

Proceedings of the Carpathian Summer School of Physics 2005

Exotic Nuclei and Nuclear/Particle Astrophysics

S Stoica • L Trache • R E Tribble
Editors

Proceedings of the Carpathian Summer School of Physics 2005

Exotic Nuclei and Nuclear/Particle Astrophysics

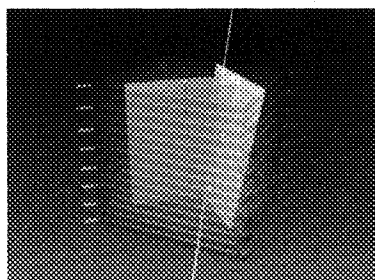
This page is intentionally left blank

Proceedings of the Carpathian Summer School of Physics 2005

Exotic Nuclei and Nuclear/Particle Astrophysics

Mamaia-Constanta, Romania

13 – 24 June 2005



S Stoica

“Horia Hulubei” National Institute for Physics & Nuclear Engineering
Bucharest, Romania

L Trache

Texas A & M University, College Station, Texas

R ETribble

Texas A & M University, College Station, Texas

 **World Scientific**

NEW JERSEY • LONDON • SINGAPORE • BEIJING • SHANGHAI • HONG KONG • TAIPEI • CHENNAI

Published by

World Scientific Publishing Co. Pte. Ltd.

5 Toh Tuck Link, Singapore 596224

USA office: 27 Warren Street, Suite 401-402, Hackensack, NJ 07601

UK office: 57 Shelton Street, Covent Garden, London WC2H 9HE

British Library Cataloguing-in-Publication Data

A catalogue record for this book is available from the British Library.

EXOTIC NUCLEI AND NUCLEAR PARTICLE ASTROPHYSICS

Proceedings of the Carpathian Summer School of Physics 2005

Copyright © 2006 by World Scientific Publishing Co. Pte. Ltd.

All rights reserved. This book, or parts thereof, may not be reproduced in any form or by any means, electronic or mechanical, including photocopying, recording or any information storage and retrieval system now known or to be invented, without written permission from the Publisher.

For photocopying of material in this volume, please pay a copying fee through the Copyright Clearance Center, Inc., 222 Rosewood Drive, Danvers, MA 01923, USA. In this case permission to photocopy is not required from the publisher.

ISBN 981-270-007-2

FOREWORD

This book contains the lectures and contributions presented at the **Carpathian Summer School of Physics 2005** (CSSP05), held in Mamaia-Constanta, Romania, June 13–24, 2005. The title of the school, *Exotic Nuclei and Nuclear/Particle Astrophysics*, is also the title of the volume. This was the 20th edition of a series which began in 1967, organized by what was then the Institute of Atomic Physics and is now “Horia Hulubei” National Institute of Physics and Nuclear Engineering (NIPNE) Bucharest, Romania. It was an event that took place, with a few exceptions, every 2 years, in the Carpathian mountain resorts of Predeal or Poiana Brasov. The latest edition was organized in 2000 in Predeal. This year the school was organized by NIPNE Bucharest in collaboration with the Cyclotron Institute, Texas A&M University in College Station, Texas and Ovidius University from Constanta. It took place under the auspices of the “World Year of Physics 2005” as part of the celebration of the WYOP in Romania and in this part of Europe. In recognition of this, it was supported by the Romanian Ministry of Education and Research and by UNESCO. The organizers decided to move the conference location to the seaside resort of Mamaia, just north of Constanta, on the Romanian shore of the Black Sea.

The lectures and contributions covered the topics announced in the school circulars: **Exotic nuclei; Exotic nuclear structures; Exotic decays; Neutrinos in Cosmos; High energy cosmic rays; Exotic Clusters and Superheavy elements; Big Bang and stellar nucleosynthesis; Experimental methods in nuclear astrophysics.**

The aim of this meeting, traditionally called a ‘school,’ but which always combined the features of a conference/workshop with that of a typical school, was to give self-consistent overviews on essential ideas, open problems and developments in these topics. We succeeded in having outstanding lecturers give up-to-date reviews on specific subjects so that students could learn about the real status of the field. The school provided a mechanism for stimulating mutual interactions between students, aspiring young scientists and well established researchers in the field. In addition, we organized a few public lectures on subjects related to the worldwide centennial celebration of Albert Einstein’s Miraculous Year. We also organized excursions and social events in order to provide school participants with a flavor of Romanian landscape and culture. We believe that the school was successful in achieving all these aims. Briefly:

- We had over 120 participants from 5 continents for the 12 day event, with 70-90 participants at any time (not everyone could stay the whole period). It was difficult to count how many countries participated, due to so many dual “affiliations”.

- We had 52 one-hour or two-hour lectures in 10 days.
- Additionally 12 communications (20 min) were presented by younger participants.
- The public lectures celebrating the World Year of Physics 2005 were excellent and we thank Lothar Buchmann, Peter Biermann, Heinigerd Rebel, Jorge Horvath and Gheorghe Stratan for their efforts. We cannot say they were a success in terms of the non-conference public attracted, but ... we tried and we'll do better next time!
- The boat trip in Danube's Delta was an occasion to see one of the Romania's natural beauties. It was taken by more than 70 people and was a wonderful surprise for all foreign participants, in terms of landscape and size, considering that we only saw 3–4% of the whole Delta. We hope that this was an occasion to see this beautiful place, a UNESCO natural preserve that belongs to all Europe and needs be protected by all of us.
- The banquet in the last evening, on June 23-rd, gave all attendants a little bit of a flavor of Romanian folklore and cuisine and was a good occasion to relax, unwind, eat, drink and dance.
- The soccer competition Romania–Rest of the World ended in a tie that needs to be resolved in future editions: the game on the beach in the first week was in favor of the international team 7-6; in the second game, on artificial grass, the Romanian team, strengthened by its international players, won 8-5!

As the title of the meeting suggests, the Organizing Committee and the International Advisory Committee intended to provide an avenue for the discussion of a common ground in the understanding of the Universe from the smallest to the largest scales, even though the emphasis was on nuclei. The study of exotic nuclei is on one end seeking answers about the structure and interactions in unique finite quantum mechanical many-body systems. On the other end, it provides data that have an impact on the understanding of the origin of the elements in the Universe. The abundance of the elements is an indelible fingerprint of the evolution of the Universe, of the large array of processes and places where nucleosynthesis took place. Many lectures were devoted to such subjects, noting their explicit or implicit ties. The school and this book offer insights on how experiments in the terrestrial nuclear physics laboratories can be combined with observations from space to enlarge our basic knowledge. This is why large experimental facilities, current or future ones, are also presented together with their research projects.

In addition, with this edition of the Carpathian Summer School, we began a series of public lectures, some of which were held in Constanta at the Ovidius University. Distinguished professors talked about “Albert Einstein, the scientist and the man” (G. Stratan, NIPNE Bucharest and Babes-Bolyai University Cluj), “The origin of elements” (L. Buchmann, TRIUMF Vancouver), “Black holes, dark matter and dark energy” (profs. P. Biermann, University of Bonn), “The

origin of high energy cosmic rays” (H. Rebel, Univ. of Karlsruhe) and “Life and death of the stars” (J. Horvath, University of Sao Paolo).

During the school, four professors also participated at the Romanian Parliament in a round table discussion with Romanian politicians and business men, on the role of the science in society and the level of its financial support, etc.

The aims of the present book are those of the conference. Immediately after the end of the school, most, if not all, of the presentations were posted on the website of the school. The full program of the school is included at the beginning of this volume. We collected manuscripts quickly for this book and we thank the authors for their very good response in providing the texts of lectures and contributions. Very few participants were not able to present their contribution here. The invited lectures form Part I of the book. The Editors organized the material in chapters following essentially the structure of the school’s sessions. However, not all sessions could be presented in well-structured chapters, and some regrouping was needed. It was done by the Editors alone. Part II contains the contributions presented. Part III contains concluding material. We included here the text of the public lecture of Peter Biermann and the notes of his intervention in the above mentioned round table organized by dr. N.V. Zamfir at the Romanian Parliament. The content of the public lecture of H. Rebel was assimilated in his lecture, in Part I. In the whole editing process, we favored speed of publication over completeness of the proceedings. Also, the texts of the lectures and contributions had to be limited in size. Readers may find it useful to consult the presentations posted on the website of the school <http://mare.tamu.edu/cssp05/> which contain typically more graphics. Pictures taken at the school are also available at the same website, for view or download.

Many thanks are due to the members of the International Advisory Committee for all their advice, valuable suggestions and recommendations for setting the program and selecting the lecturers. Members of the Organizing Committee worked hard to have the event put in place and to run it. We also thank dr. Gabriel Tabacaru (Texas A&M University) who set up and ran the website of the school. He and Mihai Horoi (Central Michigan University, Mt. Pleasant) were running the school’s computer system setup by Sabin Iacob, a young student from the University of Bucharest (who could only attend the first two days). Prof. Victor Ciupina, rector of Ovidius University Constanta, was instrumental with advice on local matters and with the support for the accommodation of a few participants. All of us would have been lost without the hard and competent work of the technical secretaries Aurora Anitoaie and Denise Cranganu and of Alexandra Olteanu, the financial officer of the school. They significantly contributed to the success of the School and we thank them. Finally, Dr. Adriana Banu (Texas A&M University) read a large part of the typescripts for this volume and helped with the editorial process.

We thank the personnel of Best Western Hotel Savoy in Mamaia, where the event took place, personnel lead by Bellamy Zahiu, for their professional, warm and discreet service during the conference and in the planning stage of it. It was a wonderful venue for a conference of this size and scope.

The school could not have taken place without the financial support of its sponsors. We thank them, in particular UNESCO-ROSTE Venice and the Romanian Ministry of Education and Research for their support. NIPNE Bucharest, the host institute, also devoted personnel and resources for the event. Without their support, the participation of young scientists would have been much reduced. Orange Romania also contributed with financial support. We also thank all the participants for making the whole event a success, without which all our efforts would have been fruitless!

Given the success of the present edition, the board of NIPNE has recently decided for the Carpathian Summer School of Physics to be a biennial event, and to put it in the list of the EPS and NUPPEC events, which means that we'll see one another in 2007! Organizers for the event are sought after.

Sabin Stoica
Livius Trache
Robert E. Tribble

Bucharest and College Station
November 2005

CONTENTS

<i>Foreword</i>	v
<i>Committee</i>	xv
<i>Pictures</i>	xvi
<i>Opening addresses</i>	xix
Part I: Invited Lectures	1
1. <i>Exotic Nuclei</i>	3
Research on neutron clusters <i>F.M. Marques</i>	5
Neutron transfer studied with a radioactive beam of ^{24}Ne , using TIARA at SPIRAL <i>W. Catford et al. for the TIARA collaboration</i>	12
Rare Isotopes INvestigations at GSI (RISING) using relativistic ion beams <i>J. Jolie et al.</i>	20
Mass formula from normal to hypernuclei <i>C. Samanta</i>	29
2. <i>Exotic Nuclear Structures</i>	37
Exotic Phenomena in Medium Mass Nuclei <i>A. Petrovici</i>	39
NUSTAR at FAIR. Nuclear structure research at GSI and the future <i>G. Muenzenberg</i>	47
From Super-Radiance to Continuum Shell Model <i>V. Zelevinski</i>	55
New methods for the exact solution of the nuclear eigenvalue problem beyond mean field approaches <i>F. Androzzi, N. Lo Iudice and A. Porrino</i>	67

Q-Phonon Approach for Low-Lying 1 ⁻ Two-Phonon States in Spherical Nuclei	75
<i>R.V. Jolos, N. Yu. Shirikova and <u>V.V. Voronov</u></i>	
Analytic description of the phase transition from octupole deformation to octupole vibrations	83
<i><u>D. Bonatsos</u>, D. Lennis, D. Petrellis, N. Minkov and P. Yotov</i>	
Three-body models in nuclear physics	91
<i>P. Descouvemont</i>	
Properties of low-lying states: Shape parameters and proton-neutron symmetry	99
<i>V. Werner</i>	
Shell model nuclear level densities	107
<i>M. Horoi</i>	
3. Exotic Decays, Clusters and Superheavy Nuclei	115
Nuclear structure and double beta decay	117
<i>J. Suhonen</i>	
Systematics of proton emission	125
<i><u>D.S. Delion</u>, R.J. Liotta and R. Wyss</i>	
Synthesis of Superheavy Elements at SHIP	133
<i><u>S. Hofmann</u> et al.</i>	
Synthesis of heaviest elements using a gas-filled recoil separator at RIKEN	144
<i>K. Morita</i>	
Fission valleys and heavy ion decay modes	152
<i><u>D.N. Poenaru</u>, R.A. Gherghescu and W. Greiner</i>	
Dynamics of mass asymmetry in dinuclear systems	160
<i>G.G. Adamian, ... <u>W. Scheid</u> et al.</i>	
4. Exotic Matter in Nuclei and Stars. Neutrinos	169
Clusters of matter and antimatter: A mechanism for cold compression	171
<i>W. Greiner</i>	

BRAHMS Experiment Quest for Early Universe Phases of Hadronic Matter <i>Z. Majka</i>	180
Strange matter in core-collapse supernova <i>J. Horvath</i>	188
Neutrino astrophysics: Gamma ray bursts <i>G.C. McLaughlin</i>	197
Neutrino emission from neutron stars <i>D.G. Yakovlev, M.E. Gusakov, A.D. Kammer and A.Y. Potekhin</i>	205
New achievements in neutrino properties <i>S. Stoica</i>	213
5. High Energy Cosmic Rays	223
The origin of cosmic rays <i>P. Biermann</i>	225
The mystery of the highest energies in the Universe <i>H. Rebel</i>	233
The cosmic ray experiment KASCADE-GRANDE <i>I.M. Brancus et al.</i>	244
Prospects for the detection of high-energy cosmic rays using radio techniques <i>Ad van den Berg</i>	253
6. Nucleosynthesis and Nuclear Physics for Astrophysics	263
Explosive nucleosynthesis: Supernovae, classical novae, and X-ray bursts <i>J. Jose</i>	265
Experimental approach to nuclear reactions of astrophysical interest involving radioactive nuclei <i>C. Angulo</i>	273
Background studies at the LUNA underground accelerator facility <i>Zs. Fulop for the LUNA collaboration</i>	281

Thoughts about two of the important reactions in nuclear astrophysics <i>L. Buchmann</i>	289
Recent experimental studies of nuclear astrophysics using intermediate-energy exotic beams <i>T. Motobayashi</i>	297
An indirect method using ANCs in nuclear astrophysics <i>R.E. Tribble et al.</i>	307
Recent applications of the Trojan-horse method in nuclear astrophysics <i>C. Spitaleri</i>	316
Nuclear astrophysics experiments at CIAE <i>Weiping Liu et al.</i>	324
Global reaction models relevant to the p process <i>S.V. Harissopoulos</i>	331
7. Large Facilities	339
TRIUMF – Canada’s national laboratory for particle and nuclear physics <i>L. Buchmann</i>	341
Status of the AGATA project <i>E. Farnea on the behalf of the AGATA collaboration</i>	349
Research at ISOLDE and the path to Eurisol <i>P.A. Butler</i>	357
Part II: Communications	365
Various types of measurements for atmospheric muons performed with the WILLI detector <i>A. Bercuci, B. Mitrica, M. Petcu, I.M. Brancus, G. Toma and M. Duma</i>	367
Few-valence-particle (hole) excitations around doubly magic nucleus ^{132}Sn <i>E. Dragulescu and D. Trancota</i>	372
Possible E(5/4) symmetry in ^{135}Ba <i>M. Fetea, R.B. Cakirli, R.F. Casten and D.D. Warner</i>	377

Cold fusion channels of $^{290}_{114}$ <i>R.A. Gherghescu</i>	382
Precise half-life measurement of ^{34}Ar , a superallowed β^+ emitter <i>V.E. Jacob, J.C. Hardy, C.A. Gagliardi, V.E. Mayes, N. Nica, G. Tabacaru, L. Trache and R.E. Tribble</i>	387
Quantum deformation of open systems <i>A. Isar and W. Scheid</i>	393
Single-particle effects in threshold fission cross section <i>M. Mirea</i>	399
Experimental and theoretical status of Borromean halo nuclei structure investigation <i>M. Petrascu</i>	405
Z(4): γ -rigid solution of the Bohr Hamiltonian for $\gamma=30^\circ$ compared to the E(5) critical point symmetry <i>D. Bonatsos, D. Lenis, D. Petrellis, P.A. Terziev, I. Yigitoglu</i>	411
Isospin distillation from a microcanonical perspective <i>Ad.R. Raduta</i>	416
Alpha half-life estimates for the superheavy elements with Z=110-116 <i>I. Silisteanu</i>	423
Part III: Conclusions	429
Public lecture: Dark energy – dark matter – and black holes: The music of the Universe <i>P.L. Biermann</i>	431
Concluding remarks. About the experimental appeal of CSSP05 <i>H. Rebel</i>	439
Towards technology in society and business through science and education <i>P.L. Biermann</i>	463
<i>List of participants</i>	467
<i>Program</i>	479

This page is intentionally left blank

Organized by

“Horia Hulubei” National Institute for Physics and Nuclear Engineering, Bucharest
Cyclotron Institute, Texas A&M University, College Station TX
Ovidius University, Constanta

Sponsored by

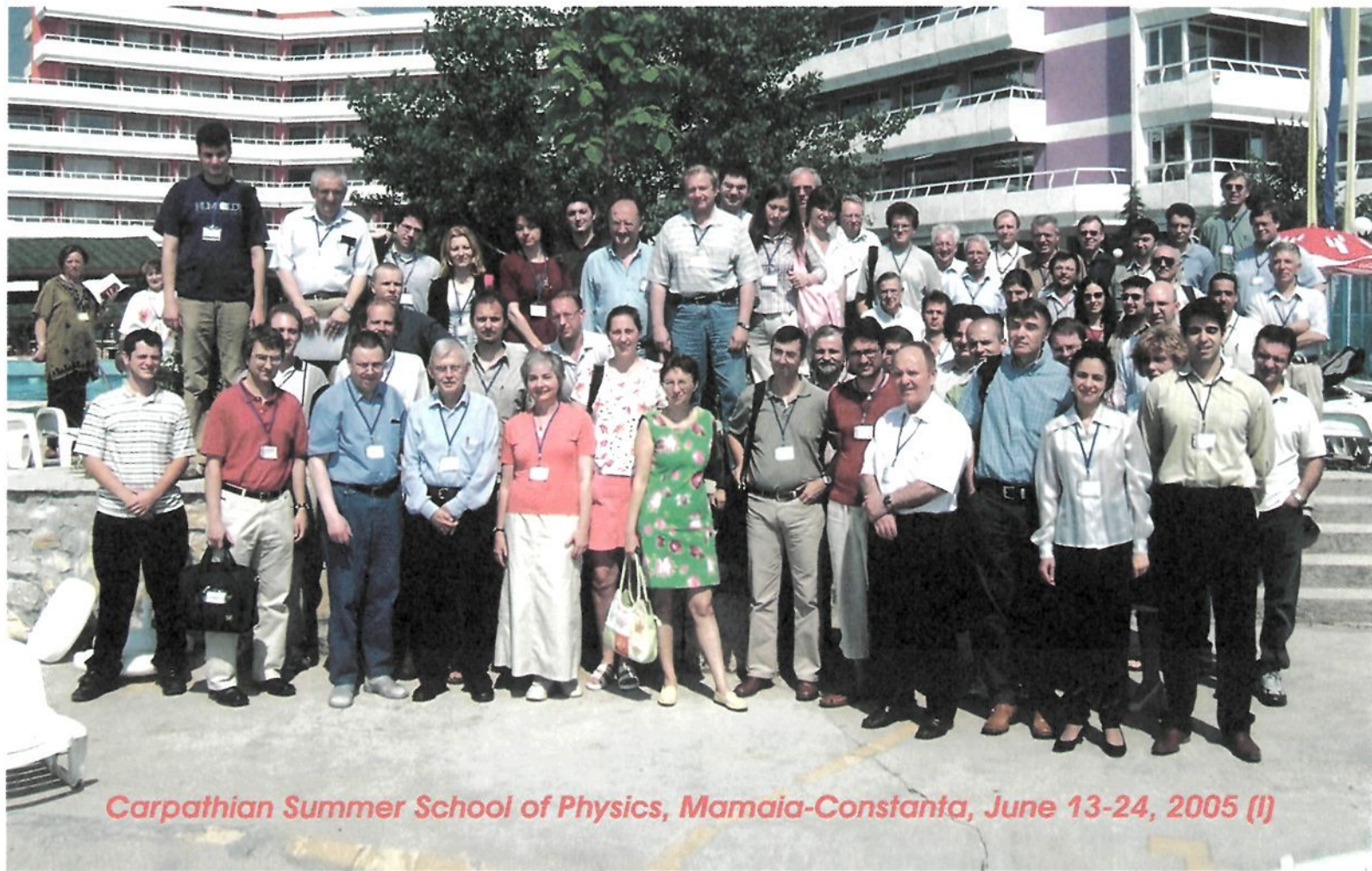
UNESCO-R.O.S.T.E., Venice, Italy
Romanian Ministry of Education and Research
Orange, Romania

International Advisory Committee:

P. Biermann (Bonn)
P. von Brentano (Cologne)
R. Casten (Yale)
W. Greiner (Frankfurt)
M. Harakeh (Groningen)
W. Haxton (Seattle)
P. Langacker (Philadelphia)
A.C. Mueller (Orsay)
Y.T. Oganessian (Dubna)
H. Rebel (Karlsruhe)
W. Scheid (Giessen)
J. Vary (Ames)
V. Voronov (Dubna)
N.V. Zamfir (Bucharest)

Organizing Committee:

S. Stoica (Bucharest) – co-chair
R.E. Tribble (Texas A&M) – co-chair
L. Trache (Texas A&M) – scientific
secretary
F. Carstoiu (Bucharest)
V. Ciupina (Constanta)
M. Horoi (Mt. Pleasant)
G. Tabacaru (Texas A&M) –
webmaster



Carpathian Summer School of Physics, Mamaia-Constanta, June 13-24, 2005 (I)



Carpathian Summer School of Physics, Mamaia-Constanta, June 13-24 2005 (II)

This page is intentionally left blank

ADDRESSES AT THE OPENING SESSION

June 13th, 2005

**The address of Dr. Nicolae Victor Zamfir
General Director, NIPNE Bucharest**

It's a great pleasure for me to welcome all of you here to this international summer school in nuclear physics. This seems to be the 20th such school, though it depends on whom you ask. The confusion comes from some uncertainty on what we consider 'international' to mean. I'm told that at the first such school there was only one foreigner, a Russian participant, as it happened. So, I wonder, can we consider it was 'international'?

Further confusion stems from the fact that after a bunch of enthusiastic nuclear physicists organized the first edition of this summer school in 1967 – Aretin Corciovei was leader of the group – many other branches of physics, mathematical physics and others, started to organize such schools, and they, too, had some connection with nuclear physics. Should they be counted as part of this series? Anyway, the consensus is that this is the 20th edition of the Romanian international school in nuclear physics.

The school has naturally evolved in terms of subjects and participants over these almost 40 years. We began with the subject of nuclear angular momenta, coefficients of fractional parentages, Clebsch-Gordon and Wigner coefficients and so on. Now, you can see what our current subjects are, which, by the way, are not so basic. In fact, they are very hot subjects in these days.

Much of these 40 years were a very tough period both for the school and for the profession of nuclear physicist in general. We survived. The school survived sometimes thanks to a very strong German support and also due to the direct involvement of Valentin Ceausescu who helped us keep the school alive (*correcting partially, for short periods and only for some, the great deal of pain and frustrations his family inflicted upon the whole nation in general and upon science in particular in the late seventies and in the eighties! – Editor's note*).

Since the political changes in the 1990s, things have become more normal. International connections have grown much better. The distribution of the participants has changed. As you can see, there now are more foreign participants than Romanian ones.

I don't know what the future will be, but we certainly hope to continue this tradition in international Romanian summer schools. Actually, these Romanian schools are a little bit different from traditional summer schools in other places, because the number of students here is not so high. You can see that there are many speakers, and the talks are very detailed. In fact, here we learn very much from one another. From this point of view, our summer school is special.

Besides, this particular summer school is special, because after a series of schools we organized in collaboration with German physicists, this is the first time the school is organized together with an American university. Maybe it is not just a coincidence that Texas A&M is sometimes called here "IFIN-West," because many physicists from IFIN-HH are working there. So, we have wonderful friends there.

I would also like to take this opportunity to thank the prefect of Constanta for participating in our ceremony. We are indeed trying to start a policy of making physics more closely connected with the public, industry, the political level, and making the public more aware of what we can do. It is not as though we sit on some Mount Olympus. We have to integrate into society. Thus, we have to integrate with the community of basic research, so that we might be part of the international exchange of ideas, but we must also become more useful to the rest of society.

In this respect, next week we will have a big meeting at the Romanian Parliament, organized by the Parliament and IFIN-HH. Andrei Dorobantu is the promoter of this. We will try to bring together politicians, both members of the Senate and Chamber of Deputies, physicists, and representatives of industry, exactly with this goal in mind of heightening the profile of physics research amid the public.

I'd like to conclude by saying that I'm sure we have set off at a good start. Even the weather is good; conditions are good; the organizing job seems very good. So, I hope we will have a very good summer school – two weeks of a very useful exchange of ideas.

Thank you very much.

Nicolae-Victor Zamfir

**The address of Honorable Dan Culetu
Prefect of the County of Constanta**

Ladies and Gentlemen,

Let me first wish you a warm welcome here, in Constanta!

I hope you will benefit not only from this conference, but also from the very nice area, a very nice weather and the warm people that are living here in Constanta. We have a good relation with the university and we are very proud that this conference is taking place here in Mamaia. We have here in our county the first nuclear power plant built in Romania and we have probably to benefit to prepare scientists for this very important enterprise, which was built with international cooperation to begin with. I also hope that you will spend a very nice time here in Mamaia with its beaches, hotels, restaurants and bars, but you'll also take time to visit the surrounding area with its natural attractions, like Danube's Delta, Murfatlar winery and the archeological sites for which whole of Dobrogea is famous. I'm not a physicist, but my best friend is physicist and we always argue because he always come with arguments.

Well, this is all for me, once again I wish you success and have a nice time in Constanta.

Thank you very much!

**The address of Dr. Livius Trache
Texas A&M University
Scientific secretary of CSSP05**

Dear Colleagues,
Guests and hosts,
Current and future friends,

Howdy! Welcome y'all to the 2005 edition of the Carpathian Summer School of Physics!

Dr. Sabin Stoica, the chair of this session and co-chair of the school, welcomed you in his opening address. The other chair of the school, prof. Robert Tribble, could not be here today, he will only arrive Thursday evening. Unfortunately he had to stay behind and go first to Washington, DC, to attend an important function related to our fight with the continuous shrinking of the US budget for science, and particularly for nuclear physics. He charged me to welcome you on his behalf, which I do now, adding my own welcome. As scientific secretary of the school, I'll be more the face and voice of the Organizing Committee and you will hear more technical details from me at the end of this welcome, please bear with me for a few words before that!

I am very glad to see you here! This is the beginning of the school, but is, in a way, the end, or the beginning of the end, of a long road for the organizers. An end that we are glad we meet with a first sign of success, that of your very presence here! We can tell you that more than 50 lecturers and a total of over 120 participants accepted the invitation to come, and are here or will arrive at some point during these two weeks. With Wilton Catford, who just told you in his short address on behalf of the participants that he's an Australian, and with the Brazilian who will arrive at the end of the week, we'll have here scientists gathered from 5 continents. And from a large number of countries which we did not even attempt to count due to the difficulties created by the double affiliations so common in modern science. We consider this presence a success and we thank you for making it possible.

I have to add my thanks to the sponsors, foremost UNESCO and MEC. Without their contribution the school itself and the participation of young scientists in particular, would be a lot weaker, if at all possible. I want to thank also, on the behalf of the organizers and on your behalf, the Honorable Mr. Dan Culetu, the Prefect of the Constanta county, the highest ranking government official in the territory, for taking time from his busy schedule to attend this brief ceremony and for his address.

Dr. Zamfir, the director of NIPNE, made in his address a short history of this school, reminding us all that this is a well established tradition, with this being,

give or take a few units, we are not sure, the 20th edition. However, there are a number of 'firsts' in this edition.

The first "first" is that it is organized for the first time on the Black Sea coast, here in Mamaia, not in the Carpathian resorts of Predeal or Poiana Brasov. The Organizing Committee is pleased with the choice, with our experience so far, and hopes that you'll all appreciate the conditions offered by the "Best Western Savoy Hotel", from the cozy atmosphere of this conference hall, next to the pool and with the beach and sea in the view, to the comfort of your rooms with beautiful sea view and the warmth and professionalism of the service and personnel. Secondly, this school is for the first time organized by a joint Romanian-American committee. We had in the past editions of the school with large contributions from our colleagues from Western Europe, in particular our German colleagues, and we had Americans present in past schools, but never involved in the organization. This time you received most of the correspondence from US, and I want to personally thank you here that you gave us the benefit of the doubt and, while receiving emails from the domain @tamu.edu trying to sell you a physics school in Romania, you did not reject our emails, mine and dr. Tribble's, as spam or such, and trusted us! Thirdly, this is the first school where we asked the lecturers to support their stay, we were nervous about what kind of response we shall get, thank you for your positive answer to that. Fourth, we are adding to the school's traditional lectures and oral contributions, a number of public lectures, which we intend to address the larger public, and be part of the celebration of the "World Year of Physics 2005". We shall have to wait and see how successful these will be. They are planned to take place at the Ovidius University, in Constanta. Prof. Victor Ciupina, Rector of the University, kindly agreed to be part of our Organizing Committee, and helped us on several local issues. I thank him for that! In his address, a few minutes ago, he told you a few facts about Ovidius University, the largest public university in the area, about his personal efforts (he is a physicist) on improving physics high education in Constanta, in particular nuclear physics, related to the proximity of the nuclear power plant in Cernavoda. And he said a few proud words about the city and the region around, about the name of the university. This encourages me to say a few words of my own on this subject.

Mamaia is a a young, 20th century sea side resort, situated just north of the city of Constanta, the largest harbor on this coast. Constanta is, arguably, the oldest city continuously inhabited in Romania. As other cities around, it was founded in the VII-th century BC by Greek colonists, named Tomis, and played a role in the contacts of the locals with the Aegean civilizations. It had periods of glory and development (that you can learn about visiting the rich history and art museums and ruins in its downtown; I encourage you to do that) and periods of decadency that ended at the end of XIX-th century when it became Romania's gate to the seas. Currently it hosts around 400,000 people. Ovidius is very much

a symbol for this city, you will see many places and things named after him: the central plaza in downtown, an island, restaurants, parks, tourism agencies, you name it, ... even the university. Indeed Publius Ovidius Naso, the Latin poet, was exiled here by Emperor Augustus, and died here. He wrote here, he learned the local language to participate in poetry contests (strange habits of the barbarians?!) with the son of the local king, but the truth is he never liked the place! He always complained is too cold and asked for clemency to go back home. His "Ponticae" are known as "Tristia" (Sad letters from Pont). I want, therefore, to challenge the locals with the name of an important son of these places, whose name also deserves our recognition, particularly because affects our lives every day. Let me try to make it simple! Today is **June 13th, 2005**. We due "**June**" to Julius Caesar of I century B.C., **13th** to pope Gregory XIII (of XVI c. AD). **2005** is due to Dionysius Exiguus (Dennis le Petit in French, Dennis the Small in English). He was born in one of the villages around here, completed his high education in the metropolitan schools of Tomis and went the same road as Ovidius, but in the opposite direction. Went to work for the patriarch in Constantinople, then to Rome, working under ten popes, to become one of the leading scholars of his century in Europe (and later sanctified). He proposed a unified system of chronology, starting from the birth of the founder of Christianity. Made a careful study of all existing facts and literature, made a timeline, and announced "this is the year 525"! The system was gradually adopted and, actually, A.D. initially meant "*Anno Dionysii*", before becoming the universal "*Anno Domini*". We know now that he was wrong by 4-6 years (that is 1% error, compare that with our typical error bars!), but I wanted to tell you the story, as many of you may not have known it. Therefore, Mr. Prefect and Mr. Rector, I want to say that I would see a "Dionysius University" in Constanta! But then, if it is Dionysius University, why in Constanta and not in Murfatlar*?!

Thank you for your attention! Enjoy your stay!

Livius Trache

*Murfatlar is one of the most prestigious wineries in Romania, nearby, in the same county (Editor's note).

Part I
Invited Lectures

This page is intentionally left blank

1. Exotic Nuclei

This page is intentionally left blank

RESEARCH ON NEUTRON CLUSTERS

F. MIGUEL MARQUÉS*

*Laboratoire de Physique Corpusculaire,
IN2P3-CNRS, ENSICAEN et Université de Caen,
F-14050 Caen cedex, France
E-mail: marques@lpccaen.in2p3.fr*

A new approach to the production and detection of multineutrons, based on breakup reactions of beams of very neutron-rich nuclei, is presented. The first application of this technique to the breakup of ^{14}Be into ^{10}Be and $4n$ revealed 6 events consistent with the formation of a bound tetra-neutron. The description of these data by means of an unbound tetra-neutron resonance is also discussed. The experiments that have been undertaken at GANIL in order to confirm this observation with $^{12,14}\text{Be}$ and ^8He beams are presented. Special attention is paid to the angular correlations of some candidate events observed in the channel ($^8\text{He}, ^4\text{He}$).

1. Neutral nuclei

Stable systems formed by few nucleons, such as ^3H and $^3,^4\text{He}$, have long played a fundamental role in testing nuclear models and the underlying N-N interaction. Their ground states, however, do not appear to be particularly sensitive to the form of the interaction. New perspectives should be provided by light nuclei exhibiting very asymmetric N/Z ratios. For example, among the $N = 4$ isotones one finds the two-neutron halo structure around the α particle in ^6He , or the ground state of ^5H observed as a relatively narrow, low-lying resonance. Concerning the lightest isotone, 4n , nothing is known.

The existence of neutral nuclei has been a long standing question in nuclear physics. Over the last forty years very different techniques have been employed in various laboratories for the search of multineutrons, mainly $^3,^4n$, without success¹. All the techniques consisted of two stages, the formation and the detection of the multineutron, and the negative results were always interpreted as due to the extremely low cross-section of the reaction

*For the DEMON-CHARISSA collaborations.

used to form the multineutron. Theoretically, *ab initio* calculations² suggest that neutral nuclei are unbound. However, the uncertainties in many-body forces, the already relatively poor knowledge of the two-body n - n interaction, and in general the lack of predictive power of these calculations, do not exclude the possible existence of a very weakly bound ${}^4\text{n}$.

2. Neutron stars

One could argue that multineutrons, bound systems of neutrons, already exist: neutron stars. They are, however, at a very different size scale and held together by gravity. Is there any straightforward link between the possible existence of multineutrons at the nuclear scale and the characteristics of neutron stars?

The possible existence of multineutrons would not have any implication in the core composition, not even in the whole interior as at densities beyond ρ_0 nuclei dissolve —also neutral nuclei would. They could only appear in the inner crust, in which ${}^{56}\text{Fe}$ coexists with very neutron-rich nuclei and free neutrons, but this is a very small part of the star and any effect would be far beyond the present experimental capabilities.

On the other hand, attempts are being made in order to link the properties of neutron stars with those of the most neutron-rich stable nucleus, ${}^{208}\text{Pb}$. Theoretical models explore in this way the N - N interaction for $N > Z$. In that sense, multineutrons could provide a very important input, as their possible existence would constraint strongly the N - N interaction in an almost proton-free environment like the one found in neutron stars.

3. A new approach

We have recently proposed a new approach to the production and detection of multineutron clusters¹. The technique is based on the breakup of energetic beams of very neutron-rich nuclei and the subsequent detection of the liberated multineutron cluster in liquid scintillator modules. The detection in the scintillator is accomplished via the measurement of the energy of the recoiling proton (E_p). This is then compared with the energy derived from the flight time (E_n), possible multineutron events being associated with values of $E_p > E_n$.

In light neutron-rich nuclei, components of the wave function in which the neutrons present a cluster-like configuration may be expected to appear. Owing to pairing and the confining effects of any underlying α -clustering on the protons, the most promising candidates may be the

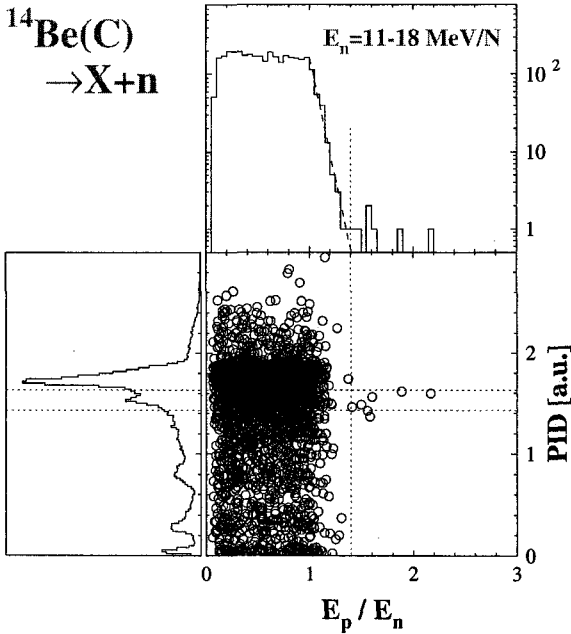


Figure 1. Scatter plot, and the projections onto both axes, of the particle identification parameter versus E_p/E_n for the data from the reaction $\text{C}(^{14}\text{Be}, \text{X} + \text{n})$. The PID has been projected for all neutron energies. The dotted lines correspond to $E_p/E_n = 1.4$ and to the region centred on the ^{10}Be peak¹.

drip-line isotopes of Helium and Beryllium, ^8He ($S_{4n} = 3.1 \text{ MeV}$) and ^{14}Be ($S_{4n} = 5.0 \text{ MeV}$). As breakup reactions present relatively high cross-sections (typically $\sim 100 \text{ mb}$), even only a small component of the wave function corresponding to a multineutron cluster could result in a measurable yield with a moderate secondary beam intensity. Furthermore, the different backgrounds encountered in previous experiments are obviated in direct breakup.

The method has been applied to data from the breakup of ^{11}Li , ^{14}Be and ^{15}B beams. In the case of ^{14}Be , some 6 events have been observed with characteristics consistent with the production and detection of a multi-neutron cluster, most probably in the channel $^{10}\text{Be} + ^4\text{n}$ (Fig. 1). Special care was taken to estimate the effects of pileup; that is the detection for a breakup event of more than one neutron in the same module. Three independent approaches were applied and it was concluded that at most pileup may account for some 10% of the observed signal. The most proba-

ble scenario was concluded to be the formation of a bound tetra-neutron in coincidence with $^{10}\text{Be}^1$.

4. Bound or resonant state?

Following the publication of our paper¹, many theoretical papers have investigated the conditions needed for the binding of a four neutron system². The overall conclusion is that the present knowledge on the n - n interaction and the physics of few-body systems do not predict a bound ^4n . Interestingly, however, the calculations of Pieper suggested that it may be possible for the tetra-neutron to exist as a relatively low-energy, broad resonance.

Two scenarios were confronted¹ in order to explain the events observed: the scattering of a bound ^4n on a proton, and the detection of several neutrons in the same module (pileup). The hypothesis of a bound ^4n was found to be consistent with the experimental observations, while the estimates of pileup obtained, mainly through Monte-Carlo simulations, were one order of magnitude too low.

If the four neutrons, however, form a resonance at low energy, the decay in flight will lead to four neutrons with very low relative momentum, and one could expect that the probability of some of them to enter the same module may increase. The simulations presented¹ have therefore been modified in order to include the decay of a ^4n resonance³.

The results of the simulations show the expected increase of the pileup probability towards low resonance energies. For a given resonance energy, the results do not depend much on the width. A significant increase of the pileup probability appears below $E = 2$ MeV, the resonance energy suggested by Pieper². A resonance below 2 MeV may, therefore, be consistent with the events observed¹. We note that preliminary results of an experiment measuring the α transfer in the reaction $^8\text{He}(d, ^6\text{Li})4n$ suggest a resonant structure about 2 MeV above threshold⁴.

5. New experiments and results

The confirmation of the multineutron candidate events observed with a higher intensity ^{14}Be beam and an improved charged particle identification system, and the search for similar events in the breakup of ^8He , were proposed at GANIL. Even if the intensity and quality of the ^8He beam, delivered by SPIRAL, should be much higher, structural effects may well lead to a stronger ^4n component in ^{14}Be g.s. than, say, in ^8He . For example, the configuration of the neutrons in a ^4n system, $(1s)^2(1p)^2$, is closer to that of

the valence neutrons in ^{14}Be than to those in ^8He . Therefore, if no events were observed during the ^8He run the question whether the tetra-neutron exists would remain open.

Unfortunately, several problems concerning the cyclotron lead to null results after two different attempts with ^{14}Be beams, in 2001 and 2002. An analysis of the channel ($^{14}\text{Be}, ^8\text{Be}$), planned in order to search in parallel for the existence of the hexa-neutron, could not be performed either. The reanalysis of data from a previous experiment on the breakup of ^{12}Be , specially the ($^{12}\text{Be}, ^8\text{Be}$) channel, was also undertaken⁶. No clear evidence of such events appeared.

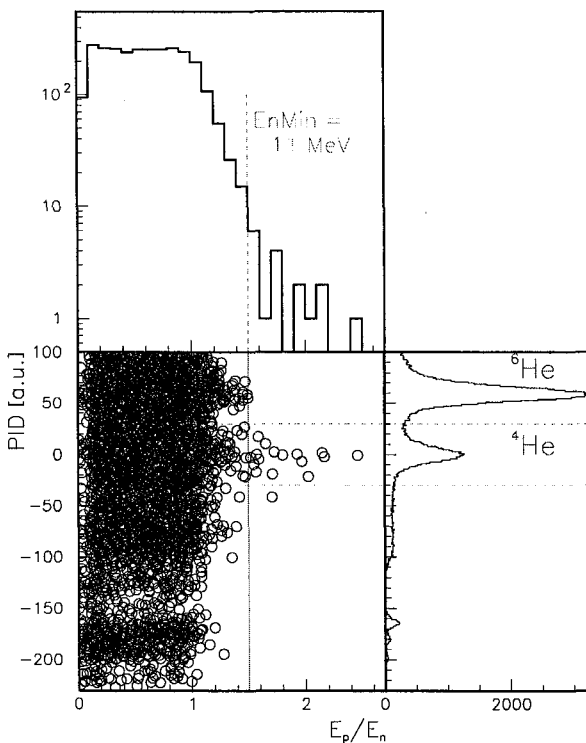


Figure 2. Same as in figure 1 for the data from the reaction $\text{C}(^8\text{He}, \text{X}+n)$. The PID has been projected for all neutron energies. The dotted lines correspond to $E_p/E_n = 1.4$ and to the region centred on the ^4He peak⁵.

On the other hand, some data were acquired with a high intensity ^8He

beam from SPIRAL. Preliminary results⁵ exhibit the same kind of signal observed previously¹, an abnormal number of high-energy proton recoils in the $-4n$ channel with respect to all other channels (Fig. 2).

6. Angular correlations and 4n resonances

Due to the (relatively) higher statistics and to the lower beam energy (13 MeV/N compared to the 35 MeV/N of the ^{14}Be beam), the analysis of the relative angle between the ^4He fragment and the neutron in the projectile frame becomes feasible. This analysis was already introduced in the ^{14}Be data¹, but was not developed in detail due to the energy constraints.

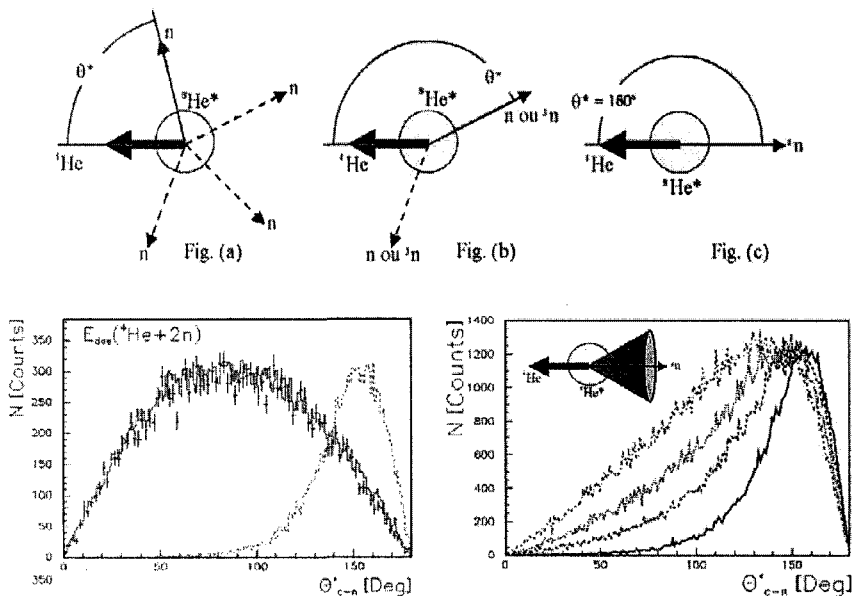


Figure 3. Angular correlations between the α particle and the neutron in the ^8He reference frame (θ_{cn}^*)⁵. On the upper row, the 5, 3 and 2 body phase-space scenarios. On the lower-left panel, all the data (points), the 5 body phase-space simulation (solid line) and the 4n bound state scenario (dotted line). On the lower-right panel, the 4n resonant state simulations from 0.1 MeV to 2 MeV (from right to left).

The results of the simulations are presented in Fig. 3. The 5 body phase-space simulation describes very accurately the whole data. But most importantly, the bound and resonant states lead to significantly different correlation patterns, being in the resonant case different for each of the

resonance energies.

This parameter is therefore sensitive to the nature of the tetraneutron state, and, in the case of the resonance hypothesis, to its energy. The 14 events observed on Fig. 2 lie in the region between 60 and 160 degrees⁵, and seem in principle closer to the low-energy resonant state hypothesis, but the analysis is still in progress.

7. Conclusion

After four decades of experimental search for multineutrons, or neutral nuclei, the new approach described here has led to the first observation of events that can, at present, be only explained through the existence of a $4n$ state. This state could be a very weakly bound (neutral) nuclei¹, or a broad low-energy resonance³. Following the most complete calculations to date², the most likely scenario should be the latter.

Among the different attempts at confirmation, only the one using an intense ^8He beam from SPIRAL was successful. The preliminary results, and the analyses in progress, seem to confirm the existence of the 4n state⁵. A new experiment aiming to study the ($^{14}\text{Be}^*$, $^{10}\text{Be}+^4n$) channel using one proton knock-out from a more intense ^{15}B beam will be undertaken at GANIL in 2005.

References

1. F.M. Marqués *et al.*, Phys. Rev. C **65**, 044006 (2002).
2. S.C. Pieper, ENAM'04 proceedings, to be published.
3. F.M. Marqués *et al.*, submitted to Phys. Rev. C.
4. D. Beaumel, private communication.
5. V. Bouchat *et al.*, in preparation.
6. G. Normand *et al.*, in preparation.

NEUTRON TRANSFER STUDIED WITH A RADIOACTIVE BEAM OF ^{24}Ne , USING TIARA AT SPIRAL

W. N. CATFORD¹, C. N. TIMIS¹, R. C. LEMMON², M. LABICHE³, N. A. ORR⁴, L. CABALLERO⁵, R. CHAPMAN³, M. CHARTIER⁶, M. REJMUND⁷,
H. SAVAJOLS⁷ AND THE TIARA COLLABORATION

¹*Department of Physics, University of Surrey, Guildford, Surrey GU2 7XH, UK*

²*CCLRC Daresbury Laboratory, Daresbury, Warrington WA4 4AD, UK*

³*University of Paisley, Paisley, Scotland PA1 2BE, UK*

⁴*LPC, IN2P3-CNRS, ISMRA and Université de Caen, F-14050 Caen, France*

⁵*IFC, CSIC-Universidad de Valencia, E-46071 Valencia, Spain*

⁶*Department of Physics, The University of Liverpool, Liverpool L69 7ZE, UK*

⁷*GANIL, BP 55027, 14076 Caen Cedex 5, France*

E-mail: W.Catford@surrey.ac.uk

A general experimental technique for high resolution studies of nucleon transfer reactions using radioactive beams is briefly described, together with the first new physics results that have been obtained with the new TIARA array. These first results from TIARA are for the reaction $^{24}\text{Ne}(d,p)^{25}\text{Ne}$, studied in inverse kinematics with a pure radioactive beam of 10^5 pps from the SPIRAL facility at GANIL. The reaction probes the energies of neutron orbitals relevant to very neutron rich nuclei in this mass region and the results highlight the emergence of the N=16 magic number for neutrons and the associated disappearance of the N=20 neutron magic number for the very neutron rich neon isotopes.

1. Introduction

A great hope for the future in radioactive beam experiments is to be able to map out the changing shell structure for very exotic nuclei, away from stability, where this arises from effects such as the monopole migration of orbital energies and the changes brought about by alterations in the surface environment and spin-orbit splitting¹. Nucleon transfer reactions such as (d,p), (p,d) etc. are an established means of populating and studying nuclear levels that have a substantial single-particle structure. The development of techniques to use such reactions with radioactive beams, across a wide range of beam energies and masses and with high energy resolution, will open the way to exploit transfer across new regions of the nuclear chart

and hence to study the new nuclear structure effects that evolve.

The technique that is described here, and implemented via the new TIARA array used in association with the VAMOS spectrometer and the EXOGAM gamma-ray array, is designed to achieve excitation energy resolution of better than 20-40 keV in the final nucleus. This is an order of magnitude better than can be achieved in a reasonable experimental setup that uses charged-particle observations only². The complete kinematical detection of the binary transfer reaction products specifies the reaction channel cleanly, where the identification of the heavy (beam-like) particle at least in Z is required, and the light (target-like)-particle detection allows angular distributions to be measured for any mass of projectile.

The present paper updates and extends results of the analysis in progress, reported elsewhere^{3,4}.

2. The TIARA Array

The requirement to use inverse kinematics in order to study nucleon transfer reactions, induced on radioactive species by protons and deuterons, imposes certain rather general requirements on the detection system to be used. The kinematics turns out to lead to particular reactions always appearing in the same characteristic range of laboratory angles and with similar energies, regardless of the mass or velocity of the incident beam^{5,4}. This allows a general purpose transfer apparatus to be designed.

The design philosophy and detailed description of TIARA has been discussed elsewhere^{3,6} but, briefly, the aim was to surround the target with a charged particle array that approached 4π coverage, with reasonable energy measurement and an angular resolution of 1 or 2 degrees. This array needed to be very compact so that a high gamma-ray efficiency of $>15\%$ (at 1.3 MeV) could be achieved, whilst avoiding the exposure of gamma-ray detectors to decay radiation from beam particles scattered in the forward 40° . In the present setup, the TIARA array covers 82% of 4π with active silicon and the gamma-ray detectors are in a close cube geometry and thus subtend 67% of 4π . The setup is mounted in front of a magnetic spectrometer which is used to separate physically the direct beam and the transfer reaction products, after the target. The region around the target is shown in Fig. 1.

3. Experimental Details

The TIARA system was set up in front of the VAMOS spectrometer at GANIL⁷, which was operated in dispersive mode at zero degrees. Direct

beam was intercepted just in front of the focal plane detectors. The support frame and four detectors of EXOGAM⁸ surrounded the TIARA chamber. All events in which a particle was detected in TIARA were recorded. The



Figure 1. The four EXOGAM detectors, in a compact cube geometry, are shown mounted around the TIARA vacuum vessel, which is symmetric (both cylindrically and forward-backward around the target) and narrows down to just 98mm in diameter near the target. The TIARA array is inside, and the beam enters through a target selection mechanism, also located inside the vessel at the lower right.

gamma ray parameters were recorded via the VAMOS acquisition system and events were correlated with TIARA in real time via an event stamping method developed at GANIL.

An isotopically pure beam of ^{24}Ne was supplied at 10 MeV/nucleon after reacceleration in the CIME cyclotron connected to the SPIRAL facility at GANIL. The beam intensity of 10^5 pps was a factor of two lower than the maximum due to a limitation placed on the emittance, which limited the beam spot on target to a diameter of approximately 2mm base width. The target was 1 mg/cm^2 of CD_2 self supporting on a thin 25mm diameter frame.

A test experiment was performed with a stable beam of ^{14}N at similar intensity and beam quality, in order to verify that normal kinematics (d,p)

results from the literature could be reproduced with the TIARA setup. Good agreement was found⁹.

4. Results

The isotopic identification for beam-like particles recorded at the focal plane of VAMOS is shown in Fig.2. This is derived from measured ΔE , E and time-of-flight parameters plus a ray tracing calculation that used the horizontal and vertical angles and positions measured at the focal plane. The ray tracing algorithm employed a neural network that was trained using a set of theoretically calculated rays obtained by numerical integration of their trajectories through VAMOS¹⁰ and this gives results identical to an algebraic algorithm developed at GANIL.

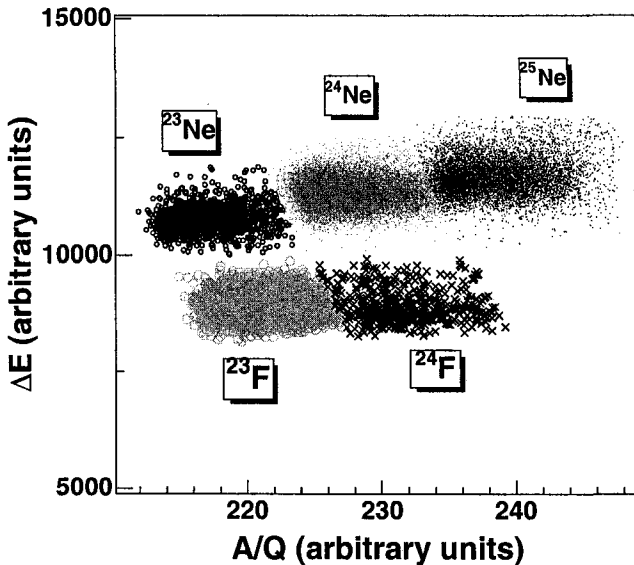


Figure 2. Particle identification for particles recorded behind the beam stop at the focal plane of VAMOS.

By selecting the ^{24}Ne ions in Fig.2, the scattered deuterons recorded in TIARA could be analysed. The ^{24}Ne momentum changes sufficiently

quickly with scattering angle that very forward scattered elastics can still avoid the beam stop. The energy of the deuterons changes rapidly with their angle⁵ and, by using energy cuts, the elastic angular distribution could be extracted (see Fig.3). A good fit was obtained using the optical potential measured for $d+^{26}\text{Mg}$ at a similar energy¹¹. The normalization obtained using these elastic data allowed absolute transfer cross sections to be extracted with confidence. From the measured energy and angle recorded for

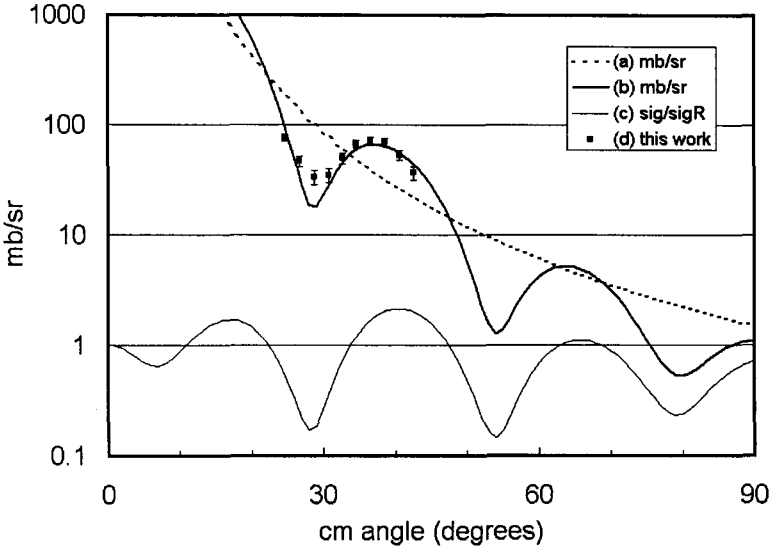


Figure 3. Angular distribution for $d + ^{24}\text{Ne}$ elastic scattering: (a) Rutherford formula, (b) optical model calculation (see text), (c) ratio of (b) to (a), and (d) present measurements.

protons from the (d,p) reaction to make ^{25}Ne (cf. Ref.3) the excitation energy spectrum for states in ^{25}Ne could be deduced. Different peaks in this spectrum could be used to gate the spectrum of associated gamma rays. Example data are included in Fig.4. An important result of this analysis was that the excitation energies of the populated states could be fixed with an accuracy of order 30 keV. The limiting factor in this accuracy was the poor statistics of the gamma ray spectrum. This was in fact severely compromised in the present experiment by an intermittent fault in an electronic discriminator unit, and the eventual aim in this type of experiment will be to use individual gamma ray peaks to apply gates in the analysis. In

the present case, however, it was still of vital importance that the gamma ray data could fix the energies and the number of peaks to be fitted to the (poorer resolution) excitation energy spectra derived from the particle energies. These fits are shown in the inset of Fig.4. The data are just sufficient to allow limited gamma-gamma coincidence analysis. In the case of the state near 4 MeV it can be seen that the 1.7 MeV and 2.4 MeV gamma rays seen in its decay [Fig.4(b)] appear to be in coincidence [Figs.4 (c) and (d)]. The excitation energy spectrum (derived from the proton energy and

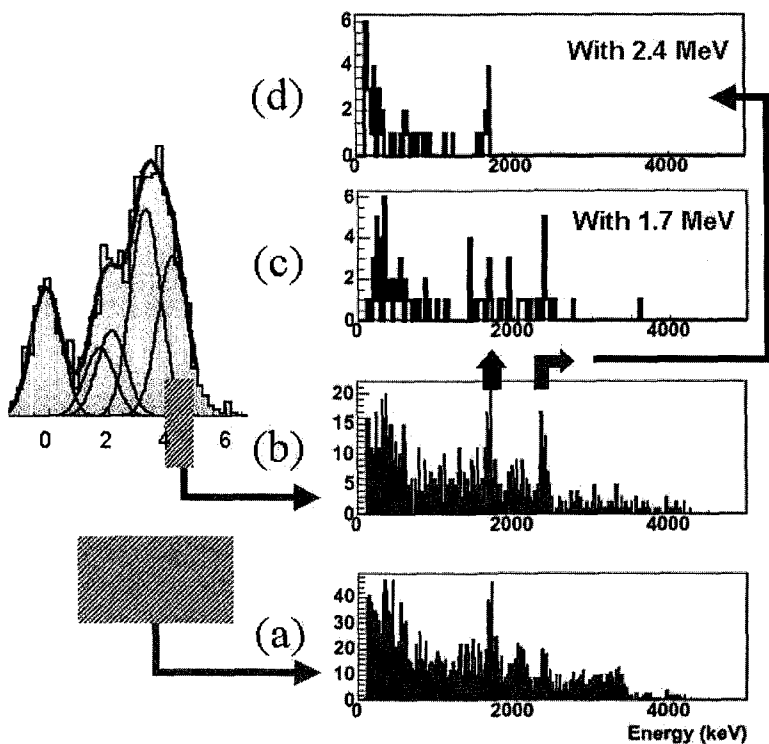


Figure 4. Gamma ray energy spectra from $d(^{24}\text{Ne}, p\gamma)^{25}\text{Ne}$ gated according to the excitation energy spectrum derived from the proton energy and angle (shown in inset): (a) all excited states, (b) peak near 4 MeV, (c) as for (b) but also requiring a coincident 1.7 MeV gamma ray, (d) as for (b) but requiring a 2.4 MeV gamma ray.

angle) was fitted with 5 peaks. The widths of these peaks depended on the experimental resolution of the system, and this was in turn dependent on the detection angle of the proton. Thus, the data were binned for angular

regions chosen to be 8° wide in order to give sufficient statistics for fitting. In order to fit the angular distributions, different optical model potentials were investigated, taken from (d,p) reactions on neighbouring nuclei $^{26}\text{Mg}^{11}$ and $^{22}\text{Ne}^{12}$. A systematic comparison with adiabatic calculations according to the prescription of Johnson and Soper¹³ was also performed. The adiabatic analysis was adopted for the extraction of spectroscopic factors, which were determined by normalising the theoretical curve to the data for each state, with particular emphasis placed on the data for the smallest center of mass angles (closest to 180° in the laboratory)¹⁴.

The results of the analysis are included in Table 1. The identifications of the spins are discussed below. In general, spectroscopic factors extracted in this fashion have an uncertainty of order 20% arising from the assumptions in the reaction theory, and this is the dominant source of uncertainty in the quoted results.

Table 1. Results for states in ^{25}Ne identified as being populated in neutron transfer on ^{24}Ne . Previous E_x is from Reed *et al.* and USD refers to a $1s0d$ shell model calculation.

E_x (MeV) present	E_x (MeV) previous	ℓ (\hbar) transfer	J^π	S present	S USD	E_x (MeV) USD
0	0	0	$1/2^+$	0.80	0.63	0
1.680	1.703	2	$5/2^+$	0.15	0.10	1.779
2.030	-	2	$3/2^+$	0.44	0.49	1.687
3.330	-	1	$3/2^-$	0.75	-	-
4.030	-	(3)	$7/2^-$	0.73	-	-

5. Discussion

The key feature emerging from Table 1 is that the state identified as the first $3/2^+$ state in ^{25}Ne , which reflects most directly the single particle energy of the $0d_{3/2}$ shell model orbital, is substantially higher than predicted. The identification rests on both the relative strength of this “particle” state compared to the $0d_{5/2}$ “hole” state and the observed gamma decay pathways. The shift of order 350 keV is presumably due to matrix elements in the USD effective interaction that are not well determined from data on less neutron rich nuclei. The shift can be understood very naturally in the monopole shift picture^{15,1}, in which the emptying of the $d_{5/2}$ proton orbital in the more neutron rich $N=15$ isotones removes an attractive interaction

that lowers the neutron $0d_{3/2}$ energy for nuclei closer to stability. This tends to make $N=16$ a magic number for neutron rich nuclei. Simultaneously, the gap to the negative parity orbitals $0f_{7/2}$ and $1p_{3/2}$ is reduced and $N=20$ loses its magicity¹⁶.

The state identified as the $5/2^+$ is almost certainly the state seen in beta decay¹⁷ at 1.703 MeV and has also been seen recently in neutron knockout from $^{26}\text{Ne}^{18}$. This latter observation also supports the identification of the 1.703 MeV level as the hole state and the newly observed level at 2.03 MeV as the $3/2^+$ state. The further implications of these results are still under investigation.

Acknowledgments

We acknowledge with thanks the support of the GANIL and LPC Caen technicians, during the installation and commissioning of the TIARA array. Mr Geoffrey Moores (University of Paisley) and the Daresbury design staff are thanked for their vital contributions. This work was supported in the UK by EPSRC grants held at Surrey, Paisley, Daresbury and Birmingham.

References

1. H. Grawe *et al.*, *Eur. Phys. J. A*, DOI:10.1140/epjad/i2005-06-025-1 (2005).
2. J.S. Winfield, W.N. Catford, N.A. Orr, *Nucl. Instr. Meths.* **A396**, 147 (1997).
3. W.N. Catford *et al.*, *J. Phys.* **G**, in press.
4. W.N. Catford *et al.*, *Eur. Phys. J.*, DOI: 10.1140/epjad/i2005-06-171-4 (2005).
5. W.N. Catford *et al.*, *Nucl. Phys.* **A701**, 1 (2002).
6. W.N. Catford *et al.*, *AIP Conference Proc.* **704**, 185 (2004).
7. H. Savajols *et al.*, *Nucl. Instr. Meths.* **B204**, 146 (2003).
8. J. Simpson *et al.*, *Acta Physica Hungaria: Heavy Ions* **11**, 159 (2000).
9. M. Labiche *et al.*, *J. Phys.* **G**, in press.
10. C.N. Timis, University of Surrey.
11. F. Meurders and A. Van Der Steld, *Nucl. Phys.* **A230**, 317 (1974).
12. A.J. Howard, J.G. Pronko, C.A. Whitten, Jr., *Nucl. Phys.* **A152**, 317 (1970).
13. R.C. Johnson and P.J.R. Soper, *Phys. Rev.* **C1**, 976 (1970).
14. X.D. Liu *et al.*, *Phys. Rev.* **C69**, 064313 (2004).
15. T. Otsuka *et al.*, *Prog. Part. Nucl. Phys.* **47**, 319 (2001); *Phys. Rev. Lett.* **87**, 082502 (2001).
16. Y. Utsuno *et al.*, *Phys. Rev.* **C64**, 011301R (2001); **C70**, 044307 (2004).
17. A.T. Reed *et al.*, *Phys. Rev.* **C60**, 024311 (1999).
18. J.R. Terry and J.L. Lecouey, *Nucl. Phys.* **A734**, 469 (2004).

**RARE ISOTOPES INVESTIGATIONS AT GSI (RISING) USING
RELATIVISTIC ION BEAMS**

J. JOLIE, G. ILIE, P. REITER, A. RICHARD, A. SCHERILLO,
T. STRIEPLING, N. WARR

Institut für Kernphysik, Universität zu Köln, Zulpicher Str. 77, 50937 Köln, Germany

A. BANU, F. BECKER, P. BEDNARCZYK, P. DOORNENBAL, J. GERL,
H. GRAWE, M. GÓRSKA, I. KOJOUHAROV, S. MANDAL, N. SAITO, T. R.
SAITO, H.-J. WOLLERSHEIM

GSI-Darmstadt, Germany

S. MALLION, G. NEYENS, K. TURZO, P. VAN DUPPEN, N. VERMEULEN
K.U. Leuven, Belgium

ZS. PODOLYAK, W. GELLETLY, P.H. REGAN, P.M. WALKER, W.N. CATFORD,
Z. LIU, S. WILLIAMS

University of Surrey, UK

A. BLAZHEV, R. LOZEVA, P. DETISTOV, L. ATANASOVA, G. DAMYANOVA
University of Sofia, Bulgaria

D. CORTINA GIL, J. BENLLIURE, T. KURTUKIAN NIETO, E. CASEREJOS
Universidad de Santiago de Compostela, Spain

J.M. DAUGAS, G. BELIER, V. MEOT, O. ROIG
CEA, Bruyères le Chatel, France

G. SIMPSON, I.S. TSEKHANOVICH
ILL Grenoble, France

I. MATEA

CENBG Bordeaux, France

R. SCHWENGER

IKHP Rossendorf, Germany

M. HASS, B.S. NARA SINGH, S.K. CHAMOLI, G. GOLDRING, I. REGEV,
S. VAINTRAUB

The Weizmann Institute, Israel

D.L. BALABANSKI, G. LO BIANCO, K. GLADNISHKI, A. SALTARELLI, C. PETRACHE
University of Camerino, Italy

G. BENZONI, N. BLASI, A. BRACCO, F. CAMERA, B. MILLION, S. LEONI, O. WIELAND
University of Milano, Italy

A. MAJ, M. KMIECIK, J. GRĘBOSZ, P. BEDNARCZYK, J. STYCZEŃ,
M. LACH, W. MĘCZYŃSKI, K. MAZUREK

IFJ PAN Krakow, Poland

M. PFÜTZNER, A. KORGUL

Warsaw University, Poland

M. IONESCU-BUJOR, A. IORDACHESCU, V. ZAMFIR

NIPNE, Bucharest, Romania

A. JUNGCLAUS

Universidad Autonoma de Madrid, Spain

G. GEORGIEV

ISOLDE-CERN, Switzerland

D.M. CULLEN, S.J. FREEMAN, A.G. SMITH, R. ORLANDI

Manchester University, UK

R.M. CLARK

Lawrence Berkeley National Lab USA

M.A. BENTLEY, G. HAMMOND, R. WADSWORTH

University of York, UK

A.BÜRGER, H. HÜBEL

University of Bonn, Germany

D. RUDOLPH, C. FAHLANDER

University of Lund, Schweden

J. SIMPSON

CLRC Daresbury, UK

R.D. HERZBERG, R.D. PAGE, P. NOLAN

University of Liverpool, UK

T. DAVIDSON, P. WOODS

University of Edinburgh, UK

A.M. BRUCE

University of Brighton, UK

T. FAESTERMANN, R. KRÜCKEN

TU-München, Germany

H. MACH

Uppsala University, Schweden

B. RUBIO, A. ALGORA

IFIC Valencia, Spain

The first experiments performed using fast fragmentation beams and the RISING gamma-ray spectrometer are reviewed and their results are discussed. Plans for future campaigns using ions which are slowed down and stopped in a catcher will also be presented, including details of experiments which measure magnetic moments (g -factor) and β decays using an active stopper.

1. Introduction

The study of atomic nuclei and their dynamics at low excitation energies has been performed over several decades using more and more sophisticated experimental techniques. The themes of modern day nuclear structure research are changing. On one hand, they are refocusing towards the study of low-spin properties and the associated complete spectroscopy. On the other hand, nuclear structure research is now able to manipulate an extremely important degree of freedom, namely the neutron-to-proton ratio, with the advent of the new radioactive beam facilities. Thus, predictions of present-day nuclear models can be tested and the effects due to the underlying neutron-proton degree of freedom can be thoroughly studied. Moreover, new

properties can be revealed, such as the coupling of bound states with the continuum, dilute nuclear matter, clustering and new decay modes. With the availability of Radioactive Ion Beams (RIBs), all essential degrees of freedom become available for experimental manipulation. However, such work requires infrastructure that can only be afforded on an international scale. That said, the discovery potential is very large and new facilities, such as RIA and the GSI extension FAIR, will be built in the coming decade.

Essential for RIB and stable-beam research is the use of high-performance detector arrays to study properties of stable and exotic nuclei. Large γ -ray spectrometers, such as EUROBALL and Gammasphere, were developed for the study of high-spin physics where they have been very successful. Nowadays they are being partly converted towards lower-spin applications. The most advanced project in this direction concerns the EUROBALL spectrometer, which was dismantled in 2003 for that specific goal. The 15 EUROBALL Cluster detectors are now installed at the Fragment Separator (FRS) at GSI as part of the RISING project [1]. It is also worth noting that the other major components of the Euroball spectrometer have been successfully installed at the RITU spectrometer in Jyvaskyla and within the CLARA array at INFN-Legnaro for use in experiments with stable beams.

2. The RISING fast beam campaign

The first RISING campaign (spokesman P. Reiter) ran from summer 2003 until spring 2005 and was aimed at γ -ray spectroscopy of exotic nuclei moving at relativistic energies. The set-up was conceived in such a way that the gamma-ray detection efficiency was maximized with the restriction on the energy resolution of one percent for each individual Euroball Cluster detector at recoil velocities of $v/c = 0.43$. Due to the Lorentz boost, it implied a strongly asymmetric set-up whereby all detectors were mounted behind the target in three rings around the 16 cm wide beam tube. With this set-up, a photopeak efficiency of 2.81% (at 1.33 MeV) and an energy resolution of 1.56% were attained [1]. For some of the fast beam experiments, two additional rings holding seven MINIBALL triple detectors were added, increasing the photopeak efficiency to 7.3%. In the backward direction, eight BaF₂ detectors from the HECTOR array were mounted. These detectors were used to measure very high-energy γ rays and also provide a very good timing reference. Behind the target the Calorimetric Telescope (CATE) [2] array was used to identify the scattered particles and break-up products. It consists of position sensitive thin Si and thick CsI(Tl) ΔE -E telescope detectors. For data analysis, each event was tracked and reconstructed. Figure 1 shows a photograph of the complete 'Fast Beam RISING setup'.

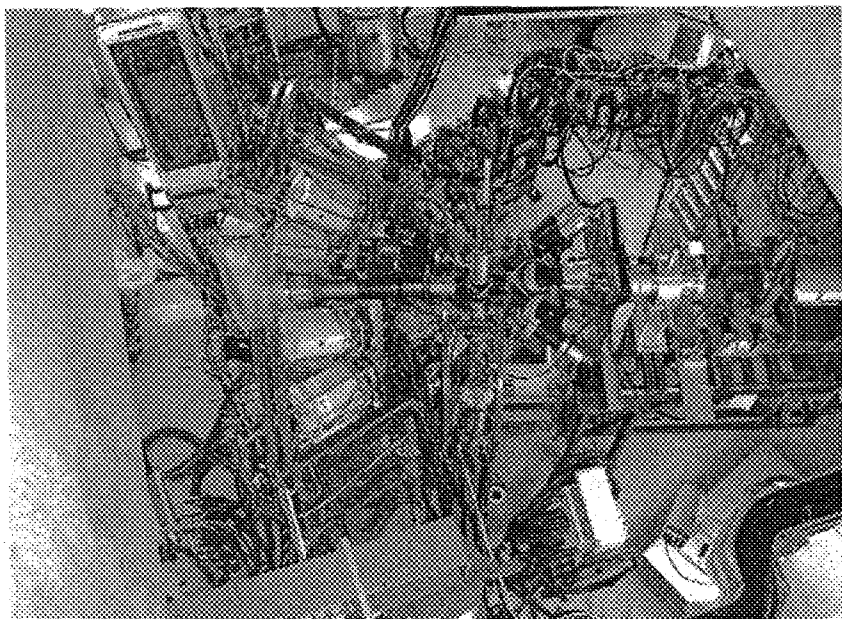


Figure 1. RISING fast beam setup. The beam enters into the set-up from the right-hand side. After hitting the target, the ions are detected in the CATE detector array. The γ rays are detected using the HECTOR array (right), the MINIBALL detectors (middle) and the EUROBALL Cluster detectors (left).

The first results of the fast campaign are now available. Relativistic Coulomb excitation was used in several experiments in order to extract the $B(E2)$ value of the first excited state in a number of unstable nuclei, providing an independent test of the collectivity of this fundamental excitation. For ^{56}Cr and ^{58}Cr , the results confirm the presence of a subshell closure at $N=32$, which was already indicated by the anomalous excitation energy of the first excited 2^+ state in ^{56}Cr [3]. The result represents a challenge for large scale shell-model calculations which overestimate the $B(E2; 2^+ \rightarrow 0^+)$ value for this nucleus. In the ^{108}Sn isotope the obtained $B(E2; 2^+ \rightarrow 0^+)$ value is in agreement with the theoretical calculations [4].

In order to study proton-rich unstable nuclei, two-step fragmentation reactions were used in several experiments. Preliminary results on the $T=3/2$ mirror nuclei in the $A \sim 50$ region show the potential of this method [5]. In addition to the first results discussed above, a significant number of other new results are expected following the completion of the complex data analysis associated with these experiments, including those performed with the addition of the MINIBALL detectors to the RISING array.

3. The g-factor campaign

Static nuclear moments (specifically magnetic dipole and electric quadrupole moments) represent critical tests for the nuclear wave functions obtained within theoretical models, since only one state is involved in the calculation of the expectation values of these observables. The magnetic moment μ , being the product of the nuclear g-factor and the spin I , is a very sensitive probe of the single-particle structure of nuclear states. High-spin isomers in the region of doubly-magic nuclei often have a rather pure single-particle configuration, for which the g-factor is a very good observable to determine the valence nucleon configuration. Measurements of nuclear g-factors can also serve as stringent tests of spin and parity assignments [6]. This is particularly true in far-from-stability regions where such assignments are often based on systematics and theoretical predictions.

Starting in the autumn of 2005, the RISING collaboration will be performing a dedicated campaign of g-factor measurements (spokeswoman G. Neyens) using the Time Differential Perturbed Angular Distribution (TDPAD) method. The method of g-factor or a spectroscopic quadrupole moment determination for an isomeric state is based on measuring the perturbation of the γ -ray anisotropy due to externally applied magnetic (or electric) interactions, following the implantation of the spin-oriented isomeric beam into a suitable stopper (i.e., a crystal or foil). This method has been used extensively over the last couple of decades for measurements of static moments of isomeric states which were produced (and spin-aligned) following in-beam fusion-evaporation reactions [6]. However, in order to investigate isomers with lifetimes in the range of $10^{-7} - 10^{-4}$ s in neutron-rich nuclei, the projectile fragmentation and projectile fission reactions are the most suitable (and often the *only* available) methods for producing spin-orienting and selecting the isomers in a fast and efficient way.

To date, only a few TDPAD measurements have been made on isomers produced in fragmentation reactions at intermediate energies of the primary beam [7,8,9]. The major difference between these and former in-beam experiments is that the isomers are first mass separated in-flight using dipole magnets. During the separation process, the reaction-induced spin orientation needs to be maintained until the moment of implantation. The hyperfine interaction between the nuclear and random-oriented electron spin can cause a loss of orientation during the flight through vacuum. To avoid it, there are two possibilities: either (i) the isomer is produced without electrons (fully stripped fragments) or (ii) the isomeric beam is selected in a noble-gas-like charge state. The primary beam high energies used in fragmentation reactions mean that most fragments can be produced fully stripped, and therefore such beams have been used so far. In a pioneering experiment, Schmidt-Ott and collaborators demonstrated that considerable alignment ($\sim 30\%$) is observed

in the $^{43\text{m}}\text{Sc}$ isomeric ensemble selected with the FRS at GSI and produced in the fragmentation of a relativistic ^{46}Ti beam (500 MeV/u) [7].

For the planned experiments at the FRS a dedicated magnet system allowing magnetic fields up to about 1.5 T (with a gap of 5 cm between the poles) and up to 1.1 T (with a gap of 10 cm) will be used. The γ decays will be detected using 8 EUROBALL Cluster detectors mounted in a close geometry in the horizontal plane (see Fig.2).

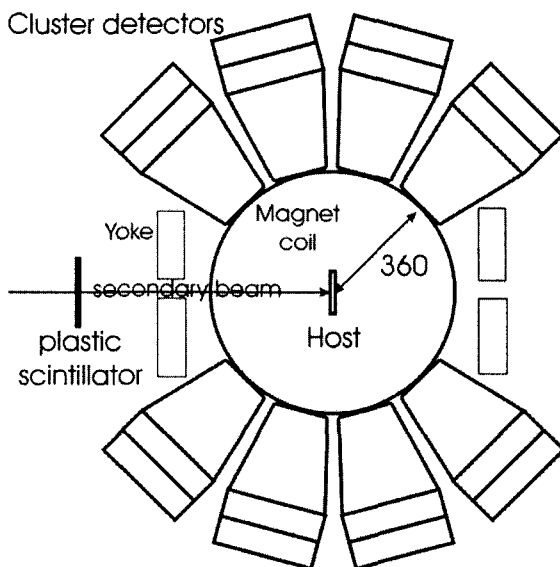


Figure 2. Schematic layout of the TDPAD set-up for measuring isomeric g-factors viewed from above. Detectors are at 36 cm from the stopper and at relative angles of 60° to each other. The total γ -ray detection efficiency is estimated of 4%.

Experiments with fully stripped fragments were limited so far to nuclei up to mass number $A_{\text{max}} \approx 80$ using intermediate energies as provided at e.g. GANIL, RIKEN and MSU. This is because the probability of picking up electrons increases with Z for a fixed beam energy, while it decreases with the beam energy for a given Z . RISING will address mass $A \approx 100 \rightarrow 200$ nuclei. The proposed experiments can be performed at present only at GSI, because the energy and charge of the primary beam at other facilities are not high enough. Furthermore, the fragmentation of a relativistic ^{238}U beam (available only at GSI) offers the unique possibility of studying isomers in neutron-rich nuclei approaching ^{132}Sn . The presence of spin-alignment in

fragments produced by a relativistic ^{238}U fission reaction will be demonstrated for the first time as part of the g-RISING campaign.

The proposed g-factor studies focus on nuclei in regions along shell closures ($Z=50$ and $Z=82$) and near doubly magic nuclei. Near the $Z=50$ shell closure, the structure of isomeric states which consist of rather pure particle and/or hole configurations with respect to the doubly-magic proton-rich ^{100}Sn and the doubly-magic neutron rich ^{132}Sn cores will be investigated. Study of the g-factors of isomers in these regions will help to pin down the suggested configurations and spin assignments, as well allowing investigation of the properties of the M1 operator and its suggested quenching at the extremes of isospin between ^{100}Sn and ^{132}Sn .

Nuclei along the $Z=82$ proton shell closure exhibit a variety of nuclear structures at low excitation energy. In the neutron mid-shell region, a transition from a typical shell model type structure towards more collective states seems to set in. The g-factors in this region are investigated to probe the onset of collectivity in the isomeric wave functions.

4. The stopped beam campaign

Following the g-factor measurements the RISING Stopped Beam Campaign (spokesman P. Regan) will start. Here the 15 EUROBALL Cluster detectors will be used to build a compact array around a passive or active stopper. They will be used to measure γ -rays following β decay to excited states and to measure the direct decay of long lived isomers. For the study of the former process, a position sensitive silicon detector will be used as an active stopper so that the incoming heavy ion can be correlated to its subsequent β decay.

The compact set-up is expected to reach a photopeak efficiency of 11% at 1.33 MeV and 20% at 0.662 keV (see Fig.3). It can be extended with 8 BaF₂ fast scintillators for fast-timing experiments. The FRS will be used in monochromatic mode which allows the stopping of selected isotopes in a 1mm thick Si stopper at the focal plane. This allows a spreading of specific species across a wide area of the focal plane, both increasing the sensitivity of the experiments and allowing longer decay times for subsequent heavy-ion-implantation β -decay correlation measurements to take place.

The physics aims of the Stopped RISING project are focused on obtaining spectroscopic information on nuclei with highly exotic proton-to-neutron ratios. These include specific studies of : (i) isospin and seniority isomers along the $N=Z$ line (specifically ^{54}Ni and $N=Z=41\rightarrow 43$); (ii) the use of 'cold fragmentation reactions' to populate rather neutron-rich nuclei and in particular isomeric states arising from the maximal spin coupling of two-particle (or hole) states in near doubly magic systems 'south' of ^{132}Sn (^{130}Cd) and ^{208}Pb (^{206}Hg , ^{204}Pt); (iii) the investigation of very neutron-rich Zr nuclei approaching the ^{110}Zr harmonic oscillator double shell closure following

projectile fission reactions; (iv) and the utilization of K-isomeric states to map out collectivity and axial symmetry around the valence proton-neutron-product (Np,Nn) maximum nucleus ^{170}Dy .

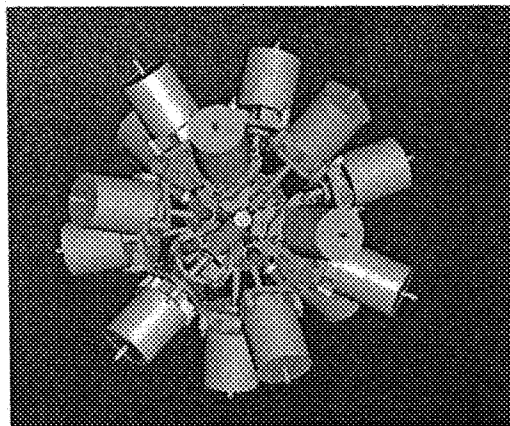


Figure 3. CAD drawing of the Stopped Beam RISING array.

5. Conclusions

The RISING project is aimed at frontier research in nuclear structure physics using relativistic RIBs. It therefore has to combine the complicated FRS infrastructure with state-of-the-art γ -ray detectors. Although as expected several technical problems can arise (e.g., atomic background, operation of the FRS in new settings) the project is moving forward and the first experiments are providing new and interesting results and, more importantly perhaps, paving new experimental pathways into the unknown regions of the Ségre chart. These experiments will be of vital importance for the future FAIR and RIA facilities. The first results of the fast beam campaign are now available and a new series of experiments using stopped beams will be performed in 2006–2007. RISING is a major effort of the European nuclear physics community and has already demonstrated that the traditional low- and high-spin communities can merge and pursue common scientific goals in the future.

Acknowledgments

This work was supported by the BMBF under grant 06K167 and the EPSRC(UK).

References

1. H.J. Wollersheim, *et al. Nucl. Instr. and Meth. In Phys. Res.* **A537**, 637 (2005).
2. R. Lozeva, *et al. Nucl. Instr. and Meth. In Phys. Res.* **B204**, 678 (2003);
R. Lozeva, *et al. Acta Phys. Pol.* **B36**, 1249 (2005).
3. A. Bürger, *et al. Phys. Lett* **B622**, 29 (2005).
4. A. Banu, *et al.*, submitted to *Phys. Rev. C*, 2005.
5. G. Hammond, *et al. Acta Physica Polonica* **B36**, 1249 (2005).
6. G. Neyens, *Reports on Progress in Physics* **66**, 633 (2003).
7. W.D. Schmidt-Ott, *et al.*, *Z. Phys.* **A350**, 215 (1994).
8. G. Georgiev, *et al.*, *J. Phys.* **G28**, 2993 (2002).
9. I. Matea, *et al.*, *Phys. Rev. Lett.* **93**, 142503 (2004).

MASS FORMULA FROM NORMAL TO HYPERNUCLEI

CHHANDA SAMANTA

Saha Institute of Nuclear Physics

1/AF Bidhannagar,

Kolkata-700064, India

E-mail: chhanda.samanta@saha.ac.in

Physics Department, Virginia Commonwealth University

Richmond, VA 23284, U.S.A.

E-mail: csamanta@vcu.edu

In recent years mass measurement of a number of nuclei away from the line of stability has revealed a host of new nuclear structure effects viz. new magic configuration, exotic size and a change in nuclear pairing. To estimate nuclear masses Bethe-Weizsacker formulated a mass formula (BW) based on a liquid drop description of the nucleus and it reproduces the gross features of the nuclear binding energies of medium and heavy nuclei. BW was extended later for light nuclei by modifying its asymmetry and pairing terms. The modified Bethe-Weizsacker mass formula (BWM) reproduces the gross features of the binding energy versus nucleon number curves of all nuclei from $Z=3$ to 83. As no shell effect is incorporated, when compared to experimental masses, BWM helps to identify appearance of some new light magic numbers and disappearance of some old known ones. BWM is extended to describe the separation energies of the Λ , $\Lambda\Lambda$, Σ , Ξ and Θ hyperons from their respective hypernuclei. Details of these mass formulae are discussed in the light of some new discoveries in the field.

1. Introduction

The nuclear mass is one of the most decisive factors governing nuclear stability. As the binding energy determines how much energy is available for a given nuclear reaction, the impact of masses in nuclear reaction and nuclear astrophysics is far reaching. While many properties of normal nuclear matter are well studied, recent investigations indicate that existence of hyperons in dense nuclear matter can influence various properties of cosmic objects. For example, mass, vibration and superfluidity of a neutron star are now predicted to depend crucially on the presence of hyperons in its high density core.

In the past decades a considerable amount of spectroscopic informa-

tions has been accumulated on the non-strange normal nuclei as well as strange hypernuclei. Non-strange normal nuclei are made of neutrons (n) and protons (p) with quark structures udd (n) and uud (p) respectively, whereas hypernuclei consist of neutron(s), proton(s) and hyperon(s). A hyperon has at least one strange quark in them. Lambda ($\Lambda^0=uds$), Sigmas ($\Sigma^0=uds$, $\Sigma^-=dds$, $\Sigma^+=uus$), Cascade ($\Xi^- =dss$) are examples of some hyperons. Recently a new hyperon called "Theta" with pentaquark structure ($\Theta^+=uudd\bar{s}$) has been discovered at SPRING-8, Japan¹, existence of which was predicted in 1997 by D. Diakonov, V. Petrov and M. Polyakov². Interestingly while a few more laboratories support this discovery, several other laboratories produced contradictory results³. Further experiments are now on at different laboratories around the world, including Spring-8, for confirmation. No bound theta hypernucleus⁴ has been discovered so far.

Hypernuclei have been a topic of continuous interest over a long period of time. For example, Λ separation energies have been determined for the ground states of about 40 Λ hypernuclei ($S=-1$) including 3 double- Λ ($S=-2$) hypernuclei^{5,6}. For Cascade hyperon, Ξ^- ($S=-2$) separation energies are measured for several Ξ^- hypernuclei⁵. Recent investigations suggest that due to strongly repulsive Σ -nucleus potential, Sigmas are possibly unbound in nuclei, except for the very special case of nuclei with mass number $A=4$. The ${}^4_2\text{He}$ is bound due to the presence of an attractive Lane term in the isospin dependent Σ -nucleus potential⁷. It has been predicted that the $1/A$ dependence of the Lane term reduces the possibility of finding bound Σ -hypernuclei with large A ^{7,8}.

Calculations in a relativistic mean-field formalism (RMF) suggest that as there is an attractive Θ^+ -nucleus interaction, the Θ^+ particle can be bound in nuclei and, the Θ^+ hypernuclei would be bound more strongly than Λ hypernuclei⁹. Recent calculations in quark mean-field (QMF) model also support existence of bound Θ^+ hypernuclei and predict that in comparison to Λ hypernuclei more bound states are there in Θ^+ hypernuclei²². While a search for bound Theta hypernuclei is on, for a large number of hypernuclei, including double Lambdas, Cascade and Sigmas, more experimental data are needed.

The n, p, Λ , Σ , Ξ and Θ are all baryons and have different masses. A generalised mass formula for non-strange normal nuclei and strange hypernuclei has been formulated which is able to predict the nuclear mass over a wide mass range. This mass formula is presented in the next section.

2. Generalised mass formula (BWMH) for strange and non-strange nuclei

The generalization of the mass formula is pursued starting from the modified-Bethe-Weizsäcker mass formula (BWM) preserving the normal nuclear matter properties. The BWM is basically the Bethe-Weizsäcker mass formula extended for light nuclei which can explain the gross properties of binding energy versus nucleon number curves of all non-strange normal nuclei from $Z=3$ to $Z=83^{10-13}$. In BWM, the binding energy of a nucleus of mass number A and atomic number Z is defined as

$$B(A, Z) = a_v A - a_s A^{2/3} - a_c \frac{Z(Z-1)}{A^{1/3}} - a_{sym} \frac{(N-Z)^2}{[(1 + e^{-A/k})A]} + \delta_{new}, \quad (1)$$

where N and Z are the number of neutrons and protons respectively and

$$\begin{aligned} a_v &= 15.777 \text{ MeV}, & a_s &= 18.34 \text{ MeV}, \\ a_c &= 0.71 \text{ MeV}, & a_{sym} &= 23.21 \text{ MeV}, \\ & & & \text{and } k = 17, \end{aligned} \quad (2)$$

and the pairing term,

$$\delta_{new} = (1 - e^{-A/c})\delta, \quad \text{where } c = 30, \quad (3)$$

and

$$\begin{aligned} \delta &= 12A^{-1/2} \text{ for even } N - \text{even } Z, \\ &= -12A^{-1/2} \text{ for odd } N - \text{odd } Z, \\ &= 0 \text{ for odd } A. \end{aligned} \quad (4)$$

When a hyperon is inserted into a normal nucleus its net charge (Z) and neutron number may change. For example, normal ${}^6\text{Li}(= 3p + 3n)$ and hyper ${}^6_\Lambda\text{Li}(3p+2n+\Lambda^0)$ have same proton number but different neutron number. Similarly, ${}^6_\Sigma\text{Li}$ may have the following configurations ($3p+2n+\Sigma^0$), or ($4p+1n+\Sigma^-$), or ($2p+3n+\Sigma^+$) each adding up the net charge $Z=3$ and net $A=6$.

Hypernuclei are found to be more bound than normal nuclei. A systematic search of hyperon separation energy (S_Y) experimental data for Λ , $\Lambda\Lambda$, Σ^0 and Ξ^- hypernuclei leads to a generalised mass formula for both hyper

and non-strange nuclei which will be, henceforth, called the BWMH. The experimental separation energy of the Λ -hypernuclei (for which experimental data are available over a wide mass range) is found to follow a relation¹⁴ $S_Y \propto A^{-2/3}$.

Baryons can be arranged on the basis of some interesting symmetry consideration. The combined spin(I)-flavour(F) invariance gives rise to the $SU(6)$ classification of Gursey and Radicati¹⁵. The flavour symmetry $SU_F(3)$ breaks by explicit consideration of the different mass of these baryons. The $SU(6)$ symmetry breaking is related to different strengths of the nucleon-nucleus and hyperon-nuclear interactions and has important consequences. For example, although small, the $\Sigma - \Lambda$ mass difference figures prominently in the smallness of the Λ -nuclear spin-orbit interaction¹⁶. The $SU(6)$ symmetry breaking term represented by the strangeness is taken here to be inversely proportional to $A^{2/3}$. An additional mass dependent term breaks the $SU_F(3)$ symmetry.

In BWMH the hypernucleus is considered as a core of normal nucleus plus the hyperon(s) and the binding energy of both normal and hypernuclei is defined as

$$B(A, Z) = a_v A - a_s A^{2/3} - a_c \frac{Z(Z-1)}{A^{1/3}} - a_{sym} \frac{(N - Z_c)^2}{[(1 + e^{-A/k})A]} + \delta_{new} + n_Y \left[0.0335 m_Y - 26.7 - 48.7 \frac{|S|}{A^{2/3}} \right], \quad (5)$$

where n_Y = number of hyperons in a nucleus, m_Y = mass of the hyperon in MeV, S = strangeness of the hyperon and mass number $A = N + Z_c + n_Y$ is equal to the total number of baryons. N and Z_c are the number of neutrons and protons respectively while the atomic number Z in Eq. (5) is now the net charge number given by

$$Z = Z_c + n_Y q \quad (6)$$

where q is the charge number (with proper sign) of hyperon(s) constituting the hypernucleus. The $n_Y = 0$ for non-strange ($S=0$) normal nuclei. The hyperon separation energy S_Y defined as

$$S_Y = B(A, Z)_{hyper} - B(A - n_Y, Z_c)_{core}, \quad (7)$$

is the difference between the binding energy of a hypernucleus and the binding energy of its non-strange core nucleus.

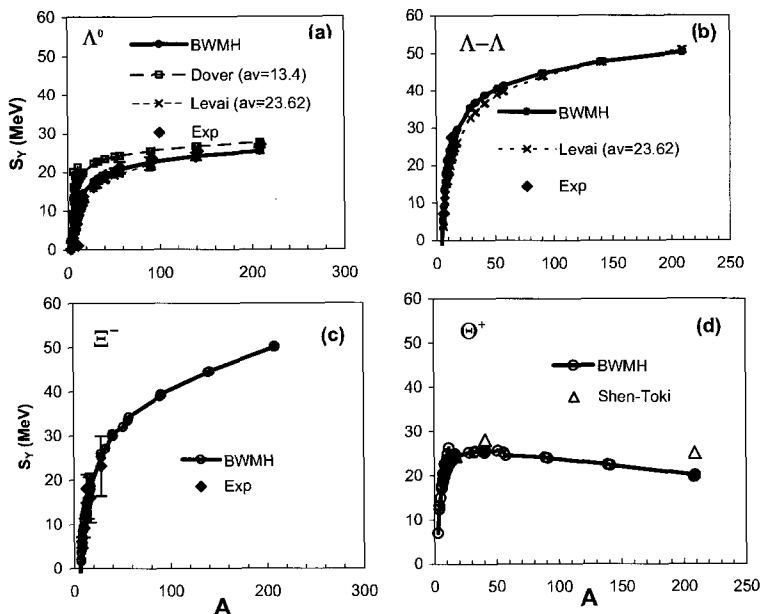


Figure 1. Hyperon separation energy S_Y versus mass number A for (a) single Λ ($m_Y = 1115.63$ MeV) and (b) double Λ separation predicted by BWMH, Dover *et al.* Ref. 24 and Levai *et al.* Ref. 23 and experimental values from Ref. 5 and Ref. 6. (c) single Ξ^- ($m_Y = 1321.32$ MeV) and experimental values Ref. 5 and, (d) single S_{Θ^+} ($m_Y = 1540$ MeV) separation and quark mean field calculations of Shen and Toki of Ref. 22.

Figs.1(a) and 1(b) show plots of S_Y versus A for Λ and $\Lambda\Lambda$ hypernuclei respectively. BWMH predictions are found to be in good agreement with the experimental data⁵. For Σ nuclei the situation is more complicated. Harada *et al.* investigated the structure of ${}^4_{\Sigma}He$ by the coupled-channel calculation between the ${}^3H + \Sigma^+$ and the ${}^3He + \Sigma^0$ channels and predicted the Σ^+ separation energy in ${}^4_{\Sigma}He$ to be 3.7 to 4.6 MeV⁷. Experimental separation energy values are $4.4 \pm 0.3 \pm 1$ MeV¹⁷, 2.8 ± 0.7 MeV¹⁸, 4 ± 1 MeV¹⁹. The BWMH predicts binding energy of Σ^0 ($m_Y = 1192.55$ MeV) and Σ^+ ($m_Y = 1189.37$ MeV) in ${}^4_{\Sigma^0}He$ ($=\Sigma^0 + {}^3_2He$) as 2.69 MeV and ${}^4_{\Sigma^+}He$ ($=\Sigma^+ + {}^3_1H$) as 1.6 MeV, respectively. Search for heavier Σ hypernuclei has been carried out by several authors^{8,17-21} without success. BWMH estimations for the Ξ^- separation energies compare well with the currently available experimental values (Fig.1(c)). On the other hand, absolutely no experimental data exists so far on bound Theta hypernuclei. Therefore, the Θ^+ separation energies are compared with the recent theoretical predictions

(Fig.1(d)). The BWMH predictions for S_Y of Θ^+ are found to be close to the quark mean field (QMF) calculations²². It is interesting to note that due to a delicate balance between the strangeness and Coulomb terms, the S_Y values of hyperons with $q = +1$ are found to have a peak near lower A values with a decreasing trend at larger A , a feature absent for hyperons with $q = 0, -1$.

Earlier BW was extended for Λ and $\Lambda\Lambda$ and Λ , $\Lambda\Lambda$ and Ξ^- by Levai *et al.*²³ and Dover *et al.*²⁴ respectively. The mass formula of Levai *et al.*²³ reproduces the line of stability, while the formulae of Dover *et al.*²⁴ show marked deviations. Moreover, both fail to reproduce the binding energy versus mass number (A) plot of normal non-strange light nuclei such as, ${}^6\text{Li}$. Those two formulae also fail to reproduce the sharp oscillations in the experimental neutron separation energy (S_n) versus A plots due to the absence of²⁴/inadequate²³ pairing term. The incompressibility of infinite nuclear matter²⁵ obtained using the energy co-efficient a_v of the volume term is about 300 MeV for BWM (and BWMH)²⁶ which is within the limits of experimental values, while the mass formula of Levai *et al.*²³ predicts values in the range of 400-480 MeV which are too high to be realistic (Table 1). While the formula of Dover *et al.* gives reasonable value for compressibility, it grossly overpredicts the hyperon separation energies (Fig.1). The presence of a Majorana term in the mass formula of Levai *et al.* [Eqs. (6) and (8) of Ref. ²³] also poses a serious problem that the binding energy per nucleon diverges as the mass number A goes to infinity. This violates the nuclear saturation properties. BWMH is not plagued with such divergence problems and nuclear saturation properties are well preserved for large A . As mentioned earlier, BWMH also reproduces the overall properties of the binding energy and nucleon separation energy curves of normal nuclei¹⁰.

Table 1. Compressibility (K_0) predictions of standard nuclear matter by BWMH, Levai *et al.*²³ and Dover *et al.*²⁴ using different volume term a_v .

Theory	<i>BWMH</i>	<i>Ref.23</i>	<i>Ref.23</i>	<i>Ref.24</i>	<i>Ref.24</i>
a_v (MeV)	15.777	22.63	23.62	18.4	13.4
K_0 (MeV)	301	403	418	340	265

3. Summary and conclusion

Since many questions in heavy-ion physics, particle physics and astrophysics are related to the effect of strangeness in nuclear matter, understanding of strange nuclei in baryonic matter is of utmost importance in the current research scenario. Many laboratories around the world are exploring the possibilities of binding of different hyperons in nuclei. In this context *a priori* estimation of binding energies of hyperons is necessary. With this in view a single mass formula (BWMH) valid for both non-strange normal nuclei and strange hypernuclei is prescribed by introducing hyperon mass and strangeness dependent SU(6) symmetry breaking terms in the modified-Bethe-Weizsäcker mass formula (BWM). Hyperon binding energies calculated by BWMH are in good agreement with the available experimental values. BWMH does not account for the repulsive hyperon-nucleus potential. It reproduces the binding energies of bound Sigma hypernuclei ${}^4_{\Sigma}He$, but would not be applicable where the Σ -nucleus potential is completely repulsive. Recently, an exotic pentaquark hyperon, called Theta, has been discovered. It is awaiting for confirmation from various laboratories. One way to verify its existence is to produce the Theta hypernuclei. BWMH predicts binding energy of Theta hypernuclei over a wide mass range from light to heavy mass nuclei and its predictions are in close agreement with the quark mean field estimates available for medium to heavy mass nuclei. The BWMH preserves the normal nuclear matter properties and gives the value of incompressibility of nuclear matter in consonance with the currently accepted values. Thus, this single mass formula relating both non-strange normal nuclei and strange hypernuclei is expected to provide a bridge between the earth and the cosmos including the neutron stars.

References

1. T.Nakano *et al.*, *Phys. Rev. Lett.* **91**, 012002 (2003).
2. D. Diakonov, V. Petrov, M. Polyakov, *Z. Phys.* **A359**, 305 (1997).
3. F. Close, *Nature* **435**, 287 (2005).
4. G. A. Miller, *Phys. Rev.* **C70**, 022202 (2004).
5. H. Bando, T. Motoba and J. Zofka, *Int. J. Mod. Phys. A* **5**, 4021 (1990); see references therein.
6. H.Takahashi *et al.*, *Phys. Rev. Lett.* **87**, 212502 (2001).
7. T. Harada *et al.*, *Nucl. Phys.* **A507**, 715 (1990).
8. S. Bart *et al.*, *Phys. Rev. Lett.* **83**, 5238 (1999).
9. X. H. Zhong *et al.*, *Phys. Rev.* **C71**, 015206 (2005).
10. C. Samanta and S. Adhikari, *Phys. Rev.* **C65**, 037301 (2002).
11. S. Adhikari and C. Samanta, *Int. Jour. Mod. Phys.* **E13**, 987 (2004).

12. C. Samanta and S. Adhikari, *Phys. Rev.* **C69**, 049804 (2004).
13. C. Samanta and S. Adhikari, *Nucl. Phys.* **A738**, 491 (2004).
14. Robert E.Chrien, *Nucl. Phys.* **A478**, 705c (1988).
15. F. Gursev and L.A. Radicati, *Phys. Rev. Lett.* **13**, 173 (1964).
16. N. Kaiser and W. Weise, *Phys. Rev.* **C71**, 015203 (2005).
17. T. Nagae *et al.*, *Phys. Rev. Lett.* **80**, 1605 (1998).
18. H. Oota *et al.*, *Prog. Theor. Phys. Suppl.* **117**, 177 (1994); H. Oota, *Hyperfine Interact.* **103**, 227 (1996).
19. R. S. Hayano, *Nucl. Phys.* **A547**, 151c (1992).
20. P.K. Saha *et al.*, *Phys. Rev.* **C70**, 044613 (2004).
21. R.I. Sawafta, *Nucl. Phys.* **A639**, 103c (1998).
22. H.Shen and H.Toki, *Phys. Rev.* **C71**, 065208 (2005).
23. G. Levai, J. Cseh, P. Van Isacker and O. Juillet, *Phys. Lett.* **B433**, 250 (1998).
24. Carl B. Dover and A.Gal, *Nucl. Phys.* **A560**, 559 (1993).
25. D.N. Basu, *Jour. Phys. G: Nucl. Part. Phys.* **30**, B7 (2004).
26. D.N. Basu and P. Roy Chowdhury, *arXiv:nucl-th/0408013*, (2004).

2. Exotic Nuclear Structures

This page is intentionally left blank

EXOTIC PHENOMENA IN MEDIUM MASS NUCLEI *

A. PETROVICI

*National Institute for Physics and Nuclear Engineering,
R-76900 Bucharest, Romania
Institut für Theoretische Physik, Universität Tübingen,
D-72076 Tübingen, Germany
E-mail: spetro@ifn.nipne.ro*

Results are presented on the influence of Coulomb-induced isospin-mixing on the superallowed Fermi β decay using the *complex* EXCITED VAMPIR variational approach for the description of the lowest excited 0^+ states in the two isovector triplets of nuclei ^{70}Se , ^{70}Br , ^{70}Kr and ^{74}Kr , ^{74}Rb , ^{74}Sr , respectively. The calculated strengths are in agreement with the experimentally available results. Particular non-analog Fermi branches to excited 0^+ states with considerable strength are predicted to coexist with the superallowed decay in some of the presently investigated nuclei giving some hope for possible experimental detection.

1. Introduction

The investigation of the structure of exotic nuclei around the $N=Z$ line in the $A \simeq 70$ mass region is one of the most exciting challenges in low energy physics today. Apart from displaying some rather interesting nuclear structure effects these nuclei play an important role in weak interaction and nuclear astrophysics. Superallowed Fermi β decays between analog states provide tests of the validity of the conserved vector current (CVC) hypothesis and the unitarity of the Cabibbo-Kobayashi-Maskawa (CKM) matrix. Combining the vector coupling constant (G_v) of nucleon β decay with that of the purely leptonic muon decay, the CKM matrix element between u and d quarks (V_{ud}) can be determined. This amplitude together with the mixing amplitudes V_{us} and V_{ub} , provides the possibility to test experimentally the standard three-generation quark model for the electroweak interaction.

Two classes of nucleus-dependent corrections must be applied to the

*This work was partially supported by Project 436RUM 113/20/0-2 of Deutsche Forschungsgemeinschaft

measured ft value of a $0^+ \rightarrow 0^+$ β transition between T=1 analog states in order to obtain the coupling constant G_ν via the relationship

$$ft(1 + \delta_R)(1 - \delta_c) = \frac{K}{2G_\nu^2(1 + \Delta_R^\nu)}, \quad (1)$$

where f is the statistical rate function, t is the partial half-life for the transition, δ_c is the isospin-symmetry-breaking correction, δ_R is the transition-dependent part of the radiative correction, Δ_R^ν is the transition-independent part, and K is a known constant.

Intens theoretical effort was devoted in the last years to the investigation of the superallowed beta decay of nuclei with $A \geq 62$ (see Ref. [1] and references therein). Several experimental programs have been recently initiated to measure the half-lives and branching ratios for the superallowed decays of odd-odd N=Z nuclei with $A \geq 62$, where the charge-dependent correction terms are expected to be large.

The microscopic nuclear structure calculations for such medium heavy nuclei are extremely involved. The adequate model spaces are far too large to allow for a complete diagonalisation of an appropriate effective many-body Hamiltonian and thus one has to rely on suitable approximate methods. Furthermore, the appropriate effective Hamiltonian itself is not known a priori and can only be determined by an iterative process of many time-consuming calculations. Both, the limitation of the particular approximate method used as well as the insufficient knowledge of the appropriate Hamiltonian, will leave some uncertainties in the quantitative results especially if small effects are to be investigated.

2. Theoretical framework

In the last decade there have been many rather successful theoretical investigations about the structure of nuclei in the $A \simeq 70$ mass region, not only of those along the valley of β -stability, but also in some exotic nuclei close to the proton drip line²⁻⁴. For these calculations the so-called *complex* EXCITED VAMPIR (EXVAM) approach has been used. This approach uses Hartree-Fock-Bogoliubov (HFB) vacua as basic building blocks, which are only restricted by time-reversal and axial symmetry. The underlying HFB transformations are essentially *complex* and do mix proton- with neutron-states as well as states of different parity and angular momentum. The broken symmetries of these vacua (nucleon numbers, parity, total angular momentum) are restored by projection techniques and the resulting symmetry-projected configurations are then used as test wave functions in

chains of successive variational calculations to determine the underlying HFB transformations as well as the configuration mixing. The HFB vacua of the above type account for arbitrary two-nucleon correlations and thus simultaneously describe, e.g., like-nucleon as well as isovector and isoscalar proton-neutron pairing. The *complex* EXCITED VAMPIR has been proven to be a rather useful tool for nuclear structure investigations in large model spaces for the $A \simeq 70$ mass region. Here the effective interaction was adjusted in many different calculations. Phenomena like shape-coexistence and γ -mixing as well as the competition between proton-neutron and like-nucleon-pairing turned out to be very important and various experimental observations in many nuclei could be nicely reproduced. Thus it is worthwhile to apply the same methods for the investigation of the influence of Coulomb-induced isospin-mixing on superallowed Fermi β decay in the $A=70$ and $A=74$ isovector triplets of nuclei, even more so, since some of these nuclei have already been studied in some detail recently ²⁻⁴.

3. Results and discussion

Few recent results concerning the structure of some investigated $A=70$ and $A=74$ nuclei obtained in the frame of the *complex* EXCITED VAMPIR approach will be illustrated in the following. In all these calculations we used a ^{40}Ca core and included the $1p_{1/2}$, $1p_{3/2}$, $0f_{5/2}$, $0f_{7/2}$, $1d_{5/2}$ and $0g_{9/2}$ oscillator orbits for both protons and neutrons in the valence space. The effective two-body interaction is constructed from a nuclear matter G-matrix based on the Bonn One-Boson-Exchange potential (Bonn A).

In ^{74}Kr a strong mixing of prolate and oblate deformed configurations could explain the irregularities observed at low spins as well as the appearance of isomeric states at low excitation energy ³. The complex band structures (see Fig.1) observed at high spins can be explained by a strong mixing of coexisting states based on configurations having different quadrupole, hexadecapole and octupole deformations in the intrinsic system as well as different pairing properties. We investigated the properties of the positive-parity states in the dd-odd ^{74}Rb nucleus at low and high spins ². The calculations revealed some striking similarities between ^{74}Kr and ^{74}Rb at low spins, while deviations appear with increasing spin.

In Figs.2 and 3 we present the EXVAM spectra of the mirror nuclei ^{70}Se and ^{70}Kr , respectively. Particular effects of oblate-prolate coexistence and mixing at low, intermediate and high spins have been obtained and strong $M1$, $\Delta I=0$ transitions have been predicted. Strong similarities, but also

significant differences characterize the behavior of the two mirror nuclei⁴.

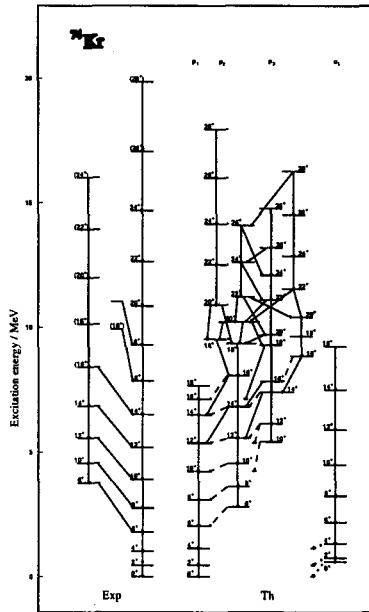


Figure 1. The EXVAM spectrum of ^{74}Kr is compared to the experimental results.

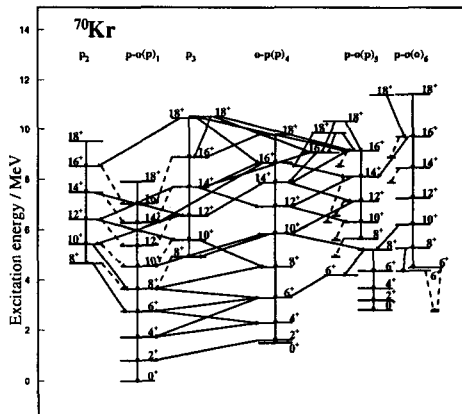


Figure 2. The theoretical EXVAM spectrum of ^{70}Kr .

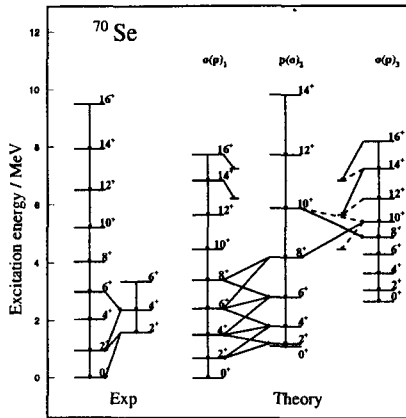


Figure 3. The EXVAM spectrum of ^{70}Se is compared to the experimental results.

In order to investigate the effect of isospin mixing on superallowed Fermi β decay we calculated the lowest 0^+ states in ^{70}Se , ^{70}Br , ^{70}Kr , ^{74}Kr , ^{74}Rb , and ^{74}Sr . For each nucleus of the $A=70$ triplet the energetically lowest 13, for the $A=74$ triplet the lowest 18 $I^\pi=0^+$ configurations have been taken into account⁵. It should be stressed that isospin is not considered as a good quantum number in the EXVAM approach. Thus, even if a charge symmetric interaction is used, good total isospin can only be expected, if the configurations form a complete set under isospin-rotations. This is obviously not the case, if only the 13 or 18 lowest states are considered.

First we used a charge symmetric effective Hamiltonian. Thus one expects degenerate isovector excitation spectra for any triplet of nuclei with proton and neutron numbers $(Z-1, Z+1)$, (Z, Z) and $(Z+1, Z-1)$, respectively. Here Z is an odd number. Furthermore, one expects for the superallowed Fermi-transitions from the ground state of the $(Z+1, Z-1)$ - to the ground state of the (Z, Z) -system and from the ground state of the (Z, Z) - to the ground state of the $(Z-1, Z+1)$ -system both a total strength of two and vanishing strengths for all the transitions from the ground state of the $(Z+1, Z-1)$ - to all excited states of the (Z, Z) -system as well as from the ground state of the (Z, Z) - to all the excited states of the $(Z-1, Z+1)$ -nucleus. Deviations from these values as well as from the degeneracy of the spectra can then be attributed to isospin-mixing effects. In order to study those, the Coulomb-interaction has been included. For this purpose we need not only the two-body matrix elements in the model space but also the Coulomb-contributions to the single particle energies resulting from the ^{40}Ca core. In

order to determine the latter, we performed spherically symmetric Hartree-Fock calculations (with partial occupations of the unfilled j -shells) for the two doubly-even nuclei $(Z-1, Z+1)$ and $(Z+1, Z-1)$ of each triplet using the Gogny-interaction D1S and a 21 major-shell model space. The contribution of the core to the proton single particle energies of the above valence orbits was calculated. We add the Coulomb-matrix elements and single-particle contributions to the charge-symmetric effective Hamiltonian defined above. The resulting Hamiltonian will be denoted by H_1 in the following.

Two different approaches have been considered : First, the Hamiltonian H_1 was diagonalized for each considered nucleus within the *complex* EXVAM solutions obtained with the charge symmetric Hamiltonian H_0 ('perturbative' approach). Second, the *complex* EXVAM calculations are repeated with H_1 right from the beginning ('variational' approach). For each triplet of nuclei we calculated the total strength (S_T) of the transitions from the parent ground state to all the calculated 0^+ states of the daughter nucleus and the strength for the ground to ground transition (S_{g-g}). A summary of the results is presented in Table 1.

Table 1. The total (S_T) and analog (S_{g-g}) Fermi β decay strengths of selected $A = 70$ nuclei for the symmetric (H_0) and Coulomb (H_1) effective Hamiltonian for the *perturbative* (p) and *variational* (v) approaches.

Parent nucleus	H_0		H_1^p		H_1^v	
	S_T	S_{g-g}	S_T	S_{g-g}	S_T	S_{g-g}
^{70}Kr	1.975	1.967	1.970	1.935	1.946	1.917
^{70}Br	1.977	1.967	1.979	1.967	1.959	1.951

Estimating the error by summing the missing strengths between all and the analog transitions for the charge symmetric case ($\epsilon_1 = (S_T(H_0) - S_{g-g}(H_0))/2$) and the missing total strengths between the variational calculations performed with H_0 and H_1 ($\epsilon_2 = (S_T(H_0) - S_T(H_1))/2$) one may conclude that the upper limit for the isospin mixing effect on the Br to Se ground to ground transition is about 0.8 % with this strength distributed over many excited states, while for the Kr to Br ground to ground transi-

tion a depletion of at least 0.7 and at most 2.5 % is obtained. In this latter case a non-analog branch feeding the fourth excited 0^+ state in Br with an upper limit of 0.7 % is obtained. The results are summarized in Fig. 4.

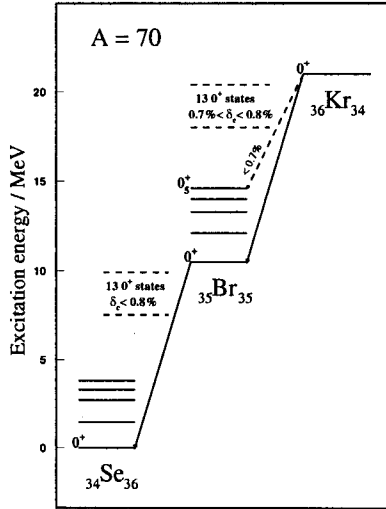


Figure 4. The isospin-mixing correction for the $A=70$ isovector triplet.

The EXVAM results for the $A=74$ triplet ^{74}Kr , ^{74}Rb and ^{74}Sr are summarized in Table 2. Estimating the errors in the same way as for the $A=70$ triplet, one obtains a depletion of the ground to ground decay from Sr to Rb in between 1.3 and 2.7 % of the sum rule strength and a non-analog branch with an upper limit of about 1 % from the ground to the second excited state. For the Rb to Kr ground to ground decay the depletion is in between 0.2 and 1.2 %. Here an upper limit of only 0.3 % is obtained for the branch feeding the second excited state in Kr. These EXVAM results are summarized in Fig. 5. Experimentally, the non-analog Fermi-decay to the first excited 0^+ state in Kr has been investigated^{6,7} and has turned out to be very weak in agreement with the result of our calculations.

The effects of the isospin mixing on the superallowed Fermi transitions are rather small and thus difficult to describe by any microscopic many-body theory quantitatively. Small changes in the effective interaction could yield considerable changes in the quantitative results. However, we think that we have obtained at least the rough magnitude of the effects to be expected. Improvements are possible in the near future.

Table 2. The total (S_T) and analog (S_{g-g}) Fermi β decay strengths of selected $A=74$ nuclei for the symmetric (H_0) and Coulomb (H_1) effective Hamiltonian for the *perturbative* (p) and *variational* (v) approaches.

Parent nucleus	H_0		H_1^p		H_1^v	
	S_T	S_{g-g}	S_T	S_{g-g}	S_T	S_{g-g}
^{74}Sr	1.954	1.947	1.940	1.918	1.932	1.893
^{74}Rb	1.957	1.948	1.948	1.929	1.946	1.924

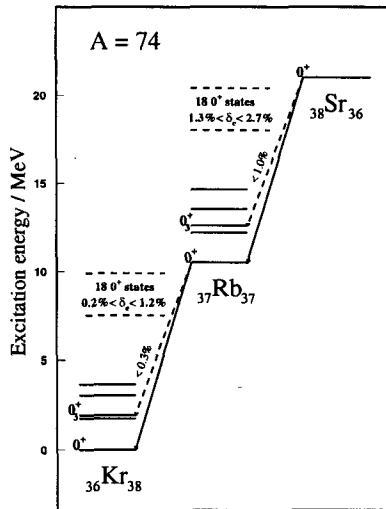


Figure 5. The isospin-mixing correction for the $A=74$ isovector triplet.

References

1. I.S. Towner and J.C. Hardy, *Phys. Rev.***C66** (2002) 035501.
2. A. Petrovici et al., *Progr. Part. Nucl. Phys.***43** (1999) 485.
3. A. Petrovici, K.W. Schmid, A. Faessler, *Nucl. Phys.***A665** (2000) 333.
4. A. Petrovici, K.W. Schmid, A. Faessler, *Nucl. Phys.* **A728** (2003) 396.
5. A. Petrovici, et al., *Nucl. Phys.* **A747** (2005) 44.
6. ISOLDE Collaboration, M. Oinonen et al., *Phys. Lett.***B511** (2001) 145.
7. E.F. Zganjar et al., *Eur. Phys. J.***A15** (2002) 229.

NUSTAR AT FAIR NUCLEAR STRUCTURE RESEARCH AT GSI AND THE FUTURE

G. MÜNZENBERG

GSI Darmstadt, Planckstr. 1, 64220 Darmstadt and
Johannes Gutenberg Universität Mainz *)

FAIR, the new international Facility for Antiproton and Ion Research at GSI, will open up a new era for nuclear research. This contribution will concentrate on Nuclear Structure, Astrophysics, and Reactions (NUSTAR). NUSTAR at GSI covers the full periodic table from light halo nuclei to superheavy elements. It includes spectroscopy, reaction studies, and direct mass measurements as first generation experiments in a heavy-ion storage ring. Storage ring experiments will play a key role in the future research and development program within NUSTAR at FAIR.

1. NUSTAR at FAIR

1.1. *Introduction to the research program*

FAIR, the new international facility for antiproton and ion research at GSI [1], will cover a broad spectrum of hadronic, nuclear, and atomic physics research and application using intense heavy ion beams of intermediate energy and secondary beams of radioactive nuclei and antiprotons.

Nuclear structure research at NUSTAR within FAIR will be extended to regions at the limits of nuclear stability. New probes for reaction studies with unstable nuclei will become available. Experimental developments include: (i) a large-acceptance fragment separator of high resolution [2] which delivers relativistic radioactive ion beams, including Uranium fission products, to a low energy branch associated with detection systems for precision spectroscopy such as an ion trap and gamma arrays with tracking capability; (ii) a high energy branch for reaction studies in reversed kinematics; (iii) a storage ring complex for experiments at high precision including direct mass measurements and reaction studies. In this contribution after a brief overview over the running program the challenges and opportunities for structure research with the new facility will be outlined.

*) retired

1.2. Facility layout

Figure 1 displays the present and future accelerator complex. The existing system consists of the UNiversal Linear ACcelerator (UNILAC), serving as accelerator for low energy beams and as injector to the synchrotron system, the heavy-ion synchrotron SIS 18, and the Experimental Storage Ring (ESR). The new facility comprises the double-ring synchrotrons SIS 100/300 and a system of storage and cooler rings: the Collector Ring (CR), the RESR (not shown in the Fig.1), the New Experimental Storage Ring (NESR), and the High Energy Storage Ring (HESR) [1].

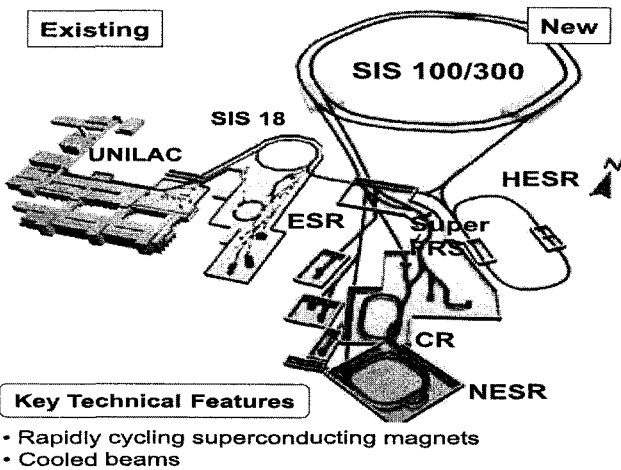


Figure 1. Layout of FAIR. The NUSTAR part is highlighted. It comprises the Super-FRS, the CR and the NESR.

The UNILAC provides beams for experiments near Coulomb barrier, primarily the superheavy-element program [3] and simultaneously serves in a time sharing mode as injector for the synchrotron complex. Two RFQ-injectors, one equipped with an ECR ion source, the other one with two high-intensity ion sources, allow for flexibility in the choice of the primary ion beams.

An important characteristic of FAIR will be the parallel operation of different experiments making use of the high flexibility of the storage rings and beamlines. For the existing UNILAC, SIS18, ESR facility parallel operation of different experiments is already routine now. For the NUSTAR program SIS 100 is operated in a fast cycling mode. It accelerates ions up to Uranium to energies of 1 AGeV at intensities of the order of $10^{12}/s$ which can be slowly

extracted for reaction experiments or with fast extraction for injection into the storage-ring complex. The SIS 300 can optionally be used as a stretcher ring for DC operation.

2. NUSTAR, the research program with radioactive beams

Central topics of NUSTAR, the research program for NUclear Structure, Astrophysics, and Reactions within FAIR are the exploration of nuclear structure at the limits of nuclear stability in isospin and charge including exotic decay modes and the evolution of shells. The aim is to understand correlations and pairing, in-medium modification of the nucleon-nucleon interaction, and the behavior of nuclear matter with extreme neutron-to-proton ratios.

The success of the first generation experiments with unstable nuclear beams motivated a number of second generation projects with improved accelerators and new experimental equipment. The major ones are SPIRALII (France), the new RIKEN accelerator facility RARF (Japan), the MSU upgrade (USA), and the planned facilities EURISOL (a European project) and RIA (USA). The new GSI facility will play a premier role among these new facilities. It will provide high beam intensities in combination with the highest energies available for unstable nuclear beams.

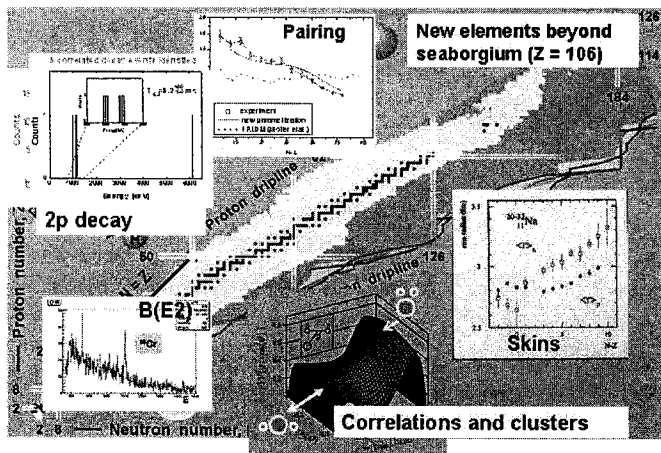


Figure 2. Highlights of nuclear structure research at GSI.

As an example, Fig. 2 displays a collection of highlights of nuclear structure research at GSI. These include: the study of halo nuclei to investigate correlations and clusters, nuclear skins to investigate neutron and proton distributions inside nuclei, the discovery of the two-proton decay in ^{45}Fe , a new decay mode far-off stability, $B(E2)$ values, the evolution of pairing in the isospin degree of freedom as an example for large-scale mass measurements to investigate the systematic behavior of the nuclear landscape far-off stability including new regions of shells and deformations and other global phenomena, and the creation and investigation of new heavy and superheavy elements [3].

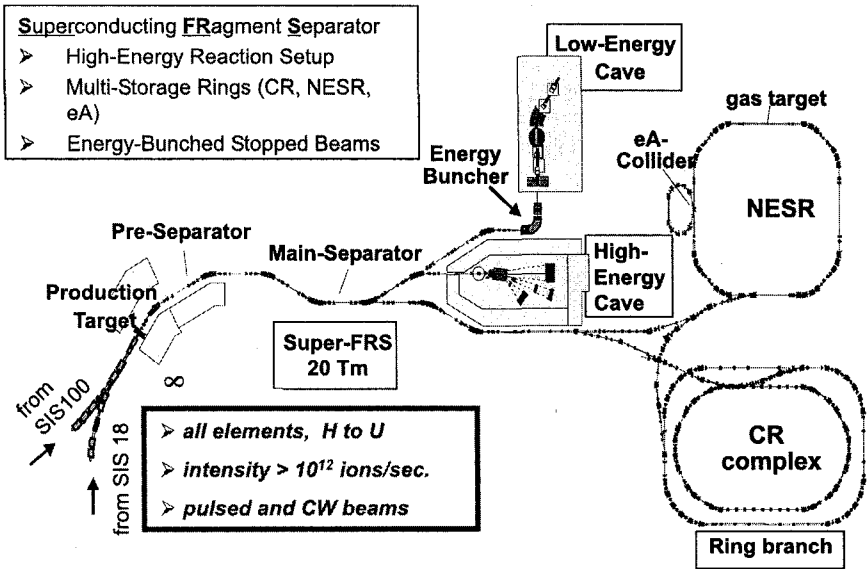


Figure 3. The GSI NUSTAR facility with the Super-FRS and its three branches: low-energy, high energy for nuclear reactions, and the storage-ring complex with the small electron-heavy ion collider.

Figure 3 displays the layout of the NUSTAR facility at FAIR [1]. Its principal instrument is the superconducting FRagment Separator (Super-FRS) [2], a two-staged high resolving energyloss-type spectrometer for in-flight separation of radioactive nuclides created in the production target by fragmentation or fission of heavy ions. Super-FRS has a high ion optical flexibility. It can optionally be operated as low resolution, high transmission

beamline, as separator for isotopic clean radioactive beams, or in a spectrometer mode for reaction studies of high resolution.

Super-FRS mostly will work as in-flight separator to provide unstable nuclei for spectroscopy and reaction studies. For these experiments the Super-FRS feeds three branches (Fig. 3):

- A low energy branch for spectroscopy, including in-beam gamma spectroscopy, and reaction studies at low and intermediate energies e.g. below 100 AMeV. The special feature is a combination of a dispersive magnet and a shaped energy degrader acting as energy buncher to create in-flight separated isotopic beams of low momentum spread. The low-energy branch can be equipped with a broad spectrum of instrumentation including an ion catcher-trap system, silicon arrays for decay studies with implanted radioactive nuclei, a laser set-up, and the advanced Germanium ball AGATA for in-beam gamma spectroscopy.
- A high energy branch for reaction studies with unstable nuclei. This branch will be an upgrade of the existing LAND-Aladin set-up with a new superconducting dipole of 4 Tm bending power, an upgraded Large Area Neutron Detector (LAND), and improved particle detectors for heavy fragments and charged particles. The set-up will also contain a target calorimeter and proton detectors to investigate proton scattering in reversed kinematics [4].
- A ring branch, equipped with the CR to collect and cool the in-flight separated fragment beams. The CR will be equipped with stochastic cooling to achieve fast cooling of radioactive heavy ion beams within the order of seconds. Operation in the isochronous mode will allow direct mass measurements of short lived species down to microsecond half-lives. Experiments will be performed in the NESR which has an electron cooler, an internal gas jet, and a cluster target. An additional ring between CR and NESR, the RESR, will match the injection energy into the NESR as required for the experiments. The internal NESR targets will allow reaction studies with highest precision and scattering at low momentum transfer. Cooled beams are well defined in momentum and angle. The use of thin targets avoids atomic interactions such as energy loss or angular scattering. The effective target thickness is enhanced by six orders of magnitude as the beam passes the target on each revolution with a frequency of $10^6/s$.

Besides decay spectroscopy and in-beam gamma spectroscopy reaction studies in reversed kinematics, precision experiments in the storage-ring systems will be the principal research fields of NUSTAR. One of the key features of NUSTAR is the high projectile energy of up to 1 AGeV for all ions up to

Uranium. The advantage is clean separation in-flight for all fragments up to Uranium as all heavy ions are bare at this high energy which is most important to separate fission fragments of the heavy group. Fission fragments will give access to the large region of practically unknown neutron-rich species. These are not only important for structure investigations but also for nuclear astrophysics as the r-process path passes through practically unexplored neutron-rich regions far off stability. The simple reaction mechanism at high energy facilitates the interpretation of reaction experiments.

Nuclear halos and skins, correlations, and giant resonance studies will be premier research fields. Specifically the access to the wide field of the still almost unexplored neutron-rich species will give new insights into the spectroscopic properties of nuclei far away from stability. Reaction studies in reversed kinematics do not only give access to unstable nuclear species. They are also a new tool for detailed structure investigations. This new experimental technique allows investigating reactions in complete kinematics. As all fragments emerging from the relativistic projectile after interaction with the target are focused in forward direction and have practically the same velocity as the projectile, they can be detected, identified, and their kinematical properties can be measured event by event. This allows to look inside nuclei, to observe the motion of the nucleons, and to investigate correlations and clusters.

A unique feature of NUSTAR is that the radioactive nuclei, separated in-flight by the Super-FRS, can be injected into the storage-ring system consisting of the Collector Ring (CR) and the New Experimental Storage-Ring (NESR) for experiments with stored and cooled beams. The storage and cooler ring system for nuclear structure investigations is a unique feature of FAIR. Electron-cooled beams are the ideal tool for precision experiments. As first generation precision experiments in a heavy ion storage ring direct mass measurements have been performed. The large acceptance of the storage ring allows systematic studies e.g. mapping the nuclear mass surface to get a first overview on the evolution of nuclear structure towards the limits of nuclear stability and to explore isospin effects. Irregularities in the nuclear mass surface are first indications for structure changes [5]. Atomic nuclei can be stored as bare, hydrogen- or helium-like systems. Decay studies in storage rings explore nuclear lifetime under interstellar conditions [6]. A small collider, the heavy-ion storage ring combined with small intersecting electron storage ring, will provide electrons as a new probe for investigations of unstable nuclei [7].

Scattering in reversed kinematics to measure matter distributions will certainly be among the first generation of reaction experiments in the NESR.

The Fig. 4 shows a feasibility study of such experiments. The left panel displays computer simulations of matter radius measurements at the internal gas target for ^{132}Sn (solid line assumed radius of 4.66 fm, dashed line assumed radius of 4.87 fm), the right panel is a simulation of charge radius measurements for ^{120}Sn (4.82 fm, solid line), and ^{132}Sn (4.95 fm, dotted line) measured in the electron-heavy ion mini-collider.

The mini-collider is a new and challenging development in the NUSTAR program. A small electron ring operated in a colliding mode with the NESR allows performing low-energy electron scattering for structure studies. With this set-up it will not only be possible to investigate electron scattering on radioactive nuclei but also to measure electron scattering in complete kinematics with the detection of all participants in the exit channel [7], not possible with the presently used stable-beam electron scattering facilities.

The following Letters of Intent have been submitted for the NUSTAR research program (see: www.gsi.de/nustar):

Low Energy Branch, (C.Scheidenberger (GSI))

HISPEC High-resolution in-flight gamma-ray spectroscopy, Z. Podolyak (U.Surrey)

DESPEC Decay spectroscopy with Implanted Ion Beams, B. Rubio (CSIC Valencia)

MATS Precision measurements of very short-lived nuclei using, K.Blaum (U.Mainz)
an advanced trapping system for highly-charged ions

LASPEC LASER spectroscopy for the study of nuclear properties, P. Campbell (U.Manchester)

NCAP Neutron capture measurements, M.Heil (FZ Karlsruhe)

Exo+pbar Antiprotonic radioactive nuclides, M. Wada (RIKEN)

High-Energy Branch

R³B A universal setup for kinematically complete measurements of reactions with relativistic radioactive beams, T. Aumann (GSI)

Ring Branch

ILIMA Study of isomeric beams, lifetimes and masses, Yu. Novikov (NPI St.Petersburg)

EXL Exotic nuclei studied in light-ion induced reactions at the NESR storage ring, M. Chartier (U.Liverpool)

ELISE Electron-ion scattering in a storage ring (e-A collider), H. Simon (GSI)

pbar-A Antiproton-ion collider: measurement of neutron and proton rms radii of stable and radioactive nuclei, P. Kienle (TU Munich)

PIONICS Spectroscopy of pionic atoms with unstable nuclei, K. Itahashi (RIKEN)

3. Organization of NUSTAR within FAIR

The GSI FAIR project is a multi-national project [1], steered by the International steering Committee ISC-FAIR. The total cost according to the CDR is 675 M€. The German government will pay 65% the state of Hessen 10%. The final decision on the construction of FAIR will be made after the

commitment of partner states to contribute 25% of construction cost. To organize funding and contracting, phase one of the project will be run on the basis of Memoranda of understanding (MOUs). The Scientific and Technical Issues STI-FAIR committee will combine the three scientific Program Advisory Committees PAC QCD, PAC NUSTAR (NUClearn Structure, Astrophysics, and Reactions), and PAC APPA (Atomic Physics, Plasma Physics, and Applications), as well as the Technical Advisory Committee TAC.

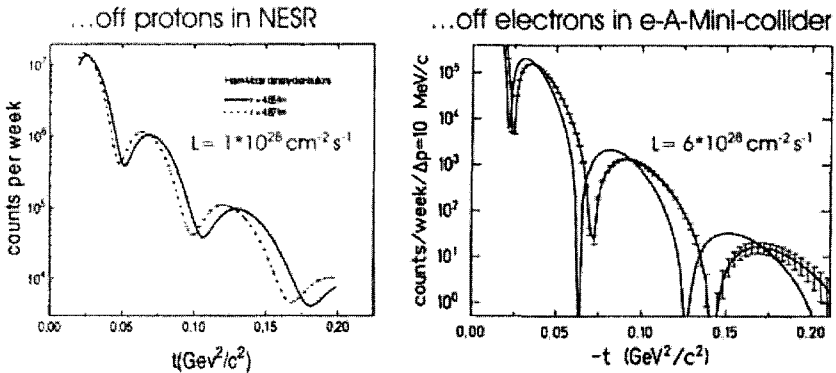


Fig. 4. Simulation of Proton scattering at the internal target of the NESR (left panel) and electron scattering using the electron-heavy-ion mini-collider for the example of Sn isotopes (right panel).

Acknowledgments

I gratefully acknowledge fruitful discussions with H. Geissel, S. Hofmann, H. Emling, L. Chulkov, H. Simon, and M. Winkler.

References

1. A. Bräuning-Demian, contribution to this conference, GSI03 Conceptual design report for "An International Accelerator Facility for Ions and Antiprotons", GSI-Darmstadt, Darmstadt, 2002.
2. H. Geissel, *et al.*, *Nucl. Instr. and Methods* **B204**, 714 (2004).
3. S. Hofmann, contribution to this conference.
4. R. Palit, *et al.*, *Phys. Rev.* **C68**, 034138 (2003).
5. T. Radon, H. Geissel, G. Münzenberg, *et al.*, *Nucl. Phys.* **A677**, 75 (2000).
6. F. Bosch, *et al.*, *Phys. Rev. Lett.* **77**, 5190 (1996).
7. G. Münzenberg, *et al.*, *Nucl. Phys.* **A626**, 249c (1997).

FROM SUPER-RADIANCE TO CONTINUUM SHELL MODEL*

VLADIMIR ZELEVINSKY

*National Superconducting Cyclotron Laboratory and Department of Physics and
Astronomy, Michigan State University, East Lansing, MI 48824-1321, USA*

ALEXANDER VOLYA

*Department of Physics, Florida State University, Tallahassee, FL 32306-4350,
USA*

Consideration of marginally stable mesoscopic systems, including nuclei on the verge of stability, requires that intrinsic structure and continuum effects be taken on equal footing. In two lectures we discuss a possible way to the continuum shell model. The approach is based on the consistent use of the effective non-Hermitian energy-dependent Hamiltonian that allows one to calculate the discrete spectrum in agreement with conventional shell model along with the reaction cross sections. We explain physics of super-radiance and trapping and show examples of first applications to long chains of neutron-rich isotopes.

1. Introduction

The subject of primary interest in nuclear physics nowadays is physics of nuclei far from stability. These studies open new aspects of nuclear structure and provide keys for understanding the chemistry of the Universe. In contrast to stable nuclei, here we deal with loosely bound formations, where the excitations easily break up the system. A theoretical description in such cases must include the continuum states, both for calculating decay probabilities or reaction cross section and as virtual states for intrinsic dynamics. More generally, we need to learn how to describe open or marginally stable many-body quantum systems encountered everywhere in mesoscopic physics (complex molecules, atomic clusters, atoms in traps, quantum wires, quantum dots etc.) Future quantum computers should be

*This work is supported by NSF grant PHY-0244453 and the DOE grant DE-FG02-92ER40750. Collaboration with V. Sokolov and N. Auerbach is highly appreciated.

open for processing information but avoiding chaos and decoherence emerging in interactions with the external world.

The most detailed calculations for nuclear structure can be performed with modern version of the shell model. However, the standard shell model considers only the discrete spectrum; the relation to continuum and reactions is built indirectly, through quantities like spectroscopic factors. For weakly bound systems, the effects of coupling with and through continuum are much more substantial and have to be accounted for in a straightforward way. In principle, there exists quantum-mechanical theory based on classical works by Wigner and Eisenbud, Kapur and Peierls, Fano, Feshbach and Lane and Thomas, summarized in a book by Mahaux and Weidenmüller¹, that formally unifies the nuclear structure in the shell model description and nuclear reactions. However, only recently practical approaches were developed still leaving many open questions.

It turns out that there are new qualitative phenomena predicted for the systems strongly coupled to continuum which, being a consequence of general theory, remained essentially unnoticed for a long time. As we discuss below, the unstable states under appropriate conditions are naturally divided into short-lived (*super-radiating*) and long-lived (*trapped*). This segregation occurs as a kind of phase transition as a function of a parameter

$$\kappa = \frac{\gamma}{D}, \quad (1)$$

where γ is a typical width of unstable intrinsic states prior to this transition, and D is their energy spacing. The transition was first recognized in numerical simulations² and theoretically explained in Refs. 3 and 4 as a phenomenon of the same type as *super-radiance* in quantum optics.

In our short review we show the roots of the super-radiance, discuss its necessary ingredients, different manifestations, and the way to constructing a version of the continuum shell model^{6,7} based on these ideas and the Feshbach projection formalism^{8,9}. More details can be found in Ref. 10. We do not discuss here other recent approaches^{11,12,13} aimed at the same target.

2. Super-radiance and trapping

The optical super-radiance, *coherent spontaneous radiation*, was predicted by Dicke⁵ 50 years ago and observed in HF gas¹⁴ and later in many other media. It appears that incoherent spontaneous radiation may acquire coherence in a system of many two-level radiators placed in a volume of a

size smaller than the wavelength of radiation. The radiators are coupled through common radiation field. This coupling creates the entangled many-body states including those with coherent mixing of atoms in the excited and ground state. Such states maximize the virtual coupling between the atoms via emission and absorption of photons. As a result, a radiation burst is observed with intensity proportional to N^2 , where N is a number of atoms.

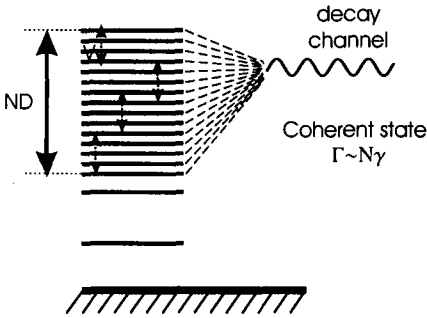


Figure 1. System of intrinsic states coupled with continuum. At $\kappa \sim 1$, a coherent state is formed accumulating a large fraction of the total width of N original levels; the remaining states are trapped.

An analog of Dicke super-radiance (SR) should exist in any quantum system coupled with continuum if certain conditions are fulfilled. The scheme of the effect is shown in Fig.1. The necessary ingredients for the appearance of the effect include (i) a set of intrinsic states $|1\rangle$ with the same exact quantum numbers, unperturbed energies ϵ_1 and typical spacing D ; (ii) continuum channel states $|c; E\rangle$, where c stands for all discrete quantum numbers including those of the residual state of the system; (iii) energy E above some of thresholds E_{th}^c so that the decay amplitudes A_1^c and partial widths $\gamma_1^c = |A_1^c|^2$ do not vanish; (iv) the unstable states overlap, $\kappa^c = \gamma^c/D \sim 1$. In this situation a sharp redistribution of widths occurs, and a number of broad (SR) states, equal to the number of open channels, is segregated from the rest of the states. The latter (trapped states) return to the no-overlap regime with narrow widths and long lifetime that exceeds the Weisskopf recurrence time $\sim \hbar/D$ and ensures the intrinsic equilibration.

Experimentally, we see in this regime the segregation of direct and compound reactions. As a well known example we can interpret from this viewpoint the single-particle resonances. Such broad structures mark the concentration of the fragmented single-particle strength and correspond to a broad background seen in neutron scattering as a direct process. Extremely narrow neutron resonances with chaotic structure and typical enhancement

of weak interactions and parity non-conservation correspond to trapped compound states. The manifestations of the same mechanism are seen in other systems, including atomic¹⁵, molecular¹⁶, condensed matter¹⁷, and particle^{18,19} physics examples.

3. Formalism

The convenient formalism that fully accounts for dynamics of intrinsic states strongly coupled with and through the continuum uses *effective non-Hermitian Hamiltonian*. The obvious advantage of working within this scheme is the opportunity to utilize rich experience and specific results obtained in the framework of the traditional shell model with effective interactions.

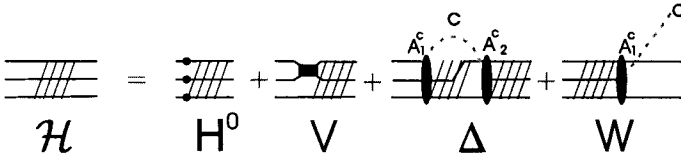


Figure 2. Diagrammatic equation for the full propagator $\mathcal{G}(E)$, Eq. (3).

In order to clarify the derivation of the effective Hamiltonian \mathcal{H} acting only in the intrinsic space $|k\rangle$ we introduce first the many-body propagator

$$G(E) = \frac{1}{E - H}, \quad (2)$$

where the intrinsic Hermitian Hamiltonian H is that of the standard shell model including the single-particle mean field levels and intrinsic effective interaction V . The total propagator

$$\mathcal{G}(E) = \frac{1}{E - \mathcal{H}} \quad (3)$$

differs from the intrinsic propagator (2) by coupling to the decay channels,

$$\mathcal{G}_{12}(E) = G_{kl}(E) + G_{13}(E)M_{34}(E)\mathcal{G}_{42}(E). \quad (4)$$

Here the complex mass operator

$$M = \text{Re } M + i \text{Im } M \equiv \Delta(E) - \frac{i}{2}W(E) \quad (5)$$

has an obvious structure, Fig. 3,

$$M_{12}(E) \sim \sum_c \int (\prod d^3p)_c \frac{H_{1c}H_{c2}}{E - E_p^{(c)} + i0}, \quad (6)$$

where all channels, open and closed at given running energy E , contribute to the sum and corresponding vertices are the matrix elements of the original Hamiltonian that was defined in full space.

The imaginary part $-W/2$ of the mass operator (6) comes from the *on-shell* processes with energy conservation [the delta-function in the denominator of Eq. (6)]. This is possible only for *open* channels c . Including the kinematic factors (phase space volume available in channel c at given energy) in the matrix elements H_{1c} , we can always write down this part in the *factorized* form,

$$W_{12}(E) = \sum_{c(\text{open})} A_1^{c*}(E)A_2^c(E), \quad (7)$$

where the effective amplitudes $A_1^c(E)$ vanish at threshold energy $E = E_{\text{th}}^c$. The real part $\Delta(E)$ corresponds to *off-shell* virtual processes of coupling via continuum which include all, open and closed, channels. This term is given by the principal value integral (6); its energy dependence is usually weak in the region of interest.

The effective Hamiltonian

$$\mathcal{H} = H + \Delta(E) - \frac{i}{2} W(E) \quad (8)$$

is non-Hermitian and energy dependent. Its eigenvalues

$$\mathcal{E}_j(E) = E_j(E) - \frac{i}{2} \Gamma_j(E) \quad (9)$$

are complex and energy dependent. One can use the Breit-Wigner approach and call the resonance energy E_r the solution of the equation $E_j(E_r) = E_r$; then $\Gamma_j(E_r)$ can be considered the width of this resonance. However in general, the decay of such state is not exponential and the resonance shape is not Breit-Wigner one. The eigenstates of the Hamiltonian (8) form a biorthogonal complete set but they also depend on running energy.

This formulation allows one to calculate the cross sections of various reactions directly, avoiding the procedure of diagonalization for the complex Hamiltonian. The amplitude of the $b \rightarrow a$ process,

$$T^{ab}(E) = e^{i\delta_a(E)} \sum_{12} A_1^a(E) \mathcal{G}_{12}(E) A_2^{b*}(E) e^{i\delta_b(E)}, \quad (10)$$

can be found by inverting the propagator (3). For practical purposes, we add here the “potential phases” δ_a and δ_b as smooth functions of energy that mimic the contributions of remote energy regions not accounted for

in the shell model approach. All strong energy dependences coming from resonances and thresholds are included explicitly. The scattering matrix

$$S^{ab}(E) = \delta^{ab} - iT^{ab}(E) \quad (11)$$

is by construction *unitary*, $S^\dagger S = 1$. This is ensured by the fact that the same entrance and exit amplitudes that enter T^{ab} explicitly are included in the denominator of the propagator $\mathcal{G}(E)$. Vice versa, one can deduce the factorized form of the Hamiltonian $W(E)$ from the unitarity requirement. Finally, the observable cross sections are proportional to $|S^{ab}(E)|^2$.

4. Transition to super-radiance

The SR phenomenon follows^{4,20} from the structure of the effective Hamiltonian (7,8). Consider, for example, a case of one open channel and energy-independent Δ and amplitudes A_1 . Let ϵ'_α be real eigenvalues of $H' = H + \Delta$, and B_α decay amplitudes of states $|\alpha\rangle$ found from A_1 after transformation to the basis $|\alpha\rangle$ (the part W remains factorized). Then the secular equation for complex energies (9) reads

$$1 = -\frac{i}{2} \sum_\alpha \frac{\gamma_\alpha}{\mathcal{E} - \epsilon'_\alpha}, \quad \gamma_\alpha = |B_\alpha|^2. \quad (12)$$

At *weak* continuum coupling, $\kappa \ll 1$, the quasistationary states are narrow well isolated resonances,

$$\mathcal{E}_\alpha \approx \epsilon'_\alpha - \frac{i}{2}\gamma_\alpha. \quad (13)$$

In the opposite limit of strong coupling, $\kappa > 1$, the total width $\Gamma = \sum_\alpha \gamma_\alpha$ of all unperturbed states (invariant under transformation from amplitudes A_1 to amplitudes B_α) is getting greater than the total energy interval $\Delta\epsilon'$ covered by relevant states (strongly coupled to a give channel). Then W becomes the main term in the effective Hamiltonian. Because of the factorized structure, the matrix of W is of rank 1, so that it has only one non-zero eigenvalue equal to its trace, Γ (for k open channels we would have k non-zero eigenvalues). Other eigenvalues vanish the corresponding states acquire only a small widths because of mixing by the Hermitian interaction.

If the real spectrum would be degenerate, $\epsilon_\alpha = \bar{\epsilon}$, the solution is obvious: one state at

$$\mathcal{E}_{\text{SR}} = \bar{\epsilon} - \frac{i}{2}\Gamma \equiv \sum_\alpha \gamma_\alpha, \quad (14)$$

accumulates the entire summed width Γ , while the remaining states are still degenerate and stable. With splitting of the levels on the interval $\Delta\epsilon' < \Gamma$, the total width of the narrow states can be found from (12) as

$$\Gamma_{\text{narrow}} = \Gamma - \Gamma_{\text{SR}} \approx 4 \left(\frac{\Delta\epsilon'}{\Gamma} \right)^2 \Gamma = 4 \frac{\Gamma}{\kappa^2} \ll \Gamma. \quad (15)$$

The SR state plays the role of the *doorway* state with respect to the trapped states as the single-particle resonance for the compound neutron resonances.

The transition to SR occurs at $\kappa^c \sim 1$ when the percolating collectivization of overlapping intrinsic states by their coupling to common decay channels leads to their coherence. The reaction processes considered in time domain form a hierarchy of different scales that is governed by two parameters, κ and N , the localization length of intrinsic states²¹: the fastest direct process, $\tau_d \sim \hbar/\Gamma_{\text{SR}}$, the intrinsic fragmentation time $\tau_f \sim \hbar/\Delta\epsilon' \sim \kappa\tau_d$, the Weisskopf recurrence time $\tau_W \sim \hbar/D \sim \kappa\tau_d N$, and the longest lifetime of compound states $\tau_{\text{comp}} \sim \hbar/(\Gamma_{\text{narrow}}/N) \sim \tau_W \kappa$.

5. Towards continuum shell model

Work on converting the nice general formalism into a practical tool with detailed calculations for nuclei far from stability is still in progress, and many technical questions still are waiting to be resolved. The main principal difficulty lies with the Hamiltonian itself. The conventional shell model, for example in the best studied region of *sd*-shell²², uses the single-particle energies and effective Hermitian two-body interaction matrix elements (63 in the *sd*-space) as input parameters; they can be smoothly scaled with mass number effectively accounting for many-body interactions and density dependence. The parameters are semi-empirical being fit long ago by the spectroscopic information available at a time. The rest, including newly discovered isotopes, should be a pure result of the large-scale diagonalization. Of course, the results are presented as discrete levels even if in reality the corresponding states are seen as resonances.

The real problem is in the absence of knowledge of what interaction should be used for calculations with the continuum. There exist only the first and technically quite complicated attempts²³ of constructing the effective interactions using the Gamow shell model approach in the so-called Berggren basis²⁴. The problem consists in identifying the resonances prior to the shell model solution and therefore the self-consistency condition become critical. The direct derivation of the *G*-matrix for a many-body

system with discrete and continuum spectra was never done, even in the low-density (Brueckner) approximation.

In this situation we utilize a pragmatic approach. We borrow the intrinsic Hermitian interaction from the traditional shell model. The dispersive part Δ of the effective Hamiltonian \mathcal{H} coming from the off-shell continuum coupling is assumed to be already included in the effective shell model interaction; its weak energy dependence is neglected. This approximation can be lifted paying the price of slightly enhanced technical difficulty but at this stage it makes no sense because of lack of knowledge of interaction. We neglect also coupling between the channels in the continuum; their coupling through intrinsic dynamics is fully accounted for, see for example the expression (10) for the scattering amplitude. Then the only element that is still missing is the set of the continuum coupling amplitudes $A_1^c(E)$.

We are interested mainly in low energy region, when only few open channels are present. Here the energy dependence of the amplitudes $A_1^c(E)$ may be crucial. Near thresholds, this dependence is in fact determined by quantum-mechanical calculations of threshold behavior of wave functions and phase space volume available in a given channel. However, the positions of thresholds in a nucleus A are defined by the levels of residual nuclei $A - 1, A - 2, \dots$. We come to necessity to solve self-consistently the problem for a *chain* of nuclei related by consecutive decays. With the amplitudes determined, one can proceed either diagonalizing the complex Hamiltonian \mathcal{H} and finding the discrete levels and resonances or inverting the propagator \mathcal{G} for calculating the cross sections.

6. How it works

Considering the chains of nuclei (until now we worked with helium, lithium and oxygen), we start with the core, alpha-particle or ^{16}O . For the heavier isotopes the one- and two-body decay channels were included. An asymptotic state in a *one-body* channel can be written as

$$|c : E\rangle_A = c_j^\dagger(\epsilon_j)|\alpha; A - 1\rangle, \quad (16)$$

where the operator c^\dagger creates one free particle, j labels its quantum numbers, ϵ_j is its kinetic energy, $|\alpha; A - 1\rangle$ is the final discrete state of the residual nucleus, and total energy is $E = E_\alpha + \epsilon_j$.

Assuming for simplicity that in the shell model space the single-particle quantum numbers j provide a unique label, we look for the coupling amplitude in the factorized form

$$A_1^c(E_\alpha + \epsilon_j) = a_j(\epsilon_j)\langle\alpha; A - 1|b_j|1; A\rangle. \quad (17)$$

The second factor here is the spectroscopic amplitude that defines the weight of the shell model quasiparticle j in the many-body initial state $|1; A\rangle$. The amplitude j describes the transformation of the internal quasiparticle into the asymptotic free particle. In the mean field approximation it can be found as

$$a_j(\epsilon) = \sqrt{\frac{2\mu}{\pi k}} \int_0^\infty dr F_l(r) U(r) u_l(r), \quad (18)$$

where $U(r)$ is the mean field potential including the Coulomb barrier for the outgoing protons, $F_l(r)$ and $u_l(r)$ are the regular solutions with orbital momentum l for free motion and in the mean field, respectively. Near threshold, where the right energy dependence is crucial, $a(\epsilon) \sim \epsilon^{(l+1)/2}$. Only far from threshold, neglecting this dependence and assuming that the removal of a particle does not lead to a significant restructuring of the mean field, one can use the closure approximation for calculating W as a single-particle operator 7.

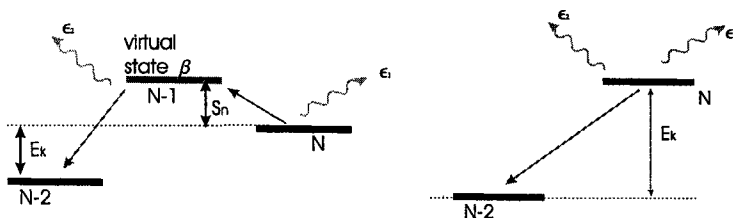


Figure 3. Diagrams for two-body decays, sequential (left part) and direct (right part).

The *two-body* decays can proceed via sequential and direct (“democratic”) mechanisms sketched in Fig.3. The total amplitude can be presented as the sum

$$A_1^c(E_\alpha + \epsilon_{j_1} + \epsilon_{j_2}) = \langle j_1 j_2; \alpha, A - 2 | H_{s.p.}^{(2)} + V_{2 \text{ body}} | 1; A \rangle. \quad (19)$$

The sequential decay is described by the second order with respect to the single-particle Hamiltonian that implements the virtual transition through a state in the intermediate nucleus ($A - 1$). or direct transitions, we considered until now only those for a correlated pair with zero angular momentum using the pairing part of the two-body interaction. Such decays are responsible for instability of such nuclei as ^{26}O . The cluster decay can be also included in a similar way.

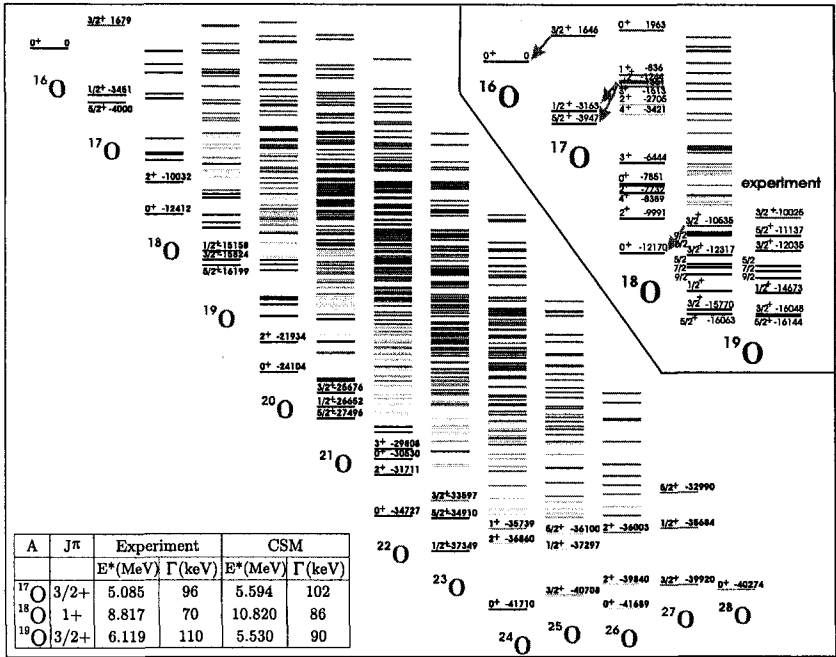


Figure 4. Continuum shell model calculations for oxygen isotopes.

An example of a realistic calculation for the chain of isotopes $^{17-28}\text{O}$ is shown in Fig. 4. An important advantage of this scheme with self-consistent threshold energies in parent-daughter relations is that for stable states the results by construction are identical with those in the standard shell model if the same residual interaction was used. For resonance states theory predicts positions and widths although the lineshape may not be given by the BW formula. The inset shows more detailed comparison with data for the lightest isotopes. Many predictions, such as the width of the ground state of ^{26}O , are expected to be tested with coming experiments.

7. Outlook

The suggested theoretical scheme for unified description of structure and reactions in open or marginally stable many-body systems is shown to work effectively and reliably. The work is in progress, and many problems are still to be solved. Below we selectively list some of them.

- Extension of calculations to new isotope chains.
- Direct calculation of reaction cross sections with loosely bound nu-

clei.

- Better treatment of decay amplitudes from first principles; inclusion of other decay modes.
- Consistent derivation of the effective interaction to be utilized in continuum shell model with possible necessity of renormalizing the interaction used for description of discrete spectra.
- Theory of pigmy-branch of the giant resonance based on the interplay of super-radiance (collectivization of widths) and collectivization of multipole strength, see Ref. 10 and references therein.
- Improved consideration of Ericson fluctuations in the region of overlapping resonances.
- Statistical properties of resonances in open quantum systems.
- Application to other mesoscopic systems.

References

1. C. Mahaux and H.A. Weidenmüller, *Shell Model Approach to Nuclear Reactions* (North Holland, Amsterdam, 1969).
2. P. Kleinwächter and I. Rotter, *Phys. Rev. C* **32**, 1742 (1985).
3. V.V. Sokolov and V.G. Zelevinsky, *Phys. Lett. B* **202**, 10 (1988).
4. V.V. Sokolov and V.G. Zelevinsky, *Nucl. Phys.* **A504**, 562 (1989).
5. R.H. Dicke, *Phys. Rev.* **93**, 99 (1954).
6. A. Volya and V. Zelevinsky, *Phys. Rev. C* **67**, 54322 (2003).
7. A. Volya and V. Zelevinsky, *Phys. Rev. Lett.* **94** (2005) 052501.
8. H. Feshbach, *Ann. Phys.* **5**, 357 (1958); **19**, 287 (1962).
9. I. Rotter, *Rep. Prog. Phys.* **54**, 635 (1991).
10. A. Volya and V. Zelevinsky, In *Nuclei and Mesoscopic Physics*, ed. V. Zelevinsky, AIP Conference Proceedings **777**, 2005, p. 229.
11. R.I. Betan, R.J. Liotta, N. Sandulescu, and T. Vertse, *Phys. Rev. Lett.* **89**, 042501 (2002).
12. N. Michel, W. Nazarewicz, M. Ploszajczak, and J. Okolowocz, *Phys. Rev. C* **67**, 054311 (2003).
13. N. Michel, W. Nazarewicz, and M. Ploszajczak, *Phys. Rev. C* **70**, 064313 (2004).
14. N. Skribanowitz, I.P. Herman, J.C. MacGillivray, and M.S. Feld, *Phys. Rev. Lett.* **30**, 309 (1973).
15. V.V. Flambaum, A.A. Gribakina, and G.F. Gribakin, *Phys. Rev. A* **54**, 2066 (1996).
16. V.B. Pavlov-Verevkin, *Phys. Lett. A* **129**, 168 (1988).
17. K. Pichugin, H. Schanz, and P. Šeba, *Phys. Rev. E* **64**, 056227 (2001).
18. N. Auerbach and V. Zelevinsky, *Phys. Rev. C* **65**, 034601 (2002).
19. N. Auerbach, V. Zelevinsky, and A. Volya, *Phys. Lett. B* **590**, 45 (2004).
20. V.V. Sokolov and V.G. Zelevinsky, *Ann. Phys. (N.Y.)* **216**, 323 (1992).
21. V. Zelevinsky, *Ann. Rev. Nucl. Part. Sci.*, **46**, 237 (1996).

22. B.A. Brown and B.H. Wildenthal, *Ann. Rev. Nucl. Part. Sci.* **38**, 29 (1988);
B.A. Brown, W. Richter, R. Julies, and B. Wildenthal, *Ann. Phys. (N.Y.)*
182, 191 (1988).
23. G. Hagen, M. Hjorth-Jensen, and J.S. Vaagen, *Phys. Rev. C* **71**, 044314
(2005).
24. T. Berggren, *Nucl. Phys.* **A109**, 265 (1968).

NEW METHODS FOR THE EXACT SOLUTION OF THE NUCLEAR EIGENVALUE PROBLEM BEYOND MEAN FIELD APPROACHES

F. ANDREOZZI, N. LO IUDICE, AND A. PORRINO

*Dipartimento di Scienze Fisiche, Università di Napoli "Federico II"
and Istituto Nazionale di Fisica Nucleare,
Monte S Angelo, Via Cintia I-80126 Napoli, Italy
E-mail: loiudice@na.infn.it*

We report on an important sampling algorithm for generating a subset of exact eigensolutions of the nuclear shell model Hamiltonian within a truncated space and its tests performed on typical nuclei. We also mention an equation of motion method, under way of development, which generates iteratively a microscopic multiphonon basis and is therefore especially suitable for the investigation of collective modes.

1. Introduction

Powerful methods for solving the nuclear eigenvalue problem have been developed in the last two decades. A notable one is a Monte Carlo method, adopted to compute ground states properties¹ or to generate stochastically a truncated basis for diagonalizing the many-body Hamiltonian². The first approach has to deal with the sign problem, the second with the redundancy of the basis states and the broken symmetries.

Alternative approaches, mostly based on Lanczos³ algorithm, face directly the diagonalization of the Hamiltonian. The critical point of these methods is the amount of memory needed and the time spent in the diagonalization process.

In a recent paper⁴, we have developed an iterative algorithm for generating a selected set of eigenvectors of a large matrix which is fast, *robust*, yielding always stable numerical solutions, free of *ghost* eigenvalues, and extremely simple to be implemented. Moreover, the algorithm could be naturally endowed with an importance sampling which allows for a drastic reduction of the space and offers other important advantages⁵.

SM is, in general, not suitable for studying nuclear collective proper-

ties. These are studied traditionally in mean field approaches, like Tamm-Dancoff (TDA) or random-phase approximation (RPA), which select the configurations building up the collective states.

TDA and RPA can be considered as harmonic approximations to the full nuclear eigenvalue problem. Anharmonic effects may be accounted for by going to higher RPA⁶ or by Boson expansion methods^{7,8}. Closely related to the latter approach is the quasiparticle-phonon model (QPM)⁹, which faces the nuclear eigenvalue problem in an enlarged phonon space spanned by a restricted set of two or, exceptionally, three RPA phonon states. The QPM has been adopted with success for studying collective states of complex structure. On the other hand, it applies only to separable Hamiltonians and does not provide precise prescriptions for keeping under control the uncertainties due to the space truncation, the quasi-boson approximation and the lack of antisymmetrization of the multiphonon basis states.

We are currently developing an equation of motion method¹⁰, which solves exactly the nuclear many body problem, for a Hamiltonian of general form, in a space with an arbitrary number of phonons.

2. Shell Model Algorithm

2.1. The Importance Sampling Algorithm

Let us consider, for simplicity, a symmetric matrix $A = \{(a_{ij}) = \langle i | \hat{A} | j \rangle\}$ representing a self-adjoint operator \hat{A} in an orthonormal basis $\{|1\rangle, |2\rangle, \dots, |N\rangle\}$. The algorithm goes through several iteration loops. The first loop consists of the following steps: 1a) Diagonalize the two-dimensional matrix (a_{ij}) ($i, j=1, 2$), 1b) select the lowest eigenvalue λ_2 and the corresponding eigenvector $|\phi_2\rangle c_1^{(2)} |1\rangle + c_2^{(2)} |2\rangle$, 1c) for $j = 3, \dots, N$ diagonalize the matrix

$$\begin{pmatrix} \lambda_{j-1} & b_j \\ b_j & a_{jj} \end{pmatrix}$$

where $b_j = \langle \phi_{j-1} | \hat{A} | j \rangle$ and select the lowest eigenvalue λ_j together with the corresponding eigenvector $|\phi_j\rangle$. This zero approximation loop yields the approximate eigenvalue and eigenvector

$$E^{(1)} \equiv \lambda_N, \quad |\psi^{(1)}\rangle \equiv |\phi_N\rangle \sum_{i=1}^N c_i^{(N)} |i\rangle. \quad (1)$$

We use these new entries to start an iterative procedure which goes through $n = 2, 3, \dots$ refinement loops, consisting of the same steps with the following

modification. At each step $j = 1, 2, \dots, N$ of the n -th loop ($n > 1$) we have to solve an eigenvalue problem of general form, since the states $|\phi_{j-1}\rangle$ and $|j\rangle$ are no longer orthogonal. The eigenvalue $E^{(n)} \equiv \lambda_N$ and eigenvector $|\psi^{(n)}\rangle \equiv |\phi_N\rangle$ obtained after the n -th loop are proved to converge to the exact eigenvalue E and eigenvector $|\psi\rangle$ respectively⁴.

The algorithm has been shown to be completely equivalent to the method of optimal relaxation¹¹ and has therefore a variational foundation. Because of its matrix formulation, however, it can be generalized with minimal changes so as to generate at once an arbitrary number n_v of eigensolutions. Indeed, we have to replace the two dimensional matrix (??) with a multidimensional one

$$\begin{pmatrix} \lambda_{j-1} & b_j \\ b_j & a_{jj} \end{pmatrix} \Rightarrow \begin{pmatrix} \Lambda_k & B_k \\ B_k^T & A_k \end{pmatrix}, \quad (2)$$

where Λ_k is a n_v -dimensional diagonal matrix whose non-zero entries are the eigenvalues $\lambda_1^{(k-1)}, \lambda_2^{(k-1)}, \dots, \lambda_{n_v}^{(k-1)}$, $A_k = \{a_{ij}\}$ ($i, j = (k-1)p+1, \dots, kp$) is a p -dimensional submatrix, B_k and its transpose are matrices composed of the matrix elements $b_{ij}^{(k)} = \langle \phi_i^{(k-1)} | \hat{A} | j \rangle$ ($i = 1, \dots, n_v; j = (k-1)p+1, \dots, kp$). A loop procedure similar, though more general, to the one adopted in the one-dimensional case, yields a set of n_v eigenvalues E_1, \dots, E_{n_v} and corresponding eigenvectors $\psi_1, \dots, \psi_{n_v}$.

When the dimensions of the Hamiltonian matrix become prohibitively large, one needs to resort to truncation methods. To this purpose we have exploited the fact that the algorithm yields quite accurate solutions already in the first approximation loop to devised a sampling which makes use of the first loop only. This now goes through the following steps :1a) Diagonalize the v -dimensional principal submatrix $\{a_{ij}\}$ ($i, j = 1, v$); 1b) For $j = v+1, \dots, N$, diagonalize the $v+1$ -dimensional matrix

$$\begin{pmatrix} \Lambda_v & \vec{b}_j \\ \vec{b}_j^T & a_{jj} \end{pmatrix}, \quad (3)$$

where $\vec{b}_j = b_{1j}, b_{2j}, \dots, b_{vj}$; 1c) Select the lowest v eigenvalues λ'_i , ($i = 1, v$) and accept the new set only if

$$\sum_{i=1,v} |\lambda'_i - \lambda_i| > \epsilon \quad (4)$$

The outcome of this procedure is that the selected states span a $n_s (< N)$ dimensional space, so that the subsequent refinement loops iterate only on the smaller set of n_s basis vectors. The number of operations is thereby

reduced by a factor N/n_s . Indeed, for large N , they are $O(n_s(N + \mu n_s))$, to be compared with $O(\mu' N^2)$ when dealing with the full matrix, having denoted by μ and μ' the number of iterations required to reach convergence in the two cases.

The sampling procedure has also the important virtue of generating a scaling law for the eigenvalues. Indeed the sampling parameter ϵ scales with n according to

$$\epsilon = b \frac{N}{n^2} \exp \left[-c \frac{N}{n} \right]. \quad (5)$$

This induces for the energies the following scaling law

$$E = E_0 + b \frac{N}{n} \exp \left[-c \frac{N}{n} \right], \quad (6)$$

where b , c , and E_0 are constants specific of each state and the full dimension N provides the scale. This law, which is somewhat different from the one proposed in Ref. 14, is valid for all states and nuclei examined and follows directly from the sampling⁵.

This is illustrated in Fig. 1 for the lowest states of the semi-magic ^{108}Sn and the $N=Z$ even-even ^{48}Cr . Similar results hold for the $N > Z$ odd-even ^{133}Xe . It must be pointed out that the asymptotic eigenvalues extrapolated by the scaling law differ from the exact ones in the second or third decimal digit.

The sampling guarantees a high accuracy also for the eigenstates ψ_n . As shown in Fig. 2, their overlap with the exact eigenvectors ψ for the first five $J^\pi = 2^+$ states of ^{108}Sn and $J^\pi = 0^+$ of ^{48}Cr converges rapidly to unity.

Correspondingly also $E2$ transition strengths converge rapidly to the exact values. Indeed, the strengths computed at a relatively large ϵ differ very little from the exact values. This rapid convergence is quite significant in view of the extreme sensitivity of the transition strengths to even very small components of the wave function.

3. Equation of Motion Method for Collective Modes

As pointed out in the Introduction, mean field approaches, like TDA or RPA, being more selective in the choice of configurations, are more suitable than SM for studying collective modes. In order to account for anharmonic effects, however, it is necessary to enlarge the space so that more complex configurations come into play. To achieve this goal we have developed an equation of motion method¹⁰, which solves exactly the nuclear many body

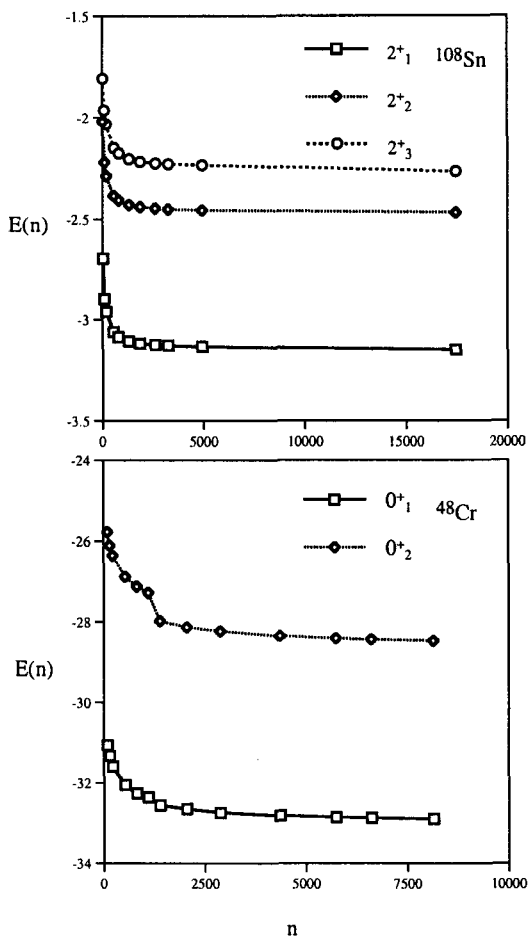


Figure 1. Eigenvalues versus the dimensions n of the truncated matrices resulting from the sampling.

problem in a space which is the direct sum of n -phonon subspaces, with n running from 0 to an arbitrary number N .

We start with a general two-body Hamiltonian written in second quantized form and solve the following eigenvalue equations in each n -phonon subspace

$$\langle n; \beta_n | [H, a_p^\dagger a_h] | n-1; \alpha_{n-1} \rangle = (E_{\beta_n} - E_{\alpha_{n-1}}) X_{\alpha_{n-1} \beta_n}^{(ph)}, \quad (7)$$

where a_p^\dagger and a_h creates a particle and a hole respectively, E_{β_n} are the unknown eigenvalues of the Hamiltonian H within the n -phonon subspace

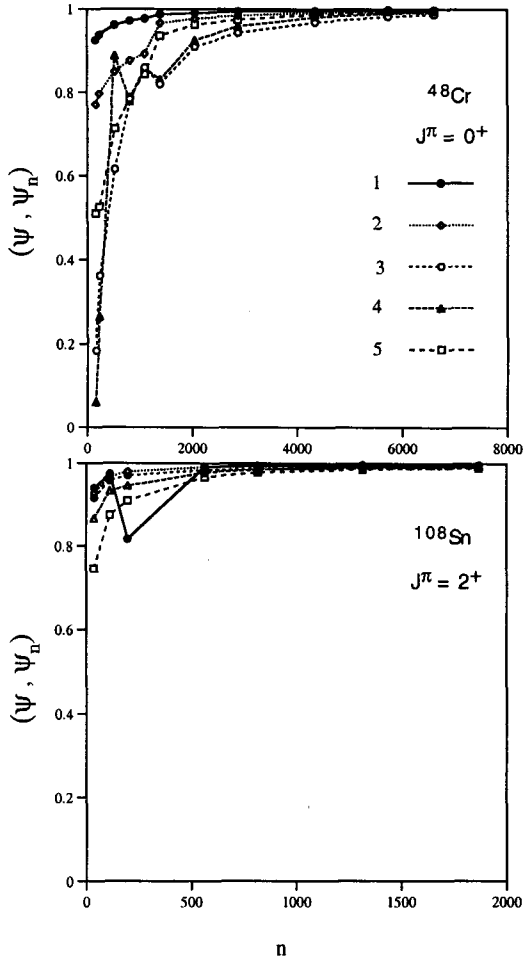


Figure 2. Overlap of sampled wave functions with the corresponding exact ones.

with eigenvectors $|n; \beta_n \rangle$, and

$$X_{\alpha_{n-1}\beta_n}^{(ph)} \equiv \langle n; \beta_n | a_p^\dagger a_h | n-1; \alpha_{(n-1)} \rangle \quad (8)$$

are the unknown amplitudes to be determined. Once the commutator is unfolded, we get after some manipulations a set of equations in $X_{\alpha_{n-1}\beta_n}^{(ph)}$. These equations establish recurrence relations between subspaces with different number of phonons. They can therefore be solved iteratively, thereby generating the full multiphonon basis up to any N . As in all methods adopt-

ing a multiphonon basis, the states so generated, being composed of products of microscopic ph phonons, cannot be properly antisymmetrized and, therefore, form an overcomplete set. We, however, eliminate exactly and completely the redundant states in each n -phonon subspace by adopting a procedure based on the Choleski decomposition, which allows to extract the correct number of linear independent states, out of the overcomplete set. The latter method leaves unchanged also the phonon structure of the basis states and, therefore, allows to eliminate naturally and maximally the spurious admixtures induced by the center of mass motion.

Once represented in the multiphonon basis so constructed, the Hamiltonian matrix has a relatively simple structure and, therefore, can be reduced drastically in sizes and easily diagonalized.

We are presently testing the method on ^{16}O . This nucleus has been studied already in several approaches^{15,16,17,18}. The goal of the test is to explore the potential of the method in relation to the other approaches and in the perspective of facing more complex nuclei. The results will be given in a forthcoming paper¹⁰.

4. Concluding Remarks

We have outlined a new algorithm for solving the nuclear shell model Hamiltonian. Such an iterative algorithm is naturally endowed with an importance sampling, which allows for a drastic truncation of the matrices, while keeping the accuracy of the solutions under strict control.

The importance sampling has the further important virtue of providing scaling laws for the energies which allow to extrapolate to the exact eigenvalues. Since the truncation is far more effective in nuclei with neutron excess, we feel confident that the sampling may be successfully applied to heavy nuclei.

We have also briefly outlined an equation of motion method, complementary to the shell model algorithm, which is intended to provide an exact and thorough description of collective modes within a microscopic multiphonon space. This work is in progress and will be presented elsewhere¹⁰

Acknowledgments

This work is partly supported by the Ministero dell' Istruzione, Università e Ricerca (MIUR).

References

1. See for instance J.A. White, S.E. Koonin, and D.J. Dean, *Phys. Rev. C* **61**, 034303 (2000).
2. T. Otsuka, M. Honma, and T. Mizusaki, *Phys. Rev. Lett.* **81**, 1588 (1998).
3. See for instance G. H. Golub and C. F. Van Loan, *Matrix Computations*, (John Hopkins University Press, Baltimore 1996).
4. F. Andreozzi, A. Porrino, and N. Lo Iudice, *J. Phys. A: Math. Gen.* **35** (2002) L61.
5. F. Andreozzi, N. Lo Iudice, and A. Porrino, *J. Phys. : Nucl. Part. Phys.* **29** (2003) 2319.
6. D. J. Rowe, *Rev. Mod. Phys.* **40**, 153 (1968).
7. S. T. Belyaev and V. G. Zelevinsky, *Nucl. Phys.* **39**, 582 (1962)
8. A. Klein and E. R. Marshalek, *Rev. Mod. Phys.* **63**, 375 (1991) and references therein.
9. V. G. Soloviev, *Theory of Atomic Nuclei: Quasiparticles and Phonons* (Institute of Physics Bristol, 1992).
10. F. Andreozzi, N. Lo Iudice, A. Porrino, F. Knapp, and J. Kvasil, to be submitted for publication.
11. I. Shavitt, C. F. Bender, A. Pipano, and R. P. Hosteny, *J. Computational Phys.* **11**, 90 (1973).
12. A. Ruhe, in *Lecture Notes in Mathematics* **527**, edited by A. Dold and B. Eckmann, (Springer-Verlag, Berlin 1977) p. 130.
13. J.H. Wilkinson, *The Algebraic Eigenvalue Problem*, (Clarendon Press, Oxford, 1965) p. 71.
14. M. Horoi, A. Volya, and V. Zelevinsky, *Phys. Rev. Lett.* **82** (1999) 2064.
15. G. E. Brown, A. M. Green, *Nucl. Phys.* **75**, 401 (1966)
16. W. C. Haxton and C. J. Johnson, *Phys. Rev. Lett.* **65**, 1325 (1990).
17. H. Feshbach and F. Iachello, *Phys. Lett.* **B 45**, 7 (1990).
18. E. K. Warburton, B. A. Brown, D. J. Millener, *Phys. Lett.* **B 293**, 7 (1992)

Q-PHONON APPROACH FOR LOW-LYING 1^- TWO-PHONON STATES IN SPHERICAL NUCLEI

R. V. JOLOS, N. YU. SHIRIKOVA AND V. V. VORONOV

*Joint Institute for Nuclear Research,
141980, Dubna, Moscow Region, Russia
E-mail: voronov@theor.jinr.ru*

The properties of 1^- two-phonon states and the characteristics of E1 transition probabilities between low-lying collective states in spherical nuclei are analyzed within the Q -phonon approach. Several relations between observables are obtained. Microscopic calculations of the E1 $0_1^+ \rightarrow 1^-$ transition matrix elements are performed on the basis of the RPA. A satisfactory description of the experimental data is obtained.

1. Introduction

In investigations of the E1 transitions¹⁻⁷ the low-lying 1^- have been observed in spherical nuclei states, which are characterized by strong $B(E1; 0_1^+ \rightarrow 1^-)$, of the order of several units $\times 10^{-3} e^2 fm^2$. It was demonstrated that these low-lying 1^- states arise as $|2_1^+ \otimes 3_1^-; 1^- M\rangle$ due to coupling of the collective quadrupole 2_1^+ and the collective octupole 3_1^- states. Similar 1^- states have been observed in the Cd, Sn, Ba, Ce, Nd, and Sm isotopes. Their two-phonon character has been proved by the observed strong E2 and E3 transitions to the corresponding one-phonon states^{5,6,7} and by the fact that the energies of these 1^- states are very close to the summed energies $E(2_1^+) + E(3_1^-)$.

Strong correlations between the values of $B(E1; 0_1^+ \rightarrow 1^-)$ and the product of average squares of the quadrupole $\langle \beta_2^2 \rangle$ and octupole $\langle \beta_3^2 \rangle$ deformation parameters in non-magic nuclei⁸ clearly show that away from the closed shells the large $B(E1)$ values have a collective nature connected with the motion of the nuclear shape. The ratio $B(E1)/(\langle \beta_2^2 \rangle \langle \beta_3^2 \rangle)$ is amazingly constant, although the $B(E1)$ strength varies by an order of magnitude in the considered nuclei. Analyzing the experimental data on the ratio $B(E1; 1_1^- \rightarrow 0_1^+)/B(E1; 3_1^- \rightarrow 2_1^+)$ it was shown in Ref. 9 that this ratio is a constant equal to 1 within a factor of 2 although these E1 transi-

tion strengths can differ by about two orders of magnitude for different nuclei. Considered nuclei are rather vibrational and can be understood, at least qualitatively, in a harmonic phonon picture. In the last model $B(E1;1_1^- \rightarrow 0_1^+)/B(E1;3_1^- \rightarrow 2_1^+) = \frac{7}{3}$. This correlation of the E1 strengths can be considered as an additional support for the quadrupole–octupole coupled character of the 1_1^- states.

The $B(E1;1_1^- \rightarrow 2_1^+)$ is small in Sn isotopes; however, it increases in Cd, Te isotopes¹⁰.

A minimum has been found in the A -dependence of $B(E1;1_1^- \rightarrow 0_1^+)$ in the Nd, Sm and Ba isotopes when the number of neutrons N is equal to 78 or 86^{11,12,13}. This characteristic feature of the behavior of $B(E1;1_1^- \rightarrow 0_1^+)$ as a function of N has been discovered earlier in the RPA-based calculations in Ref. 14.

Summarizing experimental data one can see that the microscopical model describing strong E1 transitions at low energies basing on the two-phonon quadrupole–octupole model of the low lying 1_1^- states should explain experimental data.

To analyze experimental data mentioned above we suggested the Q -phonon approach for a description of low-lying 1^- two-phonon states recently¹⁵.

2. Model

In Ref. 16 the Q -phonon approach to the description of the positive parity collective states was developed within the IBM.

In contrast to Ref. 16, where the Q -phonon approach was formulated for the bosonic configurational space of the IBM, our approach is formulated for the fermionic configurational space. In addition, we consider both positive and negative parity states.

In the Q -phonon approach the 2_1^+ state is presented by the following expression

$$|2_1^+, \mu\rangle = N_{2_1^+} \hat{Q}_{2\mu} |0_1^+\rangle, \quad (1)$$

where $|0_1^+\rangle$ is the ground state vector, $N_{2_1^+} = \left(\frac{1}{\sqrt{5}} \langle 0_1^+ | (\hat{Q}_2 \hat{Q}_2)_0 | 0_1^+ \rangle \right)^{-1/2} = \sqrt{5} / | \langle 0_1^+ || Q_2 || 2_1^+ \rangle |$ and $\hat{Q}_{2\mu}$ is in our case the standard shell model quadrupole moment operator

$$\hat{Q}_{2\mu} = \sum_{jj'mm'} \langle jm | r^2 Y_{2\mu} | j'm' \rangle a_{jm}^+ a_{j'm'}, \quad (2)$$

expressed in terms of the nucleon creation a_{jm}^+ and annihilation $a_{j'm'}$, operators.

Let us include into consideration the octupole mode

$$|3_1^-, \nu\rangle = N_{3_1^-} \hat{Q}_{3\nu} |0_1^+\rangle, \quad (3)$$

where $N_{3_1^-} = \left(\frac{1}{\sqrt{7}} \langle 0_1^+ | (\hat{Q}_3 \hat{Q}_3)_0 | 0_1^+ \rangle \right)^{-1/2} = \sqrt{7} / | \langle 0_1^+ \| Q_3 \| 3_1^- \rangle |$ and $\hat{Q}_{3\nu}$ is the fermionic octupole moment operator

$$\hat{Q}_{3\nu} = \sum_{jj'mm'} \langle jm | r^3 Y_{3\mu} | j'm' \rangle a_{jm}^+ a_{j'm'}. \quad (4)$$

As we know from the RPA type calculations¹⁷ both expressions (1) and (3) are very good approximations for the lowest collective 2^+ and 3^- states.

Continuing along this line and remembering that the 1_1^- state is mainly a quadrupole–octupole two–phonon state we suggest for the 1_1^- state vector that

$$|1_1^-, M\rangle = N_{1_1^-} \left(\hat{Q}_2 \hat{Q}_3 \right)_{1M} |0_1^+\rangle, \quad (5)$$

where for $N_{1_1^-}$ we obtain the following relation:

$$\begin{aligned} \left(N_{1_1^-} \right)^{-2} &= \left(N_{2_1^+} \right)^{-2} \left(N_{3_1^-} \right)^{-2} \\ &+ \frac{1}{\sqrt{5}} \sum_{n \neq 1} \langle 0_1^+ | (Q_2 Q_2)_0 | 0_n^+ \rangle \langle 0_n^+ | (Q_3 Q_3)_0 | 0_1^+ \rangle \\ &+ \frac{2\sqrt{30}}{35} \langle 0_1^+ | ((Q_2 Q_2)_2 (Q_3 Q_3)_2)_0 | 0_1^+ \rangle \\ &+ \frac{\sqrt{11}}{7\sqrt{5}} \langle 0_1^+ | ((Q_2 Q_2)_4 (Q_3 Q_3)_4)_0 | 0_1^+ \rangle \end{aligned} \quad (6)$$

The last three terms in the right–hand side of expression (6) can give a noticeable contribution only in the case of strong mixing of the two–phonon quadrupole–quadrupole and two–phonon octupole–octupole states. However, as it is known from the RPA type calculations¹⁸, this mixing is insignificant: less than 1%. Neglecting these terms we obtain an approximate relation

$$N_{1_1^-} \approx N_{2_1^+} N_{3_1^-}. \quad (7)$$

The wave vector (5) can be written in terms of the RPA collective phonons and the two–quasiparticle components which correspond to the noncollective RPA solutions. Written in this way the wave vector (5) has the

two-phonon component with one quadrupole and one octupole collective RPA phonons as the main component, the three-phonon component with two collective quadrupole and one collective octupole RPA phonons, and the two-quasiparticle 1^- components. It means that the results of our Q -phonon approach should be compared not with the pure RPA calculations but with the RPA based calculations which include also anharmonic effects. A contribution of the last two components to the norm of the wave vector (5) is very small for nuclei considered in the present paper.

The strength of the Q -phonon scheme lies in a possibility to derive relations between electromagnetic transition matrix elements also outside the analytically solvable harmonic vibrator and rotor limits. This is possible because of the simple form of the wave vectors in this approach. However, the wave vectors (1), (3) and (5) only look simple. The multipole moment operators in these expressions act on the exact ground state. Thus, for calculations we needed an expression for the ground state vector. In section V we take as an approximation to the ground state vector the vacuum state of the RPA phonons.

Let us apply the model formulated above to calculations of the matrix element of the $E1$ $0_1^+ \rightarrow 1_1^-$ transition. We obtain

$$\langle 1_1^-, M | M_{1M}(E1) | 0_1^+ \rangle = N_{1_1^-} \langle 0 | (Q_2 Q_3)_{1M} M_{1M}(E1) | 0_1^+ \rangle, \quad (8)$$

where $M_{1M}(E1)$ is the operator of the electric dipole transition. Since multipole operators Q_2 , Q_3 and $M(E1)$ commute with each other we can rewrite the last expression as

$$\begin{aligned} & \langle 1_1^-, M | M_{1M}(E1) | 0_1^+ \rangle = \\ & N_{1_1^-} \sum_{\mu, \nu} C_{2\mu 3\nu}^{1M} \langle 0_1^+ | (-1)^\nu Q_{3-\nu} M_{1M}(E1) (-1)^\mu Q_{2-\mu} | 0_1^+ \rangle \end{aligned} \quad (9)$$

Using expressions (1), (3) and relation (7) we can rewrite (9) in the following way:

$$\langle 1_1^-, M | M_{1M}(E1, M) | 0_1^+ \rangle = \sum_{\mu, \nu} C_{2\mu 3\nu}^{1M} (-1)^\mu \langle 3_1^-, \nu | M_{1M}(E1) | 2_1^+, -\mu \rangle$$

From the last expression using the Wigner-Eckart theorem we obtain

$$\langle 1_1^- || M(E1) || 0_1^+ \rangle = \langle 3_1^- || M(E1) || 2_1^+ \rangle, \quad (10)$$

and from (10) we get

$$B(E1; 1_1^- \rightarrow 0_1^+) / B(E1; 3_1^- \rightarrow 2_1^+) = \frac{7}{3}. \quad (11)$$

The last value coincides with that of the harmonic phonon picture. However, we did not use the assumption of harmonicity of quadrupole and octupole vibrations. Thus, the Q -phonon model explains qualitatively one of the experimental results mentioned in Introduction.

3. E1 transition $1_1^- \rightarrow 2_1^+$

Let us consider the matrix element $\langle 1_1^- M' | M_{1\mu}(E1) | 2_1^+ M \rangle$. This matrix element can be written in the following way:

$$\langle 1_1^- M' | M_{1\mu}(E1) | 2_1^+ M \rangle = N_{2_1^+} \langle 1_1^- M' | Q_{2M} M_{1\mu}(E1) | 0_1^+ \rangle \quad (12)$$

Having in mind that the $0_1^+ \rightarrow 1_1^-$ transition is the strongest one among the low-lying states we can rewrite approximately (12) as

$$\langle 1_1^- M' | M_{1\mu}(E1) | 2_1^+ M \rangle \approx N_{2_1^+} \langle 1_1^- M' | Q_{2M} | 1_1^- \mu \rangle \langle 1_1^- \mu | M_{1\mu}(E1) | 0_1^+ \rangle$$

and as a consequence we obtain

$$\frac{\langle 1_1^- || M(E1) || 2_1^+ \rangle}{\langle 1_1^- || M(E1) || 0_1^+ \rangle} = \sqrt{\frac{5}{3}} \frac{\langle 1_1^- || Q_2 || 1_1^- \rangle}{\langle 0_1^+ || Q_2 || 2_1^+ \rangle} \quad (13)$$

The quadrupole moment of the 1_1^- state can be expressed approximately in terms of the quadrupole moments of the 2_1^+ and 3_1^- states. Finally, we have

$$\frac{\langle 1_1^- || M(E1) || 2_1^+ \rangle}{\langle 1_1^- || M(E1) || 0_1^+ \rangle} \approx \frac{1}{\sqrt{35}} \frac{\langle 2_1^+ || Q_2 || 2_1^+ \rangle}{\langle 0_1^+ || Q_2 || 2_1^+ \rangle} + \frac{\sqrt{6}}{\sqrt{35}} \frac{\langle 3_1^- || Q_2 || 3_1^- \rangle}{\langle 0_1^+ || Q_2 || 2_1^+ \rangle}. \quad (14)$$

From (14) we can see that going from the magic or semimagic nuclei to nuclei with open shell the ratio $B(E1; 1_1^- \rightarrow 2_1^+)/B(E1; 1_1^- \rightarrow 0_1^+)$ increases with the quadrupole moments of the first 2^+ and 3^- states.

4. RPA based microscopic consideration

The aim of this section is to calculate the dipole transitional matrix element $\langle 1_1^- || M(E1) || 0_1^+ \rangle$, basing on expressions (1), (3) and (5) for the state vectors $|2_1^+\rangle$, $|3_1^-\rangle$ and $|1_1^-\rangle$ and on the RPA approximation for the ground state. Thus, in the calculations below it is assumed that the wave vectors of the 2_1^+ , 3_1^- and 1_1^- states are

$$|2_1^+, \mu\rangle = \tilde{N}_{2_1^+} \hat{Q}_{2\mu} |0_1^+, RPA\rangle, \quad (15)$$

$$|3_1^-, \nu\rangle = \tilde{N}_{3_1^-} \hat{Q}_{3\nu} |0_1^+, RPA\rangle, \quad (16)$$

and

$$|1_1^-, M\rangle = \tilde{N}_{1_1^-} \left(\hat{Q}_2 \hat{Q}_3 \right)_{1M} |0_1^+, RPA\rangle, \quad (17)$$

Since the derivation of relations (11) and (14) is independent of a concrete structure of the 0_1^+ state and is based only on the Q -phonon form of the wave vectors, the results obtained below are consistent with relations (11) and (14).

We assume below that the ground state contains only those correlations which are produced by the quadrupole–quadrupole and the octupole–octupole interactions. Therefore, calculating the strength of the E1 transitions we must introduce the core polarization factor χ which takes into account a shift of a part of the E1 strength to the giant dipole resonance¹⁹. We mention that the RPA-type calculations of the E1 transitions were performed in Refs.14, 20.

The components of the wave vectors of the 2_1^+ , 3_1^- and 1_1^- states, containing operators creating two–quasiparticle 1^- states, appear because the quadrupole and the octupole multipole operators representing the corresponding state vectors according to (1), (3) and (5), are not exhausted by the one–boson term expressed in collective bosons only. In the calculations based on the Quasiparticle–Phonon model^{17,18,14,20} this admixture is generated by the quasiparticle–phonon coupling term which is produced by the terms in Q_2 and Q_3 additional to the one–boson term. However, the weight of this contribution in the norm of the eigenstate is similar in both the approaches. An expression for the reduced matrix element $\langle 1_1^- \| M(E1) \| 0_1^+ \rangle$ is given in Ref. 15.

The results of the calculations of the electric dipole transition matrix elements are presented in the Tables 1,2.

Here besides the total calculated dipole transitional matrix element $|\langle 1_1^- \| M(E1) \| 0_1^+ \rangle|_{total}$ including all contributions the results obtained without inclusion of the contribution coming the $I^\pi = 1^-$ two–quasiparticle admixture denoted by $|\langle 1_1^- \| M(E1) \| 0_1^+ \rangle|_{T=0}$ are also shown.

The results presented in Tables 1 and 2 show that in Cd, Sn, Ba, Ce and partly in Nd and Sm isotopes the experimental data are between the results of calculations obtained with and without a contribution of an admixture of a dipole two–quasiparticle component to the 1_1^- state. However, in many cases the matrix element $|\langle 0_1^+ \| M \| 1_1^- \rangle|_{T=0}$, which includes only a collective contribution, is closer to the experimental data than the total matrix element, which includes both collective and two–quasiparticle contri-

Table 1. The experimental (ex) and calculated electric dipole transition matrix elements for Cd, Sn and Ba isotopes obtained including all contributions (tot) and without a contribution of the two-quasiparticle admixture to the 1_1^- state ($T=0$) (in units $e \cdot fm$).

Nucleus	$ \langle 1^- \parallel M(E1) \parallel 0^+ \rangle _{tot}$	$ \langle 1^- \parallel M(E1) \parallel 0^+ \rangle _{T=0}$	$ \langle 1^- \parallel M(E1) \parallel 0^+ \rangle _{ex}$
^{108}Cd	0.140	0.018	0.050
^{110}Cd	0.119	0.024	0.048
^{112}Cd	0.115	0.026	0.041
^{114}Cd	0.114	0.031	0.044
^{116}Cd	0.109	0.036	0.034
^{116}Sn	0.170	0.066	0.081
^{118}Sn	0.173	0.073	0.085
^{120}Sn	0.169	0.076	0.087
^{122}Sn	0.156	0.073	0.085
^{124}Sn	0.134	0.063	0.078
^{134}Ba	0.086	0.019	0.048
^{136}Ba	0.113	0.040	0.071
^{138}Ba	0.160	0.082	0.114
^{140}Ba	0.152	0.074	-
^{142}Ba	0.153	0.078	-
^{144}Ba	0.158	0.079	-

butions. Nevertheless, we can see that the two-quasiparticle admixture to the collective quadrupole–octupole two-phonon component of the 1_1^- state should be taken into account to improve agreement with the experimental data.

Both sets of the results obtained with and without inclusion of the

Table 2. The same as in Table 1 but for Ce, Nd and Sm isotopes.

Nucleus	$ \langle 1^- \parallel M(E1) \parallel 0^+ \rangle _{tot}$	$ \langle 1^- \parallel M(E1) \parallel 0^+ \rangle _{T=0}$	$ \langle 1_1^- \parallel M(E1) \parallel 0^+ \rangle _{ex}$
^{140}Ce	0.179	0.099	0.129
^{142}Ce	0.170	0.092	0.108
^{144}Ce	0.190	0.114	-
^{146}Ce	0.209	0.134	-
^{142}Nd	0.189	0.108	0.128
^{144}Nd	0.181	0.101	0.098
^{146}Nd	0.187	0.111	0.071
^{148}Nd	0.223	0.141	0.119
^{144}Sm	0.193	0.115	0.140
^{146}Sm	0.177	0.103	-
^{148}Sm	0.190	0.116	0.052
^{150}Sm	0.212	0.132	0.099

contribution of the two-quasiparticle component of the 1_1^- state reproduce also an experimental A -dependence of the reduced matrix element.

Concluding this section we should like to stress that any microscopic consideration of the enhanced E1 transitions cannot be performed in a harmonic approximation, *i.e.*, cannot be carried out in the framework of the pure RPA and requires from the beginning an inclusion of the anharmonic effects.

5. Summary

In conclusion, based on the Q -phonon representation of the wave vectors of the low-lying collective states we have derived the relations between different reduced matrix elements of the E1 transition operator. These relations explain qualitatively the experimentally observed correlations among data on E1 transitions.

It is shown that the two-quasiparticle component of the wave vector of the $|1_1^- \rangle$ state should be taken into account to achieve an agreement with the experimental data in spite of a small contribution of this component to the norm of the $|1_1^- \rangle$ state.

References

1. T. Guhr, K.D. Hummel, G. Kilgus *et al.*, *Nucl.Phys.* **A501**, 95 (1989).
2. A. Zilges, P. von Brentano, H. Friedrichs *et al.*, *Z.Phys.* **A340**, 155 (1991).
3. U. Kneissl, H.H.Pitz and A. Zilges, *Prog.Part.Nucl.Phys.* **37**, 349 (1996).
4. C. Fransen, O. Beck, P. von Brentano *et al.*, *Phys.Rev.* **C57**, 129 (1998).
5. S.J. Robinson, J. Jolie, H.G. Börner *et al.*, *Phys.Rev.Lett.* **73**, 412 (1994).
6. M. Wilhelm, E. Radermacher, A. Zilges *et al.*, *Phys.Rev.* **C54**, R449 (1996).
7. M. Wilhelm, S. Kasemann, G. Pascovici *et al.*, *Phys.Rev.* **C57**, 577 (1998).
8. M. Babilon, T. Hartmann, P. Mohr *et al.*, *Phys.Rev.* **C65**, 037303 (2002).
9. N. Pietralla, *Phys.Rev.* **C59**, 2941 (1999).
10. W. Andrejtscheff *et al.*, *Phys.Lett.* **B506**, 239 (2001).
11. F.R. Metzger, *Phys.Rev.* **C14**, 543 (1976).
12. F.R. Metzger, *Phys.Rev.* **C18**, 2138 (1978).
13. T. Eckert, O. Beck, J. Besserer *et al.*, *Phys.Rev.* **C56**, 1257 (1997).
14. V.V. Voronov *et al.*, *Bull.Acad.Sci. USSR, Ser.Phys.* **48**, 190 (1984).
15. R.V. Jolos *et al.*, *Phys. Rev.* **C70** 054303 (2004).
16. N. Pietralla *et al.*, *Phys.Rev.Lett.* **73**, 2962 (1994).
17. V.G. Soloviev, *Theory of complex nuclei*, Oxford, Pergamon Press, 1976.
18. M. Grinberg *et al.*, *Particles and Nuclei*, **29**, 1456 (1998).
19. A. Bohr and B.R. Mottelson, *Nuclear Structure*, vol. 2 (Benjamin, 1975).
20. N. Tsoneva, H. Lenske and Ch. Stoyanov, *Nucl.Phys.* **A731**, 273 (2004).

ANALYTIC DESCRIPTION OF THE SHAPE PHASE TRANSITION FROM OCTUPOLE DEFORMATION TO OCTUPOLE VIBRATIONS

DENNIS BONATSOS*, D. LENIS, D. PETRELLIS
*Institute of Nuclear Physics, N.C.S.R. "Demokritos",
GR-15310 Aghia Paraskevi, Attiki, Greece*
* E-mail: bonat@inp.demokritos.gr

N. MINKOV**, P. YOTOV
*Institute for Nuclear Research and Nuclear Energy,
Bulgarian Academy of Sciences,
72 Tzarigrad Road, BG-1784 Sofia, Bulgaria*
** E-mail: nminkov@inrne.bas.bg

An analytic collective model in which the relative presence of the quadrupole and octupole deformations is determined by a parameter (ϕ_0), while axial symmetry is obeyed, is developed. The model [to be called the Analytic Quadrupole Octupole Axially symmetric model (AQOA)] involves an infinite well potential, provides predictions for energy and $B(EL)$ ratios which depend only on ϕ_0 , draws the border between the regions of octupole deformation and octupole vibrations in an essentially parameter-independent way, and in the actinide region describes well ^{226}Th and ^{226}Ra , for which experimental energy data are shown to suggest that they lie close to this border. The similarity of the AQOA results with $\phi_0 = 45^\circ$ for ground state band spectra and $B(E2)$ transition rates to the predictions of the X(5) model is pointed out.

1. Introduction

Shape phase transitions in nuclear structure have been recently described in terms of critical point symmetries, leading to parameter-free (up to overall scale factors) predictions for spectra and transition probabilities. The $E(5)^1$ and $X(5)^2$ critical point symmetries introduced so far deal with the quadrupole degree of freedom alone. On the other hand, it is known³ that in the light actinides octupole deformations and octupole vibrations occur. It is the aim of the present work to provide an analytic description of the light actinides lying near the border between the regions of octupole vi-

brations and octupole deformation, through the use of a model containing the minimum number of free parameters, which will be called the Analytic Quadrupole Octupole Axially symmetric (AQOA) model. A non-analytic description of the same problem has been given recently in Ref. 4.

In Sec.2 the AQOA model is formulated, while numerical results and comparisons to experiment are given in Sec.3. Finally Sec.4 contains discussion of the present results and plans for further work.

2. The Analytic Quadrupole Octupole Axially Symmetric (AQOA) Model

We consider a nucleus in which quadrupole deformation (β_2) and octupole deformation (β_3) coexist. We take only axially symmetric deformations into account, which implies that the γ degrees of freedom are ignored, as in the Davydov–Chaban approach⁵. The body-fixed axes x' , y' , z' are taken along the principal axes of inertia of the (axially symmetric) nucleus, while their orientation relative to the laboratory-fixed axes x , y , z is described by the Euler angles $\theta = \{\theta_1, \theta_2, \theta_3\}$. The Hamiltonian reads^{6,7}

$$H = - \sum_{\lambda=2,3} \frac{\hbar^2}{2B_\lambda} \frac{1}{\beta_\lambda^3} \frac{\partial}{\partial \beta_\lambda} \beta_\lambda^3 \frac{\partial}{\partial \beta_\lambda} + \frac{\hbar^2 \hat{L}^2}{6(B_2\beta_2^2 + 2B_3\beta_3^2)} + V(\beta_2, \beta_3) \quad (1)$$

where B_2 , B_3 are the mass parameters.

We seek solutions of the Schrödinger equation of the form⁶

$$\Phi_L^\pm(\beta_2, \beta_3, \theta) = (\beta_2\beta_3)^{-3/2} \Psi_L^\pm(\beta_2, \beta_3) |LM0, \pm\rangle, \quad (2)$$

where the function $|LM0, \pm\rangle$ describes the rotation of an axially symmetric nucleus with angular momentum projection M onto the laboratory-fixed z -axis and projection $K = 0$ onto the body-fixed z' -axis. The moment of inertia with respect to the symmetry axis z' is zero, implying that levels with $K \neq 0$ lie infinitely high in energy⁶. Therefore in this model we are restricted to states with $K = 0$ only. The function $|LM0, +\rangle$ transforms according to the irreducible representation (irrep) A of the group D_2 , while the function $|LM0, -\rangle$ transforms according to the irrep B_1 of the same group^{6,7}. The general form of these functions is⁸

$$|LMK, \pm\rangle = \sqrt{\frac{2L+1}{16\pi^2(1+\delta_{K0})}} (D_{K,M}^L(\theta) \pm (-1)^L D_{-K,M}^L(\theta)). \quad (3)$$

In the special case of $K = 0$ it is clear that $|LM0, +\rangle \neq 0$ for $L = 0, 2, 4, \dots$, while $|LM0, -\rangle \neq 0$ for $L = 1, 3, 5, \dots$. The functions $\Psi_L^\pm(\beta_2, \beta_3)$ and

$\Psi_L^-(\beta_2, \beta_3)$ are respectively symmetric and antisymmetric with respect to reflection in the plane $x'y'$, and therefore describe states with positive and negative parity respectively⁷.

Using the solutions of Eq.(2) for the Hamiltonian of Eq.(1), introducing^{6,7} $\tilde{\beta}_2 = \beta_2\sqrt{B_2/B}$, $\tilde{\beta}_3 = \beta_3\sqrt{B_3/B}$, $B = (B_2 + B_3)/2$, reduced energies $\epsilon = (2B/\hbar^2)E$ and reduced potentials $u = (2B/\hbar^2)V$ ^{1,2}, as well as polar coordinates (with $0 \leq \tilde{\beta} < \infty$ and $-\pi/2 \leq \phi \leq \pi/2$)^{6,7} $\tilde{\beta}_2 = \tilde{\beta} \cos \phi$, $\tilde{\beta}_3 = \tilde{\beta} \sin \phi$, $\tilde{\beta} = \sqrt{\tilde{\beta}_2^2 + \tilde{\beta}_3^2}$, the Schrödinger equation takes the form

$$\left[-\frac{\partial^2}{\partial \tilde{\beta}^2} - \frac{1}{\tilde{\beta}} \frac{\partial}{\partial \tilde{\beta}} + \frac{L(L+1)}{3\tilde{\beta}^2(1+\sin^2\phi)} - \frac{1}{\tilde{\beta}^2} \frac{\partial^2}{\partial \phi^2} + u(\tilde{\beta}, \phi) + \frac{3}{\tilde{\beta}^2 \sin^2 2\phi} - \epsilon_L \right] \times \Psi_L^\pm(\tilde{\beta}, \phi) = 0. \quad (4)$$

Separation of variables in Eq.(4) can be achieved by assuming the potential to be of the form $u(\tilde{\beta}, \phi) = u(\tilde{\beta}) + u(\tilde{\phi}^\pm)$, where $u(\tilde{\phi}^\pm)$ is supposed to be of the form of two very steep harmonic oscillators centered at the values $\pm\phi_0$, i.e.

$$u(\tilde{\phi}^\pm) = \frac{1}{2}c(\phi \mp \phi_0)^2 = \frac{1}{2}c(\tilde{\phi}^\pm)^2, \quad \tilde{\phi}^\pm = \phi \mp \phi_0, \quad (5)$$

with c being a large constant. In other words, the nucleus is supposed to be rigid with respect to the variable ϕ , implying that ϕ remains close to $\pm\phi_0$ and, therefore, the relative amount of quadrupole and octupole deformation remains constant, as in Strutinsky-type potential energy calculations⁹. This assumption will be (partly) justified *a posteriori* by the fact that the spectrum remains almost unchanged for values of ϕ_0 between 30° and 60°.

In this way Eq. (4) is separated into

$$\left[-\frac{\partial^2}{\partial \tilde{\beta}^2} - \frac{1}{\tilde{\beta}} \frac{\partial}{\partial \tilde{\beta}} + \frac{1}{\tilde{\beta}^2} \left(\frac{L(L+1)}{3(1+\sin^2\phi_0)} + \frac{3}{\sin^2 2\phi_0} \right) + u(\tilde{\beta}) - \epsilon_{\tilde{\beta}}(L) \right] \times \psi_L^\pm(\tilde{\beta}) = 0, \quad (6)$$

and

$$\left[-\frac{1}{\langle \tilde{\beta}^2 \rangle} \frac{\partial^2}{\partial (\tilde{\phi}^\pm)^2} + u(\tilde{\phi}^\pm) - \epsilon_\phi \right] \chi(\tilde{\phi}^\pm) = 0, \quad (7)$$

where $\Psi_L^\pm(\tilde{\beta}, \phi) = \psi_L^\pm(\tilde{\beta})(\chi(\tilde{\phi}^+) \pm \chi(\tilde{\phi}^-))/\sqrt{2}$, while $\langle \tilde{\beta}^2 \rangle$ is the average of $\tilde{\beta}^2$ over $\psi^\pm(\tilde{\beta})$, and $\epsilon_L = \epsilon_{\tilde{\beta}}(L) + \epsilon_\phi$. It is worth noticing that Eq. (6)

has the same form for both $+\phi_0$ and $-\phi_0$, since only even functions of ϕ_0 appear in it.

In the case in which $u(\tilde{\beta})$ is an infinite well potential ($u(\tilde{\beta}) = 0$ if $\tilde{\beta} \leq \tilde{\beta}_W$; $u(\tilde{\beta}) = \infty$ if $\tilde{\beta} > \tilde{\beta}_W$), using the definitions $\epsilon_{\tilde{\beta}} = k_{\tilde{\beta}}^2$, $z = \tilde{\beta}k_{\tilde{\beta}}$, Eq. (6) is brought into the form of a Bessel equation

$$\frac{d^2\psi_{\nu}^{\pm}}{dz^2} + \frac{1}{z} \frac{d\psi_{\nu}^{\pm}}{dz} + \left[1 - \frac{\nu^2}{z^2}\right] \psi_{\nu}^{\pm} = 0, \quad \nu = \sqrt{\frac{L(L+1)}{3(1+\sin^2\phi_0)} + \frac{3}{\sin^2 2\phi_0}}. \quad (8)$$

Then the boundary condition $\psi_{\nu}^{\pm}(\tilde{\beta}_W) = 0$ determines the spectrum

$$\epsilon_{\tilde{\beta},s,\nu} = \epsilon_{\tilde{\beta},s,\phi_0,L} = (k_{s,\nu})^2, \quad k_{s,\nu} = \frac{x_{s,\nu}}{\tilde{\beta}_W}, \quad (9)$$

and the eigenfunctions

$$\psi_{s,\nu}^{\pm}(\tilde{\beta}) = \psi_{s,\phi_0,L}^{\pm}(\tilde{\beta}) = c_{s,\nu} J_{\nu}(k_{s,\nu}\tilde{\beta}), \quad (10)$$

where $x_{s,\nu}$ is the s th zero of the Bessel function $J_{\nu}(z)$, while $c_{s,\nu}$ are normalization constants, determined from the condition $\int_0^{\tilde{\beta}_W} |\psi_{s,\nu}^{\pm}(\tilde{\beta})|^2 \tilde{\beta} d\tilde{\beta} = 1$ to be $c_{s,\nu} = \sqrt{2}/J_{\nu+1}(k_{s,\nu})$. The notation has been kept similar to Ref. 2.

Eq. (7) for the potential of Eq. (5) takes the form of a simple harmonic oscillator equation. The total energy in the present model is then

$$E(s, L, \phi_0, n_{\phi}) = E_0 + A\epsilon_{\tilde{\beta},s,\phi_0,L} + Bn_{\phi}, \quad (11)$$

where n_{ϕ} is the quantum number of the above mentioned oscillator. Only the case with $n_{\phi} = 0$ will be considered in what follows.

In the axial case used here the electric quadrupole and octupole operators are

$$T_{\mu}^{(E2)} = t_2\beta_2 D_{\mu,0}^{(2)}(\theta), \quad T_{\mu}^{(E3)} = t_3\beta_3 D_{\mu,0}^{(3)}(\theta), \quad (12)$$

while the electric dipole operator reads⁶

$$T_{\mu}^{(E1)} = t_1\beta_2\beta_3 D_{\mu,0}^{(1)}(\theta). \quad (13)$$

$B(EL)$ transition rates are calculated using the standard techniques, the final result being

$$B(EL; L_i \rightarrow L_f) = c(c_{s_i,\nu_i}c_{s_f,\nu_f})^2 (L_i L L_f | 000)^2 (I_{\tilde{\beta}}^{(EL)})^2, \quad (14)$$

where the integrals over $\tilde{\beta}$ are

$$I_{\tilde{\beta}}^{(E2)} = I_{\tilde{\beta}}^{(E3)} = \int \tilde{\beta}^2 J_{\nu_i}(k_{s_i,\nu_i}\tilde{\beta}) J_{\nu_f}(k_{s_f,\nu_f}\tilde{\beta}) d\tilde{\beta}, \quad (15)$$

with $I_{\tilde{\beta}}^{(E1)}$ containing an extra factor of $\tilde{\beta}$ and all constant factors having been absorbed in c .

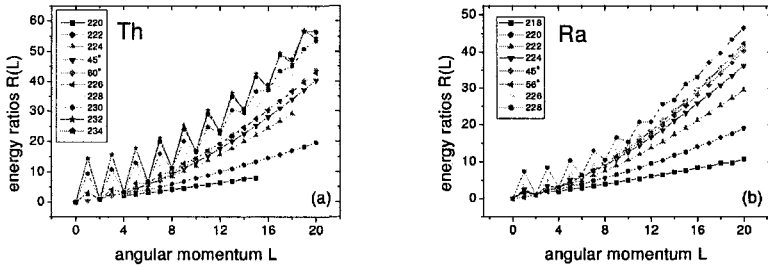


Figure 1. (a) Experimental energy ratios $R(L) = E(L)/E(2_1^+)$ for ^{220}Th [10], ^{222}Th [11], ^{224}Th [12], ^{226}Th [13], ^{228}Th [14], ^{230}Th [15], ^{232}Th [15,16], and ^{234}Th [15], compared to theoretical predictions for $\phi = 45^\circ$ and $\phi = 60^\circ$. (b) Same for ^{218}Ra [17,18], ^{220}Ra [10], ^{222}Ra [15,19], ^{224}Ra [15,19], ^{226}Ra [15,19], and ^{228}Ra [15], compared to theoretical predictions for $\phi = 45^\circ$ and $\phi = 56^\circ$.

3. Numerical Results and Comparison to Experiment

Numerical results indicate that the region of interest in the present model, in which smooth and essentially parameter independent behavior of spectra and $B(EL)$ rates is observed, is the region $30^\circ \leq \phi_0 \leq 60^\circ$, to which further considerations will be limited.

A comparison between the AQOA and X(5) results is also instructive. The ground state band of X(5) lies a little lower than the ground state band of the AQOA model with $\phi_0 = 45^\circ$, while for the $s = 2$ and $s = 3$ bands the AQOA model predictions for $\phi_0 = 45^\circ$ are larger than the X(5) values by almost a factor of two. Furthermore, the $B(E2)$ values in the ground state band of X(5) are slightly higher than the corresponding predictions of the AQOA model for $\phi_0 = 45^\circ$.

The similarities between the ground state bands of the AQOA and X(5) models can be understood as due to the fact that both models originate from the Bohr Hamiltonian and use an infinite well potential, while in addition for the properties of the ground state band the quadrupole degree of freedom, included in both models, is expected to be important. In contrast, the excited bands appear to be more sensitive to the inclusion of the octupole degree of freedom. The position of the 0_2^+ state becomes therefore an important factor in the process of comparison to experiment. One can also think of the AQOA model as an extension of the X(5) framework, in which the negative parity states, as well as the $B(EL)$ transitions involving them, are included.

Experimental data for the ground state and related negative parity

bands of $^{220-234}\text{Th}$ are shown in Fig.1(a). It is clear that ^{226}Th lies on the border between two different regions. Below ^{226}Th the odd-even staggering is very small, while from ^{228}Th up the odd-even staggering is becoming much larger, increasing with the neutron number N . It is clear that below ^{226}Th the situation corresponds to octupole deformation, in which the ground state band and the negative parity band merge into a single band, while above ^{226}Th the picture is corresponding to octupole vibrations, i.e. the negative parity band is a rotational band built on an octupole bandhead, thus lying systematically higher than the ground state band. Theoretical predictions for $\phi = 45^\circ$ lie a little below ^{226}Th , while the $\phi = 60^\circ$ results follow the ^{226}Th data very closely.

A similar picture is observed in $^{218-228}\text{Ra}$, shown in Fig.1(b). In this case octupole deformation appears below ^{226}Ra , while ^{228}Ra is already in the regime of octupole vibrations. Theoretical predictions for $\phi_0 = 45^\circ$ again lie a little below ^{226}Ra , while the ^{226}Ra data are followed quite closely by the predictions of $\phi_0 = 56^\circ$.

As far as the 0_2^+ bandhead is concerned, the experimental values (normalized to the 2_1^+ state) are 12.186 for ^{226}Ra and 11.152 for ^{226}Th , in good agreement with the 11.226 and 12.410 values predicted by the AQOA model for the ϕ_0 values of 56° and 60° used in Fig. 1 . It should be noticed that the normalized 0_2^+ bandhead is lying close to this height for all Ra and Th isotopes for which data exist, namely ^{222}Ra (8.225), ^{224}Ra (10.861), ^{228}Ra (11.300), ^{228}Th (14.402), ^{230}Th (11.934), ^{232}Th (14.794), ^{234}Th (16.347), with data taken from the references used in Fig. 1 .

Considering the AQOA model as an extension of the X(5) framework involving negative parity states implies that the search for X(5)-like nuclei in the light actinides, where the presence of low-lying negative parity bands is important, should be focused on nuclei with $R(4)$ ratio close to 3.0 and 0_2^+ bandhead higher than the X(5) value of 5.65 .

On the results presented in this section, the following additional comments apply.

1) Fig. 1 indicates that ^{226}Th (^{226}Ra) can be well described using the AQOA model with $\phi_0 = 60^\circ$ ($\phi_0 = 56^\circ$), which provides results quite similar to the $\phi_0 = 45^\circ$ case. In all these cases the value of ϕ_0 indicates that the quadrupole and octupole deformations are present in comparable amounts. This is in agreement with Strutinsky-type potential-energy calculations^{9,20}, resulting in comparable β_2 and β_3 values for these nuclei. The presence of octupole deformation in ^{226}Ra has also been realized in a study²¹ within the framework of the spdf-IBM^{22,23}.

2) Fig. 1 suggests that ^{226}Th and ^{226}Ra lie close to the border between octupole deformation and octupole vibrations. This is in agreement with Woods–Saxon–Bogolyubov cranking calculations²⁴ for the Ra and Th isotopes, suggesting shape changes from nearly spherical ($N \simeq 130$) to octupole-deformed ($N \simeq 134$) to well-deformed reflection-symmetric ($N \simeq 140$) shapes, in which negative-parity bands can be interpreted in terms of octupole vibrations.

3) One can easily see that no odd–even staggering is predicted by the AQOA model. This is in agreement to the well known fact that odd-even staggering is produced when the potential in β_3 is a double well with two symmetric minima²⁵, the staggering being sensitive to the angular momentum dependence of the height of the potential barrier²⁶. An infinitely high barrier leads to no odd-even staggering²⁵, which is indeed the case here. The introduction of a finite barrier in the present model will lead to staggering, but it will require the addition of at least one new parameter, in contrast to the main goal of the present work, which is the description of the border between octupole deformation and octupole vibrations with the minimum number of parameters possible. As shown in Figs. 1(a) and 1(b), the model does predict the border between the regions of octupole deformation and octupole vibrations in an essentially parameter independent way.

4) It should be noticed that the transition examined here is the one from octupole deformation to octupole vibrations as a function of the neutron number in a chain of isotopes, which is different from the gradual setting in of octupole deformation as a function of angular momentum in a given nucleus, usually studied by considering the odd-even staggering^{27,28}.

4. Discussion

The analytic quadrupole octupole axially symmetric (AQOA) model introduced in this work describes well the border between octupole deformation and octupole vibrations in the light actinides, which corresponds to ^{226}Th and ^{226}Ra in the Th and Ra isotopic chains respectively. Some of the main ingredients of the present model, such as the infinite well potential and the approximate separation of variables, strongly resemble the ones used in the X(5) model, describing the critical point of the shape phase transition from vibrational to axially deformed rotational nuclei², determined through the study of potential energy surfaces derived from the Hamiltonian of the Interacting Boson Model²⁹. An interesting task is the study of the potential

energy surfaces resulting in the spdf-IBM^{22,23}, the version of IBM including the octupole degree of freedom in addition to the quadrupole one, which can possibly lead to the determination of a shape phase transition from octupole deformation to octupole vibrations. Although some early results are given in Ref. 23, this task is far from complete. The inclusion of staggering in the present model, as well as its application to the rare earth region near $A = 150$, where octupole deformation is known to occur³, are also of interest.

References

1. F. Iachello, *Phys. Rev. Lett.* **85**, 3580 (2000).
2. F. Iachello, *Phys. Rev. Lett.* **87**, 052502 (2001).
3. P. A. Butler and W. Nazarewicz, *Rev. Mod. Phys.* **68**, 349 (1996).
4. P. G. Bizzeti and A. M. Bizzeti-Sona, *Phys. Rev.* **C70**, 064319 (2004).
5. A. S. Davydov and A. A. Chaban, *Nucl. Phys.* **20**, 499 (1960).
6. A. Ya. Dzyublik and V. Yu. Denisov, *Yad. Fiz.* **56**, 30 (1993) [*Phys. At. Nucl.* **56**, 303 (1993)].
7. V. Yu. Denisov and A. Ya. Dzyublik, *Nucl. Phys.* **A589**, 17 (1995).
8. A. Bohr and B. R. Mottelson, *Nuclear Structure*, Vol. II (Benjamin, New York, 1975).
9. W. Nazarewicz *et al.*, *Nucl. Phys.* **A429**, 269 (1984).
10. A. Artna-Cohen, *Nucl. Data Sheets* **80**, 157 (1997).
11. Y. A. Akovali, *Nucl. Data Sheets* **77**, 271 (1996).
12. A. Artna-Cohen, *Nucl. Data Sheets* **80**, 227 (1997).
13. Y. A. Akovali, *Nucl. Data Sheets* **77**, 433 (1996).
14. A. Artna-Cohen, *Nucl. Data Sheets* **80**, 723 (1997).
15. J. F. C. Cocks *et al.*, *Nucl. Phys.* **A645**, 61 (1999).
16. M. R. Schmorak, *Nucl. Data Sheets* **63**, 139 (1991).
17. Y. A. Akovali, *Nucl. Data Sheets* **76**, 457 (1995).
18. N. Schulz *et al.*, *Phys. Rev. Lett.* **63**, 2645 (1989).
19. J. F. C. Cocks *et al.*, *Phys. Rev. Lett.* **78**, 2920 (1997).
20. G. A. Leander *et al.*, *Nucl. Phys.* **A453**, 58 (1986).
21. N. V. Zamfir and D. Kusnezov, *Phys. Rev.* **C63**, 054306 (2001).
22. J. Engel and F. Iachello, *Phys. Rev. Lett.* **54**, 1126 (1985).
23. J. Engel and F. Iachello, *Nucl. Phys.* **A472**, 61 (1987).
24. W. Nazarewicz and P. Olanders, *Nucl. Phys.* **A441**, 420 (1985).
25. G. A. Leander *et al.*, *Nucl. Phys.* **A388**, 452 (1982).
26. R. V. Jolos and P. von Brentano, *Phys. Rev.* **C49**, R2301 (1994).
27. P. Schüler *et al.*, *Phys. Lett.* **B174**, 241 (1986).
28. W. R. Phillips *et al.*, *Phys. Rev. Lett.* **57**, 3257 (1986).
29. F. Iachello and A. Arima, *The Interacting Boson Model* (Cambridge University Press, Cambridge, 1987).

THREE-BODY MODELS IN NUCLEAR PHYSICS

P. DESCOUVEMONT

*Physique Nucléaire Théorique et Physique Mathématique, CP229
Université Libre de Bruxelles, B1050 Brussels, Belgium
E-mail: pdesc@ulb.ac.be*

We present different three-body models used in nuclear physics. Microscopic and non-microscopic models are briefly described, with emphasis on the hyperspherical formalism. Recent applications are presented on ${}^6\text{He}$ spectroscopy, on $\alpha + n + n$ scattering phase shifts, and on the ${}^7\text{Be}(p,\gamma){}^8\text{B}$ radiative-capture reaction.

1. Introduction

Three-body models play an important role in nuclear physics. For many years, several nuclei such as ${}^{12}\text{C}$ ($= \alpha + \alpha + \alpha$) or ${}^9\text{Be}$ ($= \alpha + \alpha + n$) are known to be well described by a three-body structure¹. This property is even extended to hypernuclei², such as ${}^9_{\Lambda}\text{Be}$ or ${}^6_{\Lambda\Lambda}\text{He}$, which can also be considered as three-body systems ($\alpha + \alpha + \Lambda$ or $\alpha + \Lambda + \Lambda$, respectively).

Recently, the interest for exotic nuclei³ still strengthened the importance of those models. Many exotic light nuclei are believed to have a marked three-body structure. For example the $\alpha + n + n$ structure of ${}^6\text{He}$, or the ${}^9\text{Li} + n + n$ structure of ${}^{11}\text{Li}$ are now well established.

In a theoretical point of view, two approaches are considered, according to whether the internal structure of the three constituents is taken into account or not. Neglecting this structure gives rise to the potential model, where the many-body problem is reduced to a nucleus-nucleus interaction. In this respect, the hyperspherical method⁴ has been shown to be well adapted. On the other hand, more sophisticated models do consider the internal structure of the clusters. Microscopic cluster models are based on a nucleon-nucleon interaction, and therefore present a significant predictive power. The many-body Schrödinger equation is solved by the Resonating Group Method (RGM), or the equivalent Generator Coordinate Method (GCM), which assume that the system is described by clusters, whose wave functions are defined in the shell model⁵. The RGM has been applied to

many two-cluster systems, for nuclear spectroscopy and nucleus-nucleus reactions. Extension to three-cluster models requires important computer time, and is therefore more recent. This extension has been done in two directions: (i) in nucleus-nucleus collisions, if one of the colliding nuclei presents a cluster structure, a three-body model is necessary⁶; (ii) for nuclear spectroscopy a recent development allows to combine the microscopic approach with the hyperspherical formalism⁷.

Here we briefly described the different three-body models, with recent applications.

2. Non-microscopic models

If the structure of the individual nuclei is neglected, the three-body hamiltonian reads

$$H_3 = \sum_{i=1}^3 T_i + \sum_{i<j} V_{ij}(\mathbf{r}_j - \mathbf{r}_i), \quad (1)$$

where \mathbf{r}_i is the coordinate of nucleus i , T_i its kinetic energy, and V_{ij} a two-body interaction. To solve the Schrödinger equation associated with (1), we use the hyperspherical coordinate formalism⁸. After c.m. removal, the coordinates \mathbf{r}_i are replaced by the Jacobi coordinates \mathbf{x} and \mathbf{y} . These are transformed to the hyperradius ρ , and to five angles denoted as $\Omega_5 = (\Omega_x, \Omega_y, \alpha)$; Ω_x and Ω_y are the angles associated with the Jacobi coordinates x and y , and α is the hyperangle. The wave function in partial wave $J\pi$ is written as

$$\Psi_3^{JM\pi}(\rho, \Omega_5) = \rho^{-5/2} \sum_{\gamma K} \chi_{\gamma K}^{J\pi}(\rho) \mathcal{Y}_{\gamma K}^{JM}(\Omega_5), \quad (2)$$

where K is the hypermomentum, γ a set of additional quantum numbers (ℓ_x, ℓ_y, L, S), and $\mathcal{Y}_{\gamma K}^{JM}(\Omega_5)$ the hyperspherical harmonics.

Using expansion (2) in the Hamiltonian (1), we get a set of coupled differential equations

$$\left[-\frac{\hbar^2}{2m_N} \left(\frac{d^2}{d\rho^2} - \frac{(K+3/2)(K+5/2)}{\rho^2} \right) - E \right] \chi_{\gamma K}^{J\pi}(\rho) + \sum_{K'\gamma'} V_{K'\gamma', K\gamma}^{J\pi}(\rho) \chi_{\gamma' K'}^{J\pi}(\rho) = 0, \quad (3)$$

where m_N is the nucleon mass. The potential matrix elements are obtained from a numerical integration over the hyperangle α . Integrations over Ω_x and Ω_y are performed analytically.

System (3) should be truncated at some maximal K value, K_{max} . Typical values are $K_{max} \approx 20 - 30$, which leads to large-size systems (typically $\approx 100 - 200$ equations). We use the Lagrange-mesh method⁹, where each partial wave $\chi_{\gamma K}^{J\pi}(\rho)$ is expanded over a Lagrange basis. The main advantage of this method is that the matrix elements are obtained from values of the potential at the mesh points. Without any loss of accuracy with respect to other variational methods, the calculations are very fast.

An important issue with three-body models concerns two-body forbidden states. They are accounted for either by adding a projection operator to V_{ij} , or by using its supersymmetric transform. Details are given in Ref. 10.

The method has been first applied to bound states¹⁰. Let us consider ${}^6\text{He}$ described as $\alpha + n + n$. In Fig. 1, we give the probability distribution defined as

$$P^{J\pi}(x, y) = \int d\Omega_x d\Omega_y |\Psi^{JM\pi}(x, y)|^2, \quad (4)$$

which is plotted as a function of the relative coordinates ($r_{n-n} = \sqrt{2}x$ and $r_{\alpha-nn} = \sqrt{3/4}y$). We obtain the well known wave function, with two maxima. This wave function is similar to the wave function obtained by Voronchev *et al.*¹¹ who find a maximum at large $r_{\alpha-nn}$ values ("dineutron" configuration), and one at large r_{nn} values ("cigar" configuration).

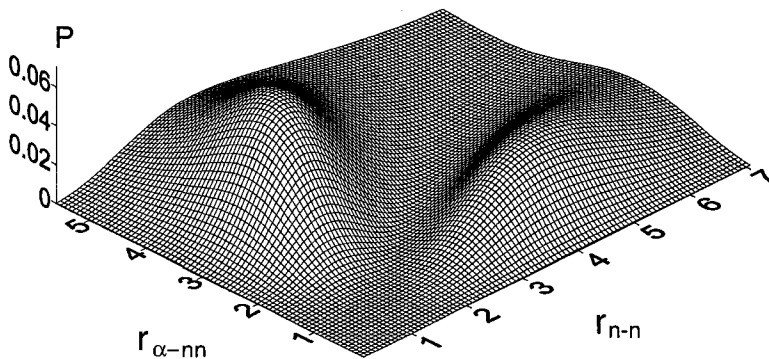


Figure 1. ${}^6\text{He}$ probability P [see Eq.(4)] for the $S = 0$ component. Distances are given in fm.

More recently, we have extended the model to three-body scattering states¹². In that case, the correct treatment of the asymptotic wave functions is restored with the R -matrix method¹³. The use of the hyperspherical framework leads to long-range three-body potentials¹⁴, and therefore requires propagation methods¹⁵. This formalism provides scattering matrices with a high accuracy with a small number of basis states (typically $20 \sim 30$). The method has also been applied to charged system.

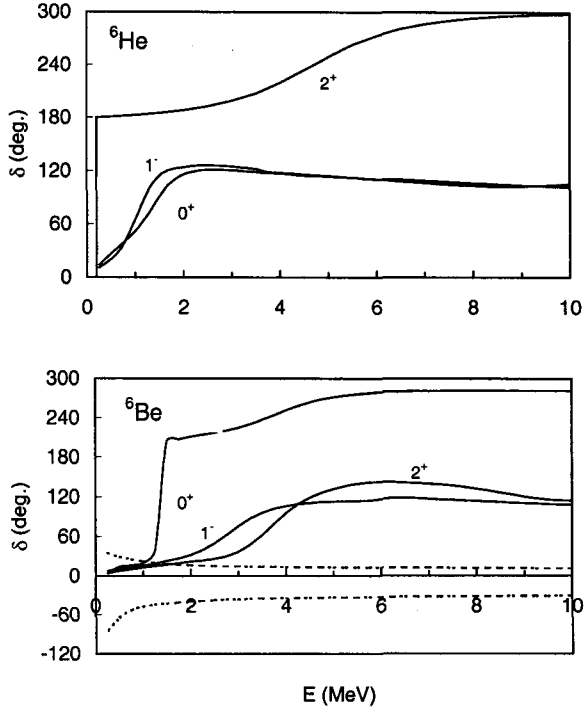


Figure 2. Eigenphases of ${}^6\text{He}$ and ${}^6\text{Be}$ for different J values (solid lines). For ${}^6\text{Be}$, dotted lines represent Coulomb eigenphases for $J = 0^+$.

In Fig. 2, we present the $\alpha + n + n$ and $\alpha + p + p$ phase shifts for $J = 0^+, 1^-, 2^+$. They are given as eigenphases, i.e. eigenvalues of the scattering matrix. As expected, the 2^+ phase shift of ${}^6\text{He}$ presents a narrow resonance. The theoretical energy (about 0.2 MeV) is however underestimated as the experimental value¹⁶ is $E = 0.82$ MeV. The 0^+ and 1^- phase shifts show broad resonances near 1.5 MeV. Similar phase shifts have been obtained by Thompson *et al.*¹⁴ with other potentials. A broad structure

has been observed recently by Nakamura *et al.*¹⁷ in the ${}^6\text{Li}(t, {}^3\text{He}){}^6\text{He}$ reaction near $E_x \approx 4.4$ MeV. This structure is dominated by negative-parity states but contains a small admixture of positive-parity states. Although the theoretical 0^+ and 1^- resonances are located near $E_x \approx 2.5$ MeV, they could be candidates for the experimental structure.

In ${}^6\text{Be}$, the ground state is found at $E = 1.26$ MeV with a width $\Gamma = 65$ keV. These values are in reasonable agreement with experiment ($E = 1.37$ MeV, $\Gamma = 92 \pm 6$ keV), the width being underestimated by the model due to the lower energy.

3. Microscopic three-body models

3.1. General definition

In the second variant, the internal structure of the constituents is explicitly taken into account through their internal wave functions. The A -body hamiltonian is therefore given by

$$H_A = \sum_{i=1}^A T_i + \sum_{i<j}^A V_{ij} \quad (5)$$

where T_i is the kinetic energy of nucleon i , and V_{ij} a nucleon-nucleon interaction. In the cluster approximation, the total wave functions of the system are defined from the cluster wave functions Φ_i of the constituents. Let us consider three particles with wave functions $\Phi_i^{S_i \nu_i}(\mathbf{P}_i)$ with spin and projection S_i and ν_i , and located at \mathbf{P}_i . A three-cluster wave function is written as

$$\Phi_{\nu_1, \nu_2, \nu_3}(\mathbf{P}_1, \mathbf{P}_2, \mathbf{P}_3) = \mathcal{A} \Phi_1^{\nu_1}(\mathbf{P}_1) \Phi_2^{\nu_2}(\mathbf{P}_2) \Phi_3^{\nu_3}(\mathbf{P}_3), \quad (6)$$

where \mathcal{A} is the antisymmetrization operator between all nucleons of the system. The locations \mathbf{P}_i are used as generator coordinates. These A -body basis functions are then projected on total spin and parity. Essentially two methods are developed, with specific angular-momentum projection. Both approaches are described in the next subsections.

3.2. Nucleus-nucleus collisions

The first variant can be applied to nucleus-nucleus reactions, where one of the particles presents a two-cluster structure. These two clusters are coupled to each other, to form one of the colliding nuclei. This approach has been applied to $p+{}^7\text{Be}(=\alpha+{}^3\text{He})$ in Ref. 6 and $\alpha+{}^{20}\text{Ne}(={}^{16}\text{O}+\alpha)$ in

Ref. 18, for example. In that case, basis functions involve two generator coordinates, one associated with the two-cluster nucleus, and the other one with the relative motion.

As an example we choose the ${}^7\text{Be}(p,\gamma){}^8\text{B}$ S -factor, which plays a crucial role in the solar-neutrino problem¹⁹. Many direct as well as indirect measurements have been performed in order to reduce the uncertainties on the S -factor at zero energy (see Ref. 20 for an overview). As a high precision is required for $S(0)$, the extrapolation down to astrophysical energies should be done very carefully. Current experiments are performed in a limited energy range, which requires the use of a theoretical model to derive $S(0)$. The reliability of the model can be tested in the energy range where data exist, which provides some "confidence level" on the extrapolation. In most experiments, a microscopic cluster model⁶ (hereafter referred to as DB94) is used for the extrapolation. This model takes account of the ${}^7\text{Be}$ deformation, of inelastic and rearrangement channels, and has been tested with spectroscopic properties of ${}^8\text{B}$ and ${}^8\text{Li}$, as well as with the ${}^7\text{Li}(n,\gamma){}^8\text{Li}$ mirror cross section. An update of the calculation has been performed recently²¹. The S -factor is shown in Fig. 3.

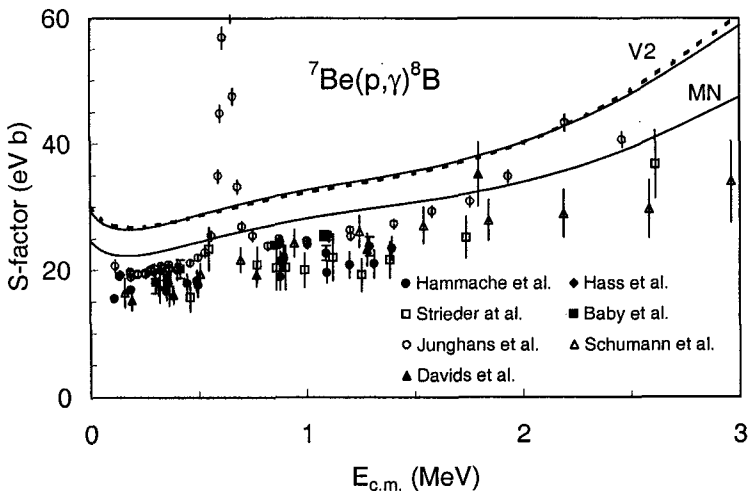


Figure 3. ${}^7\text{Be}(p,\gamma){}^8\text{B}$ S factor with two nucleon-nucleon interactions (V2 and MN). The results of DB94 are shown as a dashed line. See Ref. 21 for references to the data.

3.3. Nuclear spectroscopy

Recently the hyperspherical formalism has been applied to microscopic three-cluster models⁷. A direct extension of Eq. (2) reads

$$\Psi_A^{JM\pi} = \mathcal{A} \phi_1 \phi_2 \phi_3 \rho^{-5/2} \sum_{\gamma K} \chi_{\gamma K}^{JM}(\rho) \mathcal{Y}_{\gamma K}^{JM}(\Omega_5), \quad (7)$$

where ϕ_i represent the internal wave functions. In that case the relative functions are expanded over a gaussian basis, involving a single generator coordinate, denoted as R . We refer the reader to Ref. 7 for details.

This model has been applied to ${}^6\text{He}$ and ${}^6\text{Li}$. Here we show some selected results on ${}^6\text{He}$. In Fig. 4, we diagonalize the Hamiltonian in the basis states with fixed hyperradius R , and obtain the eigenvalues $E(R)$, or "energy curves". Although these energy curves do not directly correspond to the effective potentials of the hyperspherical method, they provide a useful insight into the cluster structure of the system.

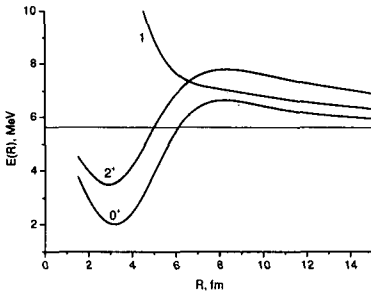


Figure 4. Energy curves for ${}^6\text{He}$. The horizontal solid line is the center-of-mass kinetic energy $\hbar\omega/4 = 5.61$ MeV.

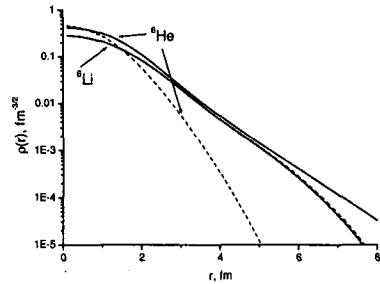


Figure 5. Proton (dashed lines) and neutron (solid lines) densities of the ground states of ${}^6\text{He}$ and ${}^6\text{Li}$.

Both positive-parity curves exhibit a similar behavior with pronounced minima around $R = 3$ fm and maxima around 8 fm. Such a behavior suggests the existence of either a bound state or a resonance. The 2^+ minimum is located 1.5 MeV higher, which is compatible with the experimental gap between the ground 0^+ state and the 2^+ resonance. Figure 4 suggests that the energy curve is not consistent with the existence of a low-energy 1^- resonance.

The present calculation confirms the existence of a neutron halo in ${}^6\text{He}$. Apart from the value of the r.m.s. radius, this is evident from the nucleon

densities (Fig.5). The neutron density decreases noticeably slower than the proton one.

4. Conclusion

Three-body models represent powerful tools for the study of many light nuclei. We have outlined here the main characteristics of two complementary approaches: a potential-model description, where the three constituents interact through nucleus-nucleus potentials, and a microscopic formalism, where the three clusters are described by shell-model wave functions.

We have presented different applications of both approaches. Calculations are essentially limited to bound states. However the low separation energies of exotic nuclei make continuum states quite important. A significant progress has been recently achieved in non-microscopic models. An extension to microscopic descriptions of three-body continuum states raises several problems, namely in the treatment of boundary conditions, but will be certainly considered in the next years.

References

1. Y. Fujiwara *et al.*, *Prog. Theor. Phys. Suppl.* **68**, 29 (1980).
2. M. Theeten, D. Baye, and P. Descouvemont, *Nucl. Phys.* **A753**, 233 (2005).
3. B. Jonson, *Phys. Rep.* **389**, 1 (2004).
4. F.T. Smith, *Phys. Rev.* **120**, 1058 (1960).
5. K. Wildermuth and Y.C. Tang, "A Unified Theory of the Nucleus", ed. by K. Wildermuth and P. Kramer, Vieweg, Braunschweig (1977).
6. P. Descouvemont and D. Baye, *Nucl. Phys.* **A567**, 341 (1994).
7. S. Korennov and P. Descouvemont, *Nucl. Phys.* **A740**, 249 (2004).
8. M.V. Zhukov *et al.*, *Phys. Rep.* **231**, 151 (1993).
9. D. Baye, M. Hesse, and M. Vincke, *Phys. Rev.* **E65**, 026701 (2002).
10. P. Descouvemont, C. Daniel, and D. Baye, *Phys. Rev.* **C67**, 044309 (2003).
11. V.T. Voronchev *et al.*, *Yad. Fiz.* **43**, 1149 (1986).
12. P. Descouvemont, E. Tursunov, and D. Baye, to be published.
13. A.M. Lane, R.G. Thomas, *Rev. Mod. Phys.* **30**, 257 (1958).
14. I.J. Thompson *et al.*, *Phys. Rev.* **C61**, 024318 (2000).
15. V.M. Burke and C.J. Noble, *Comput. Phys. Commun.* **85**, 471 (1995).
16. D.R. Tilley *et al.*, *Nucl. Phys.* **A708**, 3 (2002).
17. T. Nakamura, *Eur. Phys. J.* **A13**, 33 (2002).
18. P. Descouvemont and D. Baye, *Phys. Lett.* **228B**, 6 (1989).
19. J.N. Bahcall *et al.*, *Phys. Lett.* **B433**, 1 (1998); *Astrophys. J.* **555**, 990 (2001).
20. A.R. Junghans *et al.*, *Phys. Rev.* **C68**, 065803 (2003).
21. P. Descouvemont, *Phys. Rev.* **C70**, 065802 (2004).

PROPERTIES OF LOW-LYING STATES: SHAPE PARAMETERS AND PROTON-NEUTRON SYMMETRY*

V. WERNER

This report summarizes some past and ongoing works on quadrupole shape invariants and mixed-symmetry states. The role of quadrupole shape invariants as model independent measures for nuclear deformation is shown. A method is presented to derive approximate values for the lowest invariants from only few E2 transition data, as well as how to obtain relations among E2 matrix elements, both involving the lowest-lying excited states. In the second part the current status of the investigation of mixed-symmetry states in N=52 nuclei is briefly discussed, showing the importance of measuring g factors in this region, and the decay from the scissors mode to the γ -vibrational band in well-deformed rotors is addressed.

1. Quadrupole Shape Invariants

1.1. Nuclear deformation from E2 properties

The nuclear shape is usually discussed in terms of geometrical deformation parameters β and γ , which parametrize the elongation and the triaxiality of a drop-like nucleus, respectively. However, this parametrization is naturally model dependent, as the view of the nucleus as a geometrical object is involved, and the deformation parameters are derived from comparison of data to a geometrical model, *e.g.*, the rigid triaxial rotor model (RTRM)¹.

An alternative, model independent approach to nuclear deformation is given by the concept of quadrupole shape invariants, which was introduced by Kumar² and widely used by Cline and co-workers³ in the evaluation of large sets of E2 matrix elements. Quadrupole shape invariants are higher order moments of the quadrupole operator and, considering the ground state, have the form

$$q_n \propto \langle 0_1^+ | \underbrace{[Q \dots Q]}_n^{(0)} | 0_1^+ \rangle . \quad (1)$$

*This work is supported by USDOE under grant number DE-FG02-91ER-40609 and the DFG under contract number Br 799/12-1

We use the shape parameters K_n defined⁴ by

$$K_n = q_n / (q_2^{n/2}) . \quad (2)$$

These parameters are model independent, which means that they can be calculated from any model, or directly from measured E2 matrix elements. Writing the q and K parameters in terms of the geometrical model, one gets for the lowest invariants

$$q_2 = \left(\frac{3ZeR^2}{4\pi} \right)^2 \langle \beta^2 \rangle = \left(\frac{3ZeR^2}{4\pi} \right)^2 \beta_{\text{eff}}^2 \quad (3)$$

$$\text{and } K_3 = - \frac{\langle \beta^3 \cos 3\gamma \rangle}{\langle \beta^2 \rangle^{3/2}} = - \cos(3\gamma_{\text{eff}}) , \quad (4)$$

showing their relation to the geometrical deformation parameters. The K parameters take fluctuations of the deformation, *i.e.*, vibrations in β and γ , into account. Therefore above equations define *effective* deformation parameters β_{eff} and γ_{eff} , while higher invariants relate to fluctuations in those.

1.2. Shape invariants and the shape/phase transition

A model accounting for fluctuations and covering a broad range of nuclear structures is the interacting boson model (IBM)⁵. The simple Hamiltonian^{6,4}

$$H_{IBM} = (1 - \zeta) n_d - \frac{\zeta}{4N} Q^\chi \cdot Q^\chi \quad (5)$$

with only two free parameters ζ and χ , where χ is inert in the quadrupole operator Q^χ , can be used to interpolate between the dynamical symmetry limits of the *sd*-IBM-1, U(5), SU(3), and O(6), which correspond to vibrations, axially symmetric rigid rotors, and γ -soft nuclei, respectively. Here, n_d is the d -boson number operator, N is the number of bosons, and an absolute energy scale is omitted. It was shown⁴ that the K parameters vary smoothly over the space of structures spanned by the Hamiltonian (5) and can be used as benchmarks for nuclear structure.

Quadrupole shape invariants also mirror phase transitional behavior in shape/phase transitional regions^{7,8}. For example, K_4 , which relates to β -softness, has values around 1.4 for vibrational (U(5)) nuclei, while it equals 1.0 for axially symmetric rigid (SU(3)) and γ -soft (O(6)) rotors. In between, K_4 shows a rapid change in the region corresponding to the vibrator-rotor phase transition, as depicted in Fig. 1, showing the derivative of K_4 with

respect to the control parameter ζ for $N = 10$ bosons. The derivative peaks where the rapid change in K_4 between spherical and deformed nuclei appears, marking the critical point. Different lines correspond to different values of χ , which controls the effective triaxiality ($\gamma_{\text{eff}} = 30^\circ$ for $\chi = 0$ and $\gamma_{\text{eff}} = 0^\circ$ for $\chi = -1.32$).

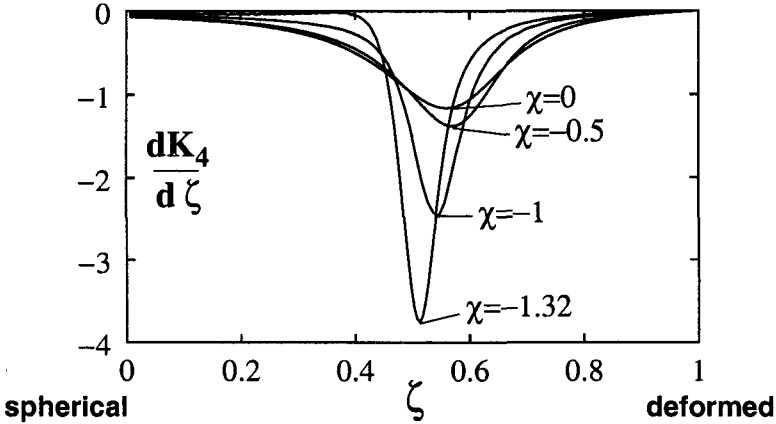


Figure 1. Derivative of K_4 with respect to ζ , calculated⁷ for different values of χ within the IBM.

The shape invariant most sensitive to the oblate/prolate phase transition⁸ is K_3 , which changes sign at the $O(6)$ dynamical symmetry limit of the IBM. Figure 2 shows K_3 on the transition from the prolate $SU(3)$ to the oblate $\overline{SU}(3)$ limit. K_3 correlates strongly to the quadrupole moment of the 2_1^+ state, as $Q(2_1^+)$ dominates the main term in K_3 , as seen below.

1.3. Q -phonon approximations

Using different intermediate couplings of two quadrupole operators in the definition of q_4 , as

$$\langle 0_1^+ | [QQ]^{(J)} [QQ]^{(J)} | 0_1^+ \rangle, \quad J = 0, 2, 4, \quad (6)$$

useful approximations to the parameter K_4 can be obtained. Expanding the expressions (6) into sums over E2 matrix elements one derives large sums. These sums can be truncated using the Q -phonon scheme^{10,11}. In this

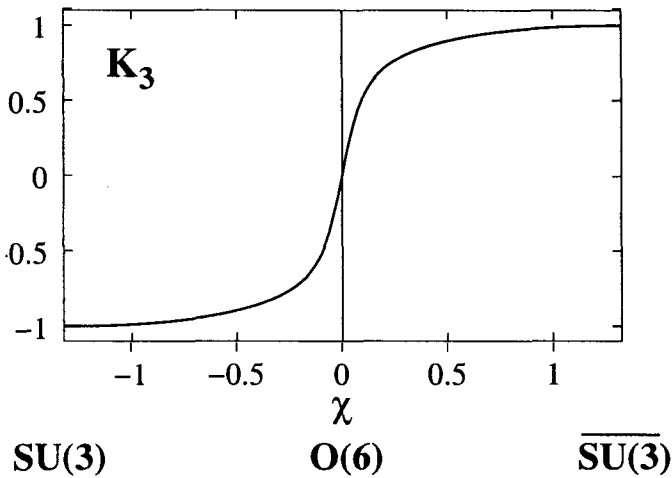


Figure 2. K_4 as a function of χ , calculated between the prolate and oblate $SU(3)$ and $\overline{SU(3)}$ dynamical symmetry limits of the IBM.

scheme only E2 transitions between states which differ by one Q -phonon ($\Delta Q = 1$) are allowed. Applying this selection rule, the sums reduce drastically. In addition, it was found that the expressions (6) are approximately proportional to each other. Thus one obtains¹² a simple expression¹³ for K_4 ,

$$K_4^{appr.} = \frac{7}{10} \frac{B(E2; 4_1^+ \rightarrow 2_1^+)}{B(E2; 2_1^+ \rightarrow 0_1^+)}, \quad (7)$$

which approximates the exact value of K_4 within a few percent. Also by application of the Q selection rule q_2 is approximated by

$$q_2^{appr.} = B(E2; 0_1^+ \rightarrow 2_1^+), \quad (8)$$

and the 3-B(E2)-relation

$$B(E2; 2_1^+ \rightarrow 2_1^+) \approx B(E2; 4_1^+ \rightarrow 2_1^+) - B(E2; 2_2^+ \rightarrow 2_1^+) \quad (9)$$

is obtained, with $B(E2; 2_1^+ \rightarrow 2_1^+)$ being proportional to the squared value of the 2_1^+ quadrupole moment¹².

It was found⁹ that the first order approximation to K_3 is not sufficient in order to derive a good approximative value for K_3 . A second order approximation is needed, which includes at most one matrix element with

$\Delta Q = 2$, leading to the expression

$$K_3^{appr.} = \sqrt{\frac{7}{10}} \text{sign}(Q(2_1^+)) \left[\frac{\sqrt{\frac{B(E2; 2_1^+ \rightarrow 2_1^+)}{B(E2; 2_1^+ \rightarrow 0_1^+)}}}{-2 \frac{\sqrt{B(E2; 2_2^+ \rightarrow 0_1^+) \cdot B(E2; 2_2^+ \rightarrow 2_1^+)}}{B(E2; 2_1^+ \rightarrow 0_1^+)}} \right], \quad (10)$$

which involves 4 $B(E2)$ values only.

2. Mixed-Symmetry States

2.1. Shell effects at $N=52$

Nuclear eigenstates which are symmetric with respect to the proton-neutron (pn) degree of freedom usually make up the lowest excited states in even-even nuclei. Typical collective phenomena are vibrations of spherical nuclei, or rotations of deformed nuclei, in which protons and neutrons are in phase. An additional class of collective excited states exists, in which not all protons and neutrons move in phase. These states are known as mixed-symmetry (MS) states^{14,15}. In the proton-neutron version of the IBM, the IBM-2, they are characterized by the F -spin quantum number, which is the bosonic analog to the isospin quantum number. Symmetric states have a maximum F -spin, F_{max} , while the here discussed MS states have $F = F_{max} - 1$.

In vibrational nuclei, showing the typical patterns of multi-phonon excitations, the first excited state built on the 0^+ ground state is a pn-symmetric one-phonon 2^+ state. From the isovector part of the quadrupole operator, another one-phonon 2^+ state with MS character can be excited from the ground state. The main signature of this state is a strong M1 transition to the symmetric 2_1^+ state, with a transition matrix element in the order of $1 \mu_N^2$.

MS structures are so far best investigated²¹ in ^{94}Mo , including MS multi-phonon states. The one-phonon $2_{1,ms}^+$ state was found at about 2 MeV excitation energy and the strong M1 transition to the 2_1^+ state was identified¹⁷. A similar result was obtained¹⁸ in ^{96}Ru . Another $N=52$ isotope, ^{92}Zr was found to behave differently, with the $2_{1,ms}^+$ state being identified at lower energy¹⁹ - even below the two-phonon symmetric 2^+ state - with larger E2 excitation strength, and a smaller M1 transition strength to the 2_1^+ state.

The reason for this behavior was found in the underlying shell structure and is due to the closure of the proton $p_{1/2}$ orbital. Proton $j = 2$ configurations are suppressed in the light Zr nuclei, and thus the 2_1^+ state has enhanced neutron character, as it is mirrored in its measured²⁰ negative g factor of $g(2_1^+) = -0.18(1)$. If F -spin is a good quantum number, one would expect about equal amounts of protons and neutrons in the wave functions of the symmetric and the MS one-phonon 2^+ states. Therefore, the broken pn-symmetry in the 2_1^+ state suggests broken F -spin in ^{92}Zr , and the missing proton component should be found in the $2_{1,\text{ms}}^+$ state. This is supported by a shell model calculation¹⁹ predicting a positive g factor for the $2_{1,\text{ms}}^+$ state. The calculation also predicted the observed²¹ M1 strength (see Fig. 3) between the lowest 4^+ states, identifying them as being dominated by g boson like configurations.

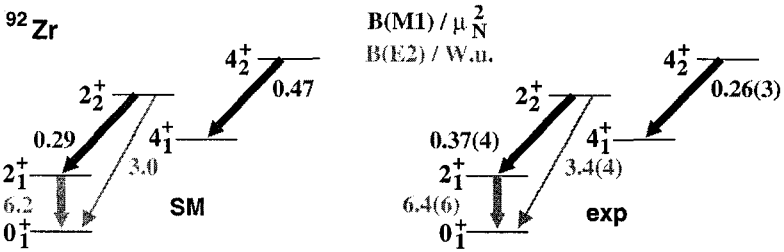


Figure 3. Comparison of shell model predictions and data for the lowest 2^+ and 4^+ states in ^{92}Zr .

Current experiments at WNSL at Yale University aim on measuring the g factor of the MS 2_2^+ state in Zr isotopes using the transient field setup of the Rutgers group²². The principle of the measurement is that Zr nuclei are Coulomb excited on a carbon target in inverse kinematics and then pass magnetized Gd. As the high-energetic ions in their excited states pass the transient magnetic field, the spin of the oriented nuclei precesses. This causes a rotation in the angular distribution of the γ -rays, when the nucleus decays to its ground state. This rotation is proportional to the magnetic moment, and thus the g factor, of the excited state. The experiments are challenging due to the short lifetime of the MS states in the order of 100 fs, making the effect small.

First experiments have been performed on ^{94}Zr , the structure of which is expected to be very similar to that of ^{92}Zr . This is depicted schematically

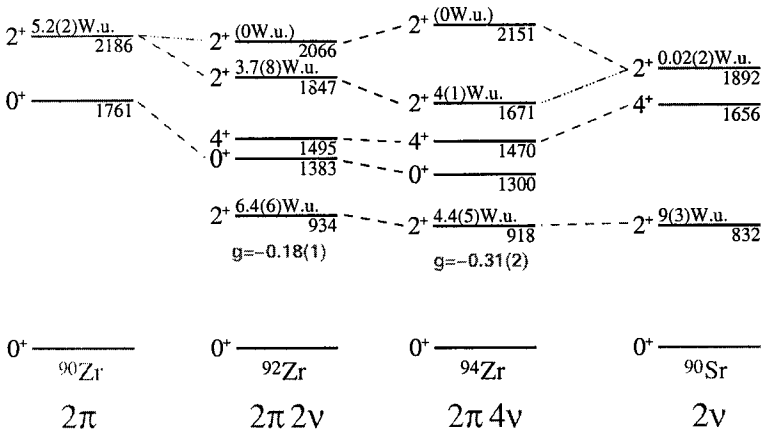


Figure 4. Scheme of low-lying levels in $^{90-94}\text{Zr}$ and ^{90}Sr . Structures of connected states are expected to be similar.

in Fig. 4, showing a correspondence of levels in both Zr isotops to their neighboring nuclei with only two valence protons, or neutrons, respectively, explaining intuitively the enhanced neutron content of the 2_1^+ states, which is known²⁰ to be even more pronounced in ^{94}Zr as seen from its g factor.

2.2. The scissors mode in ^{164}Dy

The coupling of isovector resonances to γ -vibrations has been subject of investigation already years ago in terms of a search for a decay of the giant dipole resonance (GDR) to the γ -band in well deformed rotors²³. The GDR is a collective counter motion of the nuclear proton body versus the neutron body. It was described within a geometrical approach by a mixture of $K = 0$ and $K = 1$ components of the GDR, and within the IBM involving a p boson modeling the dipole excitation.

The IBM-2 predicts¹⁵ another dipole mode, which can be seen as a relative of the GDR in the valence space, the scissors mode²⁴. In a geometrical picture, the scissors mode is a scissors-like counter oscillation of the deformed proton and neutron bodies, involving only valence nucleons. Similarly to the findings for the GDR, the IBM-2 predicts a decay of the scissors mode to the band-head of the γ -band, which was so far unobserved in well deformed rotational nuclei.

Recent experiments using photon scattering techniques with incident photons from bremsstrahlung at Stuttgart University, and an almost monoenergetic polarized photon beam from the free electron laser at TUNL reveal

such a decay in ^{164}Dy . Final experimental results and a detailed comparison to IBM-2 predictions, that will be published soon²⁵, solve ambiguities in the level scheme of ^{164}Dy that were left in the past, and show a good agreement of the observed decays and the model.

Acknowledgments

I wish to thank all who contributed to the topics presented in this report, especially P. von Brentano and N. Pietralla, who were involved in all parts, A. Tonchev for his collaboration in the TUNL experiment, U. Kneissl and H.H. Pitz for the long collaboration in Stuttgart experiments, N. Benczer-Koller and G. Kumbartzki for the ongoing work on g factors, as well as R.F. Casten and J. Jolie for fruitful discussions especially on the topic of shape invariants and phase transitions.

References

1. A.S. Davydov and G.F. Fillipov, Nucl. Phys. **8**, 237 (1958).
2. K. Kumar, Phys. Rev. Lett. **28**, 249 (1972).
3. D. Cline, Ann. Rev. Nucl. Part. Sci. **36**, 683 (1986).
4. V. Werner *et al.*, Phys. Rev. C **61** 021301(R) (2000).
5. F. Iachello and A. Arima, *The Interacting Boson Model* (Cambridge University Press, Cambridge, 1987).
6. D.D. Warner and R.F. Casten, Phys. Rev. Lett. **48**, 1385 (1982).
7. V. Werner *et al.*, Phys. Lett. B **527**,55 (2002).
8. J. Jolie *et al.*, Phys. Rev. Lett. **87**, 162501 (2001).
9. V. Werner, C. Scholl, and P. von Brentano, Phys. Rev. C **71**, 054314 (2005).
10. T. Otsuka and K.-H. Kim, Phys. Rev. C **50**, R1768 (1994).
11. G. Siems *et al.*, Phys. Lett. B **320**, 1 (1994).
12. V. Werner, P. von Brentano, and R.V. Jolos, Phys. Lett. B **521** (2001) 146.
13. R.V. Jolos *et al.*, Nucl. Phys. A **618**, 126 (1997).
14. A. Faessler, Nucl. Phys. **85**, 653 (1966).
15. F. Iachello, Phys. Rev. Lett. **53**, 1427 (1984).
16. C. Fransen *et al.*, Phys. Rev. C **71**, 054304 (2005).
17. N. Pietralla *et al.*, Phys. Rev. Lett. **83**, 1303 (1999).
18. N. Pietralla *et al.*, Phys. Rev. C **64**,031301(R) (2001).
19. V. Werner *et al.* Phys. Lett. B **550**, 219 (2002).
20. G. Jakob *et al.*, Phys. Lett. B **468**, 13 (1999).
21. C. Fransen *et al.*, Phys. Rev. C **71**, 054304 (2005).
22. N. Benczer-Koller, M. Hass, and J. Sak, Ann. Rev. Nucl. Part. Sci. **30**, 53 (1980).
23. A.M. Nathan and R. Moreh, Phys. Lett. B **91**, 38 (1980).
24. A. Richter, Prog. Part. Nucl. Phys. **34**,261 (1995).
25. V. Werner *et al.*, in preparation.

SHELL MODEL NUCLEAR LEVEL DENSITIES

M. HOROI*

*Department of Physics,
Central Michigan University,
Mount Pleasant, Michigan 48859, USA
email: horoi@phy.cmich.edu*

The knowledge of the nuclear spin and parity-dependent level densities $\rho(E, J, \pi)$ is important for understanding statistical properties of nuclei and reaction rates. We review recent methods for calculating spin and parity-dependent shell model nuclear level using the formalism of statistical spectroscopy and the exponential convergence method.

1. Introduction

Knowledge of the level density is an important element of the description of highly excited many-body systems. In application to nuclei, as well as other finite systems, such as atomic clusters, the many-body level density determines all statistical properties, both for the discrete spectrum and for reactions. The importance of the level densities is obvious, especially in connection to neutron resonances in heavy nuclei and related applications, nuclear reactions in general and advances far from stability in particular, and the astrophysical problem of nucleosynthesis¹. The most common semi-phenomenological approaches to the problem of the nuclear level density use basically the noninteracting Fermi-gas model of a nucleus^{2,3}. One of the shortcomings of the Fermi-gas approach to the nuclear level density (NLD) is its inability to correctly predict the ratio of negative to positive number of levels in the energy region of interest for nuclear astrophysics calculations. Some mean-field solutions have been recently proposed⁴, however there are no practical solutions to this problem. The residual interaction can be fully taken into account in modern large-scale shell model calculations based on a direct diagonalization. One would hope that at not very high excitation

*Work supported by grant PHY-0244453 of the US National Science Foundation.

energy the finiteness of model space is not crucial because of a relatively low statistical weight of intruder configurations. Furthermore, one can try to smoothly match the exact shell model results using methods of statistical spectroscopy^{5,6}. Recent developments in this area of research are presented in this contribution.

2. Spin-Dependent Nuclear Level Density

As the dimensions of the shell model Hamiltonian matrices grow beyond the directly tractable limits, the approach of using the methods of statistical spectroscopy^{5,6} is still possible. One needs to build the Hamiltonian matrix and calculate the traces of its moments without an explicit diagonalization. According to the central limit theorem, the distributions of level densities, strength functions and related quantities are converging to Gaussians so that the lowest moments are expected to provide sufficient information⁷. The standard partitioning of Hilbert space according to the particle configurations, which is a usual tool in the construction of the shell model basis, is very convenient here since it facilitates the calculation of the traces. The propagation procedure for the traces including the projection operators for additional quantum numbers is more complicated⁸. Meanwhile, reliable information on the level density $\rho(E, J^\pi, T)$ as a function of total spin J , parity and isospin T is highly desirable.

Taking into account only the first two scalar moments (of total density) seems to be insufficient in cases where the inclusion of many major shells and other shell effects distort the shape of the level density. The approach developed by Jacquemin *et al.*⁸ allows to calculate exactly shell model centroids $\bar{E}(J)$ and widths $\sigma(J)$ for the level densities at fixed spin J . Recently^{9,10}, we proposed⁹ a method of calculating the nuclear level density as a function of excitation energy E , spin J , and parity π , in the following way:

$$\rho(E, J, \pi) = \sum_{\vec{m}} D(n\vec{m}JT_z)(FRG)(E + E_0 - E_{n\vec{m}T_z}(J), \sigma_{n\vec{m}T_z}(J)). \quad (1)$$

Here $\vec{m} = [m_1, m_2, \dots, m_p]$ labels a configuration of n particles in p spherical single-particle levels, $D(n\vec{m}JT_z)$ is a number of states with given J and isospin projection T_z one can build in the configuration \vec{m} ¹⁰, $E_{n\vec{m}T_z}(J)$ and $\sigma_{n\vec{m}T_z}(J)$ are the fixed- J configuration centroid and width (see below), E is the excitation energy, E_0 is the ground state (g.s.) energy, and $(FRG)(x, \sigma)$ are the finite range Gaussians defined in Horoi *et al.*⁹.

In this approach each partition has a definite number of particles and parity; no special effort for conserving number of particles and parity is required, as in the case of a model that cannot select subspaces with correct symmetries, such as Shell Model Monte Carlo¹¹. The generalization to fixed-isospin level density is straightforward. $\bar{E}_p(J)$ and $\sigma_p(J)$ are calculated using techniques similar to those described by Jacquemin^{8,10}.

A part of the present approach was sometimes mentioned in the literature as a method to determine the shape of the J -dependent level density $\rho(E, J)$ as a function of the absolute energy of the system. Equation (1) indicates that one needs the g.s. energy to obtain the NLD as a function of the excitation energy. Finding the energies of low-lying states can be achieved using the exponential extrapolation^{12,13}. It was established¹⁴ that the remote tails of the generic strength function are exponential. This can be translated into exponentially small admixtures of highly excited states, located beyond threshold of 3-4 scalar widths from the scalar centroid, to the exact wave functions of low-lying states. The exponential convergence was rigorously proved in some models and tested by the full matrix diagonalization when possible. A practical algorithm was worked out¹³ to establish the onset of the exponential regime by several progressive truncations keeping the partitions in their entirety. Using this algorithm it is usually possible to locate the ground and low-lying states very close (better than 200–300 keV) to the exact energy value using shell model spaces of dimensions that are less than 1% of the full dimension^{13,15}.

The results obtained using this procedure are shown in Fig. 5 of Horoi *et al.*⁹ for the lowest part of spectrum in the cases of $J = 0$ and $J = 3$. Fig. 6 shows the density of 0^+ and 0^- states for 6 particles in *psd* model space using the PSDMK interaction¹⁰. The comparison with exact shell model calculations proves to be extremely good. No attempt to address the contribution of the center-of-mass (CoM) spurious components was done; methods of removal of the CoM spurious states from the nuclear level density are presented in Secs. 4 and 5.

3. Spin-Cutoff Approach to Spin-Dependent Level Density

The calculation of the fixed- J widths in the middle of the *fp*-shell could take days on a single modern workstation (similar times may be necessary to accurately estimate the yrast states energies). However the all-averaged configuration centroids and widths can be calculated in seconds using Eqs. (129–133) of French and Ratcliff⁵. In addition, calculations of the restricted

configuration widths require about the same amount of time when using Eqs. (134–140) of French and Ratcliff⁵. As recently shown⁹, these moments can be used to calculate very accurately the total density of states. It will thus be interesting to investigate if a method of calculating the fixed- J density of states using the spin cutoff factor could be an efficient and accurate alternative. Knowing the total density of states $\rho(E)$ one can calculate⁶ the fixed- J density of states $\rho_J(E)$.

$$\rho_J(E) = \frac{(2J+1)^2}{\sqrt{8\pi\sigma^3}} e^{-(J+1/2)^2/(2\sigma^2)} \rho(E) . \quad (2)$$

Here, σ is the spin cutoff factor. A quick and accurate summation over J at each energy would indicate a simple relation between the density of levels $\rho_{\text{lev}}(E)$ and the total density of states,

$$\rho_{\text{lev}}(E) = \frac{1}{\sqrt{2\pi\sigma^2}} \rho(E) . \quad (3)$$

Equation (3) can be used as a definition of the spin cutoff factor as a function of energy. However, using Eq. (3) to calculate the spin cutoff factor would not be any easier than solving exactly, or very accurately, the problem of fixed- J density of states. One alternative would take advantage of the fact that^{9,6}

$$\sigma^2(E) = \langle M^2 \rangle (E) , \quad (4)$$

and try to estimate $\langle M^2 \rangle$ using methods of statistical spectroscopy (see *e.g.* Wong⁶ p. 45). In the lowest zeroth-order expansion one can calculate (see p. 45, 171⁶) the energy dependence of $\langle M^2 \rangle (E)$ using

$$\langle M^2 \rangle (E) = \frac{1}{\rho(E)} \sum_{\bar{m}} d_{\bar{m}}(FRG)_{\bar{m}}(E) \langle M^2 \rangle_{\bar{m}} . \quad (5)$$

Figure 3 of Horoi *et al.*¹⁶, summarizes the results of three different calculations based on methods of statistical spectroscopy and compares them with the exact shell model results (staircase): (i) the fixed- J centroids and widths method^{9,10}, (ii) the spin cutoff factor formula of Eq. (2) using the exact spin cutoff factor from Eq. (4), and (iii) the spin cutoff factor formula of Eq. (2) using the zeroth-order spin cutoff factor from Eqs. (4–5).

One can summarize that: (i) the shell model nuclear level density describes very well the experimental data, at least up to the particle emission threshold; (ii) the fixed- J level density is accurately described by the fixed- J

centroids and widths method^{9,10}; (iii) the fixed- J level density is reasonably well described, except for high spins, by the spin cutoff factor formula of Eq. (2) when one uses the exact spin cutoff factor extracted with the help of Eq. (4); (iv) the fixed- J level density is not sufficiently well described by the spin cutoff factor formula of Eq. (2) when one uses the zeroth-order spin cutoff factor extracted with the help of Eqs. (4-5).

4. Nuclear Level Density for a Restrictive Class of Configurations

Equation (1) provides a good description of the exact shell model level density for cases when all possible configurations of a given single-particle model space are taken into account⁹; this is usually the case for $0\hbar\omega$ calculations. However, in order to describe unnatural parity states, one should be able to include only a restricted number of configurations, *e.g.* those corresponding to $1\hbar\omega$, $3\hbar\omega$, etc. Moreover, to reduce the effect of the spurious center-of-mass states, one would restrict the set of configurations to that of factorizable wave functions (*e.g.* $1\hbar\omega$ for two major shells), and use the Lawson¹⁷ technique to push up the contribution of the low-lying spurious states to higher energies. Even in these cases Eq. (1) can be used. However, the J -dependent configuration widths, $\sigma_{n\bar{m}T_z}(J)$, have to be calculated by including only the restricted class of configuration in the intermediate states (see below). Recently¹⁰, we published explicit expressions for matrix elements that can be used to calculate the fixed- J configuration centroids and widths entering Eq. (1) for cases (i) when all intermediate configurations are considered, and (ii) when only a restricted class is included. They are similar to the configuration centroids and widths averaged over all values of M and T_z as given by French and Ratcliff in their classical paper⁵. Their Eqs. (129-133) for the centroids and widths that include all intermediate configurations, and Eqs. (134-140) for the widths, that include only a restrictive class of intermediate configurations, have been recently extended¹⁰ for fixed spin and isospin and parity.

We recently proposed⁹ a precise recipe of calculating the fixed- J configuration centroids and widths using traces of powers of the two-body Hamiltonian $\langle\langle H^p \rangle\rangle_{n\bar{m}JT_z}$, *e.g.*

$$E_{n\bar{m}T_z}(J) = \langle H \rangle_{n\bar{m}JT_z} = \left[\langle\langle H \rangle\rangle_{n\bar{m}(M=J)T_z} - \langle\langle H \rangle\rangle_{n\bar{m}(M=J+1)T_z} \right] / D(n\bar{m}JT_z), \quad (6)$$

$$\sigma_{n\bar{m}T_z}(J) = \sqrt{\langle H^2 \rangle_{n\bar{m}JT_z} - \langle H \rangle_{n\bar{m}JT_z}^2}, \quad (7)$$

where the averages $\langle H^p \rangle_{n\bar{m}JT_z}$ are related to the traces by $\langle H^p \rangle_{n\bar{m}JT_z} D(n\bar{m}JT_z) = \langle \langle H^p \rangle \rangle_{n\bar{m}JT_z}$. In the case that one has to include only a restricted class of configurations into the calculation, the centroids can still be calculated from Eq. (6), but the widths have to be calculated in the same spirit as Eqs. (134–140) of French and Ratcliff⁵. The results for the contribution to the fixed- J traces of H^2 from configurations \bar{m}' that belong to the class under consideration are [see also Eqs. (6-7) above]

$$\langle \langle H^2 \rangle \rangle_{n\bar{m}MT_z} = \sum_{\bar{m}'} \sum_{m' \in \bar{m}'} \langle \langle H^2 \rangle \rangle_{n\bar{m}MT_z}(m'), \quad (8)$$

where

$$\langle \langle H^2 \rangle \rangle_{n\bar{m}MT_z}(m' \in \bar{m}') \equiv \sum_{m \in \bar{m}} \langle m | H | m' \rangle \langle m' | H | m \rangle. \quad (9)$$

Explicit expression for $\langle \langle H^2 \rangle \rangle_{n\bar{m}MT_z}(m' = m)$, $\langle \langle H^2 \rangle \rangle_{n\bar{m}MT_z}(m' = m : r^{-1}s^{+1})$, and $\langle \langle H^2 \rangle \rangle_{n\bar{m}MT_z}(m' = m : r^{-1}s^{-1}t^{+1}u^{+1})$ are given in Horoi *et al.*¹⁰. The $rstu$ labels denote single-particle states rather than single-particle orbits⁵.

An application of the formalism was presented¹⁰ for the case of 16 particles in the $p - sd$ single-particle space, where we calculated the density of 1^- levels, the most affected by the spurious center-of-mass motion, in a class of configurations restricted to $1\hbar\omega$ excitations. The calculations were performed adding to the nuclear Hamiltonian the center-of-mass term multiplied by a constant β : $H = H_N + \beta[H_{\text{CoM}}/(\hbar\omega) - 3/2]$. This is the standard procedure of pushing up the spurious states out of the energy range of interest¹⁷. We use $\beta = 2$ to eliminate the spurious states and compare with the case when $\beta = 0$ (no center-of-mass corrections). The results are presented in Fig.1¹⁰, where the staircases are the results of the full shell model diagonalization, while the curves are the results of calculations according to our approach. The results of our model follow well the exact shell model results in both cases, and the level density for the center-of-mass corrected case is lower than the one without such corrections, indicating that the spurious states were pushed up to higher energy.

5. Cases of Exact Removal of the Contribution of Center-of-Mass Spurious State to the Nuclear Level Density

One can show that if the model space includes a complete set of $N\hbar\omega$ excitations (such as $1\hbar\omega$), the many-body wave functions factorize in a center-of-mass component and an intrinsic part. We recently¹⁸ found recursive formulae to exactly remove the contribution of the center-of-mass spurious states from the fixed- J and parity shell model nuclear level density if one knows the level densities for restricted class of shell model configurations:

$$\begin{aligned} & \rho_{nsp}[E, J, (n) + (n+2) + \dots + (n+2m)] = \\ & \rho[E, J, (n) + (n+2) + \dots + (n+2m)] - \\ & \sum_{K=1}^N \sum_{J_K=J_{Kmin}}^{K, \text{ step } 2} \sum_{J'=|J-J_K|}^{J+J_K} \rho_{nsp}[E, J', (n-K) + \dots + (n+2m-K)], \quad (10) \end{aligned}$$

with the condition that if $(n-K) < 0$ then

$$\begin{aligned} & \rho_{nsp}[E, J', (n-K) + (n+2-K) \dots + (n+2m-K)] = \\ & \rho_{nsp}[E, J', (n+2-K) \dots + (n+2m-K)]. \quad (11) \end{aligned}$$

Here $\rho_{nsp}[E, J, (n) + (n+2) + \dots + (n+2m)]$ represents the nuclear level density free of CoM spurious states for an exactly factorizable shell model space that includes (n) , $(n+2)$ and up to $(n+2m)$ $\hbar\omega$ excitations. We note that the recursive system of Eqs. (10) and (11) can always start from the level density in the $0\hbar\omega$ model space, which does not contain CoM spurious states. This method is valid for a large class of problems that use a harmonic oscillator shell model basis and translational invariant shell model Hamiltonians. Using our methods for calculating nuclear level density utilizing fixed- J configuration centroids and widths for restricted class of shell model configuration^{10,9}, such as $N\hbar\omega$ excitations, one can calculate very accurately nuclear level densities free of center-of-mass spurious states. This approach could be also applicable to other many-fermion systems such as ${}^3\text{He}$ or ${}^6\text{Li}$ atomic clusters.

6. Conclusions and Outlook

In conclusion, we proposed a new practical method of calculating the total density of states using the procedures of statistical spectroscopy in a given

shell model space. We show that a sum of Finite Range Gaussians over partitions with the J -dependent centroids and widths can successfully describe spin- and parity-dependent partial level densities; the essential ingredient is an accurate estimate of the ground state energy of the system, which is possible with the aid of the exponential convergence method. We explicitly showed for the first time how to calculate the fixed- J widths when only a restricted class of shell model configurations, such as $N\hbar\omega$ excitations, is allowed in the intermediate states. A specific example is the case when the elimination of the spurious states from the lowest part of the spectrum is desired; it can be very useful to accurately calculate the ratio of negative and positive parity level densities, a quantity of acute interest for a reliable description of the astrophysical reaction rates⁴. The suggested methods are also applicable for the description of other many-fermion systems with degenerate single-particle orbits, such as complex atoms or atomic clusters.

References

1. T. Rauscher, F.-K. Thielemann and Karl-Ludwig Kratz, *Phys. Rev.* **C56**, 1613 (1997).
2. A. Bohr and B. Mottelson, *Nuclear Structure*, vol. 1 (Benjamin, New York, 1969); vol. 2 (Benjamin, New York, 1974).
3. A. S. Iljinov *et al.*, *Nucl. Phys.* **A543**, 517 (1992).
4. Y. Alhassid, G.F. Bertsch, S. Liu, and H. Nakada, *Phys. Rev. Lett.* **84**, 4313 (2000).
5. J. B. French and K. F. Ratcliff, *Phys. Rev.* **C3**, 94 (1971).
6. S.S.M. Wong, *Nuclear Statistical Spectroscopy*, Oxford Univ Press, 1986.
7. V. Kota, *Phys. Rep.* **347**, 223 (2001).
8. C. Jacquemin, *Z. Phys.* **A303**, 135 (1981); C. Jacquemin, G. Auger and C. Quesne, *Z. Phys.* **A309**, 55 (1982).
9. M. Horoi, J. Kaiser, and V. Zelevinsky, *Phys. Rev.* **C67**, 054309 (2003).
10. M. Horoi, M. Ghita and V. Zelevinsky, *Phys. Rev.* **C69**, 041307(R), (2004).
11. Y. Alhassid, S. Liu, and H. Nakada, *Phys. Rev. Lett.* **83**, 4265 (1999).
12. M. Horoi, A. Volya and V. Zelevinsky, *Phys. Rev. Lett.* **82**, 2064 (1999).
13. M. Horoi, B. A. Brown and V. Zelevinsky, *Phys. Rev.* **C65**, 027303 (2002).
14. N. Frazier, B. A. Brown and V. Zelevinsky, *Phys. Rev.* **C54**, 1665 (1996).
15. M. Horoi, B. A. Brown, and V. Zelevinsky, *Phys. Rev.* **C67**, 034303 (2003).
16. Mihai Horoi, Monica Ghita, and Vladimir Zelevinsky, *Nucl. Phys.* **A758**, 142c (2005).
17. D. H. Gloekner and D. R. Lawson, *Phys. Lett.* **B 53**, 313 (1974).
18. M. Horoi, INT-04-3 *Microscopic Nuclear Structure*, Seattle, Sep. 2004, http://mocha.phys.washington.edu/~int_talk/WorkShops/int_04_3/ to be submitted to *Phys. Rev. Lett.*, (2005).

3. Exotic Decays, Clusters and Superheavy Nuclei

This page is intentionally left blank

NUCLEAR STRUCTURE AND DOUBLE BETA DECAY

JOUNI SUHONEN

Department of Physics, University of Jyväskylä
P.O.Box 35, FIN-40014, Jyväskylä, Finland
E-mail: jouni.suhonen@phys.jyu.fi

The nuclear-structure problems related to the double beta decays are reviewed. The present status of the nuclear matrix element calculations of the neutrinoless double beta decay is presented. The structure of the involved nuclear matrix elements and the related universal behaviour are discussed. Independent probes of the involved virtual transitions are proposed.

1. Motivation

The recent neutrino-oscillation experiments Super-Kamiokande, SNO, KamLAND, and CHOOZ¹ have confirmed the existence of the neutrino mass. These experiments can only probe the differences of the squares of the masses, not the absolute mass scale of the neutrino. On the contrary, the neutrinoless double beta ($0\nu\beta\beta$) decay can probe the absolute mass scale using the effective neutrino mass, $\langle m_\nu \rangle$, extracted from the results of the underground double-beta-decay experiments. To extract the absolute neutrino masses one needs information about the involved nuclear matrix elements², neutrino mixing³, and the associated charge parity (CP) violation phases⁴. In fact, knowing the underlying nuclear matrix elements accurately enough, one can extract from the double-beta experiments information about the CP phases of the neutrino-mixing matrix⁴. One more fundamental piece of information would emerge if the $0\nu\beta\beta$ decay were detected, namely that the neutrino would be a Majorana particle, naturally contained in various particle-physics theories going beyond the standard model of electroweak interactions.

Given the above impressive list of important qualitative and quantitative neutrino properties, potentially probed by the $0\nu\beta\beta$ decay, one can not stress enough the importance of a reliable calculation of the involved nuclear matrix elements (NME). Lack of accuracy in the values of these matrix elements is the source of inaccuracy in the information on neutrino

properties, extracted from the $0\nu\beta\beta$ -decay experiments. Along the years a host of different nuclear models have been used to compute values of these matrix elements^{2,5}. At the same time the calculation of the half-lives and the corresponding NME's of the two-neutrino double beta ($2\nu\beta\beta$) decay has served as a first test for theories aimed at the description of the $0\nu\beta\beta$ decay process. The $2\nu\beta\beta$ decay mode proceeds as a second order perturbative process within the standard model.

2. Nuclear Matrix Elements

Both for the $2\nu\beta\beta$ and $0\nu\beta\beta$ decay the initial and final nuclei are even-even ones, two charge units apart from each other. In the present work we consider only decays between the 0^+ ground states of these nuclei.

The $2\nu\beta\beta$ decay can be thought of as two successive Gamow–Teller beta-decay transitions, and the corresponding NME can be simply written as a sum over virtual transitions through the 1^+ states of the involved odd-odd intermediate nucleus. For a recent study where these transitions are displayed and discussed see Ref.6.

For the neutrino-mass mode of the $0\nu\beta\beta$ decay the half-life can be written as

$$\left[t_{1/2}^{(0\nu)}(0_i^+ \rightarrow 0_f^+) \right]^{-1} = G^{(0\nu)} \left| M_{\text{FGT}}^{(0\nu)} \right|^2 \frac{\langle m_\nu \rangle^2}{m_e^2}, \quad (1)$$

where m_e is the electron rest mass and $\langle m_\nu \rangle$ is the effective neutrino mass

$$\langle m_\nu \rangle = \sum_{i=1}^3 m_i \lambda_i |U_{ei}|^2, \quad (2)$$

with the CP phases λ_i , mass eigenstates m_i , and the mixing matrix elements U_{ei} for the electron neutrino. The quantity $M_{\text{FGT}}^{(0\nu)}$ is the nuclear matrix element

$$M_{\text{FGT}}^{(0\nu)} = M_{\text{GT}}^{(0\nu)} - \left(\frac{g_V}{g_A} \right)^2 M_{\text{F}}^{(0\nu)}, \quad (3)$$

containing the double Gamow–Teller NME, $M_{\text{GT}}^{(0\nu)}$, and the double Fermi NME, $M_{\text{F}}^{(0\nu)}$, as given in detail, *e.g.*, in Ref. 7. The factor $G^{(0\nu)}$ is a leptonic phase-space factor, as given in Refs. 2 and 7. The constants g_V and g_A are the vector and axial-vector coupling constants of the effective nucleon current within a nucleus.

The most notable nuclear models used in the evaluation of the NME of Eq. (3) are the nuclear shell model (SM) and the proton-neutron quasiparticle random-phase approximation (pnQRPA). The SM calculations can be divided into three categories, namely the early calculations, with heavily truncated configuration spaces, the later, more realistic calculations for the light nuclei, like ^{48}Ca , and the large-scale SM calculations of the first half of the 90's, when some medium-heavy and heavy nuclei were calculated by using realistic interactions in single-particle bases, considered large in the SM framework.

The pnQRPA calculations are characterized by an adjustable particle-particle part of the proton-neutron two-body interaction^{2,6}. Determination of the value of the corresponding strength parameter, g_{pp} , has been a key issue since the mid 80's. The NME of the $2\nu\beta\beta$ decay is very sensitive to the value of this parameter, leading to the so-called g_{pp} problem of the pnQRPA. An example is shown in Fig. 1 for the decay of ^{76}Ge . The value $g_{pp} = 1$ corresponds to the bare proton-neutron two-body interaction and the value $g_{pp} = 0$ to the disappearance of this interaction. As seen from the figure, the increasing strength of the proton-neutron interactions drives the $2\nu\beta\beta$ NME towards zero, and finally across it to the negative side. Hereby it reaches the values allowed by the measured $2\nu\beta\beta$ decay half-life. These experimentally allowed regions of the NME, extracted from several different measurements with their ranges of error included, are shown in the figure as two shaded horizontal stripes.

Contrary to the $2\nu\beta\beta$ decay, the NME of the $0\nu\beta\beta$ decay is much less dependent on the value of g_{pp} within the framework of the pnQRPA. This has been shown in Fig. 2 for the decay of ^{76}Ge . Here the four different values of g_{pp} correspond to the borders of the experimentally allowed regions of the $2\nu\beta\beta$ NME in Fig. 1. The decomposition to different multipoles has been done according to

$$M_{\text{GT}}^{(0\nu)} = \sum_{J^\pi} M_{\text{GT}}^{(0\nu)}(J^\pi), \quad (4)$$

where the different multipoles stem from the Fourier-Bessel expansion of the neutrino-exchange potential corresponding to the propagator of the Majorana neutrino between the two decaying neutrons⁷.

From Fig. 2 we notice that the 1^+ component of the NME (4) is strongly dependent on g_{pp} , as was the case for the $2\nu\beta\beta$ NME. This is the main uncertainty of the $0\nu\beta\beta$ NME with respect to the value of g_{pp} . On the other hand, the multipoles other than $J^\pi = 1^+$ depend only weakly on g_{pp}

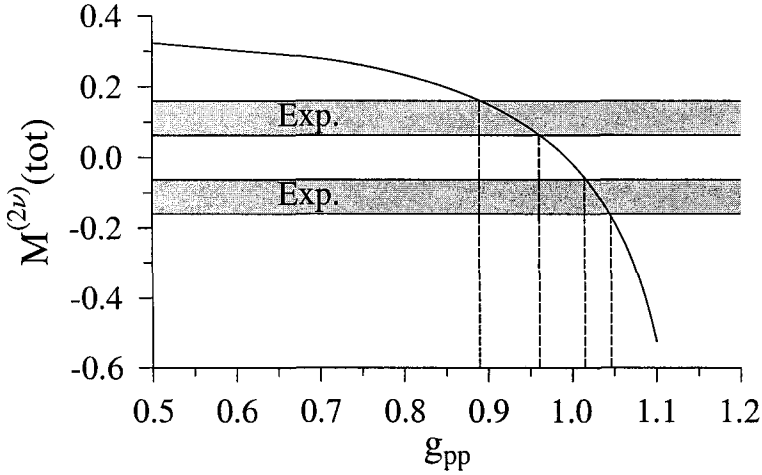


Figure 1. The NME for the $2\nu\beta\beta$ decay of ^{76}Ge as a function of the interaction strength parameter g_{pp} . The two horizontal stripes define the experimentally allowed values.

reducing the overall dependence of $M_{\text{GT}}^{(0\nu)}$ on g_{pp} . In addition, we notice that the multipoles 2^- , 3^+ and possibly 4^- give a substantial contribution to the total $M_{\text{GT}}^{(0\nu)}$. In fact, studying several other $0\nu\beta\beta$ NME's of medium-mass nuclei it seems that the 2^- contribution is by far the most important and describes a kind of universal behaviour of the $0\nu\beta\beta$ NME's⁸.

A chronologically ordered compilation of the available NME's (3) for a selection of most relevant $0\nu\beta\beta$ decaying nuclei has been summarized in Fig. 3. The coding of the figure is the following: for each nucleus the left bar includes NME's calculated before the end of the year 1995. The used theories are mainly the pnQRPA and the shell model. The middle bar contains NME's computed between the years 1996 and 2000. The used theories are mainly the pnQRPA and the renormalized pnQRPA (pnRQRPA, a higher-order version of the pnQRPA⁹). Finally, the right bar shows NME's computed from the year 2001 on. The used theories are the pnQRPA and pnRQRPA, and other higher-order extensions of the pnQRPA.

As can be seen in Fig. 3, the uncertainties in the computed half-lives, and thus in the computed NME's, are unacceptable in view of the determination of the absolute mass scale and the CP phases from the potential results of the underground experiments. Hence, the problem remains: how to

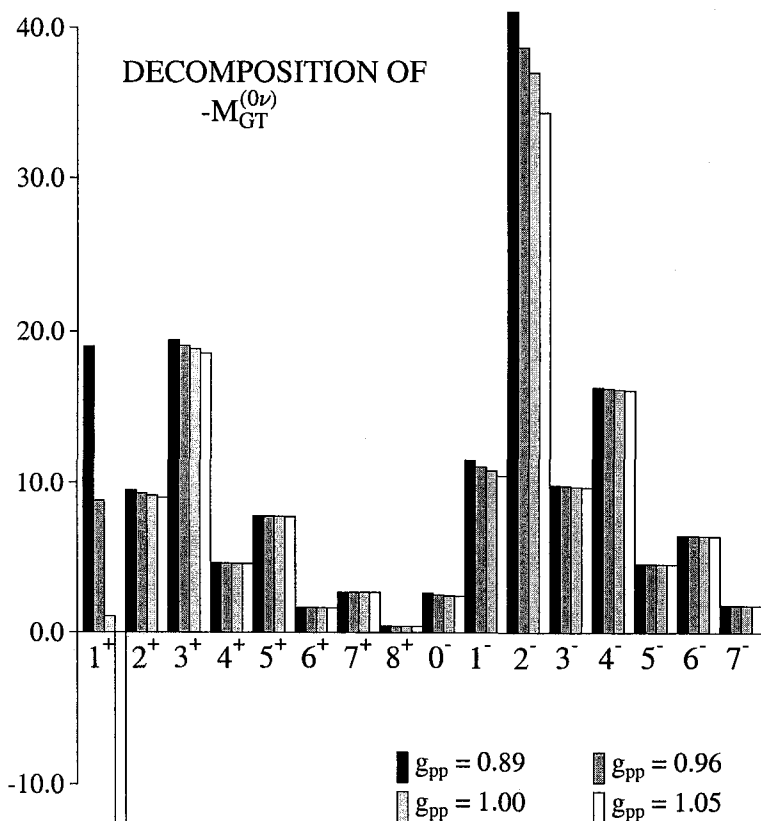


Figure 2. Multipole decomposition of the negative of the $0\nu\beta\beta$ NME $M_{GT}^{(0\nu)}$ of Eq. (4) for the decay of ^{76}Ge within the pnQRPA description. Four different values of g_{pp} , indicated in the figure, have been included in the analysis.

probe independently the involved virtual transitions and to obtain useful information to constrain the parameter spaces of the used nuclear models.

3. Independent Probes

As mentioned in the previous subsection, it is important to find independent probes of the virtual transitions involved in the NME's of both types of double beta decay. The probe which most likely first enters one's mind

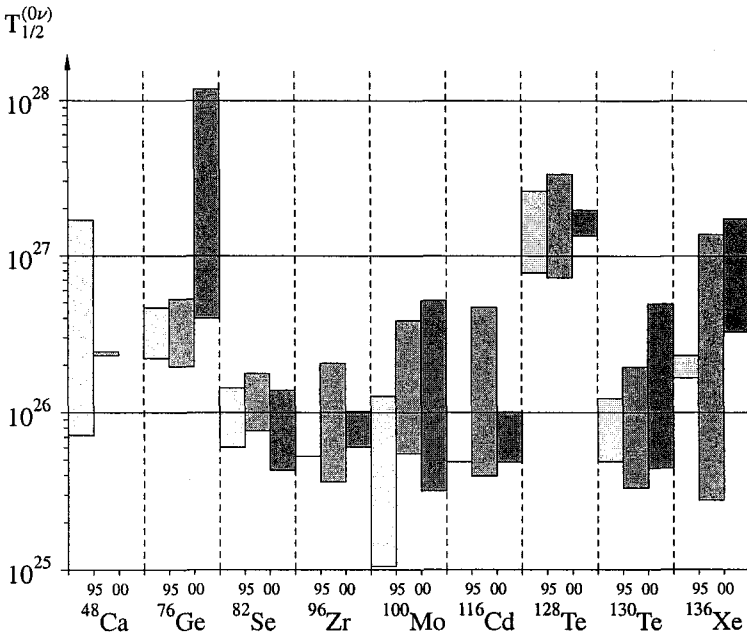


Figure 3. Compilation of the computed $0\nu\beta\beta$ -decay half-lives for selected nuclei. For each nucleus the left, middle, and right bars include the computed NME's, up to 1995, 1996-2000, from 2001 on, respectively.

is the measurement of single beta decays from the intermediate odd-odd nucleus of the double beta decay to the adjacent even-even nuclei. Typical examples of the available data is shown in Fig. 4 for double-beta chains involving medium-mass nuclei. As seen from the figure the available data on relevant beta decays is scarce and other independent probes are called for to access higher intermediate multipoles (see Fig. 2) and higher intermediate energies.

Beyond the beta decays other independent probes of the virtual transitions have been proposed. They are the charge-exchange reactions¹⁰ and possibly neutrino-nucleus charged-current scattering¹¹. In addition, in¹² it was proposed to use the ordinary muon capture (OMC) as a probe of the virtual transitions to the J^π states of the intermediate odd-odd nucleus. In particular in light nuclei the OMC seems to be a powerful probing device¹³. An example is given in Fig. 5 for the OMC on ^{48}Ti , i.e. for the process $^{48}\text{Ti} + \mu^- \rightarrow ^{48}\text{Sc} + \nu_\mu$ which probes virtual transitions to the states of the

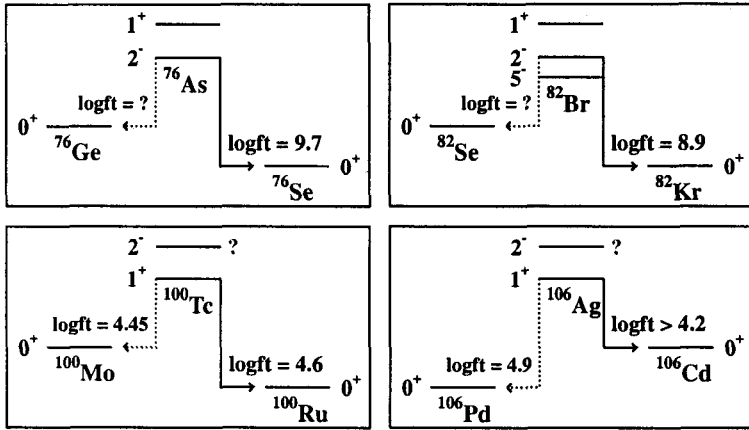


Figure 4. Available experimental data for the beta decays of medium-mass odd-odd nuclei involved in double beta decays.

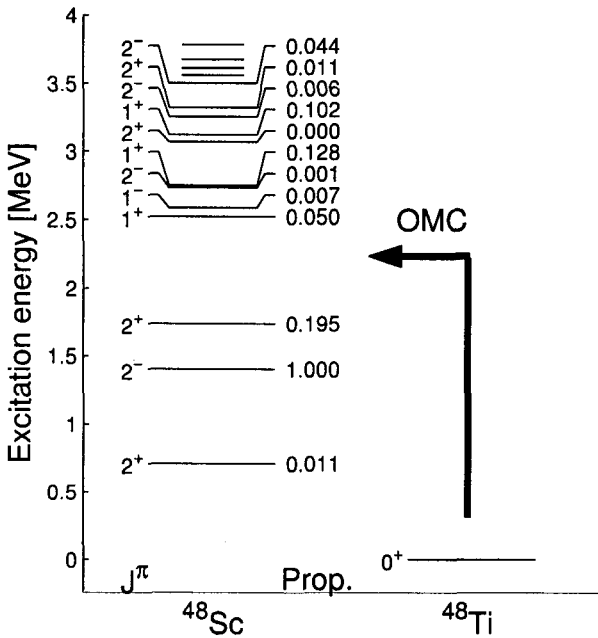


Figure 5. Calculated rates for the OMC on the nucleus ⁴⁸Ti.

intermediate nucleus ^{48}Sc of the ^{48}Ca double beta decay. The presented relative capture rates (relative to the capture rate to the first 2^- state) can be compared with the experimental ones in the near future when the analyses of the experiments performed recently at the PSI are finished (see Ref. 14 for more information).

Acknowledgments

This work has been supported by the Academy of Finland under the Finnish Centre of Excellence Programme 2000–2005 (Project No. 44875, Nuclear and Condensed Matter Programme at JYFL).

References

1. Super-Kamiokande Collaboration, S. Fukuda et al., *Phys. Rev. Lett.* **86**, 5651 (2001) ; SNO Collaboration, Q.R. Ahmad et al., *Phys. Rev. Lett.* **89**, 011302 (2002) ; KamLAND Collaboration, K. Eguchi et al., *Phys. Rev. Lett.* **90**, 021802 (2003) ; M. Appollonio et al., *Phys. Lett.* **B466**, 415 (1999).
2. J. Suhonen and O. Civitarese, *Phys. Rep.* **300**, 123 (1998).
3. O. Civitarese and J. Suhonen, *Nucl. Phys.* **A729**, 867 (2003).
4. S. Pascoli, S. T. Petcov and W. Rodejohann, *Phys. Lett.* **B549**, 177 (2002).
5. J. Suhonen, *Phys. Atom. Nucl.* **61**, 1286 (1998) ; *ibid* **65**, 2176 (2002).
6. J. Suhonen, *Phys. Lett.* **B607**, 87 (2005).
7. M. Doi, T. Kotani and E. Takasugi, *Prog. Theor. Phys. Suppl.* **83**, 1 (1985).
8. O. Civitarese and J. Suhonen, submitted to *Phys. Lett.* **B**.
9. J. Toivanen and J. Suhonen, *Phys. Rev. Lett.* **75**, 410 (1995).
10. H. Ejiri, *Phys. Rep.* **338**, 265 (2000) ; S. Rakers et al., *Phys. Rev.* **C71**, 054313 (2005).
11. C. Volpe, *J. Phys.* **G31**, 903 (2005).
12. M. Kortelainen and J. Suhonen, *Eur. Phys. Lett.* **58**, 666 (2002) ; *ibid.*, *Nucl. Phys.* **A713**, 501 (2003).
13. M. Kortelainen and J. Suhonen, *J. Phys.* **G30**, 2003 (2004).
14. H. O. U. Fynbo et al., *Nucl. Phys.* **A724**, 493 (2004).

SYSTEMATICS OF PROTON EMISSION

D.S. DELION

*National Institute of Physics and Nuclear Engineering, POB MG-6, Bucharest,
Romania*

R.J. LIOTTA AND R. WYSS

KTH, Alba Nova University Center, SE-10691, Stockholm, Sweden

A simple formula that relates the Coulomb parameter to the logarithm of the proton emission half-life, corrected by the centrifugal barrier, is presented. The corresponding experimental data lie on two straight lines corresponding to different regions of charge numbers, independently of the angular momentum of the outgoing proton. We also present a simple relation between the logarithm of the spectroscopic function and the quadrupole deformation. These dependencies provide a powerful tool to assign quantum numbers to the experimentally observed decay processes.

1. Introduction

Nearly a century ago one of the most challenging problems in physics was the understanding of the Geiger-Nuttall rule, which says that the logarithm of the half life in alpha decay is proportional to the energy of the outgoing alpha particle, *i.e.*, its Q-value. It can be asserted that the probabilistic interpretation of quantum mechanics started by the explanation given by Gamow to that rule as a consequence of the quantum penetration of the alpha particle through the Coulomb barrier¹. Nowadays the challenge in nuclear physics is related to rare nuclei, *i.e.*, nuclei lying very far from the stability line which, therefore, decay rapidly by particle emission (proton and neutron drip lines). When a rare isotope is reached at the proton drip line it desintegrates through various open channels, but proton radioactivity is of a primordial importance because the decaying proton is relatively easy to detect and the information that it carries, as *e.g.*, its kinetic energy and angular momentum, provides precious knowledge of the dynamics of rare nuclei.

2. Theoretical background

The purpose of this lecture is to present a simple formula that allows one to determine precisely the spin and parity of the mother nucleus independently of any model calculation. To achieve this we use the strong dependence of the half-lives upon the proton Q -values (Q_p). One may think that by just plotting the logarithm of the half-lives as a function of Q_p , as in the Geiger-Nuttall rule, one would obtain a clear graphical pattern of the experimental data. However, such a plot which is the standard way to present proton decay² does not show any obvious trend, see Fig.1(a). The data corresponding to different deformations and spins are all mixed up and it is impossible from that plot to deduce what state corresponds to a given spin and parity. The reason of this disorder is that it is not Q_p , i. e. the kinetic energy of the emitted proton, that determines the decay, but rather the height and width of the Coulomb and centrifugal barriers in which the proton is trapped before decaying. Or, in other words, it is the probability of penetration through the total barrier that determines the decay. The centrifugal barrier, and the corresponding penetrability, is determined by the orbital angular momentum l of the proton, which in deformed nuclei is the l -value of the spherical partial wave used to expand the deformed potential. The decay process is strongly dependent upon l , specially since parity conservation requires that adjacent l -values differ by two units. One therefore expects that there will be one dominant partial wave also in deformed nuclei.

Assuming that the proton is located at a point R , the half-life corresponding to that wave can be written as³

$$T_{1/2} = \frac{\ln 2}{v} \left| \frac{H_l^{(+)}(\chi, \rho)}{s_{lj}(R, \beta)} \right|^2, \quad (1)$$

where $H_l^{(+)}$ is the Coulomb-Hankel spherical wave, $\chi = 2(Z-1)e^2/(\hbar v)$ is the Coulomb parameter (which determines the Coulomb barrier), Z is the charge number of the mother nucleus, $v = \hbar k/\mu = \sqrt{2Q_p/\mu}$ is the velocity of the outgoing proton, μ is the reduced mass of the proton-daughter system, $\rho = kR$ and $s_{lj}(R, \beta)/R$ is the deformed proton wave function at the radius R projected into the outgoing channel (l, j) ⁴, which depends upon the deformation parameters β . For spherical emitters $s_{lj}(R, 0)/R$ is the radial component of the wave function.

A good approximation of the function $H_l^{(+)}$ for physical situations is

given by the WKB value, *i.e.*³,

$$H_l^{(+)}(\chi, \rho) \approx G_l(\chi, \rho) \approx C_l(\chi, \rho) \sqrt{ctg \alpha} e^{\chi(\alpha - \sin \alpha \cos \alpha)}, \quad (2)$$

where G_l is the irregular Coulomb function. The influence of the centrifugal barrier is fully contained in the function C_l , which is given by

$$C_l(\chi, \rho) = e^{\left[\frac{l(l+1)}{x} t g \alpha\right]}, \quad \cos^2 \alpha = \frac{Q_p}{V_c(R)}, \quad (3)$$

and $V_c(R)$ is the Coulomb potential at distance R . We will choose this distance as the matching radius, for which we will adopt the standard form, *i.e.*, $R = 1.2(A_d^{1/3} + A_p^{1/3})$, where A_d is the mass number of the daughter nucleus and $A_p = 1$. It is worthwhile to point out that the results do not depend upon R as long as it is chosen beyond the range of the nuclear potential.

Defining the reduced half-life as

$$T_{red} = \frac{T_{1/2}}{C_l^2} = \frac{F(\chi, \rho)}{|s_{lj}(R, \beta)|^2} \quad (4)$$

where

$$F(\chi, \rho) = \frac{\ln 2}{v} ctg \alpha e^{[2\chi(\alpha - \sin \alpha \cos \alpha)]} \quad (5)$$

one finds that T_{red} does not depend upon the angular momentum l if plotted against the dimensionless Coulomb parameter χ . Moreover, $\log_{10} T_{red}$ which, according to Eq. (5), is proportional to $2\chi(\alpha - \sin \alpha \cos \alpha)$, is a linear function of χ independently of the value of l , provided the velocity v and the parameter α , which depend upon the Q-value, have a smooth behaviour. Only in the case of a sudden transition, in the Q-value or in shape of the nucleus, the value of $\log_{10} F(\chi, \rho)$ or $\log_{10} s_{lj}$ may change. But it is important to stress that the entire analysis is based upon the assumption that the proper value of l , that is the one that determines the experimental half-life $T_{1/2}$, is used. Otherwise, and since $T_{1/2}$ is strongly l -dependent, that straight line pattern would be completely spoiled.

3. Systematics of experimental data

To check these rather straightforward conclusions we evaluated $\log_{10} T_{red}$ in cases where experimental data are available, which we took from Ref. 2. For odd-odd emitters with integer angular momenta J_m the proton spins j_m are extracted from calculations that estimate the main component of the proton-neutron mother state.

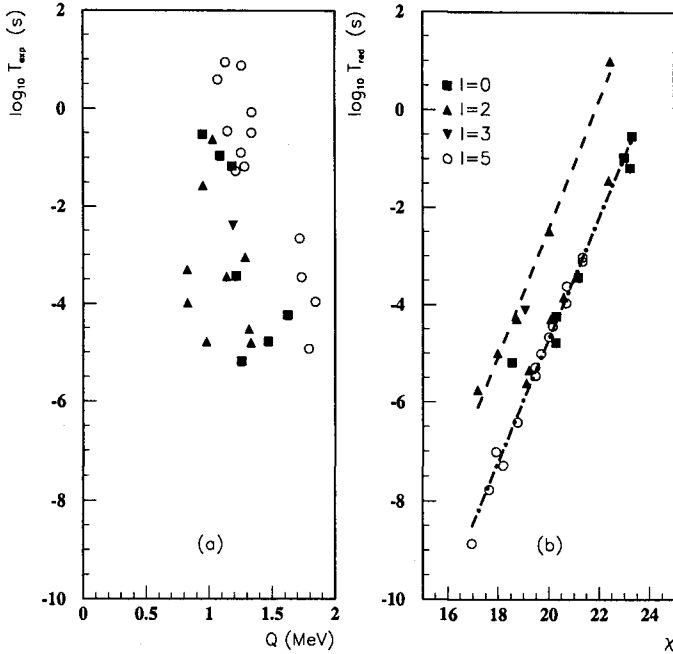


Figure 1. (a) Logarithm of the experimental half-lives corresponding to proton decay as a function of the Q-value. (b) The reduced half-life $\log_{10} T_{red}$, Eq. (4), as a function of the Coulomb parameter χ . The numbers labelling the different symbols correspond to the l -values of the outgoing proton. The two lines are computed according to Eq. (6).

Angular momentum conservation requires that $\vec{J}_m = \vec{J}_d + \vec{j}$, where J_d is the angular momentum of the daughter nucleus and $\vec{j} = \vec{l} + \vec{s}$ ($s=1/2$) is the spin of the outgoing proton. In the case of odd decaying nuclei to the ground state with $J_d = 0$ it is $J_m = j_m$. If, in addition, the nucleus is spherical then $j_m = j$ and $l_m = l$, where l_m is the orbital angular momentum of the single quasiproton state in the mother nucleus.

The relation between j_m and l is more complex if the mother nucleus is deformed. The values of j_m in ² are often extracted from theoretical predictions.

With the values of l , χ and $\log_{10} T_{red}$ as extracted from experiment we produced the plot shown in Fig.1(b). Amazingly, the points lie all

approximately along two straight lines. The seven nuclei on the upper line bear proton number $Z \leq 67$.

Using a fitting procedure we found that the experimental half-lives can be reproduced by the formula

$$\begin{aligned} \log_{10} T_{red}^{(k)} &= a_k(\chi - 20) + b_k, \\ a_1 &= 1.31, \quad b_1 = -2.44, \quad Z \leq 67, \\ a_2 &= 1.25, \quad b_2 = -4.71. \quad Z > 67. \end{aligned} \quad (6)$$

where $k = 1(2)$ corresponds to the upper (lower) line in Fig.1(b).

The standard errors are $\sigma_1 = 0.26$ and $\sigma_2 = 0.23$, corresponding to a mean factor less than two. These differences are small in our logarithmic scale.

As pointed out above, these two straight lines, which are the equivalent of the Geiger-Nuttall rule, may have been induced either by a brusque change in the Q-values or in the structure of the different emitters, or by both. The Q-value dependence affects only the function $F(\chi, \rho)$. We therefore plotted this function against χ in Fig.2. One recognizes similarities in this figure with the pattern of Fig.1(b), namely there appear two lines, but now the upper line excludes three of the seven emitters of the upper line in Fig.1(b). These are just the ones with $Z=67$, *i.e.*, ^{141}Ho and $^{141}\text{Ho}^*$ as well as $Z=64$, ^{131}Eu . In fact the deviations from the two lines in Fig.2 are much larger here than in Fig.1(b), corresponding to an error of about one order of magnitude. This forces us to conclude that although there is a dependence upon the Q-value, this effect is not the only reason behind the two remarkable straight lines of Fig.1(b). The only other source that may contribute to the shift is an abrupt change in the nuclear structure of the emitters.

In order to extract the influence of the Coulomb barrier we computed the spectroscopic factor s_{ij}^{-2} , defined by Eq.(4). In Fig.3(a) we plot the logarithm of this quantity as a function of the charge number Z . In Fig.3(b) we show the deformation parameter β , taken from Ref. 5, as a function of Z . One sees that it has an obvious similarity with the dependence in Fig.3(a). At the proton drip line between $Z=67$ and $Z=69$, there occurs a pronounced change: from a large prolate shape with $\beta \approx 0.3$ to oblate shape with $\beta \approx -0.2$ deformation. These shapes are substantiated by measurements of the moments of inertia. After this phase transition, nuclei with increasing Z acquire a shape close to spherical.

There is a point in Fig.1(b) that deviates conspicuously from the upper straight line. That is the solid square corresponding to $^{141}\text{Ho}^*$. In Fig.3(b)

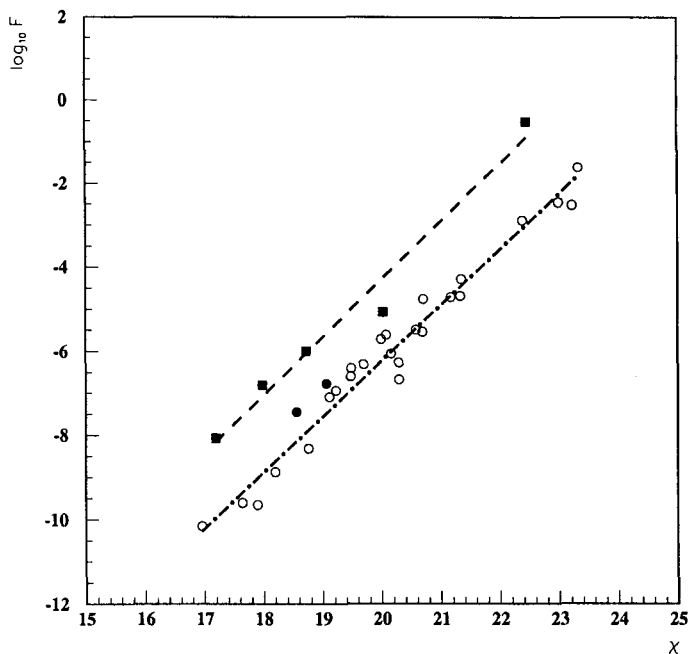


Figure 2. The logarithm of $F(\chi, \rho)$, Eq. (5), as a function of χ . Solid symbols correspond to nuclei with $Z \leq 67$. The solid circles correspond to the emitters ^{141}Ho and $^{141}\text{Ho}^*$.

one sees that this nucleus is situated at the border between the two regions of deformation, which is consistent with the interpretation given here to the behaviour of $\log_{10} T_{red}$.

The remarkable agreement between the data and the straight lines behavior shown in Fig.1(b) can hardly be considered accidental. Will all nuclei lie on these two lines or will another region in the nuclear chart occur, with yet another line? These are important questions to answer and we encourage further experimental efforts directed to the measurement of half-lives and Q-values in proton decays, not only from rare nuclei, with the aim of probing the assumptions made here to arrive to Eq. (6). Besides the possibility thus opened to determine angular momenta the consistency of angular momentum assignment in nuclei, this may even help to parametrize the

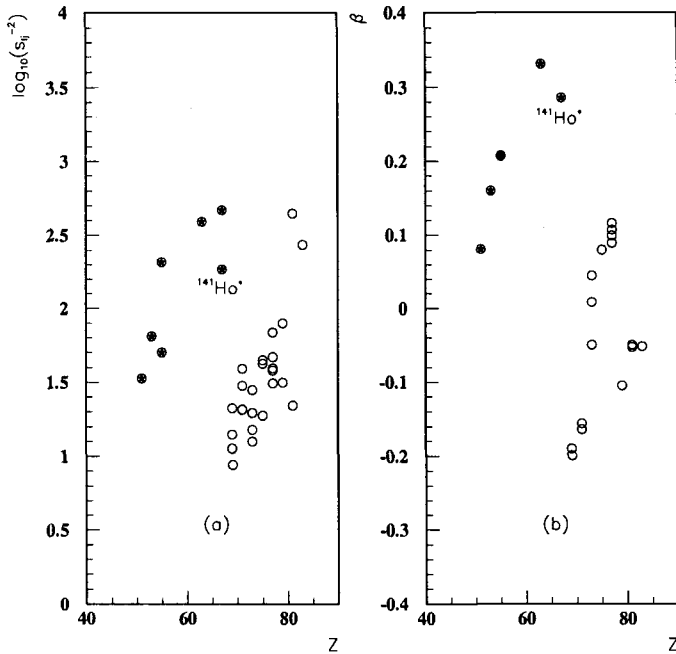


Figure 3. (a) Logarithm of the spectroscopic factor, defined by Eq.(4), versus the charge number Z . Solid circles correspond to nuclei with $Z \leq 67$. (b) Dependence of the quadrupole deformation parameter β upon the charge number Z . Solid circles correspond to nuclei with $Z \leq 67$.

systematics of other processes where the centrifugal barrier plays a role.

4. Conclusions

In conclusion we have presented in this lecture a simple formula [Eq.(6)] which is the equivalent of the Geiger-Nuttall rule for proton emission. This formula allows one to assign rather precisely the spin and parity of proton decaying states. The only quantities that are needed are the half-life of the mother nucleus and the proton Q -value. As a function of these quantities, corrected by the centrifugal barrier [Eq.(4)], the experimental data lie along two straight lines. Since the decay probability is strongly dependent upon the orbital angular momentum l of the decaying proton, only properly

assigned l -values will fit into the straight lines. Moreover, these two lines appear as a result of a sharp change in the nuclear shape and therefore they correspond to two regions of deformation, one being between oblate and spherical with $Z \leq 67$ and the other being between prolate and spherical with $Z > 67$. Indeed, we showed that the spectroscopic factor is directly correlated with the deformation parameter. Therefore proton emission can be a powerful tool to determine experimentally quantum numbers as well as deformations in rare nuclei close to the proton drip line.

References

1. G. Gamow, *Z. f. Phys.* **51**, 204 (1928).
2. A. A. Sonzogni, *Nucl. Data Sheets* **95**, 1 (2002).
3. P. O. Fröman, *Mat. Fys. Skr. Dan. Vid. Selsk.* **1**, no. 3 (1957).
4. G.R. Satchler, *Direct Nuclear Reactions* (Clarendon Press, New York, 1983).
5. P. Möller, R. J. Nix, W. D. Myers, and W. Swiatecki, *At. Data Nucl. Data Tables* **66**, 131 (1995).

SYNTHESIS OF SHE AT SHIP

S.HOFMANN^{1,*}, D. ACKERMANN^{1,†}, S. ANTALIC², H.G. BURKHARD¹,
R. DRESSLER³, F.P. HEBBERGER¹, B. KINDLER¹, I. KOJOUHAROV¹,
P. KUUSINIEMI⁴, M. LEINO⁴, B. LOMMEL¹, R. MANN¹,
G. MÜNZENBERG^{1,†}, K. NISHIO⁵, A.G. POPEKO⁶, S. SARO²,
H.J. SCHÖTT¹, B. STREICHER², B. SULIGNANO^{1,†},
J. UUSITALO⁴, AND A.V. YEREMIN⁶

¹GSI, D-64220 Darmstadt, Germany

²DNP, Comenius University, SK-84248 Bratislava, Slovakia

³PSI, 5232 Villigen, Switzerland

⁴DP, University of Jyväskylä, FIN-40351 Jyväskylä, Finland

⁵JAERI, Tokai, Ibaraki 319-1195, Japan

⁶FLNR at JINR, Ru-141 980 Dubna, Russia

An overview of present experimental investigation of superheavy elements is given. The data are compared with theoretical descriptions. Results are reported from an experiment to confirm production of element 112 isotopes in irradiation of $^{238}\text{UF}_4$ with ^{48}Ca . One spontaneous fission event was measured, which agrees with three events of previously measured data assigned to the decay of $^{283}112$. However, more experimental work is needed in order to obtain an independent and unambiguous confirmation of previous results.

1. Introduction and Status of Experiments

For the synthesis of heavy and superheavy elements (SHE) fusion-evaporation reactions are used. Two approaches have been successfully employed. Firstly, reactions with medium mass ion beam impinging on targets of stable Pb and Bi isotopes (cold fusion) were used. These reactions have been successful to produce elements up to $Z=112$ at GSI [1] and to confirm these experiments at RIKEN [2] and LBNL [3]. Using a ^{209}Bi target the isotope $^{278}113$ was recently synthesized at RIKEN [2]. Secondly, reactions between lighter ions, especially with beams of ^{48}Ca , and radioactive actinide targets (hot fusion) have been used to produce more neutron-rich isotopes of elements from $Z=112$ to 116 and 118 at FLNR [4]. Figure 1 summarizes the data as they are presently known or under investigation.

* and University Frankfurt, Josef-Buchmann-Professor of Physics

† and University Mainz

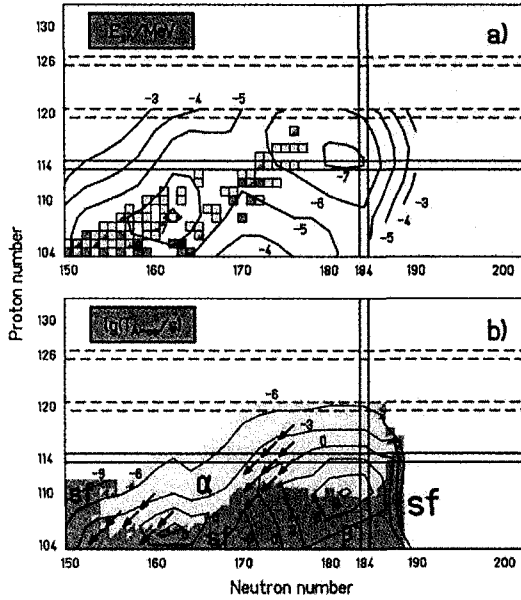


Figure 1. Calculated ground-state shell correction energy (a) and dominating partial half-lives for α , β^+ or EC, β^- decay and spontaneous fission (SF) of even-even nuclei (b). The calculated data were taken from Refs. [5,6]. The squares in (a) show the isotopes of heavy and superheavy elements, which are known or presently under investigation, and the arrows in (b) mark the measured decay chains. In all cases the decay chains end, in agreement with theoretical predictions, at nuclei decaying by SF.

Besides the discovery of the existence of these high-Z elements, two more important observations emerged. Firstly, the expectation that half-lives of the new isotopes should lengthen with increasing neutron number as one approaches the island of stability seems to be fulfilled. Secondly, the measured cross-sections for the relevant nuclear fusion processes reach values up to 5 pb, which is surprisingly high. Furthermore, they seem to be correlated with the variation of shell-correction energies as predicted by macroscopic-microscopic calculations [5,6].

A number of excitation functions was measured for the synthesis of elements from Nobelium to Darmstadtium using cold fusion reactions. Some of the curves are shown together with the two data points for $^{277}_{112}$ in Fig. 2. Maximum evaporation residue cross-sections (1n channel) were measured at beam energies well below a contact configuration, where projectile and target nucleus come to rest according to the fusion model by Bass [7].

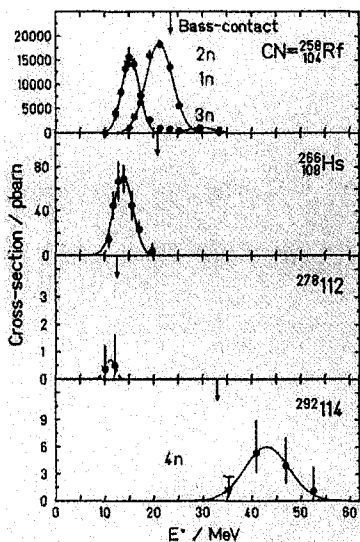


Figure 2. Excitation functions measured at SHIP for the synthesis of elements Rf and Hs plus two data points measured for $Z=112$ using cold fusion reactions (^{208}Pb target) [1] and at the DGFRS of FLNR for the synthesis of element $Z=114$ [4] using hot fusion reaction (^{244}Pu target). The arrows mark the excitation energy for reactions, when the kinetic energy of the projectile is just sufficient high to reach a contact configuration according to the fusion model by Bass [7]. The excitation energies were calculated using binding energies for the compound nuclei from Ref. [8].

Excitation functions for hot fusion reactions were measured recently at FLNR [4]. The data for the reaction $^{48}\text{Ca} + ^{244}\text{Pu} \rightarrow ^{288}114 + 4n$ is shown in the lowest panel in Fig. 2. Here the peak is located well above the contact configuration calculated from a mean value of the nuclear potential of the deformed target nucleus. This shift as well as the increased width of the curve (10.6 MeV instead of 4.6 MeV FWHM for ^{265}Hs) are in accord with an orientation effect on fusion using a deformed target nucleus. The shift to higher energy indicates collisions in direction of the short deformation axis.

It was pointed out in the literature [9] that closed shell projectile and target nuclei are favorable for the synthesis of SHEs. The reason is not only a low (negative) reaction Q -value and thus a low excitation energy, but also that fusion of such systems is connected with a minimum of energy dissipation. The fusion path proceeds along cold fusion valleys, where the reaction partners maintain kinetic energy up to the closest possible distance. Recent theoretical studies are able to reproduce the measured data. That work is continued by various groups (see *e.g.* Refs.[10,11]) aiming to work out reliable predictions for the production cross-sections of SHEs.

2. Study of the $^{48}\text{Ca} + ^{238}\text{U}$ reaction

2.1. Results from previous investigations

Data from studies of the reaction $^{48}\text{Ca} + ^{238}\text{U} \rightarrow ^{286}112^*$ are contradictory concerning half-lives and cross-sections. A summary of the published data is shown in Table 1.

Most comprehensive studies of hot fusion reactions with ^{48}Ca beams were performed at the DGFRS of FLNR, Ref. [4]. The results from this group are based not only on the reaction $^{48}\text{Ca} + ^{238}\text{U}$, but also on data from reactions for the synthesis of nuclei of elements beyond $Z=112$. These data served as a basis for the preparation of our experiment to search for $^{283}112$ at SHIP using the reaction $^{48}\text{Ca} + ^{238}\text{U}$.

Table 1. Published data from investigation of the reaction $^{48}\text{Ca} + ^{238}\text{U} \rightarrow ^{286}112^*$.

days	E^* / MeV	dose / 10^{18}	events	event type	$T_{1/2}$ / s	xn	σ / pb	Ref.
25	33	3.5	2	ER-SF	81	3	5.0	12
15	39	2.2	0	—	—		<7.3	12
29	33	5.9	0	—	—		<2.2	13
15	35.5	4.7	2	ER-SF	568	3	3.0	13
14	31.4	5.8	1	ER-(α)-SF	(3.4)	3	0.5	4
17	35.0	7.1	2	ER-(α)-SF	(1.4)	3	2.5	4
			3	ER- α -SF	2.7	3		
			1	ER-4 α -SF	6.1	3		
13	39.8	5.2	1	ER-SF	0.00014	4	0.6	4
22.5	34.2	2.8	7	SF	≥ 60	3	2	14
≈ 8.7	31.9	2.26	0	—	—		<0.80	15
≈ 7.1	36.3	1.85	0	—	—		<0.96	15

E^* at half thickness of the target layer; cross-section limits given are "one-event" limits which do not include errors from statistical fluctuations.

2.2. Technical aspects and test reactions

The ^{48}Ca beam was prepared from the ECR ion source and accelerator UNILAC at GSI. Metallic, isotopically enriched (89.5 %) ^{48}Ca and the ECR oven technique were used. Ions with charge state 10^+ were extracted and accelerated by the high charge state injector (RFQ + IH structure) and the UNILAC to Coulomb barrier energies. A mean current of $1.2 \mu\text{A}$ were reached on target at a duty factor of 28 % (5.5 ms wide pulses at 20 Hz repetition frequency). The consumption of ^{48}Ca was 0.6 mg/h on the average.

The targets were prepared from the chemical compound UF_4 . Layers of 488, 408 and 451 $\mu\text{g}/\text{cm}^2$ were evaporated on backing foils of 42 $\mu\text{g}/\text{cm}^2$ C and subsequently covered with C layers of 10 or 20 $\mu\text{g}/\text{cm}^2$. Details of the target preparation are given in [16]. The target thickness was controlled on-line by registration of elastically scattered projectiles and scattering of 20 keV electrons [17]. The data showed a continuous decrease of the thickness during irradiation. The target wheel was replaced at the latest, when the losses reached a value of 30 %. We estimated a mean fading of 20 % of target thickness for the calculation of the cross-section. A total of 14 uranium target wheels were used. The Uranium content of new and irradiated targets including the performance of the whole experimental set-up was tested by measuring the yield of fusion products from reactions with a ^{22}Ne beam supplied for two days at half time of the experiment. This test confirmed the results obtained by the measurements using scattered projectiles or electrons.

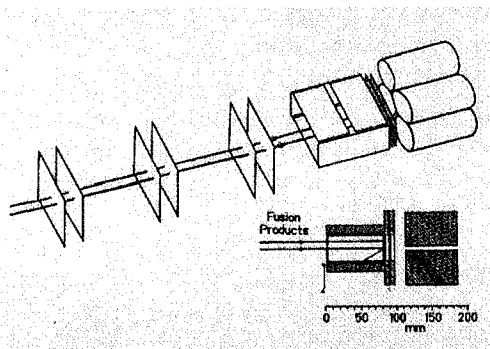


Figure 3. Detector set-up at SHIP. For details see text and description in Ref. [1].

Properties of SHIP and of the detector system are described in Ref. [1]. Since that time, however, the detector system was modified. A Si veto detector was mounted behind the stop detector and the Ge detectors were replaced by a four-crystal Ge clover detector. The new set-up is shown in Fig. 3. During the Uranium irradiation the first of the TOF detectors was removed after few days, which resulted in reduced scattering of the ions and deeper implantation into the Si stop detector.

Two different field settings for SHIP were calculated using a Monte Carlo method, in order to optimize efficiency for the separation of fusion products from the $^{48}\text{Ca} + ^{238}\text{UF}_4$ reaction. Values of 17 % and 24 % were obtained. Test reactions using a ^{208}Pb target confirmed the dependence and, because the back-

ground did not increase more than proportional, we used the setting with higher efficiency.

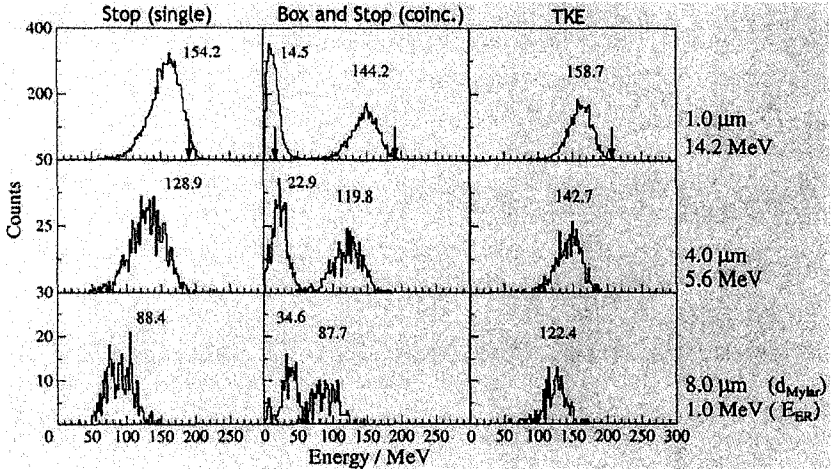


Figure 4. Detector response to SF events of ^{252}No produced in the reaction $^{48}\text{Ca} + ^{206}\text{PbS}$ for three different implantation depth obtained by mylar degrader foils of 1, 4 and 8 μm thickness located in front of the Si detector array. The measured energy (α calibration) of the implanted nuclei is given on the right. The three columns show from the left the energy singles spectra obtained from the stop detector, coincident signals detected in the box and the stop detector (here combined in one spectrum) and the total kinetic energy (TKE) as sum of the coincident signals. The energy values given in MeV are the peaks centre of gravity. The energy calibration is based on α particles and does not include heavy ion deficit energies. Note that at 14.2 MeV implantation energy both fission fragments are detected simultaneously in the stop and the box detector with a probability of 42 % relative to all SF signals in the stop detector. This probability is slightly increasing at less deep implantation, because then the probability decreases that both SF fragments are stopped in the stop detector. The arrows in the first row mark the energy values measured from the SF event on May 8th, 2005. The implantation energy was 19.5 MeV (see Fig. 6), which corresponds roughly to the same implantation depth as for ^{252}No shown in row one, assuming implantation of a heavy isotope of element 112.

The response of the detector system to SF events was investigated especially carefully, expecting that fission will terminate the decay chains of element 112 isotopes. These measurements were performed using the ^{48}Ca beam and targets of ^{208}Pb and ^{206}Pb before and after the main irradiation, respectively. Half time the main irradiation the reaction $^{22}\text{Ne} + ^{238}\text{UF}_4$ was also used for testing purposes. The isotopes produced were ^{254}No , ^{252}No and $^{255,256}\text{No}$, ^{256}Md (p3n channel) and their daughter products, respectively. In order to give an impression of the detector response, we plot in Fig. 4 part of the data.

The response of the Ge clover detector to SF was obtained from 10,000 SF events. SF- γ coincidences were measured with fractions of 25.6, 31.0, 23.8, and

7.7 % for signals in 1, 2, 3 or all 4 of the 4 Ge crystals, respectively. Only in 11.0 % of all cases no signal from the clover detector was in coincidence with SF. Vice versa the response of the clover detector to background events was also measured. From 19,000 background events in the Si stop detector with energies >150 MeV the corresponding fractions are 1.8, 0.4, 6×10^{-4} , 5×10^{-5} , and 97.7 %.

2.3. The experiment at SHIP

The irradiations at SHIP, including various test reactions, took place from April 6th to June 9th, 2005. Duration of the $^{238}\text{UF}_4$ irradiation, beam energies, beam doses and results are summarized in Table 2. Chronologically, energies were chosen as given in the table from top to bottom.

Table 2. Parameters and results of the $^{48}\text{Ca} + ^{238}\text{UF}_4$ irradiation studied at SHIP.

days	$E_{\text{proj}} / \text{MeV}$	E^* / MeV	dose / 10^{18}	event	event type	$T_{1/2} / \text{s}$	xn	σ / pb
20.9	239.3	37.0	12	0	—	—	—	<0.6
16.8	236.2	34.5	10	1	ER—SF	5.2	?	$0.7 + 1.6 - 0.6$
14.8	233.3	32.0	7	0	—	—	—	<0.8

For E^* and cross-section limits see footnote to Table 1.

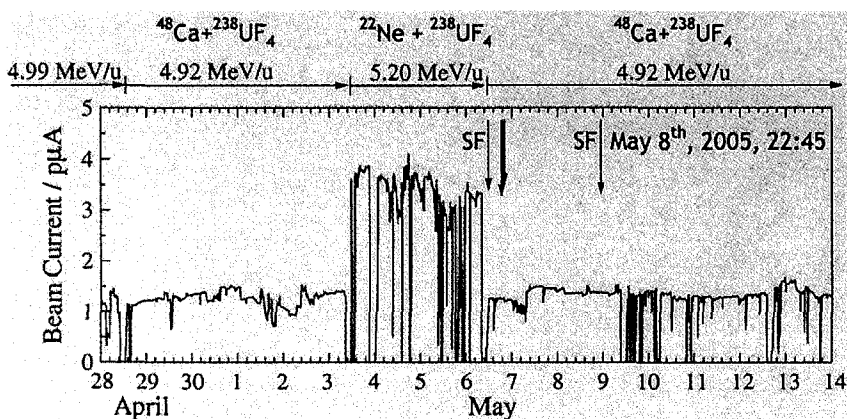


Figure 5. Mean beam currents in particle μA and appearance of SF events during irradiation of an $^{238}\text{UF}_4$ target with ^{48}Ca projectiles. From May 3rd to 6th a ^{22}Ne beam was used for testing purposes.

No SF events were measured at excitation energies of 37.0 and 32.0 MeV. At the beginning of the irradiation at $E^* = 34.5$ MeV within 12 hours after the

test reaction $^{22}\text{Ne} + ^{238}\text{UF}_4$, we measured 3 SF events. The period of interest is shown in Fig. 5. The TKE (energy calibration based on α particles) of these SF events is 149.4, 141.3, and 154.8 MeV, respectively, which agrees well with the energies of SF events from ^{255}No or ^{256}Fm measured during the test reaction. We assign these events to the decay of ^{256}Fm on the basis of well known half-lives and SF branching ratios.

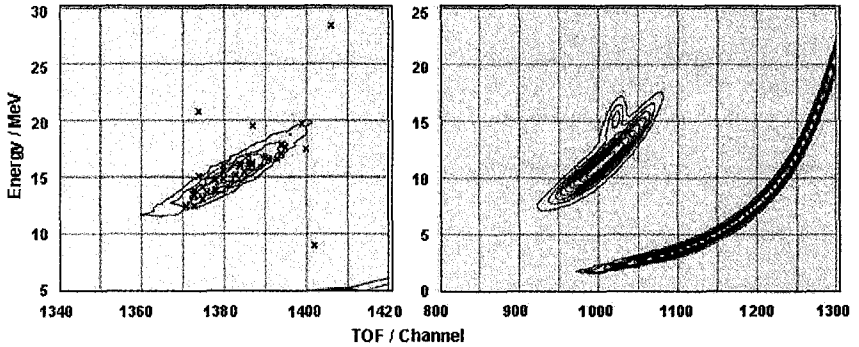


Figure 6. TOF (inverse time scale)–energy spectrum from the reaction $^{48}\text{Ca} + ^{238}\text{UF}_4$ with all signals (marked by crosses) appearing 1000 s before the SF event from May 8th, 2005 and within a position window of ± 1 mm (left side) in comparison with a similar plot from the test reaction $^{48}\text{Ca} + ^{206}\text{PbS}$ (right side). In that plot the branches show, with increasing energy, scattered projectiles, scattered target nuclei and ^{252}No evaporation residues. It was taken from an 11.5 hours irradiation in which a beam dose of 3.4×10^{17} was reached. Contour lines begin at 201 counts and are plotted in steps of 201 counts. The structure on the projectile branch is an artifact from the graphics program. The contour lines on the left plot begin with 49 counts and are plotted in steps of 49 counts. For this underlying contour plot all data of the $^{238}\text{UF}_4$ irradiation at 236.2 MeV beam energy were taken, which were measured after the test with the ^{22}Ne beam during a period of 12.1 days and at a beam dose of 7.1×10^{18} projectiles.

A fourth SF event was measured on May 8th, 2005, also shown in Fig. 5. The measured parameters clearly identify this event as SF. The energies, based on α calibration, are $E_{\text{stop}} = 190.4$ MeV and $E_{\text{box}} = 15.3$ MeV. These data are shown together with the energies from SF of ^{252}No in Fig. 4. The considerable high TKE is clearly visible. In order to determine the true TKE we used the known TKE of the ^{252}No decay, which is 195 MeV [18] (see Fig. 7). The difference to the peak position at 158.7 MeV in Fig. 4 is 36 MeV. This energy difference was added to the TKE of the SF event from May 8th, which resulted in a TKE of 242 MeV. Assuming a width of the TKE distribution similar to that of ^{252}No , we determine a one σ uncertainty of ± 15 MeV for this one event.

The following properties of the SF event were measured further: no signals from the TOF detectors, signals of 386 and 2068 keV in two of the Ge detectors,

appearance during the beam pause at 12.508 ms after beginning of the macro-pulse period which starts with the 5.5 ms wide beam pulse. Finally, the event occurred in strip number 9 of the 16 strip stop detector at a vertical position of 30 mm from the bottom. The signal from the 28 segment box detector was derived from segment number 13.

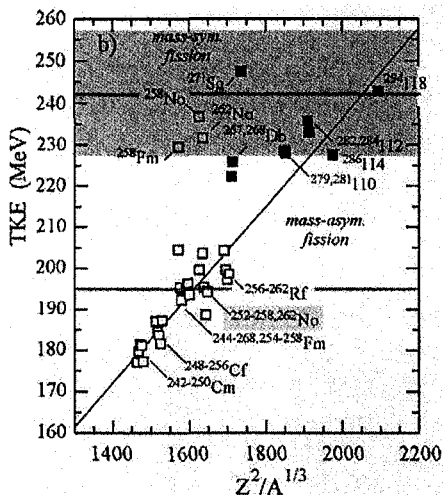


Figure 7. Shown is the Viola-Seaborg systematic of SF nuclei. The horizontal line at 242 MeV marks the TKE value of the SF event measured on May 8th in our experiment. The $\pm 1\sigma$ uncertainty of the mean TKE for this SF decay is also given. Marked at 195 MeV is the TKE of ^{252}No [18], which was used for calibration. The TKE of our event was added to a Fig. taken from Ref. [4], which shows data recently measured at FLNR (filled squares) and previously measured data (open squares) [19].

At the position of the SF event in the stop detector we searched for preceding α particles and the implanted evaporation residue. Within a reasonable position window of ± 1 mm (a more accurate position calibration is in preparation) and a time window of 1000 s, we found a total of 36 implantations, but no α particle was measured. Due to the low discriminator level (200 keV) for detection of α particles escaping from the stop detector, we exclude non-registration of such events with high probability. TOF and energy values of the 36 implanted nuclei are plotted in Fig. 6, left side. Most of the events coincide with background events from elastically scattered target nuclei. Only one appears at a position where we expect signals from implanted evaporation residues. Where this region is located relative to the background distribution is clearly seen in Fig. 6, right side, which was taken from the test reaction $^{48}\text{Ca} + ^{206}\text{PbS}$. The

measured time difference between implantation and SF is 7.57 s, which corresponds to a half-life of $(5.2 + 25.1 - 2.4)$ s.

Finally, we show in Fig. 7 the Viola-Seaborg systematic of SF nuclei.

3. Conclusion and Outlook

The data measured for the decay of nuclei in the region of heavy and super-heavy nuclei agree well with the predictions from the macroscopic-microscopic model.

Using fission barriers from these models, the production cross-sections were reasonably well described in recent theoretical work. Aiming at confirmation of results on element 112 using hot fusion reaction, we measured one SF event which agrees with data measured in Dubna. However, if we tentatively assign the

SF to the isotope $^{283}112$ in accordance with the interpretation given in [4], then we have to introduce an adequate SF branching of this nucleus, because no α particle was measured between implantation and SF. More experimental work is needed in order to obtain an independent and unambiguous confirmation of previous results. As a next step, we will explore the production of metallic uranium targets which result in higher efficiency of the SHIP separator than targets of chemical compounds, in order to study the reaction $^{54}\text{Cr} + ^{238}\text{U} \rightarrow ^{292}116^*$ and to repeat the reaction $^{48}\text{Ca} + ^{238}\text{U} \rightarrow ^{286}112^*$ under further improved conditions.

Acknowledgement

We thank the UNILAC staff for excellent performance of the ^{48}Ca beam with respect to high stability, high current and low consumption of material.

References

1. S. Hofmann and G. Münzenberg, *Rev. Mod. Phys.* **72**, 733 (2000).
2. K. Morita et al., *J. Phys. Soc. Jpn.* **73**, 2593 (2004) and this conference.
3. T.N. Ginter et al., *Phys. Rev.* **C67**, 064609 (2003).
4. Yu.Ts. Oganessian et al., *Phys. Rev.* **C70**, 064609 (2004).
5. R. Smolanczuk et al., *Phys. Rev.* **C52**, 1871 (1995).
6. P. Möller et al., *Atomic Data and Nucl. Data Tables* **66**, 131 (1997).
7. R. Bass, *Nucl. Phys.* **A231**, 45 (1974).
8. W.D. Myers and W.J. Swiatecki, *Nucl. Phys.* **A601**, 141 (1996).
9. A. Sandulescu et al., *Phys. Lett.* **60B**, 225 (1976).
10. G. Adamian et al., *Phys.Rev.* **C69**, 14607 and 44601 (2004).
11. A.S. Zubov et al., *Eur. Phys. J.* **A23**, 249 (2005).

12. Yu.Ts. Oganessian et al., *Eur. Phys. J. A* **5**, 63 (2002).
13. Yu.Ts. Oganessian et al., *Eur. Phys. J. A* **19**, 3 (2004).
14. A.B. Yakushev et al., *Radiochim. Acta.* **91**, 433 (2003).
15. K.E. Gregorich et al., *Phys. Rev. C* **72**, 014605 (2005).
16. B. Lommel et al., *Nucl. Instr. Meth.* **A480**, 16 (2002).
17. R. Mann et al., *GSI Scientific Report 2004-1*, 224 (2004).
18. E.K. Hulet, *Physics of Atomic Nuclei* **57**, 1099 (1994).
19. D.C. Hoffman and M.R. Lane, *Radiochim. Acta.* **70/71**, 135 (1995).

SYNTHESIS OF HEAVIEST ELEMENTS USING A GAS-FILLED RECOIL SEPARATOR AT RIKEN

KOSUKE MORITA[†]

RIKEN (The Institute of Physical and Chemical Research), Hirosawa 2-1, Wako-shi, Saitama 351-0198, Japan

Using heavy-ion fusion reactions with one neutron evaporation, production and decay of isotopes of the heaviest elements with atomic numbers 108, 110, 111, 112, and 113, were studied. The reactions used were $^{208}\text{Pb}(^{58}\text{Fe}, n)$, $^{208}\text{Pb}(^{64}\text{Ni}, n)$, $^{209}\text{Bi}(^{64}\text{Ni}, n)$, $^{208}\text{Pb}(^{70}\text{Zn}, n)$, and $^{209}\text{Bi}(^{70}\text{Zn}, n)$, respectively. A gas-filled recoil separator was used to separate the isotopes of our interest from the primary beams from the accelerator, and from the other background particles. Our results clearly confirmed the productions of ^{265}Hs , ^{271}Ds , ^{271}Rg ($Z=111$), and $^{277}112$ reported previously by a GSI group. The convincing candidate event of the isotope of the 113th element, $^{278}113$, and its daughter nuclei, ^{274}Rg and ^{270}Mt were observed for the first time.

1. Introduction

To produce the isotopes of very heavy elements, including the new elements, and study their properties has attracted both experimental nuclear physicists and chemists continuously. The results of the activities have been providing information about the interesting nuclear structure of the very heavy region where the fission barrier of a nucleus as determined by the liquid-drop model is very low and the nucleus could only exist because of the stabilization by a quantum-mechanical shell effect, and about possibly interesting chemical behavior expected by the relativistic effect because of the high Coulomb-field provided by a large Z nucleus. The steps of discoveries of the new elements have not been so fast however, because the production cross-sections of the heaviest elements are known to be very small. In the case of producing an isotope of the 113th element $^{278}113$ [1], the value reached the order of 0.1 picobarn which is almost at the lowest limit of performing the experiment within a reasonable accelerator-time, even using the highest performances of the experimental setups of recent days.

In the Institute of Physical and Chemical Research, RIKEN, we have performed a series of experiments to study the production and the decay properties of

[†] e-mail: morita@rarfexp.riken.jp

isotopes of the heaviest elements using so-called ‘cold-fusion’ reactions which have been studied intensively by a group at the Gesellschaft für Schwerionenforschung (GSI), Germany [2]. We started the experiments with the reactions which have already been studied at GSI in order to confirm their results with an independent setup by a different experimental group. These were studies of production and decay of isotopes, whose atomic numbers were 108, 110 [3], 111 [4], and 112 [5]. The reactions used were $^{208}\text{Pb}(^{58}\text{Fe}, n)$, $^{208}\text{Pb}(^{64}\text{Ni}, n)$, $^{209}\text{Bi}(^{64}\text{Ni}, n)$, and $^{208}\text{Pb}(^{70}\text{Zn}, n)$, respectively. The results provided clear confirmations of the productions and decay of the isotopes ^{265}Hs , ^{271}Ds , ^{272}Rg , and $^{277}112$ reported in Ref. [2]. Because there were quite a few confirmation experiments performed [6] for these nuclei, the importance of our results should be highly stressed.

As an extension of the work mentioned above, we performed experiments aimed at synthesizing an isotope of larger atomic number, $Z = 113$, using the $^{209}\text{Bi} + ^{70}\text{Zn}$ reaction. We observed one decay chain which can be assigned to subsequent α -decays from $^{278}113$, using the genetic correlation of α -decays connected to the known nuclides, ^{266}Bh and ^{262}Db [1]. The production of element 113 was first reported by Oganessian *et al.* [7] in 2004 in the decay products of the reaction $^{235}\text{Am}(^{48}\text{Ca}, xn)(x=3, 4)$. Recently, the production was reported by Oganessian *et al.* [8], with additional results of an identification of atomic numbers of the long lived Db-products by means of nuclear-chemical technique.

2. Experimental Procedure

Setups were almost the same in the series of experiments. Details of the experimental procedures were described in Refs. [1, 3, 4].

Beams accelerated and extracted by the RIKEN Linear Accelerator (RILAC) irradiated the targets mounted on the rotating wheel which was turning at 2000~3000 rpm to prevent the damage of the targets by the intense beams. Targets were prepared by vacuum evaporation of metallic material (^{208}Pb enriched up to 98.4% or ^{209}Bi) of about $450 \mu\text{g}/\text{cm}^2$ in thickness onto carbon foils of $30 \mu\text{g}/\text{cm}^2$ in thickness. Conditions of the beams and the targets were monitored by measuring the elastically scattered beam particles by the targets with using a PIN photodiode.

Fusion-evaporation residues of our interest, recoiling out of the target in the same direction as the beam particles, were separated by a gas filled recoil ion separator GARIS [2] from the intense ($\sim 3 \times 10^{12}$ /s) beam particles, target recoils ($\sim 10^3$ /s), and other unwanted particles, and were collected at the focal plane of

GARIS where a detection system was set. The separator GARIS was filled with helium gas at a pressure of 86 Pa.

The focal plane detection system consists of two sets consisting of a timing detector and a silicon semiconductor detector box (SSD box). The timing detector is an assembly of micro-channel-plates (MCP) that detect secondary electrons emitted from a thin foil by the impact of ions passing through the foil. The SSD box placed downstream of the timing detector consists of five silicon detectors. The active area of each detector is 60 mm×60 mm. One of the silicon detectors, which faces the direction of the incoming particles, is placed at the bottom of the SSD box and consists of 16 strip detectors (PSD). The strip detectors are position sensitive along the longer dimension. Other four detectors are set to detect decaying particles from the radioactive reaction products implanted in the PSD.

Evaporation residues transported through GARIS pass through two MCP assemblies where the time-of-flight of the ions is measured, are then implanted in a semiconductor detector set at the focal plane of GARIS.

A schematic drawing of the setup of the separator is shown in Fig. 1.

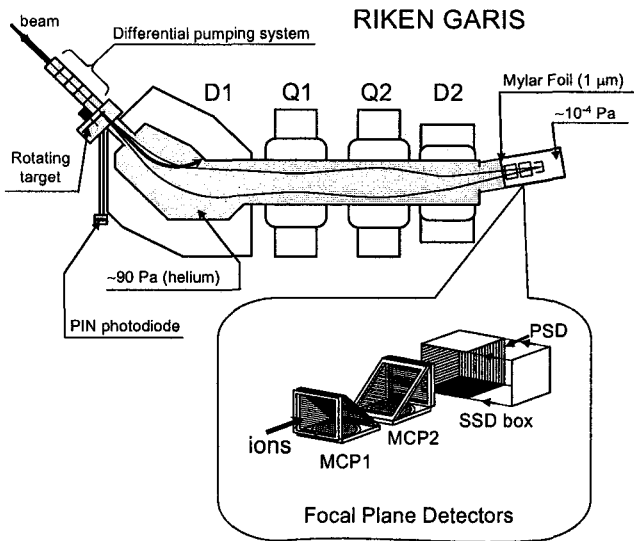


Figure 1. Plane view of RIKEN GARIS. Envelopes of evaporation residues' trajectories are shown by lines. Typical trajectory of primary beam is also shown by a thick line. A schematic drawing of detection system at the focal plane is superimposed.

3. Experimental Results

3.1. Synthesis of ^{265}Hs ($Z=108$), ^{271}Ds ($Z=110$), and ^{272}Rg ($Z=111$).

In July 2002, an experiment on the synthesis of ^{265}Hs by the $^{208}\text{Pb}(^{58}\text{Fe}, n)$ reaction, which was intensively studied at GSI by Hofmann et al. [9], was made for the purpose of total system check, checking the background conditions, and the transmission of the separator. Ten atoms of the isotope ^{265}Hs were produced and detected in 3 days of beamtime. The transmission of GARIS was deduced to be 80% using the cross section value 68 pb reported in Ref. [9]. The counting rate of the PSD was measured to be 10 cps at a typical beam intensity of 3×10^{12} /s. The measured small counting rate indicates a high reliability of the correlation analysis of the decay chains.

In the latter half of the year 2002, the production and decay of ^{271}Ds produced by the $^{208}\text{Pb}(^{64}\text{Ni}, n)$ reaction were investigated. Fourteen atoms of ^{271}Ds were detected in total. The measured decay energies and decay times in the decay chains, assigned to the subsequent decay starting from ^{271}Ds , provided a clear confirmation of production and decay of ^{271}Ds previously reported by Hofmann et al. [10]. In Table 1 improved half-lives of ^{271}Ds and ^{267}Hs are listed together with the isomeric state of $^{271\text{m}}\text{Ds}$ and possible isomeric states of $^{267\text{m}}\text{Hs}$.

Table 1. Half-lives of ^{271}Ds , $^{271\text{m}}\text{Ds}$, ^{267}Hs , and $^{267\text{m}}\text{Hs}$. To deduce them, the values obtained in the present work and those reported in Ref. [10] were combined. For $^{267\text{m}}\text{Hs}$, only present data are used. The second column (n) denotes the number of decays observed.

Nuclei	n	$T_{1/2}$	
^{271}Ds	11	$1.63^{+0.44}_{-0.29}$ ms	improved
$^{271\text{m}}\text{Ds}$	3	69^{+56}_{-21} ms	confirmed
^{267}Hs	12	52^{+13}_{-8} ms	improved
$^{267\text{m}}\text{Hs}$	1	$0.80^{+3.8}_{-0.3}$ s	possible

The excitation function, that is the incident energy dependence of the production cross section, was measured. The beam energy giving the maximum cross section was 316 MeV. The corresponding center-of mass energy at the half-thickness of the target is 240 MeV. The FWHM value of the excitation

function is deduced to be 4 MeV assuming that the shape of the curve is Gaussian. Other results are reported in Ref. [3].

In the first half of the year 2003, the production and decay of ^{272}Rg by the $^{209}\text{Bi}(^{64}\text{Ni}, n)$ reaction were studied. Fourteen atoms of ^{272}Rg were detected in total. Measured decay energies and decay times of decay chains, assigned to the subsequent decays starting from ^{272}Rg , provided a clear confirmation of productions and decays of ^{272}Rg previously reported by Hofmann *et al.* [11, 12]. We observed fourteen atoms of ^{272}Rg , while the GSI group obtained six atoms of that [12]. Because of the better statistics than the one obtained at GSI, more information on decay properties of decay chains started from ^{272}Rg was obtained, beside the confirmation. Results are summarized in Table 2.

Table 2. Decay properties of ^{272}Rg and its daughters observed in the present experiment.

Nuclei	n	$T_{1/2}$	E_{α}	
			MeV	
^{272}Rg	14	$3.8^{+1.4}_{-0.8}$	ms	10.2 ~ 11.56
^{268}Mt	14	21^{+8}_{-5}	ms	9.4 ~ 10.77
^{264}Bh	14	$0.89^{+0.31}_{-0.19}$	s	8.86 ~ 9.83
^{260}Db	12	$5.7^{+2.3}_{-1.3}$	s	8.35 ~ 9.4
^{256}Lr	8	18^{+10}_{-5}	s	8.35 ~ 8.65

The excitation function for the production cross section was also measured. From a Gaussian fit assuming the width (FWHM) of 4 MeV which is the same value as in the case of ^{271}Ds described in the previous paragraph, it was found that the maximum cross section was at $E_c = 318.9$ MeV which corresponds to the center-of-mass energy of 244.1 MeV. Results are reported in detail in Ref. [4].

3.2. $^{208}\text{Pb} + ^{70}\text{Zn}$ reaction

In April to June 2003, we performed an experiment to study the production and decay of $^{277}112$ using the $^{208}\text{Pb}(^{70}\text{Zn}, n)$ reaction. The beam energy at the half-thickness of targets was estimated to be 345.9 MeV. During the irradiation we observed two decay-chains that can be assigned to subsequent decays originated from $^{277}112$. The result has provided a confirmation of the discovery of $^{277}112$ and its daughter nucleus ^{273}Ds reported by Hofmann *et al.* [12]. The total dose of ^{70}Zn was 4.4×10^{18} . The production cross section of the isotope $^{277}112$ by the

$^{208}\text{Pb}(^{70}\text{Zn}, n)$ reaction was deduced to be $0.44^{+0.59}_{-0.29}$ pb using a transmission efficiency of 0.8 for GARIS¹. Observed decay chains are shown in Fig. 2. In the figure, energies, decay times, and detected positions are indicated. For both chains, decay ended by spontaneous fissions after four sequential alpha decays. Results are reported in detail in Ref. [5].

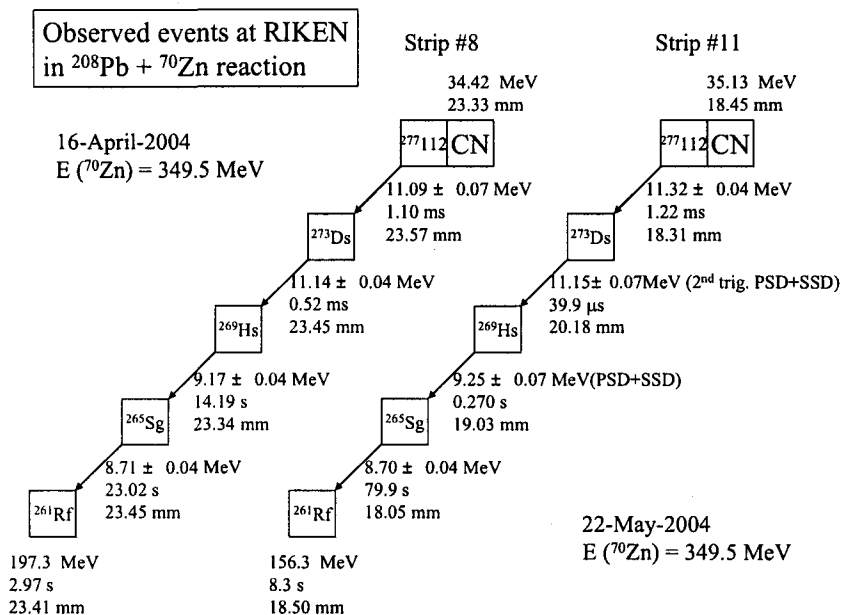


Figure 2. Observed decay chains in the reaction $^{208}\text{Pb}(^{70}\text{Zn}, n)$. CN denotes compound nucleus $^{278}112$.

3.3. $^{209}\text{Bi} + ^{70}\text{Zn}$ reaction

The experiment was designed to produce the isotope $^{278}113$ by the one-neutron evaporation channel in the $^{209}\text{Bi} + ^{70}\text{Zn}$ complete fusion reaction. On the basis of a systematic study of the most probable reaction energies for the one-neutron evaporation channel in the $^{208}\text{Pb}(^{64}\text{Ni}, n)^{271}\text{Ds}$, $^{209}\text{Bi}(^{64}\text{Ni}, n)^{272}\text{Rg}$, and $^{208}\text{Pb}(^{70}\text{Zn}, n)^{277}$ reactions mentioned in the previous sessions, a reaction energy of 349.0 MeV at the half-thickness of the targets was adopted to maximize the relevant cross section for producing $^{278}113$.

As a result, the convincing candidate event of the isotope of the 113th element, $^{278}113$, and its daughter nuclei, ^{274}Rg and ^{270}Mt , was observed, for the

first time, in the $^{209}\text{Bi} + ^{70}\text{Zn}$ reaction at a beam energy of 349.0 MeV with a total dose of 1.7×10^{19} . The alpha decay energies and decay times of the candidates, $^{278}113$, $^{274}111$, and ^{270}Mt , were $(11.68 \pm 0.04 \text{ MeV}, 0.344 \text{ ms})$, $(11.15 \pm 0.07 \text{ MeV}, 9.26 \text{ ms})$, and $(10.03 \pm 0.07 \text{ MeV}, 7.16 \text{ ms})$, respectively. The production cross section of the isotope was deduced to be $55^{+150}_{-45} \text{ fb}$ (10^{-39} cm^2). The decay chain is shown in Fig. 3, together with decay energies (E_α and/or E_{SF}) and decay times. Results are reported in detail in Ref. [1].

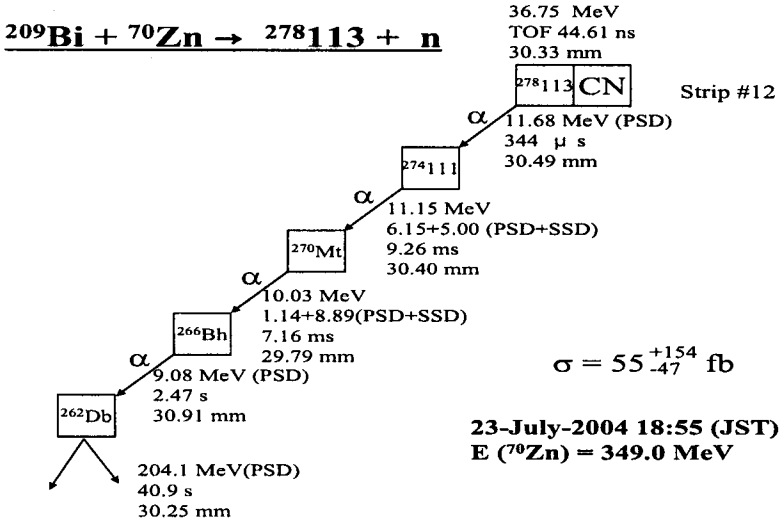


Figure 3. Decay chain observed in the irradiation of ^{209}Bi by ^{70}Zn projectiles. Measured energies, decay time, and measured positions are indicated in the figure. CN denotes the compound nucleus $^{289}113$.

4. Summary

At the RILAC facility in RIKEN, we have studied the production and decay properties of isotopes of the heaviest elements, ^{265}Hs , ^{271}Ds , ^{272}Rg , $^{277}112$, and $^{277}113$, using a gas-filled recoil separator GARIS. The reactions used were $^{208}\text{Pb}(^{58}\text{Fe}, n)$, $^{208}\text{Pb}(^{64}\text{Ni}, n)$, $^{209}\text{Bi}(^{64}\text{Ni}, n)$, $^{208}\text{Pb}(^{70}\text{Zn}, n)$, and $^{209}\text{Bi}(^{70}\text{Zn}, n)$, respectively. The results clearly confirmed the production and decay properties of ^{265}Hs , ^{271}Ds , ^{271}Rg ($Z=111$), and $^{277}112$ reported previously by a GSI group. The convincing candidate event of the isotope of the 113th element, $^{278}113$, and its daughter nuclei, ^{274}Rg and ^{270}Mt were observed for the first time.

Acknowledgments

The series of experiments at RIKEN were performed in collaboration with K. Morimoto, D. Kaji, T. Akiyama, T. Suda, A. Yoshida, H. Haba, T. Ohnishi, A. Yoneda, R. Kanungo, K. Katori, I. Tanihata (RIKEN, Wako); H. Koura (JAERI, Tokai); K. Ozawa, K. Sueki (Univ. of Tsukuba, Tsukuba); T. Yamaguchi (Saitama Univ., Saitama); E. Ideguchi (CNS, Univ. of Tokyo, Wako); S. Goto, H. Kudo (Niigata Univ., Niigata); F. Tokanai (Yamagata Univ., Yamagata); N. Sato (Tohoku Univ., Sendai); Y-L. Zhao (IHEP Chinese Academy of science, Beijing); H-S. Xu (IMP Chinese Academy of Science, Lanzhou); T. Zheng (Peking Univ., Beijing); A. V. Yeremin (FLNR JINR, Dubna); and J. Peter (LPC/ISMRA, Caen).

References

1. K. Morita *et al.*, *Jap. Phys. Soc. J.* **73**, 2593 (2004).
2. S. Hofmann and G. Münzenberg, *Rev. Mod. Phys.* **72**, 733 (2000).
3. K. Morita *et al.*, *Eur. Phys. J.* **A21** 257 (2004).
4. K. Morita *et al.*, *K. Jap. Phys. Soc. J.* **73**, 1738 (2004).
5. K. Morita *et al.*, in *Proceedings of International Symposium on Exotic Nuclei, EXON 2004, Peterhof, Russia, (World Scientific, Singapore)*.
6. C.M. Folden III *et al.*, *Pys. Rev. Lett.* **93**, 212702-1 (2004).
7. Yu. Ts. Oganessian *et al.*, *Phys. Rev.* **C69**, 021601(R) (2004).
8. Yu. Ts. Oganessian *et al.*, *Phys. Rev.* **C72**, 034611 (2005).
9. S. Hofmann, *Rep. Prog. Phys.* **61**, 639 (1998).
10. S. Hofmann *et al.*, *Z. Phys.* **A350**, 277 (1995).
11. S. Hofmann *et al.*, *Z. Phys.* **A350**, 281 (1995).
12. S. Hofmann *et al.*, *Eur. Phys. J.* **A14**, 147 (2002).

FISSION VALLEYS AND HEAVY ION DECAY MODES

DORIN N. POENARU AND RADU A. GHERGHESCU

*Horia Hulubei National Institute of Physics and Nuclear Engineering,
RO-077125, Bucharest-Magurele, Romania, E-mail: poenaru@ifn.nipne.ro*

WALTER GREINER

*Frankfurt Institute for Advanced Studies, J. W. Goethe Universität,
Max-von-Laue-Str. 1, D-60438 Frankfurt am Main, Germany*

Potential energy surfaces are calculated by using the most advanced asymmetric two-center shell model allowing to obtain shell and pairing corrections which are added to the Yukawa-plus-exponential model deformation energy. Shell effects are of crucial importance for experimental observation of spontaneous disintegration by heavy ion emission. Results for ^{242}Cm illustrate the main ideas and show for the first time a potential barrier for a cluster emitter obtained by using the macroscopic-microscopic method.

1. Introduction

Recently we performed a systematic analysis¹ of the experimental results concerning heavy particle radioactivities² showing that our predictions within the analytical superasymmetric (ASAF) model (see ³ and the references therein) have been confirmed and that the strong shell effects of the daughter ^{208}Pb were not fully exploited. In this way we could make suggestions for the candidates to be used in the future experiments.

A new method allowing to explain qualitatively the fission fragments mass asymmetry was derived⁴ by finding the saddle-point shapes as a result of integrating a Euler-Lagrange eq. associated to the variational problem of minimizing the deformation energy. The cranking inertia of a simple shell model can be expressed by an analytical relationship.⁵

In the present work we take advantage of using the most advanced two center shell model⁶ to study the potential energy surfaces (PES) of cluster emitting nuclei showing deep valleys due to the doubly magic fragments ^{208}Pb and ^{132}Sn . Strutinsky's⁷ macroscopic-microscopic method is used. A particularly deep valley is that of ^{208}Pb which proved to be of practical

importance not only for the production of superheavy nuclei but also for the experimental search of cluster decay modes. Even for alpha decay it is possible to see such a valley if the emitter is ^{212}Po or ^{106}Te . In the latter case the fragment ^{102}Sn plays the important role. The potential barrier shape for a heavy ion decay mode may be obtained by cutting the PES at a given value of the mass and charge asymmetry. In this way one can compare the difference between the macroscopic barrier and the total one with shell and pairing corrections taken into account. This provides a further justification of the ASAF barrier shape.

2. The method

In a binary fission process ${}^AZ \rightarrow {}^{A_1}Z_1 + {}^{A_2}Z_2$ the phenomenological energy E_{Y+EM} is calculated within Y+EM by taking into account the difference between charge and mass asymmetry.⁸ In the following we would like to outline the calculations of the shell⁷ and pairing⁹ corrections $\delta E = \delta U + \delta P$ leading to the total deformation energy

$$E_{def}(R, \eta) = E_{Y+EM}(R, \eta) + \delta E(R, \eta) \quad (1)$$

By choosing two intersected spheres for nuclear shape parametrization one can take the separation distance between fragment centers, R , as a deformation parameter. Initially, for a parent nucleus $R_i = R_0 - R_2$. At the touching point $R_t = R_1 + R_2$. The mass asymmetry $\eta = (A_1 - A_2)/A$.

The two-center shell model⁶ gives at every pair of coordinates (R, η) the sequence of doubly degenerate discrete energy levels $\epsilon_i = E_i/\hbar\omega_0^0$ in units of $\hbar\omega_0^0 = 41A^{-1/3}$, arranged in order of increasing energy. The smoothed-level distribution density is obtained by averaging the actual distribution over a finite energy interval $\Gamma = \gamma\hbar\omega_0^0$, with $\gamma \simeq 1$,

$$\tilde{g}(\epsilon) = \left\{ \sum_{i=1}^{n_m} [2.1875 + y_i(y_i(1.75 - y_i/6) - 4.375)]e^{-y_i} \right\} (1.77245385\gamma)^{-1} \quad (2)$$

where $y = x^2 = [(\epsilon - \epsilon_i)/\gamma]^2$. The summation is performed up to the level n_m fulfilling the condition $|x_i| \geq 3$.

The Fermi energy, $\tilde{\lambda}$, of this distribution is given by

$$N_p = 2 \int_{-\infty}^{\tilde{\lambda}} \tilde{g}(\epsilon) d\epsilon \quad (3)$$

with $N_p = Z$ for proton levels and $N_p = A - Z$ for neutron levels, leading to a non-linear equation in $\tilde{\lambda}$, solved numerically. The total energy of the

uniform level distribution

$$\tilde{u} = \tilde{U}/\hbar\omega_0^0 = 2 \int_{-\infty}^{\tilde{\lambda}} \tilde{g}(\epsilon)\epsilon d\epsilon \quad (4)$$

In units of $\hbar\omega_0^0$ the shell corrections are calculated for each pair (R, η) :

$$\delta u(n, R, \eta) = \sum_{i=1}^n 2\epsilon_i(R, \eta) - \tilde{u}(n, R, \eta) \quad (5)$$

$n = N_p/2$ particles. Then $\delta u = \delta u_p + \delta u_n$. Similarly, for pairing corrections

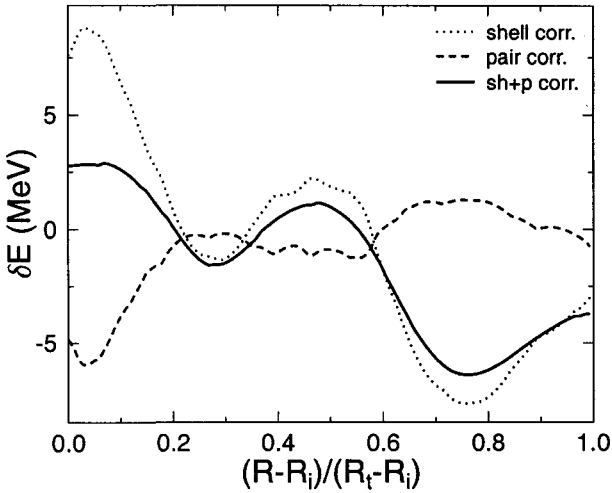


Figure 1. Shell and pairing corrections for a symmetric ($\eta = 0$) fission of ^{236}Pu .

we take the doubly degenerate levels $\{\epsilon_i\}$ in units of $\hbar\omega_0^0$. $Z/2$ levels are occupied with n levels below and n' above Fermi energy contributing to pairing, $n = n' = \Omega\tilde{g}_s/2$. The cutoff energy, $\Omega \simeq 1 \gg \tilde{\Delta} = 12/\sqrt{A}\hbar\omega_0^0$. The gap Δ and Fermi energy λ are solutions of the BCS eqs:

$$0 = \sum_{k_i}^{k_f} \frac{\epsilon_k - \lambda}{\sqrt{(\epsilon_k - \lambda)^2 + \Delta^2}} ; \quad \frac{2}{G} = \sum_{k_i}^{k_f} \frac{1}{\sqrt{(\epsilon_k - \lambda)^2 + \Delta^2}} \quad (6)$$

where $k_i = Z/2 - n + 1$, $k_f = Z/2 + n'$, and

$$\frac{2}{G} \simeq 2\tilde{g}(\tilde{\lambda}) \ln \left(\frac{2\Omega}{\tilde{\Delta}} \right) \quad (7)$$

As a consequence of the pairing correlation, the levels below the Fermi energy are only partially filled, while those above the Fermi energy are only partially empty. Occupation probability by a quasiparticle (u_k) or hole (v_k) is given by

$$v_k^2 = [1 - (\epsilon_k - \lambda)/E_k]/2; \quad u_k^2 = 1 - v_k^2 \quad (8)$$

The quasiparticle energy is expressed as

$$E_\nu = \sqrt{(\epsilon_\nu - \lambda)^2 + \Delta^2}. \quad (9)$$

The pairing correction $\delta p = p - \tilde{p}$, represents the difference between the pairing correlation energies for the discrete level distribution

$$p = \sum_{k=k_i}^{k_f} 2v_k^2 \epsilon_k - 2 \sum_{k=k_i}^{Z/2} \epsilon_k - \frac{\Delta^2}{G} \quad (10)$$

and for the continuous level distribution

$$\tilde{p} = -(\tilde{g}\tilde{\Delta}^2)/2 = -(\tilde{g}_s\tilde{\Delta}^2)/4 \quad (11)$$

Compared to the shell correction, the pairing correction is out of phase and smaller (see Fig.1) leading for $\eta = \text{constant}$ to a smoother total curve $\delta e(R) = \delta u(R) + \delta p(R)$ where $\delta p = \delta p_p + \delta p_n$. In the present work we prefer to use the dimensionless separation distance $x = (R - R_i)/(R_t - R_i)$ instead of R . In this way one can clearly see the initial parent nucleus at $x = 0$ and the touching point configuration at $x = 1$.

3. Results

In the following we shall present results for ^{242}Cm — the heaviest cluster emitter observed until now. The PES versus the normalized separation distance $(R - R_i)/(R_t - R_i)$ and the mass asymmetry $\eta = (A_1 - A_2)/(A_1 + A_2)$ are plotted in Fig. 2. The macroscopic Y+EM deformation energy is shown at the bottom, followed by the microscopic shell plus pairing corrections (center), and their sum (the total deformation energy) at the top. Very deep valleys due to the doubly magic fragments ^{208}Pb and ^{132}Sn can be seen in the center of Fig. 2 and on the corresponding contour plot (Fig. 3) at large and small mass asymmetry, respectively. Such cold valleys were used in the sixties by Walter Greiner to motivate the search for superheavy elements, and the development of Heavy Ion Physics worldwide and in Germany, where GSI was built. These valleys may also be seen on the total PES at the top of Fig. 2. Here the deepest valley remains that of Sn, which

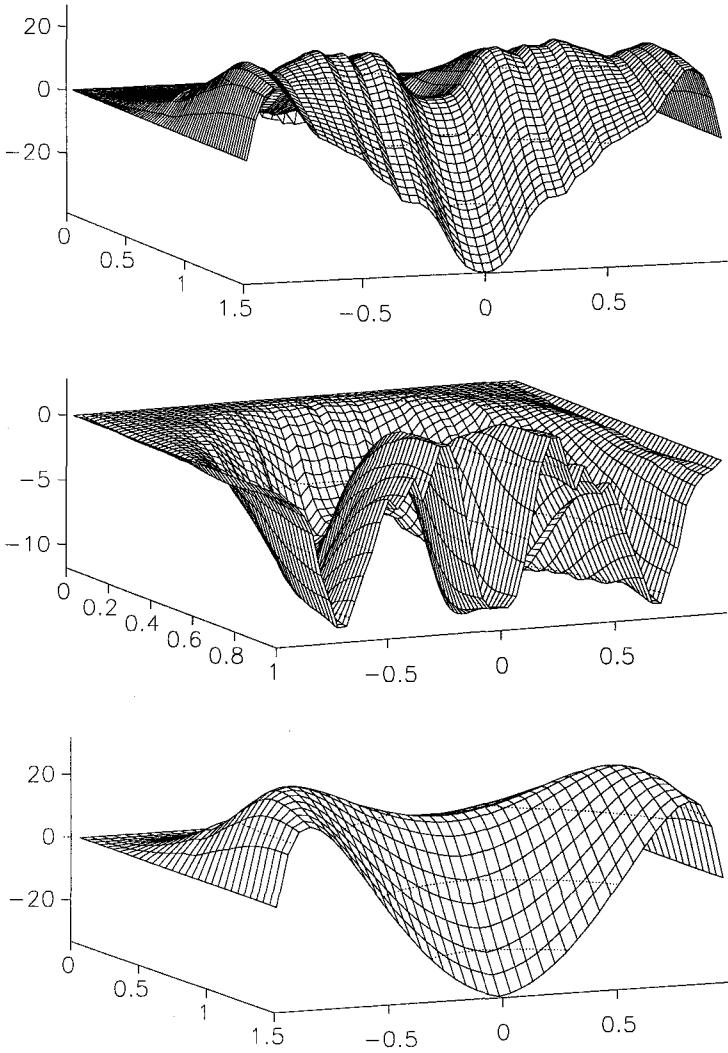


Figure 2. PES of ^{242}Cm vs $(R - R_i)/(R_t - R_i)$ and $\eta = (A_1 - A_2)/(A_1 + A_2)$. Y+EM (bottom), Shell + Pairing corrections (center), and total deformation energy (top). The energies are expressed in MeV.

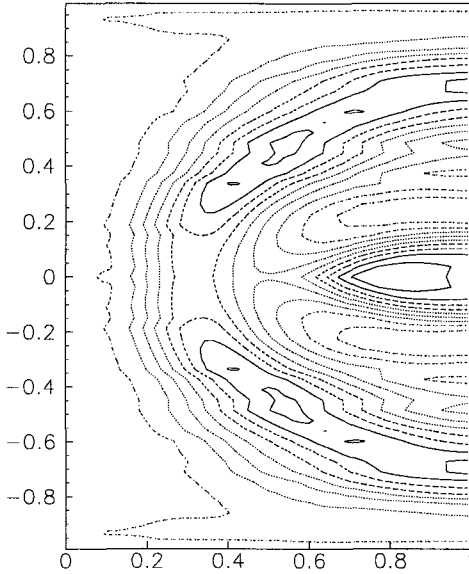


Figure 3. Contour plot of shell and pairing corrections for ^{242}Cm vs $(R - R_i)/(R_t - R_i)$ and η .

is responsible for the cold fission; the $^{208}\text{Pb} + ^{34}\text{Si}$ valley, explaining the ^{34}Si radioactivity of ^{242}Cm , is laying on the Businaro-Gallone mountain, hence it is shallower.

Two plots obtained by cutting the PES at a given value of the asymmetry are shown in Fig. 4. We adopt the usual convention of having zero deformation energy and shell plus pairing corrections for the initial spherical shape, leading to $E_{def} = E_{Y+EM} = \delta E = 0$ at $R = R_i$ for all values of η and at $\eta = \pm 1$ for all values of R . In the upper part one can see an expected two hump barrier at $\eta = 0$. The typical example for ^{34}Si emission from ^{242}Cm , shown at the bottom, provide justification for one of the basic assumptions of the analytical supersymmetric fission (ASAF) model, which was very successful in predicting the half-lives of cluster decay modes. It is remarkable to see for the first time a potential barrier obtained by using the macroscopic-microscopic method for a cluster emitter. Having a smaller height and width compared to the (dotted line) macroscopic Y+EM barrier, it is very similar to the barrier used in ASAF which was based on the Myers-Swiatecki's liquid drop model.¹⁰

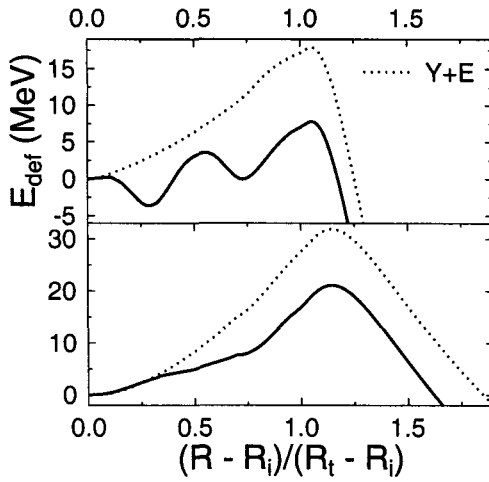


Figure 4. A cut through the PES of ^{242}Cm at symmetry $\eta = 0$ (top) and for ^{34}Si radioactivity with ^{208}Pb daughter (bottom).

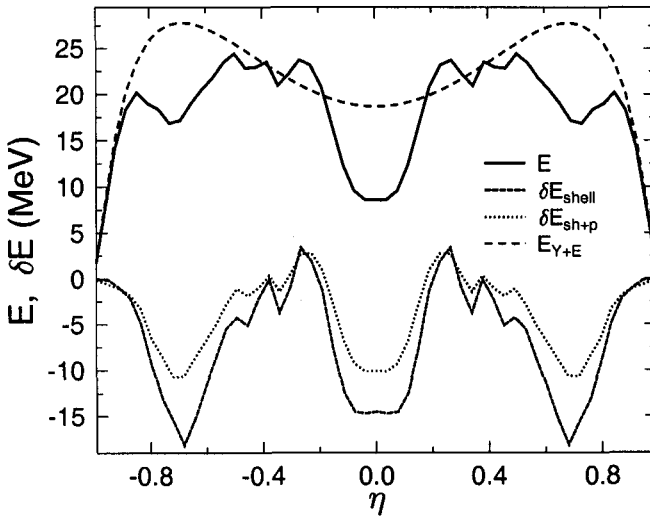


Figure 5. Deformation energies at the touching point configurations ($R = R_t$) of ^{242}Cm vs the asymmetry η : E_{Y+EM} and E_{def} (top); shell + pairing corrections and only shell corrections (bottom).

One can see how deep are the two main valleys on the PES by plotting in Fig. 5 a cut of the PES at the touching point configuration, $R = R_t$. In the upper part of this figure the macroscopic energy E_{Y+EM} (the smooth dashed line) and the total deformation energy E_{def} (heavy line) can be seen. They exhibit few valleys of which that of Sn at lower values of η and that of Pb at higher η are the deepest ones. In the lower part of Fig. 5 there are two other curves representing the shell plus pairing correction (dotted curve) and only the shell corrections (dashed line). As we already mentioned when Fig. 1 was discussed, there are two effects of pairing corrections leading to a smoother variation and to a shallower valley.

In conclusion the strong shell effect associated to the doubly magic character of the daughter ^{208}Pb observed in the systematic analysis of experimental results¹ comes from a deep valley present on the potential energy surfaces. The potential barrier shape of heavy ion radioactivity obtained from the first time by using the macroscopic-microscopic method provides further support for the particular choice of the barrier within the ASAF model.

Acknowledgments

This work was partly supported by Deutsche Forschungsgemeinschaft, Bonn, and by Ministry of Education and Research, Bucharest. We acknowledge also the support by Prof. S. Hofmann, Gesellschaft für Schwerionenforschung (GSI), Darmstadt.

References

1. D.N. Poenaru, Y. Nagame, R.A. Gherghescu, W. Greiner, *Phys. Rev.*, **C65** (2002) 054308; Erratum **C66** 049902.
2. D.N. Poenaru, W. Greiner, in *Nuclear Decay Modes*, (IOP Publishing, Bristol, 1996), Chap. 6, pp. 275.
3. D. N. Poenaru, D. Schnabel, W. Greiner, D. Mazilu, R. Gherghescu, *Atomic Data Nucl. Data Tables*, **48** (1991) 231.
4. D. N. Poenaru, R.A. Gherghescu, W. Greiner, *Nucl. Phys. A* **747** (2005) 182.
5. D. N. Poenaru, R.A. Gherghescu, W. Greiner, *Europ. Phys. J. A* **24** (2005) 355.
6. R. A. Gherghescu, *Phys. Rev.* **67** (2003) 014309.
7. V. M. Strutinsky *Nucl. Phys. A* **95** (1967) 420.
8. D. N. Poenaru, M. Ivaşcu, D. Mazilu, *Comput. Phys. Comm.* **19** (1980) 205.
9. M. Bolsterli, E. Fiset, J. R. Nix, J. Norton, *Phys. Rev C* **5** (1972) 1050.
10. W. D. Myers, W. J. Swiatecki, *Nucl. Phys. A* **81** (1966) 1.

DYNAMICS OF MASS ASYMMMETRY IN DINUCLEAR SYSTEMS

G. G. ADAMIAN¹, A. ANDREEV^{1,2}, N. V. ANTONENKO^{1,2},
R. V. JOLOS^{1,2}, S. P. IVANOVA^{1,2}, YU. V. PALCHIKOV¹, W. SCHEID^{2*},
T. M. SHNEIDMAN¹

¹*Joint Institute for Nuclear Research, 141980 Dubna (Moscow Region), Russia*

²*Institut für Theoretische Physik der Universität Giessen, D-35392, Germany*

* *E-mail: werner.scheid@theo.physik.uni-giessen.de*

The dinuclear system concept assumes two touching nuclei which can exchange nucleons by transfer. This concept can be applied to nuclear structure, to fusion reactions leading to superheavy nuclei and to multi-nucleon transfer.

1. Introduction

The dinuclear system (DNS) concept was introduced by V. V. Volkov¹. A dinuclear system is a configuration of two touching nuclei (clusters) which keep their individuality. Other notations for such a system are nuclear molecule or bi-cluster configuration. Two main degrees of freedom govern the dynamics of the DNS: (1) the relative motion between the nuclei describing the decay of the dinuclear system which is called quasifission and (2) the transfer of nucleons between the nuclei. The latter process changes the mass and charge asymmetries which are defined by the coordinates

$$\eta = \frac{A_1 - A_2}{A_1 + A_2} \quad \text{and} \quad \eta_Z = \frac{Z_1 - Z_2}{Z_1 + Z_2}. \quad (1)$$

These coordinates can be assumed as continuous or discrete quantities. For $\eta = \eta_Z = 0$ we have a symmetric clusterization with two equal nuclei, and if η approaches the values ± 1 or if A_1 or A_2 is equal to zero, a fused system has been formed.

The dinuclear system model has a large variety of applications. In this article we consider nuclear structure phenomena, e. g. normal- and superdeformed bands, the fusion dynamics in producing superheavy nuclei, and the decay of the dinuclear system, i. e. the quasifission since no compound nucleus is formed.

2. Dinuclear configuration

The dinuclear configuration describes quadrupole- and octupole-like deformations corresponding to normal, super- and hyperdeformed states. To demonstrate the deformation we calculated² the mass (m) and charge (c) moments of a nucleus described by a dinuclear configuration with a (mass and charge) density $\varrho(\mathbf{r}) = \varrho_1(\mathbf{r}_1) + \varrho_2(\mathbf{r}_2)$, where ϱ_i ($i = 1, 2$) is the density of the nucleus i . The moments can be compared with those of an axially deformed nucleus by use of a shape expansion with multipole deformation parameters $\beta_\lambda = \beta_0, \beta_1, \beta_2, \beta_3 \dots$. Then one obtains these parameters β_λ as functions of η or η_Z , nearly independent of A for spherical clusters and with a specific dependence on the surface thickness, the radius parameter and the deformation of the clusters².

The dinuclear system model can be applied in the range of $\eta = 0 - 0.3$ to hyperdeformed (HD) states (nuclei with large quadrupole deformation), in the range of $\eta = 0.6 - 0.8$ to superdeformed (SD) states (similar quadrupole and octupole deformations) and around $\eta \approx 1$ to the parity splitting of bands (linear increase of deformations). As example let us discuss the ^{152}Dy system². The potential energy of the DNS as a function of η shows significant minima for $\eta = 0.34$ ($^{50}\text{Ti} + ^{102}\text{Ru}$), $\eta = 0.66$ ($^{26}\text{Mg} + ^{126}\text{Xe}$) and $\eta = 0.71$ ($^{22}\text{Ne} + ^{130}\text{Ba}$). The DNS $^{50}\text{Ti} + ^{102}\text{Ru}$ is compatible with HD properties, the dinuclear systems $^{26}\text{Mg} + ^{126}\text{Xe}$ and $^{22}\text{Ne} + ^{130}\text{Ba}$ have SD properties. For $^{26}\text{Mg} + ^{126}\text{Xe}$ we calculated a moment of inertia of $J=104 \hbar^2/\text{MeV}$ and an electric quadrupole moment of $Q_2=24 \text{ eb}$ in comparison with the experimental values of SD states with $J=(85\pm 3) \hbar^2/\text{MeV}$ and $Q_2=(18\pm 3) \text{ eb}$.

3. Normal- and superdeformed bands

The DNS model can be used to describe the ground state (GS) and superdeformed (SD) bands of various nuclei. Let us apply this model to the structure of ^{60}Zn ³. This nucleus has a threshold of 2.7 MeV above ground state for its decay into $^{56}\text{Ni} + \alpha$. Therefore, one can assume that the ground state band contains an α -component. Further thresholds are positioned at 10.8 and 11.2 MeV above the ground state for the decays into $^{52}\text{Fe} + ^8\text{Be}$ and $^{48}\text{Cr} + ^{12}\text{C}$, respectively. The extrapolated band head of the SD band has an energy of 7.5 MeV and a moment of inertia of $(692-795)M \text{ fm}^2$ in comparison with the moment of inertia of the $^{52}\text{Fe} + ^8\text{Be}$ system of $750 M \text{ fm}^2$. Hence one can assume that the SD band of ^{60}Zn contains a ^8Be component.

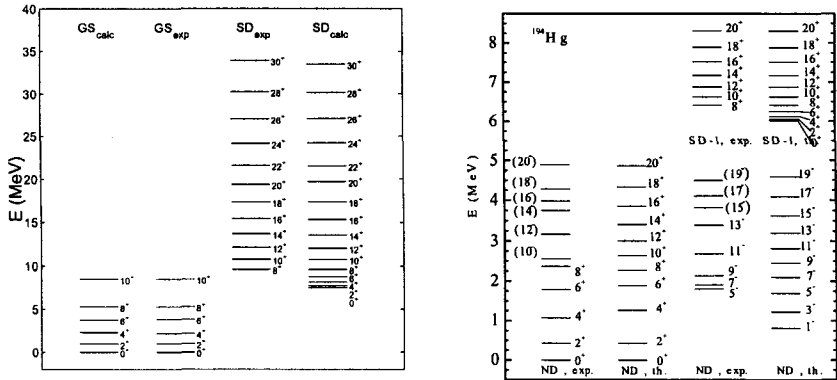


Figure 1. Calculated and experimental levels of the ground state and superdeformed bands of ^{60}Zn (l.h.s.) and ^{194}Hg (r.h.s.) .

The cluster picture of the GS and SD bands can be consistently described by a collective dynamics in the mass asymmetry coordinate η . To achieve this aim we formulate a Schrödinger equation in η . The calculated potential $U(\eta)$ for ^{60}Zn has minima for α -type clusterizations, namely for $^{56}\text{Ni} + \alpha$, $^{52}\text{Fe} + ^8\text{Be}$ and so on. Then the probability $|\psi_I(\eta)|^2$ expressed with the intrinsic wave function is peaked around these potential minima indicating a corresponding cluster structure of the states. In Figure 1 we demonstrate calculated and experimental level spectra of ^{60}Zn and also of ^{194}Hg ⁴. The electromagnetic transition probabilities can be evaluated^{3,4} with the intrinsic wave functions $\psi_I(\eta)$ and agree with the experimental ones. Also the effect of parity splitting is reproducible with the dynamics in η which is related to the octupole degree of freedom near $|\eta| = 1$.

4. Dinuclear dynamics in the fusion process

Heavy and superheavy nuclei can be produced by fusion reactions with heavy ions. We discriminate Pb or Bi based reactions, e. g. $^{70}\text{Zn} + ^{208}\text{Pb} \rightarrow ^{278}112 \rightarrow ^{277}112 + n$ with an evaporation residue cross section of $\sigma = 1$ pb and an excitation energy of the $^{278}112$ compound nucleus of about 11 MeV, and actinide based reactions, e. g. $^{48}\text{Ca} + ^{244}\text{Pu} \rightarrow ^{289}114 + 3n$, with the emission of more neutrons. The cross sections are small because of the strong competition between complete fusion and quasifission.

4.1. Models for production of superheavy nuclei

The models for the production of superheavy nuclei can be discriminated by the dynamics in the most important collective degrees of freedom of the system, i. e. the relative and mass asymmetry motions. The description of the fusion process depends sensitively whether an adiabatic or a diabatic potential in the internuclear coordinate R is assumed.

a) *Models using adiabatic potentials*: These models minimize the potential energy and apply an adiabatic dynamics in the internuclear distance. In that case the nuclei first change their mass asymmetry in the direction of more symmetric clusters and then they fuse together by crossing a smaller fusion barrier in the relative coordinate around $\eta = 0$. The models yield large probabilities for fusion if similar target and projectile nuclei are taken which seems to contradict the exponential fall-off of the evaporation residue cross section with increasing projectile nuclei in Pb based reactions.

b) *Dinuclear system concept*: The fusion proceeds by a transfer of nucleons between the nuclei in a touching configuration, i. e. in the dinuclear configuration. Here, mainly a dynamics in the mass asymmetry degree of freedom occurs. The potential is of diabatic type with a minimum in the touching range and a repulsive part towards smaller internuclear distances prohibiting the dinuclear system to amalgamate to the compound nucleus in the relative coordinate. Such a potential can be achieved with a diabatic two-center shell model and can also be justified with structure calculations based on group theoretical methods⁵.

c) *Comparison of fusion probabilities calculated with adiabatic and dynamical diabatic potentials*⁶: We studied fusion probabilities for the compound system ^{246}Fm using adiabatic and dynamical diabatic potentials obtained with the Strutinsky formalism and single-particle energies of the asymmetric two-center shell model. The fusion is assumed as a statistical diffusion process and estimated with the Kramers formula by taking into account the quasifission. The fusion probabilities are calculated as functions of the initial mass asymmetry $\eta_i = 0 - 0.6$ of the projectile and target for an optimal incident energy. The fusion proceeding in the internuclear coordinate has a large probability of $0.8 - 1$ for the adiabatic potential and an extremely small probability of $10^{-17} - 10^{-6}$ for the dynamical diabatic potential. If the nuclei fuse along the mass asymmetry coordinate, we find fusion probabilities of $10^{-6} - 10^{-1}$ in agreement with the experimental observed ones. Therefore, the experimental fusion probabilities support a fusion process in η as predicted with the DNS model.

4.2. Evaporation residue cross section

The cross section for the production of superheavy nuclei can be written

$$\sigma_{ER}(E_{c.m.}, J) = \sum_{J=0}^{J_{max}} \sigma_{cap}(E_{c.m.}, J) P_{CN}(E_{c.m.}, J) W_{sur}(E_{c.m.}, J). \quad (2)$$

The three factors are the capture cross section, the probability for complete fusion and the survival probability. The maximal contributing angular momentum J_{max} is of the order of 15 - 20. The capture cross section σ_{cap} describes the formation of the dinuclear system at the initial stage of the reaction when the kinetic energy of the relative motion is transferred into potential and excitation energies. The DNS can decay by crossing the quasifission (Coulomb) barrier B_{qf} which is of the order of 0.5 - 5 MeV.

After its formation the DNS evolves in the mass asymmetry coordinate. The center of the mass distribution moves towards more symmetric fragmentations and its width is broadened by diffusion processes. The part of the distribution, which crosses the inner fusion barrier B_{fus}^* of the driving potential $U(\eta)$, yields the probability P_{CN} for complete fusion. The DNS can also decay by quasifission during its evolution. Therefore, the fusion probability P_{CN} and the mass and charge distributions of the quasifission have to be treated simultaneously. The fusion probability can be quantitatively estimated with the Kramers formula and results as $P_{CN} \sim \exp(-(B_{fus}^* - B_{qf})/T)$ where the temperature T is related to the excitation energy of the DNS. Since the inner fusion barrier increases with decreasing mass asymmetry, we find an exponential depression of the fusion probability towards symmetric projectile and target combinations.

The excited compound nucleus undergoes fission and neutron emission besides other negligible decays. The probability to reach the ground state of the superheavy nucleus by neutron emission is denoted as survival probability W_{sur} . In the case of the one-neutron emission in Pb-based reactions the survival probability is roughly the ratio of the width Γ_n for neutron emission to the fission width Γ_f because of $\Gamma_f \gg \Gamma_n$. The survival probability depends sensitively on the nuclear structure properties of the superheavy elements as level density, fission barriers and deformation.

With the DNS concept we can reproduce the measured evaporation residue cross sections of the Pb- and actinide-based reactions with a precision of a factor of two. This concept also yields the excitation energies of the superheavy compound nuclei at the optimal bombarding energies (largest production cross sections) in agreement with the experimental data.

4.3. Isotopic dependence of production cross section

An opinion is that the production cross section is increasing with the neutron number for isotopic superheavy nuclei. For example, the cross sections for Ds ($Z = 110$) increase with the neutron number: $^{62}\text{Ni} + ^{208}\text{Pb} \rightarrow ^{269}\text{Ds} + n$ and $^{64}\text{Ni} + ^{208}\text{Pb} \rightarrow ^{271}\text{Ds} + n$ have evaporation residue cross sections 3.5 and 15 pb, respectively. This opinion can not be generalized. When

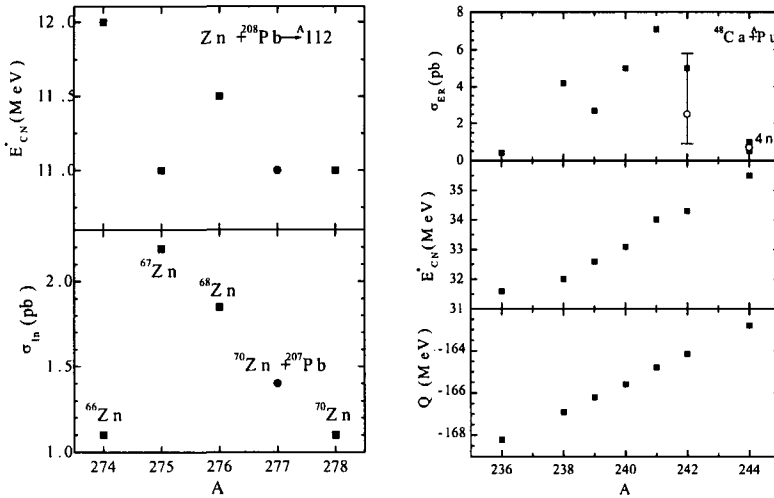


Figure 2. Excitation energy E_{CN}^* , evaporation residue cross section σ_{1n} and Q -value for $Zn + ^{208}Pb \rightarrow ^A112$ (l.h.s.) and $^{48}Ca + ^A Pu$ (r.h.s.). The experimental points are from Ref. [8].

the neutron number of the projectile is increasing, the dinuclear fragmentation gets more symmetrical and the fusion probability decreases if the more symmetric DNS does not consist of more stable nuclei. Also the survival probability is of importance. For compound nuclei with closed neutron shells the survival probability is larger. Hence the product of P_{CN} and W_{sur} determines whether the production cross section increases or decreases with increasing neutron number. Figure 2 shows examples for cold and hot fusion reactions⁷. These calculations are very valuable for an adequate choice of projectile and target nuclei in experiment.

5. Quasifission as a signature for dinuclear systems

The process of quasifission is the decay of the dinuclear system. Since quasifission leads to a large quantity of observable data like mass and charge

distributions, distributions of total kinetic energies (TKE), variances of total kinetic energies and neutron multiplicities, a comparison of the theoretical description with experimental data provides sensitive information about the applicability and correctness of the used model. For this reason we studied the dynamics of mass and charge transfer and the succeeding quasifission with master equations⁹. At the starting point we consider the shell model Hamiltonian of all dinuclear fragmentations of the nucleons. This Hamiltonian can be used to derive master equations for the probability $P_{Z,N}(t)$ to find the dinuclear system in a fragmentation with $Z_1 = Z$, $N_1 = N$ and $Z_2 = Z_{tot} - Z$, $N_2 = N_{tot} - N$. The master equations are

$$\begin{aligned} \frac{d}{dt}P_{Z,N}(t) = & \Delta_{Z+1,N}^{(-,0)}P_{Z+1,N}(t) + \Delta_{Z-1,N}^{(+,0)}P_{Z-1,N}(t) \\ & + \Delta_{Z,N+1}^{(0,-)}P_{Z,N+1}(t) + \Delta_{Z,N-1}^{(0,+)}P_{Z,N-1}(t) \\ & - \left(\Delta_{Z,N}^{(-,0)} + \Delta_{Z,N}^{(+,0)} + \Delta_{Z,N}^{(0,-)} + \Delta_{Z,N}^{(0,+)} \right) P_{Z,N}(t) \\ & - \left(\Lambda_{Z,N}^{qf} + \Lambda_{Z,N}^{fis} \right) P_{Z,N}(t). \end{aligned} \quad (3)$$

The one-proton and one-neutron transfer rates $\Delta^{(\dots)}$ depend on the single particle energies and the temperature of the DNS where the occupation of the single-particle states is taken into account by a Fermi distribution. The simultaneous transfer of more nucleons is neglected. The quantities $\Lambda_{Z,N}^{qf}$ and $\Lambda_{Z,N}^{fis}$ are the rates for quasifission in the coordinate R and for the fission of the heavier fragment, respectively, and are calculated with the Kramers formula. These rates cause a loss of the total probability $\sum P_{Z,N}(t) \leq 1$. Then the mass yield is obtained as

$$Y(A_1) = \sum_{Z_1} \int_0^{t_0} \Lambda_{Z_1,A_1-Z_1}^{qf} P_{Z_1,A_1-Z_1}(t) dt, \quad (4)$$

where $t_0 \approx (3 - 5) \times 10^{-20}$ s is the reaction time. The DNS dynamics was also studied by Li *et al.*¹⁰ with similar master equations.

a) *Results for quasifission*⁹: We calculated quasifission distributions, TKEs, variances of TKE and neutron multiplicities for cold and hot fusion reactions and found satisfying agreement with the experimental data of Itkis *et al.*¹¹. For heavier systems, e. g. $^{48}\text{Ca} + ^{248}\text{Cm}$, the contribution of fission products to the mass distribution can be neglected since the probability for forming a compound nucleus is very small.

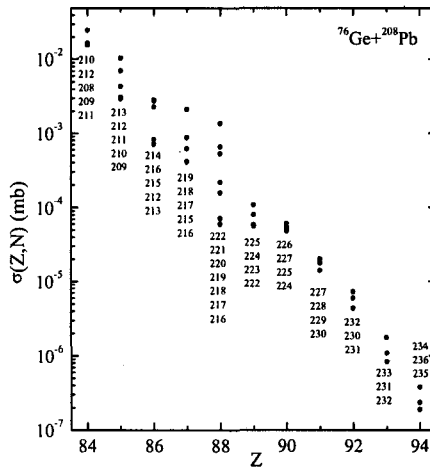


Figure 3. Production cross section in the reaction $^{76}\text{Ge} + ^{208}\text{Pb}$ as a function of Z and A of the heavier fragment.

b) *Production cross sections for asymmetric systems:* The master equations give also probabilities for more asymmetric systems than the initial one. In Figure 3 we present production (transfer) cross sections for asymmetric fragmentations in the reaction $^{76}\text{Ge} + ^{208}\text{Pb}$. The measurement of these observable cross sections would be an unique prove for the fusion dynamics in the dinuclear system concept.

Acknowledgements

We thank DFG (Bonn), VW-Stiftung (Hannover) and RFBR (Moscow) for supporting this work.

References

1. V. V. Volkov, *Izv. AN SSSR ser. fiz.* **50**, 1879 (1986).
2. T. M. Shneidman *et al.*, *Nucl. Phys.* **A671**, 119 (2000).
3. G. G. Adamian *et al.*, *Phys. Rev.* **C67**, 054303 (2003).
4. G. G. Adamian *et al.*, *Phys. Rev.* **C69**, 054310 (2004).
5. G. G. Adamian *et al.*, *Phys. Lett.* **B451**, 289 (1999).
6. G. G. Adamian *et al.*, *Nucl. Phys.* **A671**, 233 (2000).
7. G. G. Adamian *et al.*, *Phys. Rev.* **C69**, 011601 and 014607 (2003).
8. Yu. Ts. Oganessian *et al.*, *Eur. Phys. J.* **A13**, 135 (2002); **A15**, 201 (2002).
9. G. G. Adamian *et al.*, *Phys. Rev.* **C68**, 034601 (2003).
10. W. Li *et al.*, *Europhys. Lett.* **64**, 750 (2003).
11. M. G. Itkis *et al.*, lecture at this school, see <http://mare.tamu.edu/cssp05/>.

This page is intentionally left blank

4. Exotic Matter in Nuclei and Stars.

Neutrinos

This page is intentionally left blank

CLUSTERS OF MATTER AND ANTIMATTER: A MECHANISM FOR COLD COMPRESSION

WALTER GREINER

I will first present the vacuum for the e^+e^- field of QED and show how it is modified for baryons in nuclear environment. Then I discuss the possibility of producing new types of nuclear systems by implanting an antibaryon into ordinary nuclei. The structure of nuclei containing one antiproton or antilambda is investigated within the framework of a relativistic mean-field model. Self-consistent calculations predict an enhanced binding and considerable compression ($4 \dots 5\rho_0$) in such systems as compared with normal nuclei. I present arguments that the life time of such nuclei with respect to the antibaryon annihilation might be long enough for their observation. This yields a mechanism for cold compression.

1. Introduction

It is generally accepted that the physical vacuum has nontrivial structure. This conclusion was first made by Dirac on the basis of his famous equation for a fermion field which describes simultaneously particles and antiparticles. The Dirac equation in the vacuum has a simple form

$$(i\gamma^\mu\partial_\mu - m)\Psi(x) = 0, \quad (1)$$

where $\gamma^\mu = (\gamma^0, \boldsymbol{\gamma})$ are Dirac matrices, m is the fermion mass and $\Psi(x)$ is a 4-component spinor field. For a plane-wave solution $\Psi(x) = e^{-ipx}u_p$ this equation is written as

$$(\hat{p} - m)u_p = 0, \quad (2)$$

where $\hat{p} = \gamma^0 E - \boldsymbol{\gamma}\mathbf{p}$. Multiplying by $(\hat{p} + m)$ and requiring that $u_p \neq 0$ one obtains the equation $E^2 - \mathbf{p}^2 - m^2 = 0$ which has two solutions

$$E^\pm(\mathbf{p}) = \pm\sqrt{\mathbf{p}^2 + m^2}. \quad (3)$$

Here the $+$ sign corresponds to particles with positive energy $E_N(\mathbf{p}) = E^+(\mathbf{p})$, while the $-$ sign corresponds to solutions with negative energy. To ensure stability of the physical vacuum Dirac has assumed that these negative-energy states are occupied, forming what is called now the Dirac sea. Then the second solution of Eq.(3) receives a natural interpretation:

it describes holes in the Dirac sea. These holes are identified with antiparticles. Their energies are obviously given by $E_{\bar{N}}(\mathbf{p}) = -E^{-}(-\mathbf{p}) = \sqrt{\mathbf{p}^2 + m^2}$. Unfortunately, the Dirac sea brings divergent contributions to physical quantities such as energy density, and one should introduce a proper regularization scheme to get rid of these divergences. This picture has received numerous confirmations in quantum electrodynamics and other fields.

One of the most fascinating aspects is the structure of the vacuum in QED and its change into charged vacuum states under the influence of strong (supercritical) electric fields¹, which we briefly remind of.

Figure 1 shows the diving of the deeply bound states into the lower energy continuum of the Dirac equation. In the supercritical case the dived

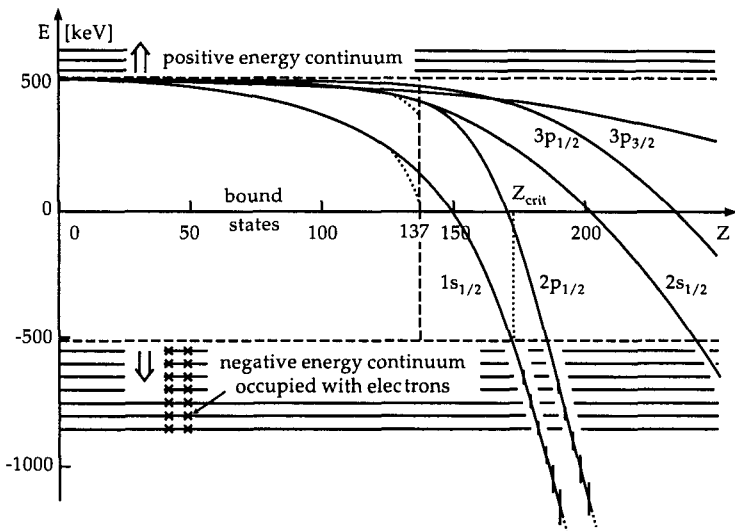


Figure 1. Lowest bound states of the Dirac equation for nuclei with charge Z . While the Sommerfeld fine-structure energies (dashed line) for $s_{1/2}$ and $p_{1/2}$ states end at $Z = 137$, the solutions for extended Coulomb potentials (full line) can be traced down to the negative-energy continuum reached at the critical charge Z_{cr} for the $1s$ state. The bound states entering the continuum obtain a spreading width as indicated.

state is degenerate with the (occupied) negative electron states. Hence spontaneous e^+e^- pair creation becomes possible, where an electron from the Dirac sea occupies the additional state, leaving a hole in the sea which escapes as a positron, while the electron's charge remains near the source. This is a fundamentally new process, whereby the neutral vacuum of QED

becomes unstable in supercritical electrical fields. It decays within about 10^{-19} s into a charged vacuum. The charged vacuum is now stable due to the Pauli principle, i.e., the number of emitted particles remains finite. The vacuum is first charged twice because two electrons with opposite spins can occupy the $1s$ shell. After the $2p_{1/2}$ shell has dived beyond $Z_{cr} = 185$, the vacuum is charged four times, etc. This change of the vacuum structure is not a perturbative effect, as are the radiative QED effects (vacuum polarization, self-energy, etc.). It is hoped to observe it in narrow energy windows in collisions of very heavy ions (e.g. U + Cm) near the Coulomb barrier, where “sticking” of the nuclei by about 10^{-19} s could be possible. Such sticking is important for observing a line-structure in the positron spectrum.

2. The vacuum structure in nuclear physics

It has been noticed already many years ago (see *e.g.* Ref. 2) that nuclear physics may provide a unique laboratory for investigating the Dirac picture of vacuum. The basis for this is given by relativistic mean-field models which are widely used now for describing nuclear matter and finite nuclei. Within this approach nucleons are described by the Dirac equation coupled to scalar and vector meson fields. Scalar S and vector V potentials generated by these fields modify the plane-wave solutions of the Dirac equation as follows

$$E^{\pm}(\mathbf{p}) = V \pm \sqrt{\mathbf{p}^2 + (m - S)^2}. \quad (4)$$

Again, the $+$ sign corresponds to nucleons with positive energy $E_N(\mathbf{p}) = V + \sqrt{\mathbf{p}^2 + (m - S)^2}$, and the $-$ sign corresponds to antinucleons with energy $E_{\bar{N}}(\mathbf{p}) = -E^-(-\mathbf{p}) = -V + \sqrt{\mathbf{p}^2 + (m - S)^2}$. It is remarkable that changing sign of the vector potential for antinucleons is exactly what is expected from the G-parity transformation of the nucleon potential. As follows from Eq. (4), in nuclear environment the spectrum of single-particle states of the Dirac equation is modified in two ways. First, the mass gap between positive- and negative-energy states, $2(m - S)$, is reduced due to the scalar potential and second, all states are shifted upwards due to the vector potential. These changes are illustrated in Fig. 2.

It is well known from nuclear phenomenology that a good description of nuclear ground state is achieved with $S \simeq 350$ MeV and $V \simeq 300$ MeV so that the net potential for nucleons is $V - S \simeq -50$ MeV. Using the same values one obtains for antinucleons very a deep potential, $-V - S \simeq -650$ MeV. Such a potential would produce many strongly bound states

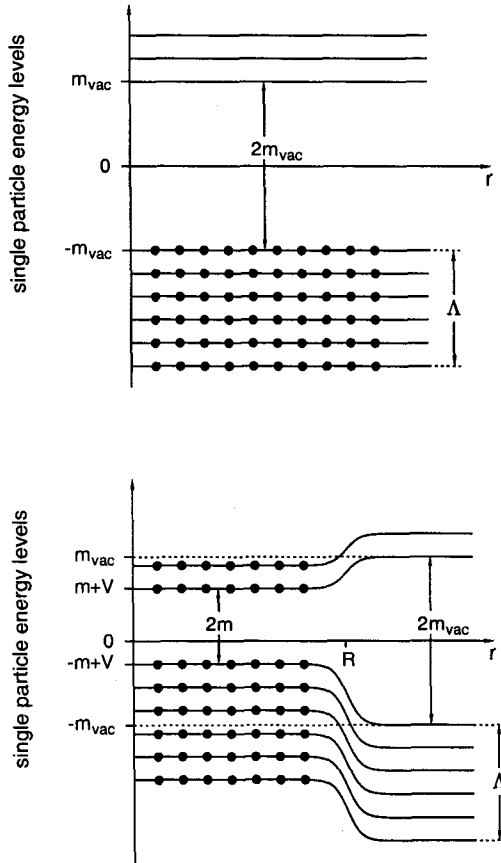


Figure 2. Schematic spectrum of the Dirac equation in vacuum (upper panel) and in a nucleus of radius R (lower panel). A divergent contribution of negative-energy states is often regularized by introducing a cut-off momentum Λ

in the Dirac sea. However, if these states are occupied they are hidden from direct observation. Only creating a hole in this sea, *i.e.* inserting a real antibaryon into the nucleus, would produce an observable effect. If this picture is correct one should expect the existence of strongly bound states of antinucleons with nuclei. Below we report on our recent studies of antibaryon-doped nuclear systems^{3,4}.

3. Systems made of baryons and antibaryons

Unlike some previous works, we take into account the rearrangement of nuclear structure due to the presence of a real antibaryon. The structure of such systems is calculated using several versions of the relativistic mean-field model (RMF): TM1 ⁵, NL3 and NL-Z2 ⁶. Their parameters were found by fitting binding energies and charge form-factors of spherical nuclei from ¹⁶O to ²⁰⁸Pb. The general Lagrangian of the RMF model is written as

$$\begin{aligned}
 \mathcal{L} = & \sum_{j=B, \bar{B}} \bar{\psi}_j (i\gamma^\mu \partial_\mu - m_j) \psi_j \\
 & + \frac{1}{2} \partial^\mu \sigma \partial_\mu \sigma - \frac{1}{2} m_\sigma^2 \sigma^2 - \frac{b}{3} \sigma^3 - \frac{c}{4} \sigma^4 \\
 & - \frac{1}{4} \omega^{\mu\nu} \omega_{\mu\nu} + \frac{1}{2} m_\omega^2 \omega^\mu \omega_\mu + \frac{d}{4} (\omega^\mu \omega_\mu)^2 \\
 & - \frac{1}{4} \vec{\rho}^{\mu\nu} \vec{\rho}_{\mu\nu} + \frac{1}{2} m_\rho^2 \vec{\rho}^\mu \vec{\rho}_\mu \\
 & + \sum_{j=B, \bar{B}} \bar{\psi}_j (g_{\sigma j} \sigma + g_{\omega j} \omega^\mu \gamma_\mu + g_{\rho j} \vec{\rho}^\mu \gamma_\mu \vec{\tau}_j) \psi_j \\
 & + \text{Coulomb part}
 \end{aligned} \tag{5}$$

Here summation includes valence baryons B , in fact the nucleons forming a nucleus, and valence antibaryons \bar{B} inserted in the nucleus. They are treated as Dirac particles coupled to the scalar-isoscalar (σ), vector-isoscalar (ω) and vector-isovector ($\vec{\rho}$) meson fields. The calculations are carried out within the mean-field approximation where the meson fields are replaced by their expectation values. Also a "no-sea" approximation is used. This implies that all occupied states of the Dirac sea are "integrated out" so that they do not appear explicitly. It is assumed that their effect is taken into account by nonlinear terms in the meson Lagrangian. Most calculations are done with antibaryon coupling constants which are given by the G-parity transformation ($g_{\sigma \bar{N}} = g_{\sigma N}$, $g_{\omega \bar{N}} = -g_{\omega N}$) and $SU(3)$ flavor symmetry ($g_{\sigma \bar{\Lambda}} = \frac{2}{3} g_{\sigma \bar{N}}$, $g_{\omega \bar{\Lambda}} = \frac{2}{3} g_{\omega \bar{N}}$). In isosymmetric static systems the scalar and vector potentials for nucleons are expressed as $S = g_{\sigma N} \sigma$ and $V = g_{\omega N} \omega^0$.

Following the procedure suggested in Ref. 7 and assuming axial symmetry of the nuclear system, we solve effective Schrödinger equations for nucleons and an antibaryon together with differential equations for mean meson and Coulomb fields. We explicitly take into account the antibaryon contributions to the scalar and vector densities. It is important that antibaryons give a negative contribution to the vector density, while a positive

contribution to the scalar density. This leads to increased attraction and decreased repulsion for surrounding nucleons. To maximize attraction, nucleons move to the center of the nucleus, where the antiproton has its largest occupation probability. This gives rise to a strong local compression of the nucleus and leads to a dramatic rearrangement of its structure.

Results for the ^{16}O nucleus are presented in Fig. 3 which shows 3D plots of nucleon density distributions. The calculations show that inserting an antiproton into the ^{16}O nucleus leads to the increase of central nucleon density by a factor 2–4 depending on the parametrization. Due to a very deep antiproton potential the binding energy of the whole system is increased significantly as compared with 130 MeV for normal ^{16}O . The calculated binding energies of the \bar{p} - ^{16}O system are 830, 1050 and 1160 MeV for the NL-Z2, NL3 and TM1, respectively. Due to this anomalous binding we call such systems super bound nuclei (SBN). In the case of antilambdas we rescale the coupling constants with a factor 2/3 that leads to the binding energy of 560–700 MeV for the $\bar{\Lambda}$ - ^{16}O system. As a second example, we investigate the effect of a single antiproton inserted into the ^8Be nucleus. The normal ^8Be nucleus is not spherical, exhibiting a clearly visible 2α structure with the ground state deformation $\beta_2 \simeq 1.20$. As seen in Fig. 4, inserting an antiproton in ^8Be results in a much less elongated shape ($\beta_2 \simeq 0.23$) and disappearance of its cluster structure. The binding energy increases from 53 MeV to about 700 MeV. Similar, but weaker effects have been predicted⁸ for the K^- bound state in the ^8Be nucleus.

The calculations have been performed also with reduced antinucleon coupling constants as compared to the G-parity prescription. We have found that the main conclusions about enhanced binding and considerable compression of \bar{p} -doped nuclei remain valid even when coupling constants are reduced by a factor 3 or so.

4. Life-time estimates

The crucial question concerning possible observation of the super-bound nuclei (SBNs) is their life time. The main decay channel for such states is the annihilation of antibaryons on surrounding nucleons. The energy available for the annihilation of a bound antinucleon equals $Q = 2m_N - B_N - B_{\bar{N}}$, where B_N and $B_{\bar{N}}$ are the corresponding binding energies. In our case this energy is at least by a factor 2 smaller as compared with the vacuum value of $2m_N$. This should lead to a significant suppression of the available phase space and thus to a reduced annihilation rate in medium. We have

Sum of proton and neutron densities for ^{16}O (top),
 ^{16}O with $\bar{\Lambda}$ (bottom left) and ^{16}O with \bar{p} (bottom right)

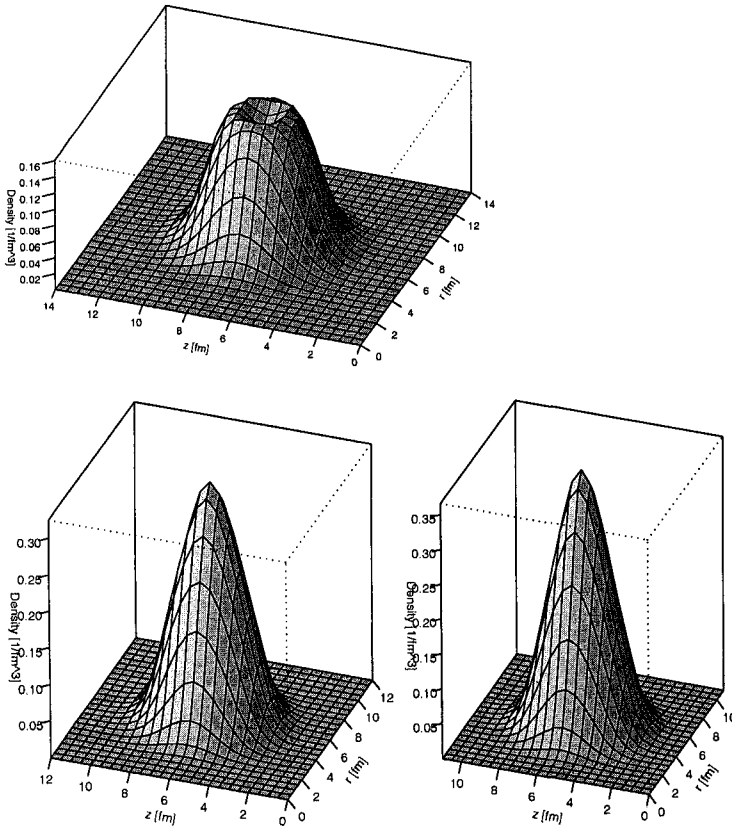


Figure 3. Sum of neutron and proton densities for ^{16}O (top), ^{16}O with \bar{p} (bottom right) and ^{16}O with $\bar{\Lambda}$ (bottom left) calculated with the parametrization NL-Z2.

performed detailed calculations assuming that the annihilation rates into different channels are proportional to the available phase space. All intermediate states with heavy mesons like ρ , ω , η as well as multi-pion channels have been considered. Our conclusion is that decreasing the Q value from 2 GeV to 1 GeV may lead to the reduction of total annihilation rate by a factor of 20÷30. Then we estimate the SBN life times on the level of 5-25 fm/c which makes their observation feasible. This large margin in the life times is mainly caused by uncertainties in the overlap integral between antinucleon and nucleon scalar densities. Longer life times may be expected for SBNs containing antihyperons. The reason is that instead of pions more heavy kaons must be produced in this case. We have also analyzed multi-

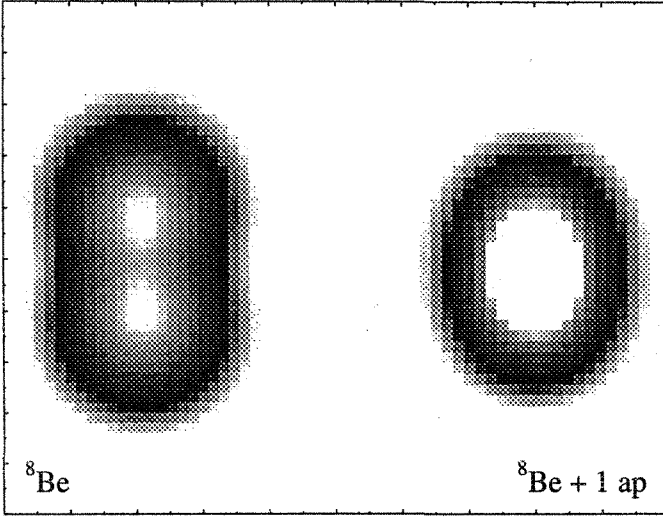


Figure 4. Contour plot of nucleon densities for ${}^8\text{Be}$ without (left) and with (right) antiproton calculated with the parametrization NL3.

nucleon annihilation channels (Pontecorvo-like reactions) and have found their contribution to be less than 40% of the single-nucleon annihilation^{3,4}.

We believe that such exotic nuclear states can be produced by using antiproton beams of multi-GeV energy, *e.g.* at the future GSI facility. It is well known that low-energy antiprotons annihilate on the nuclear periphery (at about 5% of the normal density). Since the annihilation cross section drops significantly with energy, a high-energy antiproton can penetrate deeper into the nuclear interior. Then it can be stopped there in an inelastic collision with a nucleon, *e.g.* via the reaction $A(\bar{p}, N\pi)\bar{p}A'$, leading to the formation of a \bar{p} -doped nucleus. Reactions like $A(\bar{p}, \Lambda)\bar{\Lambda}A'$ can be used to produce a $\bar{\Lambda}$ -doped nuclei. Fast nucleons or lambdas can be used for triggering such events. In order to be captured by a target nucleus final antibaryons must be slow in the lab frame. Rough estimates of the SBN formation probability in a central $\bar{p}A$ collision give values in the order of $10^{-5} - 10^{-6}$. With the \bar{p} beam luminosity of $2 \cdot 10^{32} \text{ cm}^{-2}\text{s}^{-1}$ planned at GSI this will correspond to the reaction rate of a few tens of desired events per second.

Several signatures of SBNs can be used for their experimental observation. First, annihilation of a bound antibaryon can proceed via emission

of a single photon, pion or kaon with an energy of about 1 GeV (such annihilation channels are forbidden in vacuum). So one may search for relatively sharp lines, with width of $10\div 40$ MeV, around this energy, emitted isotropically in the SBN rest frame. Another signal may come from explosive disintegration of the compressed nucleus after the antibaryon annihilation. This can be observed by measuring radial collective velocities of nuclear fragments. Such systems serve as a tool for creating cold compression of nuclear matter, in contrast to nuclear compression in high energy nucleus-nucleus encounters where nuclear shock waves – due to the Rankine-Hugoniot relation – yield compression and heating closely connected. For more details on all the points discussed here I refer to our comprehensive paper by Mishustin *et al.*⁴.

Acknowledgments

I am grateful to T. J. Bürvenich, I.N. Mishustin and L.M. Satarov for fruitful discussions and help in the preparation of this talk.

References

1. W. Greiner, B. Müller, J. Rafelski, *Quantum electrodynamics of strong fields*, Springer Verlag, 2nd edition, December 1985
2. N. Auerbach, A.S. Goldhaber, M.B. Johnson, L.D. Miller, A. Picklesimer, *Phys. Lett.* **B182** (1986) 221.
3. T. Bürvenich, I.N. Mishustin, L.M. Satarov, J. A. Maruhn, H. Stöcker, W. Greiner, *Phys. Lett.* **B542** (2002) 261.
4. I. N. Mishustin, L. M. Satarov, T. J. Bürvenich, H. Stöcker, and W. Greiner, *Phys. Rev.* **C71**, 035201 (2005)
5. Y. Sugahara and H. Toki, *Nucl. Phys.* **A579** (1994) 557.
6. M. Bender, K. Rutz, P.-G. Reinhard, J.A. Maruhn, and W. Greiner, *Phys. Rev.* **C60** (1999) 34304.
7. G. Mao, H. Stöcker, and W. Greiner, *Int. J. Mod. Phys.* **E8** (1999) 389.
8. Y. Akaishi and T. Yamazaki, *Phys. Rev.* **C65** (2002) 044005.
9. I.N. Mishustin, L.M. Satarov, H. Stöcker, W. Greiner, *Phys. Rev.* **C 59** (1999) 3343.

THE BRAHMS EXPERIMENT QUEST FOR EARLY UNIVERSE PHASES OF HADRONIC MATTER*

ZBIGNIEW MAJKA[†]

*M. Smoluchowski Institute of Physics, Jagiellonian University
ul. Reymonta 4, 30-059 Kraków, Poland*

We report BRAHMS experiment study of hadronic matter phases created at RHIC. Heavy ion collisions at RHIC energies are characterized by a high degree of transparency of colliding nuclei leading to the formation of a baryon-poor central region. An initial energy density in this zone is well above the energy density considered necessary for the formation of quark-gluon plasma. Some forward rapidity results suggest the possible color glass condensate phase in colliding nuclei.

1. Introduction

Thirty years ago, Collins and Perry [1], realized that the asymptotic freedom property of Quantum Chromodynamics (QCD) suggests the existence of an extremely dense form of hadronic matter with deconfined quarks and gluons, called later by Shuryak [2], and others [3], the Quark Gluon Plasma (QGP). This theoretical background led to the construction of the Relativistic Heavy Ion Collider (RHIC) at the Brookhaven National Laboratory [4]. Since the year 2000, four complementary experiments, namely BRAHMS [5], PHENIX [6], PHOBOS [7], and STAR [8], are investigating this novel abnormal dense state of nuclear matter. Some results obtained by these four experiments can be rather easily understood in the frame of the theoretical picture that has been developed before RHIC started taking data, but some of the results are quite puzzling. It has been proposed that some effects observed by the BRAHMS experiment might be related to the possible existence of the nuclei prior to the collisions in the Color Glass Condensate phase (CGC) [9].

2. Quark Gluon Plasma

The fact that a single quark has never been observed has been the greatest puzzle of elementary particle physics for years. This basic experimental fact has led theorists to conjecture that quarks may be permanently confined within hadrons as a result of the fundamental nature of the chromo-dynamic force. The

* Work partially supported by the Rector of the Jagiellonian University grants.

[†] For BRAHMS Collaboration.

quantum field theory describes the interaction of quarks through the strong color field whose quanta are gluons. This theory called Quantum Chromodynamics (QCD) is a gauge theory with non-Abelian symmetry group.

The non-Abelian nature of QCD gives rise to the confining force which does not decrease with increasing separation distance of quarks. The intrinsic strength of the color force between quarks decreases as they are brought closer together. At asymptotically small separations, the quarks are virtually free (asymptotic freedom). Now the physics of quark confinement in QCD is well established experimentally and by numerical simulations of lattice gauge theories. However, little is known about the confinement mechanism and how the parton physics at short distances smoothly evolves into hadron physics at large distances. The understanding of this transition requires non-perturbative knowledge of the parton dynamics at all length scales. It was mentioned in the introduction that QCD predicts the existence of a deconfined form of hadronic matter called a quark gluon plasma [1, 10], in which the quarks and gluons normally confined within hadrons are liberated. This transition might occur at the energy density of an order of magnitude higher than the energy density inside of atomic nuclei, that is larger than $1 \text{ GeV}/\text{fm}^3$ [11]. It is possible that the condition for deconfinement could exist in neutron star cores, in exploding black holes, or may have been present in the early Universe, a few microseconds after Big Bang. It was suggested in the mid 70s by W. Greiner and others [12], that QGP can be formed in a laboratory by use of relativistic heavy ion collisions. This theoretical motivation led to the construction of the Relativistic Heavy Ion Collider (RHIC) at the Brookhaven National Laboratory.

3. Color Glass Condensate

The ideas for a new form of hadronic matter which controls the high energy limit of strong interactions are motivated by HERA experiment data on the gluon distribution function inside protons, $xG(x, Q^2)$ [13]. The issue of x and Q^2 dependence of parton distributions at very small values of the Bjorken x variable is one of the most interesting and challenging problems in QCD related to our understanding of hadrons. The wave function of a very high energy hadron has contributions from quarks, anti-quarks and gluons with energies from values of the order of the scale of light hadron masses, $E \sim 200 \text{ MeV}$, up to that of hadron energies. A useful variable, x which characterizes these quark degrees of freedom is the typical energy of the constituent scaled by that of the hadron. The quantity Q^2 is the resolution scale measured in the inverse momentum of the probe, which is usually a virtual photon. The essential feature of small x physics is that the gluon density is very large. These high density gluons exist in a very coherent configuration, the color glass condensate. The gluon density can be thought of as a momentum scale squared at saturation, Q_s^2 . Here, the saturation means that the density of gluons approaches a fixed limit as x goes toward

smaller values. The gluon phase space density in a hadron or nucleus of radius R for $p_T^2 \leq Q_s^2$ is given by:

$$\frac{1}{\pi R^2} \frac{dn_g}{dy d^2 p_T} \propto \frac{1}{\alpha_s}$$

Because the strong interaction coupling, α_s , is evaluated at $Q_s^2 \gg \Lambda_{QCD}^2$, the coupling is small ($\alpha_s \ll 1$). This means that the quantum mechanical states of the system are multiply occupied and share some properties of Bose condensates - hence the gluons are in a condensate. The gluons at small x are generated from gluons at larger values of x , and in the infinite momentum frame their natural time scales are Lorentz time-dilated. This time-dilated scale is transferred to the small x degrees of freedom which therefore evolve very slowly as compared to natural time scale - this is the property of the glass. The gluons which make up this glass condensate are colored and now the Color Glass Condensate (CGC) phrase has been explained. The CGC is considered as a universal form of QCD matter which describes high energy strongly interacting particles and nuclei.

While the QGP is the incoherent thermal limit of QCD matter at high temperature, the CGC is the coherent limit of QCD matter at high energies. If the QGP has been created at RHIC from the interaction of initial nuclear matter, then the CGC has to be also present at RHIC collisions.

4. BRAHMS Experimental Setup

The BRAHMS experimental setup [5], has the unique capability among the four RHIC experiments [5-8], to measure identified hadrons with high transverse momenta that can reach up to about 5 GeV/c and can access rapidities close to the beam value for the top RHIC energy. The very different momenta and particle densities at mid-rapidity and forward angles has led to a design with two moveable magnetic spectrometers [14]. The BRAHMS experiment also has four global detector systems. A perspective view of the experimental setup is presented in Fig. 1. The Forward Spectrometer (FS) has a solid angle of 0.8 msr and measures identified particles having momenta up to 25 GeV/c in the angular range of $2.3^\circ < \theta < 30^\circ$. Four magnets (D1-D4) are used for sweeping and analyzing particles emerging from the reaction. The forward arm of the FS tracking detectors (T1 and T2) are Time Projection Chambers (TPCs) which provide good three-dimensional track recognition and rejection of background in a high multiplicity environment. The back arm of the FS tracking detectors (T3-T5) are Drift Chambers (DCs) and each consists of three identical modules that contain 10 (8) detection planes for T3 (T4-T5). Particle identification in the FS is based on two time-of-flight hodoscopes

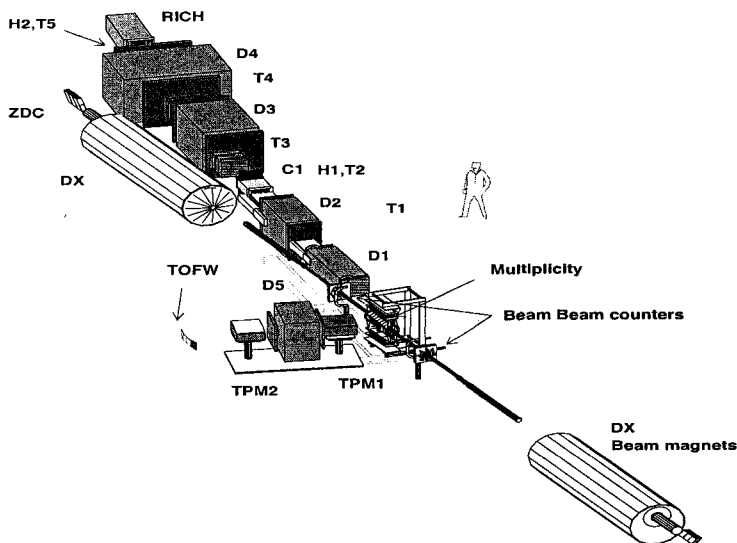


Figure 1. The BRAHMS experimental setup in perspective.

(H1-H2) as well as on Čerenkov measurements. Higher momentum particles are identified with a threshold Čerenkov detector (C1) placed behind the H1 magnet and a ring imaging Čerenkov detector (RICH) placed behind H2. The Mid-Rapidity Spectrometer (MRS) has a solid angle of 6.5 msr and measures identified particles having momenta in the range $0.2 \text{ GeV}/c < p < 5 \text{ GeV}/c$ and in the angular range of $30^\circ < \theta < 95^\circ$. The single dipole magnet (D5) of the MRS is placed between two TPC's which are used for tracking. Particle identification is obtained with a time-of-flight wall. Four global detector systems are used to enable event characterization. Around the interaction vertex a global multiplicity array is used to estimate event-by-event centrality. The Multiplicity Array (MA) consists of two independent systems with a modestly segmented silicon strip detector array (SiMA) surrounded by an outer plastic scintillator tile array (TMA) in a double, hexagonal-side barrel arrangement.

The silicon strip detectors also provide information on overall charged particle yields, with an effective coverage in pseudorapidity of $-3.0 \leq \eta \leq 3.0$. Beam - Beam Counters (BBC) are located 220 cm from the nominal interaction vertex near the beam pipe. They are constructed from two sizes of Čerenkov radiators glued to photo-multiplier tubes. The primary task for the BB counters is to provide a start time and a level 0 trigger. The 50 ps time resolution of the array allows the determination of the vertex position to an accuracy of 0.9 cm. These detectors also provide multiplicity information at high pseudo-rapidity with $2.1 \leq |\eta| \leq 4.7$. The Zero Degree Calorimeters (ZDCs) are located $\pm 18 \text{ m}$

from the nominal interaction vertex and detect neutrons emitted in a small cone ($\theta < 2$ mrad) around the downstream beam directions. The neutron multiplicity is correlated with the event geometry and can therefore be used along with the multiplicity array and beam-beam counters to estimate the centrality of the collision. The ZDCs coincidence can provide a minimum-bias selection making it useful as an event trigger as well as a luminosity monitor. Clean selection of minimum-biased events required a coincidence between the two ZDCs and a minimum of 4 hits in the TMA. Such selections include 95% of the total nuclear cross section of 7.1 b. There are identical sets of ZDCs in all of the RHIC experiments. This enables a cross check of results from all four experiments and provides luminosity measurements for the RHIC machine group.

5. Selected Results from the BRAHMS Experiment

The main focus here is to give an overview of the main BRAHMS results on the properties of hot and high energy density hadronic matter produced in ultra-relativistic heavy ion collisions at RHIC. The kinetic energy that is removed from the beam and which is available for the production of new states of hadronic matter (e.g. QGP) depends on the amount of stopping between the colliding nuclei. BRAHMS has measured the net proton rapidity distribution in (0–10)% central Au+Au collisions at full RHIC energy [15], and the results are displayed in Fig. 2 together with the results of measurements at AGS [16], and SPS accelerators [17].

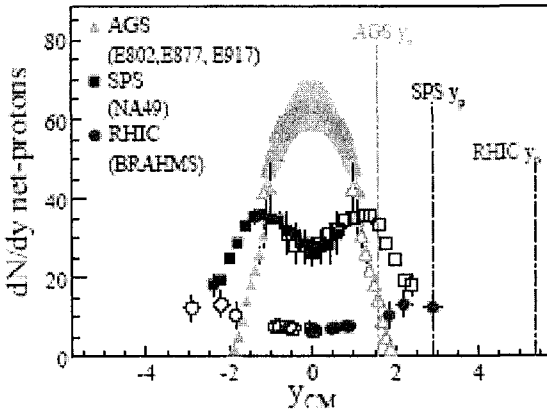


Figure 2. Rapidity density of net protons (i.e. number of protons minus number of antiprotons) measured at AGS [16], SPS [17], and RHIC by BRAHMS [15].

The net number of protons per unit of rapidity around $y = 0$ is only about 7 and the distribution is flat over at least ± 1 unit of rapidity. The distribution rises in the rapidity range $y = 2-3$ to an average $dN/dy \approx 12$. These results indicate that heavy ion collisions at RHIC energies are characterized by a high degree of transparency of colliding nuclei leading to the formation of a baryon-poor central region. From such measurements one may deduce the upper and lower limits for both the rapidity and energy losses at RHIC. The analysis of the data establishes that 26 TeV of kinetic energy is removed out of 35 TeV available energy per central Au+Au collision and this energy is available for particle production in a small volume immediately after collision.

The multiplicity distribution of emitted particles is a fundamental observable in ultra-relativistic collisions due to its sensitivity to all stages of the reaction. It was observed that the production of charged particles in central Au + Au collisions at $\sqrt{s_{NN}} = 200$ GeV exceeds the particle production per participant pair observed in elementary p + p collisions at the same energy by 40–50% [18]. This means that nucleus-nucleus collisions at the considered energies are far from being the simple superposition of elementary collisions. The measurement of charged particle density $dN_{ch}/d\eta$ can be used to estimate the so called Bjorken energy density, ε [19]. For the central Au+Au reaction at $\sqrt{s_{NN}} = 200$ GeV this estimation gives the value $4 \text{ GeV}/\text{fm}^3$. This value exceeds by the factor 4 the predicted energy density for the boundary between hadronic and QGP phases [11].

The first collisions of gold ions at nucleon-nucleon center-of-mass energies of 130 GeV at RHIC revealed a dramatic decrease of pion production at high transverse momentum p_T as compared to an incoherent sum of pions produced in p+p collisions at the same energy [20]. High p_T hadrons are primarily produced from the fragmentation of the hard-scattered partons and the observed suppression could be either due to the initial state shadowing of the gluon distribution inside the nuclei [21], or due to the final state jet energy degradation [22]. The crucial test of these different mechanisms has been performed during the third RHIC run when collisions between deuterium and gold ions at $\sqrt{s_{NN}} = 200$ GeV were investigated. Figure 3 shows the so-called modification factor measured for central Au+Au collisions and minimum bias d+Au collisions at $\sqrt{s_{NN}} = 200$ GeV [23]. The modification factor is defined as a ratio of the particle yield produced in a nucleus-nucleus collision scaled with the number of binary collisions and the particle yield produced in an elementary nucleon-nucleon collision. The absence of the suppression around midrapidity in the d+Au collisions suggests that the suppression observed in the Au+Au collisions is indeed due to final state interactions. However it was also observed in the

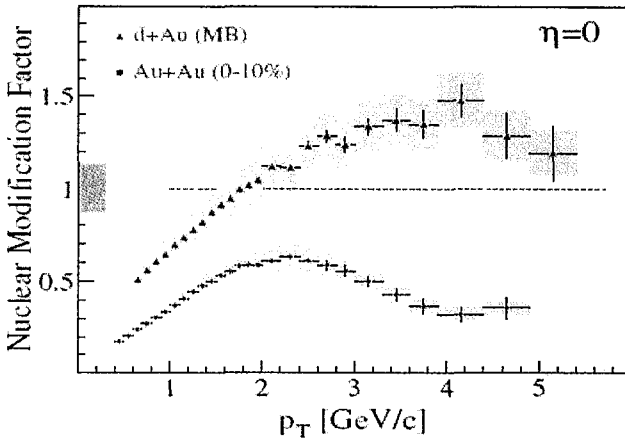


Figure 3. Nuclear modification factors measured for central Au+Au collisions and minimum bias d+Au collisions at $\sqrt{s_{NN}} = 200$ GeV [23].

BRAHMS experiment that at forward pseudorapidity $\eta = 2.2$ inclusive negatively charged hadrons are suppressed in both Au+Au and minimum-bias d+Au collisions [23,27]. This observation suggests the possible existence of nuclei prior to the collisions in the CGC state.

6. Summary

The matter that is created at RHIC differs from anything that has been seen before. The overall scenario of ultra-relativistic heavy ion collisions at RHIC is consistent with particle production from a color field formation of a QGP and subsequent hadronization. The suppression of high p_T particles seen at forward rapidities in nucleus-nucleus collisions is a novel effect and may be related to the CGC. We must wait for deeper a understanding of the observed matter.

References

1. J. C. Collins and M. J. Perry, *Phys. Rev. Lett.* **34**, 1353 (1975).
2. E. V. Shuryak, *Phys. Lett.* **B78**, 150 (1978).
3. O. K. Kalashnikov and V. V. Klimov, *Phys. Lett.* **B88**, 328 (1979);
J. I. Kapusta, *Nucl. Phys.* **B148**, 461 (1979).
4. RHIC: <http://www.bnl.gov/rhic/default.htm>
5. BRAHMS experiment home pages:
<http://www4.rcf.bnl.gov/brahms/WWW/brahms.html>.
6. PHENIX experiment home pages: <http://www.phenix.bnl.gov>
7. PHOBOS experiment home pages: <http://www.phobos.bnl.gov>
8. STAR experiment home pages: <http://www.star.bnl.gov>

9. D. Kharzeev *et al.*, *Phys. Lett.* **B561**, 93, (2003).
10. G. Baym and S. A. Chin, *Phys. Lett.* **B62**, (1976);
B. A. Freedman and L. D. McLerran, *Phys. Rev. D* **16**, 1169 (1977);
G. Chaplin and M. Nauenberg, *Phys. Rev. D* **16**, 450 (1977).
11. F. Karsch, *Nucl. Phys.* **A698**, 199 (2002).
M. Gyulassy and T. Matsui, *Phys. Rev. D* **29**, 419 (1984).
12. J. Hofmann *et al.*, Bear Mountain Workshop, New York, Dec. 1974;
H. G. Baumgardt *et al.*, *Z. Phys.* **A273**, 359 (1975).
13. J. Breitweg *et al.*, *Eur. Phys. J.* **67**, 609 (1999).
14. A. Adamczyk, *Nucl. Instr. and Meth.*, **A499**, 227 (2001).
15. I. G. Bearden *et al.*, *Phys. Rev. Lett.* **93**, 1020301 (2004).
16. B. B. Back *et al.*, *Phys. Rev. Lett.* **86**, 1970 (2001).
L. Ahle *et al.*, *Phys. Rev.* **C60**, 064901 (1999).
J. Barette *et al.*, *Phys. Rev.* **C62**, 024901 (2000).
17. H. Appelshauser *et al.*, *Phys. Rev. Lett.* **82**, 2471 (1999).
18. I. G. Bearden *et al.*, *Phys. Lett.* **B523**, 227 (2001);
I. G. Bearden *et al.*, *Phys. Rev. Lett.* **88**, 202301 (2002).
19. J. D. Bjorken, *Phys. Rev. D* **27**, 140 (1983).
20. K. Adcox *et al.*, *Phys. Rev. Lett.* **88**, 022301 (2002).
21. D. Kharzeev, E. Levin and L. McLerran, *Phys. Lett.* **B561**, 93 (2003).
22. J. D. Bjorken, Fermilab-Pub-82-059 THY;
D. Appell, *Phys. Rev. D* **33**, 717 (1986);
M. Gyulassy and M. Plamer, *Phys. Lett.* **B243**, 432 (1990).
23. I. Arsene *et al.*, *Phys. Rev. Lett.* **91**, 072305 (2003).
24. I. Arsene *et al.*, *Phys. Rev. Lett.* **93**, 242303 (2004).

STRANGE MATTER IN CORE-COLLAPSE SUPERNOVAE

J.E. HORVATH[†]

*Instituto de Astronomia, Geofísica e Ciências Atmosféricas,
Universidade de São Paulo R. do Matão 1226, Cidade Universitária
05508-900 São Paulo SP – BRAZIL*

We present a discussion of the main features of the appearance and propagation of hypothetical strange quark matter inside massive star collapsing cores, expected to add energy to the explosion of a Type II supernova. We show first the different approaches and results obtained for the critical conditions for the nucleation of a small chunk of this matter. Then, issues related to the type of outward propagation (quite analogous to a thermonuclear combustion, but in the supranuclear density regime) are discussed, with emphasis on the several dynamical instabilities of the flame and combustion regimes, a problem not yet solved and of considerable complexity. Finally we outline other applications of these models including "short" GRB and gamma flares from galactic neutron stars.

1. Introduction

1.1. *Early Days of Quark Matter and the Rise of a Wild Hypothesis*

The first reports addressing the possible existence of quarks inside stars are over three decades old now [1]. We are still not completely sure about their relevance for relativistic astrophysics, but it must be also acknowledged that the "standard" assumption of a normal (i.e. confined hadrons) composition is nothing but an act of faith given the observational set of constraints. Therefore, it has become fashionable to construct and test quark matter models by calculating stellar properties and other astrophysical features. Generally speaking, the original expectation was that quark matter may appear at high pressure forming a compact core above a certain critical density, while the external layers of the star were still composed of normal hadrons.

After this early work, a handful of very interesting papers [2] entertained the idea of a metastable or even *absolutely stable* quark matter (SQM), in which the

[†] Available at foton@astro.iag.usp.br

“opening” of a third Fermi sea (the strange quark one) was fundamental to share the energy by reducing its value per baryon number unit. A sketch of this hypothetical situation is depicted in Fig. 1.

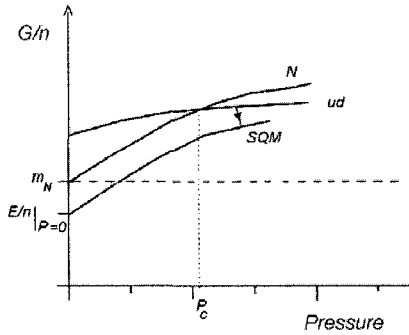


Figure 1. The free energy per baryon number unit as a function of the pressure. If a transition to deconfined quark matter happens at a certain critical pressure (dotted line), the possibility of creating a third Fermi sea by the decay to s quarks could lower the energy per baryon, perhaps to a value which is lower than the nucleon mass at zero pressure (vertical axis). In this case, the three-flavor uds matter would not decay back into hadrons, and received the special name of Strange Quark Matter, or SQM for short.

It is important to remark at this point that, by hypothesis, the energy release in the transition (indicated with an arrow in Fig. 1) is not purely due to latent heat, but rather to the existence of a “chemical” difference between the phases. Therefore, the two-step process globally seen as $n \rightarrow uds$ renders an analogous to a laboratory combustion [3].

Several issues arise, related to the appearance, propagation and astrophysical consequences of the SQM hypothesis. In what follows we shall sketch some of these issues, and finally list a number of open questions useful for those who wish to contribute to this field.

2. Appearance (nucleation) of SQM

An initial seed of SQM is needed if a combustion of the star will happen. This can be achieved either by the presence of a “dormant” strangelet(s) present from earlier phases of stellar evolution (i.e. by accretion from the interstellar medium), or by the decay to SQM of a small blob of two-flavor ud matter (much in the same way as described in Fig. 1), a process that involves the *nucleation* of

a quark phase. The first mechanism has been shown to be likely, actually so likely that it is almost impossible to avoid a contamination in every neutron star. Therefore, these ideas lead to a SQM of most of “neutron stars”, an observation that prompted early objections [4] against the Bodmer-Terazawa-Witten hypothesis. An assessment of these problems can be found in Ref. [5] and references therein.

The probability of nucleation, on the other hand, has been calculated by a number of works using nucleation theories, both classical [6] and quantum [7]. The expectation of nucleation in a “hot” environment (see below) suggests that at \approx few TeV the classical thermal regime would be the most relevant. However, if this stage is bypassed without SQM nucleation, all the relevant temperatures would be ineffective and the quantum regime be the most relevant. The expressions of the first regime are controlled by exponentials of the work needed to create a bubble of SQM with radius r , of the form

$$W = -\frac{4}{3}\pi r^3(P_i - P_e) + 4\pi\sigma r^2 - 8\pi\gamma r + \frac{4}{3}\pi r^3 n_i(\mu_i - \mu_e) \quad (1)$$

where P_i, P_e are the quark and hadron pressures, μ_i, μ_e their chemical potentials and σ, γ the surface and curvature coefficients at the interface.

We draw the attention to the third and fourth terms, which are unlike other nucleation situations. The linear one is the so-called *curvature* term, which is proper of light fermions confined to a cavity [8]. It is known to disfavor the nucleation of the quark phase in general. The last term contains the composition effects, and it is quite dependent on the specific hypothesis made about the nucleation process.

The nucleation rates happen to be (no surprise) extremely dependent on the temperature and density respectively. Since the temperatures needed for SQM nucleation in the thermal regime are at least one order of magnitude lower than the physical temperatures inside a collapsing core, we believe that is quite difficult to “hold” the protostar in the hadronic state after several seconds. Another reason is that, for generic equations of state, the difference between the central density of a $\approx 1.5M_\odot$ model and the maximum mass model along the same sequence is something like $\Delta\rho/\rho \approx 2$. This means that if the star does not convert to SQM at birth, the critical density must be fine-tuned. The situation is shown in Fig. 2.

In summary, even though it is not clear that nucleation of SQM happens at all, there are strong indications that if that ever happens, the high-temperature, high-density regime in a collapsing core would be the ideal place. It has also been shown that the presence of neutrinos quench the nucleation [9], in addition to the fact that the star rises its central density only when neutrino diffusion happens. This again suggests that the moment of nucleation might be \sim seconds after a supernova bounce.

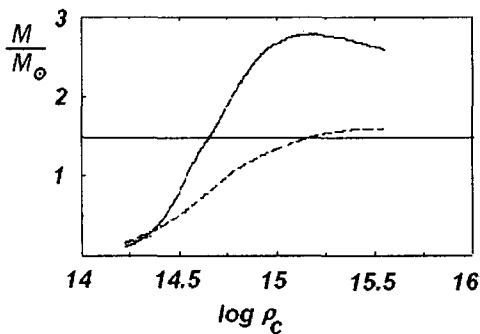


Figure 2. The mass of the stellar models as a function of their central density, for two different equations of state. In the cases of the stiffer equation of state, the difference between the central density of the 1.5 solar mass model and the maximum mass is around a factor of 2, and much less for the softer one. Accretion of, say 0.1–0.5 solar masses would not change the central density of the star a lot, and then the critical value must be “tuned” for a mixed hadronic/strange population.

3. What Happens Next?

The inevitable propagation of the phase change converting the star to SQM is quite different from the case in which quark matter appears only at high pressure. Descriptions using kinetic formalisms employed for ordinary combustions led to the idea that *deflagrations* (slow combustions) are the preferred mode [10]. However, fast combustions (*detonations*) are a possibility in spite of the relative slowness of weak interactions that limit the rate at which matter creates its strangeness content. This issue is still open, given that several examples of two-step detonations which start with an endothermic reaction are known. In addition, if there is some “overshooting” and the initial seed happens to be macroscopic, the star would face a sudden build of an overpressure almost instantaneously, a situation known to be favorable for the launch of a shock of strength $\approx \Delta P / 2$ (Fig. 3), capable of starting a detonation wave.

Another feature that points towards a non-laminar combustion mode is the occurrence of instabilities on very short timescales, of the order of $\approx \text{ms}$. The most conspicuous are the Landau-Darrieus and Rayleigh-Taylor instabilities, which distort the laminar front and wrinkle the flame, thus increasing the burning rate depending on the area of the interface. A first study devoted specifically to this problem [11] concluded that, within a linear treatment, there is no way that even if initially laminar, a deflagration remains as such. This means that very quickly an acceleration of the flame should ensure, leading the process towards the turbulent combustion branch, and perhaps boosting it to the detonation region.

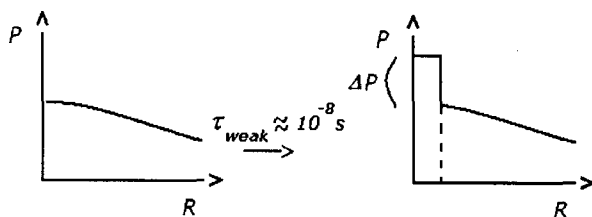


Figure 3. If a macroscopic region makes the transition to *ud* matter inside a collapsing core, it will become (by hypothesis) a SQM core after a timescale typical of weak interactions, orders of magnitude faster than dynamical timescales of $\approx \text{ms}$. Then the core has no time to readjust itself and it would be an effectively isocoric transition. The overpressure due to the released energy could be important for the start of a detonation.

In any case, it is clear that because of the microphysics, instabilities can not be ignored and the actual speed of the burning would be much faster than the laminar deflagration. A similar picture has been developed by Khlokhov and collaborators [12] for Type Ia supernovae, namely thermonuclear combustions in degenerate white dwarfs. The SQM case would be a high-density analogue to the SN Ia case.

The possible effects in a Type II supernova are summarized at a glimpse in Fig. 4. Several important issues remain to be established, and numerical simulations may be the only form to address them. These include the very propagation of a detonation, the efficiency of energy transfer to the stalled shock at the bottom of the stellar envelope and of course the effectiveness of neutrino capture by the shock after \sim seconds after bounce (provided a supernova can hold that much without recollapsing to a black hole). The instabilities must be revised, if possible going beyond the linear level. It is also

important to take a detailed look at the coupled problem of reaction kinetics + hydrodynamics, since a non-trivial interplay of both is known to exist.

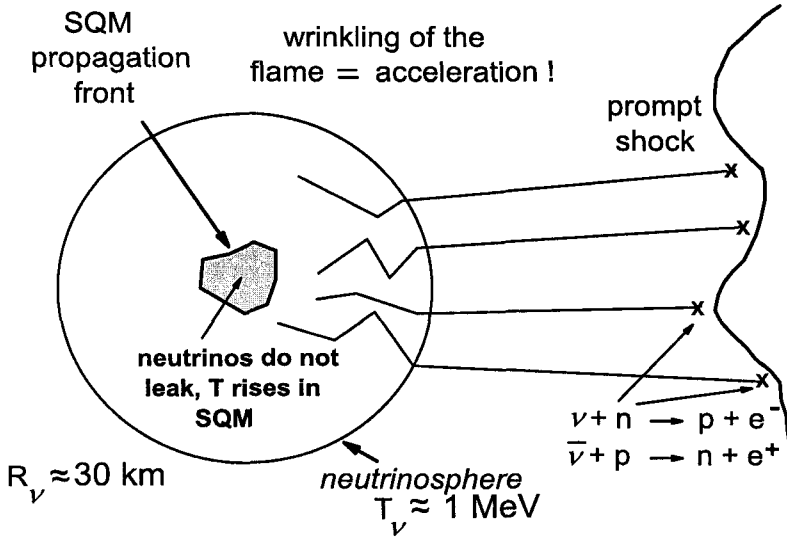


Figure 4. A Type II supernova scenario. After deleptonization SQM nucleates in the protonneutron star and begins to propagate inside the core, probably in a non-laminar mode. While the simplest shock-piston one dimensional models suggest that energy could be added to the stalled prompt shock mechanically [13], it is also possible that the main effect could be the addition of neutrinos from the hot matter [14], which do leak promptly but rather diffuse out with a higher mean energy than the "standard" ones.

4. Propagation of flames with magnetic fields

Up to now we have implicitly assumed a zero-magnetic field environment, thus neglecting possible effects on the nucleation and propagation of SQM. However, it is well-known that magnetic fields are ubiquitous in astrophysical environments, and in (proto)neutron stars in particular. In fact, compact stars are the most magnetized objects in the Universe, and thus a look at the magnetic field issue would be in order.

There is no need to worry about *structural* properties of magnetic fields deep inside stars, since their energy density in several orders of magnitude lower than degeneracy pressures (this is true even for the highest magnetic fields suggested for *magnetars*, if they exist at all). However, we have calculated quite recently a more subtle effect, namely the influence of a magnetic field on the

propagation of a combustion *via* the dispersion relations. We found, in agreement with other studies, that the development of instabilities is quenched across field lines, while it proceeds unimpeded along them. This generates an asymmetry of the propagation of the order of the quotient of polar to equatorial velocities (assuming that a simple ordered dipole is a good description inside the star and that both velocities represent a suitable average over the fluid elements)

$$\xi = v_p / v_e = \left[1 + B^2 / (4\pi\rho v_{\text{lam}}^2) \right]^{D-2} \quad (2)$$

with v_{lam} the laminar deflagration velocity and D the fractal dimension of the turbulent deflagration, a number to be extracted from numerical simulations. The asymmetry has a “threshold” value of B around $\approx 10^{13}$ G, fields smaller than this would not be important at all for the propagation, while very large fields would cause an approximate scaling $\xi \approx B$, and a needle-shaped front [14].

Applications of the above model suggest a continuum of explosive phenomena, perhaps including “short” GRBs and Type II supernovae in the same class provided SQM is relevant for the physical evolution of these systems. The same model may be useful for applications to a different phenomenon, namely the giant flares from Soft-Gamma Repeaters like the recent event Dec 27 2004 suffered by SGR 1806-20 which released at least 10^{47} erg in gamma-rays, provided only one of such flares happens per source (Lugones, Horvath and Gouveia Dal Pino, in preparation). Finally, recent calculations [15] have shown that the possibility of self-bound quark matter is *greatly enhanced* if the effects of pairing are considered. Therefore, we stress again the importance of more detailed studies of SQM in physics and astrophysics, well beyond these “first generation” outline.

5. Conclusions

We have presented an overview of the possible features and effects of SQM inside protoneutron stars, and suggested that important consequences are potentially affecting the very explosions through direct transfer or neutrino energy leak. In spite of the appeal of these models, we must acknowledge that after 20 years or so SQM theory is still a speculative area [16]. In particular, a list of questions we would like to answer include (but is not limited to):

- How strong and firm are the experimental limits on the abundance of SQM? Is there a body of candidates still supporting the SQM hypothesis?

- To what extent does SQM violate some sacred facts in astrophysics? Are we clever enough to rule out SQM on purely astrophysical grounds?
- Is there a definitive answer on the stability issue, from some reliable theoretical method?
- Can we be sure about the nucleation of SQM in so-called “delayed” timescales in a supernova environment?
- Do we know the hydrodynamics of the combustions well enough? If so, can we calculate/simulate the propagation [17]?
- Is there a significant energetic modification for Type II supernovae from these models? In which conditions?

If answers could be obtained with some confidence, we could provide a firmer ground to study exotic possibilities in physics and astrophysics.

Acknowledgments

We wish to acknowledge the partial financial support of FAPESP and CNPq Agencies (Brazil) along many years of work on these subjects. I would like to thank the Organizers of the Mamaia School for their invitation and assistance for delivering this lecture at the event.

References

1. D.D. Ivanenko and D.F. Kurdgelaidze, *Fizika* **8**, 39 (1970) ; J.C. Collins and M.J. Perry, *Phys. Rev. Lett.* **34**, 1353 (1975); G. Baym and S.A. Chin *Phys. Lett.* **B62**, 241 (1976); G. Chapline and M. Nauenberg, *Phys. Rev. D* **16**, 450 (1977).
2. A. R. Bodmer, *Phys. Rev. D* **4**, 1601 (1971);, E. Witten *Phys. Rev. D* **30**, 272 (1984); H. Terazawa, *Jour. Phys. Soc. Japan* **59**, 1199 (1990).
3. C. Alcock, E. Farhi and A.V. Olinto, *ApJ* **310**, 261 (1986); A.V. Olinto *Phys.Lett.* **B192**, 71 (1987).
4. M.A. Alpar *Phys. Rev. Lett.* **58**, 2152 (1987); R.R. Caldwell and J.L. Friedman, *Phys. Lett.* **B264**, 143 (1991).
5. J.E. Horvath and G. Lugones, astro-ph/0311449 (2003).
6. J.E. Horvath, O.G. Benvenuto and H.Vucetich, *Phys. Rev. D* **45**, 3865 (1992); M. Olesen and J. Madsen *Phys. Rev. D* **49**, 2698 (1994); J.E. Horvath, *Phys. Rev. D* **49**, 5590 (1994).
7. W. Slominski, *Acta. Phys. Pol.* **B21**, 245 (1990); K. Iida and K. Sato, *Prog. Theor. Phys.* **98**, 277 (1997).
8. I. Mardor and B. Svetitsky, *Phys. Rev. D* **44**, 878 (1991).
9. G. Lugones and O.G. Benvenuto, *Phys. Rev. D* **58**, 083001 (1998).

10. G. Baym *et al.*, *Phys. Lett.* B160, 181 (1985); A.V. Olinto *Phys.Lett.* **B192**, 71 (1987), J. Madsen and M.L. Olesen, *Nucl. Phys. B Proc. Supp.* **24**, 170 (1991), H. Heiselberg, G. Baym and C. Pethick, *Nucl. Phys. B Proc. Supp.* **24**, 144 (1991).
11. J.E. Horvath and O.G. Benvenuto, *Phys. Lett.* **B213**, 516 (1988).
12. A.M. Khlokhov, E. S. Oran and J.C. Wheeler, *ApJ* **478**, 678 (1997).
13. O.G. Benvenuto and J.E. Horvath, *Phys. Rev. Lett.* **63**, 716 (1989); O.G. Benvenuto, J.E. Horvath and H. Vucetich, *Int. Jour. Mod. Phys.* **A4**, 257 (1989).
14. G. Lugones *et al.*, *ApJ* **581**, L101 (2003).
15. G. Lugones and J.E. Horvath, *Phys. Rev. D* **66**, 074017 (2002).
16. See the recent review by F. Weber, astro-ph/0407155 (2004).
17. I. Tokareva and A. Nusser, astro-ph/0502344 (2005).

NEUTRINO ASTROPHYSICS: GAMMA RAY BURSTS

G. C. MCLAUGHLIN *

*Department of Physics
North Carolina State University
Raleigh, NC, 27608 USA
E-mail: Gail.McLaughlin@ncsu.edu*

We discuss the importance of neutrinos in astrophysics and consider the particular case of accretion disks which may power gamma ray bursts. We examine accretion rates of $0.1M_{\odot}/s - 10M_{\odot}/s$, which are sufficiently large to produce strong fluxes of neutrinos. In many cases significant regions of trapped neutrinos are created in the accretion disk. We discuss the implications for the nucleosynthesis that occurs in these objects, as well the energy deposited by neutrino-antineutrino annihilation.

1. Introduction

Neutrinos have importance in many areas of astrophysics. Experimental detection of neutrinos has been used to confirm models of the sun. While there is still much to learn about core collapse supernovae, the handful of neutrinos detected from supernova 1987a confirmed our basic picture of these objects, which is that the core of a massive star collapses to nuclear density, forms a “proto-neutron” star, and that most of the gravitational binding energy leaks out in the form of neutrinos.

Neutrinos in both of these environments are indicators of the type of nucleosynthesis that is occurring. In the sun, the neutrinos which are emitted are products of nuclear burning. Most of the neutrinos which have been detected are produced in the decay of Boron-8, which was synthesized in the sun. In the supernova, most of the neutrinos are produced thermally, not as a by product of nucleosynthesis. However, they greatly influence element synthesis near the core of the proto-neutron star, in the so called neutrino driven wind, by setting the neutron-to-proton ratio in outflowing

*Work partially supported by grant DE-FG-02ER4166 of the Department of Energy

material through the reactions

$$\nu_e + n \rightarrow p + e^+ \quad (1)$$

$$\bar{\nu}_e + p \rightarrow n + e^- \quad (2)$$

Neutrinos have a similar influence in Big Bang Nucleosynthesis, where the same reactions determine in part the neutron-to-proton ratio and therefore the amount of Helium that exists in the universe today.

In this contribution we will discuss the role of neutrinos in accretion disks surrounding black holes, and their impact on the nucleosynthesis that comes from these objects. We are motivated by recent observation and theoretical work on gamma ray bursts^{1–11}. While gamma ray bursts were first observed more than thirty years ago, it is only recently that great strides have been made observationally. The current evidence points to explosions of massive stars as being responsible for long duration bursts, i.e. some sort of exotic supernova. Less data exists on short duration bursts, but these have been suggested to be formed by neutron star mergers.

The neutrinos from accretion disks may be responsible for powering a gamma ray burst, by providing the energy for the ejection of small amounts of material at highly relativistic velocities. We explore the energy deposition that comes from neutrino-antineutrino annihilation above the gamma ray burst.

Also, although a large part of the material in the disk is accreted into the black hole up to half can be ejected vertically off of the disk. The wind will produce a variety of elements that will contribute significantly to the abundance of certain isotopes observed in our solar system today. We explore the elements that are produced in the course of the outflow from the accretion disk. We begin by discussing the neutrinos in the disk.

2. Neutrinos from Accretion Disks

We first calculate the nuclear composition of matter in the accretion disks surrounding stellar mass black holes. We use accretion disk parameters from^{12,13} and as in Ref. 14 we follow mass elements in the accretion disk starting at the point of nuclear dissociation and determine the evolution of the electron fraction. We find that the initial neutronization of the disk material by electron capture can be reversed by neutrino interactions in the inner regions of disks with accretion rates of $1 M_\odot/s$ and higher. For these cases the inner disk regions are optically thick to neutrinos. In order to estimate the emitted neutrino fluxes we calculate the surface of

last scattering for the neutrinos for each optically thick disk model. Figure 1 shows the surfaces of last scattering for the neutrinos in two different accretion disks. Optical depths of neutrinos in accretion disks have also been considered in Ref. 15.

In order to determine what sort of nucleosynthesis may occur we must examine the composition of matter as it flows away from gamma ray burst accretion disks¹⁶. Since there is a large flux of neutrinos leaving the surface of the disk, the electron fraction of the outflowing material will change due to charged current neutrino interactions. We calculate the electron fraction in the wind using detailed neutrino fluxes from every point on the disk and study a range of trajectories and outflow conditions for several different accretion disk models. We find that low electron fractions only appear in outflows from disks with high accretion rates ($\dot{M} = 10M_{\odot}/s$) that have a significant region of both trapped neutrinos and antineutrinos. Disks with lower accretion rates, e.g. ($\dot{M} = 1M_{\odot}/s$) only have a significant region of trapped neutrinos, but not antineutrinos, and can have outflows with very high electron fractions. The low accretion rate disks with little trapping ($\dot{M} = 0.1M_{\odot}/s$) have outflow electron fractions closer to one half.

Although a large part of the material in the disk is accreted into the black hole up to half can be ejected vertically off of the disk. A self-consistent model for this outflow has not yet been developed, therefore we use a parameter study for the conditions in this outflow. There are three parameters in the outflow which primarily influence the final element abundance distribution: the entropy per baryon, s/k , the acceleration and final velocity of the material, β and v_{∞} respectively, and the radial distance from the center of the disk where the material is ejected¹⁶.

3. Nucleosynthesis in the Outflow of Accretion Disks

For the highest ($\dot{M} = 10M_{\odot}/s$) and medium ($\dot{M} = 1M_{\odot}/s$) accretion rate disks, the electron neutrino and antineutrino interactions play the dominant role in determining the nucleosynthesis that takes place in the material which is ejected from the disk. These accretion rates reflect those that would occur in the neutron star - neutron star merger scenario. In the highest accretion rate disks the electron fraction is driven quite low in the ejecta, so the material is very neutron rich. Our preliminary calculations show that this is a potentially viable environment for the r-process¹⁷. Figure 2 shows two nucleosynthesis calculations using the high accretion disk model.

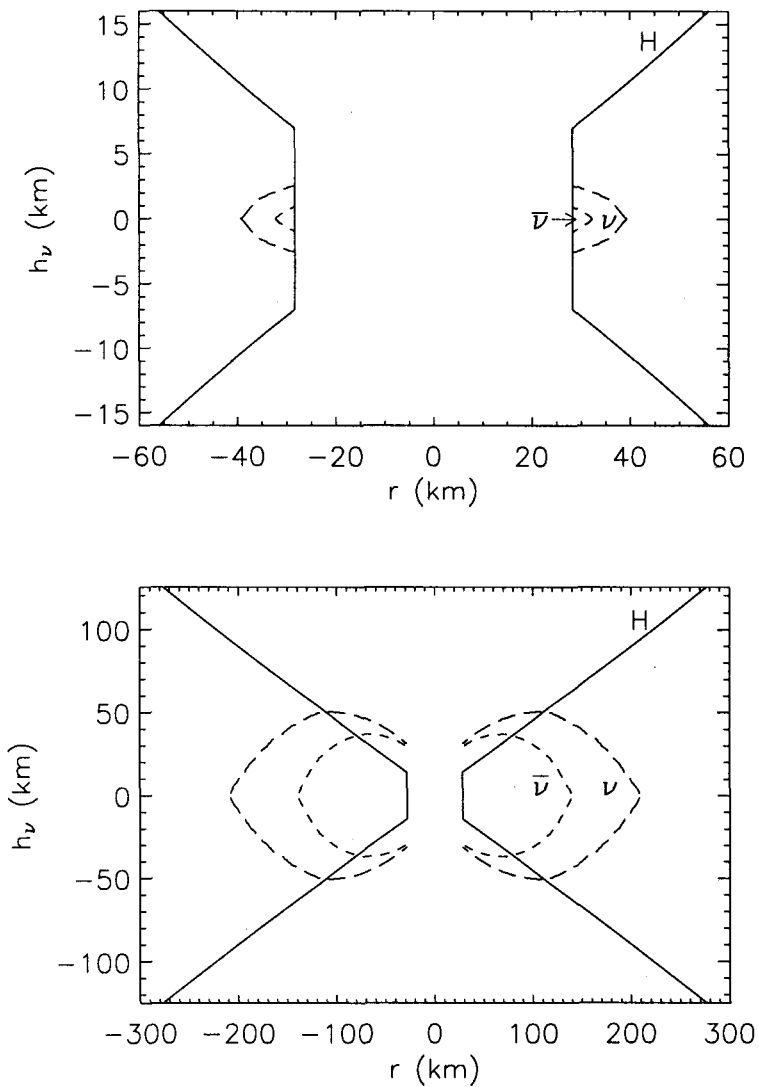


Figure 1. Neutrino and antineutrino surfaces in a $\dot{M} = 1 M_\odot/s$, $a = 0$ (a, on the top) and a $\dot{M} = 10 M_\odot/s$, $a = 0$ (b, on the bottom) accretion disk. The solid line shows the density scale height of the disk.

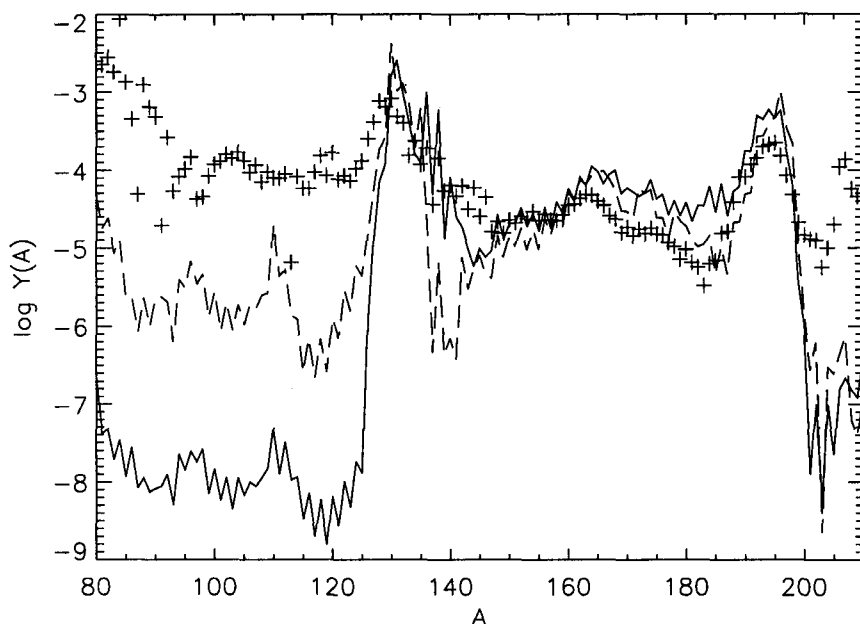


Figure 2. R-process nucleosynthesis abundances resulting from a reaction network calculation using a $\dot{M} = 10M_{\odot}/s$ model and outflow conditions of $\beta = 2.0$, $s/k = 48$ (solid line) as well as $\beta = 0.8$ and $s/k = 12$ (dashed line). The starting disk radii for both trajectories is $r_0 = 250$ km. The crosses show the solar system abundances.

Lower accretion rate disks ($\dot{M} = 1M_{\odot}/s$) are currently predicted by the collapsar model^{9,18} which describes exploding massive stars. For low accretion rates and entropies per baryon around $s/k \sim 40$ the electron fraction is closer to $1/2$, i.e. equal numbers of neutrons and protons. In this case rare nuclei such as Zinc and p-process nuclei may be produced^{19,20}. Figure 3 shows overproduction factors for Zinc-64 in outflow from an accretion disk of $\dot{M} = 0.1M_{\odot}/s$ (Ref. 21).

4. Neutrino–Antineutrino Annihilation from Accretion Disk Neutrinos

The energy which makes a gamma ray burst explosions possible may derive from the large neutrino luminosity that is emitted from the accretion disk surrounding a stellar mass black hole. Calculations of the flux com-

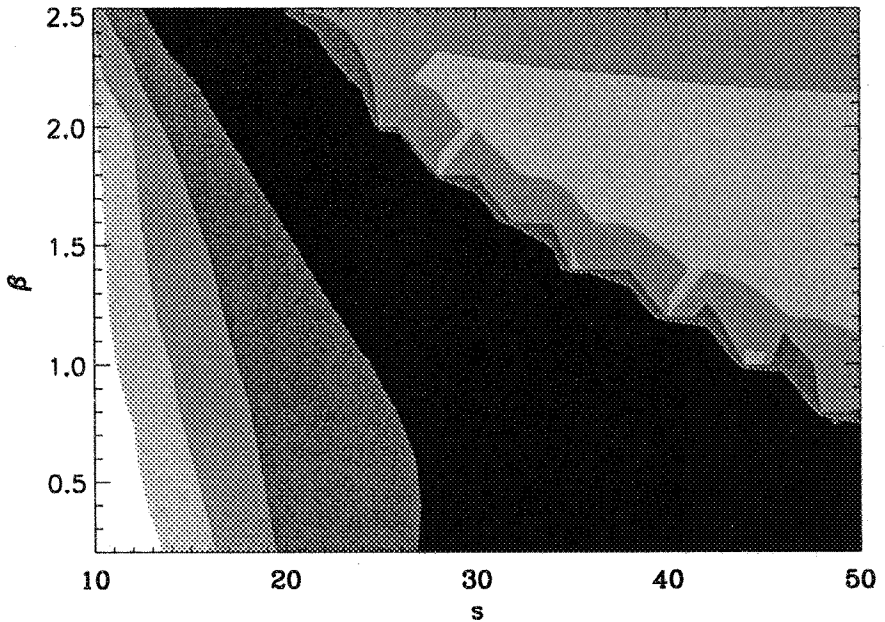


Figure 3. Shows the overproduction factor for Zinc. The shaded regions correspond, from darkest to lightest, of 1000, 100, 10 and 1. The horizontal axis shows entropy per baryon, while the vertical axis, β is related to inverse acceleration as in a stellar wind parameterization. This was calculated using the neutrino flux from a $\dot{M} = 0.1 M_{\odot}/s$ disk model.

ing from the accretion disk surrounding the black hole from¹⁴ can be used to estimate the neutrino-antineutrino annihilation rate. The strongest neutrino flux emerges from a ring at the inner edge of the disk and the extended source leads to a considerable departure from spherical symmetry. The non-spherical geometry increases the efficiency of neutrino annihilation and can cause a collimation of scattered material into a jet along the axis of the disk. The spatial distribution of annihilation efficiencies is shown in Fig.4, similar to the calculations in²². Different disk models^{12,13} not only give neutrino-antineutrino annihilation rates that differ by several orders of magnitude, but also produce a pattern of energy deposition that varies²². Particularly in the region near the inner edge of the accretion disk, the neutrino flux depends very strongly on the model, and future, more sophisticated models will help to better determine the total rate and the deposition pattern.

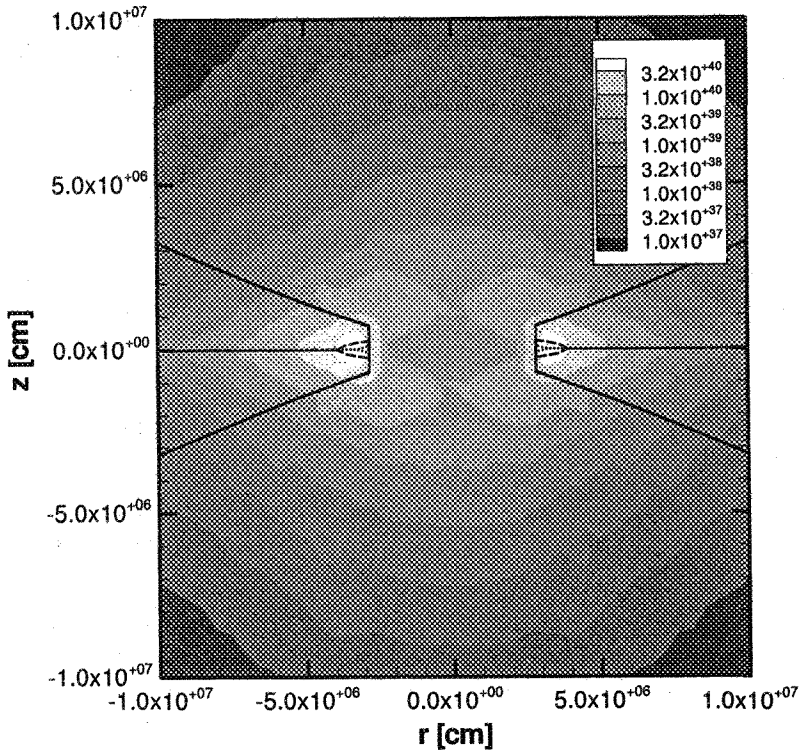


Figure 4. Shows the rate of neutrino-antineutrino annihilation, in units of $\text{eV}/\text{cm}^{-3}/\text{s}$ above a GRB accretion disk. The black hole is in the center and the solid lines show the density scale height of the disk.

5. Conclusions

Neutrinos are important in many environments in astrophysics and the disks that are thought to surround black holes in gamma ray burst models are no exception. The rapidly accreting disks that are thought to be produced by neutron-star mergers produce regions of trapped electron neutrinos and antineutrinos. The less rapidly accreting disks thought to be produced by the explosions of some massive stars, also release copious numbers of neutrinos. A wide variety of nucleosynthesis is possible in the outflow from these disks. This depends primarily on the accretion rate, but also on the entropy and outflow timescale of the ejected material. For a rapid accretion rate and rapid outflow, the conditions are viable for producing an r-process. For lower accretion rates, the conditions are favorable for producing certain rare nuclei, such as p-process nuclei and 64-Zinc.

Energy deposition from the neutrinos above the disk may power the gamma ray burst. The flux depends greatly on the accretion rate of the of the disk. Future models will tell us whether neutrino-antineutrino annihilation is responsible for providing the energy which drives gamma ray bursts.

References

1. T. J. Galama et al., *Nature* **395**, 670 (1998).
2. S. R. Kulkarni et al. *Astrophys. J.* **522**, L97 (1999).
3. K. Z. Stanek et al., *Astrophys. J.*, **591**, L17 (2003).
4. J. Hjorth et al., *Nature* **424**, 751 (2003).
5. P. Garnavich et al., *Astrophys. J.* **582**, 924 (2003).
6. M. Della Valle et al., *Astron. and Astrophys.* **406**, L33 (2003).
7. B. Thomsen, *Astron. and Astrophys.* **419**, L21 (2004).
8. D. Malesani, *Astrophys. J.* **609**, L5 (2004).
9. A. I. MacFadyen, S. E. Woosley, *Astrophys. J.* **524**, 262 (1999).
10. H.-Th. Janka, T. Eberl, M. Ruffert, C. L. Fryer, *Astrophys. J.* **527**, L39 (1999).
11. S. Rosswog, M. Liebendoerfer, *MNRAS* **342**, 673 (2003); S. Rosswog et al., *MNRAS* **345**, 1077 (2003).
12. R. Popham, S. E. Woosley, and C. Fryer, *Astrophys. J.* **518**, 356 (1999).
13. T. DiMatteo, R., Perna, and R. Narayan, *Astrophys. J.* **579**, 706 (2002).
14. R. Surman and G. C. McLaughlin, *Astrophys. J.* **603**, 611 (2004) [arXiv:astro-ph/0308004].
15. W. H. Lee, E. Ramirez-Ruiz and D. Page, *Astrophys. J.* **608**, L5 (2004) [arXiv:astro-ph/0404566].
16. R. Surman and G. C. McLaughlin, arXiv:astro-ph/0407206.
17. G. C. McLaughlin and R. Surman, arXiv:astro-ph/0407555.
18. D. Proga, A. I. MacFadyen, P. J. Armitage and M. C. Begelman, *Astrophys. J.* **599**, L5 (2003)
19. J. Pruet, R. Surman and G. C. McLaughlin, *Astrophys. J.* **602**, L101 (2004) [arXiv:astro-ph/0309673].
20. S. Fujimoto, M. Hashimoto, K. Arai and R. Matsuba, *Astrophys. J.* **614**, 847 (2004) [arXiv:astro-ph/0405510].
21. R. Surman, G. C. McLaughlin and W. R. Hix, arXiv:astro-ph/0509365.
22. J. P. Kneller, G. C. McLaughlin and R. Surman, arXiv:astro-ph/0410397.

NEUTRINO EMISSION FROM NEUTRON STARS *

D. G. YAKOVLEV, M. E. GUSAKOV † A. D. KAMINKER, AND
A. Y. POTEKHIN

*Ioffe Physical Technical Institute,
Politekhnikeskaya 26, 194021, Saint-Petersburg, Russia*

The main mechanisms of neutrino emission from the matter of supranuclear density in superfluid cores of neutron stars are reviewed, with the emphasis on the cores composed of nucleons. The effects of neutrino emission on the thermal evolution of neutron stars are described. The prospects of exploring the fundamental (but still poorly known) properties of supranuclear matter by comparing simulations of neutron star thermal evolution with observations are outlined.

1. Introduction

Neutron stars are the most compact stellar objects in the Universe. Their typical masses are $M \sim 1.4 M_{\odot}$ (where M_{\odot} is the solar mass), while their radii are only ~ 10 km. Their mean mass density reaches a few ρ_0 ($\rho_0 \approx 2.8 \times 10^{14}$ g cm $^{-3}$ is the standard nuclear matter density); their central density can exceed $10 \rho_0$. Accordingly, neutron stars can be regarded as unique astrophysical laboratories of supranuclear matter.

It is currently thought (*e.g.*, Ref. 1) that a neutron star consists of a thin crust (of mass $\lesssim 10^{-2} M_{\odot}$) and a core (where the mass density $\rho \gtrsim \rho_0/2$). The crustal matter contains atomic nuclei, electrons, and (at $\rho \gtrsim 4 \times 10^{11}$ g cm $^{-3}$) free neutrons. The core can be subdivided into the outer ($\rho \lesssim 2\rho_0$) and inner parts. The outer core consists of neutrons (n), with an admixture of protons (p), electrons (e), and muons (all constituents being strongly degenerate). The composition of the inner core is unknown. It may be the same as in the outer core but may also contain hyperons, pion or kaon condensates, quark matter, or a mixture of different phases.

*Supported by grants 05-02-16245 and 03-07-90200 of the Russian Foundation for Basic Research and by grant 1115.2003.2 of the Russian Leading Science School Program.

†Partially supported by the INTAS grant YSF 03-55-2397 and by the Russian Science Support Foundation

Table 1. Main processes of neutrino emission in nucleon matter

Process	Reactions	L_ν , erg s ⁻¹	Comment
Direct Urca	$n \rightarrow pe\bar{\nu}$ $pe \rightarrow n\nu$	$\sim 10^{44-46} T_9^6 \mathcal{R}$	fast
Modified Urca	$nN \rightarrow pNe\bar{\nu}$ $pNe \rightarrow nN\nu$	$\sim 10^{39-40} T_9^8 \mathcal{R}$	slow
Bremsstrahlung	$NN \rightarrow NN\nu\bar{\nu}$	$\sim 10^{37-39} T_9^8 \mathcal{R}$	very slow
Cooper pairing	$\tilde{N}\tilde{N} \rightarrow \nu\bar{\nu}$	$\lesssim 10^{40-42} T_9^8$	moderate

Nucleons, hyperons, and quarks can be in superfluid state. Microscopic theories of dense matter are model dependent. The fundamental problem of the equation of state (EOS) and composition of the matter in neutron star cores is still unsolved.

Here, we briefly review neutrino processes in neutron stars with nucleon cores and their effect on neutron star cooling (see, *e.g.*, Refs. ²⁻⁶ for more details).

2. Neutrino Emission Processes

Neutron stars are born hot in supernova explosions, with the internal temperature $T \sim 10^{11}$ K, producing a powerful neutrino outburst. In one minute after the birth a star becomes transparent for neutrinos. We discuss the following neutrino-transparent stage when the neutrino emission is much weaker than at the supernova stage but still important for neutron star cooling.

We outline the neutrino emission from stellar cores which is usually more powerful than from crusts. The main neutrino reactions in nucleon cores are listed in Table 1. It is important to know the neutrino emissivities Q (erg cm⁻³ s⁻¹) for these reactions and the associated neutrino luminosities L_ν (erg s⁻¹), which are the emissivities integrated over the star volume.

The most powerful is the direct Urca process⁷. In the matter composed of n , p , and e , this is the beta decay of a neutron and subsequent electron capture by a proton (Table 1). The process occurs if the proton fraction is sufficiently high (to satisfy momentum conservation). This happens only for some EOSs in the inner cores of massive stars, where the density exceeds a certain density threshold ρ_D .

In addition, there are slower neutrino processes (Table 1), which operate in the outer and inner cores. They are two modified Urca processes (for $N=n$ or p) and three bremsstrahlung processes (nn , pp and np). The modified Urca processes differ from the direct Urca by an additional nucleon-spectator N (which simplifies momentum conservation). In the presence of

muons there are additional Urca processes, with muons instead of electrons.

Neutrino reactions are greatly affected by nucleon superfluidity. When the temperature T drops much below the critical temperature T_c for a given nucleon species, the energy gap in the nucleon energy spectrum greatly (exponentially) suppresses all reactions involving such nucleons (*e.g.*, Ref. 3).

Also, superfluidity initiates a specific neutrino process owing to *Cooper pairing of nucleons*⁸ (annihilation of Bogoliubov quasi-nucleons \tilde{N} into neutrino pairs, Table 1). This process is forbidden in nonsuperfluid matter. With decreasing T , it becomes allowed at $T = T_c$, produces the maximum emissivity at $T \sim 0.8 T_c$, and is exponentially suppressed at $T \ll T_c$. For realistic density profiles $T_c(\rho)$ at T much below the maximum value of $T_c(\rho)$, the neutrino luminosity due to this process behaves as $L_\nu^{\text{CP}} \propto T^8$ and may exceed the luminosity provided by the modified Urca process in a nonsuperfluid star by up to two orders of magnitude^{5,9}.

Order-of-magnitude estimates of neutrino luminosities for the cited processes are given in Table 1, where $T_9 = T/10^9$ K and \mathcal{R} describes the reduction of the luminosity by superfluidity (with $\mathcal{R} = 1$ and $L_\nu^{\text{CP}} = 0$ in a nonsuperfluid star).

3. Neutrino Emission and Cooling Neutron Stars

Because the neutrino emission depends on the internal structure of neutron stars and affects their cooling, it allows one to explore the internal structure by comparing the cooling theory with observations. Here we follow Ref. 10.

Observations of isolated neutron stars, whose thermal surface radiation has been detected or constrained, are summarized in Fig. 1 (the data are the same as in Refs. ^{9,10}). We present the stellar ages t and effective surface temperatures T_s^∞ inferred from observations; ‘ ∞ ’ means the quantity redshifted to the reference frame of a distant observer. Arrows show the upper limits on T_s^∞ (in cases no thermal radiation has been detected).

The cooling theory gives *cooling curves*, $T_s^\infty(t)$ (*e.g.*, Fig. 1). In $t \lesssim 100$ years the stellar interiors become thermally relaxed. At $t \lesssim 10^5$ years, a star cools mainly via neutrino emission; at $t \gtrsim 10^5$ years it cools via thermal surface emission of photons.

Figure 1 shows the *basic cooling curve*. It is calculated for a star with a non-superfluid nucleon core which cools slowly via the modified Urca process. This curve is almost independent of the EOS and neutron star mass. It cannot explain the observations – some sources are hotter and some colder than predicted by the curve.

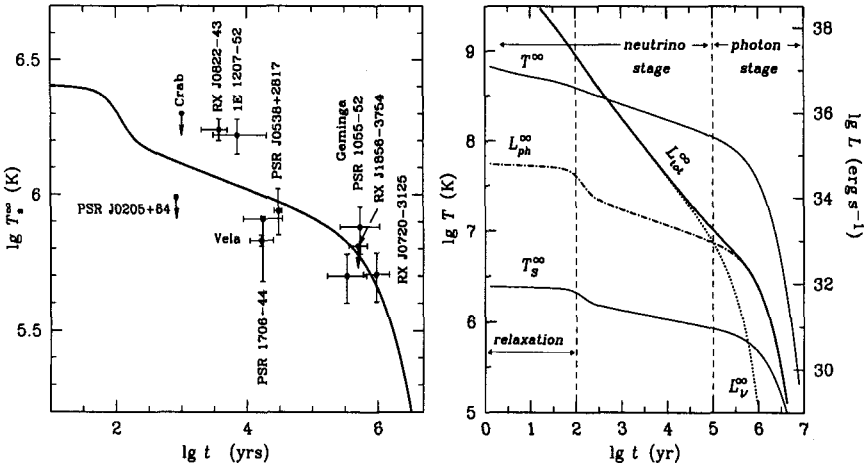


Figure 1. *Left*: Observational limits of surface temperatures for several isolated neutron stars compared with the basic theoretical cooling curve. *Right*: Internal and surface temperatures; neutrino, photon and total luminosities (red-shifted for a distant observer) for the basic cooling model.

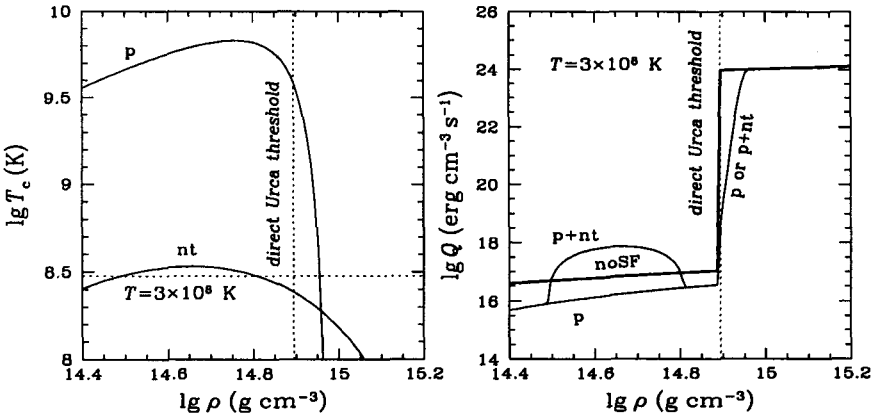


Figure 2. *Left*: Illustrative models of critical temperatures for singlet-state proton (p) and triplet-state neutron (nt) pairing in a neutron star core. *Right*: Neutrino emissivity in the same core at $T = 3 \times 10^8$ K for non-superfluid matter (thick line; noSF) and either for proton pairing (p) or for proton and neutron pairing (p+nt). The vertical dotted line shows the direct Urca threshold.

At the next step let us take into account the effects of enhanced neutrino emission in massive neutron stars (Fig. 2). We adopt a moderately stiff EOS of dense nucleon matter from Ref. 11 (the same modification as in Ref. 4).

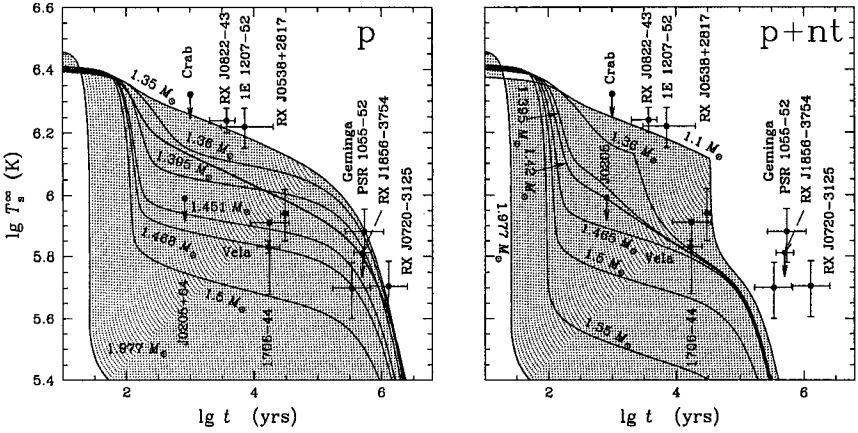


Figure 3. *Left:* Cooling of neutron stars of several masses (indicated near the curves) with proton superfluidity p from Fig. 2 in the cores. *Right:* Same as in the left panel but adding the effect of neutron superfluidity nt .

It opens the direct Urca process at $\rho > \rho_D = 7.851 \times 10^{14} \text{ g cm}^{-3}$, i.e., at $M > M_D = 1.358 M_\odot$ (M being the gravitational mass) and gives the maximum neutron-star mass $M_{\text{max}} = 1.977 M_\odot$. In non-superfluid matter the direct Urca process switches on sharply at $\rho > \rho_D$. If M exceeds M_D only by 0.1%, the neutrino luminosity owing to the direct Urca process is already so strong that $T_s^\infty(t)$ falls much below the T_s^∞ for coldest observed stars in Fig. 1 (close to the lowest curves in Fig. 3). Therefore, we have either the basic curve for $M \leq M_D$ or much lower curves for more massive stars; these curves are inconsistent with the data.

However, protons and neutrons in neutron star cores can be in superfluid state. As a rule, protons undergo singlet-state pairing, whereas neutrons undergo triplet-state pairing (e.g., Ref. ¹²) with density dependent critical temperatures $T_{\text{cp}}(\rho)$ and $T_{\text{cnt}}(\rho)$ which are very sensitive to theoretical models. Figure 2 shows some phenomenological $T_{\text{cnt}}(\rho)$ and $T_{\text{cp}}(\rho)$ curves ⁴ and their effect on the neutrino emissivity.

First we assume strong proton superfluidity p alone. It extends to densities $\rho > \rho_D$ and suppresses the modified Urca process in low-mass stars ($M < M_D$). The neutrino luminosity of these stars becomes lower (Fig. 2), being determined by a weaker mechanism (nn bremsstrahlung, unaffected by proton superfluidity). This *raises* the cooling curves of low-mass stars and allows one to explain the observations of stars hottest for their age, such as RX J0822-43, 1E 1207-52, PSR B1055-52 (left panel of Fig. 3).

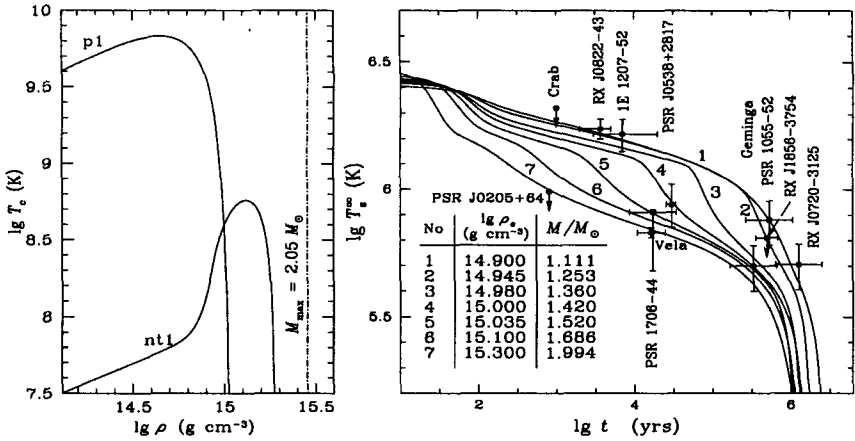


Figure 4. *Left:* Model density dependence for critical temperatures of protons (p1) and neutrons (nt1) in a nucleon stellar core for the EOS which forbids the direct Urca process. *Right:* Cooling of neutron stars of several masses (indicated in the inset) with pairing p1 and nt1 for the same EOS.

Thus, we may treat these sources as low-mass neutron stars.

Proton pairing p suppresses even the direct Urca process at $\rho \sim \rho_D$. At higher ρ pairing gradually dies out, opening the direct Urca process. The gradual opening broadens the direct Urca threshold (Fig. 2) and ensures the gradual decrease of cooling curves with increasing M . In this way we may attribute masses to observed neutron stars¹³, as shown in the left panel of Fig. 3, and explain all the data. For instance, we obtain $M \approx 1.47 M_\odot$ for the Vela pulsar. However, this *weighing* of neutron stars is sensitive¹⁴ to the EOS of dense matter, to the direct Urca threshold, and to superfluidity model $T_{cp}(\rho)$. Even strong pairing p dies out in the centers of massive stars ($M \sim M_{\max}$), where direct Urca process is allowed. Thus, massive stars cool very rapidly, as if they are non-superfluid, and become very cold.

Now let us include also neutron pairing nt with the peak of $T_{cnt}(\rho)$ as low as $\sim 4 \times 10^8$ K at $\rho \sim 4 \times 10^{14}$ g cm⁻³. This pairing is mild and insignificant, according to nuclear physics standards, but crucial for the cooling. It appears in a cooling star when the internal temperature falls below the peak value. It creates then a powerful neutrino emission owing to Cooper pairing of neutrons in outer stellar cores, especially efficient in low-mass stars. The emission accelerates the cooling (the right panel of Fig. 3) and violates the interpretation of the observations of such sources as PSR B1055-52. Thus, this mild neutron superfluidity contradicts the

observations.

The opposite example is given in Fig. 4. Let us consider neutron stars with nucleon cores and employ the EOS¹⁵ which forbids the direct Urca process in all stars with $M \leq M_{\max} = 2.05 M_{\odot}$. Furthermore, let us adopt the model of strong proton pairing p1 and mild neutron pairing nt1 (the left panel of Fig. 4). Pairing p1 is similar to pairing p in Fig. 2; it suppresses the modified Urca process in low-mass stars. The peak of $T_{\text{cnt}}(\rho)$ for pairing nt1 is as low as for pairing nt but shifted to higher densities. Accordingly, pairing nt1 is inefficient in low-mass stars and does not affect their cooling. However, the enhanced neutrino emission owing to this pairing operates in massive stars and accelerates their cooling. Then the cooling of stars with different masses enables us to explain the data (the right panel of Fig. 4), but only under stringent constraints on the $T_{\text{cnt}}(\rho)$ profile⁹. Note that a discovery of a neutron star slightly colder than those observed now would ruin this interpretation.

4. Conclusions

We have outlined the main neutrino emission mechanisms in nucleon cores of neutron stars. We have shown that these mechanisms are greatly affected by the EOS and by superfluid properties of dense matter. We have demonstrated that the neutrino emission strongly regulates the cooling of isolated neutron stars. Current observations of cooling neutron stars can be explained by different theoretical models of dense matter. Nevertheless the theory rules out some theoretical models (*e.g.*, the model in the right panel of Fig. 3).

Neutron star cooling can also be regulated by the surface magnetic fields and by the presence of light (accreted) elements on stellar surfaces (see, *e.g.*, Refs. ^{4,6,10}). The fields and accreted elements affect the thermal conductivity of surface layers. They may increase the surface temperature $T_s^{\infty}(t)$ of middle-aged stars and decrease $T_s^{\infty}(t)$ for $t \gtrsim 10^5$ yrs. In addition, the neutrino emission and cooling can be modified⁶ by the presence of different forms of matter (hyperons, pion or kaon condensates, deconfined quarks) in neutron stars (and in strange quark stars). Also, the cooling can be affected by some reheating mechanisms, for instance, by the viscous dissipation of rotational energy or Ohmic decay of magnetic field. All in all, current observations of cooling neutron stars can be explained by drastically different physical models of dense matter.

New observations of neutron stars are required for a better understand-

ing of their internal structure. Observations of cooling neutron stars should be analyzed together with other observational data. The data should be combined with new theoretical results, particularly, with new studies of nucleon superfluidity and neutrino emission properties. This would allow one to obtain more stringent constraints on neutron star structure.

Acknowledgments

DY is grateful to the organizers of CSSP-2005 and to the RFBR (travel grant 05-02-26668z) for financial support which allowed him to participate in CSSP-2005.

References

1. P. Haensel, In: *Final Stages of Stellar Evolution*, C. Motch and J.-M. Hameury (eds.), EAS Publications Series: EDP Sciences, 249 (2003).
2. C.J. Pethick, *Rev. Mod. Phys.* **64**, 1133 (1992).
3. D.G. Yakovlev, A.D. Kaminker, O.Y. Gnedin, and P. Haensel, *Phys. Rep.* **354**, 1 (2001).
4. D.G. Yakovlev and C.J. Pethick, *Ann. Rev. Astron. Astrophys.* **42**, 169 (2004).
5. D. Page, J.M. Lattimer, M. Prakash, and A.W. Steiner, *Astroph. J. Suppl.* **155**, 623 (2004).
6. D. Page, U. Geppert, and F. Weber, *Nucl. Phys. A*, accepted (2005) [astro-ph/0508056].
7. J.M. Lattimer, C.J. Pethick, M. Prakash, and P. Haensel, *Phys. Rev. Lett.* **66**, 2701 (1991).
8. E.G. Flowers, M. Ruderman, and P.G. Sutherland, *Astrophys. J.* **205**, 541 (1976).
9. M.E. Gusakov, A.D. Kaminker, D.G. Yakovlev, and O.Y. Gnedin, *Astron. Astrophys.* **423**, 1063 (2004).
10. D.G. Yakovlev, O.Y. Gnedin, M.E. Gusakov, A.D. Kaminker, K.P. Levenfish, and A.Y. Potekhin, *Nucl. Phys. A* **752**, 590c (2005).
11. M. Prakash, T.L. Ainsworth, and J.M. Lattimer, *Phys. Rev. Lett.* **61**, 2518 (1988).
12. U. Lombardo and H.-J. Schulze, In: *Physics of Neutron Star Interiors*, D. Blaschke, N.K. Glendenning, and A. Sedrakian (eds.), Springer: Berlin, 30 (2001).
13. A.D. Kaminker, P. Haensel, and D.G. Yakovlev, *Astron. Astrophys.* **373**, L17 (2001).
14. A.D. Kaminker, D.G. Yakovlev, and O.Y. Gnedin, *Astron. Astrophys.* **383**, 1076 (2002).
15. F. Douchin and P. Haensel, *Astron. Astrophys.* **380**, 151 (2001).

NEW ACHIEVEMENTS IN NEUTRINO PROPERTIES

S. STOICA

*Horia Hulubei National Institute of Physics and Nuclear Engineering,
407 Atomistilor Street, P.O. Box MG-6
077125 Magurele-Bucharest, Romania
E-mail: stoica@ifn.nipne.ro*

Neutrino oscillation experiments, from solar and atmospheric to reactor and accelerator ones, have firmly proved that neutrinos have mass and mix. However, the absolute scale of the neutrino mass remains still unknown. In the last years cosmological data allow us to extract stringent constraints on the sum of neutrino masses. On the other side, accurate information about the absolute neutrino mass can be extracted from direct measurements performed in beta and double-beta decay experiments. Moreover, double-beta decay experiments can provide us with information about the nature of neutrino. This lecture makes a short review of the main achievements in neutrino properties based on data obtained recently in these experiments.

1. Introduction

Fundamental properties of neutrinos, like their absolute mass and their nature (Majorana or Dirac particle), are still unknown, while others, like the number of neutrino flavors or the precise values of their mixing angles, are not yet fully settled. Since neutrinos play a key role in major domains like particle and nuclear physics, astrophysics and cosmology, there is a continuous effort, both theoretical and experimental, to give answers to these issues.

During the last years there was a significant progress in the knowledge of the neutrino properties. Shortly, the present situation can be characterized by: i) important results obtained in different neutrino oscillation experiments which confirm that neutrinos have mass and mix, ii) stringent constraints on the sum of the neutrino masses derived from recent cosmological data and iii) a hope that the next generation of double-beta decay experiments will provide us with meaningful information about the nature and absolute mass of the electron neutrino.

This lecture makes a short review of the main achievements in neutrino

properties based on data obtained recently in these experiments.

The paper is organized as follows: in sect. II we present recent results obtained in neutrino oscillation experiments, including atmospheric, solar, reactor and accelerator experiments. Section III is devoted to the presentation of cosmological data including WMAP, 2dFGRS, SDSS and Ly α analysis. In sect. IV we refer to direct measurements of the neutrino mass: tritium and double-beta decay experiments and in the last section we end up with some conclusions and prospectives in this field.

2. Neutrino oscillation experiments

2.1. Channel $\mu \rightarrow \tau$

Atmospheric neutrinos are produced mainly in the decay of pions and muons:

$$\pi \rightarrow \mu + \nu_\mu \quad \mu \rightarrow e + \nu_\mu + \nu_e \quad (2.1)$$

Experiments have measured the ratio $R_{\mu/e}$ which is compared to the (expected) theoretical one. The experimental values were found significantly smaller than the expected ones. Particularly, we refer to the SuperKamiokande (SK) experiment⁷ which produced the most conclusive results during its 1996-2000 run. They measured $R_{\mu/e}$ in two energy regimes and got the following results: i) $E_\nu \leq 1.33$ GeV; $(R_{\mu/e})_{meas}/(R_{\mu/e})_{th} \sim 0.638$ instead of ~ 2 and ii) $E \geq 1.33$ GeV; $(R_{\mu/e})_{meas}/(R_{\mu/e})_{th} \sim 0.658$ instead of > 2 . This result was also confirmed by other atmospheric experiments like Soudan, MACRO, etc.

In addition, they found a significant zenith angle asymmetry of the high energy muon events $[(U/D)_{meas}]/[(U/D)_{th}] \sim 0.54$, while no asymmetry was found for the electron events. This result was explained by a standard neutrino oscillation between two species in the channel $\mu \rightarrow \tau$ with the following most probable values of the oscillation parameters:

$$\Delta m^2 = 2.6 \times 10^{-3} eV^2; \quad \sin^2 2\theta_{12} \sim 1.00 \quad (2.2)$$

A nice confirmation of this interpretation came from the K2K terrestrial experiment⁷: neutrino oscillations in the same range of values of the oscillation parameters as atmospheric neutrinos measured by SK were searched for neutrinos coming from the decay of pions produced by 12 GeV protons accelerated at the KEK proton accelerator hitting a dump target at KEK and detected at SK, at about 250 km distance. Near KEK (300m away) two detectors were placed to count the number of neutrinos which go to the SK detector and then this number was compared with what the

SK detector has found. The reaction $\nu + n = e^- + p$ was chosen to measure the neutrino energy. The last result reported by the K2K group is: the total number of neutrinos observed at KEK was 151 as compared with 108 observed at SK. In terms of oscillation parameters this result gives values of these parameters very closed to those obtained in the SK atmospheric experiment:

$$\Delta m^2 = 2.4 \times 10^{-3} eV^2; \quad \tan^2 2\theta_{12} \sim 0.44 \quad (2.3)$$

which is an independent confirmation of the neutrino oscillations in this channel.

2.2. Channel $e \rightarrow \mu, \tau$

a) Solar neutrino experiments

The main sources of solar neutrinos are presented in Table below.

Reaction	Neutrino energy	SSM flux
$p + p \rightarrow d + e^+ + \nu_e$	$\leq 0.42 \text{ MeV}$	$5.95 \times 10^{10} \text{ cm}^{-2} \text{ s}^{-1}$
$e^- + {}^7\text{Be} \rightarrow \nu_e$	0.86 MeV	$4.77 \times 10^9 \text{ cm}^{-2} \text{ s}^{-1}$
${}^8\text{B} \rightarrow {}^8\text{Be}^* + e^+ + \nu_e$	$\leq 15 \text{ MeV}$	$5.05 \times 10^6 \text{ cm}^{-2} \text{ s}^{-1}$

Several experiments (Homestake, GALLEX-GNO, SAGE, SK, etc.) have measured the neutrino fluxes from the last reaction and found a significant difference between the measured fluxes and the theoretical ones predicted by the Standard Solar Model (SSM). A possible explanation of this result was advanced from the beginning: a transition of ν_e into ν_μ and ν_τ . However, the range of oscillation parameters which accommodate all these results allows several proposed solutions (scenarios) for the neutrino oscillations: Large mixing angle (LMA), Small mixing angle (SMA), Low mass (LOW), Mikheev-Smirnov-Wolfenstein solution (MSW); vacuum oscillations (VAC). Very recently, the new results from SNO⁷ and from the reactor experiment KamLAND⁷ lead to a unique solution for the solar neutrino problem. The essential step forward in the SNO experiment was the construction of a detector that has multiple detection channels. They use the following reactions:

$$\nu_e + d \rightarrow e + p + p \quad (CC) \quad (2.4a)$$

$$\nu_x \rightarrow \nu_x + n + p \quad (NC) \quad (2.4b)$$

$$\nu_x \rightarrow \nu_x + e \quad (ES) \quad (2.4c)$$

recording the ν_e by one reaction and the total flux of all neutrinos by another. In the SK measurement for solar neutrinos only the ES process was investigated.

In addition, the spectrum of the recoil electrons was measured in both experiments and no deviation from the spectrum expected, calculated in the hypothesis that the shape of the ν_e spectrum on the Earth is given by the known initial 8B spectrum, was observed. In the SNO experiment the fluxes in all three processes were measured. Combination the SK and SNO results the ν_μ and ν_τ fluxes were derived and found different from zero, although the initial flux (from the 8B decay) contained only ν_e . This is a demonstration that ν_e oscillate into the other neutrino species. The best fit for the oscillation parameters accomodating this result gives:

$$\Delta m^2 \sim 5 \times 10^{-5} eV^2; \quad \tan^2 \theta_{23} \sim 0.34 \quad (2.5)$$

The SNO result together with measurements of the recoil electron spectrum disfavored the SMA-MSW regions. Furthermore, the results got from the KamLAND reactor experiment excluded SMA, LOW and VAC solutions.

In the KamLAND experiment the $\bar{\nu}$ are detected in the 1kt liquid scintillator detector located in the Kamioka mine, via the observation of the process $\bar{\nu}_e + p \rightarrow e^+ + n$ with $E_\nu \sim 1.8$ MeV. The $\bar{\nu}$ flux is expected from 26 reactors in Japan and Korea with distances in the range of 138-214 km. Both prompt photons from the annihilation of positrons in the scintillator and the 2.2 MeV delayed photons from the neutron capture $n + p \rightarrow d + \gamma$ are detected. During 145.1 days of running they got $(N_{obs} - N_{bg})/N_{expected} = 0.611 \pm 0.085$ and the best fit values of the oscillation parameters derived from this result are:

$$\Delta m^2 = 6.9 \times 10^{-5} eV^2; \quad \sin^2 2\theta_{23} = 1.00 \quad (2.6)$$

Conclusion: KamLAND confirms the solar neutrino results leaving LMA the only solution for the solar neutrino problem. It provides strong evidence of neutrino oscillations obtained for the first time with terrestrial reactor antineutrinos with the initial flux under control. It is, however, worth mentioning that while the results of the KamLAND experiment restrained the range of the Δm^2 parameter derived in SNO and SK experiments, it can not reduce the uncertainty in the values of the mixing angle.

2.3. Channel $e \rightarrow \tau$

CHOOZ and Palo Verde experiments⁷ (finished in 1998) provide us with information on the third mixing angle θ_{13} . Like in the KamLAND experiment, the $\bar{\nu}_e$ disappearance was searched via the same reaction: $\bar{\nu}_e + p \rightarrow e^+ + n$. No indication for the disappearance of $\bar{\nu}_e$ on the way 300 m from reactor to detector was found. The ratio of the measured and expected number of $\bar{\nu}_e$ was found $R \sim 1.01$. The values of the best fit parameters are:

$$\Delta m^2 \sim 2.5 \times 10^{-3} eV^2 \quad \sin^2 2\theta \leq 0.15 \quad (2.7)$$

At this point we mention the result of the LNSD experiment⁷ that used decays of stopped $\bar{\nu}_\mu$ at the LAMPF facility at Los Alamos to look for the appearance of electron antineutrinos. They reported the oscillation probability:

$$P(\bar{\nu}_\mu \rightarrow \bar{\nu}_e) = (0.264 \pm 0.067 \pm 0.045) \quad (2.8)$$

with

$$\Delta m^2 \sim 1 eV^2$$

Thus, LSND claims evidence for conversion $\bar{\nu}_\mu \rightarrow \bar{\nu}_e$. Having in mind that solar and atmospheric experiments give for Δm^2 values with four and two orders of magnitude, respectively, smaller than the LSND value, the presence of this disparate value requires the introduction of a fourth neutrino flavor in order to accommodate the results from all the neutrino oscillation experiments. However, the LSND result is controversial and should be checked independently by other experiments. MiniBooNE is now running to check this result.

3. Cosmological constraints for neutrino masses

Neutrino oscillation experiments provide us with convincing evidence that neutrino have mass and mix. The scale of the masses can be derived from other kind of experiments. At present, there are still no conclusive experimental results giving this scale, but to put limits as stringent as possible for neutrino masses is also meaningful. Recently, cosmological observations have started to provide valuable upper limits for the sum of the neutrino masses, which now are more stringent than those from laboratory experiments. The Gerstein-Zeldovich model makes the connection between the total neutrino mass and their associated energy density:

$$\Omega(\nu)h^2 = \Sigma m(i)/(93MeV) \quad (3.1)$$

where h is the Hubble parameter. From the analysis of the cosmic microwave background (CMB) power spectrum, measured by WMAP, for instance, one can extract the temperature fluctuations. Since the temperature fluctuations of the CMB spectrum display a spatial homogeneity, they can be expanded in spherical harmonics:

$$(\Delta T)/T^0 = \Sigma a(lm)Y_{lm}(\theta, \phi) \quad (3.2)$$

with $a(lm)$ aleatory variables which fulfil the relations $a(lm)a(l'm') = C(l)\delta_{ll'}\delta_{mm'}$. $C(l)$ is called the angular power spectrum and is conventionally shown when presenting the CMB results.

The massive neutrinos affect the CMB anisotropy spectrum (but to a lesser extent than was previously thought) by i) shifting the peaks to lower l 's (small effect) and ii) by enhancing the magnitude of peaks for high l (more significant effect). The anisotropies in the energy density power spectrum of the CMB are measured accurately within WMAP experiment[?]. However, from WMAP data only one can not extract stringent constraint on the sum of the neutrino masses because one can not fix precisely the other cosmological parameters.

Massive neutrinos contribute to the critical density of the universe. They also affect the formation of the large scale structures, particularly the power spectrum of matter fluctuations at small scales (within the horizon, when they are still relativistic), suppressing it.

This effect can be studied via the observation of the distribution of galaxies. Large samples of galaxy redshifts in surveys such as the 2 degree Field Galactic Red Shift Survey (2dFGRS)[?] and Sloan Digital Sky Survey (SDSS)[?] provide a tool for studying the power spectrum of matter fluctuations with very small random errors.

One can extract an upper limit for the sum of neutrino masses combining data from WMAP and fixing the other cosmological parameters from the analysis of 2dFGRS and SDSS data. The most stringent limit found in literature from such an analysis is $\Sigma m_i = 0.65$ eV. This limit can be even improved when Lyman- α ($Ly\alpha$) analysis is also included.

The matter density fluctuations are locally related to the optical depth for the absorption of light emitted by quasars by the Lyman clouds. Thus the analysis of $Ly\alpha$) forest can give us constraints on the matter power spectrum on scales within horizon, where the effect of massive neutrinos is most visible.

Combined data of WMAP, SDSS and $Ly\alpha$ give $\Sigma m_i = 0.42$ eV. There is a tendency to more stringent upper limits for the sum of neutrino masses

coming from cosmology. However, when performing such analysis one should have good constraints on the other cosmological parameters. For instance, Hannestad⁷ showed that when dark energy is taken as a free (but constant parameter) the limits relax: $\Sigma m_i \sim 1.48$ eV which leave still possible all the results on the neutrino masses.

4. Direct measurements of the neutrino mass

Neutrino oscillation experiments have proved that neutrinos have mass, which is the first evidence for beyond Standard Model physics. However, still remain the questions: what is the scale of this mass and what is the nature of neutrino, is it a Dirac or a Majorana particle? Answers to these questions are expected from direct measurements of neutrino mass. For example, neutrino mass can be derived by measuring the energy end point part of the beta-spectrum of tritium:

$${}^3\text{He} \rightarrow {}^3\text{He} + e^- + \nu_e \quad (4.1)$$

In spite of some advantages of this method (β decay is superallowed, nuclear matrix elements are constant, the electron spectrum is determined by only the phase space, the energy released E_0 is a convenient quantity), it has a reduced sensibility. The present most advanced experiments (Mainz and Troisk) give an upper limit of neutrino mass of $m_\nu \leq 1.8$ eV. The next generation beta decay experiment KATRIN⁷ aims at reaching a sensitivity of $m_\nu \sim 0.2$ eV. The tritium experiment measures the quantity:

$$m_\beta^2 = \Sigma |U_{ei}|^2 m^2 \quad (4.2)$$

In the normal hierarchy hypothesis $m_\beta \sim 0.012$ eV, in inverted hierarchy $m_\beta \sim 0.05$ eV, while for the eventuality of 4 neutrino flavors it results: $0.45m_\beta \sim 1.4$ eV. One can see that the sensibility of KATRIN would not be sufficient to measure the neutrino masses if there are 3 flavors of neutrinos.

Double-beta decay is a nuclear process in which an even-even nucleus of (A, Z) decays into another even-even nucleus of the same mass but having the number of protons (or neutrons) changed by two units. It can occur with the emission of two neutrinos in the final states, the so called $2\nu\beta\beta$ decay mode, which is allowed within the Standard Model (SM). However, in GUTs beyond the SM, a second decay mode in which no neutrino is found in the final state is also allowed: the $0\nu\beta\beta$ decay mode. The observation of this process would prove that ν_e is a Majorana particle and would allow the derivation of the electron neutrino mass. The decay rate of the neutrinoless

decay mode reads:

$$\Gamma = GF[M(GT), M(F)] < m_{\beta\beta} >^2 : < m_{\beta\beta} >^2 = |\Sigma_i |U_{ei}|^2 e^{\alpha(i)} m_i|^2 \quad (4.3)$$

To derive neutrino masses one needs to calculate of the nuclear matrix elements (of Gamow-Teller and Fermi type) and the phase space G and use the experimental neutrinoless double-beta decay half-lives. Assuming CP conservation and taking into account the ν -oscillation results one obtains:

$$< m_{\beta\beta} > \sim |U_{ei}|^2 \pm |U_{ei}|^2 (m_1 + \Delta m_{12})^{1/2} \quad (4.4)$$

This relation can be used to derive the scale of neutrino mass values for different scenarios concerning the neutrino mass hierarchy: normal, inverted and degenerate. Unfortunately, at present the range of possible values for the neutrino masses is still too large, with a lower limit fixed at the $\sqrt{\Delta m_{atm}}$, which is out of the sensitivity of the most ambitious future $\beta\beta$ decay experiments. However, in the inverted and degenerate hierarchy scenarios the lower limits for the absolute neutrino masses are of the order of several tens of meV, which is in the range of sensibility of experiments like GENIUS and GEM, for instance.

We also mention the result of the Heidelberg-Moscow $\beta\beta$ decay experiment which reported a positive result for the $0\nu\beta\beta$ decay observation⁷. They found $m_{\nu_e} = (0.11 - 0.59)$ eV, with 0.39 eV the most probable value. However, this result is not yet confirmed by other independent experiments.

Combining the results from ν -oscillation experiments and the analysis of the cosmological data (including $Ly\alpha$ analysis), this result seems to be excluded. However, as we already mentioned, a recent analysis of the present data, involving a better parametrization of the dark energy⁷, may relax the upper limit for this sum and thus this result can not yet be excluded. From the future $\beta\beta$ decay experiments, aiming to reach a sensitivity ~ 0.015 eV there is a hope to find out new information about the absolute mass and the nature of neutrinos.

5. Conclusions

During many years there were indications in favor of the disappearance of solar ν_e (solar neutrino problem) or atmospheric ν_μ (atmospheric anomaly).

In the last years there were impressive experimental results for the explanation of these "unexpected" results by neutrino oscillations between different flavors. The essential steps forward made in these last years were: the up-down asymmetry observed in the atmospheric multi-GeV muon events

in the SK experiment, the confirmation of this result by the K2K terrestrial experiment, the evidence of transition of solar ν_e into ν_μ and ν_τ from the observation of the ν 's through the detection of CC, NC and ES processes by the SNO experiment, the evidence of disappearance of reactor $\bar{\nu}_e$ in the KamLAND experiment.

On the other hand many cosmological data allow us to extract stringent limits for the sum of the neutrino masses. However, these limits are dependent on cosmological models, whose parameters should be properly fixed.

Direct experiments for measuring the neutrino mass, especially $\beta\beta$ decay experiments remain the only able in a predictable future to provide us with absolute values of the neutrino masses and nature. In the next future there is good chance to find answers for the following still unsolved questions: a more precise determination of the neutrino oscillation parameters (for instance how small is the θ_{13} mixing angle (this information is expected from the large baseline neutrino oscillation experiments); how many neutrino flavor exist? (MiniBooNe experiment will check soon the LSND result, which still leaves some room for 4 neutrino flavors); neutrino mass scale and hierarchy (from improved analysis of cosmological data and direct measurements of the neutrino mass); nature of neutrino: is it a Majorana or a Dirac particle (from $\beta\beta$ decay experiments).

So, we expect in the next future more answers to fundamental questions related to the neutrino properties, maintaining this domain of research among the most exciting ones.

References

1. SK collaboration, S. Fukuda *et al.*, *Phys. Lett.* **B539**, 179 (2002); Y. Ashie *et al.*, *hep-ex/0501064*.
2. K2K collaboration, M.H. Ahn *et al.*, *Phys. Rev. Lett.* **90**, 041801 (2003); E. Alin *et al.*, *Phys. Rev. Lett.* **94**, 081802 (2005).
3. SNO collaboration, S.N. Ahmed *et al.*, *Phys. Rev. Lett.* **92**, 181301 (2004); B. Aharmim *et al.*, *nucl-ex/0502021*.
4. KamLAND collaboration, K. Eguchi *et al.*, *Phys. Rev. Lett.* **94**, 081801.
5. CHOOZ collaboration, M. Apollonio *et al.*, *Eur. Phys. J.* **C27**, 331 (2003); Palo Verde collaboration, F. Boehm *et al.*, *Phys. Rev. D* **64** 112001 (2001).
6. LSND collaboration, A. Aguilar *et al.*, *Phys. Rev. D* **64**, 112007 (2001).
7. WMAP collaboration, C.L. Bennet *et al.* *ApJ, Suppl.* **149** 1 (2003).
8. 2dFGRS collaboration, W.J. Percival *et al.*, *Mon. Nat. Roy. Astron. Soc.* **327** 1297 (2001).
9. SDSS collaboration, M. Tegmark *et al.*, *Phys. Rev. D* **69**, 103501 (2004).
10. A. Osipowicz *et al.*, *hep-ex/0109033*.

11. Beta-beta experiments *et al.*, *Phys. Rep.* **21**, 121 (2004).
12. H.V. Klapdor-Kleingrothaus, A. Dietz, H.L. Harvey and I.V. Krivosheina, *Mod. Phys. Lett.* **A16**, 2409 (2001).
13. H. Hannestad, *astro-ph/0509320*

5. High Energy Cosmic Rays

This page is intentionally left blank

THE ORIGIN OF COSMIC RAYS

PETER L. BIERMANN

*Max-Planck Institute for Radioastronomy, Bonn, Germany
and Department of Physics and Astronomy,
University of Bonn, Germany
E-mail: plbiermann@mpifr-bonn.mpg.de*

Here we review some arguments of recent years about the origin of cosmic rays, both Galactic and extragalactic. The final decision has not been made, but for Galactic cosmic rays supernova explosions, into a predecessor stellar wind, or into the interstellar medium are the option explored the most. Other candidates are microquasars and Gamma Ray Bursts. It appears likely, that the physics of very massive star explosions, Gamma Ray Bursts, and the origin of cosmic rays is tightly linked. For extragalactic cosmic rays the situation is even less clear: The activity by nearby active galactic nuclei is perhaps the most compelling, but the decay of relic particles seems still quite plausible, while new particles produced in interactions close to active black holes, or perhaps even near the merger of two massive black holes are avenues that remain to be investigated. The future work on this quest remains fascinating.

1. Introduction

Ever since their discovery almost 100 years ago, cosmic rays have challenged the physics community with both the search to understand their origin, but also with the attempt to learn more fundamental physics through their properties.

2. Spectrum of Galactic Cosmic Rays

The basic idea is that particles go back and forth across a shock, with a small step in momentum gain each time. This is called diffusive Fermi acceleration, since the particles go back and forth diffusively. Fermi acceleration was invented by Fermi and subsequently refined through the explicit use of a shock wave by many others (Fermi 1949, 1954; Axford *et al.* 1977; Krymskii 1977; Bell 1978; Blandford & Ostriker 1978; Ptuskin *et al.* 1980). Recent key theoretical work was done by I. Axford, A. Bell, E. Berezhko, R. Blandford, A. Bykov, L. Drury, D. Ellison, T. Gaisser, F. Jones, R.

Jokipii, M. Malkov, J. Ostriker, M. Ostrowski, R. Protheroe, V. Ptuskin, R. Schlickeiser, T. Stanev, A. Strong, H. Völk, and many others. In the references we only list a selection of reviews and books, in order to limit space. Classical references are the books by V. Ginzburg, S. Hayakawa, and W. Heisenberg. One attempt to collate all data was done by B. Wiebel-Sooth & P. Biermann, another in the book by P. Grieder.

An early hypothesis was that this acceleration happens in the interstellar medium near the exploded star, when the shock produced by the explosion travels through the Interstellar Medium at very high speed. After all, this shock is directly observable.

Another hypothesis is that acceleration in shocks in winds plays a key role for cosmic rays (CRs). A general theory was proposed in a series of papers starting with P. Biermann (1993), based on earlier work with H. Völk (1988). This approach gave quantitative predictions, that have held up so far.

Since the environment of the exploded star is often still under the influence of the earlier star, both approaches have similarities.

In the concept that particles go back and forth across a shock, the energy gain/loss of particles of various kinds has several contributions:

- Injection: from the winds of Wolf Rayet (WR) stars, the winds of red supergiant stars (RSG), and/or the interstellar medium (ISM). In some approaches these different sites are critical. A variant on the idea that the injection is from the winds, is that the injection is from the hot and partially unmixed gas in a hot bubble around a number of recently exploded supernovae.
- Momentum kick: the Lorentz transformation at a shock with velocity U ; scattering with diffusion coefficient κ , particle energy E and charge Z
- Adiabatic loss: in an expanding spherical shock system, in stellar wind, radial distance r
- Injection history: in a wind of density $\rho \sim r^{-2}$, in the interstellar medium obviously with the local clumpy structure (work by, e.g., E. Berkhuisen)
- Drifts: in curved magnetic fields, in magnetic fields perpendicular to shock normal, in a stellar wind. The knee is due to a scale change in the relevant curvature, leading to a small loss in acceleration efficiency at a specific rigidity E/Z . The line of reasoning about drift motions, and the associated energy gains has been emphasized

most by R. Jokipii. An alternate approach is to argue that the acceleration is enhanced by an instability in the shock (recent work by A. Bell), leading to much higher magnetic fields and so also higher particle energies, and that the acceleration just becomes less efficient at the knee. A third idea is to have the spectrum straight at the source site to the largest energies, and to bend the spectrum via a loss from the Galaxy, which depends on rigidity $\sim E/Z$

- Supersonic turbulence: observable in shear, radio polarization in post shock region, temporal variations: this leads to

$$\kappa \sim \Delta r \times \Delta U \quad (1)$$

An alternate concept is to just use microscopic scale turbulence, scattering the particles within a very small distance from the shock.

- In winds injection spectrum of $E^{-7/3}$. In WR winds acceleration to $Z 10^{17}$ eV, reaching the ankle with heavy elements. In RSG winds a smaller maximum energy due to the limited size, but the same predicted spectrum. In ISM injection spectrum of $E^{-2.42}$. The earlier papers give an error estimate of these predictions, a prediction for the knee energy, and the final cutoff energy (both proportional to charge Z). In other work, for the explosions into the ISM the initial spectrum is much closer to E^{-2} . However, in a standard explosion “downstream” is inside the supernova shock, and only when the shock disappears do get the cosmic rays released into the outside world; the final spectrum of cosmic rays injected into the interstellar medium is an integral over the accumulated losses and gains and so different from any instantaneous spectrum; the spectrum can be curved, and is usually steeper than E^{-2} .
- **Reference injection spectrum** $E^{-2.3}$ to $E^{-2.4}$, for one proposal (P. Biermann *et al.*), and closer to $E^{-2.1}$ for the second proposal (e.g. H. Völk *et al.*).

A full description of arguments is in the Calgary review (P. Biermann 1993), in the Tucson review (P. Biermann 1997), and in the Landolt-Börnstein data listing and review (B. Wiebel-Sooth & P. Biermann 1999).

Alternate recent arguments have been made by A. Bell, P. Blasi *et al.*, and H. Völk *et al.* The main observable difference is that the injection in the first approach is slightly steeper than in the second one; this implies a different interaction scenario, in the material close to the source mostly

in the first proposal, and distributed across the interstellar medium in the second one.

3. Transport Galactic Cosmic Rays

Here the basic idea is to rely on ISM data, Solar wind analogy, CR electron spectrum data, and CR anisotropy, but use the secondary/primary ratio from spallation as a test of the spallation site.

The original key paper is by N. Kardashev (1962). Electrons are observed to have a spectrum of $E^{-3.3}$. In the energy range beyond 5 - 10 GeV electron energy losses by Synchrotron and IC emission dominate over leakage from the Galaxy, so steepening by unity. Therefore injection with $E^{-2.3}$. Protons/Helium in CRs show $E^{-2.7}$. So difference gives leakage energy dependence as $\tau_L \sim E^{-0.3...0.4}$. Including error bars and anisotropy limits gives exponent in $\tau_L \sim E^{-\alpha_L}$ with $\alpha_L \leq 0.4$. This implies Kolmogorov turbulence governs CR transport (A. Kolmogorov 1941). So the key result is

- **Transport** $\tau_L \sim E^{-1/3}$.

This implies a steepening of the spectrum by 1/3: so for wind final spectrum $E^{-8/3}$. The time scale implied has been checked, spallation versus IC and synchrotron loss. Data confirm very closely the spectrum of $E^{-2.67}$. Other tests have been done with the available KASKADE data (work with A. Vasile, S. Ter-Antonyan).

The alternative is to seek to resolve the discrepancy between the spallation derived grammage as a function of energy, and the implied leakage time energy dependence in a reacceleration throughout the medium.

3.1. Spallation Galactic Cosmic Rays

Here first hypothesis, most spallation in region close to an exploding star, so local turbulence spectrum governed by injected cosmic rays.

Key initial papers are by A. Kolmogorov (1941), R. Kraichnan (1965), W. Matthaeus *et al.* (1992) and later; early work was done by L. Prandtl in the 1920ies and Th. Karman in the 1930ies.

Injecting energy into turbulence at some specific length scale of wavenumber k_0 gives usually a spectrum $I(k)$ of energy per volume per wavenumber of k^{+2} at long wavelengths $k < k_0$, and $k^{-5/3}$ at short wavelengths $k > k_0$.

Injecting with lots of power leads to a saturated spectrum of k^{-1} at long wavelengths or short wavenumbers, as seen in the Solar wind. This has also been called an inverse cascade.

Injecting power in a 2D medium, such as dominated by a magnetic field, gives a $k^{-3/2}$ spectrum.

The turbulence describing a series of shocks running through a medium is k^{-2} , a saw-tooth pattern.

However, injecting power at all scales simultaneously (see A. Bell 1978) with a CR $E^{-7/3}$ spectrum at a discontinuity such as a shock, gives a spectrum of $I(k) \sim k^{-13/9}$, leading to an energy dependence as

$$\text{spallation grammage} \sim E^{-5/9}$$

Hirschegg review (P. Biermann 1997), confirmed by V. Ptuskin at the ICRC 1999 with $E^{-0.54}$. A preliminary analysis suggests that 2/3 of the grammage or more are near the source, and 1/3 or less are in the average ISM (work with R. Sina, E.-S. Seo). Tests are the precise spectra of positrons, antiprotons, and of the spallation secondary nuclei.

In the alternate picture this reasoning leads to difficulties, which some have used to suggest that supersymmetry is required. There may be a solution by adducing secondary acceleration in the ISM.

4. Predictables and Answers Galactic Cosmic Rays

At the workshop the challenge arose to give answers to a number of questions. Here we try to give the answers based on the approach by the author.

- Very massive stars explode with about $E_{SN} \approx 10^{52}$ erg (work with G. Pavalas).
- The mechanism of explosion for the most massive stars is the magneto-rotational mechanism proposed by G. Bisnovaty-Kogan 1970, following an earlier idea of N. Kardashev 1964; many papers now G. Bisnovaty-Kogan & S. Moiseenko 2004/2005.
- Observed knee caused by He and C, and so $\Delta E/E \approx 3$. $E_{knee} \simeq E_{ankle}(U/c)^2$. Knee energy universal for all contributing stars, the WR star explosions.
- Inner Galaxy in γ -rays corresponding to a CR interaction spectrum of $E^{-7/3}$, outer Galaxy corresponding to a CR interaction spectrum of $E^{-8/3}$ (work with S. Casanova *et al.* 2004). TeV emission predicted to be much more patchy than matter distribution. This appears to be consistent with both the EGRET and the MILAGRO results.

- CR abundances composite of WR stars (some He, all heavy elements), RSG stars (some H, some He), and some ISM (only part of H) (work with A. Popescu; here at meeting R. Binns).
- CR power of Galaxy 3×10^{41} erg/s. Galaxy has wind, with k^{-2} turbulence spectrum, dominated by shocks (work by V. Ptuskin, V. Zirakashvili *et al.*, with E.-J. Ahn *et al.*, and L. Caramete).

The most comprehensive approach using the ISM as the main interaction site has been made by A. Strong & I. Moskalenko.

For literature see the many quotations in those review articles and books listed here at the end.

4.1. Tests

In the next few years we can expect that the new TeV spectra of cosmic ray acceleration sources may help bring a decision, whether any one of the proposals above is what Nature chose. A second avenue is the high precision spectra for various nuclei at relatively high particle energy. And the ultimate test will be the neutrino spectra of our inner Galaxy.

5. Extragalactic Cosmic Rays

Here we have explored the concept that the radio galaxy M87 can contribute most at the highest energies, and the radio galaxy Cen A around 10 EeV; many weaker radio galaxies contribute at yet lower energies. We have explored in some detail the physics of relativistic jets in microquasars to active galactic nuclei, in order to understand the cosmic ray role; these papers are not listed here (work with H. Falcke, W. Krüßls, K. Mannheim, S. Markoff, R. Rachen, F. Yuan, *et al.*).

An alternate picture is to invoke the decay of some postulated plausible relic particle (work by D. Schramm, P. Bhattacharjee, G. Sigl, *et al.*). The difficulty reconciling the AGASA data and the HiRes data, now again found in the AUGER analysis, illustrate that the resolution may not come for some more years.

Tests will be the isotropy of cosmic rays on the sky, the spectra, any possible directional correlation of ultra high energy cosmic rays with distant known sources, and any insight on the nature of the particles arriving. An indirect test will be provided by the modelling of the magnetic field around our Galaxy, perhaps in an extended halo, perhaps in a large magnetic wind; for a small number of CR sources such an environment is

required to isotropize the arrival directions (work with A. Bogdan, L. Caramete, and A. Curutiu). Just as for Galactic cosmic ray sources, gamma ray and neutrino spectra as well as their variability characteristics of active galactic nuclei may provide the ultimate test.

6. Conclusions

The evolution of our understanding of the origin of Galactic cosmic rays is beginning to show convergence towards an origin mostly connected to the supernova explosions of very massive stars and their environment. The possible relation of the origin of galactic cosmic rays and their progenitor stars to the origin of Gamma Ray Bursts, and the mechanism of explosion of very massive stars promises just like the unknown origin of extragalactic cosmic rays to be an exciting field of research in the future.

For the extragalactic cosmic rays the remaining discrepancy between the different avenues of measurements leaves the debate wide open, between an activity of cosmologically nearby black holes on one end of the range of discussion, there mostly M87 and Cen A, and an origin from the decay of relic particles of some unknown sort at the other end of the range.

Ultimately, this physical understanding can hopefully be used to deepen our understanding of the fundamental physics of matter.

Acknowledgements

P.L. Biermann would like to acknowledge W. Bednarek, V. Berezhinsky, G. Bisnovatyi-Kogan, P. Blasi, H. Blümer, D. Bosanac, W. Cui, D. Durisen, T. Enßlin, H. Falcke, G. Farrar, P. Frampton, L. Gergely, M. Ostrowski, K. Otmianowska-Mazur, R. Juskiewicz, A. Kandus, H. Kang, P.P. Kronberg, A. Kusenko, N. Langer, P. Lipari, K. Mannheim, S. Markoff, G. Medina-Tanco, S. Moiseenko, A. Olinto, M. Ostrowski, C. Pilachowski, D. Ryu, A. Shukurov, R. Sina, E.-S. Seo, T. Stanev, S. Ter-Antonyan, M. Urbanik, Y. Wang, T. Weiler, G. Yodh, F. Yuan, and J. Ziolkowski for many comments and discussions of these questions. Special support comes from the European Sokrates / Erasmus grants in collaboration with East-European Universities and academy institutes, with partners W. Bednarek, L. Gergely, M. Ostrowski, K. Petrovay, A. Petrusel, R. Roman, M.V. Rusu, and S. Vidrih, and VIHROS through the FZ Karlsruhe. Work with PLB is being supported through the AUGER theory and membership grant 05 CU 5PD1/2 via DESY/BMBF (Germany); further support for the work with PLB has come from the DFG, DAAD, and Humboldt Foundation.

References

1. Aharonian, F. A., Völk, H. J., Horns, D., Eds., *International Symposium on High Energy Gamma-Ray Astronomy*, Proceedings of the conference held in Heidelberg, Germany, 26-30 July 2004, 821 p. With CD-ROM. Berlin: Springer (2005).
2. Berezhko, E. G., *Advances in Space Research*, **35**, p. 1031 - 1040 (2005).
3. Berezhinskii, V.S., *et al.*, *Astrophysics of Cosmic Rays*, North-Holland, Amsterdam (especially chapter IV) (1990).
4. Bhattacharjee, P. & Sigl, G., *Physics Reports*, **327**, 109 - 247 (2000), astro-ph/9811011.
5. Biermann, P.L., at 23rd International Conference on Cosmic Rays, in Proc. *Invited, Rapporteur and Highlight papers*; Eds. D. A. Leahy *et al.*, World Scientific, Singapore, p. 45 (1994).
6. Biermann, P.L., in *Cosmic winds and the Heliosphere*, Eds. J. R. Jokipii *et al.*, Univ. of Arizona press, p. 887 - 957 (1997), astro-ph/9501030.
7. Biermann, P.L., Bisnovatyi-Kogan, G., Moiseenko, S., in Proc. of the Brazil Nov 2004 meeting, Ed. E.d. Pino Gouveia, AIP proc. vol. 784 (2005).
8. Drury, L. O'C., *Rep. Progr. Phys.* **46**, 973 - 1027 (1983).
9. Gaisser, T.K., *Cosmic Rays and Particle Physics*, Cambridge Univ. Press (1990).
10. Ginzburg, V.L. & Syrovatskii, S.I., *The origin of cosmic rays*, Pergamon Press, Oxford (1964), Russian edition (1963).
11. Grieder, P. K. F., *Cosmic Rays at Earth*, Elsevier Science (2001).
12. Hillas, A. M., *Ann. Rev. Astron. Astrophys.* **22**, 425 (1984).
13. Kronberg, P.P., *Rep. Prog. Phys.*, **57**, 325 - 382 (1994).
14. Kulsrud, R.M., *Annual Rev. of Astron. & Astrophys.* **37**, 37 (1999).
15. Learned, J.G. & Mannheim, K., *Ann. Rev. Nucl. & Part. Sci.* **50**, 679 - 749 (2000)
16. Malkov, M. A., O'C Drury, L., *Rep. Progr. Phys.*, **64**, p. 429-481 (2001).
17. Moskalenko, I. V., Strong, A. W., in *Int. Conf. on Astrophysical Sources of High Energy Particles and Radiation* (Torun, Poland, June 20-24, 2005). To be published in AIP Conf. Proc., eds. T. Bulik *et al.*, (2005), astro-ph/0509414.
18. Nagano, M., Watson, A.A., *Rev. Mod. Phys.*, **72**, 689 - 732 (2000).
19. Piran, T., *Physics Reports* **314**, 575 (1999).
20. Ptuskin, V. S., *et al.*, *Adv. Space Res.*, **35**, p. 162 - 166 (2005), astro-ph/0301420.
21. Schlickeiser, R., *Cosmic ray astrophysics*, Astronomy and Astrophysics Library, Berlin, XV + 519 pp: Springer (2002).
22. Matthews, J.M., Ed., *High Energy Astrophysics. Models and Observations from MeV to EeV*, Singapore: World Scientific (1994).
23. Stanev, T., *High energy cosmic rays*, Springer, (2004).
24. Völk, H. J., *Nuclear Physics B*, **138**, p. 492 - 501 (2005).
25. Wiebel-Sooth, B., Biermann, P.L., Landolt-Börnstein, vol. VI/3c, Springer Verlag, p. 37 - 90 (1999).

THE MYSTERY OF THE HIGHEST ENERGIES IN THE UNIVERSE

HEINIGERD REBEL

Institut für Kernphysik, Forschungszentrum Karlsruhe, D 76021 Karlsruhe, Germany

The present status of the experimental research looking for the end of the cosmic ray energy spectrum and the some aspects of this question are briefly discussed

1. Introduction

Our Universe is filled with many kinds of radiation: Electromagnetic radiation and particles in a broad range of wavelengths and energies, respectively, visible and invisible for our eyes. Some of the radiation is produced in stars and galaxies, while some is the ubiquitous cosmological background radiation, a relic from the cosmic evolution starting with the Big-Bang (as we believe in terms of the standard understanding). Among all these radiations, the most energetic are cosmic rays particles, dominantly protons, helium, carbon, nitrogen ... up to Fe ions in a appreciable amount. They continuously bombard our Earth from the cosmos by an isotropic stream of high energy particles.

Roughly once per second, a subatomic particle enters the Earth's atmosphere carrying as much energy as a well thrown rock. That fact implies that there are somewhere in Universe forces that can impart to a single proton 100 millions times the energy achievable by the most powerful Earthbound accelerators.

Cosmic rays were discovered in 1912 by the Austrian Victor Hess through a series of balloon flights, in which he carried electrometers to over 5000 m altitudes. Nowadays we know that the energy spectrum of these particles extends from 1 GeV to beyond 10^{20} eV (or 100 EeV), the highest energies of known individual atomic particles in the Universe.

But we have only a rudimentary understanding where these cosmic particles are coming from, how they are accelerated to such high energies and how they propagate through the interstellar space. The difficulty is that cosmic rays are overwhelmingly charged particles (stripped nuclei), and the galactic magnetic fields are sufficiently strong to scramble their paths. Perhaps except at highest energies cosmic rays have lost all their memory about the location of the emission sources, when they eventually arrive the Earth's atmosphere. Hence the only observable quantities, which may give us some information are **the energy distribution and the elemental composition of primary cosmic rays, at highest energies eventually with deviations from isotropic incidence.** The experimental determination of these observables are topics of contemporary

research and of current interest, especially in regions which exceed the energies provided by man-made accelerators [1].

The rather featureless energy spectrum of primary cosmic rays comprises more than 12 orders of magnitude in the energy scale. The flux of primary cosmic rays falls from 1 particle/m²/s to 1 particle/km²/century at the highest energies. It follows an overall power-law ($\propto E^{-2.7}$) with a distinct change of the index to ($\propto E^{-3}$) around $3 \cdot 10^{15}$ eV, called the „knee“. This feature and other discontinuities are more distinctly displayed, when the flux is multiplied with the power law dependence of the flux (Fig.1). The origin of the knee is still not consistently explained, though discovered 40 years ago by German Kulikov and George Khristiansen from the Moscow State University with studies of the intensity spectrum of Extensive Air Showers (EAS), of the so-called shower size, which roughly reflects the primary energy [2].

A great deal of interest and current efforts concern the shape of the spectrum in the EeV – region, i.e. above 10^{18} eV, where the spectrum seems to flatten (“ankle”), especially around $5 \cdot 10^{19}$ eV. There is the theoretically predicted Greisen-Zatsepin-Kuzmin (GZK) cut-off originating from the photo-interaction of protons with the 2.7 K background radiation. The AGASA experiment in Akeno (Japan) [3], in particular, but also others, has shown that this limit may not exist. Other experiments see a tendency for the GZK cut-off.

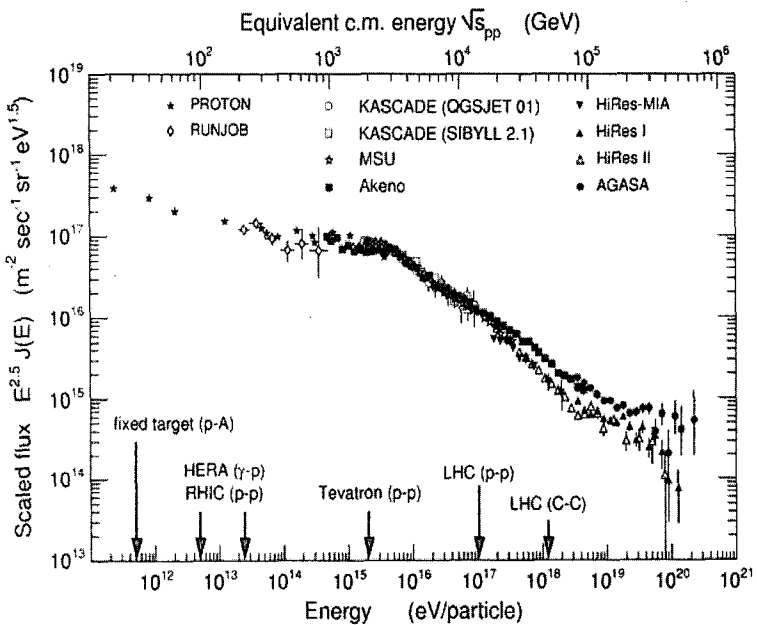


Figure 1. The primary energy spectrum of cosmic rays.

This fact (and the controversy features) is an issue of extreme astrophysical and cosmological relevance. This lecture will be particularly focussed to these highest energies. One should realise that the energy range we are considering is many orders of magnitude higher than of artificial accelerators on Earth.

Something is hurling incredibly energetic particles around the universe. Do these particles come from some unknown superpowerful cosmic explosion?

From a huge blackhole sucking stars to their violent deaths? From colliding galaxies? From the collapse of massive invisible relics of the origin of the Universe? We don't yet know the answers!

2. Methodical Features and Techniques

Above 10^{14} eV the techniques used to study cosmic rays employ the phenomenon of Extensive Air Showers discovered independently by Auger and Kohlhörster in 1938 [4,5].

An extensive air shower is a natural phenomenon of our environment that happens when a high energy particle from the cosmos enters into the Earth atmosphere and dissipates the energy by **multiparticle production**. Thus the atmosphere acts globally as a particle multiplier and enables the detection of the rare single particle by large-area ground-based detector arrays.

Most of the produced particles in the hadronic interactions are pions and kaons, which can decay into muons and neutrinos before interacting, thus producing the most penetrating component of atmospheric showers. The most intensive component - electrons and photons - originates from the fast decay of neutral pions into photons, which initiate electromagnetic showers in the target, thus distributing the originally high energy over millions of charged particles.

The backbone of an air shower is the hadronic component of nucleons, pions and more exotic particles. The electromagnetic component is accompanied by an additional EAS phenomenon, the production of atmospheric Cerenkov light which carries further information about the shower development.

However, in ground-based experiments, in general, we are not in the situation to see the longitudinal development, we observe only the developed status of the air shower cascade at a certain observation level. From the observables there, that means from the intensity, the lateral and eventually the energy distributions, we must deduce the characteristic properties of the primary particle.

The analysis of the observations invokes extensive Monte Carlo simulations of the development of air showers. They serve as references for pattern recognition methods considering the correlations (multivariate distributions) of the observables [1].

In an EAS experiment the lateral distributions of the particles are sampled by more or less regular arrangements of a large number of various types of

particle detectors: scintillators, streamer tubes, gas counters, water - Cerenkov detectors. They cover only a small fraction of the total area. An example of a modern experiment of this kind is the KASCADE (-Grande) experiment [6] in Forschungszentrum Karlsruhe, which attempts to explore the region of the knee.

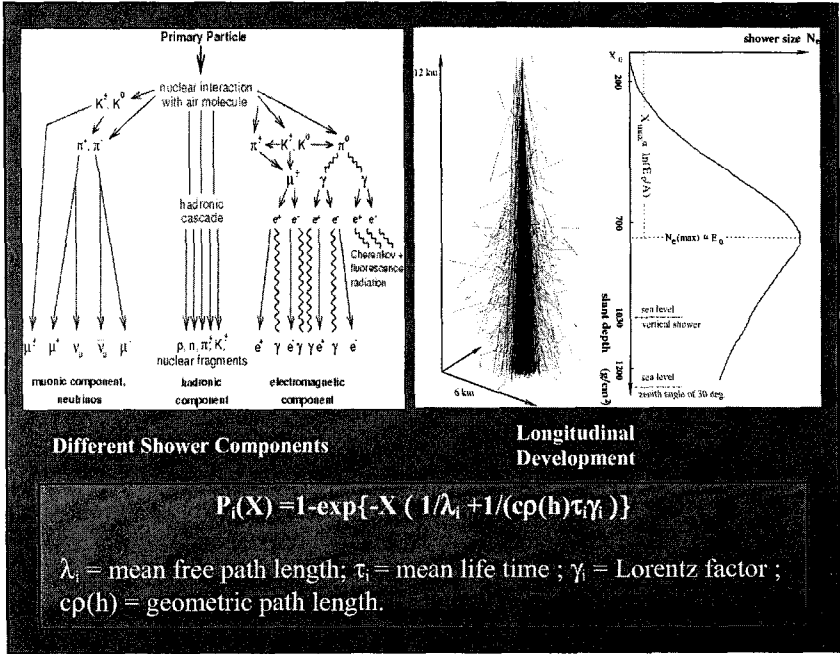


Figure 2. Schematic display of the structure of Extensive Air Showers.

3. Air Fluorescence Technique

For the experimental research at higher primary energies above 10^{17} eV, we are discussing briefly an efficient method applicable there, which informs even about the longitudinal development of the EAS: *Air fluorescence observations*.

The technique relies on the fact that an ionising particle can excite N_2 molecules in the atmosphere, Such excited molecules emit fluorescence photons (typically within 10 to 50 ns after excitation: rigorously speaking it is "luminescence"). The optical fluorescence come from various bands of molecular nitrogen of the molecular nitrogen ion, with light emitted between 3000 and 4000 Å, which happens to be the wave band for which the atmosphere is quite transparent. The attenuation length is approximately 15 km for vertical incidence. The fluorescence yield per particle is mildly dependent on altitude.

An EAS of 10^{17} eV has more than 100 millions of electrons in the shower maximum, so that there are many fluorescence photons, even with 0.5 % fluorescence efficiency.

The fluorescence light is isotropically emitted and can be detected at large distances from the shower axis. Thus it can be distinguished from air-Cerenkov light which is induced by the fast electrons and is emitted in forward direction, confined to near distances from the shower axis. The problem is to identify the weak light traces from a 40-Watt glue ball, flying some microseconds through the atmosphere in some kilometres distance.

The effective area for recording showers is very large as compared with conventional detector arrays and compensates the low duty cycle resulting from observations only on clear dark moonless nights. There are special techniques used for discrimination against night sky background and terrestrial light noise.

The fluorescence light (a flash of a few microseconds of duration) is collected using a lens or a mirror and imaged to a camera, located in the focal plane. Essentially the camera is an assembly of a large number of photo multipliers, each looking to a certain region of the sky. The camera pixelizes the image and records the time interval of the light arrival in each pixel element. We just inspect in Fig. 3 an air fluorescence *telescope* prepared in Forschungszentrum Karlsruhe and installed as a building stone of the Pierre Auger detector [7] in Argentina for studying the highest energies.

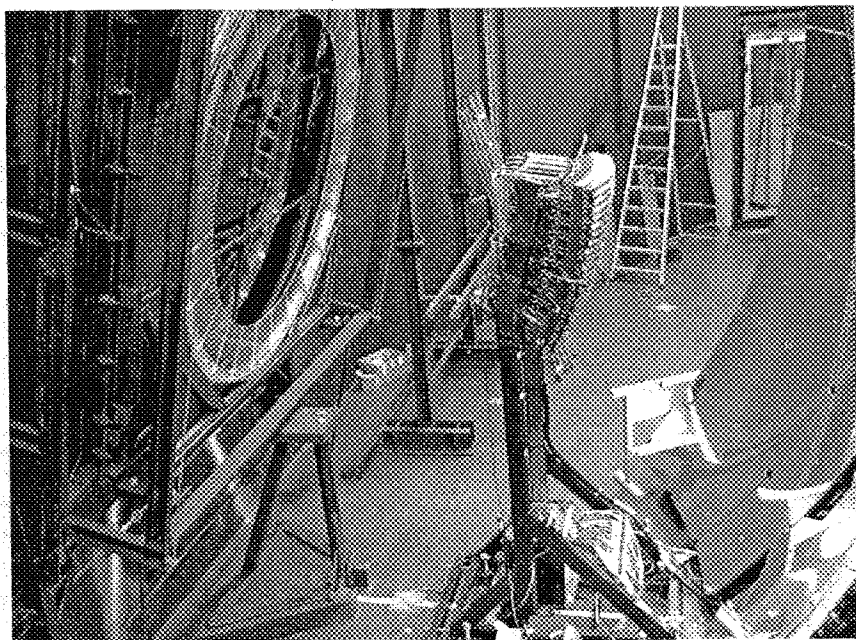


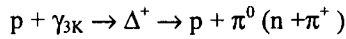
Figure 3. Fluorescence telescope assembled for the Pierre Auger Observatory [7].

The detector is in fact a large area spherical mirror telescope of 11 m² collecting area of aluminum segments, assembled with a correcting lens (Schmidt optics), covering a field of 30° x 30°. The camera is an assembly of 20 x 22 photomultipliers in the focus. The light trace is stored by a digital film in 100 ns distances .

From such traces together with the timing information, or more accurately by a stereoscopic procedure using two telescopes , the longitudinal development of the extended air shower in the atmosphere could be reconstructed. The fluorescence technique has been developed and effectively used by the Fly's Eye detectors installed in Dugway, Utah, 160 km from Salt Lake city, US [8].

4. The Spectral Region of the Ankle and Above

There the first remarkable feature results from the interaction with the 2.7 K microwave background radiation filling the universe. Above a certain threshold the cosmic particles interact with these photons, which appear to be blue-shifted to high gamma ray energies. For protons at about 5·10¹⁹ eV these gamma rays reach 300 GeV and start photo production of pions and cool down the proton in this way:



That is the **Greisen–Zatsepin–Kuz'min (GZK) spectral cut off** [9]. The consequence is that above 5·10¹⁹ eV, the cosmic radiation have rather short attenuation lengths, in the order of, say several tens Mpc and the Universe gets relatively opaque for them. To state this more explicitly: It is impossible for ultrahigh energy cosmic ray (UHECR) particles to reach us from sources whose distance would exceed 100 Mps, unless rather exotic particles or interaction mechanisms are envisaged. The size of 100 Mps is roughly the size of our local supercluster, the home of our Galaxy in the Universe.

A second feature is related to the chemical composition of ultrahigh energy primary cosmic rays. If the highest energy cosmic rays would be mainly protons, as some experimental results are tentatively interpreted, the trajectories of single charged ultrahigh energy particles through the galactic and extra-galactic magnetic fields (which are believed to be in the order of μG and nG, respectively) get no more noticeably deflected over distances limited by the Greisen-Zatsepin-Kuzmin cut-off. Typically the angular deviation of a 10²⁰ eV proton from a source of 30 Mps distance would be about 2 degrees. In other words, above the cut-off, the direction of incidence of such particles should roughly point to the source: Proton astronomy should become possible to some extent, defined by the box of the consequences of the cut-off. However, looking in our astrophysical surroundings, the number of objects within a few degrees of the observed arrival directions and within a distance of a few Mpc is quite

limited, if such objects should be able to accelerate particles to such extremely high energies at all. Some short remarks about that in a moment.

What is the present experimental knowledge? The data around the ankle and above come from a few large-aperture ground based detector arrays with two types of techniques. Alternatively to particle detector arrays [3,10] the observation method based on the nitrogen fluorescence is used [8,11].

Figure 4 displays the highest energy region of the cosmic ray spectrum as observed by the AGASA detector (1999) [3]. The figures near the data points indicate the number of events and the bars show the 90% confidence level. The energy spectrum is multiplied by E^3 , so that the part below 10^{18} eV becomes flat. The ankle structure becomes evident and the deviation from the cut-off predictions. "Impossible" events beyond the cut-off (see Fig.4) seem to be existing! There are of course large error bars, but the tendency is confirmed when other 13 events are included, detected by other detectors.

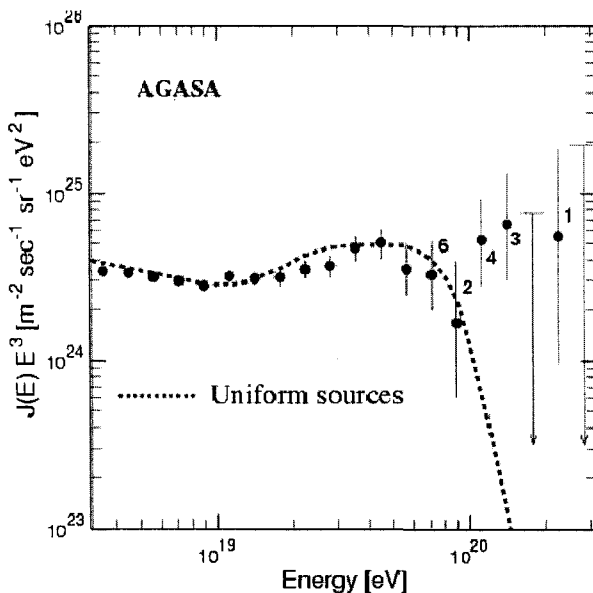


Figure 4. Highest energy region of the cosmic ray spectrum [3].

It should be noted that first results of the Pierre Auger Observatory, communicated at the 29th ICRC in Pune, India, 3-10. August, tentatively agree with results of the HiRes detector, which, in contrast to the AGASA results, do not find events beyond the GZK cut-off within the actual statistical accuracy. Such trans-GZK UHECR events would finally constitute a mystery, when we ask: Where are the sites and what are the acceleration mechanisms being capable to impart energies of macroscopic orders (in the most energetic case of

3· 10²⁰ eV: 50 joules) to a microscopic particle. Many processes have been proposed, where in an astrophysical plasma large scale macroscopic motion is transferred to individual particles, for example in a turbulence and by shock waves. The crucial role is played by the size of the acceleration region and the magnetic field embedded in the plasma and keeping the gyroradius of the particle in the acceleration region. That depends also from the velocity β of the motion.

In the conventional approach of shock wave acceleration by the Fermi mechanism, say in supernova remnants, β is in the order of 0.01. This is usually demonstrated by the so-called Hillas plot [12] (which neglects various sources of possible energy losses). It shows that we hardly find objects which might be able to accelerate cosmic rays beyond the 10²⁰ eV limit.

If all parameters related to the question are taken into account, one has to admit that none of the proposed scenarios seems fully convincing. In addition we have to keep in mind that the sources should be nearby in cosmological scales. Within the present statistical accuracy the data do also not show a distinct correlation with nearby point sources. There are only two potential candidates: the radio galaxy M87 in the Virgo cluster (about 20 Mpc away) and the radio galaxy NGC 315 at about 85 Mpc.

In order to associate some observed UHECR with this source it has been assumed that the two cosmic particles registered with the highest energies (2·10²⁰ eV and 3.2·10²⁰ eV) are He particles. When such a hypothesis of a galactic wind accelerator would turn out to be real, proven by larger statistics, we would have discovered a gigantic accelerator reaching energies many orders of magnitude higher than any conceivable man-made machine.

However, if future studies would exclude “conventional” astrophysical acceleration mechanisms, one would need to consider another class of theories proposed as possible explanation, so-called “top-down” processes, where even the violence of the Lorentz invariance has been considered. Most of the top-down models consider the possibility that UHECR arise from decay of some super-heavy X particle whose mass is in the Grand Unification range (10²⁵ eV) produced during some phase transition period during the early Universe. The models differ mainly, how to produce the density of X particles to fit the UHECR observations and their survival since some 10⁻³⁵ s after Big Bang. One should mention that such models (“one new suggestion per week”) have quite specific features and experimental signatures (spectrum and mass composition) so that a discrimination appears to be not impossible, provided the experimental knowledge could get increased. That is just our challenge for the next generation of detectors with large apertures!

5. The Next and Over-Next Generation of Detectors

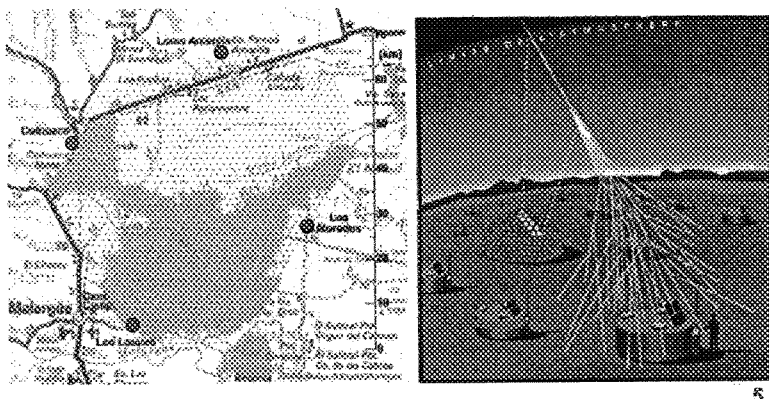
The next detector is the Pierre Auger Observatory with 14.000 km² sr aperture over two sites (30 times the size of Paris), one in each hemisphere. The installation of the Southern observatory has started in 2000 with a prototype

array of 55 km² and an air fluorescence telescope, near the small town of Malargüe in the province of Mendoza, Argentina. In final the site will be equipped with 1600 detector stations (12 m³ tanks filled with water detecting Cerenkov light produced by secondary particles), distributed in a grid with 1.5 km spacing. Four “eyes” composed of 33 air fluorescence telescopes will view 3000 km² of the site and measure during clear moonless nights i.e. with a duty cycle of 10 % the giant showers through the fluorescence generated in air.

This hybrid detector provides unique advantages. A subsample of 10% of the total number of events simultaneously observed with both techniques, enables a cross calibration and yield an unprecedented quality for shower identification. It is expected to detect some 60 to 100 events per year above 10²⁰ eV, and 100 times more above 10¹⁹ eV.

Hybrid measurement

- 4 Fluorescence stations: 180° x 30° by 4 x 6 Telescopes
- 1600 Water-Cherenkov-Tanks: 1.5 km Grid; 3000 km²



5

Figure 5. Hybrid layout of the Southern Pierre Auger Observatory [7].

The Pierre Auger Observatory was just started by a collaboration of 19 contributing countries, and the community looks already forward to the next generation of detectors. There is less doubt that this will be an airborne detector observing the giant shower development in the atmosphere with a huge aperture quasi “from above”. This is envisaged with the EUSO project [13]: fluorescence detectors installed on the International Space Station. Another proposal is a balloon borne project using the Antarctic ice as reflector of Cerenkov light [14].

Such projects are particularly interesting, when in few years the Pierre Auger Observatory will have shown that the spectral cut-off exceeds the present reach and that larger statistics is necessary for studies of the focal points of Extremely High Energy Cosmic Ray Observations. However, the lesson of the advanced studies [1] of the knee region like with KASCADE, that the investigation of the

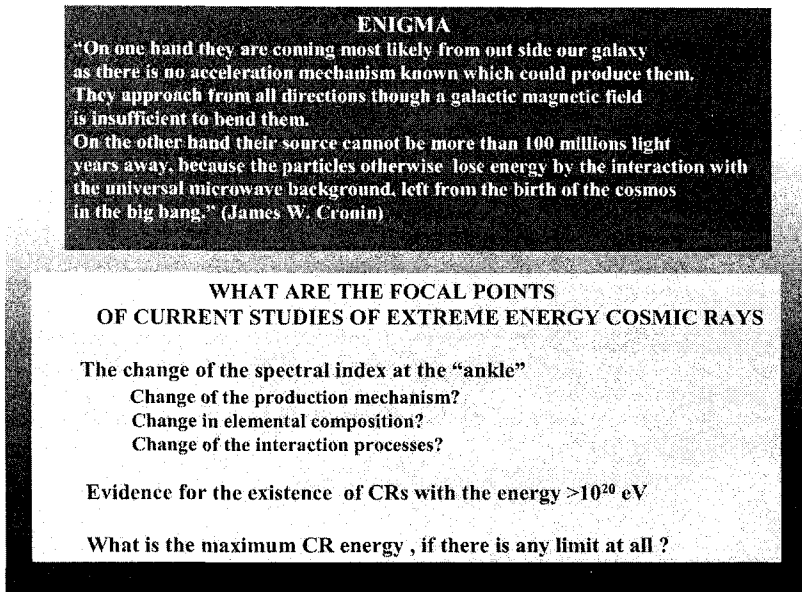


Figure 6. Focal points of UHCR investigations.

far-reaching astrophysical aspects by EAS observations has to be accompanied by a serious and quantitative understanding of the hadronic interactions in that energy range. That is the other side of the medal of all necessary efforts!

Without that, even the energy determination of EAS and scale of the spectrum may remain finally under debate! This debate got recently some new impact since the HiRes collaboration presented a new calibration inducing some doubt on the non-existence of Greisen-Zatsepin cut-off.

6. Conclusions

The most remarkable feature of the cosmic radiation is that the investigators have not yet found a natural end of the energy spectrum, albeit with decreasing intensity. We do not know the cosmic source of such a radiation, and the

features establish a mystery of great cosmological relevance at the frontier of natural science.

Acknowledgements

I would like to thank the organising committee of the CSSP05 for the nice opportunity to present this topic. Fruitful discussions with Dr. Ralph Engel are gratefully acknowledged.

References

1. A. Haungs, H. Rebel, M. Roth, *Rep. Prog.* **66**, 1145 (2003).
2. G.V. Kulikov and G.B. Khristiansen, *Soviet Physics JETP* **35** 441 (1959) 441
3. M.Takeda *et al.*- AGASA Collaboration, *Phys.Rev.Lett.* **81**, 1163 (1998).
4. P.Auger, R.Maze, T.Grivet-Mayer, *C.R. Acad. Sci. Ser. 2*, **206**, 172 (1938); *ibidem* **207**, 228 (1938).
5. W.Kohlhörster, I.Mathes, E.Weber, *Naturwissenschaften* **26**, 576 (1938).
6. T.Antoni *et al.* -KASCADE Collaboration, *Nucl. Instrum. Methods* **A513**, 490 (2003); A. Haungs *et al.*- KASCADE-Grande Collaboration, *Proc.28th ICRC (Tsukuba, Japan)*, vol. 2, p. 985 (2003).
7. M.T.Dova *et al.* - Pierre Auger Observatory Collaboration, *Proc 27th International Cosmic Ray Conf. (Hamburg)*, vol 2, p. 699.
8. G.L.Cassidy *et al.*, *Rev. Nucl. Part. Sci.* **35**, 351 (1985).
9. K.Greisen, *Phys.Rev.Lett.* **16**, 748 (1966); G.T. Zatsepin and V.A.Kuz'min, *Sov. Phys. JETP* **4**, 78 (1966).
- 10.M.Ave *et al.* , *Astropart. Phys.* **3**, 105 (1995).
- 11.D.J.Bird *et al.*, *Phys.Rev.Lett.* **71**, 3401 (1993).
12. A. M.Hillas, *Ann. Rev. Astron. Astrophys.* **22**, 425 (1984).
13. L.Scarsi *et al.*-EUSO team, in *Proc.27th Int.Cosmic Ray Conf.(Hamburg)* vol. 2, p.839
14. R.A. Antonov *et al.*, *Proc.27th Int.Cosmic Ray Conf.(Hamburg)* vol. 2, p.828

THE COSMIC RAY EXPERIMENT KASCADE-GRANDE

I. M. BRANCUS^{*B}, W.D. APEL^A, F.A. BADEA^A, K. BEKK^A, A. BERCU^C^B,
M. BERTAINA^C, J. BLÜMER^{A,D}, H. BOZDOG^A, M. BRÜGGEMANN^E, P. BUCHHOLZ^E,
A. CHIAVASSA^C, K. DAUMILLER^A, F. DI PIERRO^C, P. DOLL^A, R. ENGEL^A,
J. ENGLER^A, P.L. GHIA^F, H.J. GILS^A, R. GLASSTETTER^G, C. GRUPEN^E, A. HAUNGS^A,
D. HECK^A, J.R. HÖRANDEL^D, K.-H. KAMPERT^G, H.O. KLAGES^A, Y. KOLOTAEV^E,
G. MAIER^A, H.J. MATHES^A, H.J. MAYER^A, J. MILKE^A, B. MITRICA^B, C. MORELLO^F,
G. NAVARRA^C, R. OBENLAND^A, J. OEHLISCHLÄGER^A, S. OSTAPCHENKO^A, S.
OVER^E, M. PETCU^B, T. PIEROG^A, S. PLEWNIA^A, H. REBEL^A, A. RISSE^H, M. ROTH^D,
H. SCHIELER^A, O. SIMA^B, M. STÜMPERT^D, G. TOMA^B, G.C. TRINCHERO^F,
H. ULRICH^A, J. VAN BUREN^A, W. WALKOWIAK^E, A. WEINDL^A, J. WOCHLE^A,
J. ZABIEROWSKI^H, D. ZIMMERMANN^E

^A Institut für Kernphysik, Forschungszentrum Karlsruhe, Germany

^B National Inst. of Physics and Nuclear Engineering, Bucharest, Romania

^C Dept. of General Physics, Università degli Studi di Torino, Italy

^D Institut für Experimentelle Kernphysik, Universität Karlsruhe, Germany,

^E Fachbereich Physik, Universität Siegen, Germany

^F Institute for Interplanetary Space Physics INAF, Torino, Italy

^G Fachbereich Physik, Uni Wuppertal, Germany

^H Soltan Institute for Nuclear Studies, Lodz, Poland

* E-mail: iliana@ifin.nipne.ro

The cosmic ray experiment KASCADE, set up in Forschungszentrum Karlsruhe, Germany as a multi-detector installation, studying the electromagnetic, the muonic and the hadronic extensive air showers (EAS) component for each observed shower event, has explored the primary energy spectrum and the mass composition of cosmic rays in the energy range of the so called „knee“ (around 3 PeV). The multi-dimensional analyses reveal a distinct knee (change of the spectral index of a power-law description) in the energy spectra of the light primary cosmic rays and the dominance of heavy particles with increasing energy. This result provides some important implications, discriminating various conjectures and astrophysical models of the origin of the knee. The KASCADE-Grande experiment is an upgrade of the KASCADE experiment extending the detection area by a factor of 10. It is motivated by studies of a higher primary energy range, looking for the knee-like features of the heavy components, which are expected to appear in the range of 100 PeV. The lecture describes details of motivation, of experimental lay-out and of first studies with KASCADE-Grande.

1. Introduction

The energy spectrum of cosmic rays comprises more than 12 orders of magnitude, up to 10^{20} eV, following overall power laws, decreasing first $\propto E^{-2.7}$, with a distinct

change of the spectral index around 10^{15} eV, called „knee“ and a further change, called „ankle“ at ultrahigh energies [1], see Fig. 1.

At energies higher than 10^{14} eV, the observation of Extensive Air Showers (EAS) produced in the interaction of cosmic ray particles with atmospheric nuclei, can be done only by indirect observation with large surface experiments. From the lateral and longitudinal development of the particle cascades the energy and the mass of the primary particle can be inferred. The main EAS components are muons, hadrons and e^+ , e^- , γ , usually observed by large arrays like KASCADE [2,3], recently upgraded to KASCADE Grande [4,5].

The analysis of EAS observables to deduce properties of the primary particles relies on comparison with Monte Carlo (MC) simulations of the shower development, performed with the CORSIKA program [6], including the detector response. Using multivariate parameter distributions and advanced statistical methods, like Bayesian decision method [7] or neural network approaches [8], it is possible to infer the energy spectrum and mass composition of cosmic rays.

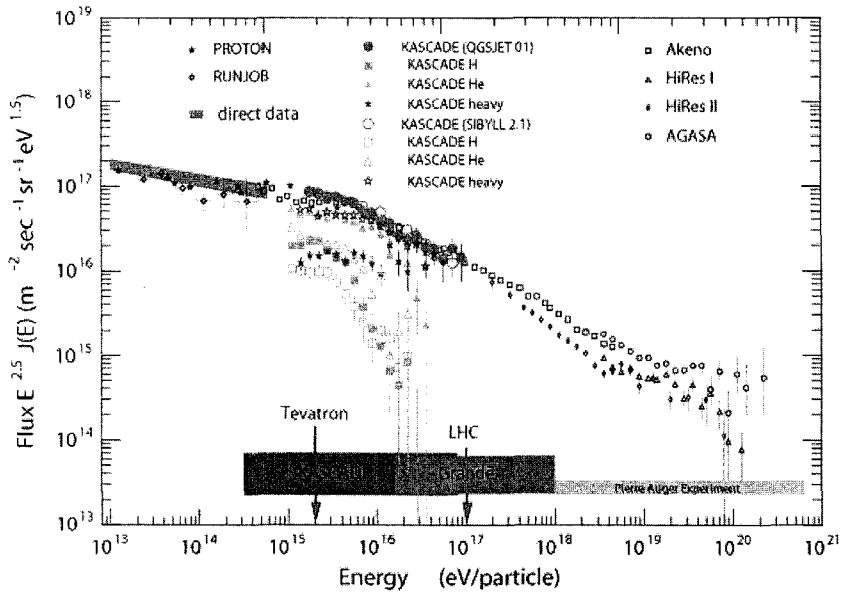


Figure 1. Primary cosmic ray flux covered by KASCADE and KASCADE Grande indicating the knee of the light component and the expectation for the heavy on (from Ref. [9]).

2. The KASCADE Experiment

2.1. Results of KASCADE Data Analysis

The KASCADE experiment, located in FZK, Germany (8°E , 49°N and 110 m a.s.l.) is the main part of KASCADE-Grande, being able to measure all three main components of EAS for primary energies 10^{14} - 10^{16} eV, (Fig. 2).

It consists of an array spanning 200 m x 200 m with 252 scintillation detectors (with detection threshold for electrons $E_e > 5$ MeV and for muons, $E_\mu > 230$ MeV), a central detector, 320 m², (formed by a hadronic calorimeter using liquid ionization chambers, a trigger plan of scintillation counters in the third layer and at bottom, 2 layers of position sensitive, MWPC and Limited Streamer Tubes, LST, for muon tracking at $E_\mu > 2.4$ GeV) and a muon tracking detector MTD, (in a 44m x 54m x 2.4m tunnel, using limited streamer tubes MWPC, $E_\mu > 0.8$ GeV).

For an approximate energy identification, the KASCADE experiment uses the truncated muon number, N_μ^{tr} , the muon intensity integrated between 40 m and 200 m from the shower axis, as simulations studies have shown a nearly independence of this estimator on the primary mass.

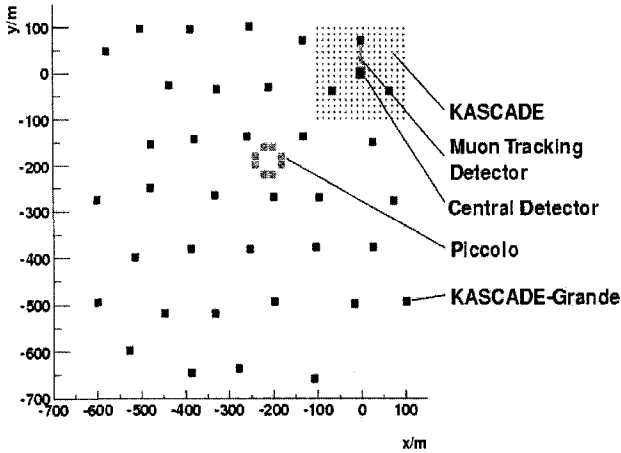


Figure 2. Schematic layout of KASCADE-Grande experiment (from Ref. [9])

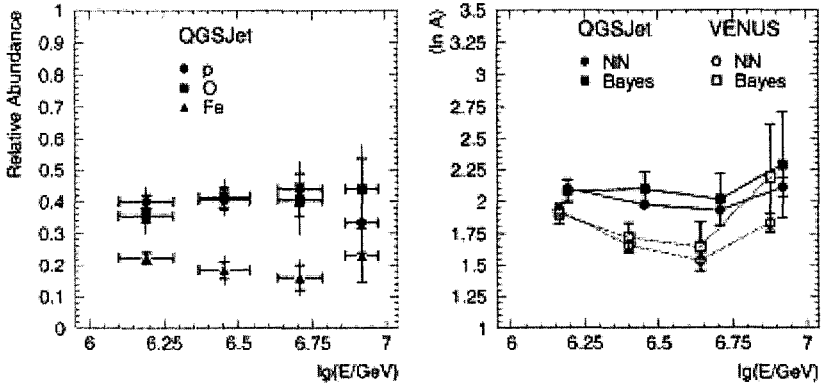


Figure 3. The relative abundances of the classes H, O and Fe vs. $\log N_{\mu}^{\text{tr}}$, reconstructed on the basis of two hadronic interaction models and using the EAS observables N_c and N_{μ}^{tr} . The right graph shows the corresponding mean logarithmic mass $\langle \ln A \rangle$ vs. N_{μ}^{tr} , (from [8]). Statistical (thick) and methodical (thin lines) uncertainties are indicated as error bars.

The most powerful quantity measured by KASCADE about the primary mass is the correlation between the electron size and the muon component.

The non-parametric statistical methods can be used to explore the significance of the observed features for a discrimination of different EAS primaries, by applying Bayesian decision rules [7] or neural networks [8], (Fig. 3).

The data indicate a mixed composition [8] which becomes heavier above the knee.

2.2. Main Conclusions from KASCADE Data

Using CORSIKA code for different hadronic interaction models, studies of some hadronic observables indicate that the QGSJET seems to be more adequate [1].

Different procedures of analysis lead to the interesting result that *the knee* is a change of the spectral index in the all-particle spectrum due to the light component.

A change towards a heavier composition above the knee is expected in acceleration models, where the knee is supposed to be rigidity dependent. A verification of this model would be the observation of the knee in the heavy component in a primary energy region around $E_0 = 10^{17}$ eV.

The question where is the knee of the iron component [9,10], determined the extension of KASCADE to KASCADE-Grande.

3. The KASCADE Grande Experiment

3.1. Description of KASCADE-Grande Array

KASCADE Grande covers a large area of detection 0.5 km^2 , (Fig. 2), making possible to measure EAS produced by primaries cosmic rays with energies 10^{14} eV - 10^{18} eV . It consists of three arrays: KASCADE (previously described), Grande and Piccolo [5,6].

Grande is formed by 37 stations at a distance about 130 m on an area of 0.5 km^2 . Each of 10 m^2 station is split into 16 individual scintillators, $80 \text{ cm} \times 80 \text{ cm}$ area, 4 cm thick. Each scintillator is viewed by photo-multipliers for timing and particle measurements, with a dynamic range of 0.3 to $750/10 \text{ m}^2$ mips.

Piccolo consists of an array of 8 huts (10 m^2 each), with 12 scintillator plates each. The aim of Piccolo is to provide an external trigger to KASCADE and Grande for coincidence events, allowing the recording of data from all detectors of KASCADE-Grande. A trigger condition of 1 Hz will provide an efficiency $\varepsilon > 0.6$ at 10^{16} eV .

The basic observables obtained from both KASCADE and the new detectors from KASCADE-Grande are the following: the shower core position, the angle-of-incidence, the total number of charged particles, given from Grande array data, the muon density, ρ_μ , the reconstruction of the total muon number, provided by KASCADE muon detectors, the lateral electron density profile from the extended electromagnetic array and the total electron number (by subtracting the muon number from the charged particle number), the reconstructed production height, h_μ , from the tracking modules,

3.2. Results of KASCADE-Grande data

Figure 4 (left) shows for a single shower, the lateral distribution of electrons and muons measured by KASCADE and the charge particle densities measured by the Grande station [9]. The good agreement between the two sets of data indicates the capability of KASCADE Grande experiment and the high quality of the data.

For simulated H and Fe showers at 10^{17} eV primary energy and 22° zenith angle, the reconstruction accuracy of the shower core position and direction is in the order of 4 m (13 m) and 0.18° (0.32°) with 68% (95%) confidence level. For both primaries, the statistical uncertainty of the shower is around 15%.

The critical point of KASCADE-Grande reconstruction is the estimation of the muon number due to the limited range of KASCADE muon detectors. The

systematic uncertainty of the muon number depends on the radial range of the data measured by the KASCADE array and the chosen lateral distribution.

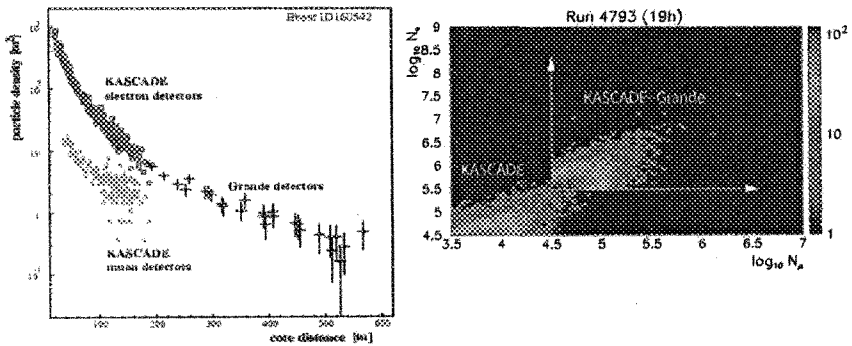


Figure 4. Left: particle densities in the different detectors of KASCADE Grande measured for a single event (from Ref. [9]); Right: the comparison between KASCADE and KASCADE-Grande data for a combined test-run (from Ref. [9])

Figure 4 (right) compares the correlation of the electron and muon distributions for KASCADE and KASCADE-Grande in a 1-day test-run [9]. Due to the larger area of KASCADE-Grande, about 10 times larger than KASCADE array, the numbers of showers increases significantly at primary energies approximately 10 times higher.

3.3 Event-by-event Studies

Based on the SHOWREC program [10] to reconstruct the charged particle component for KASCADE-Grande taking into account the response of the Grande detectors, extensive studies have been done to explore features for energy estimation and mass discrimination around 10^{17} eV [11]. A set of H, C and Fe induced EAS have been simulated with CORSIKA program for hadronic interaction QGSJET, (CORSIKA version 6.023), distributed randomly over an angle-incidence range 0° – 45° , calculated with a spectral index of the power-law slope of -2.0 for 8 energy ranges from 10^{16} eV to 10^{18} eV. The reconstructed charged particle density in a range 500–600 m from the EAS center, observed with KASCADE-Grande array was found sensitive to the energy of the primary particle with a relation nearly

independent from the primary mass. The observables S^{500}/S^{600} and the charged particle number $N_{ch}^{400-600}$ can be used for energy estimation.

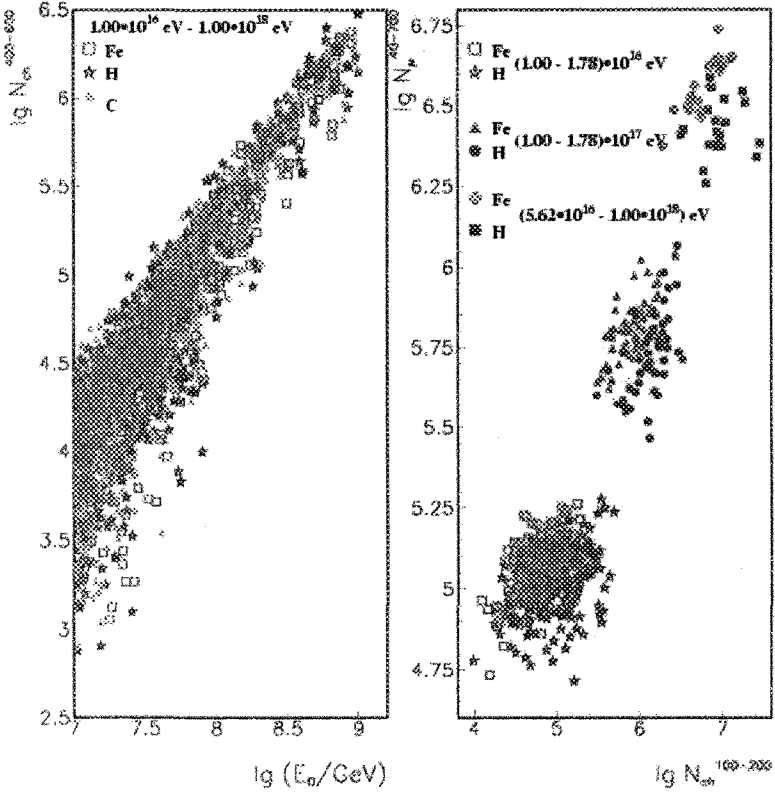


Figure 5. Left: the energy variation of the mean value of $\lg N_{ch}^{400-600}$ corresponding to single events showers, the error bars represent the statistical errors (from Ref. [11]). Right: the $N_{ch}^{40-700} - N_{ch}^{100-200}$ correlation for selected energy ranges (from Ref. [11]).

Figure 5 (left) displays the energy variation of $\lg N_{\text{ch}}^{400-600}$ of 400 reconstructed showers in the energy range $10^{16}-10^{18}$ eV, the energy variation of the mean value indicates no variation between different primaries, but appreciable fluctuations.

While the lateral distribution of EAS particle in the radial range of 500–600 m does practically not show significant differences for different primary masses at the same primary energy, the region 100–200 m exhibits features for mass discrimination. S^{100}/S^{200} or the particle number $N_{\text{ch}}^{100-200}$ could play for KASCADE-Grande a similar role as the electron size N_e in KASCADE experiment, which has to be correlated with an observable representing the muon component, a muon number N_{μ}^{40-700} , integrated on the fit range 40–700 m.

Figure 5 (right) compares the relevant correlation for mass discrimination $N_{\mu}^{40-700}-N_{\text{ch}}^{100-200}$ in selected energy ranges, indicating a better mass discrimination for higher primary energies.

4. Concluding Remarks

1. The extension of KASCADE to KASCADE-Grande experiment, accessing higher primary energies, is expected to prove the existence of the knee-like structure in the heavy component.
2. KASCADE-Grande experiment [4,5] keeps the multi-detector concept of KASCADE, but for a larger area of detection, being possible to test different interaction models for primary energies 10^{16} eV– 10^{18} eV.
3. The first measurements of KASCADE-Grande, in comparisons with KASCADE [9], shows the capability of KASCADE Grande to perform unfolding procedure like in KASCADE and the high quality of the data.
4. Event-by-event studies give the charged density S^{500}/S^{600} and the charged particle number $N_{\text{ch}}^{400-600}$, with similar dependence for all primaries, indicating such observables as suitable for energy identification [11].
5. The correlations of the reconstructed particle density S^{100}/S^{200} or the particle number $N_{\text{ch}}^{100-200}$ with a muon number N_{μ}^{40-700} , integrated on the fit range 40–700 m, presents features for mass discrimination being analogous to $N_{\mu}^{\text{tr}}-N_e$ correlation used in KASCADE experiment [11].
6. KASCADE-Grande provides the environment detecting radio emission in extensive air showers, what is the aim of LOPES project [12].

Acknowledgments

I.M.B would like to express her thanks to the Organizing Committee for the kind invitation to present KASCADE-Grande experiment and to Prof. H. Rebel and Dr. A. Haungs for useful discussions.

References

1. A. Haungs, H. Rebel, M. Roth, *Rep. Prog. Phys.* **66**, 1145 (2003).
2. G. Schatz *et al.* - KASCADE collab., *Nucl. Phys. Proc. Suppl.* **60B**, 151 (1998).
3. T. Antoni *et al.* - KASCADE collab., *Nucl. Instr. Meth. in Phys. Res.* **A513**, 490 (2003).
4. K.-H. Kampert *et al.* - KASCADE-Grande collab., *Nucl. Phys. Proc. Suppl.* **122** (2003).
5. G. Navarra *et al.* -KASCADE-Grande collab., *Nucl. Instr. Meth. in Phys. Res.* **A518**, 207 (2004).
6. D. Heck *et al.*, *Report FZKA 6019*, (1998).
7. A.A. Chilingarian, G.Z.Zasian, *Nuovo Cim.* **14**, 355 (1991).
8. T. Antoni *et al.* - KASCADE collab., *Astropart. Phys.* **16**, 245 (2002).
9. A. Haungs *et al.* - KASCADE-Grande collab., *Proc. 22nd Texas Symp.*, Conf. C041213, 2413, (2004).
10. O. Sima, I.M. Brancus, H. Rebel, A. Haungs, *FZKA-Report 6985*, (2004).
11. I.M. Brancus *et al.* - KASCADE-Grande collab., *Proc. 29th ICRC, Pune, India (2005)*.
12. A.F. Badea *et al.* - KASCADE-Grande and LOPES collabs., *Nucl. Phys. Proc. Suppl.* **136**, 384 (2004).

PROSPECTS FOR THE DETECTION OF HIGH-ENERGY COSMIC RAYS USING RADIO TECHNIQUES*

A.M. VAN DEN BERG

*Kernfysisch Versneller Instituut, Rijksuniversiteit Groningen, Zernikelaan 25
NL 9747 AA Groningen, the Netherlands*

The determination of the origin of cosmic events with energy beyond 10^{18} eV remains a challenge in cosmic-ray physics. To determine the nature of these particles, their origin, and the way they are being accelerated, requires new efforts where radio detection will play a crucial role. Recently, the LOPES collaboration employed techniques based on the detection of geomagnetic synchrotron radiation. They achieved the first calibration between conventional techniques and digital radio. The cosmic-ray induced emission mechanism in more dense and radio-transparent media is called the Askaryan effect, presently exploited or under study at several experiments. I will discuss the initiatives from the Netherlands UHE Cosmic-ray Community (NUCC). At AUGER, we anticipate to deploy antennas from the radio telescope LOFAR using the 100% duty cycle of radio as a clear advantage. Both at Auger and at LOFAR itself, radio will be used to get additional information on the shower development in the atmosphere leading to a better understanding on the very origin of these rays. LOFAR will also be used to detect radio signals emitted during the impact of cosmic events on the surface of the Moon. Finally, the existence of salt domes in the northern-eastern part of the Netherlands offers the possibility to detect neutrinos in rock salt.

1. Cosmic Rays in the Year 2005: pushing back the frontiers

This year, the World Year of Physics, marks important events in the field of ultra-high-energy (UHE) cosmic-ray (CR) physics. From many, I mention only a few. Of course, the biannual International CR Conference in Pune (ICRC2005) is a highlight; others are the inauguration of and the first data from AUGER [1], being the largest CR experiment in the world. And finally, the first calibration by the LOPES collaboration [2] of radio signals using coincidence data from surface detectors is a land-marking event, opening a new window of opportunities in CR physics, eventually leading to new and advanced detector systems. In the early years of CR research, important contributions were made using rather simple pieces of equipment [3]. Hess ascended balloon-born

* This work was performed as part of the research program of the Stichting voor Fundamenteel Onderzoek (FOM) with financial support from the Nederlandse Organisatie voor Wetenschappelijk Onderzoek (NWO).

electroscopes into the atmosphere and concluded from their rapid discharge, that we are constantly bombarded by ionizing particles. Millikan, studying the nuclear interactions between these 'rays' and atmospheric nuclei, was the name giver for these ghostly events, and because of their extraterrestrial nature, he called them 'cosmic rays'. Also Auger and his collaborators used rather simple equipment, Geiger-Muller counters, separated from each other by about 100 m, leading to the discovery of extended air showers (EAS's), a concept which has led to the construction of the largest detector areas in the world. Using EAS detectors, it was Linsley and his colleagues in New Mexico, who discovered in 1962 the first CR with energy larger than 10^{20} eV; ever since scientists (of different kind: physicists and astronomers alike, united in the field of astroparticle physics) are hunting for these extremely high energy events and are building models to explain them.

2. The quest for events around and beyond 10^{20} eV

One of the aims of the most recent experiments in high-energy astroparticle physics is to discover the sources of UHE CR events which have been detected with various detector systems [1,4,5] especially beyond the critical limit of 6×10^{19} eV, known as the Greisen-Zatsepin-Kuzmin (GZK) limit [6]. This limit is related to nuclear scattering processes between a proton and the abundant 2.7 K cosmic microwave background photons. In case the CR is a hadron, traveling to us over a distance of more than 100 Mpc (thus from an extra-galactic origin), it will almost certainly interact on its path with cosmic microwave background photons. Because of this interaction, the kinetic energy of the ray will drop below the GZK limit and therefore the detected flux should sharply diminish beyond this limit. In case the GZK limit holds for UHE CR's, as supported by the HiRes data [4] (see Fig. 1a), there should be a flux of UHE ν 's, produced through this scattering process, peaking at an energy just below this critical limit. On the other hand, in case the UHE CR spectrum continues to follow a more or less constant power-law behavior as suggested by the AGASA [5] and AUGER [1] data (Fig 1b), it may point either to very nearby sources of UHE CR's with a chemical composition of these UHE CR's close to iron nuclei, or to new physics at the highest energies. In this last scenario the decay of relics from the Big Bang has been proposed as the source for these UHE CR's, which therefore at the same time could also be a source of UHE ν 's [7]. So both the presently apparent inconsistency in the flux spectrum of UHE CR's and the predicted existence of UHE ν 's [8], calls for new initiatives, e.g. looking specifically for UHE ν 's or extending existing CR set ups. At the highest

energies, ν 's are the only events which can travel over cosmological distances without being distorted by scattering or absorption processes; nor are they deflected by intergalactic or interstellar magnetic fields. Therefore, a UHE ν telescope with a good pointing accuracy provides the unique opportunity for

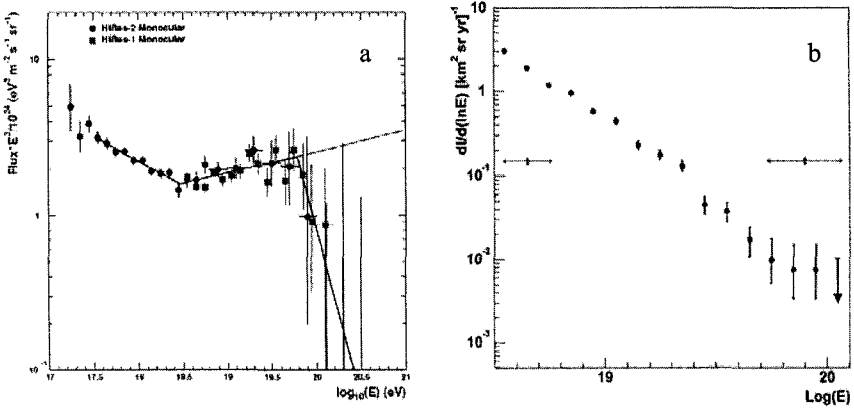


Figure 1. Flux spectra for UHE CR's. Panel a shows the recent compilation from the HiRes experiments (taken from Ref. [4]); the thick solid line shows a fit to the data using a double-broken power-law spectrum, with an indication for the GZK cutoff. Panel b displays the first estimated energy spectrum from AUGER (taken from Ref. [1]), where $dI/d\ln E \approx E dI/dE$. The Auger data can be described by a single power-law spectrum.

precise backtracking to the cosmological sources. If we summarize the present situation in the field of UHE CR physics, we conclude that many theoretical and experimental efforts are taking place, but that the fundamental questions remain unanswered: what is the nature of the CR's, what is their composition, what are the cosmological sources, and will we identify UHE extraterrestrial ν 's? The recent rapid development of digital radio offers new opportunities for this field, taking advantage of the special properties of radio signals, such as the frequency spectrum, the correlation with magnetic fields and the polarization degrees of freedom.

3. Radio as a tool to listen into CR's

The use of radio techniques [9], being one of the tools to get more information on events happening in the cosmos, goes back to the Inter-bellum, when Jansky at the Bell laboratories investigated at a wavelength of 15 m atmospheric disturbances. He concluded that, in addition to local and remote thunderstorms, extraterrestrial sources located in the direction of the center of our Galaxy could be detected using rather simple radio equipment. Signals received with radio

antennas or telescopes, can be of various nature. The most important mechanisms responsible for observed radio signals are: 1) blackbody radiation where the temperature of an astronomical object is an essential parameter, 2) synchrotron radiation where the direction and strength of magnetic fields are important, 3) Cherenkov radiation caused by fast moving charges in dielectric media, and 4) human-induced radiation, e.g. radar signals reflected from remote bodies. All these different radio signals have specific properties, e.g. with respect to the shape of the spectrum as function of frequency, or to the existence and direction of polarization. For our present discussion coherent emission of synchrotron radiation and Cherenkov radiation is important.

3.1. Coherent Synchrotron Radiation induced in the Earths atmosphere

The standard techniques for the detection of UHE CR's rely either on EAS detectors which are located on the Earths surface over large areas (many squared kilometers) or on imaging techniques where fluorescence light from excited air molecules are detected with optical telescopes. The detection system of Auger [10] encompasses both the detection of EAS's by 1600 ground-based water tanks and the tracking of fluorescence light emitted by the ionization trail in the atmosphere using 24 optical telescopes. The covered area of Auger south in the Mendoza Province in Argentina will be 3000 km²; a site in Colorado in the USA, having the same area has been selected this year. Therefore, by and large Auger will be the leading experiment in CR physics for the next decade. Recent results [11] using radio techniques for the detection of CR's in the Earths atmosphere make it possible to open a new window of opportunities for CR physics. Within EAS's leptons gyrate in the magnetic field of the Earth, thus emitting synchrotron radiation. The thickness of an EAS is only 1 m, leading to coherent emission at small enough frequencies (less than 100 kHz). This coherent emission with a strength of about 1 $\mu\text{V}/\text{m}/\text{MHz}$ can easily be detected with simple radio antennas. The new digital radio telescope LOFAR [12] operates in this frequency domain and can therefore be used to 'listen' into EAS's induced by a UHE CR. This telescope has a diameter of 350 km and is centered about 60 km south of the city of Groningen. Its antennas are very simple crossed dipoles; beam forming is done using digital techniques where signals from many antennas are brought together to direct the beam to a fixed point in the sky, or to look back for a short period of time in case a transient event (a supernova or an EAS) passed the field of the telescope. The use of radio for the detection of CR's goes back to middle of the last century, but only in recent years a breakthrough was established, especially because of the results

obtained by the LOPES collaboration [2], which demonstrated that indeed the detected radio strength has a strong correlation with the energy of the primary CR and with the strength and direction of the magnetic field of the Earth; see Fig. 2. They proved that coherent geomagnetic synchrotron radiation lies at the basis of the observed radio pulses induced by UHE CR's. The advantage of radio compared to other detector systems is large: radio signals are not absorbed or deflected on their path, the signal is proportional to the primary energy of the incoming event, and one can study the shower front in

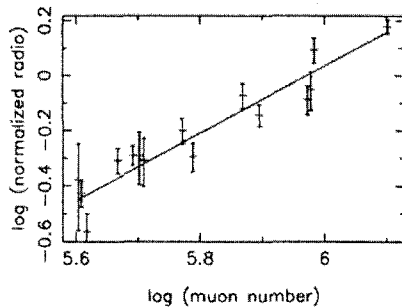


Figure 2. Correlation between radio signal strength and primary CR energy after correction for the geomagnetic field [2].

detail. In addition, radio has a 100% duty cycle, which is a factor of 10 higher than fluorescence detection, which works only during cloudless and moonless nights. In the coming years more R&D will be done by the NUCC to extend the energy range of the radio calibration and to use the high pointing accuracy of radio interferometers to search for point sources emitting UHE CR's. The results of this R&D phase will also break the ground for the CR research program at LOFAR.

3.2. Coherent Cherenkov Radiation induced in dielectric media.

As was proposed by Askaryan [13], the detection of radio signals originating from the coherent Cherenkov radiation emitted in a suitable dielectric medium by a fast moving CR-induced electromagnetic cascade, may offer good prospects for targets with a volume of several km^3 . Because of the interactions of the leptons with the medium, a net negative charge remains in the cascade. The shower front has the shape of a pancake with a thickness of a few centimeters and a diameter of about 10 cm. Although each individual charge emits Cherenkov radiation, there will be coherency near a frequency of 1 GHz and lower, because of the small dimension of this shower. After the initial proposal of Askaryan, the first experimental proof of coherent radio Cherenkov emission was reported by Saltzberg *et al.* [14]. Presently, several experiments [11] based on this effect are running using the polar icecaps or the Moon [15,16] as targets. Also the properties of rock salt are being investigated as another suitable candidate [17]. Table 1 lists some relevant bulk properties of dielectric media. The advantage of coherent Cherenkov radio emission is that a small

number of receivers can be used to reconstruct the direction of the initial ray, to determine its full energy for contained events and to use its linear polarization to reduce random signals. Recently, Alvarez-Muñiz and coworkers [18] have made calculations on the strength of radio signals induced by UHE events in dense materials, such as ice, regolith and salt. These calculations indicate that at lower frequencies the width of the Cherenkov radiation cone increases from less than 10° at a frequency of 1 GHz to more than 90° at frequencies in the 100 MHz region. If the frequency is low enough even down-going showers in the lunar regolith give rise to radio signals escaping from the lunar surface. In addition, because of the increased width of the Cherenkov cone, the chance to observe the signals with a telescope increases rapidly. New calculations [19] confirm this effect, which has led to the first lunar observations by the New Moon collaboration [16] using the Westerbork Synthesis Radio Telescope. This device consists of 14 dishes each with a diameter of 25 m and it can operate in the window of 117-175 MHz. A 100 hour observation time with this telescope will increase the sensitivity for observing UHE ν 's in the energy range beyond 10^{22} eV by several orders of magnitude as compared to the GLUE results [15] (Fig. 3), thus imposing strong limits on the flux of UHE ν 's predicted by several models [8]. In a later stage the collaboration will also use LOFAR.

Table 1. Properties [18] of dielectric materials useful as a target for the detection of CR's and ν 's.

Material	Ice	Rock salt	Lunar regolith
Density (g/cm ³)	0.9	2.2	1.8
Radiation length (cm)	39	10	13
Cherenkov angle (°)	56	66	55
Width Cherenkov angle at 1 GHz (°)	3	8	9
Attenuation length at 250 MHz (m)	~1000	~250 ?	~10
Field strength at 1 GHz (V/MHz/TeV)	$1.2 \cdot 10^{-7}$	$5.3 \cdot 10^{-8}$	$6.2 \cdot 10^{-8}$
Experiments (see also Ref. [11])	RICE ANITA	SalSA [20] ZESANA [21]	GLUE [15] New Moon [16]

In addition to the lunar regolith, rock salt offers interesting opportunities to detect UHE ν 's. Substantial salt deposits from the Zechstein period can be found in the shallow underground of the Netherlands. After the Zechstein period (in the late Perm) these salt deposits were covered with several other sediments during more recent geological periods. However, because rock salt is relatively flexible and light compared to other geological deposits, domes could be formed; a few of them with an overburden of less than 100 m. The storage of natural gas under a pressure of about 200 bar is a new application for these

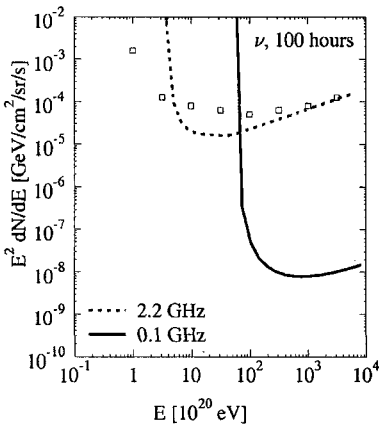


Figure 3. Flux spectrum predicted for the detection of UHE ν 's with the New Moon experiment [19]. The lines indicate the sensitivity at 0.1 and 2.2 GHz for an observation period of 100 hours of the Westerbork telescope. The squares are the results from GLUE [15].

attenuation lengths of only (22 ± 2) m and (77 ± 11) m at a frequency of 0.3 and 1.0 GHz, respectively [22]. These data deviate strongly from those determined for other sites, which might hint to problems with the samples, e.g. surface effects may play an important role in the determination of the bulk properties. This project for the development of a Zechstein SAIt Neutrino Array (ZESANA [21]) in one of the Dutch salt domes can take advantage of the infrastructure of LOFAR. One of the spiraling arms of this radio telescope runs very near the dome, allowing for fast data transmission to central computing systems.

4. Conclusion and outlook

In the past century important contributions have been made by many scientists in the field of astroparticle physics, initially using rather simple techniques. Because of recent developments, such as digital and high speed data transmission, which will be fully employed for radio detection, it is now possible to construct large detector arrays in the hunt for the rare events at end of the CR spectrum. The nature and the origin of these events may shed new light onto processes taking place in the cosmos, within our Galaxy or far away at the boundary of the Universe. The research program in the Netherlands will

domes. In the coming years a consortium formed by several companies will make a grid of about 10 caverns separated by distances of 200 m in the Zuidwending salt dome, located near the city of Groningen. This Zuidwending dome is one the largest and shallowest in the Netherlands, actually consisting of two almost overlapping domes, the northern and the southern lobe. The depth of the dome is about 2.5 km and the surface cross section roughly 0.5 by 5 km². The roof of the caverns for fast gas storage will be at a depth of about 1 km; the height and diameter of these caverns are 300 m and 50 m, respectively. Initial measurements were made at 2 frequencies, resulting in rather short

contribute to this research area using amongst other things radio as a new and very promising technique to make a decisive step forward in CR physics.

Acknowledgments

I thank J. Alvarez-Muñiz, the members of NUCC (J. Bacelar, H. Falcke, M.N. Harakeh, A. Horneffer, S. de Jong, J. Kuijpers, O. Scholten, C. Timmermans), from LOPES (H. Gemmeke, A. Haungs, A. Horneffer, T. Huege), and from SaLSA (P.W. Gorham, D. Salzberg) for stimulating discussions.

References

1. P. Sommers for the AUGER collaboration, 29th ICRC, Pune, India, 2005.
2. H. Falcke for the LOPES collaboration, *Nature* **435**, 313 (2005).
3. For a comprehensive review on CR physics, see e.g. M. Nagano and A.A. Watson, *Rev. Mod. Phys.* **72**, 689 (2000); P.L. Biermann and G. Sigl, *Lecture Notes in Physics*, **576**, 1 (2001)
4. R. Bergmann for the HiRes collaboration, 29th ICRC, Pune, India, 2005.
5. M. Takeda *et al.*, *Phys. Rev. Lett.* **81**, 1163 (1998).
6. K. Greisen, *Phys. Rev. Lett.* **16**, 748 (1966); G.T. Zatsepin and V.A. Kuzmin, *Sov. Phys. JETP Lett. (Engl. Transl.)* **4**, 78 (1966).
7. G. Gelmini and A. Kusenko, *Phys. Rev. Lett.* **84**, 1378 (2000).
8. See for example: R. Engel, D. Seckel, and T. Stanev, *Phys. Rev. D* **64**, 093010 (2001); O.E. Kalashev *et al.*, *Phys. Rev. D* **66**, 063004 (2002).
9. For reviews on radio techniques for astrophysical and astroparticle physics applications see J.S. Hey, *The Radio Universe (Pergamon, Oxford, 1971)*; P.W. Gorham and H. Falcke, *Astropart. Phys.* **19**, 477 (2003).
10. See: <http://www.auger.org>
11. For an overview of these results and experiments see: *Proc. ARENA Workshop*, May 17-19, 2005, DESY-Zeuthen.
12. See <http://www.lofar.org>
13. G. Askaryan, *Sov. Phys. JETP* **14**, 441 (1962); *ibid* **21**, 658 (1965).
14. D. Saltzberg *et al.*, *Phys. Rev. Lett.* **86**, 2802 (2001).
15. P. Gorham *et al.*, *Phys. Rev. Lett.* **93**, 41101 (2004).
16. J. Bacelar *et al.*, *Proc. ARENA Workshop*, May 17-19, 2005, DESY-Zeuthen, and references therein.
17. P. Gorham *et al.*, *Nucl. Instr. Meth. A* **490**, 476 (2002), A.M. van den Berg, *Proc. ARENA Workshop*, May 17-19, 2005, DESY-Zeuthen; M. Chiba, *ibid.*
18. J. Alvarez-Muñiz *et al.*, *Phys. Rev. D* **68**, 043001 (2003); *Proc. ARENA Workshop*, May 17-19, 2005, DESY-Zeuthen; private communication.
19. O. Scholten *et al.*, *astro-ph/0508580*; submitted to *Astropart. Phys.*

20. See: <http://www.physics.ucla.edu/astroparticle/salsa/www/home/>
21. See: <http://www.kvi.nl/~berg/zesana/>
22. M. Chiba *et al.*, *Proc. ARENA Workshop*, May 17-19, 2005, DESY-Zeuthen.

This page is intentionally left blank

6. Nucleosynthesis and Nuclear Physics for Astrophysics

This page is intentionally left blank

EXPLOSIVE NUCLEOSYNTHESIS: SUPERNOVAE, CLASSICAL NOVAE, & X-RAY BURSTS

JORDI JOSÉ

*Dept. Física i Enginyeria Nuclear (UPC),
Sor Eulàlia d'Anzizu s/n, B5, E-08034 Barcelona, Spain
& Institut d'Estudis Espacials de Catalunya (IEEC),
Ed. Nexus-201, C. Gran Capità 2-4, E-08034 Barcelona, Spain
E-mail: jordi.jose@upc.edu*

The first nucleosynthetic processes occurred about 200 seconds after the *Big Bang*, when the Universe was cool enough to allow the formation of light elements. Hydrogen, Helium-4, and traces of only a handful of isotopes (c.f., Deuterium, Helium-3, and Lithium-7), constitute the legacy of this *primordial nucleosynthesis*, that lasted only about 10 minutes. Synthesis of heavier species requires stellar furnaces and more or less violent events that provide a suitable way to contaminate this pristine primordial material, and therefore had to wait for the formation and evolution of the first stars. This took place about 180 Myr after the Big Bang, according to the recent analysis of the cosmic microwave background performed with the WMAP satellite. In this paper, we outline the nuclear processes associated with explosive stellar sites, namely supernovae, classical novae and x-ray bursts, and their interplay with the Galactic abundances.

1. Introduction: Setting the Scene

Core collapse (or types II and Ib/c) supernova explosions constitute the most dramatic fate for a single star (with $M > 10 - 12 M_{\odot}$). During these violent events, most of the star is expelled into the interstellar medium, leaving only an extremely compact remnant, either a neutron star (an object of $1 - 2 M_{\odot}$ and a very small diameter, 20 to 30 km) or a black hole behind. In contrast, single stars with masses $M < 10 - 12 M_{\odot}$ end their lives in a less violent fashion, typically evolving from the steady Main Sequence phase through the Red Giant stage, and leaving a white dwarf remnant (an object of planetary dimensions and masses in the range $0.6 - 1.4 M_{\odot}$). In the process, the ejected shells likely give rise to a bright *planetary nebula*.

Stars forming binary systems can revitalize these final, inert stellar corpses (c.f., white dwarfs and neutron stars) by mass transfer episodes. This can give rise to other explosive scenarios, including type Ia (or

thermonuclear) supernovae, classical nova outbursts (both involving white dwarf stars), as well as X-ray bursts (for which the explosion takes place on the surface of an accreting neutron star). Classical novae and type Ia supernovae have been extensively observed during the past two millennia. In contrast, X-ray bursts have been discovered much recently, since a major fraction of their energy output is emitted in X rays, and hence, detection requires the use of space observatories. About 65 Galactic low-mass X-ray binaries that exhibit such bursting behavior have been found since the independent discovery by Grindlay *et al.* (1976) and Belian *et al.* (1976). In all these cataclysmic systems, mass transfer episodes, caused by Roche lobe overflows of the Main Sequence companion, proceed through the inner Lagrangian point of the system, forming an accretion disk around the compact star. A fraction of the material contained in the accretion disk ultimately falls on top of the white dwarf (as a result of angular momentum losses driven by dissipative forces in the disk), where it is gradually compressed to degenerate conditions, thus leading to a thermonuclear runaway (TNR). Contrary to type Ia supernovae, for which the white dwarf is fully disrupted by the strength of the explosion, classical novae are expected to recur within a timescale of the order of $10^4 - 10^5$ yr; in contrast, X-ray bursts recur on timescales from hours to days. All these stellar explosions are characterized by a remarkable energy output, of the order of 10^{39} ergs (X-ray bursts), 10^{45} ergs (classical novae), and 10^{51} ergs (supernovae). A major difference between these cataclysmic events is the amount of mass ejected as well as the mean ejection velocities, whereas in a type Ia supernova, the whole star (c.f., $1.4 M_{\odot}$) is ejected at $> 10^4$ km s $^{-1}$, the explosion in both classical novae and X-ray bursts is restricted to the accreted envelope. Hence, $10^{-4} - 10^{-5} M_{\odot}$ are typically ejected during a nova outburst, at mean ejection velocities ranging from $10^2 - 10^3$ km s $^{-1}$. In contrast, it is likely that in a typical X-ray burst no mass ejection takes place because of the extreme escape velocities from a neutron star (the energy required to escape from the strong gravitational field of a neutron star of mass M and radius R is $GMm_p/R \sim 200$ MeV/nucleon, whereas the nuclear energy released from fusion of solar-like matter into Fe-group elements is just ~ 5 MeV/nucleon).

2. Supernova Explosions

Spectroscopically, type Ia supernovae (SNIa) are defined by the lack of Hydrogen and the presence of a P Cygni feature associated with Si II at 6355

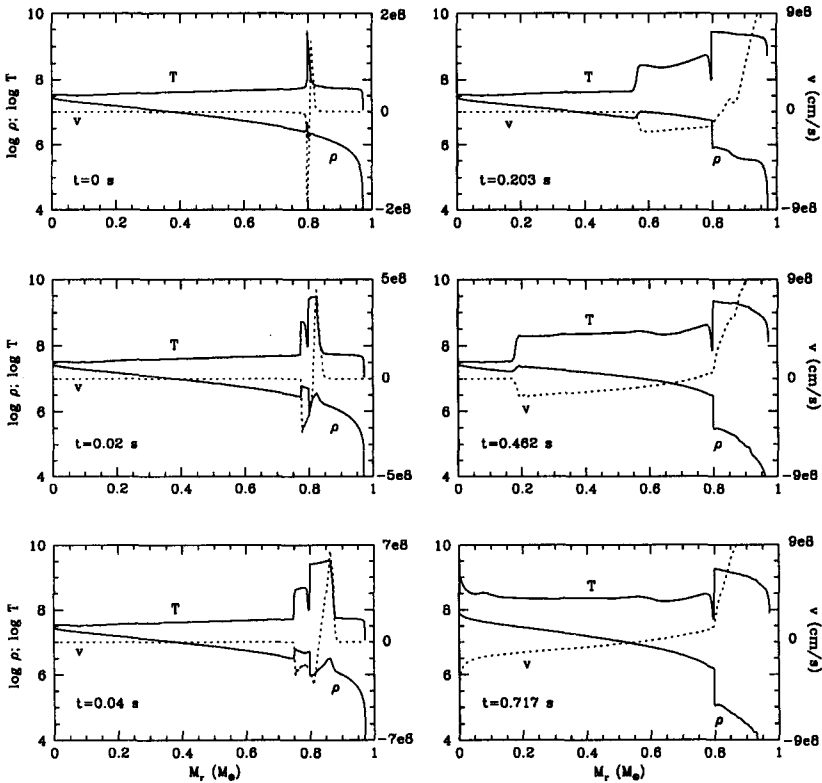


Figure 1. Temperature, density and velocity profiles, following the progress of a detonation front originated at the thick envelope's base, by He-rich accretion of matter at a rate of $\dot{M} = 3.5 \times 10^{-8} M_{\odot} \text{ yr}^{-1}$ onto a $0.8 M_{\odot}$ CO white dwarf, up to the time when C ignites near the center. See José & Hernanz (2005) for details.

Å. They constitute a quite homogeneous class of objects (c.f., 90% of all SNIa share similar spectra, light curves and peak absolute luminosities), which suggests a unique progenitor. Indeed, these supernovae appear in both elliptical and spiral galaxies, and hence, are not attributed to young progenitors. The scenario leading to SNIa is not fully settled, although it is likely associated with the thermonuclear disruption of a mass-accreting white dwarf reaching the Chandrasekhar mass (see Hillebrandt & Niemeyer 2000). One possible scenario (the so-called *single degenerate scenario*) involves a white dwarf accreting H- and/or He-rich matter from a “normal”

companion. The difficulty here is how the white dwarf can reach the Chandrasekhar mass, avoiding mass-loss episodes such as classical nova outbursts (see Section 3). A second, competing scenario (*double degenerate*) deals with a pair of white dwarfs in a close binary system. Here, He- or CO-rich accretion is expected, which somewhat helps to overcome the problems faced by the single degenerate scenario. However, there is a problem of statistics since the number of double white dwarf systems observed so far is not able to account for the Galactic SNIa rate. An additional problem faced in the modeling of SNIa deals with uncertainties in the propagation of the burning front. Several models involving detonations, deflagrations or a combined deflagration/detonation have been proposed to date. From the nucleosynthesis point of view, it is worth mentioning that SNIa constitute the main source of Fe in the Universe.

A less fashionable model involves low mass (or sub-Chandrasekhar) CO-white dwarfs accreting He-rich matter from a closeby companion (see Woosley & Weaver 1994). When accretion takes place at a moderate rate (about $10^{-8} M_{\odot} \text{ yr}^{-1}$), a detonation is found at the core-envelope interface, which propagates outwards and incinerates most of the envelope to Ni, whereas a second shock wave propagates inwards and ultimately provokes a near-center C-ignition. This powers a second detonation front that incinerates the central layers of the white dwarf before dying out. Unfortunately, these models have been criticized because the expected velocity profiles do not fit those corresponding to “canonical” supernova explosions, but because of the lower amount of ^{56}Ni synthesized, they have been claimed to account for some subluminous supernovae. Indeed, it has been recently claimed that sub-Chandrasekhar models (see Fig. 1) can account for the whole bunch of p-nuclei, including the puzzling Mo & Ru isotopes (Goriely *et al.* 2002).

In contrast, all other supernova type (SNII and/or SNIb/c) are attributed to the explosion of massive stars (with $M > 10 M_{\odot}$). Despite the lack of a self-consistent model for the explosion several “tricks” have been proposed to qualitatively derive the associated nucleosynthesis. One possibility is to artificially induce an explosion (c.f., the *thermal bomb* model; See Thielemann *et al.* 1996) by injecting energy in the central Fe core, in such a way that the total kinetic energy in the ejecta matches the required $\sim 10^{51}$ ergs. An alternative (c.f., the *piston model*; See Woosley & Weaver 1995) implies the injection of momentum. A critical issue affecting the final nucleosynthesis in SNII is the pre-supernova evolution. An interesting debate has been recently raised as regards the contribution of SNII to the

Galactic amounts of both ^{26}Al and ^{60}Fe , which are coproduced in the same regions within SNII. It is yet a matter of debate if current models match the observed values.

3. Classical Nova Outbursts

In nova outbursts, the main nuclear activity is associated with (p,γ) and (p,α) reactions, running between the line of stable nuclei and the proton drip line. Most of these rates have been measured at the right energy range in the laboratory since at the typical temperatures achieved during nova outbursts, measurements of nuclear cross sections in the region of the Gamow peak are, except for a few exceptions, feasible. In this sense, classical nova are unique stellar explosions, and represent the only explosive site for which the nuclear physics input is (or will be in the near future) primarily based on experimental information (see José *et al.* 2005).

Recent estimates of several CNO-breakout reactions (see, for instance, Davids *et al.* 2003, for $^{15}\text{O}(\alpha,\gamma)$), demonstrate that at the typical temperatures attained during nova outbursts the CNO cycle does not break out (contrary to what happens for X-ray bursts, for which peak temperatures are almost an order of magnitude higher than in novae). Indeed, it is important to stress that the injection of ‘seed’ nuclei in the Ne-Si mass region, resulting from mixing with the outer layers of the underlying white dwarf core, withdraws the main argument in support of CNO-breakout in classical novae.

The moderately high peak temperatures achieved during nova explosions, $T_{\text{peak}} \sim (2 - 3) \times 10^8$ K, suggest that abundance levels of the intermediate-mass elements in the ejecta must be significantly enhanced, as confirmed by spectroscopic determinations in well-observed nova shells. This raises the issue of the potential contribution of novae to the Galactic abundances, which can be roughly estimated as the product of the Galactic nova rate (~ 30 events yr^{-1}), the average ejected mass per nova outburst ($\sim 2 \times 10^{-5} M_{\odot}$), and the Galaxy’s lifetime (~ 10 Gyr). This order of magnitude estimate points out that novae scarcely contribute to the Galaxy’s overall metallicity (as compared with other major sources, such as supernova explosions or AGB stars), but nevertheless they can substantially contribute to the synthesis of some largely overproduced species. Indeed, studies suggest that classical novae are likely sites for the synthesis of most of the Galactic ^{13}C , ^{15}N , and ^{17}O , whereas they can partially contribute to the Galactic abundances of other species with $A < 40$, such as ^7Li , ^{19}F , or

^{26}Al (Starrfield *et al.* 1998, José & Hernanz 1998). Because of the lower peak temperatures achieved in CO models (together with the lack of significant amounts of 'seed' nuclei in the NeNa-MgAl region), the main nuclear activity in CO novae does not extend much beyond oxygen. In contrast, ONe models show a much larger nuclear activity, extending up to Silicon (for $1.15 M_{\odot}$ ONe) or Argon (for $1.35 M_{\odot}$ ONe). Hence, the presence of significantly large amounts of intermediate-mass nuclei in the spectra, such as phosphorus, sulfur, chlorine or argon, may reveal the presence of an underlying massive ONe white dwarf.

Despite of the problems associated with the modeling of the explosion, there is in general good agreement between theory and observations as regards nucleosynthesis (*i.e.*, including atomic abundances -H, He, C, O, Ne, Na...-, and a plausible endpoint for nova nucleosynthesis around Ca) is quite remarkable.

Among the isotopes synthesized during classical nova outbursts, several radioactive species have deserved special attention. Short-lived nuclei, such as $^{14,15}\text{O}$ and ^{17}F (and to some extent, ^{13}N) have been identified as the key isotopes that power the expansion and further ejection of the envelope during nova outbursts through a sudden release of energy, a few minutes after peak temperature (Starrfield *et al.* 1972). Other isotopes have been extensively investigated in connection with the predicted γ -ray output from novae. Hence, ^{13}N and ^{18}F are responsible for the predicted prompt γ -ray emission at and below 511 keV, whereas ^7Be and ^{22}Na , which decay much later (when the envelope is optically thin), are the sources that power line emission at 478 and 1275 keV, respectively (see Gómez-Gomar *et al.* 1998, and references therein). ^{26}Al is another important radioactive isotope that can be synthesized during nova outbursts, although only its cumulative emission can be observed because of its slow decay.

4. X-Ray Bursts

Accretion onto neutron stars in close binary systems can also give rise to some nova-like events known as X-ray bursts. Because of the stronger surface gravity in a neutron star (as compared with that of a white dwarf), temperatures and densities in the accreted envelope during X-ray bursts are typically an order of magnitude larger than in a typical nova outburst. As a result, detailed nucleosynthesis studies involve several hundreds of isotopes (up to the so-called SnSbTe cycle. See Schatz *et al.* 2001) and thousands of nuclear reactions. Indeed, the main reaction flow moves far away from

the valley of stability, and even merges with the proton drip-line beyond $A = 38$ (Schatz *et al.* 1999). Until recently, because of computational limitations, many simulations of X-ray bursts were performed in the framework of reduced nuclear reaction networks. Recent hydrodynamic simulations with a reasonably extended network containing 298 isotopes (up to Te) have been performed by Fisker *et al.* (2004). An unprecedented attempt, coupling detailed hydrodynamic stellar models in one-dimension with a complete nuclear reaction network (up to 1300 isotopes, in the framework of an adaptive network) has been recently performed by Woosley *et al.* (2004).

Contrary to classical novae, where the main nuclear activity is driven by proton-capture reactions in competition with β^+ -decays, X-ray bursts are triggered by a combination of nuclear reactions, including H-burning (via rp-process) and He-burning (that initiates with the triple α -reaction, and is followed both by the breakout of the CNO cycle by $^{14,15}\text{O}$ plus α , and a competition of proton captures and (α, p) reactions – the so-called αp -process). Initially, the CNO breakout is led by $^{15}\text{O}(\alpha, \gamma)^{19}\text{Ne}$, which is followed by two consecutive proton-captures through ^{20}Na and ^{21}Mg , where the flow faces strong photodisintegration reactions on ^{22}Al . Following ^{21}Mg -decay, the flow shifts through $^{21}\text{Na}(p, \gamma)^{22}\text{Mg}$. As the temperature rises and enough ^{14}O is build-up through the triple- α reaction, followed by $^{12}\text{C}(p, \gamma)^{13}\text{N}(p, \gamma)^{14}\text{O}$, an alternative path through $^{14}\text{O}(\alpha, p)^{17}\text{F}$ reaction dominates the flow, by-passing the $^{15}\text{O}(\alpha, \gamma)^{19}\text{Ne}$ link to ^{21}Na through $^{17}\text{F}(p, \gamma)^{18}\text{Ne}(\alpha, p)^{21}\text{Na}$, where $^{18}\text{Ne}(\alpha, p)^{21}\text{Na}$ represents the main path towards heavier species. The rates for these breakout reactions have huge associated uncertainties and are subject to intense experimental studies both at stable and radioactive beam facilities. Of special interest is the fact that H-burning continues after the peak of the explosion through the rp-process, which extends the main path much beyond ^{56}Ni , up to the SnSbTe region.

5. Nuclear Physics Inputs for Novae & X-Ray Bursts

Significant experimental information is already available at the typical temperatures reached in classical nova outbursts and we are confident that, in the near future, novae will become the first explosive stellar site for which all relevant nuclear physics input will be primarily based on experimental information. Main uncertainties are localized in only a handful of nuclear reaction rates (namely, $^{18}\text{F}(p, \alpha)$, $^{25}\text{Al}(p, \gamma)$ and $^{30}\text{P}(p, \gamma)$, for which several experiments have been already proposed in different facilities).

In contrast, the situation is much more complex as regards X-ray bursts: nuclear physics requirements include mass measurements along the rp-process path, and a much better knowledge of key reactions and effective lifetimes at the *waiting points* under rp-process conditions.

Acknowledgments

This work has been partially supported by the Spanish MCYT grant AYA2004-06290-C02-02.

References

1. Belian, R.D., Conner, J. P., and Evans, W. D, *ApJ* **206**, L135 (1976).
2. Davids, B., *et al.*, *Phys. Rev. C* **67**, 065808 (2003).
3. Fisker, J.L., Thielemann, F.-K., and Wiescher, M.C., *ApJ* **608**, L61 (2004).
4. Gómez-Gomar, J., *et al.*, *MNRAS* **296**, 913 (1998).
5. Goriely, S., *et al.*, *A&A* **383**, L27 (2002).
6. Grindlay, J., *et al.*, *ApJ* **205**, L127 (1976).
7. Hillebrandt, W., and Niemeyer, J.C., *ARA&A* **38**, 191 (2000).
8. José, J., and Hernanz, M., *ApJ* **494**, 680 (1998).
9. José, J., and Hernanz, M., in preparation (2005).
10. José, J., Hernanz, M., and Iliadis, C., *Nucl. Phys. A*, in press (2005).
11. Schatz, H., *et al.*, *ApJ* **524**, 1014 (1999).
12. Schatz, H., *et al.*, *Phys. Rev. Lett.* **86**, 3471 (2001).
13. Starrfield, S., *et al.*, *ApJ* **176**, 169 (1972).
14. Starrfield, S., *et al.*, *MNRAS* **296**, 502 (1998).
15. Thielemann, F.-K., Nomoto, K., and Hashimoto, M., *ApJ* **460**, 408 (1996).
16. Woosley, S.E., and Weaver, T.A., *ApJ* **423**, 371 (1994).
17. Woosley, S.E., and Weaver, T.A., *ApJS* **101**, 181 (1995).
18. Woosley, S.E., *et al.*, *ApJS* **151**, 75 (2004).

EXPERIMENTAL APPROACH TO NUCLEAR REACTIONS OF ASTROPHYSICAL INTEREST INVOLVING RADIOACTIVE NUCLEI

CARMEN ANGULO

*Centre de Recherches du Cyclotron, Université catholique de Louvain,
Chemin du cyclotron 2, B-1348 Louvain-la-Neuve, Belgium,
E-mail: angulo@cyc.ucl.ac.be*

Nuclear reactions are responsible for the nucleosynthesis and energy generation in stars. From all the stellar sites, explosive events have attracted great attention in the last years. Due to the high temperatures and short reaction time scales in these events, nuclear reactions on unstable nuclei play a crucial role. However, substantial uncertainties remain in reaction rates on unstable nuclei due to limited experimental data. In recent years some remarkable developments in radioactive ion beam production and experimental techniques have allowed many key reaction rates to be experimentally determined with reasonable accuracy for the first time. Some experimental methods that have recently been exploited are reviewed here. Remaining experimental challenges are outlined.

1. Introduction

It is well known that it is through nuclear reactions that stars are powered, and also through them the chemical elements all living beings and celestial objects are made of, are created¹. The stellar environment being considered determines the energy region within which the nuclear reaction processes need to be studied. This region is known as the Gamow Window², and the specific nuclear properties within it can play a vital role in investigating the nucleosynthesis that occurs. Thus, a reaction that may play an important role in a certain stellar environment can be completely negligible in different temperature and density conditions. Therefore, each nuclear reaction must be treated as a unique process.

Among the many sites where astrophysical nuclear reactions occur, explosive environments, such as novae, supernovae, and X-ray bursts are fascinating cases. Stellar explosions are dramatic events characterized by high temperatures and densities that produce energy at a rate greater than in almost any other astrophysical phenomena. The rates of the nuclear reactions

taking place during the explosion become then sufficiently large so that any particular nucleus can undergo a series of light particle captures forming nuclei far from the line of stability. Because such nuclei have shorter beta decay lifetimes and are more loosely bound, the sequence of reactions in these environments is determined by a balance between capture rates and rates for intrinsic beta decay or photo-dissociation. Higher temperatures and densities naturally lead to faster reaction rates, and thus in such environments one expects the nucleosynthesis to involve nuclei with shorter lifetimes which are farther from stability.

In general, for any particular explosive event, reactions between many hundreds of different stable and unstable nuclei will be involved. However, in order to gain an understanding of the explosion mechanism it is often the case that only a few of these reactions are important. Though even for those our knowledge of crucial nuclear information is often incomplete, the main reason being the experimental difficulties related to the study of those interactions in the laboratory. The information needed includes nuclear masses, excited state properties, decay properties and lifetimes, electron capture rates, neutrino and photon interaction rates, as well as light particle reaction rates. To obtain such information for unstable nuclei is experimentally very challenging; for some nuclei, especially for the upper limits of the r-process paths, this information will remain inaccessible for many years to come.

The most important reactions can be identified by studying the sensitivity of astrophysical models to the nuclear physics input. For example, at very high temperatures some capture and photo-dissociation rates come into equilibrium, and the reaction network path is insensitive to the individual reaction rates. In this scenario, of main interest are the so-called "waiting-point" nuclei, and the most important nuclear parameters are the masses and α -decay half lives of these particular nuclei³. However, knowledge of individual reaction rates is of critical importance. While the statistical model of nuclear reactions can be used to estimate nuclear reaction rates, care must be taken since the Q-value for a capture reaction will be lower for nuclei far from stability than for those near stability, and the density of the energy states in the compound nucleus will be similarly lower. For certain light nuclei, the compound system may only have one or two nuclear states contributing at the relevant astrophysical temperature. In this case, there is no alternative other than to measure the properties of individual resonances. Some innovative experimental techniques have been developed to indirectly determine energy level information for certain nu-

clei, but direct measurements with radioactive ion beams are needed. The typically weak intensity of radioactive ion beams necessitates to use efficient and highly-selective experimental techniques.

This paper is not intended to as a comprehensive review, it contains selected examples of experimental techniques and relevant reactions^a. Details can be found in a recent review paper by Blackmon, Angulo and Shotter⁴ and complementary information may be found in other recent reviews (see, for example, works by Smith and Rehm⁵, Kubono⁶, and Geissel, Kratz and Sherrill⁷).

2. Experimental methods

2.1. Accelerators and beams

Much experimental information is difficult or impossible to determine through indirect techniques, and many reactions involving radioactive nuclei remain largely uncertain. This has focused world-wide attention on the development of radioactive ion beams. There are mainly two methods for producing radioactive species^b: the Isotope Separation On Line (ISOL) method in connection with a post-acceleration facility, and the projectile fragmentation method. Present ISOL facilities include CYCLONE at Louvain-la-Neuve (Belgium), REX-ISOLDE at CERN, SPIRAL at GANIL (France), HRIBF at Oak Ridge National Laboratory (USA), and ISAC at TRIUMF (Canada). Two major projects for next generation of ISOL facilities are the Rare Isotope Accelerator (RIA) in the USA and the EURISOL project in Europe. First-generation radioactive beam facilities using the fragmentation method are GANIL at Caen (France), GSI at Darmstadt (Germany), Flerov Laboratory at Dubna (Russia), NSCL at Michigan State University (USA), RIKEN at Saitama (Japan), and IMP at Lanzhou (China). The Radio-Isotope Beam Factory (RIBF) currently under construction at RIKEN, RIA in the USA, and the new international Facility for Antiproton and Ion Research (FAIR) proposed for GSI at Darmstadt are next generation facilities that will use the projectile fragmentation method of radioactive ion beam production. A similar technique called the "in-flight" method, which is limited to nuclei very close to stability, uses a heavy ion beam at lower energies, typically just above the Coulomb barrier, to induce single nucleon transfer reactions. The resulting beam energy

^aThe choice here is exclusively based on the author's preferences and experience.

^bSee ⁴ for details.

is usually near the Coulomb barrier. This approach has been used at many facilities including ATLAS at Argonne National Laboratory (USA), CRIB at CNS/RIKEN, Texas A&M University, and the University of Notre Dame.

2.2. Targets

Reactions involving Hydrogen and Helium are the most important in explosive burning. Therefore, experimental techniques involving radioactive beams require the use of hydrogen-rich or helium-rich targets. The choice of the target must be adapted to the physics goal and the other experimental conditions (such as beam energy and intensity, detection system, etc). Polyethylene foils $[(\text{CH}_2)_n]$ are easy to handle and have been one of the most popular and successful type of targets for investigation of Hydrogen burning reactions. Foils with thicknesses between $40 \mu\text{g}/\text{cm}^2$ and several mg/cm^2 have been used with beam intensities as high as 10^9 pps^{8,9} without significant degradation, though care must be taken to distribute the beam power by, for example, rotating the target. Solid targets containing Helium must be produced by implantation. Implanted helium targets have been developed at Louvain-la-Neuve with helium thicknesses up to 10^{18} atoms/ cm^2 , sufficient for measurements of elastic scattering and some reactions with radioactive ion beams¹⁰. Gas targets are an obvious alternative to foils. Gas cells with thin windows are easy to handle, but with windows similar challenges are faced as with foil targets, degrading the beam energy and inducing background reactions. Windowless gas targets eliminate the problems associated with windows. However, many pumping stations are required to decrease the pressure down to the 10^{-7} mbar range as required for accelerators, so the targets are large and costly, and the target thickness is limited¹¹.

2.3. Detectors

The usually low intensity of radioactive ion beams places particular importance on the efficient detection of the reaction products, and arrays of gamma, neutron and charged-particle detectors have been constructed at many facilities in order to maximize the detection efficiency (see Ref. 4 for references). The advent of large-area silicon strip detectors has played a crucial role. These detectors may be segmented in one or two dimensions (double-sided detectors) to any practical level of pixelation. The shape of the strips can also be tailored to experimental requirements. For example, strips are curved in a circular pattern in many annular detector designs

to allow better reaction angular resolution in a strip. This approach was used in the Louvain–Edinburgh Detector Array (LEDA), one of the pioneering charged-particle arrays used with radioactive ion beams for nuclear astrophysics¹². A broader range of detector thicknesses has recently become available, and detectors between 50 μm and 1 mm are commonly used. This broad range of thicknesses allows Z identification of a broad range of charged particles through $\Delta E - E$ energy loss techniques.

Arrays of gamma-ray detectors have played an important role in several new approaches using both stable and radioactive ion beams. The high total efficiency of the Gammasphere array¹³ allowed $\gamma - \gamma$ coincidence measurements that accurately determined excitation energy levels that are important in studying proton-rich nuclei. The inverse reaction kinematics technique applied in radioactive ion beam measurements also allows heavy fragments to be efficiently collected using recoil separators. Several laboratories have developed recoil separators that are designed to collect these heavy products and disperse them by their mass-to-charge ratio. For example, ARES at Louvain-la-Neuve, DRAGON at ISAC, the RMS at the HRIBF, and the FMA at ANL.

2.4. *Examples of experimental techniques*

2.4.1. *Elastic scattering*

The elastic scattering technique is a well-known method to study resonant states. As a natural extension, the elastic scattering technique in inverse kinematics¹⁴, used normally to investigate reactions involving radioactive species, makes use of the sensitivity of the protons (or α particles) to the presence of a resonant state in the compound nucleus. When a resonant state is scanned with the appropriate ion beam and target, the recoil proton spectra show an interference pattern that is indicative of the resonance energy, angular momentum and width. All experimental effects, mainly the beam energy resolution inside the target and angular resolution of the detectors, must be properly taken into account to precisely extract the resonant properties. Fitting procedures, such as the R-matrix method¹⁵, are used to evaluate these quantities and to obtain the resonance properties. This method is an invaluable tool prior to any capture reaction study.

One of the main advantages with the resonant elastic scattering technique is the large elastic scattering cross section that allows measurements with radioactive beam intensities as low as 10^4 s^{-1} . Another advantage is that the energy of the recoil protons is usually sufficiently high to be de-

tected readily in standard Si particle detectors or in more sophisticated strip detector arrays¹². The β -radioactivity of the beam species may induced background in the particle detectors at low energies. This background can limit the lowest energies measurable, but this time uncorrelated background can be distinguished from the events of interest by time-of-flight techniques.

2.4.2. *Transfer reactions*

Much of our understanding of nuclear spectroscopy has been shaped by four decades of study of transfer reactions, which have proved to be a particularly powerful tool for characterizing energy levels of importance for astrophysical reaction rates. One advantage of these measurements is that states covering a broad region of excitation energy are populated, but this necessitates high-resolution particle detection in order to resolve the states of interest. Many of these reactions are well-described by the Distorted Wave Born Approximation (DWBA), so that the shape of the angular distribution of the differential cross section is distinctive of the transferred angular momentum, and the magnitude of the cross section is a reflection of the single particle-character of the state¹⁷. For example, proton-transfer reactions, most notably ($^3\text{He},d$), are the best surrogate for proton-induced reactions like (p,α). Proton single-particle states are preferentially populated, and if the reaction mechanism is well understood, proton partial widths can be extracted from the magnitude of the cross section. This approach has been applied to many nuclei that can be formed into suitable targets¹⁸, and alpha-transfer reactions have also been used to determine the alpha-particle character of those states¹⁹. The only proton transfer reactions that have been studied in inverse kinematics so far have focused on low-lying bound states important for direct capture. Difficult targets and problematic kinematics make studies of resonant states via proton transfer in inverse kinematics particularly challenging.

The properties of mirror nuclei are used to indirectly infer properties of single-particle resonances that are crucial for (p,α) reaction rates. The properties of neutron single-particle states can be studied by the (d,p) reaction on the mirror nucleus, and the properties of proton resonances are determined under the assumption of mirror symmetry. This technique was first applied with a radioactive ion beam to ^{56}Ni at Argonne National Laboratory²⁰. More recently the $^{18}\text{F}(d,p)^{19}\text{F}(\alpha)^{15}\text{N}$ has been investigated at Louvain-la-Neuve²¹ and at the HRIBF at Oak Ridge²². The aim of these measurements was to determine neutron spectroscopic factors for states in

^{19}F that are mirrors to ^{19}Ne states important for the $^{18}\text{F}(p,\alpha)^{15}\text{O}$ reaction. Under the assumption of mirror symmetry, these spectroscopic factors can constrain the $^{18}\text{F}(p,\alpha)^{15}\text{O}$ reaction rate. In the Louvain-la-Neuve experiment, a 14 MeV ^{18}F radioactive beam of about 2×10^6 pps bombarded a CD_2 target. Two LEDA silicon strip detector arrays¹² were used to detect protons in coincidence with α particles or ^{15}N ions from the breakup of alpha-unbound states in ^{19}F . Differential cross sections for the $^{18}\text{F}(d,p)^{19}\text{F}$ reaction were fitted with theoretical DWBA distributions to extract neutron spectroscopic factors for excited states in ^{19}F . A similar approach was used in the HRIBF measurement, except that a higher bombarding energy (108 MeV) was used. Cross sections for transfer to bound states (with well known excitation energies) were also measured by detecting ^{19}F ions in the Daresbury Recoil Separator, which allowed a more accurate energy calibration. Spectroscopic factors extracted from both of these measurements place important new limits on contributions of low-energy resonances to the rate of the $^{18}\text{F}(p,\alpha)^{15}\text{O}$ reaction. The uncertainty in the $^{18}\text{F}(p,\alpha)^{15}\text{O}$ reaction rate is substantially reduced. However, interference effects between several low energy resonances remain to be investigated²³, having important consequences for novae nucleosynthesis and application to nova γ -ray emission.

3. Conclusions

The quest to understand explosive stellar events confronts physicists with many challenges across a wide range of physical phenomena. The energy source that drives the macroscopic explosive evolution originates from nuclear reactions involving many unstable nuclei. Our understanding of the energy sources and nucleosynthesis in explosive events is reflected in our knowledge of the properties of these unstable nuclei and reaction rates involving them. Improving our understanding requires a source to produce these unstable species and efficient experimental techniques for studying them. In the last few years, there have been great strides in meeting these challenges for certain case studies.

Experimental approaches that were undertaken traditionally with stable beams (*i.e.*, elastic scattering, inelastic scattering, and transfer reactions) have been employed to obtain much of the initial information on energy levels in radioactive nuclei. Indirect techniques like transfer reactions are particularly appealing for measurements with low intensity radioactive ion beams, but such approaches are model dependent, and uncertainties related

to the model will be reflected in the confidence of the final result. Much progress has been made in the last few years, but many key nuclei reactions remain largely unconstrained by experiment. The remaining reactions are the most challenging ones. New and more intense radioactive beams, as well as more sophisticated detection systems, are thus required. On the other hand, nuclear physics theory must be extensively exploited to avoid misinterpretation of experimental data.

Finally, while new facilities and innovative techniques provide great promise for the future, it cannot be stressed strongly enough that a close collaboration with observers and astrophysical modellers is as essential as ever.

Acknowledgments

I would like to thank A.S. Murphy for useful comments on the manuscript.

References

1. E.M. Burbidge, G. Burbidge, W.A. Fowler, and F. Hoyle, *Rev. Mod. Phys.* **29**, 547 (1957).
2. D.D. Clayton, *Principles of Stellar Evolution and Nucleosynthesis*, University of Chicago Press, Chicago, 1968.
3. H. Schatz, *et al.*, *Phys. Rep.* **294**, 168 (1998).
4. J.C. Blackmon, C. Angulo, A.C. Shotton, *Nucl. Phys. A*, in press.
5. M.S. Smith, K.E. Rehm, *Annu. Rev. Nucl. Part. Sci.* **51**, 91 (2001).
6. S. Kubono, *Nucl. Phys.* **A693**, 221 (2001).
7. H. Geissel, K.L. Kratz, B. Sherrill, *Nucl. Phys. A*, in press.
8. W. Galster, *et al.*, *Phys. Rev.* **C44**, 2776 (1991).
9. K.E. Rehm, *et al.*, *Nucl. Instrum. Methods Phys. Res.* **449**, 208 (1998).
10. F. Vanderbist, *et al.*, *Nucl. Instrum. Methods Phys. Res.* **B197**, 165 (2002).
11. D.A. Hutcheon, *et al.*, *Nucl. Instrum. Methods Phys. Res.* **A498**, 190 (2003).
12. T. Davinson, *et al.*, *Nucl. Instrum. Methods Phys. Res.* **A454**, 350 (2000).
13. I.Y. Lee, *Nucl. Phys.* **A520**, 641c (1990).
14. C. Angulo, *Nucl. Phys.* **A746**, 222 (2004), and references therein.
15. A.M. Lane and R.G. Thomas, *Rev. Mod. Phys.* **30**, 257 (1958).
16. J.-S. Graulich, *et al.*, *Phys. Rev.* **C63**, 011302 (R) (2001).
17. G.R. Satchler, *Direct Nuclear Reactions*, Clarendon Press, Oxford, 1983.
18. R.B. Vogelaar, *et al.*, *Phys. Rev.* **C53**, 1945 (1996).
19. C.R. Brune, *et al.*, *Nucl. Phys.* **A688**, 263c (2001).
20. K.E. Rehm, *et al.*, *Phys. Rev. Lett.* **80**, 676 (1998).
21. N. de Séréville, *et al.*, *Phys. Rev.* **C67**, 052801 (R) (2003).
22. R.L. Kozub, *et al.*, *Phys. Rev.* **C71**, 032801 (R) (2005).
23. N. de Séréville, *et al.*, *Nucl. Phys.* **A758**, 745c (2005).

BACKGROUND STUDIES AT THE LUNA UNDERGROUND ACCELERATOR FACILITY

ZS. FÜLÖP FOR THE LUNA COLLABORATION

ATOMKI, H-4001 Debrecen, POB51, Hungary

The LUNA (Laboratory Underground for Nuclear Astrophysics) facility has been designed to study nuclear reactions of astrophysical interest. It is located deep underground in the Gran Sasso National Laboratory, Italy, where low energy electrostatic accelerators in combination with solid and gas target set-ups allowed to measure the total cross sections of the radiative capture reactions ${}^2\text{H}(p,\gamma){}^3\text{He}$ and ${}^{14}\text{N}(p,\gamma){}^{15}\text{O}$ within their relevant Gamow peaks. In the present work, the laboratory and beam induced background conditions for radiative capture studies at energies of astrophysical interest are discussed.

1. Introduction

Stars generate energy and synthesize chemical elements in thermonuclear reactions¹. All reactions induced by charged particles in a star take place in an energy window called the Gamow peak. In the static burning of stars, the cross section $\sigma(E)$ has a very low value at the Gamow peak. This prevents a direct cross section determination at the Earth's surface, where the signal-to-background ratio is too small partly because of the cosmic ray background. Therefore, the relevant cross sections are usually measured at higher energies and the astrophysical $S(E)$ factor is used to extrapolate the data to the corresponding Gamow peak:

$$\sigma(E) = \frac{S(E)}{E} e^{-2\pi\eta} \quad (1)$$

where η is the Sommerfeld parameter with $2\pi\eta = 31.29 Z_1 Z_2 \sqrt{\frac{\mu}{E}}$. Here Z_1 and Z_2 are the charge numbers of projectile and target nucleus, respectively, μ is the reduced mass in amu, and E is the center of mass energy in keV units. Although $S(E)$ varies only slowly with energy for a direct process, resonances and resonance tails may hinder an extrapolation¹. Therefore, the primary goal of experimental nuclear astrophysics remains

to measure cross sections at energies inside the Gamow peak, or at least to approach it as closely as possible.

The Laboratory Underground for Nuclear Astrophysics (LUNA) has been designed for this purpose and is located in the Laboratori Nazionali del Gran Sasso (LNGS) in Italy. LUNA uses high current accelerators with small energy spread in combination with high efficiency detection systems. At the 50 kV LUNA1 accelerator², the ${}^3\text{He}({}^3\text{He}, 2\text{p}){}^4\text{He}$ cross section was measured for the first time within its solar Gamow peak^{3,4}. Subsequently, a windowless gas target set-up and a 4π bismuth germanate (BGO) summing detector⁵ have been used to study the radiative capture reaction ${}^2\text{H}(\text{p}, \gamma){}^3\text{He}$, also within its solar Gamow peak⁶.

The 400 kV LUNA2 accelerator⁷ has been used to study the radiative capture reaction ${}^{14}\text{N}(\text{p}, \gamma){}^{15}\text{O}$, which is the bottleneck of the Hydrogen burning CNO cycle. The LUNA data — based on experiments down to $E = 130$ keV using solid state targets and HPGe detectors^{8,9} — resulted in a total extrapolated S factor that was a factor two smaller than the adopted values¹⁰, leading to considerable astrophysical consequences on the age of globular clusters and the CNO cycle induced neutrino yield from the Sun¹¹. In order to extend the ${}^{14}\text{N}(\text{p}, \gamma){}^{15}\text{O}$ cross section data down to $E = 70$ keV, a gas target set-up similar to the one used for the ${}^2\text{H}(\text{p}, \gamma){}^3\text{He}$ study and a bore hole BGO detector have been installed at the LUNA2 400 kV accelerator^{12,13}.

2. Background conditions at the Gran Sasso underground laboratory

The Gran Sasso underground laboratory consists of three experimental halls and several connecting tunnels. Its site is protected from cosmic rays by a rock cover equivalent to 3800 m water (3800 m w.e.). The overlying rock suppresses the flux of cosmic ray induced muons by six orders of magnitude¹⁴, resulting in a flux of muon induced neutrons of the order of $\Phi_{n_\mu} \approx 10^{-8} \frac{\text{n}}{\text{cm}^2 \cdot \text{s}}$ ¹⁵. At LNGS, a reduction in the γ continuum of about a factor 100 was observed¹⁶ for $E_\gamma < 2$ MeV when compared to a low level counting facility at the Earth's surface. Radiative capture reactions, however, often lead to the emission of γ rays of higher energy.

2.1. Laboratory background at LUNA

The laboratory background up to $E_\gamma < 8$ MeV taken with a Germanium detector is shown in Fig. 1, where spectra recorded at the Earth's surface

and inside the Gran Sasso Laboratory are compared. In the plot, the region of interest (ROI) for the LUNA $^{14}\text{N}(p,\gamma)^{15}\text{O}$ ($Q = 7.30$ MeV) experiment is marked. One can see that the Gran Sasso mountain effectively eliminates the muon induced continuum which dominates the surface spectrum above 2.6 MeV. A similar suppression in cosmic ray induced background can be observed for BGO detectors.

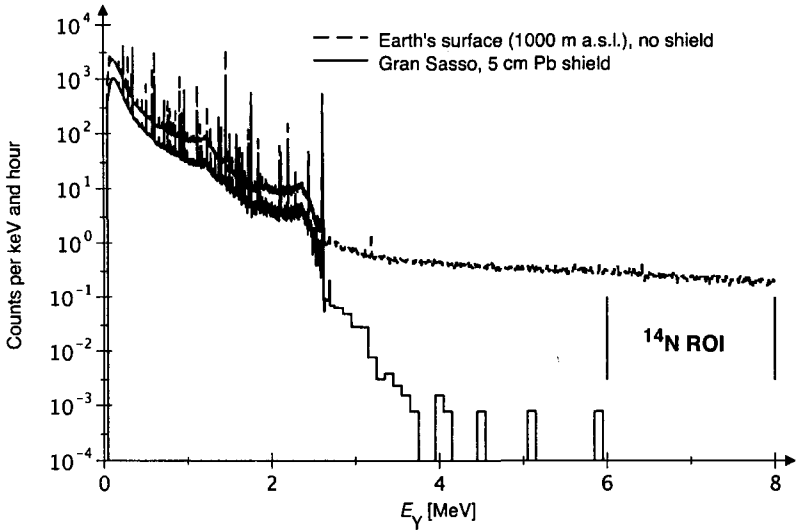


Figure 1. Laboratory γ -background as seen with a Germanium detector at the Earth's surface (1000 m above sea level) and inside the Gran Sasso underground facility. Above the 2.61 MeV line from ^{208}Tl , the surface spectrum has been rebinned in 10 keV bins, and the underground spectrum has been rebinned in 100 keV bins.

2.2. Background induced by the incident proton beam

While the laboratory background can be reduced by proper shielding, it is difficult and in some cases impossible to shield the detector against γ rays arising from parasitic reactions induced by the ion beam incident on the target system. For the LUNA solid target study of the $^{14}\text{N}(p,\gamma)^{15}\text{O}$ reaction, the proton beam induced background has been investigated in the energy region $E_p = 140$ -400 keV¹⁹. It was found that the principal background reactions were $^{11}\text{B}(p,\gamma)^{12}\text{C}$, $^{18}\text{O}(p,\gamma)^{19}\text{F}$, and $^{19}\text{F}(p,\alpha\gamma)^{16}\text{O}$. They originated from the target itself, and a reduction in their yield was achieved by making adjustments in target production.

As an example for the background conditions of the gas target experiments, a spectrum obtained with the Germanium detector at $E_p = 200$ keV proton energy and with 1 mbar nitrogen as target gas is shown at the top of Fig. 2. In the spectrum, the most important background lines as well as the lines from the $^{14}\text{N}(p,\gamma)^{15}\text{O}$ reaction are identified. The $^{15}\text{N}(p,\gamma)^{16}\text{O}$ and $^{15}\text{N}(p,\alpha\gamma)^{12}\text{C}$ background results from the natural isotopic composition of the target gas. The $^{18}\text{O}(p,\gamma)^{19}\text{F}$ and the $^{19}\text{F}(p,\alpha\gamma)^{16}\text{O}$ reactions play an important role for runs close to their resonance energies at $E_p = 151$ and 224 keV, respectively.

At the bottom of Fig. 2, two spectra obtained with a bore hole BGO detector at $E_p = 200$ keV are shown: one denoted as ‘nitrogen’ with 1 mbar Nitrogen as target gas, the other denoted as ‘helium’ with 1 mbar Helium as target gas. It is clear that the high resolution Germanium detector is needed in order to identify the background visible in the spectra taken with the BGO detector. The lines at $E_\gamma = 4.4$ and 12 MeV, evident in both BGO spectra, are from reactions on ^{11}B and ^{15}N . The line at 16 MeV is due to the $^{11}\text{B}(p,\gamma)^{12}\text{C}$ reaction caused by a ^{11}B impurity on the final collimator. At 7.7 MeV in the helium spectrum, there is a line due to the $^{13}\text{C}(p,\gamma)^{14}\text{N}$ reaction which is not visible in the nitrogen spectrum, because it is buried under the 7.5 MeV sum peak from $^{14}\text{N}(p,\gamma)^{15}\text{O}$. The small structure at 8.2 MeV in both BGO spectra is due to the $^{18}\text{O}(p,\gamma)^{19}\text{F}$ reaction. The peaks at 5.2, 6.2 and 6.8 MeV in the nitrogen spectrum are due to ^{14}N , with possible contributions from ^2H at 5.6 MeV and ^{19}F at 6.1 MeV.

The place of origin of ion beam induced gamma background can be localized using spectra taken with a Germanium detector using the Doppler shift of the γ lines. For a given transition and beam energy, the sign and magnitude of this shift depend only on the angle of emission θ , as measured from the beam direction, allowing to localize the source of the γ rays²⁰.

3. Further possibilities to improve the figure of merit of the LUNA set-ups

In the LUNA gas target $^{14}\text{N}(p,\gamma)^{15}\text{O}$ study^{12,13}, the lowest energy point has been obtained with a target current of 0.2 mA, leading to a counting rate two times lower than the laboratory background in the Gran Sasso underground facility with no additional shielding applied. With that set-up, the limit for a $^{14}\text{N}(p,\gamma)^{15}\text{O}$ experiment has been reached.

In order to study the $^{14}\text{N}(p,\gamma)^{15}\text{O}$ reaction at even lower energies than in the LUNA gas target $^{14}\text{N}(p,\gamma)^{15}\text{O}$ experiment, four approaches are possible:

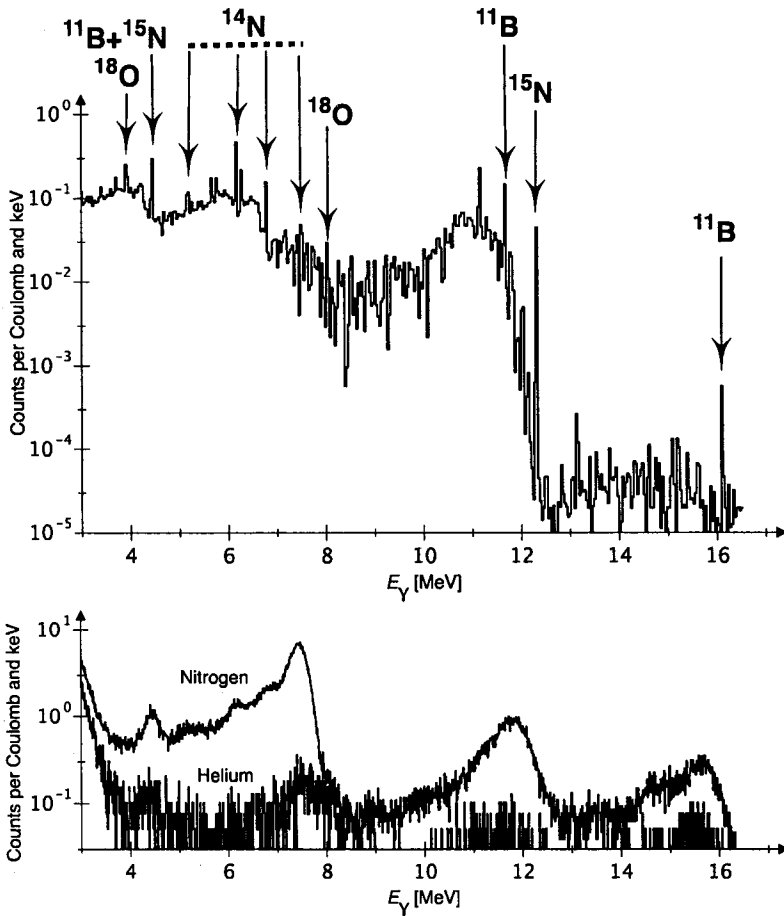


Figure 2. Spectra for $E_p = 200$ keV with 1 mbar gas in the target. Top panel: Germanium detector, Nitrogen gas. Bottom panel: BGO detector, one run with Nitrogen gas and one run with Helium gas.

(A) Reduce the laboratory background while keeping the ion beam induced background at the present level. (B) Increase the detection efficiency and improve the signal-to-noise ratio in the detection system. (C) Increase the beam current. (D) Increase the target density.

(A) The laboratory background in the present BGO detector is dominated by (n, γ) reactions in the detector itself and in parts of the setup²⁰. By shielding the set-up against neutrons, a reduction of

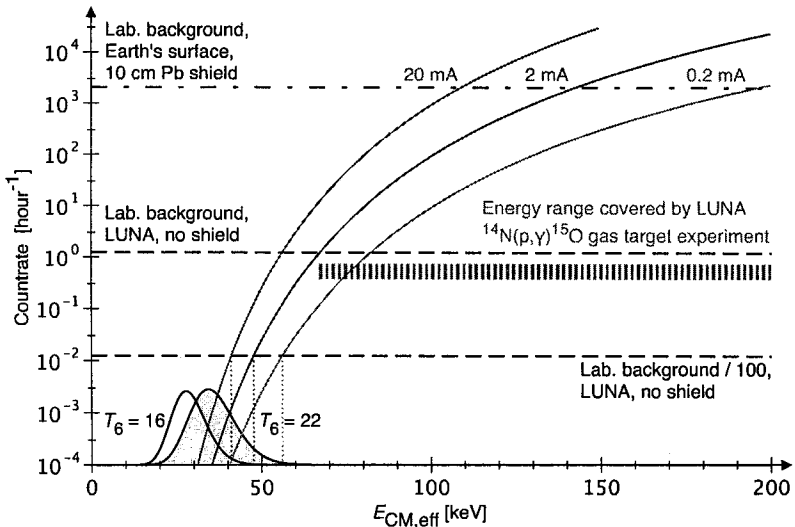


Figure 3. Counting rates from the $^{14}\text{N}(p,\gamma)^{15}\text{O}$ reaction in the LUNA 4π BGO summing detector⁵, region of interest from $\eta_\gamma = 0.5$, under the assumption of a constant S factor of 1.7 keV barn at low energy. Curves are shown for a hypothetical target of thickness $4 \cdot 10^{17} \frac{\text{atoms}}{\text{cm}^2}$ and several target currents. Also shown are Gamow peaks for $T_6 = 22$ and 16 (temperature at the center of the Sun) and laboratory background levels at the surface of the Earth, and at the LUNA site²⁰.

the laboratory background seems feasible. A reduction by a factor 100 is, however, an optimistic limit, since at this level (μ,n) neutron production in the shield will likely dominate.

- (B) The detection efficiency is already $\eta_\gamma \approx 60\%$ in the gas target experiment, depending on the individual run^{12,13}. A segmentation of the BGO detector and setting a coincidence requirement for primary and secondary γ rays would reduce the detection efficiency, but also reduce single (n,γ) background lines, possibly by a higher factor.
- (C) An increase of the ion beam current seems feasible, since many implanters with currents in the mA range exist in the world. This would, however, require a jet gas target instead of a solid or streaming gas target as in the LUNA $^{14}\text{N}(p,\gamma)^{15}\text{O}$ experiments. With jet gas targets, target thicknesses of $4 \cdot 10^{17} \frac{\text{atoms}}{\text{cm}^2}$ have been obtained²¹, and the target density was found to be unaffected by the beam heating effect, up to a deposited power of $700 \frac{\text{mW}}{\text{mm}}$ for protons in Nitrogen gas and $4000 \frac{\text{mW}}{\text{mm}}$ for Oxygen nuclei in Argon gas, with an

ion beam limited by an aperture of 3 mm diameter²². For comparison, the ion beam in the LUNA $^{14}\text{N}(p,\gamma)^{15}\text{O}$ gas target experiment was limited by an aperture of 7 mm diameter²⁰, and the maximum deposited power in the data taking runs was $30 \frac{\text{mW}}{\text{mm}}$, leading to a beam heating correction of the target density of at most 15%. An $E_p = 60$ keV proton beam in a $4 \cdot 10^{17} \frac{\text{atoms}}{\text{cm}^2}$ thick jet gas target will lose 7 keV energy²³. For a jet width of 3.3 mm²¹, this corresponds to 420, 4200, and 42000 $\frac{\text{mW}}{\text{mm}}$ for 0.2, 2, and 20 mA proton current, respectively. For 0.2 and 2 mA proton current, based on the data of Görres²² one can therefore predict no beam heating correction for a jet gas target. It has to be noted, however, that the space required for the jet nozzle and above all for the pumping arrangement will reduce the solid angle available for γ ray detection. In Fig. 3, calculated counting rates are plotted for a reduced detection efficiency due to solid angle restrictions, but the laboratory background counting levels are not reduced in proportion, because it is assumed the detector size will remain unchanged. It is clear that while entering the solar Gamow peak ($T_6 \approx 16$) will only be possible in the 20 mA case, with 2 mA target current one might be able to obtain some information for globular cluster stars at the main sequence turnoff ($T_6 \approx 22$). Assuming a 50% accelerator uptime, with the accelerator downtime entirely dedicated to laboratory background measurements, the time required to obtain a statistical precision of 12% for an $E = 47$ keV point with a 2 mA beam current and the quoted target density would be five years, with an estimated number of 220 counts from the reaction and 220 counts from laboratory background.

- (D) Already in the LUNA gas target $^{14}\text{N}(p,\gamma)^{15}\text{O}$ experiment, the cross section varied by a factor five over the target length. A further increase in target density, while in principle possible, will therefore not lead to an appreciable increase in the yield.

4. Summary

The installation of accelerators at the Gran Sasso underground laboratory with its effective cosmic ray shield allows to measure the cross sections of astrophysically relevant reactions at energies that are much lower than those accessible in laboratories at the Earth's surface. In many cases, one can even reach the Gamow peak for important stellar scenarios making

extrapolations unnecessary. This is possible also because of the successful elimination of beam induced backgrounds at the LUNA set-ups. Even for the experiments with BGO detectors, a background study with high resolution Germanium detectors is needed to identify the beam induced background. The careful analysis of the Doppler shift of the background peaks can help in the localisation of background sources. Further background studies are needed for the ${}^3\text{He}(\alpha,\gamma){}^7\text{Be}$ cross section determination to be completed in the near future.²⁴

Acknowledgments

This work was supported in part by: INFN, ILIAS/TARI RII3-CT-2004-506222, OTKA T42733 and T49245, BMBF (05CL1PC1-1), and FEDER-POCTI/FNU/41097/2001. Zs. F. is supported by Bolyai.

References

1. C. Rolfs and W. Rodney, *Cauldrons in the Cosmos*, University of Chicago Press, Chicago, (1988).
2. U. Greife *et al.*, *Nucl. Inst. Meth.* **A350**, 327 (1994).
3. M. Junker *et al.*, *Phys. Rev.* **C57**, 2700 (1998).
4. R. Bonetti *et al.*, *Phys. Rev. Lett.* **82**, 5205 (1999).
5. C. Casella *et al.*, *Nucl. Inst. Meth.* **A489**, 160 (2002).
6. C. Casella *et al.*, *Nucl. Phys.* **A706**, 203 (2002).
7. A. Formicola *et al.*, *Nucl. Inst. Meth.* **A507**, 609 (2003).
8. A. Formicola *et al.*, *Phys. Lett.* **B591**, 61 (2004).
9. G. Imbriani *et al.*, *Eur. Phys. J. A* in press, nucl-ex/0509005 (2005).
10. C. Angulo *et al.*, *Nucl. Phys.* **A656**, 3 (1999).
11. G. Imbriani *et al.*, *Astronomy & Astrophysics* **420**, 625 (2004).
12. D. Bemmerer, *PhD thesis*, Technische Universität Berlin, 2004.
13. A. Lemut, *PhD thesis*, Genova University, 2005.
14. S. Ahlen *et al.*, *Phys. Lett.* **B249**, 149 (1990).
15. H. Wulandari *et al.*, (2004), hep-ex/0401032.
16. C. Arpesella, *Appl. Radiat. Isot.* **47**, 991 (1996).
17. R. Wordel *et al.*, *Nucl. Inst. Meth.* **A369**, 557 (1996).
18. G. Heusser, *Nucl. Inst. Meth.* **B83**, 223 (1993).
19. F. Strieder *et al.*, *Nucl. Phys.* **A718**, 135c (2003).
20. D. Bemmerer *et al.*, *Eur. Phys. J. A* **24**, 313 (2005).
21. H. Becker *et al.*, *Nucl. Inst. Meth.* **198**, 277 (1982).
22. J. Görres *et al.*, *Nucl. Instr. Meth.* **A241**, 334 (1985).
23. J. Ziegler, SRIM version 2003.26, <http://www.srim.org>, 2004.
24. H. Costantini *et al.*, *Eur. Phys. J. A*, direct submitted.

THOUGHTS ABOUT TWO OF THE IMPORTANT REACTIONS IN NUCLEAR ASTROPHYSICS

L. BUCHMANN
TRIUMF
4004 Wesbrook Mall
Vancouver B.C.
Canada, V6T 2A4

Some aspects of the $^{12}\text{C}(\alpha,\gamma)^{16}\text{O}$ as well as the $^7\text{Be}(\text{p},\gamma)^8\text{B}$ reactions are discussed. Emphasis is placed more on theoretical and experimental methods rather than on results. In particular, phase shifts and angular distributions are discussed in the $^{12}\text{C}(\alpha,\gamma)^{16}\text{O}$ case with some concentration on the underlying theory. A short description of the TRIUMF-Seattle $^7\text{Be}(\text{p},\gamma)^8\text{B}$ experiment will then be given. At the end an outlook on a $^7\text{Be}(\text{p},\text{p})^7\text{Be}$ elastic and inelastic scattering experiment planned at TRIUMF is presented including a discussion of a new cylindrical time projection chamber (TACTIC) with a radial drift field.

1. The $^{12}\text{C}(\alpha,\gamma)^{16}\text{O}$ reaction

The $^{12}\text{C}(\alpha,\gamma)^{16}\text{O}$ reaction in static core helium burning of red giant stars proceeds at the same time as the 3α -reaction. This has as a consequence that for a given energy output the ratio of these reactions is fixed. A possible variation of this ratio, due to the uncertainty of our knowledge of either rate, has then rather drastic consequences on the evolution of massive stars and the composition of white dwarfs remainders from lower mass stars.

The radiative α -capture on ^{12}C has been the subject of many investigations for more than 30 years. The reason is that the center-of-mass-energy corresponding to static helium burning is quite low, *i.e.* 300 keV, and therefore the reaction has not been measured at this energy directly as the cross section there is very small. In addition, the total cross section at 300 keV consists of many components with none of them absolutely dominant and no narrow resonance present for α -capture, as is the case of the 3α -reaction. Therefore, extensive extrapolation to low energies for each component of the cross section is necessary. To illustrate the situation, the structure of

^{16}O and radiative capture paths of α -particles on ^{12}C are shown on Fig. 1.

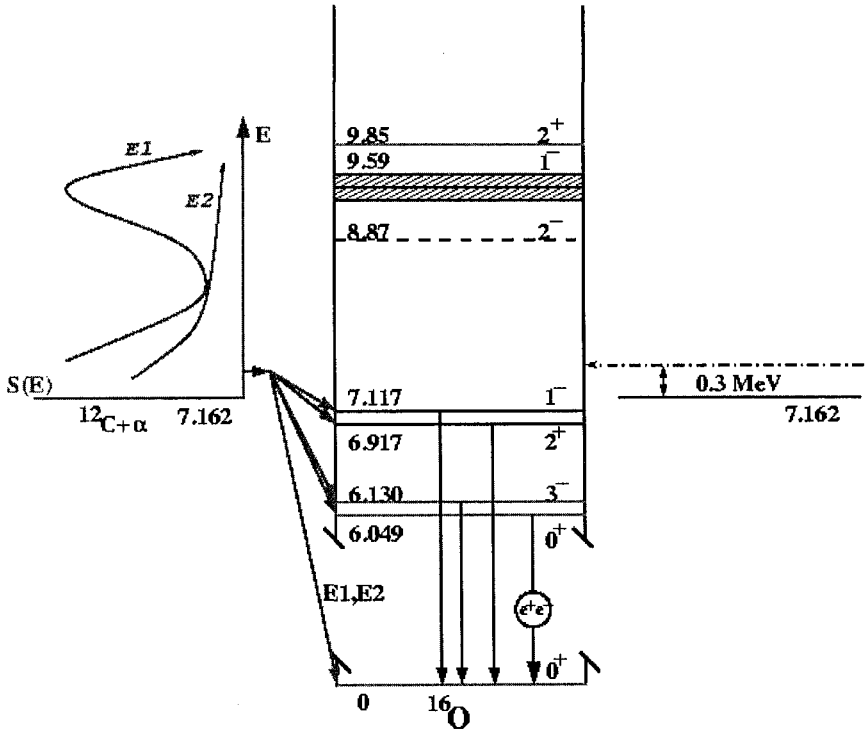


Figure 1. ^{16}O structure relevant for $^{12}\text{C}(\alpha, \gamma)^{16}\text{O}$. The energy dependence of the S factor for the two ground state components is also indicated.

The components of the cross section that must be known to evaluate the total $^{12}\text{C}(\alpha, \gamma)^{16}\text{O}$ cross section are the $E1$ and $E2$ radiative capture to the ground state that likely provide the dominant cross section and similar transitions to each of the subthreshold excited states of ^{16}O . Also the cascade transitions show frequently mixed angular momenta and $E1$ and $E2$ γ -ray multipoles. Therefore, to extrapolate with confidence, as

many as possible data at higher energies are necessary. These data include radiative capture measurements including angular distributions as well as other pieces of information which are elastic scattering data, direct reactions and the special case of the β -delayed α -decay of ^{16}N (Ref. 1). An extensive discussion of these individual components of the $^{12}\text{C}(\alpha,\gamma)^{16}\text{O}$ cross section can be found in the the overview article about helium burning in stars by Buchmann and Barnes².

However, while the extrapolation demands cross sections sorted by electromagnetic multipole transitions and angular momenta, the data typically do not provide them directly. While a decomposition into, *e.g.* different multipole transitions by angular distributions, is in principle possible, it can be shown that such an analysis produces correlations between the different components as well as correlations of errors. This problem has been discussed extensively in Buchmann *et al.*^{3,4}. It is therefore recommended to fit generic experimental data by incorporating as many theoretical components as necessary.

Extrapolations of the different cross sections involved in $^{12}\text{C}(\alpha,\gamma)^{16}\text{O}$ are typically done with the help of the *R*-matrix theory. However, there is a lot of confusion, how to apply it, see *e.g.* Kunz *et al.*⁵ ^a. It is recommended to use the *R*-matrix prescription of Barker and Kajino⁶ for fitting and extrapolation. This formalism includes a correct description of direct radiative processes which are of relevance whenever *E2* type γ radiation is involved^b.

Recently, measurements of the radiative capture cross section have been improved by the use of recoil separators^{7,8}. In this method the recoiling ^{16}O is observed either in single or in coincidence mode with the γ ray. The separator typically consist of electric and magnetic fields that separate the lower energy recoils from the beam. As beam and recoil momentum are approximately identical, electric fields are necessary for separation. These are provided in the two cases either as electromagnetic bending elements or as Wien Filters, *i.e.* crossed electric and magnetic fields. Previously, mostly γ rays have been detected often suffering from background problems due to either room background, or at higher energies neutron induced γ radiation. Sometimes problems with the response of the γ -detector made

^aThe fit in Kunz *et al.*⁵ does not include direct radiative processes both in the ground state as well as cascade transitions. The error estimates do furthermore not explore the full range of allowed interaction radii *a*, an important input in *R*-matrix theory.

^b*E1* direct capture is suppressed by the effective mass factor $Z_{\alpha}A_{\alpha} - Z_{12}A_{12}$ for the α and ^{12}C charge and mass, respectively.

the analysis of measurements difficult. A recoil separator largely overcomes these problems.

2. A measurement of the ${}^7\text{Be}(p,\gamma){}^8\text{B}$ reaction in Seattle

A small fraction of the hydrogen in the core of the sun is consumed via the ${}^7\text{Be}(p,\gamma){}^8\text{B}$ reaction producing the unstable isotope ${}^8\text{B}$ which has a very high β^+ decay Q-value. The emanating high energy neutrinos have been detected on earth and are now shown to oscillate between different weak flavours⁹. To determine the parameters of this oscillation, input from a model of the sun is necessary, which as a key ingredient requires a good knowledge of the ${}^7\text{Be}(p,\gamma){}^8\text{B}$ reaction.

This reaction involving the radioactive nucleus ${}^7\text{Be}$ ($T_{1/2}=53.4$ d) has been subject to controversy over a long time. Therefore, a new measurement of this cross section was performed by a group from TRIUMF and the University of Washington, Seattle trying to improve on all possible systematic errors and reducing the statistical uncertainty. The experiment is completely described in the article of Junghans *et al.*¹⁰ and only a few features are repeated here.

The target was produced at TRIUMF employing the TR13 cyclotron with a 13 MeV proton beam of 50 μA intensity^c and a metallic, molten lithium target. The ${}^7\text{Be}$ present in the target was chemically separated, evaporated in reduction and finally reevaporated on a finite spot, forced to be 4 mm and situated on a molybdenum watercooled backing. The proton beam was rastered over this spot so that in first order only the total amount of ${}^7\text{Be}$ was to be known, but not its area distribution. As the decay of ${}^7\text{Be}$ can be easily monitored, in fact, that amount was known throughout the bombardment with the proton beam. The three targets contained about 50% of ${}^7\text{Be}$, considerably higher than achieved in previous experiments.

The measurement of the ${}^7\text{Be}(p,\gamma){}^8\text{B}$ reaction was carried at the tandem accelerator, operated in terminal ion source mode, of the University of Washington. The ${}^7\text{Be}$ target was activated by the proton beam and swung after 1.5 seconds in front of a silicon detector where the α -spectrum from the β -delayed α -decay of ${}^8\text{B}$ was registered. The integrated proton current was both measured at the target as well as in a Faraday cup when the target was swung away. A target depth profile was obtained by employing a narrow resonance in the ${}^7\text{Be}(\alpha,\gamma){}^{11}\text{C}$ reaction. In another experimental

^cLimited by the cyclotron.

run, the possible backscattering of ^8B in activation out of the target was measured to be negligible. After correcting for the solid angle of the α -detector, the excitation function is derived as shown in Fig. 2 as S factor. These data were made subject to fits to extrapolate the S factor to low

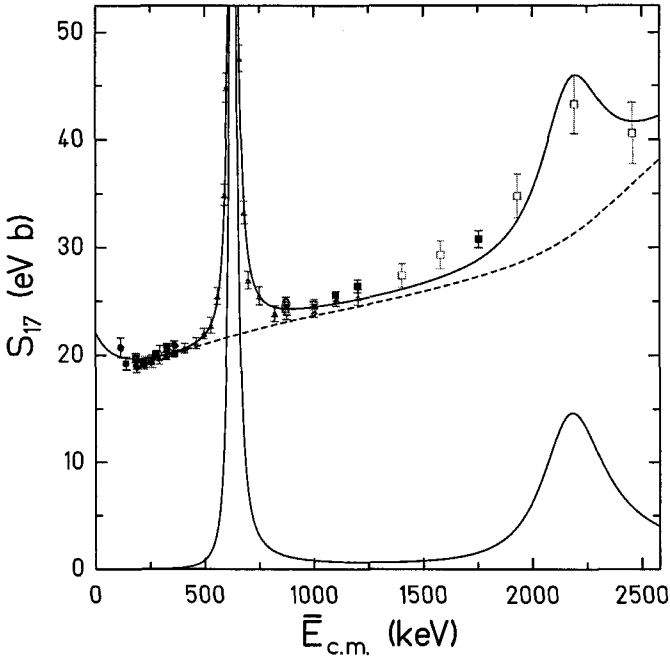


Figure 2. Data from the TRIUMF-Seattle measurement of the $^7\text{Be}(p,\gamma)^8\text{B}$ reaction and fit to these data. The p -wave part of the fits invokes a resonance description while the s wave part is scaled from a calculation by Descouvemont and Baye¹¹.

energies.

While the model of Descouvemont and Baye¹¹ gives the best apparent agreement with the data, we used several models to fit the low energy region of our data^d and estimate the theoretical uncertainty

^dIn the low energy region the interaction takes place farthest away from the nucleus and should be most easily handled by theory. Also no inelastic excitation to the first excited state of ^7Be at $E_x=418$ keV is possible.

for the extrapolation to the zero energy S factor^e. For our measurement, we derive $S_{17}(0)=22.1\pm 0.6(\text{expt})\pm 0.5(\text{theor})$ eV·b. For the average of all direct ${}^7\text{Be}(p,\gamma){}^8\text{B}$ measurements we obtain a weighted value of $S_{17}(0)=21.4\pm 0.5(\text{expt})\pm 0.5(\text{theor})$ eV·b.

3. Elastic proton scattering on ${}^7\text{Be}$ and TACTIC

As it is noticeable from our estimate of $S_{17}(0)$, the error from the theoretical extrapolation in ${}^7\text{Be}(p,\gamma){}^8\text{B}$ has become approximately as large as the one associated with the direct measurement. This error, from an experimental point of view, can be tackled by providing high precision elastic scattering data of protons on ${}^7\text{Be}$. The reason is that the nuclear part in the elastic scattering is identical to the one in radiative capture. In particular the *s*-wave scattering lengths are of interest as well as the phase shift sign of the ${}^3\text{S}_1$ wave at higher energies. It was pointed out by Descouvemont¹² that this phase shift sign is positive at about 1–2 MeV in his cluster model, but negative in potential models. In any case, a model of the radiative capture should also be capable of fitting elastic scattering data which can be obtained, in principle, at much higher precision.

With the newly installed laser ion source (TRILIS) at TRIUMF-ISAC, it will be possible to produce a ${}^7\text{Be}$ beam of considerable intensity. This beam can be accelerated to energies between 0.15 to 6 MeV/u using either ISACI or ISACII. As we wish to invoke a secondary stripper to strip ${}^7\text{Be}$ to the 4^+ charge state to remove any possible ${}^7\text{Li}$ contamination, indistinguishable by the scattered recoil protons, we will restrict the lower beam energy to 0.25 MeV/u, where the full stripping efficiency for ${}^7\text{Be}$ is about 10%.

As target we propose a hydrogen filled gas chamber (avoiding problems with solid polyethylene targets) being at the central part of a time projection chamber with a radial electric field. This chamber, named TACTIC, is now at its design stage at TRIUMF and Daresbury¹³. The principle layout is shown in Fig. 3. The recoil protons from the elastic scattering of then ${}^7\text{Be}$ beam will be detected. As the TACTIC detector will be surrounded by a BGO array, also inelastic scattering into the first excited state of ${}^7\text{Be}$ at 418 keV will be observable.

The TACTIC detector consists of an inner target region which is not visible to the detection system and an outer region into which scattered charged particles can penetrate and leave a trace. The resulting electrons

^eThe Gamow peak for this reaction in the sun is at about 20 keV; however, traditionally the S factor is quoted for zero energy with a possible estimate of the first derivative.

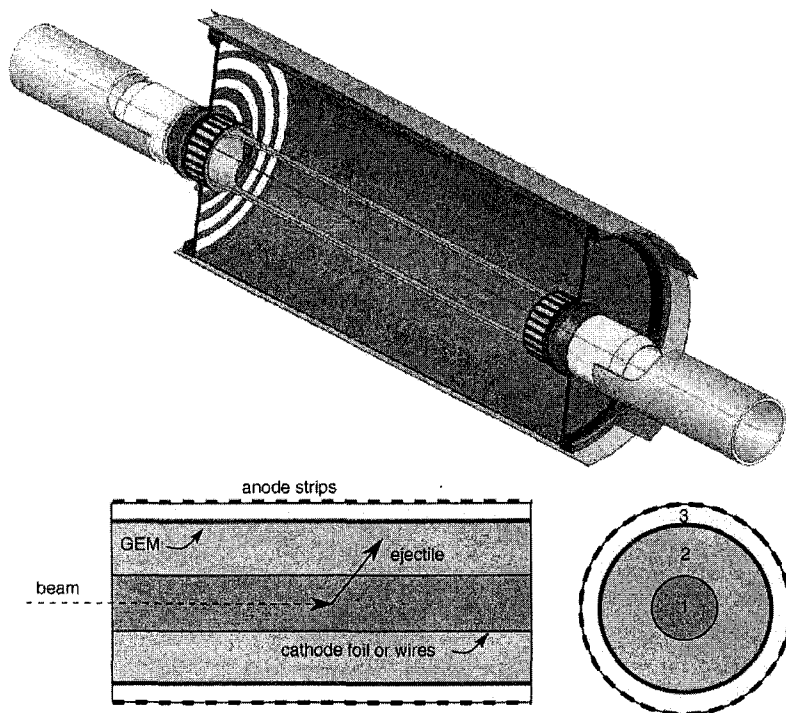


Figure 3. Layout of the TACTIC detector (upper panel) and working principle (lower panel).

are then drawn in a radial electric field toward the anode. However, on the way they encounter a GEM (Gas Electron Multiplier) foil. This GEM is a thin foil, copper plated on both side with microholes penetrating. The voltage applied between the two sides of the foil will lead to electron amplification in the strong field of the holes. With the GEM in place we obtain a very strong signal for heavy ion traces as shown in our test chamber where we used an α source to test signals and tracing¹³. Basically the GEM allows us to process the signals directly without preamplification. The inner target region can be configured in two ways: (i) with inner and outer region sharing the gas volume (a wire cage will collect beam induced electrons) and (ii) the inner and outer region separated by a foil which also serves as cathode. For the ${}^7\text{Be}(p,p){}^7\text{Be}$ experiment the second configuration will be employed.

The data acquisition system will consist of VM48 cards developed at the University of Montreal which will digitize each pulse. From that we

hope to not only get good timing and energy loss information but also some knowledge about the radial position of pulse generation. The anode will be segmented in Φ and Θ to allow for high rates, the thorough determination of scattering angles and also the detection of reactions with multiple charged particles emanating, e.g. ${}^7\text{Be}(p, {}^3\text{He } p)\alpha$ at higher energies. We have already shown that tracing the α tracks in our test chamber is possible.

This summary report is based on the work of many people, in fact too many to list here. Quite a few are co-authors of articles with the author names, but there are more who must stay anonymous here. Nevertheless that does not diminish their contributions.

References

1. R.E. Azuma, L. Buchmann, F.C. Barker, C.A. Barnes, J.M. D'Auria, M. Dombisky, U. Giesen, K.P. Jackson, J.D. King, R.G. Korteling, P. McNeely, J. Powell, G. Roy, J. Vincent, T.R. Wang, S.S.M. Wong, P.R. Wrean, *Phys. Rev. C* **50**, 1194 (1994).
2. L. Buchmann and C.A. Barnes, *Nucl. Phys. A*, in press, 2005.
3. L. Buchmann, *Nucl. Phys. A* **758**, 355c (2005).
4. L. Buchmann, R. E. Azuma, C. A. Barnes, J. Humblet, and K. Langanke, *Phys. Rev. C* **54**, 393 (1996).
5. R. Kunz, M.Fey, M.Jaeger, A. Mayer, J.W. Hammer, G. Staudt, S. Harissopoulos, and T. Paradellis, *Astr. Phys. J.* **567**, 643 (2002).
6. F.C. Barker and T. Kajino, *Aust. J. Phys.* **44** 396 (1991).
7. D. Schürmann, A. Di Leva, N. De Cesare, L. Gialanella, G. Imbriani, C. Lubritto, A. Ordione, V. Roca, H. Röcken, C. Rolfs, D. Rogalla, M. Romano, F. Schümann, F. Strieder, F. Terasi and H.-P. Trautvetter, *Nucl. Phys. A* **758**, 367c (2005).
8. D.A. Hutcheon, S. Bishop, L. Buchmann, M.L. Chatterjee, A.A. Chen, J.M. D'Auria, S. Engel, D. Gigliotti, U. Greife, D. Hunter, A. Hussein, C.C. Jewett, N. Khan, M. Lamey, A.M. Laird, W. Liu, A. Olin, D. Ottewell, J.G. Rogers, G. Roy, H. Sprenger, and C. Wrede, *Nucl. Inst. Meth. A* **498**, 190 (2003).
9. Q.R. Ahmad et al., *Phys. Rev. Lett.* **87**, 071301 (2001).
10. A.R. Junghans, E.C. Mohrmann, K.A. Snover, T.D. Steiger, E.G. Adelberger, J.M. Casandjian, H.E. Swanson, L. Buchmann, S.H. Park, A. Zyuzin, and A. Laird, *Phys. Rev. C* **68**, 065803 (2003).
11. P. Descouvemont and D. Baye, *Nucl. Phys. A* **567**, 341 (1994) and private communication.
12. P. Descouvemont, *Phys. Rev. C* **70**, 065802 (2004).
13. G. Ruprecht, D. Gigliotti, P. Amaudruz, L. Buchmann, S. P. Fox, B. R. Fulton, T. Kirchner, A. M. Laird, P. D. Mumby-Croft, R. Openshaw, M. M. Pavan, J. Pearson, G. Sheffer, and P. Walden, submitted to *EPJ* July, 2005.

RECENT EXPERIMENTAL STUDIES OF NUCLEAR ASTROPHYSICS USING INTERMEDIATE-ENERGY EXOTIC BEAMS

TOHRU MOTOBAYASHI

RIKEN, 2-1 Wako, Saitama 351-0198, Japan

E-mail: motobaya@riken.jp

Intermediate-energy Coulomb dissociation has been applied to nuclear astrophysics studies using fast radioactive-isotope (RI) beams. This method helps to overcome the low intensity and low emittance of the beams. Recent studies on several reactions involved in steady and explosive hydrogen burning are presented.

1. UNSTABLE NUCLEI in ASTROPHYSICS

Certain nuclear reactions with short-lived nuclei are expected to play important roles in explosive nuclear burning scenarios. These reactions may become faster than their β decays in high-temperature and high-density conditions. Non explosive situations as in the hydrogen burning in the sun sometimes involves unstable nuclei. These reactions are, however, difficult to study in laboratory experiments, because the short-lived nucleus is hard to be made in a target. Use of radioactive ion (RI) beams is useful in such cases. Direct measurements can be performed by a low-energy RI beam of the nucleus of interest. Another solution is to employ an indirect method such as the one based on the transfer reaction (ANC method)¹, the “Trojan Horse” method² or the Coulomb dissociation. The first and third methods are used for radiative capture reactions, whereas the second one is for transfer reactions.

Compared with ordinary beams of stable particles, the beam intensity is quite low and the emittance is large especially for intermediate-energy RI beams produced by the fragmentation scheme. Therefore, measurements should be quite efficient and reactions with large cross sections should be employed. Efforts to overcome the poor quality of the beams should also be made in order to resolve the final states of the reaction.

2. COULOMB DISSOCIATION

For a Coulomb dissociation experiment in reversed kinematics, the residual nucleus A of the radiative capture reaction of interest, $B(x,\gamma)A$, bombards a high- Z target and is Coulomb excited to its unbound state that decays to the $B+x$ channel. The cross sections of these reactions can be related since the dissociation process can be regarded as the absorption of a virtual photon, *i.e.* $A(\gamma,x)B$, the inverse of the astrophysical reaction of interest. The idea of applying this Coulomb dissociation method to astrophysical radiative capture has been first proposed by Baur, Bertulani and Rebel³, and some review articles are available^{4,5}. In addition to the advantage of using thick targets, the Coulomb dissociation method enhances the original capture cross section by a large factor.

The cross sections of the radiative capture and the photoabsorption are connected by the detailed balance relation,

$$\sigma_{A+\gamma\rightarrow B+x} = \frac{(2j_B + 1)(2j_x + 1)}{2(2j_A + 1)} \frac{k^2}{k_\gamma^2} \sigma_{B+x\rightarrow A+\gamma}. \quad (1)$$

The spins of A, B and x are denoted by j 's, respectively. The wave number k in the $B+x$ channel is given by $k^2 = 2\mu E_{\text{cm}}/\hbar^2$ with the reduced mass μ of the $B+x$ system, while the photon wave number is given by $k_\gamma = E_\gamma/\hbar c = (E_{\text{cm}} + Q)/\hbar c$, where Q denotes the Q -value of the (x,γ) reaction. Due to the large phase space volume for the $B+x$ channel, the photoabsorption cross section is enhanced. For example the factor k^2/k_γ^2 in Eq. 1 is calculated to be about 1,000 for the case of ${}^7\text{Be}(p,\gamma){}^8\text{B}$ reaction.

The energy-dependent Coulomb-dissociation cross section $d\sigma_{\text{CD}}/dE_\gamma$ and that of photoabsorption can be related with the number of virtual photon n_γ as,

$$\frac{d\sigma_{\text{CD}}}{dE_\gamma} = \frac{1}{E_\gamma} n_\gamma \sigma_{\text{photo}}. \quad (2)$$

The intense flux of virtual photons produced by a large- Z target enhances the Coulomb dissociation cross section. For example, the n_γ value is evaluated to be about 1,000 for the ${}^8\text{B}$ Coulomb dissociation at around 50 MeV/nucleon.

In Coulomb dissociation experiments, the relative energy of the two fragments B and x, which corresponds to the center-of-mass energy of the $B(x,\gamma)A$ capture reaction, is obtained from their invariant mass extracted from the velocities of B and x and their relative angle. The relative energy resolution depends on the accuracy of energy and angle determination in

detecting outgoing particles, whereas it is independent of the energy and angular spreads of the incident beam. For example, the relative energy resolution is evaluated to be 200 keV at the relative energy of 1 MeV with the angular resolution of 0.6° and the energy resolution of 2%. This indicates that this method is suitable for experiments with RI beams of intermediate energies with poor qualities.

3. ${}^7\text{Be}(p,\gamma){}^8\text{B}$

The ${}^7\text{Be}(p,\gamma){}^8\text{B}$ reaction is a sort of bench mark case where various methods are employed. It is important for estimating high-energy neutrino flux relevant to the solar neutrino puzzle, defined as the discrepancy between the measured and predicted neutrino yields from the sun⁶. Direct proton-capture measurements have been and are being performed with a radioactive ${}^7\text{Be}$ target. The Coulomb dissociation experiments provide an opportunity of independent determination of this important reaction cross section. We performed several experiments of the Coulomb dissociation of ${}^8\text{B}$ at RIKEN^{7,8,9} and GSI^{10,11}.

At RIKEN, unstable ${}^8\text{B}$ nuclei were produced by the ${}^{12}\text{C}+{}^9\text{Be}$ fragmentation at 92 MeV/nucleon, and were analyzed by the RIPS fragment separator¹². The ${}^8\text{B}$ beam energy in the center of the target, 50 mg/cm² ${}^{208}\text{Pb}$, was approximately 50 MeV/nucleon. The breakup fragments, ${}^7\text{Be}$ and p, were detected in coincidence, and their relative energy was extracted. The experimental breakup cross sections were converted to the ${}^7\text{Be}(p,\gamma){}^8\text{B}$ cross section with the help of a Monte-Carlo simulation calculation which included the detection efficiency and the theoretical Coulomb-dissociation cross sections calculated by the distorted-wave theory. In one of the experiments, the DALI setup, an array of sixty NaI(Tl) scintillators, measured the deexcitation γ rays from the first excited state of ${}^7\text{Be}$ at 429 keV populated in the dissociation process. The contribution from this process was measured to be about 5% of the Coulomb dissociation yield, and was subtracted to extract the cross section of interest.

In Fig. 1 the astrophysical S_{17} -factors obtained in the two experiments at RIKEN are shown together with the results from several direct (p, γ) measurements. The S -factor is related to the capture cross section σ by,

$$S = \sigma E \exp[2\pi\eta], \quad (3)$$

with the Sommerfeld parameter $\eta = e^2 Z_1 Z_2 / \hbar v$ and center-of-mass energy E . Our Coulomb dissociation data are consistent within errors with the results by Filipponi *et al.*¹³ and Vaughn *et al.*¹⁴. The second experiment

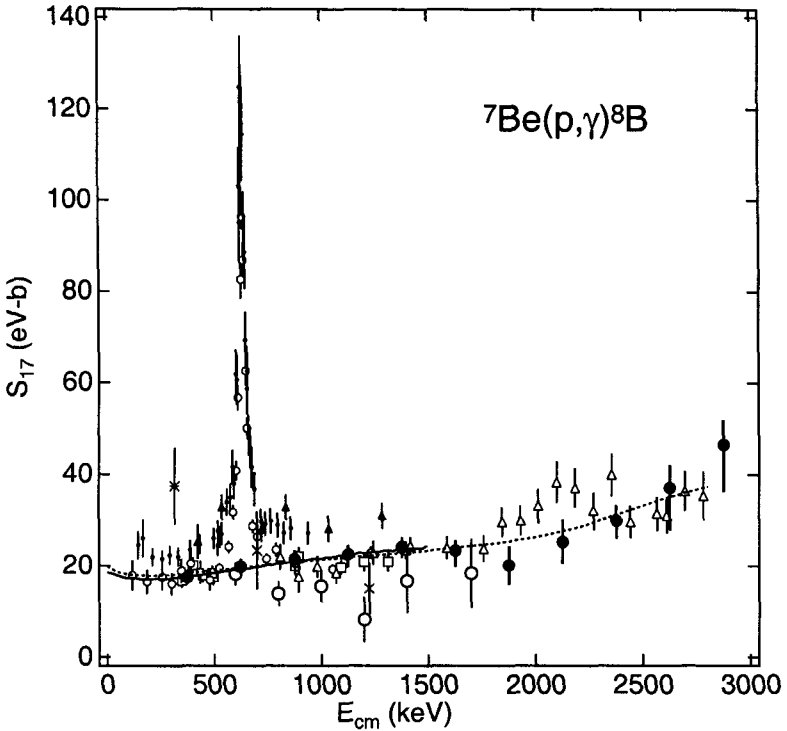


Figure 1. Astrophysical S_{17} -factors for the ${}^7\text{Be}(p,\gamma){}^8\text{B}$ reaction extracted from the first (large open circles) and second (large solid circles) experiments at RIKEN. Existing direct (p,γ) data are also shown. The solid and dashed curves represent the fits to the data from the second Coulomb dissociation experiment with the theoretical energy dependence of Barker and Spear and that of Descouvemont and Baye, respectively.

yielded the S factor extrapolated to $E=0$ as $S_{17}(0)=18.9_{-1.5}^{+1.8}$ eV-b⁹, which agrees with the recent recommendation $S_{17}(0)=19_{-2}^{+4}$ eV-b¹⁵ evaluated essentially from the direct capture data by Filippone *et al.*¹³

Experiments at a higher incident energy of 254 MeV/nucleon^{10,11} provided a good test for the reaction mechanism by comparison with the lower energy results of the RIKEN experiments, because higher order processes is less important in general at higher incident energies. The results basically agrees with the RIKEN data and hence the direct capture data with lower S -factors.

The Coulomb dissociation measurement was made also at MSU¹⁶. Although the data themselves taken at the incident energy of 83 MeV/nucleon

essentially agree with the RIKEN data, the authors deduce a slightly lower S factor by subtracting their evaluated E2 component based on their analysis on the parallel momentum distribution of ${}^7\text{Be}$ from the ${}^8\text{B}$ Coulomb dissociation¹⁷. On the other hand, the angular distribution measurement at RIKEN⁸ and the second GSI experiment¹¹ with precise angular correlation data both point to an E2 mixture much smaller than the one evaluated in the MSU experiment. This discrepancy affects the extracted S_{17} factors by 10-15%.

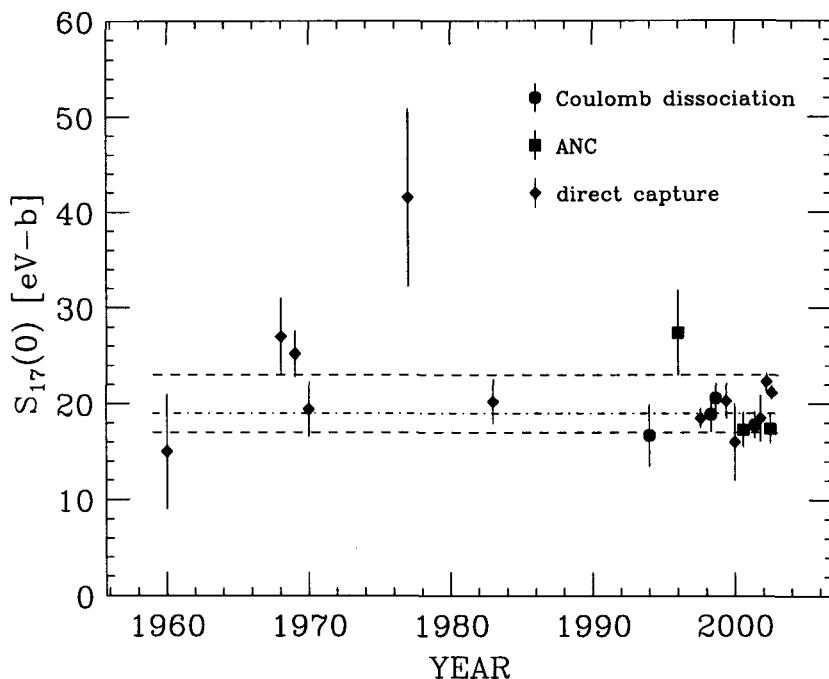


Figure 2. The $S_{17}(0)$ values extracted by the Coulomb dissociation method (solid circles) and the ANC method (solid squares). The ones obtained by direct capture measurements are also shown by solid diamonds. The latest recommendation $S_{17}(0)=19_{-2}^{+4}$ eV-b is indicated by the dashed and dot-dashed lines.

Figure 2 summarizes the $S_{17}(0)$ values reported with the direct, Coulomb dissociation and ANC methods. Though recent results are generally in good agreement with the evaluation in 1998¹⁵, more works might be necessary to resolve the discrepancy mentioned above for the Coulomb dissociation results and to improve the accuracy to the level of 5%, which

is expected to be the accuracy of future solar neutrino measurements. It should be noted that new attempts to improve the accuracy to the 5% level have been made for direct capture experiments^{18,19}. However, the disagreement among the existing data with various experiments has not been fully understood.

4. EXPLOSIVE HYDROGEN BURNING

Recently we performed experiments of the dissociation of ${}^9\text{C}$, ${}^{12}\text{N}$, and ${}^{13}\text{O}$, which are intended to determine reaction rates relevant to the hot-pp mode nuclear burning in hydrogen-rich massive objects²⁰. The experiments have been performed by essentially the same procedures as in the ${}^8\text{B}$ dissociation experiments. Figure 3 shows a relative energy spectrum of the ${}^9\text{C}$ dissociation. The data follow essentially the simulation assuming an energy-independent S factor of 100 eV-b except for the excess of yield seen at around 0.9 MeV, which corresponds to the excitation of the first resonant state of ${}^9\text{C}$.

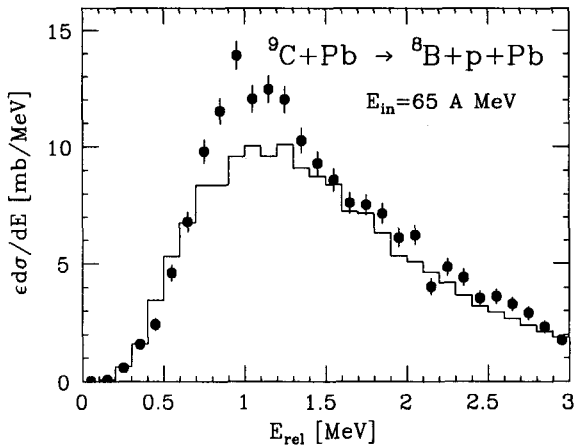


Figure 3. Experimental cross sections $\epsilon d\sigma/dE_{\text{rel}}$ for the dissociation of ${}^9\text{C}$ on Pb plotted as a function of the relative energy E_{rel} . The cross sections include the energy-dependent detection efficiency ϵ . The closed circles represent the experimental data, and the histogram shows the result of the Monte-Carlo simulation assuming Coulomb dissociation mechanism with a constant $E1$ S factor of 100 eV-b.

After considering the data taken with a carbon target, which are sensitive essentially to the dissociation due to nuclear force, the S factor for the direct capture through continuum states and the radiative widths of the

resonance in the M1 and E2 multipolarity could be extracted. The dominant M1 width is directly related to the capture cross section through the Breit-Wigner one-level formula. These results are summarized in Table 1 together with the experimental S factors obtained by the ANC method^{21,22} and theoretical estimates^{20,23,24}.

Table 1. Astrophysical S factor for the ${}^8\text{B}(p,\gamma){}^9\text{C}$ reaction at low energies and radiative widths of the 0.92 MeV resonance in ${}^9\text{C}$.

	S_{18} (energy range) (eV-b) (MeV)	$\Gamma_\gamma(\text{M1})$ (meV)	$\Gamma_\gamma(\text{E2})$ (μeV)	method
(1)	77 ± 15 (0.2-0.6)	21 ± 6	4.3 ± 1.0	${}^9\text{C}$ dissociation
(2)	45 ± 13 (0-0.1)			ANC
(3)	46 ± 6			ANC
(4)	210 (0-0.8)	34^c		shell model (S_{18}) ^e
(5)	$72^a, 80^b$ (0.2-0.6)	100^d	600^d	cluster model
(6)			4.6^c	AMD

(1) present, (2) Beaumel *et al.*, (3) Trache *et al.*, (4) Wiescher *et al.*, (5) Decouvemont, (6) Kanada-En'yo and Horiuchi

^a Minnesota force, ^b Volkov force, ^c $j_\pi=1/2^-$, ^d $j_\pi=5/2^-$, ^e Γ_γ is evaluated by systematics

As seen in the table, the extracted S_{18} factor agrees with the one predicted by Descouvemont²³ and is slightly larger than the results obtained by the ANC method. The estimate by Wiescher *et al.*²⁰ is considerably larger. For the 0.92 MeV resonance, the dominant M1 width is consistent with the estimate by Wiescher *et al.*²⁰, but is smaller than the prediction of Descouvemont²³. The extracted E2 width agrees well with the prediction of the antisymmetrized molecular dynamics by Kanada-En'yo and Horiuchi²⁴. A complete set of experimental information of astrophysical interest was extracted from the Coulomb dissociation experiment, demonstrating the usefulness of the method.

Encouraged by the success of the ${}^8\text{B}$ dissociation experiments, we extended the Coulomb dissociation method to a heavier system, the ${}^{22}\text{Mg}(p,\gamma){}^{23}\text{Al}$ reaction²⁵. This reaction might play a role in the rp-process relevant in thermonuclear runaway expected to occur in certain novae. The resultant relative energy spectrum is shown in Fig. 4. We could obtain the radiative width of the first resonant state in ${}^{23}\text{Al}$, and provided the first experimental support to the recent evaluation of the reaction rate²⁶. It should be noted that in a direct capture measurement data with equivalent

statistics can be obtained only by the ^{22}Mg beam intensity of the order of 10^{12} s^{-1} , which is impossible in the current technology.

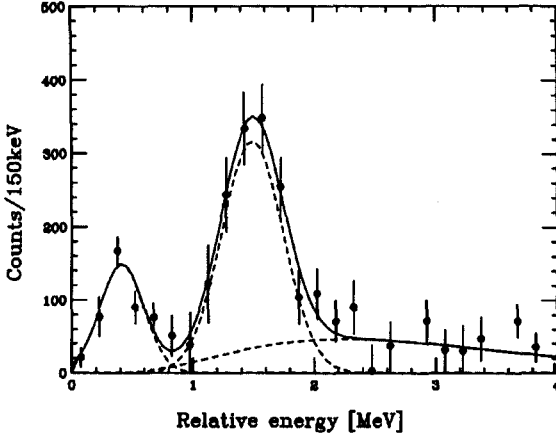


Figure 4. Experimental relative energy spectrum for the dissociation of ^{23}Al on Pb plotted as a function of the relative energy E_{rel} . The lowest-energy peak corresponds to the dissociation through the first excited state in ^{23}Al , which is expected to play a important role in the rp process hydrogen burning.

5. COULOMB EXCITATION for SUBTHRESHOLD STATES

Recently, we studied the Coulomb excitation of ^{15}O to its $3/2^+$ state at $E_{\text{ex}}=6.793 \text{ MeV}$, which can affect the low-energy behavior of the $^{14}\text{N}(p,\gamma)^{15}\text{O}$ reaction, a key process in the CNO cycle hydrogen burning. This might add an independent information to the recent life-time measurement²⁷.

Figure 5 shows the energy spectrum of γ rays associated with the inelastic ^{15}O scattering with a lead target. The fits of simulated line shapes result in an upper limit of the cross section for the $3/2^+$ excitation, leading to its radiative width $\Gamma_{\gamma} < 1.6 \text{ eV}$. This result suggests a negligible effect of the state to the low energy (p,γ) behavior. This is consistent with the recent lifetime measurement²⁷, but is in contrast to the result of R-matrix fits to the direct capture data²⁸.

6. SUMMARY

Indirect determinations of astrophysical (p,γ) cross sections involving unstable nuclei through the Coulomb dissociation method are discussed. The

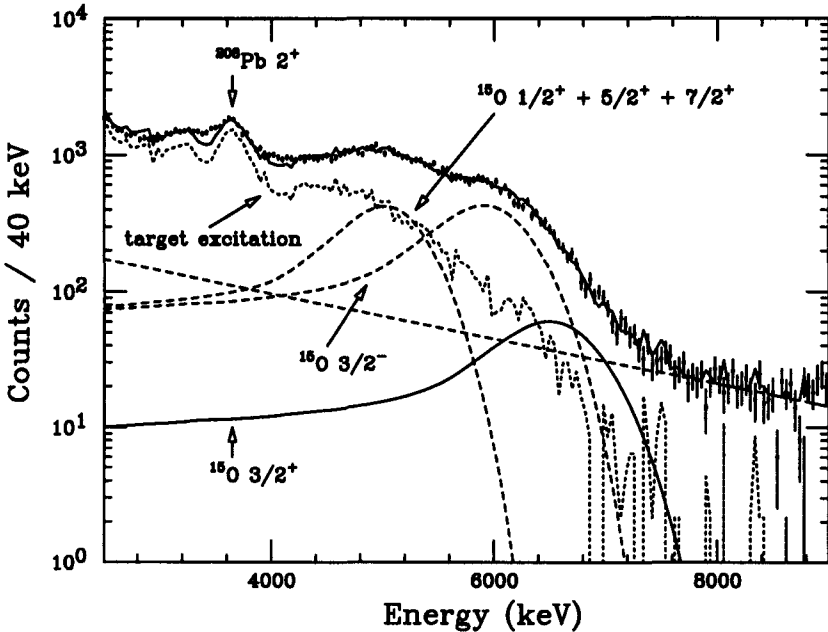


Figure 5. Experimental γ -ray spectrum observed for the $^{15}\text{O}+\text{Pb}$ inelastic scattering measured at $\theta_\gamma=63^\circ$. The curves show the result of the best fit with the six components, four spectra due to the ^{15}O excitation, target excitation component, and background.

^8B dissociation has been studied at two different energy domains, 50-80 and 250 MeV/nucleon. Extracted astrophysical S_{17} factors are consistent with a recent recommendation $S_{17}(0)=19_{-2}^{+4}$ eV-b 15 . The hot pp chain is an explosive burning process involving short-lived nuclei. The $^8\text{B}(p,\gamma)^9\text{C}$ reaction in the chain was studied by the Coulomb dissociation method. More reactions in explosive hydrogen-burning processes have been also studied by the Coulomb dissociation method: the radiative proton captures on ^{12}N , ^{13}O , and here $^{22}\text{Mg}(p,\gamma)^{23}\text{Al}$. Low-energy behavior of the $^{14}\text{N}(p,\gamma)^{15}\text{O}$ reaction, a key process in the CNO cycle hydrogen burning, was studied by the Coulomb excitation. The role of the subthreshold $3/2^+$ state to the astrophysical reaction rate was clarified.

The advantages of these experimental studies are the large cross section and the possibility to use thick targets. This enables investigations of astrophysical reactions involving unstable nuclei with reasonable yield. This may open a possibility of measuring further (p,γ) , (n,γ) and even $(2p,\gamma)$ processes by the indirect methods using RI beams provided by the RIKEN

RI Beam Factory project, which is expected to start operation in the end of the year 2006.

References

1. R.E. Tribble, this school.
2. C. Spitaleri, this school.
3. G. Baur, C.A. Bertulani, and H. Rebel, *Nucl. Phys.* **A458**, 188 (1986).
4. G. Baur and H. Rebel, *J. Phys.* **G20** 1 (1994); *Ann. Rev. Nucl. and Part. Sci.* 46 (1996) 321.
5. T. Motobayashi, *Nucl. Phys.* **A693** 258 (2001).
6. J.N. Bahcall, *Neutrino Astrophysics*, Cambridge University Press, New York, 1989.
7. T. Motobayashi *et al.*, *Phys. Rev. Lett.* **73** 2608 (1994); N. Iwasa *et al.*, *J. Phys. Soc. Jpn.* **65**, 1256 (1996).
8. T. Kikuchi *et al.*, *Phys. Lett.* **B391**, 261 (1997).
9. T. Kikuchi *et al.*, *Eur. Phys. J.* **A3**, 209 (1998).
10. N. Iwasa *et al.*, *Phys. Rev. Lett.* **83**, 2910 (1999).
11. F. Schümann *et al.*, *Phys. Rev. Lett.* **90**, 232501 (2003); F. Schümann *et al.*, submitted to *Phys. Rev. C*.
12. T. Kubo *et al.*, *Nucl. Instr. Meth.* **B70**, 309 (1992).
13. B. Filippone, S.J. Elwyn, C.N. Davids, and D.D. Koetke, *Phys. Rev. Lett.* **50** 412 (1983); *Phys. Rev.* **C28** 2222 (1983).
14. F.J. Vaughn, R.A. Chalmers, D. Kohler, and L.F. Chase, Jr., *Phys. Rev.* **C2**, 1657 (1970).
15. E.G. Adelberger *et al.*, *Rev. Mod. Phys.* **70**, 1265 (1998).
16. B. Davids *et al.*, *Phys. Rev. Lett.* **86**, 2750 (2001).
17. B. Davids *et al.*, *Phys. Rev. Lett.* **81**, 2209 (1988).
18. A.R. Junghans *et al.*, *Phys. Rev. Lett.* **86**, 041101 (2002) .
19. L.T. Baby *et al.*, *Phys. Rev. Lett.* **90**, (2003) 022501; *Phys. Rev.* **C67** 065805 (2003).
20. M. Wiescher, J. Görres, S. Graff, L. Buchmann, and F.-K. Thielemann, *Astrophys. J.* **343**, 352 (1989).
21. D. Beaumel *et al.*, *Phys. Lett.* **B514**, 226 (2001).
22. L. Trache, F. Carstoiu, A.M. Mukhamedzhanov, R.E. Tribble, *Phys. Rev.* **C66**, 035801 (2002).
23. P. Descouvemont, *Astrophys. J.* **405**, 518 (1993).
24. Y. Kanada-En'yo and H. Horiuchi, *Phys. Rev.* **C55**, 2860 (1997).
25. T. Gomi *et al.*, *Nucl. Phys.* **A734**, E77 (2004).
26. J.A. Caggiano *et al.*, *Phys. Rev.* **C64**, 025802 (2001).
27. P.F. Bertone *et al.*, *Phys. Rev. Lett.* **87**, 152501 (2001).
28. U. Schröder *et al.*, *Nucl. Phys.* **A567**, 240 (1987).

AN INDIRECT METHOD USING ANCS IN NUCLEAR ASTROPHYSICS

R.E. TRIBBLE, T. AL-ABDULLAH, C. FU, C.A. GAGLIARDI, A.M.
MUKHAMEDZHANOV, F. PIRLEPEOV, G. TABACARU, X. TANG*, L.
TRACHE

Cyclotron Institute, Texas A&M University, College Station, Texas 77843

P. BEM, V. BURJAN, V. KROHA, J. NOVÁK, Š. PÍSKOŘ, E. ŠIMEČKOVÁ,
F. VESELÝ, J. VINCOUR

*Institute for Nuclear Physics, Czech Academy of Sciences, Prague-Řež, Czech
Republic*

F. CÂRSTOIU

Institute for Atomic Physics, Bucharest, Romania

During the last decade, new indirect techniques have been developed to determine reaction rates of interest in nuclear astrophysics. One of these involves measurements of asymptotic normalization coefficients (ANCs). ANCs, which provide the normalization of the tail of the overlap function, determine S factors for direct capture reactions at astrophysical energies. They also can be related to resonance capture rates and are particularly useful for determining proton-capture reaction rates that involve subthreshold resonance states. Proton ANCs have been measured by peripheral transfer reactions using both stable beams and targets and radioactive beams. Recently neutron ANCs have been measured by heavy-ion transfer reactions. Using mirror symmetry, the neutron ANCs can be related to proton ANCs and the results can then be used to determine direct capture reaction rates. Following an introduction to ANCs, recent experiments are discussed along with the astrophysical implications of these measurements.

1. Introduction

Understanding stellar evolution requires detailed information about nuclear reactions and decays that are important in using nuclear fuel in burning

*present address: Physics Division, Argonne National Laboratory

processes that provide energy to a star. Stellar nuclear burning is complicated, involving sequences of capture reactions and beta decays, and depends on density, temperature and nuclear abundances. Reaction and decay cycles, beginning with the p - p chain and extending to the CNO, Ne-Na, etc., cycles, process the nuclear fuel, primarily through hydrogen and helium burning, yielding increasingly massive nuclei and producing energy. Explosive stellar processes involve similar sequences of reactions and decays. Some of the important reactions in the burning cycles and most in explosive processes involve unstable nuclei. New direct and indirect techniques have been developed over the last decade to measure these reaction rates. Most of these new approaches are being discussed in contributions to this summer school proceedings.

The ANC technique is based on the fact that direct proton-capture reactions of astrophysical interest involve systems where the binding energy of a captured charged particle is low. Hence at stellar energies, the capture proceeds through the tail of the nuclear overlap function. The shape of the overlap function in this tail region is determined by the Coulomb interaction, so the amplitude of the overlap function alone dictates the rate of the capture reaction. The asymptotic normalization coefficient (ANC), C , specifies the amplitude of the tail of the overlap function for the system. Astrophysical S factors for peripheral direct radiative capture reactions can be determined through measurements of ANC's using traditional nuclear reactions such as peripheral nucleon transfer^{1,2}. Also the ANC can be used to determine the external part of Γ_γ ³. Thus the ANC is connected to both the resonant and nonresonant capture amplitudes, and it can be used to determine astrophysical S factors when the capture occurs through a sub-threshold resonance state³.

2. ANC Measurements

The connection between ANCs and the direct proton capture rate at low energies is straightforward to obtain. The cross section for the direct capture reaction $A + p \rightarrow B + \gamma$ can be written as

$$\sigma = \lambda | \langle I_{Ap}^B(\mathbf{r}) | \hat{O}(\mathbf{r}) | \psi_i^{(+)}(\mathbf{r}) \rangle |^2, \quad (1)$$

where λ contains kinematical factors, I_{Ap}^B is the overlap function for $B \rightarrow A + p$, \hat{O} is the electromagnetic transition operator, and $\psi_i^{(+)}$ is the scattering wave in the incident channel. If the dominant contribution to the matrix element comes from outside the nuclear radius, the overlap

function may be replaced by

$$I_{Ap}^B(r) \approx C \frac{W_{-\eta, l+1/2}(2\kappa r)}{r}, \quad (2)$$

where C , the ANC, defines the amplitude of the tail of the radial overlap function I_{Ap}^B , W is the Whittaker function, η and l are the Coulomb parameter and orbital angular momentum for the bound state $B = A + p$, and κ is the bound state wave number. If resonance parameters are known either from measurements or calculations and ANCs are known, the resonant and nonresonant components can be used together in an R -matrix calculation to obtain capture cross sections.

Peripheral transfer reactions provide an excellent way to determine ANCs. Consider the proton transfer reaction $a + A \rightarrow c + B$, where $a = c + p$, $B = A + p$. The DWBA cross section can be written in the form⁴

$$\frac{d\sigma}{d\Omega} = \sum_{j_B j_a} \frac{(C_{Apl_B j_B}^B)^2 (C_{cpl_a j_a}^a)^2}{b_{Apl_B j_B}^2 b_{cpl_a j_a}^2} \tilde{\sigma}_{l_B j_B l_a j_a}^{DW}, \quad (3)$$

where $\sigma_{l_B j_B l_a j_a}^{DW}$ is the reduced DWBA cross section and j_i, l_i are the total and orbital angular momenta of the transferred proton in nucleus i . The factors $b_{cpl_a j_a}$ and $b_{Apl_B j_B}$ are the ANC's of the bound state proton wave functions in nuclei a and B . They are related to the corresponding ANC of the overlap function by

$$(C_{cpl_a j_a}^a)^2 = S_{cpl_a j_a}^a b_{cpl_a j_a}^2, \quad (4)$$

where $S_{cpl_a j_a}^a$ is the spectroscopic factor. If the reaction under consideration is peripheral, the ratio

$$R_{l_B j_B l_a j_a} = \frac{\tilde{\sigma}_{l_B j_B l_a j_a}^{DW}}{b_{Apl_B j_B}^2 b_{cpl_a j_a}^2} \quad (5)$$

is independent of the single particle ANC's $b_{Apl_B j_B}$ and $b_{cpl_a j_a}$. Thus for surface reactions the DWBA cross section is best parametrized in terms of the product of the square of the ANCs of the initial and final nuclei $(C^B)^2 (C^a)^2$. The ANCs, (C^B) , are just those needed in Eq. 1 to determine the capture reaction cross section.

As examples of measurements with stable beams and targets, ANCs for $^{15}\text{O} \rightarrow ^{14}\text{N} + p$ and $^{21}\text{Na} \rightarrow ^{20}\text{Ne} + p$ have been determined using the $^{14}\text{N}(^3\text{He}, d)^{15}\text{O}$ and $^{20}\text{Ne}(^3\text{He}, d)^{21}\text{Na}$ reactions. The experiments were carried out with ^3He beams supplied by the U-120M isochronous cyclotron of the Nuclear Physics Institute of the Czech Academy of Sciences. ANCs

were obtained for the ground and five excited states in ^{15}O and the ground and first three excited states in ^{21}Na . Capture in both reactions at stellar energies is dominated by a subthreshold state. In ^{15}O the state that dominates is at $E_x = 6.79$ MeV and for ^{21}Na the subthreshold state is at $E_x = 2.425$ MeV. ANC's have been used to obtain the astrophysical S factors for both systems^{5,6}.

Recent measurements with radioactive beams include the determination of the ANC's for $^{14}\text{O} \rightarrow ^{13}\text{N} + p$ which have been extracted from the $^{14}\text{N}(^{13}\text{N}, ^{14}\text{O})^{13}\text{C}$ reaction. The experiment was carried out at Texas A&M University. A beam of ^{13}C at 15 MeV/A from the K500 superconducting cyclotron was used to bombard a 9 cm long gas target filled with 2 atmospheres of H_2 gas cooled to LN_2 temperature. Recoil ions were collected by the MARS recoil spectrometer to produce a pure (>99%) secondary beam of ^{13}N at 11.8 MeV/A. A 1.5 mg/cm² melamine target was placed at the focal plane of the recoil spectrometer and reaction products from the $^{14}\text{N}(^{13}\text{N}, ^{14}\text{O})^{13}\text{C}$ reaction were observed in 5 cm \times 5 cm ΔE - E Si detector telescopes. A plastic scintillator detector was used to measure the beam particles. The angular distribution for ^{14}O reaction products populating the ground state of ^{13}C is shown in Fig. 1. The ANC's for $^{14}\text{O} \rightarrow ^{13}\text{N} + p$ have been extracted and used to predict the direct capture contribution to the $^{13}\text{N}(p, \gamma)^{14}\text{O}$ reaction⁷.

In addition to the proton transfer reactions mentioned above, neutron ANC's have been measured for several systems. As an example, the ANC's for $^8\text{Li} \rightarrow ^7\text{Li} + n$ have been obtained from the neutron transfer reaction $^{13}\text{C}(^7\text{Li}, ^8\text{Li})^{12}\text{C}$. By mirror symmetry, these ANC's can be related to those for the $^8\text{B} \rightarrow ^7\text{Be} + p$ system⁸. Thus the neutron transfer reaction can be used to determine the S factor for $^7\text{Be}(p, \gamma)^8\text{B}$. The $^{13}\text{C}(^7\text{Li}, ^8\text{Li})^{12}\text{C}$ reaction was measured at Texas A&M University with a ^7Li beam at 9 MeV/A from the K500 superconducting cyclotron bombarding a 300 $\mu\text{g}/\text{cm}^2$ ^{13}C target. After passing through the beam analysis system, the primary beam was focused at the target chamber of the MDM magnetic spectrometer. Reaction products from the ^{13}C target were observed in the focal plane of the spectrometer. The high-quality beam from the analysis system allowed for a measurement of the angular distribution even at 0° . This made it possible to separate the $1p_{1/2}$ and $1p_{3/2}$ components in the transfer. The angular distribution for the reaction and the DWBA fit using optical model parameters from ^7Li elastic scattering are shown in Fig. 2. More details can be found elsewhere⁹.

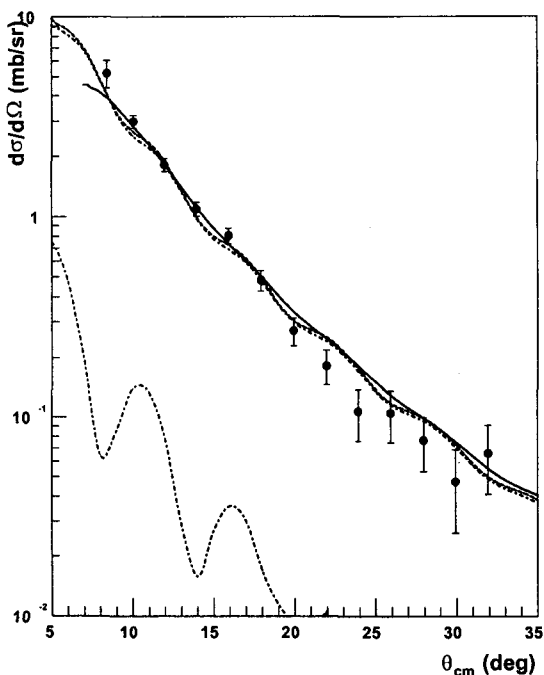


Figure 1. Angular distribution for $^{14}\text{N}(^{13}\text{N}, ^{14}\text{O})^{13}\text{C}_{g.s.}$. The dashed curve is the DWBA prediction. The solid curve is the smeared prediction taking into account the finite size of the secondary beam spot and the angular spread in the beam. The upper and lower dashed-dotted lines represent the $^{14}\text{N}(p_{1/2}) \rightarrow ^{14}\text{O}(p_{1/2})$ and $^{14}\text{N}(p_{3/2}) \rightarrow ^{14}\text{O}(p_{1/2})$ proton transfer reactions, respectively.

3. Astrophysical S factors from ANCs

The $^{14}\text{N}(p, \gamma)^{15}\text{O}$ reaction is one of the most important reactions in the CNO cycle. As the slowest reaction in the cycle, it defines the rate of energy production¹⁰ and, hence, the lifetime of stars that are governed by hydrogen burning via CNO processing. Previously a measurement of the $^{14}\text{N}(p, \gamma)^{15}\text{O}$ reaction was carried out¹¹ in 1987 and a total astrophysical factor $S(0) = 3.20 \pm 0.54$ keV b was deduced. This measurement determined that $^{14}\text{N}(p, \gamma)^{15}\text{O}$ capture at low energies is dominated by capture through the first resonance at $E_{R1} = 259.5$ keV (the resonance energy in the c.m.) and a subthreshold state at $E_s = -504$ keV. At very low energies appropriate for stellar burning, the reaction was found to be dominated by a combination of direct and resonant capture and interference from the tail of the subthreshold resonance and the first resonance. Recently the first

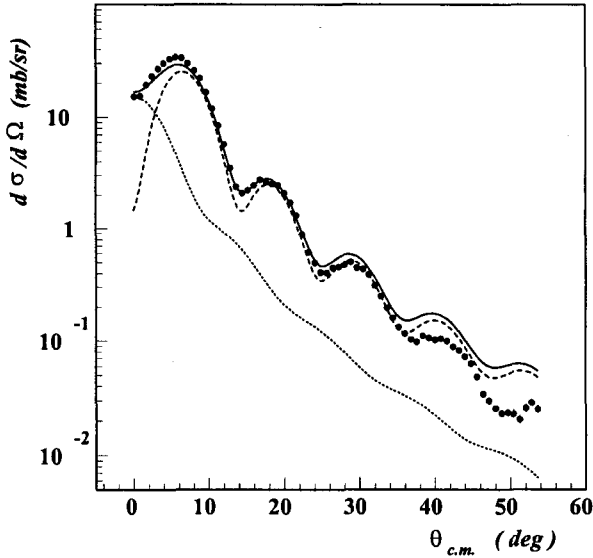


Figure 2. The angular distribution for the $^{13}\text{C}(^7\text{Li},^8\text{Li})^{12}\text{C}$ reaction. The data are shown as points and the solid line is the best fit. The $p_{1/2} \rightarrow p_{1/2}$ component is shown as the dotted line, and the $p_{1/2} \rightarrow p_{3/2}$ component is the dashed line.

measurement of the radiative width of the subthreshold state in ^{15}O to the ground state was reported¹². The new result for the width, $0.41^{+0.34}_{-0.13}$ eV, is about 15 times smaller than the value used in the analysis of the data from 1987. Due to the small width only direct capture to the subthreshold state in ^{15}O is important for the S factor and the ANC thus determines the reaction rate at stellar energies.

The ANCs that were found from the transfer reaction have been used in an R-matrix analysis to determine the S factor for $^{14}\text{N}(p,\gamma)^{15}\text{O}$. Extrapolating to stellar energies gives $S(0) = 1.40 \pm 0.20$ keVb for the contribution from the subthreshold state. Including all contributions, the total calculated astrophysical factor at zero energy is $S(0) = 1.70 \pm 0.22$ keVb⁵. This rate is about a factor of 2 smaller than that obtained from the earlier analysis and makes the energy production in the CNO cycle smaller than previously estimated.

With increasing temperature, the rates of the proton capture reactions in the cold CNO cycle exponentially increase. Eventually the reaction rate for $^{13}\text{N}(p,\gamma)^{14}\text{O}$ exceeds the rate of ^{13}N β decay ($t_{1/2}=9.965$ min) and the hot (β limited) CNO-cycle takes over. But $^{14}\text{N}(p,\gamma)^{15}\text{O}$ is still the slowest reaction and it controls the energy generation rate. As the temperature con-

tinues to increase, all of the proton capture reaction rates in the hot CNO cycle exceed the β -decay rates of ^{14}O and ^{15}O (with half lives $t_{1/2}=70.6$ s and 122 s, respectively). The energy generation rate of the hot CNO cycle will remain constant until some break out processes begin to occur. Indeed the thermonuclear runaway in novae is driven by the energy release of the hot CNO cycle. Because the peak temperature in the thermonuclear runaway is typically below 3.5×10^8 K, break out processes are inhibited by their limited reaction rates. Observation of the abundance distribution in nova ejecta indicate large over abundances of nitrogen produced by the β -decay of the bottleneck nuclei, ^{14}O and ^{15}O , in the hot CNO cycle¹³.

For $T_9=0.2$, the Gamow window for the $^{13}\text{N}(p,\gamma)^{14}\text{O}$ reaction is located at 148 keV with a width of 117 keV. At this energy the reaction is dominated by the low-energy tail of the s-wave capture on the broad 1^- resonance at $E_r=0.529$ MeV¹⁴. The direct capture contribution is significantly smaller than that due to the tail of the resonance within the Gamow window. But since both resonant and nonresonant capture proceed via s waves and then decay by E1 transitions, there is an interference between the two components. Thus the resonant tail can be enhanced through constructive interference or reduced through destructive interference.

The cross section for direct capture and resonant capture through the broad first excited state was calculated from the measured ANC and the experimental resonance parameters using the R -matrix approach⁷. In the calculation, the same parameters ($E_R^{c.m.} = 527.9 \pm 1.7$ keV, $\Gamma_{total} = 37.3 \pm 0.9$ keV and $\Gamma_\gamma = 3.36 \pm 0.72$ eV) as Magnus *et al.*¹⁵ adopted were used for the first resonance. A theoretical calculation by Descouvemont¹⁶ suggested that constructive interference occurs between the resonant and nonresonant amplitudes for the low energy tail, but there is no experimental confirmation of this so far. Thus both constructive and destructive interference were calculated. The new result for direct capture alone, is about 30% larger than the result obtained by Decrock *et al.*¹⁴ At $E_{c.m.} = 140$ keV where the Gamow peak is located for $T_9=0.2$, the calculation with constructive interference is about 38% higher than the previous result. This is due to the larger direct capture contribution from the ANC measurement. The estimated destructive interference is smaller than the constructive interference result by a factor of 3 at $E_{c.m.} = 140$ keV. Verifying by a direct measurement that constructive interference is indeed correct would be quite useful.

As material leaks out of the CNO cycle, the Ne-Na cycle can begin. The $^{20}\text{Ne}(p,\gamma)^{21}\text{Na}$ reaction is one of the reactions in the Ne-Na cycle. Its reaction rate is extremely hard to measure since, like the $^{14}\text{N}(p,\gamma)^{15}\text{O}$

reaction, it is dominated by a subthreshold state. The important state in ^{21}Na at $E_x = 2.425$ MeV is only 7 keV below threshold. Thus even a small Γ_γ will result in a substantial resonant contribution to the reaction rate. The reaction rate at stellar energies was estimated previously to be about 3500 keV b^{17} . The ANCs that were determined for this state fix the direct capture through the subthreshold state. At proton energies below about 150 keV, resonant capture through the subthreshold state dominates the S factor. Based on the present information available about the γ width of the state, $S(0) = 5900 \pm 1200 \text{ keV b}$. A new measurement of the width of this state, would substantially reduce the uncertainty in this result.

Previously, we used ($^7\text{Be}, ^8\text{B}$) proton transfer reactions to measure the ANCs for the $^8\text{B} \rightarrow ^7\text{Be} + p$ process, from which we determined the astrophysical factor $S_{17}(0)^{18}$. This reaction is a very small branch in the $p - p$ chain but the resulting ^8B produces essentially all of the high-energy neutrinos from the sun. And it is these neutrinos that are detected in the water based solar neutrino detectors. Thus knowing the rate of ^8B production in the sun is quite important.

^8B and ^8Li are mirror nuclei, and charge symmetry implies that the spectroscopic amplitudes for the proton single particle orbitals entering the ^8B wave function are nearly the same as those of the neutron single particle orbitals in the ^8Li wave function. This leads to a proportionality between the asymptotic normalization coefficients in $^8\text{B} \rightarrow ^7\text{Be} + p$ and $^8\text{Li} \rightarrow ^7\text{Li} + n$. Thus the neutron transfer reaction allows us to determine the ANCs for $^8\text{B} \rightarrow ^7\text{Be} + p$ and, consequently, the astrophysical factor S_{17} . Indeed the results from using charge symmetry agree well with those from the direct reaction. This is a new variation of the ANC approach that will also be useful in other nuclear systems.

This work was supported in part by the U.S. Department of Energy under Grant number DE-FG02-93ER40773, the U.S. National Science Foundation under Grants No. INT-9909787, PHY-0140343, ME 385(2000) project NSF and MSMT, CR, grant GACR 202/01/0709 and the Robert A. Welch Foundation.

References

1. H.M. Xu *et al.*, Phys. Rev. Lett. **73**, 2027 (1994).
2. A.M. Mukhamedzhanov and N.K. Timofeyuk, JETP Lett. **51**, 282 (1990).
3. A.M. Mukhamedzhanov and R.E. Tribble *Phys. Rev.* **C59**, 3418 (1999).
4. A.M. Mukhamedzhanov *et al.*, Phys. Rev. C **56**, 1302 (1997).
5. A.M. Mukhamedzhanov *et al.*, Phys. Rev. C **67**, 065804 (2003).

6. A.M. Mukhamedzhanov *et al.*, Phys. Rev. C (submitted).
7. X. Tang *et al.*, Phys. Rev. C **69**, 055807 (2004).
8. N. Timofeyuk, R.C. Johnson and A.M. Mukhamedzhanov, Phys. Rev. Lett. **91**, 232501 (2003).
9. L. Trache *et al.*, Phys. Rev. C **67**, 062801 (2003).
10. C. Rolfs, W. S. Rodney, *Cauldrons in the Cosmos*. (The University of Chicago Press, 1988).
11. U. Schröder *et al.*, Nucl. Phys. **A 467**, 240 (1987).
12. P. F. Bertone *et al.*, Phys. Rev. Lett. **87**, 152501 (2001).
13. M. Wiescher, J. Gorres and H. Schatz, J. Phys. G **25**, R133 (1999).
14. P. Decroock *et al.*, Phys. Rev. C **48**, 2057 (1993).
15. P.V. Magnus, E.G. Adelberger and A. Garcia, Phys. Rev. C **49**, R1755 (1994).
16. P. Descouvemont, Nucl. Phys. **A646**, 261 (1999).
17. C. Rolfs and W.S. Rodney, Nucl. Phys. **A241**, 460 (1975).
18. A. Azhari *et al.*, Phys. Rev. C **63**, 055803 (2001).

RECENT APPLICATIONS OF THE TROJAN HORSE METHOD IN NUCLEAR ASTROPHYSICS

C. SPITALERI

*Dipartimento di Metodologie Fisiche e Chimiche per l'Ingegneria, Università di
Catania and Laboratori Nazionali del Sud - INFN*

Via S. Sofia, 44

95123 Catania, ITALY

E-mail: spitaleri@lns.infn.it

The basic features of the Trojan Horse Method are discussed together with a review of recent applications, aimed to extract the bare nucleus astrophysical $S_b(E)$ factor for several two body processes. In this framework information on electron screening potential U_e was obtained from comparison with direct experiments.

1. General Introduction

In order to overcome the experimental difficulties arising from small cross sections involved in charged particle induced reactions at astrophysical energies and from the presence of the electron screening, a number of indirect methods, *e.g.* the Coulomb dissociation¹, the ANC², and the Trojan Horse Method (THM)³ were developed. Some of them make use of direct reaction mechanisms, such as transfer processes and quasi-free reactions. In particular, the THM is a powerful tool which selects the quasi-free (QF) contribution of an appropriate three-body reaction, performed at energies well above the Coulomb barrier, to extract a charged particle two-body cross section at astrophysical energies free of Coulomb suppression. The THM has already been applied several times (Table I) to reactions connected with fundamental astrophysical problems^{4,5}. In this paper, the role of the THM as complementary tool for studying reactions of astrophysical interest as well as fusion reactions for energy production in nuclear power plants is stressed, and some results are shown.

2. Theory

2.1. Quasi-Free mechanism

The quasi-free $A + a \rightarrow c + C + S$ reaction, having a strong $x \oplus S$ cluster structure, can be described by a pseudo-Feynman diagram (Fig. 1 in Ref. 3), where only the first term of the Feynman series is retained. The upper pole describes the virtual break-up of the target nucleus a into the clusters x and S ; S is then considered to be spectator to the $A + x \rightarrow c + C$ reaction, which takes place in the lower pole.

In Plane Wave Impulse Approximation (PWIA) the cross section of the three-body reaction can be factorized^{6,7} as given by:

$$\frac{d^3\sigma}{dE_c d\Omega_c d\Omega_C} \propto KF \left(\frac{d\sigma}{d\Omega_{cm}} \right)^{off} \cdot |\Phi(\vec{p}_s)|^2, \quad (1)$$

where:

- $[(d\sigma/d\Omega)_{cm}]^{off}$ is the off-energy-shell differential cross section for the two-body $A(x,c)C$ reaction at the center-of-mass energy E_{cm} given in post collision prescription by:

$$E_{cm} = E_{c-C} - Q_{2b} \quad (2)$$

where Q_{2b} is the two body Q -value of the $A + x \rightarrow c + C$ reaction and E_{c-C} is the relative energy between the outgoing particles c and C ;

- KF is a kinematical factor containing the final state phase-space factor and it is a function of the masses, momenta and angles of the outgoing particles;
- $\Phi(\vec{p}_s)$ is the Fourier transform of the radial wave function $\chi(\vec{r})$ for the x - S inter-cluster motion, usually described in terms of Hankel, Eckart and Hulthén functions, depending on the x - S system properties.

3. From Quasi-free Reactions to the Trojan Horse Method

The application of the quasi-free mechanism to the study of reactions at astrophysical energies^{3,8} derives from previous researches on the quasi-free mechanism at very low energies⁹⁻¹³. In particular, it is an extension of the indirect excitation function measurements for the two-body cross section of the ${}^7\text{Li}(p,\alpha)\alpha$ and ${}^6\text{Li}(p,\alpha){}^3\text{He}$ reactions^{14,15} at low energies.

This phenomenological approach derives from the theory of the THM proposed by Baur¹⁶, whose basic idea is to extract a two-body $A+x \rightarrow C+c$

reaction cross section at low energies from a suitable three-body $A + a \rightarrow C + c + s$ reaction.

Under appropriate kinematical conditions, the three-body reaction is considered as the decay “of the Trojan Horse”, a , into the clusters x and S and the interaction of A with x inside the nuclear region, whereby the nucleus S can be considered as a spectator during the reaction.

If the bombarding energy E_A is chosen high enough to overcome the Coulomb barrier E_C in the entrance channel of the three-body reaction, the two-body channel is not affected by Coulomb Barrier, and electron screening effects are negligible.

In the original paper by Baur¹⁶, it was proposed that the initial velocity of the projectile A is compensated for by the Fermi-motion of particle x . In this framework, a momentum of the order of hundreds MeV/c could be needed. However, in the case of a nuclei with a predominant $l=0$ inter-cluster motion, such momenta populate the tail of the momentum distribution for particle x , making very critical the separation from eventual background reaction mechanisms, like sequential decays feeding the same exit channel.

Moreover, as already mentioned, the tail of the calculated momentum distribution entering Eq. 1 changes depending on the theoretical approach applied, thus a very sophisticated treatment might be required in order to get the relevant two-body cross section. In order to overcome these problems, we have introduced a different approach^{17–21,14,22–29}, based on the idea that the initial projectile velocity is compensated for by the binding energy of particle x inside a .

Thus, the two-body reaction can be induced at very low (even vanishing) relative energy²⁶. Moreover, the role of the cutoff in the momentum distribution consists in fixing the accessible astrophysical energy region, as given by:

$$\Delta E_{qf} = E_{Ax} - B_{xs} \pm E_{xs}, \quad (3)$$

where E_{Ax} is the beam energy in the center-of-mass of the two-body A - x system, B_{xs} represents the binding energy for the x - b system, and E_{xs} describes their inter-cluster motion within the chosen cutoff in momentum.

In this way, it is possible to extract the two-body cross section from Eq. (6) after inserting the appropriate penetration function P_l in order to account for the penetrability effects affecting the direct data below the

Coulomb barrier^{22,19}. The complete formula is given by:

$$\left(\frac{d\sigma}{d\Omega}\right) \propto \left[\frac{d^3\sigma}{dE_c d\Omega_c d\Omega_C}\right] \cdot [KF|\Phi(\vec{p}_s)|^2]^{-1} \cdot P_l. \quad (4)$$

If $|\Phi(\vec{p}_s)|^2$ is known and P_l and KF are calculated, it is possible to derive $(d\sigma/d\Omega)$ from a measurement of $d^3\sigma/dE_1 d\Omega_1 d\Omega_2$ by using Eq.(1).

When the projectile energy is not very high and off-energy-shell effects are not negligible, a more sophisticated approach based on a Modified Plane Wave Born Approximation (*MPWBA*)^{30,31}, turned out to be useful since Coulomb and off-energy-shell distortions in the two-body entrance channel are included^{21,23,24,25,26}.

4. Experimental Details and Results

As already mentioned, the THM applies to a suitable three-body reaction, which is performed in a kinematically complete experiment. The experimental set-up is optimized in order to cover the angular regions where the quasi-free process is expected to be favored. The two-body cross section is then extracted from the three-body coincidence yield within a spectator momentum window usually ranging from -30 to +30 MeV/c. Note that the deduced two-body cross section is the nuclear part alone, this being the main feature of the THM. In order to deduce the experimental $S(E)$ factor from the standard definition²¹, the nuclear cross section is multiplied by the proper transmission coefficient $P_l(E)$. An experimental program has already been undertaken to study proton capture reactions on ${}^6,{}^7\text{Li}$, main responsible for their destruction^{19,21,25,26}. The extracted astrophysical $S(E)$ factors for these reactions are shown in Fig. 1. Recently, proton capture reactions on ${}^{11}\text{B}$ and ${}^9\text{Be}$ were also investigated by selecting the quasi-free contribution to the ${}^{11}\text{B}(d,\alpha^8\text{Be})n$ and ${}^9\text{Be}(d,\alpha^6\text{Li})n$ three-body processes²⁹. Their importance is indeed strongly related to cosmology as well as to stellar structure and evolution^{33,34}. The $S(E)$ factor of the bare nucleus for the ${}^{11}\text{B}+p$ interaction is reported in Fig. 2. Moreover, we have performed the experimental study of the ${}^3\text{He}(d,p){}^4\text{He}$ ²⁷ reaction in order to get an independent estimate of the electron screening potential. This investigation can give more hints concerning the electron screening effect, responsible of the very pronounced enhancement in the cross section at low energy, significantly larger than could be accounted for from the adiabatic limit. Results are shown in Fig. 3. The THM was also applied to study the ${}^{15}\text{N}(p,\alpha){}^{12}\text{C}$ reaction via the break-up of ${}^2\text{H}$ nucleus. Its reaction rate affects the production of Fluorine, removing both protons and ${}^{15}\text{N}$ nuclei

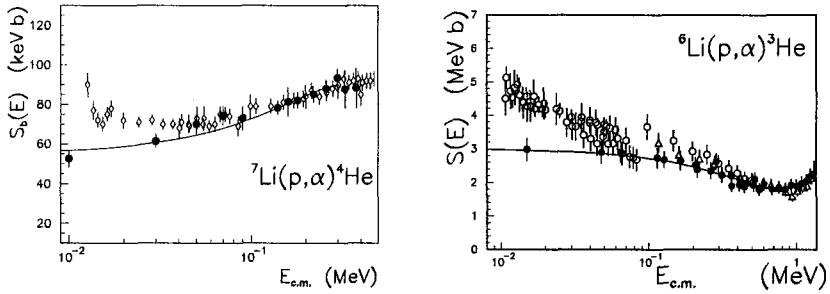


Figure 1. $S(E)$ factors for the ${}^7\text{Li}(p,\alpha){}^4\text{He}$ and ${}^6\text{Li}(p,\alpha){}^3\text{He}$ reactions. Full dots represent THM data, open symbols refer to direct data³². The solid line is the result of a second order polynomial expansion which gives in both cases the $S(0)$ value reported in Table 1.

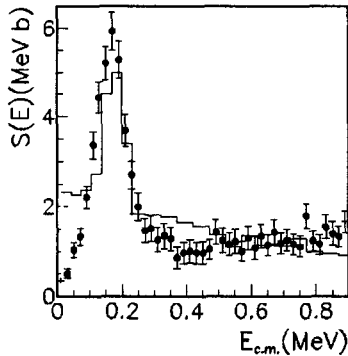


Figure 2. THMS(E) factor for the ${}^{11}\text{B}(p,\alpha){}^8\text{Be}$ reaction (full dots) compared with direct data (histogram)³⁵, both averaged out at the same bin energy of 20 keV.

from the ${}^{19}\text{F}$ production chain⁴⁴. This introduces a 8 % of uncertainty in the debated Fluorine surface abundance estimate. The indirect $S(E)$ factor is reported in Fig. 4, together with direct data and extrapolations. The normalization to the direct data was performed in all cases in an energy region where screening effects on the direct measurements are negligible. At energies above $E \sim 100$ keV, the agreement between direct and THM data sets is quite good, while they disagree at lower energies as expected, thus fully supporting the validity of the THM. Once parameterized the two behaviors, it was possible to get also independent estimates of the screening potential from one free-parameter fit. The resulting values together with the $S(0)$ parameters extracted from second order polynomial fits/R-matrix

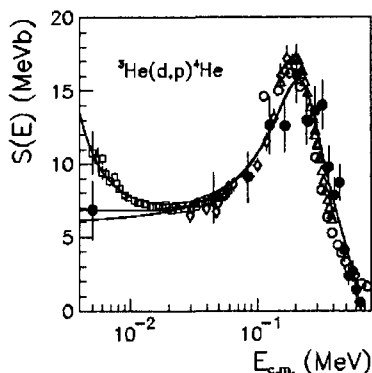


Figure 3. THM $S(E)$ factor for the ${}^3\text{He}(d,p){}^4\text{He}$ reaction (full dots) compared with direct data (open circles)^{37,38,39,40}. The solid line represents the result of the fit to get the $S(0)$ value²⁷.

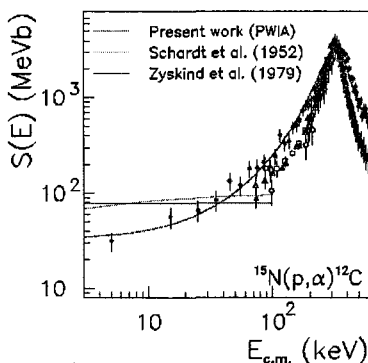


Figure 4. THM bare nucleus $S(E)$ factor for the ${}^{15}\text{N}(p,\alpha){}^{12}\text{C}$ reaction (full dots) compared with direct data (open symbols)⁴⁶. The solid red line represents the result of a fit on the THM data to get the $S(0)$ value⁴⁵. For comparison, the extrapolations from^{46,47} are also reported.

calculations on the data are quoted in Table 1. Values from direct experiments are also reported. The electron screening potential estimates are also reported, compared with the adiabatic limits and the extracted values in the direct experiments.

Our results, affected by smaller uncertainties than direct data, agree with both the extrapolated $S(0)$ and U_e direct estimates, with the exception of the ${}^{11}\text{B}+p$ $S(0)$ value which turns out to be a factor of 6 smaller than the direct estimate. This disagreement is not fully understood yet. A further

Table 1. Reactions studied via THM.

	$S(0)_{dir}$ (MeVb)	$S(0)_{THM}$ (MeVb)	$(U_e)_{teor.}$ (eV)	$(U_e)_{dir.}$ (eV)	$(U_e)_{THM}$ (eV)
${}^7\text{Li}(p,\alpha){}^4\text{He}$	0.058	0.055 ± 0.003	186	300 ± 160	330 ± 40
${}^6\text{Li}(d,\alpha){}^4\text{He}$	17.4	16.9 ± 0.5	186	330 ± 120	340 ± 50
${}^{11}\text{B}(p,\alpha_o){}^8\text{Be}$	2.1	0.31 ± 0.05	340	430 ± 80	
${}^6\text{Li}(p,\alpha){}^3\text{He}$	2.97	3.00 ± 0.19	186	450 ± 160	440 ± 100
${}^3\text{He}(d,p)\alpha$	6.51	6.0 ± 1.8	120	219 ± 7	180 ± 40
${}^9\text{Be}(p,\alpha){}^6\text{Li}$	16.4		240	800	
${}^2\text{H}(d,p){}^3\text{H}$	0.056		14	25 ± 5	
${}^{15}\text{N}(p,\alpha){}^{12}\text{C}$	65 ± 7	32 ± 6			

experiment is planned to study both ${}^{11}\text{B}(p,\alpha_o){}^8\text{Be}$ processes. Moreover, our U_e estimates for $p+{}^{6,7}\text{Li}$ processes confirm within the experimental errors the isotopical independence of the screening potential. The large discrepancy (about a factor 2) with the adiabatic limit (186 eV) is still present. As concerns with the ${}^3\text{He}+d$ interaction, the extracted U_e value (180 ± 40 eV) confirms the discrepancy with the adiabatic limit, while for the ${}^{15}\text{N}+p$ reaction, the result provides a reduced rate in the relevant energy region for astrophysics, confirming the value reported in CF88, in contrast with the one cited in the NACRE compilation.

5. Conclusions

The present paper reports the basic features of the THM together with a general review of recent applications to several relevant reactions in astrophysics. In particular, these results show the possibility to extract the bare nucleus two-body cross section via the THM, which has proven to be a powerful tool for measuring nuclear reaction cross sections at sub-Coulomb energies. However, a lot remains to be done in the future to obtain reliable information for many key reactions and processes, especially for the electron screening effects in fusion reactions where new theoretical developments are strongly needed to meet progress in the experimental field.

References

1. G. Baur and H. Rebel, *Annu. Rev. Nucl. Part. Sci.* **46**, 321 (1996).
2. A.M. Mukhamedzhanov, C.A. Gagliardi, and R.E. Tribble, *Phys. Rev.* **C63**, 024612 (2001).
3. C. Spitaleri *et al.*, *Nucl. Phys.* **A719**, 99c (2003).
4. C.J. Copi *et al.*, *Science* **627**, 192 (1995).
5. L. Piau and S. Turck-Chieze, *Ap.J.* **566**, 419 (2002).

6. U.G. Neudatchin, Y.F.Smirnov, *At. Energy Rev.* **3**, 157 (1965).
7. G. Jacob, Th. A. Maris, *Rev. Mod. Phys.* **38**, 121 (1966).
8. C. Spitaleri, *Problems of Fundamental Modern Physics II*, World Scientific, p. 21-35, 1990 and references therein.
9. M. Furic *et al.*, *Phys. Lett.* **B 39**, 629 (1972).
10. Dj. Miljanić *et al.*, *Phys. Lett.* **B 50**, 330 (1974).
11. J. Kasagi *et al.*, *Nucl. Phys.* **A239**, 233 (1975).
12. M. Zadro *et al.*, *Nucl. Phys.* **A474**, 373 (1987).
13. S. Blagus *et al.*, *Z. Phys. A-Atomic Nuclei* **337**, 297 (1990).
14. M. Zadro *et al.*, *Phys. Rev.* **C40**, 181 (1989).
15. G. Calvi *et al.*, *Phys. Rev.* **C41**, 1848 (1990).
16. G. Baur, *Phys. Lett.* **178B**, 135 (1986).
17. C. Spitaleri *et al.*, *Eur. Phys. J. A* **7**, 181 (2000).
18. G. Calvi *et al.*, *Nucl. Phys.* **A621**, 139c (1997).
19. C. Spitaleri *et al.*, *Phys. Rev.* **C60**, 055802 (1999).
20. M. Aliotta *et al.*, *Eur. Phys. J. A* **9**, 435 (2000).
21. M. Lattuada *et al.*, *Ap.J.* **562**, 1076 (2001).
22. S. Cherubini *et al.*, *Ap. J.* **457**, 855 (1996).
23. C. Spitaleri *et al.*, *Phys. Rev.* **C63**, 005801 (2001).
24. A. Musumarra *et al.*, *Phys. Rev.* **C64**, 068801 (2001).
25. A. Tumino *et al.*, *Nucl. Phys.* **A718**, 499c (2003).
26. A. Tumino *et al.*, *Phys. Rev.* **C67**, 065803 (2003).
27. M. La Cognata *et al.*, *Nucl. Phys.* **A758**, 98 (2005).
28. A. Rinollo *et al.*, *Nucl. Phys.* **A758**, 146 (2005).
29. C. Spitaleri *et al.*, *Phys. Rev.* **C69**, 055806 (2004) and references therein.
30. S. Typel and H. Wolter, *Few Body Syst.* **29**, 7 (2000).
31. S. Typel and G. Baur, *Ann. Phys.* **305**, 228 (2003).
32. S. Enstler *et al.*, *Z. Phys.* **A342**, 471 (1992).
33. R.N. Boyd and T. Kajino, *Ap. J.* **336**, 55 (1989).
34. A. Stephens and A.M. Boesgaard, *Astroph. Journ.* **491**, 339 (1997).
35. H.W. Becker *et al.*, *Z. Phys.* **A327**, 341 (1987).
36. A.J. Sierck and T.A. Tombrello, *Nucl. Phys.* **A210**, 341 (1973).
37. M. Aliotta *et al.*, *Nucl. Phys.* **A690**, 790 (2001).
38. W.H. Geist *et al.*, *Phys. Rev.* **C60**, 054003 (2001).
39. A. Krauss *et al.*, *Nucl. Phys.* **A465**, 150 (1987).
40. G.S. Chulick *et al.*, *Nucl. Phys.* **A551**, 255 (1993).
41. R.L. Schulte *et al.*, *Nucl. Phys.* **A192**, 609 (1972).
42. R.E. Brown and N. Jarmie *et al.*, *Phys. Rev.* **C41**, 1391 (1990).
43. H.S. Bosch and G.M. Hale, *Nucl. Fusion* **32**, 611 (1992).
44. M. Lugaro *et al.*, *Ap. J.* **615**, 934 (2004).
45. M. La Cognata *et al.*, *Eur. Phys. Journ.* (2005) to be published.
46. A. Redder *et al.*, *Z. Phys.* **A305**, 325 (1982).
47. J.L. Zyskind *et al.*, *Nucl. Phys.* **A320**, 404 (1979).

NUCLEAR ASTROPHYSICS EXPERIMENTS AT CIAE

WEIPING LIU*

ZHIHONG LI, XIXIANG BAI, GANG LIAN, BING GUO, SHENG ZENG,
SHENGQUAN YAN, BAOXIANG WANG, NENGCHUAN SHU
AND YONGSHOU CHEN

*China Institute of Atomic Energy, P. O. Box 275(1),
Beijing 102413, P. R. China*

This paper described the nuclear astrophysical studies using the unstable ion beam facility, GIRAFFE. We measured in inverse kinematics the angular distributions for some low energy reactions, such as ${}^7\text{Be}(d,n){}^8\text{B}$, ${}^{11}\text{C}(d,n){}^{12}\text{N}$, ${}^8\text{Li}(d,n){}^9\text{Be}$, ${}^8\text{Li}(d,p){}^9\text{Li}$ and ${}^{17}\text{F}(d,n){}^{18}\text{Ne}$, and derived the astrophysical S factors or reaction rates of ${}^7\text{Be}(p,\gamma){}^8\text{B}$, ${}^{11}\text{C}(p,\gamma){}^{12}\text{N}$, ${}^8\text{Li}(n,\gamma){}^9\text{Li}$, ${}^{17}\text{F}(p,\gamma){}^{18}\text{Ne}$ by asymptotic normalization coefficient approach at astrophysically relevant energies.

1. Description of unstable ion beam facility GIRAFFE

Aiming at the studies of nuclear astrophysics, the secondary beam facility (GIRAFFE)^{1,2} for producing and utilizing low energy beams of unstable nuclei has been constructed at the HI-13 tandem laboratory in 1993. The facility made use of the transfer and charge exchange reactions in inverse kinematics to yield some beams of unstable ions ($A < 20$) near the β -stability line with the acceptable intensities ($10^4 - 10^6$ pps). It comprises a primary reaction chamber, a dipole-quadrupole doublet (D-Q-Q) magnetic separation and focusing system, as well as a secondary reaction chamber, as shown in Fig. 1. Up to now, the ion beams of ${}^6\text{He}$, ${}^7\text{Be}$, ${}^8\text{Li}$, ${}^{11}\text{C}$, ${}^{13}\text{N}$, ${}^{15}\text{O}$, ${}^{17}\text{F}$ and ${}^{10}\text{C}$ have been delivered. They are summarized in Table 1. A velocity filter was installed between quadrupole doublet and focal plane by the end of 2004, which greatly improved the secondary beam purity.

*e-mail: wpliu@iris.ciae.ac.cn

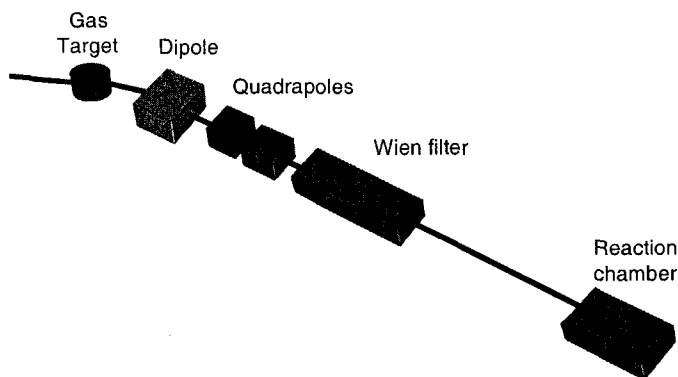


Figure 1. Sketch of GIRAFFE.

Table 1. Summary of the produced unstable ion beams at GIRAFFE.

RNB	Reaction	Energy (MeV)	FWHM (MeV)	Purity (%)	Beam intensity (pps) ^a
⁶ He	² H(⁷ Li, ⁶ He) ³ He	35.3	0.5	90	500
⁷ Be	¹ H(⁷ Li, ⁷ Be)n	23.0	1.3	99	1000
⁸ Li	² H(⁷ Li, ⁸ Li) ¹ H	39.0	0.5	90	500
¹¹ C	¹ H(¹¹ B, ¹¹ C)n	38.2	2.7	85	1000
¹³ N	² H(¹² C, ¹³ N)n	57.8	2.1	86	500
¹⁵ O	² H(¹⁴ N, ¹⁵ O)n	66.0	3.6	91	300
¹⁷ F	² H(¹⁶ O, ¹⁷ F)n	76.1	3.7	90	300
¹⁰ C	¹ H(¹⁰ B, ¹⁰ C)n	55.9	3.5	96	200

^aWith 2 mm diameter collimator and primary beam intensity 100–700 enA.

2. Experiments and theoretical analysis

The astrophysical S factor for the ${}^7\text{Be}(p,\gamma){}^8\text{B}$ reaction at solar energies is a crucial nuclear physics input for the “solar neutrino problem”. The S factor can be indirectly determined through the asymptotic normalization coefficient (ANC) ³ extracted from the proton pickup reaction of ${}^7\text{Be}$, with accuracy comparable to that from direct radiative capture or Coulomb Dissociation reaction, providing thus a significant cross examination. We measured the ${}^7\text{Be}(d,n){}^8\text{B}$ angular distribution in inverse kinematics at $E_{\text{cm}} = 5.8$ MeV and extracted the ANC for the virtual decay ${}^8\text{B} \rightarrow {}^7\text{Be} + p$ based on DWBA ⁴ analysis. The astrophysical S factor for the ${}^7\text{Be}(p,\gamma){}^8\text{B}$ reaction at zero energy was found to be $S_{17}(0) = 27.4 \pm 4.4$ eV·b ⁵. Our experimental data were re-analyzed by other groups, as shown in Fig. 5.

One of the key reactions in the hot pp chains is the ${}^{11}\text{C}(p,\gamma){}^{12}\text{N}$, which

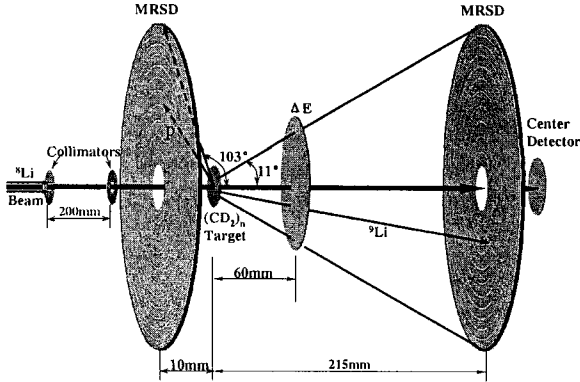


Figure 2. Experimental set-up.

is believed to play an important role in the evolution of Pop III stars. As a result of the low Q -value, its cross section at astrophysically relevant energies is likely dominated by the direct capture into the 1^+ ground state of ^{12}N , and the resonant captures into the first and second excited states of ^{12}N at 2^+ 0.960 MeV and 2^- 1.191 MeV, respectively. Angular distribution of the $^{11}\text{C}(d,n)^{12}\text{N}$ reaction at $E_{\text{cm}} = 9.8$ MeV was measured with the secondary ^{11}C beam. The experimental data were analyzed with DWBA calculations and thereby the $(\text{ANC})^2$ was extracted to be $2.86 \pm 0.91 \text{ fm}^{-1}$ for the virtual decay $^{12}\text{N} \rightarrow ^{11}\text{C} + \text{p}$. The zero energy astrophysical S factor for the direct capture $^{11}\text{C}(p,\gamma)^{12}\text{N}$ reaction was then derived to be $157 \pm 50 \text{ eV}\cdot\text{b}$. We have also estimated the contributions from resonant captures into the first and second excited states of ^{12}N and the interference between direct capture into the ground state and resonant capture into the second excited state. The astrophysical S factor of $^{11}\text{C}(p,\gamma)^{12}\text{N}$ in the astrophysically relevant energies are illustrated in Fig. 3. The temperature dependence of the direct capture, resonant capture and total reaction rates for $^{11}\text{C}(p,\gamma)^{12}\text{N}$ were derived ⁶. This work shows that the direct capture dominates the $^{11}\text{C}(p,\gamma)^{12}\text{N}$ in the wide energy range of astrophysical interest except the ranges corresponding to two resonances.

In the baryon inhomogeneous big-bang models for primordial nucleosynthesis, (IBBNs) ⁷, many nuclear reactions of unstable nuclei are involved, which can bridge the stability gap at mass number $A = 8$, and predict a higher production of elements beyond ^7Li and a larger universal mass-density parameter of baryons Ω_B . The reaction chains involving unstable nuclei ^8Li , ^9Li , ^8B , etc. are found to play a pivotal role in IBBNs. The

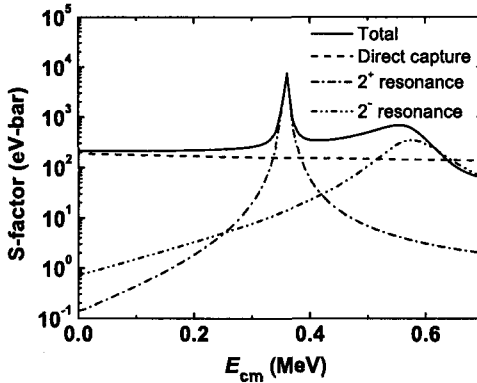


Figure 3. Deduced $^{11}\text{C}(p,\gamma)^{12}\text{N}$ astrophysical S factors.

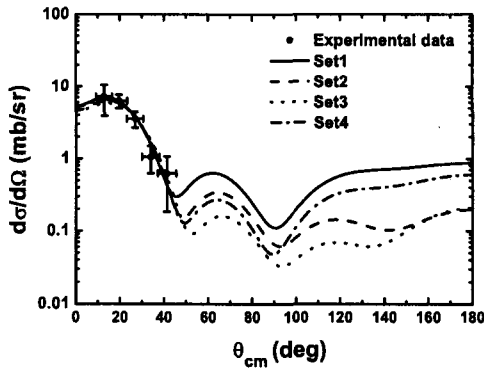


Figure 4. Angular distribution of $^8\text{Li}(d,p)^9\text{Li}$ at $E_{cm} = 7.8$ MeV.

production of succeeding heavier elements scales with the abundances of these unstable isotopes during primordial nucleosynthesis and thus all the reactions for generating or destroying them are of importance. We have measured the angular distribution of $^8\text{Li}(d,p)^9\text{Li}$ reaction at $E_{cm} = 7.8$ MeV through coincidence detection of ^9Li and recoil proton, and obtained the cross section and astrophysical S factor. By using spectroscopic factor deduced from the $^8\text{Li}(d,p)^9\text{Li}_{g.s.}$ angular distribution, we have successfully derived the $^8\text{Li}(n,\gamma)^9\text{Li}$ direct capture cross section and astrophysical reaction rate for the first time¹¹.

The typical experimental set-up for the $^8\text{Li}(d,p)^9\text{Li}$ reaction is shown in Fig. 2, the set-up of $^7\text{Be}(d,n)^8\text{B}$ reaction and that of $^{11}\text{C}(d,n)^{12}\text{N}$ were

described elsewhere^{5,6}, respectively. Two Multi-Ring Semiconductor Detectors (MRSDs) with center hole were used in this experiment. The upstream one aimed at detection of the recoil protons, and the downstream one served as a residue energy (E_r) detector, which composed a $\Delta E - E_r$ silicon counter telescope. This set-up enabled the ${}^9\text{Li}$ -recoil proton coincidence measurement. We applied the similar experimental set-up to other reactions except upstream MRSD. Such a detector configuration covered the full laboratory angular region. This setup also facilitated to precisely determine the accumulated quantity of incident unstable beams because the beams themselves were recorded by the counter telescope simultaneously.

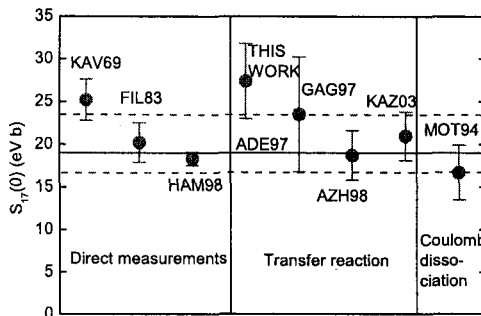


Figure 5. The ${}^7\text{Be}(p,\gamma){}^8\text{B}$ $S_{17}(0)$ factor by different approach.

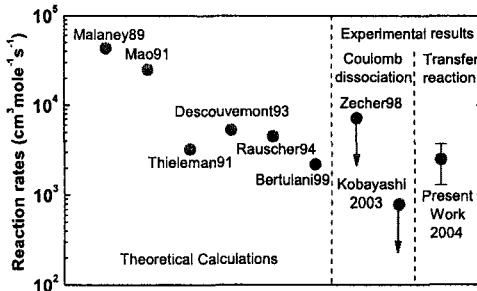


Figure 6. Comparison for reaction rates of ${}^8\text{Li}(n,\gamma){}^9\text{Li}$.

As examples, Fig.4 demonstrates the angular distribution of ${}^8\text{Li}(d,p){}^9\text{Li}$ reaction, where set1 to set4 refer to four sets of optical potential parameters; Fig. 5 shows the comparison of ${}^7\text{Be}(p,\gamma){}^8\text{B}$ $S_{17}(0)$ factor with other

measurements described in Ref. 8 and references therein; Fig.6 displays the reaction rate of ${}^8\text{Li}(n,\gamma){}^9\text{Li}$ derived through transfer reaction approach and those of theoretical calculations and Coulomb dissociation measurements presented in Ref. 9 and references therein. This data was also used to extract the ANC of mirror system by assuming the identical nuclear spectroscopic factor as a result of mirror symmetry¹². Recently the measurement of ${}^{17}\text{F}(d,n){}^{18}\text{Ne}$ reaction angular distribution at center-of-mass energy of 7.0 MeV was finished. The data analysis is underway; this data will be very important to determine the contribution of direct capture component of ${}^{17}\text{F}(p,\gamma){}^{18}\text{Ne}$ reaction.

All astrophysical reactions and their deduced parameters are summarized in Table 2.

Table 2. Summary of astrophysics experiment results.

Reaction	E_{cm} (MeV)	σ_{tot} (mb)	(ANC) ² (fm ⁻¹)	Indirect Reaction	S factor or reaction rate	Ref.
${}^7\text{Be}(d,n){}^8\text{B}$	5.8	58±8	0.711±0.090	(p,γ)	27±4 eV·b	5
${}^7\text{Be}(d,n){}^8\text{B}$	8.3	28±3	0.62±0.12	(p,γ)	24±5 eV·b	10
${}^{11}\text{C}(d,n){}^{12}\text{N}$	9.8	23±5	2.86±0.91	(p,γ)	157±50 eV·b	6
${}^8\text{Li}(d,p){}^9\text{Li}$	7.8	7.9±2.0	1.25±0.25	(n,γ)	3970±950 cm ³ mole ⁻¹ s ⁻¹	11
${}^8\text{Li}(d,p){}^9\text{Li}$	7.8	7.9±2.0	1.10±0.23 ^a	(p,γ) ^a	42±9 eV·b	12
${}^{17}\text{F}(d,n){}^{18}\text{Ne}$	7.0	tbd	tbd	(p,γ)	tbd	13

^aFor ${}^8\text{B}(p,\gamma){}^9\text{C}$ mirror system.

3. Summary

In summary, GIRAFFE, a tandem-based-one-stage unstable beam facility, proved to be effective to produce beams suitable for the study of nuclear astrophysics reactions. Angular distribution measurements of transfer reaction in inverse kinematics together with DWBA/ANC theoretical approach have been used to study the astrophysical reactions indirectly. The astrophysical S factors and/or reaction rates for ${}^7\text{Be}(p,\gamma){}^8\text{B}$, ${}^{11}\text{C}(p,\gamma){}^{12}\text{N}$, ${}^8\text{Li}(n,\gamma){}^9\text{Li}$, ${}^{17}\text{F}(p,\gamma){}^{18}\text{Ne}$ were deduced by using the measurements of ${}^7\text{Be}(d,n){}^8\text{B}$, ${}^{11}\text{C}(d,n){}^{12}\text{N}$, ${}^8\text{Li}(d,p){}^9\text{Li}$ and ${}^{17}\text{F}(d,n){}^{18}\text{Ne}$ reactions at the energies of astrophysical interest.

Acknowledgements

The above research programs were supported by the Major State Basic Research Development Program under Grant Nos. G200077400 and

2003CB716704, the National Natural Science Foundation of China under Grant Nos. 19935030, 10025524 and 10375096.

References

1. X. Bai, W. Liu, J. Qin *et al.*, *Nucl. Phys.* **A588**, 273c (1995).
2. W. Liu, Z. Li, X. Bai *et al.*, *Nucl. Instr. Meth.* **B204**, 62 (2003).
3. H. Xu, C. Gagliardi, R. Tribble, *Phys. Rev. Lett.* **73**, 2027 (1994).
4. P. Kunz, *computer code DWUCK4*.
5. W. Liu, X. Bai, S. Zhou *et al.*, *Phys. Rev. Lett.* **77**, 611 (1996).
6. W. Liu, Z. Li, X. Bai *et al.*, *Nucl. Phys.* **A728**, 275 (2003).
7. T. Kajino and R. N. Boyd, *Astrophys. J.* **359**, 267 (1990).
8. K. Ogata, M. Yahiro, Y. IseriH *et al.*, *Phys. Rev.* **C67**, 011602(R) (2003).
9. H. Kobayashi, K. Ieki, A. Horvath *et al.*, *Phys. Rev.* **C67**, 015806 (2003).
10. Y. Wang, W. Liu, X. Bai *et al.*, *Chin. Phys. Lett.* **16**, 873 (1999).
11. Z. H. Li, W. P. Liu, Z. H. Li *et al.*, *Phys. Rev.* **C71**, 052801(R) (2005).
12. G. Guo, W. P. Liu, Z. H. Li *et al.*, *Nucl. Phys.* (in press) (2005).
13. G. Lian, W. P. Liu, Z. H. Li *et al.* (unpublished).

GLOBAL REACTION MODELS RELEVANT TO THE p PROCESS *

SOTIRIOS V. HARISSOPOULOS

*Tandem Accelerator Facility, Institute of Nuclear Physics,
National Centre for Scientific Research "Demokritos",
POB 60228, 153.10 Aghia Paraskevi, Athens, Greece.
E-mail: sharisop@inp.demokritos.gr*

This contribution reports on a systematic work on cross section measurements of 22 ($p;\gamma$) and 7 (α,γ) reactions on nuclei in the Se-Sb region at energies well below the Coulomb barrier. The aim is to contribute to a cross-section database relevant to the modelling of the p process and to obtain global input parameters for Hauser-Feshbach (HF) calculations. The results are compared with HF calculations using various microscopic and phenomenological models of nuclear level densities (NLD) and optical model potentials (OMP).

1. Introduction

The trans-Iron elements are known to be synthesized in various stellar sites by three different mechanisms, the so-called s , r , and p processes. The first two develop via successive neutron captures, *i.e.* (n,γ) reactions that can be followed by β^- decays, thus producing most of the stable nuclei lying along the stability valley or "southeast" of it. These processes are comprehensively reviewed in Ref.[1]. Both the s - and r -process pathways bypass a class of 35 proton-rich nuclei, called p nuclei, which lie "northwest" of the stability valley between ^{74}Se and ^{196}Hg (see Fig.1 in Ref.[2]). The production of the p nuclei via the s and r processes is blocked by some stable ("seed") nuclei shielding them from the β decay of more neutron-rich isobars. Consequently, p nuclei are typically 10–100 times less abundant than the corresponding more neutron-rich isotopes. The most striking exception hereby is ^{92}Mo having an isotopic abundance of 14.8%.

*Supported by NATO (CRG961086), the German Academic Exchange Service (DAAD) and the Greek State Scholarship Foundation (IKY) within the IKYDA program.

The synthesis of the *p* nuclei requires a special mechanism known as *p* process that is extensively reviewed in Ref.[3]. This process has been described by various nucleosynthetic scenaria in which *p* nuclei are synthesized mainly by sequences of (γ, n) , (γ, p) and (γ, α) reactions. In some of these scenaria (p, γ) as well as (α, γ) reactions are also involved. So far, all the models of *p*-process nucleosynthesis are able to reproduce most of the *p*-nuclei abundances within a factor of 3, but they fail completely in the case of the light *p* nuclei. These discrepancies could be attributed to astrophysics uncertainties, *e.g.* those associated with the modelling of the preceding *s* process that provides the "seed" nuclei from which *p* nuclei are produced. However, nuclear physics uncertainties may also be involved because of the huge number of reaction cross sections needed to perform the extended reaction network calculations. A typical network includes more than 20000 reactions involving almost 2000 nuclei from Ga up to Bi as shown in Fig. 1. As the vast majority of these reactions refer to unstable nuclei, it is hardly possible to measure all the relevant cross sections. To overcome this problem, the Hauser-Feshbach (HF) theory is extensively used to calculate the relevant cross sections. The reliability of the HF calculations however can

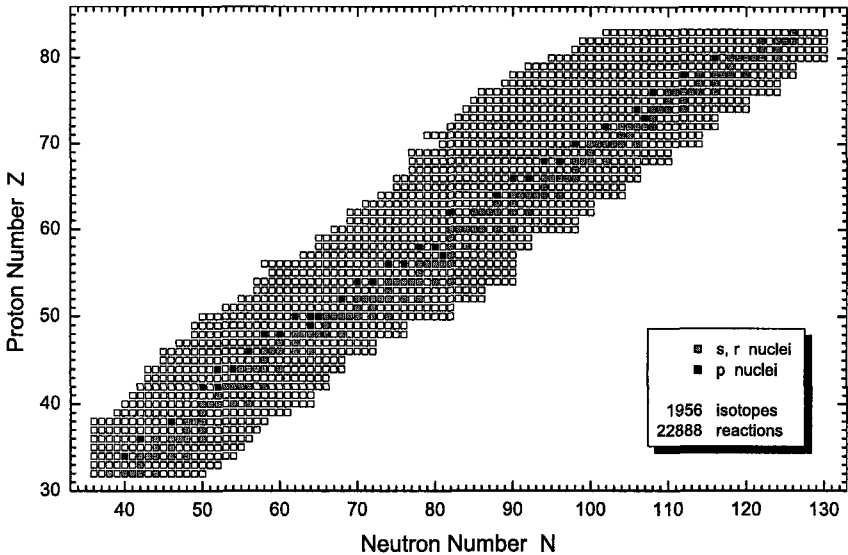


Figure 1. Chart of the nuclides involved in a typical *p*-process reaction network. The open squares correspond to unstable nuclei whereas the black ones to the *p* nuclei. Grey squares indicate stable nuclei produced by the *s* and/or the *r*process (from Ref.[4]).

be strongly affected by the uncertainties of the parameters entering the HF calculations. These refer mainly to the NLDs and the nucleon–nucleus and α -particle nucleus OMPs.

In view of these problems, we have performed several in-beam cross sections measurements of proton- as well as α -capture reactions in the Se-Sb region at energies well below the Coulomb barrier that are relevant to the p process. Such measurements can provide a sensitive reliability check of the existing OMPs and NLD models. Moreover, they can be used to improve the global features of these models and their ability to provide reliable predictions for a wide range of energies and atomic masses. The cross-section database obtained by our systematics can additionally be employed for the development of microscopic OMPs and NLD models. Such models can be of paramount importance for abundance calculations involving mass regions inaccessible in the laboratory. This is because the majority of the nuclei involved lie far from the valley of stability where no data exist and, therefore, the use of phenomenological approaches for OMPs and NLDs instead of microscopic ones may give rise to uncertainties.

2. Measurements and setups

The present work includes 22 (p,γ) and 7 (α,γ) reactions. The target nuclei for the (p,γ) reactions are shown in Fig. 2. The cross sections have been determined from γ -singles spectra taken in measurements of a) γ -angular distributions, b) angle-integrated γ fluxes and c) activations. The targets used in the former two types of measurements were highly enriched. The activation spectra of the Se isotopes were taken at the 5 MV Van de Graaff Tandem accelerator facility at “Demokritos”, Athens, using one HPGe detector of 50% relative efficiency to measure γ activities off-line in the 3–5 MeV region.

The γ -angular distributions were measured at the 4 MV DYNAMITRON accelerator at the University of Stuttgart by means of an array of 4 HPGe detectors with a relative efficiency of 100%. They were all shielded with BGO crystals for Compton suppression. This setup is described in detail in Ref.[2], where typical spectra and γ -angular distributions are also given. More details on this set of experiments as well as the data-analysis procedure are given in Ref.[4].

Angle-integrated γ fluxes have been measured at the 4 MV Dynamitron-Tandem-Laboratorium (DTL) of the University of Bochum using the setup shown in Fig. 3. This consists of a $12'' \times 12''$ 4π NaI summing monocrys-

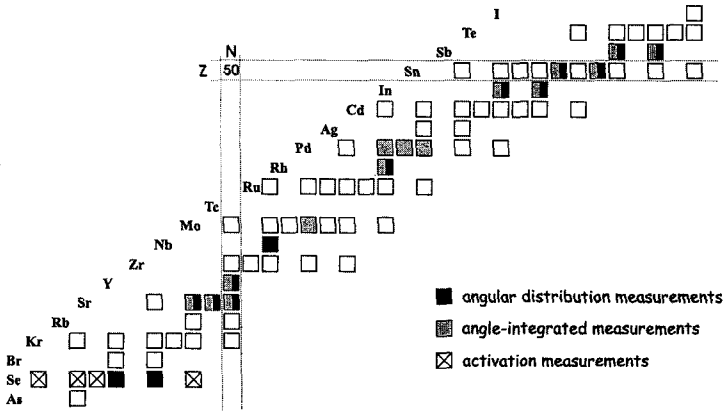


Figure 2. Stable target nuclei on which (p, γ) reactions have been studied. Targets used in γ -angular distribution measurements are indicated by black squares. Nuclei studied in angle-integrated γ -flux measurements are shown as grey squares. The hatched boxes refer to Se isotopes studied via activation.

tal of cylindrical shape with a borehole of 35 mm diameter along its axis. The targets were cooled with air and were placed at the center of the crystal, which covers a solid angle of $\approx 98\%$. Cross sections of (p, γ) reactions on the "grey"-shaded target nuclei of Fig. 2, as well as of (α, γ) reactions on ^{72}Ge , $^{91,92}\text{Zr}$, ^{92}Mo , ^{104}Pd , and $^{116,118}\text{Sn}$, have been measured with this setup. Typical spectra measured in these experiments can be found in Ref.[5], where more details on experimental procedures and the data analysis are also given. In addition to these experiments, angle-integrated cross-section measurements of the $^{89}\text{Y}(p, \gamma)^{90}\text{Zr}$ reaction have been per-

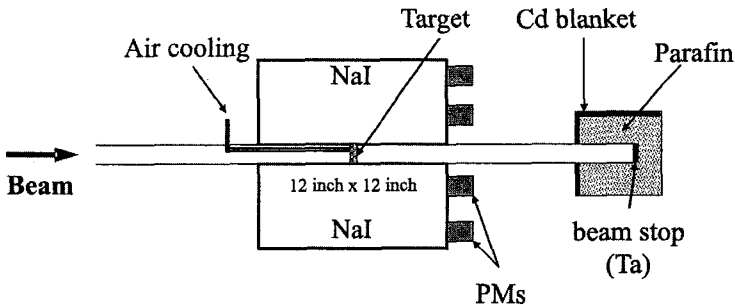


Figure 3. The 4π NaI summing monocrystal used to measure angle-integrated γ fluxes in DTL, Bochum (see text).

formed at "Demokritos", Athens, using a 12" × 12" 10-fold segmented NaI summing crystal. The latter work together with the experimental setup are presented in detail in Ref.[6]. Spectra of the latter reaction at $E_p=3$ MeV obtained with the 3 different setups mentioned above are shown in Fig. 4, to demonstrate their sensitivity in the detection of γ rays from proton capture reactions at energies far below the Coulomb barrier. As shown in Fig. 4, the spectrum taken with a HPGe detector of $\approx 100\%$ relative efficiency contains all the γ transitions de-populating the excited states of the produced nucleus. Of these γ rays, those feeding the ground state have to be analyzed at each angle measured (peaks marked in Fig. 4 with numbers indicating their energy). In addition to these peaks, the γ_0 transition, *i.e.* the primary γ ray de-exciting the entry level and feeding the ground state also has to be analyzed. Obviously, the data analysis can be time consuming. The main advantage of using HPGe detectors in these kind of measurements is that not only does the excellent energy resolution allows one to "follow" the

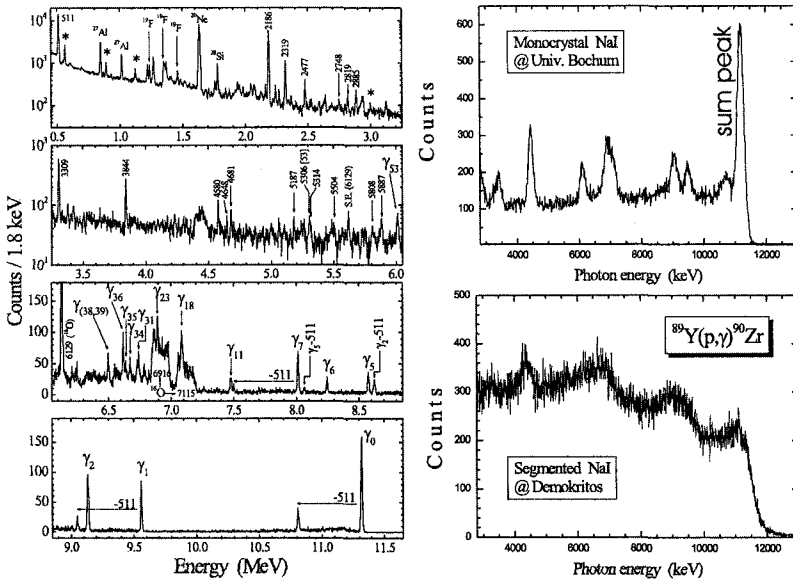


Figure 4. Gamma-singles spectra measured at 3 MeV for the $^{89}\text{Y}(p,\gamma)^{90}\text{Zr}$ reaction using a) a HPGe detector of 100% relative efficiency shielded with a BGO crystal for Compton Suppression (left panel), b) a 12 inch × 12 inch 4π NaI summing monocrystal and c) a 12 inch × 12 inch 4π NaI segmented crystal.

feeding pattern of the produced nucleus transparently, but above all, the absolute efficiency —one of the main sources of uncertainties in the data analysis— can be easily determined with an accuracy of 3-5%. On the other hand, the main advantage of using a 4π NaI(Tl) summing detector is that the response leads predominantly to a single peak, called *sum peak*, at an energy equal to the sum of the energies of the γ cascades stemming from the entry state of the produced nucleus. Such a sum peak is shown in Fig. 4 for a photon energy of ≈ 11.2 MeV. In addition, due to the 4π geometry covered by the detector, no γ -angular distributions have to be measured and, hence, the data analysis is a straightforward task as described in Ref.[5]. However, the main problem in using such a detector is the absolute efficiency, which may depend strongly on the —often unknown— decay pattern of the produced nucleus, *i.e.* on the multiplicity of γ cascades de-exciting the nucleus to the ground state. Hence, the absolute efficiency of such a detector has to be very well investigated in order to derive reliable results. In our case, this was done by measuring resonant as well as non-resonant reactions with very well known cross sections as described in Ref.[5].

3. Cross-section calculations

In the HF theory, the cross section for compound nucleus emission depends on a) the transmission coefficients for particle and photon emission, b) the nuclear level densities of the compound and residual nuclei in the different decay channels, and c) the Q-values of the involved nuclei.

To derive global input parameters for HF calculations, we took into account all existing cross section data of capture reactions on the targets displayed in Fig. 2. The calculations were carried out using the statistical model code MOST [7]. All available experimental data on nuclear masses, deformation, spectra of low-lying states, and GDR energies and widths were taken into account. The nuclear masses were taken from the compilation of Audi and Wapstra Ref.[8] and the ground state properties (matter density, single-particle level scheme) from the microscopic Hartree-Fock-BCS model of Ref.[9]. At the low incident energies studied in our experiments, the most dominant decay channels are those of photon and neutron emission, the α -particle emission channel becoming important at energies above ≈ 7 MeV. On the other hand, the effect of using different Lorentz-type or microscopic strength functions for the photon transmission coefficient turns out to be negligible. Therefore, in all the following calculations we adopt the same α -particle-nucleus potential of Demetriou *et al.* Ref.[10] and E1

strength functions given by the hybrid model of Goriely Ref.[11]. The M1 strength functions are parametrized according to Ref.[12] with the energies and widths chosen according to the latest recommendations of Ref.[13]. While the HF cross sections do not seem to be sensitive to the aforementioned nuclear ingredients, they show a strong dependence on the NLDs and nucleon OMPs. We, therefore, use different combinations of NLDs and OMPs in order to investigate the range of uncertainties they give rise to.

In particular, we use the OMPs of Koning and Delaroche Ref.[14], Jeukenne *et al.* Ref.[15] and Bauge *et al.* Ref.[16]. The first potential is purely phenomenological whereas the last two are based on microscopic infinite nuclear matter calculations applied with the local density approximation. We adopt two NLD formulae, namely the purely macroscopic formula of Thielemann *et al.* Ref.[17] and the statistical microscopic one of Demetriou and Goriely Ref.[19].

Five different combinations of these OMPs and NLDs have been considered in the HF calculations as follows: a) the microscopic NLDs of Demetriou and Goriely Ref.[19] with the OMPs of Jeukenne *et al.* Ref.[15], b) the same NLDs as in a) with the OMP of Bauge *et al.* Ref.[16], c) the same NLDs as in a) with the OMP of Koning and Delaroche Ref.[14], d) the macroscopic NLDs of Thielemann *et al.* Ref.[17] with the microscopic OMP of Jeukenne *et al.* Ref.[15] and e) the same NLDs as in d) with the phenomenological OMP of Koning and Delaroche Ref.[14].

4. Conclusions

From the comparison of all the existing (p,γ) cross sections with the predictions of the aforementioned combinations of OMPs and NLDs, one can conclude that the HF theory agrees with experiment within a factor 2–3. The predictions are more sensitive to the OMPs than to the NLDs used. Moreover, assuming always the microscopic NLDs of Demetriou and Goriely Ref.[19], we observe that the OMP of Bauge *et al.* Ref.[16] overestimates the data systematically, whereas the OMP of Jeukenne *et al.* Ref.[15] either reproduces the data satisfactorily or underestimates them by at most a factor of ≈ 1.3 . Finally, the OMP of Koning and Delaroche Ref.[14], shows no systematic behaviour, *i.e.* in some cases there is agreement, in others disagreement of at most 20-40%. The most important conclusion of astrophysical relevance, however, is that uncertainties of the above mentioned magnitude in the nuclear data input in nucleosynthesis calculations are of minor importance compared to the huge uncertainties (often exceed-

ing orders of magnitudes) associated with the "pure astrophysics" modelling. These findings however have to be further confirmed in the case of α -particle capture reactions. The data analysis of the (α, γ) cross sections measurements is in progress.

References

1. G. Wallerstein *et al.*, *Rev. Mod. Phys.* **69**, 995 (1997).
2. S. Galanopoulos *et al.*, *Phys. Rev.* **C64**, 015801 (2003).
3. M. Arnould and S. Goriely, *Phys. Rep.* **384**, 1 (2003).
4. S. Harissopulos, *AIP Conference Proceedings* **704**, 422 (2004).
5. S. Harissopulos *et al.*, *Nucl. Phys.* **A758**, 505c (2005).
6. P. Tsagari *et al.*, *Phys. Rev.* **C70**, 015802 (2004).
7. S. Goriely, in *Nuclei in the Cosmos V*, edited by N. Prantzos and S. Harissopulos, (Edition Frontières, Paris, 1998), p. 314 (see also <http://www-astro.ulb.ac.be>).
8. G. Audi and A. H. Wapstra, *Nucl. Phys.* **A595**, 409 (1995).
9. S. Goriely, F. Tondeur, and J. M. Pearson, *At. Data. Nucl. Data Tables* **77**, 311 (2001).
10. P. Demetriou, C. Grama, and S. Goriely, *Nucl. Phys.* **A707**, 141 (2002).
11. S. Goriely, *Phys. Lett.* **B 436**, 10 (1998).
12. J. Kopecky and R. E. Chrien, *Nucl. Phys.* **A468**, 285 (1987).
13. Reference Input Parameter Library, IAEA-Tecdoc-1034 (1998), (see also <http://iaeand.iaea.or.at/ripl>).
14. A. Koning and J. P. Delaroche, *Nucl. Phys.* **A713**, 231 (2003).
15. J. P. Jeukenne, A. Lejeune, and C. Mahaux, *Phys. Rev.* **C16**, 80 (1977).
16. E. Bauge, J. P. Delaroche, and M. Girod, *Phys. Rev.* **C63**, 024607 (2001).
17. F.-K. Thielemann, M. Arnould, and J. W. Truran, in *Advances in Nuclear Astrophysics*, edited by E. Vangioni-Flam, J. Audouze, M. Cassé, J.-P. Chieze, and J. Tran Thanh Van, (Editions Frontières, Gif-sur-Yvette, 1986), p.525.
18. P. Demetriou and S. Goriely, *Nucl. Phys.* **A695**, 95 (2001).

7. Large Facilities

This page is intentionally left blank

TRIUMF - CANADA'S NATIONAL LABORATORY FOR PARTICLE AND NUCLEAR PHYSICS

L. BUCHMANN
TRIUMF
4004 Wesbrook Mall
Vancouver B.C.
Canada, V6T 2A4

Throughout the last decade TRIUMF has developed into the only national laboratory in Canada dedicated to subatomic physics. Most of Canadian subatomic physics is indeed now either done at TRIUMF or one way or another supported by TRIUMF. The in-house physics at TRIUMF concentrates around the 500 MeV H^- cyclotron, though, in addition, there are three commercial cyclotrons for medical radioisotope production and another medical research cyclotron around. Research on the main cyclotron either uses the secondary π^- and μ^- beams or radioactive beams at the newly built ISAC facility. Details of the research done at TRIUMF will be reported with emphasis on ISAC and its future program.

1. General Information

The TRIUMF laboratory, a collaboration of several major Canadian universities, is situated on the campus of the University of British Columbia in Vancouver and centers around a large 520 MeV H^- cyclotron. TRIUMF was started in the early seventies by the construction of the accelerator and a few experimental facilities. This cyclotron was a revolutionary concept at its time for it allowed the extraction of several proton beam simultaneously. The energy of cyclotron was chosen to allow for the copious production of pions, and thus also muons. The cyclotron is still the very heart of TRIUMF's operation. Over the years many experimental facilities evolved: throughout the eighties new proton scattering and pion/muon beamlines were added. In this time the μSr technique evolved as a major resource for the investigation of condensed matter, in particular internal magnetic fields. At the same time radioisotope production for commercial purposes began at TRIUMF and is operated now by a company called MDS-Nordion, employing three medium energy cyclotrons. A reliable production of PET isotopes was also developed and is being continued for research at the UBC

hospital. In 1995 TRIUMF saw a major expansion from the outset of the construction of the ISAC facility which was followed in 2000 by an additional facility allowing to accelerate these beams to higher energies. An overview of the cyclotron and present facilities at TRIUMF is shown in Fig. 1

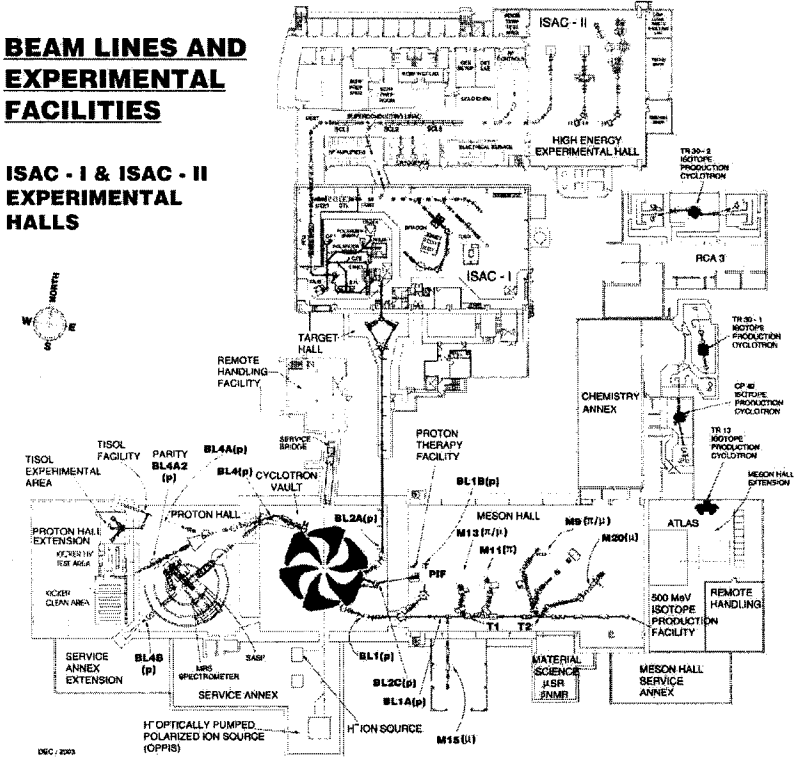


Figure 1. Overview of the TRIUMF complex. The shape of the cyclotron pole tips is indicated schematically.

2. The Cyclotron and Primary Beamlines

The TRIUMF cyclotron accelerates proton beams of up to $350 \mu\text{A}$ into several beamlines. The cyclotron is of about 20 m diameter. The diameter is chosen large to suppress relativistic magnetic stripping of H^- ions by having a relatively small magnetic field (7 kG). The poles of the cyclotron have a characteristic hill/valley structure (Fig. 1) which allows both focusing

and compensation for relativistic effects at the outside of the cyclotron. The cyclotron operates at 23 MHz. For servicing the upper magnet, the resonators (lid) of the cyclotron can be raised, see Fig. 2. The cyclotron



Figure 2. View of the inside of the TRIUMF cyclotron with lid raised.

beams are extracted by thin stripper foils leading to charge exchange and a switch of proton curvature in the magnetic field. Three extraction ports are used, numbered '1', '2', and '4'. Beamline 1A takes the majority of the current ($140 \mu\text{A}$, 520 MeV) and has two carbon or beryllium targets to produce pions and muons. Several secondary beamlines diverge from the two target points. Beamline 1B takes off from beamline 1A to the north and is used for irradiating materials at low currents.

Extraction port 2 serves two beamlines: Port 2C takes proton beams at the relatively low energies of 60-110 MeV. These are either used for commercial isotope production or proton eye tumor therapy. Port 2A serves a beamline running north to the ISAC facility. It is configured to take up to $100 \mu\text{A}$ at 500 MeV and has been operated to $70 \mu\text{A}$ on ISAC targets.

Beamline 4 has served several proton scattering experiments. It splits into two beamlines, 4A and 4B. Beamline 4A has housed a parity violating experiment and TISOL, the predecessor of ISAC. Beamline 4B houses two spectrometers that have been used in proton scattering experiments. These

experiments are inactive now and it is planned in the long term future to use an extension of beamline 4 as a second beamline for ISAC isotope production.

3. Non-ISAC Physics at TRIUMF

The range of physics done at TRIUMF is very wide and includes such subjects as condensed matter physics and life sciences. Only three examples are discussed below.

The TWIST experiment is placed at beamline M13 which starts at the first muon producing target in beamline 1A. The TWIST experiment does a precise measurement of the muon decay by doing precision spectroscopy of the decay positron. The polarized surfaced muon beam is stopped in the center of the detector. After decay the positron circles in the magnetic field of the detector where its momentum is precisely measured in a drift chamber that is inserted in the bore of the superconducting magnet. A fit to the spectrum allows to derive the so-called Michel parameters which can be predicted from the Standard Model. Values with improved precision compared to previous measurements of two of them have just been published.

The proton therapy program aims to cure certain kinds of eye tumours that are inoperable without losing eyesight. As the energy deposited per stopping length is the highest shortly before a charged particle comes to rest (Bragg peak), the protons from the cyclotron are brought to rest in the tumor while producing relative little damage in healthy tissue being still at high velocity. The patient treated is fixed by a special chair behind the end of beamline 2C.

One of the tools of condensed matter physics is now the μSr method. Muons from the decay of pions can be selected, polarized and implanted into materials. The positive variety will stop in the crystal lattice (while the negative one will be absorbed by some nucleus). There the μ^+ will decay. Because of the weak interaction nature of this decay, the decay will be asymmetric around the polarization axis. If a magnetic field is present in the solid, the magnetic moment will cause the polarization axis to rotate around the magnetic field. Thus, in a typical μ^+ decay experiment the decay curve will be sinusoidally modulated. By applying a RF field equal in frequency to the precision frequency of the muon around the magnetic axis, an absorption signal can be observed, and hence the strength of the magnetic field been measured. Several beamlines at TRIUMF are now

dedicated to the μ Sr user community all situated at the two primary targets of beamline 1A.

4. The External Program

As the only subatomic laboratory of larger size in Canada, TRIUMF has taken up the task of being an infrastructure laboratory for groups who have experiments at laboratories outside of Canada. In addition, some contributions to laboratories, where such groups are working, have been organized and often paid by TRIUMF.

The recent largest involvement of TRIUMF was with the LHC and the ATLAS detector there. Hitherto, TRIUMF has built or supervised the production of beam elements for the LHC accelerator chain and the main rings. These are now largely delivered and have been found satisfactory. In addition, parts of the liquid argon calorimeter for the ATLAS detector have been assembled at TRIUMF requiring a large clean room facility. For the future, an involvement in ATLAS computing is planned with computing facilities (clusters) at TRIUMF.

TRIUMF has been involved in the production of part of the detector for the g_0 experiment at the Jefferson Laboratory. There has been the construction of a manipulator system for source placement in SNO. TRIUMF is also involved in the construction of a near detector of the J2K neutrino oscillation experiment.

TRIUMF had a longtime involvement in the experiment E787 at the AGS at the Brookhaven National Laboratory which measured the pion-neutrino decay of the K^+ . This involvement has led to the independent funding of a detector laboratory named LADD at TRIUMF by the Canadian Foundation for Innovation.

5. The ISAC Facility

In 1995 it was decided to add a radioactive beams facility named ISAC to TRIUMF. The facility is of the ISOL type, *i.e.* the proton beam intercepts a massive solid target, held on high temperature by heating and/or the beam power. The radioactive atoms diffuse out of the target matrix, effuse from its surface and are guided into an ion source. After mass separation, they are either transported into a low energy area for decay studies or are accelerated by a RFQ-DTL chain to energies from 0.15 to 1.5 MeV/u for a charge-to-mass ratio better or equal than 1/30. The accelerated beam has been largely used for nuclear astrophysics studies. The facility is laid out

to tolerate $100 \mu\text{A}$ of proton beam on a Uranium target. The ISAC facility is shown in Fig. 3.

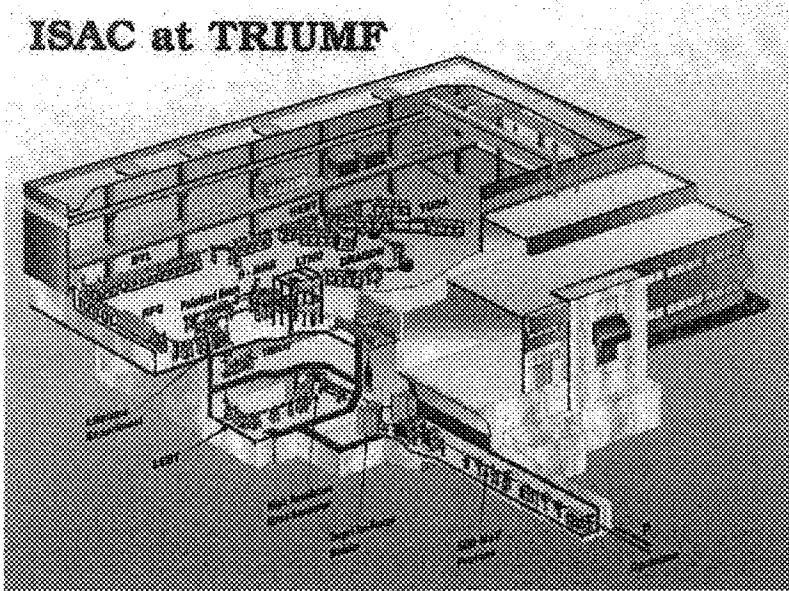


Figure 3. The ISAC facility at TRIUMF.

Because of the radiation produced by the proton beam, the two target ion source areas are in a special vault which allows for remote handling of these complex devices. In particular, the target-ion source is at the bottom of a two meter long iron plug that provides the primary shielding against the protons scattered from the target. Services are mazed through this plug. The plug can be remotely lifted and transported by a crane to hot cells where the target-ion source can be exchanged or repaired by manipulators.

The targets are typically contained in a 20 cm long tantalum tube and are often in the form of thin disks to keep diffusion lengths short. Several targets have been run so far, among them Ta and SiC with proton currents up to $70 \mu\text{A}$. A surface ion source, a laser source (TRILIS), and an ECR source are available.

The two beamlines from the east and west station join at the preseparator, where a coarse mass separation of the beam is performed. Better resolution is achieved at the high resolution mass spectrometer adjacent to

the target ion sources. After the desired mass has been separated, the beam is guided upstairs either into the TRINAT laser, atom trap laboratory, or to the ground level experimental hall where a multitude of experimental facilities are installed.

In the low energy area the 8π spectrometer and the GPS stations have been expanded by several facilities, including a β -detection array named SCEPTAR, a Si(Li)-array for E0 measurements and BaF₂ detectors. In these facilities detailed studies of electromagnetic decays following β -decay are performed including precision half life measurements.

A facility, which works similar as μ Sr has been installed in the ISAC hall named β NMR. In this case polarized ions are implanted into a probe and time and magnetic field dependent asymmetries in the β -decay are detected. The method is complementary to μ SR as the range of the radioactive ions (that can be even slowed down by a counterpotential) is shorter and the half lives are longer. The polarized ions, at the moment largely ⁸Li, are produced in a collinear laser-atomic beam arrangement by optical pumping. To obtain an atomic beam, the radioactive ion beam is neutralized in a sodium vapour cell and after polarization re-ionized in a helium gas cell.

A new mass measuring device, named TITAN, has been funded by NSERC and is now being installed in the ISAC hall. It is based on ionic Penning traps like similar devices worldwide, however ions will be in addition brought to a high charge state by an EBIS charge breeder. The unit consists of a RFQ trap to macrobunch the ion beam, the EBIS charge breeder, a first cooling Penning trap and a second precision Penning trap with subsequent ion detection outside. The commissioning of TITAN is planned for 2006.

Radioactive beams that are accelerated can be brought to three stations: a straight through one for general purposes, and the TUDA and the DRAGON facilities. TUDA is a scattering chamber with a geometry adapted to inverse kinematic experiments. Detectors and targets are rearranged for each experiment, but typically large area silicon detectors of the LEDA type (~ 26 cm diameter) are involved. TUDA has 512 separate channels of electronics available using peak sensing ADCs for high resolution and associated TDCs. The electronic is housed in a specially shielded and grounded shack.

DRAGON is a recoil separator to measure radiative capture reactions on typically Hydrogen or Helium targets, for largely astrophysical purposes. As the recoil particle and the beam approximately move with the same momentum in the same direction, DRAGON contains electrostatic benders

to separate the two beams. The target is a windowless gas target, where the emanating γ rays can be detected in a BGO array. After the target, the beam and recoils pass a bending magnet to separate to one charge state. Then, an electrostatic bender follows to separate recoil and beam particles. As scattered beam particles can mimic recoil ones, a second stage of the same configuration (magnet-electrostat) follows. Recoil particles are detected at the end of DRAGON in a silicon detector or an ionization chamber.

6. ISAC2 and the Future

In the year 2000 it was approved to boost the energy of the ISAC beam to 6.5 MeV/u. For this purpose a new building housing the accelerator and an experimental hall have been built, see Fig. 1. Initially the beam from the ISAC DTL will be used at 1.5 MeV/u and brought into a newly superconducting accelerator chain. The first helium cooled cavities of this accelerator were tested this July and indeed accelerated beam. The first stage of the accelerator going to 4.5 MeV/u will be ready by December of 2005. To allow the acceleration of masses higher than 30, a charge state booster, *i.e.* an ECR source with ion beam injection, will be installed close to the high resolution mass separator in early 2006. The energy of the superconducting linac will then be boosted in 2008 to 6.5 MeV/u. Eventually a bypass accelerator for the ISAC1 chain to allow more efficient acceleration of heavy masses ($A > 60$) will be installed.

Facilities available for ISACII will be a Germanium array in construction, named TIGRESS, and a spectrometer/separator now in the planning stage, named EMMA. TIGRESS will eventually have 12 large Germanium detectors, each of them separated into 8 segments with digital readout and γ -ray tracking. The first prototype detector has been proven now in beam to work properly. EMMA will be mounted behind a target station that can be configured with a selection of front-end detectors, among them TIGRESS or silicon detectors. EMMA consists of an electric dipole followed by a magnet and another electric dipole in a symmetric configuration like the FMA at Argonne.

More information about TRIUMF and its experiments can be found at www.triumf.ca. I wish to thank Alan Shotter for proofreading this manuscript.

STATUS OF THE AGATA PROJECT

E. FARNEA

*INFN, Sezione di Padova
via Marzolo 8,
35131 Padova, Italy
E-mail: farnea@pd.infn.it*

on behalf of the AGATA Collaboration

The AGATA project aims at the construction of an array of highly segmented, High-Purity Germanium detectors based on the novel concepts of pulse shape analysis and γ -ray tracking. The present status of the project is reviewed.

1. Introduction

In the past few years, many exciting results in the field of gamma spectroscopy have been obtained by using arrays of Compton-suppressed High-Purity Germanium (HPGe) detectors, which are extensively described in the review paper by Beausang and Simpson[?]. Given the technology on which such devices are based, it is apparent that the present generation arrays will not meet the requirements posed by the presently planned and under construction radioactive beam facilities.

In fact, as discussed thoroughly in the above mentioned work, these devices are characterized by a quantity, called the *resolving power*, which is proportional to the peak-to-total (P/T) ratio in the spectra and is inversely proportional to the *effective* energy resolution of the detectors. Following in-flight emission of the photons, the effective energy resolution is given in practice by the Doppler broadening caused by the finite solid angle covered by the individual counters, resulting in much worse values than the intrinsic detector resolution. In the case of radioactive beam facilities based on primary beam fragmentation and in-flight separation, where broad recoil velocity range and dispersion are expected, each individual counter should cover a very small solid angle to keep the effective energy resolution to acceptable values. As a consequence, in order to have a sufficiently high detection efficiency, which is obviously a major issue for any device oper-

ating in a radioactive beam facility where the expected beam intensities will be orders of magnitude lower than those at the present stable beam accelerators, an array should be composed of a very large number (even thousands) of such elements which would be impractical and economically unfeasible.

Concerning the P/T ratio of the spectra, which is, as discussed in the aforementioned work, the other important parameter for the resolving power of an array, it should be observed that at present the most widely used technique to increase such value is the use of anti-Compton (or Compton suppression) shields, that is, veto detectors shielded from the direct radiation and surrounding the individual Germanium counters. This technique is quite reliable, but has the drawback of limiting the maximum solid angle coverage (and therefore the detection efficiency) of an array because of the fraction of solid angle unavoidably covered by the anti-Compton shields.

In order to overcome the limitations discussed above, an alternative solution has been proposed and investigated in the past few years which implies investing on the signal processing software rather than on the detector hardware. This technique requires the use of highly electrically segmented Germanium crystals combined with digital electronics in order to identify the positions of the single energy depositions within the crystals through a detailed analysis of the signal shape (*pulse shape analysis*). The energies of the individual photons will be subsequently extracted by powerful algorithms of tracking the scattering sequences of each γ ray.

Presently two major projects aim at the construction of an array of High-Purity Germanium detectors based on the novel concepts of pulse shape analysis and γ -ray tracking: GRETA in the USA and AGATA in Europe.

In the following, the general ideas on which pulse shape analysis and γ -ray tracking are based will be described and the present status of the AGATA project will be discussed.

2. Pulse-Shape Analysis

As mentioned in Sec. ??, the experimental conditions at many of the planned radioactive beam facilities will be extremely harsh compared to the existing stable beam facilities because of the high recoil velocities and of the large recoil velocity dispersion. In order to perform a good quality Doppler correction, it will be of the outmost importance to determine the position of the first interaction of each photon at a much better level than

the usual assumption of the center of gravity of the whole crystal. The techniques to extract such information from the signal shapes are generically known as *pulse shape analysis*.

The state-of-the art pulse shape analysis techniques presently under development for AGATA involve the comparison of the digitized pulses from highly segmented Germanium crystals with a basis of reference signals, each of them corresponding to a well localized single interaction point. Ideally such basis should be constructed experimentally, but in practice this is not feasible and the basis is constructed via detailed electric field and charge transportation calculations[?]. The precision with which the interaction point can be extracted from the experimental pulses depends critically on the reference basis, therefore a large effort is being put into the calculation of as realistic as possible reference signals, which should then be compared with a few selected experimental points.

Several techniques are presently under development and test within the collaboration to perform the comparison of the experimental signals with the reference basis. Powerful computer codes exploiting ideas from the artificial intelligence fields, for instance genetic algorithms[?], have been shown to be quite reliable, although their present speed is not sufficiently high to be used for an on-line implementation at the counting rates foreseen for AGATA. The position resolution which can be achieved with these techniques is of the order of 5 mm FWHM for a low-energy photon, as shown by two in-beam tests performed respectively with the MARS segmented prototype[?] and with the GRETA prototype[?], which is certainly adequate for the requirements of the project. More schematic approaches such as grid searches have been shown to produce, in simple cases, results comparable to the most sophisticated algorithms[?]. The use of sophisticated mathematical tools, such as wavelet transformations, has been attempted recently within the collaboration and the preliminary results are promising (see for instance the contribution of P. Desesquelles in[?]).

3. γ -ray Tracking

In High-Energy Physics, the techniques to track the path of charged particles are well developed and commonly used. Photons, on the other hand, are quite different, since they do not release energy continuously along their motion, rather they deposit their energy in discrete steps, where each interaction point may be well separated from the other ones. Once the individual interaction points are known, it is in principle possible to reconstruct the

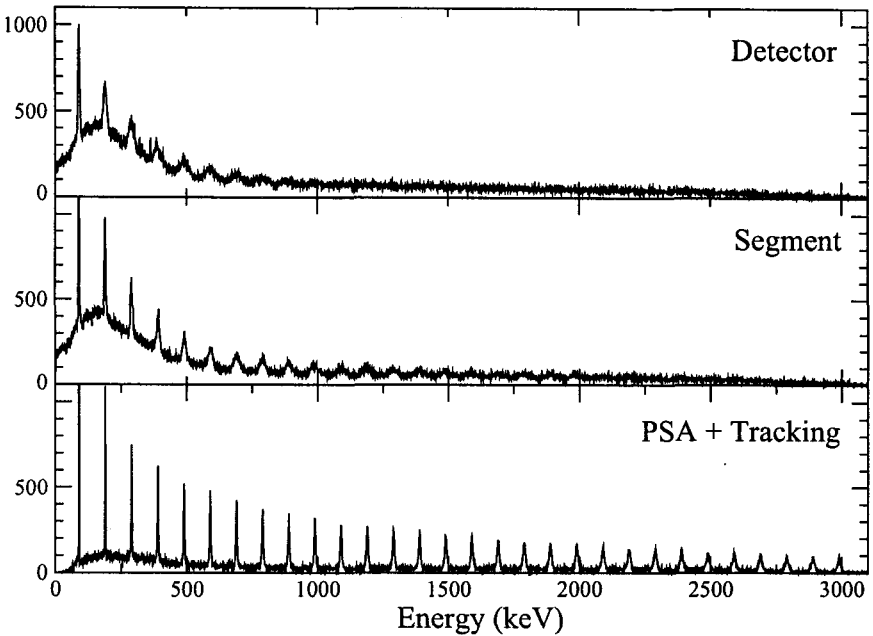


Figure 1. Comparison between the simulated spectra obtained with AGATA performing the Doppler correction respectively at the level of the whole detector, of a segment and of the first interaction point as extracted from the combination of pulse shape analysis and γ -ray tracking. The velocity of the emitting nuclei was $\beta = 50\%$.

scattering sequence of a photon, since for each Compton scattering there is a relation between the scattering angle and the energies of the incoming and of the scattered photon.

The case of a single interacting photon is actually not realistic, and in most cases the algorithm should disentangle the interaction points belonging to each photon before attempting the reconstruction of the scattering sequence. Since the number of permutations which should be explored would be too high to allow for a complete analysis, typically smaller clusters of points are extracted from the full set of points using proximity criteria based on the angular distance and on the effective distance in Germanium crystals⁷.

The state-of-the-art tracking algorithms developed for AGATA rely on two different (and complementary) approaches. In the case of the *forward tracking*, the scattering sequence is followed from the origin of the γ rays up to the last interaction point⁷. In the case of the *backward track-*

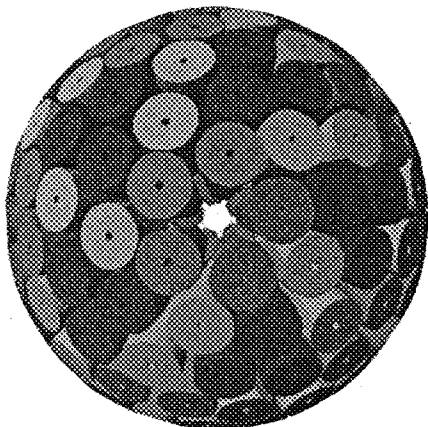


Figure 2. Pictorial view of the AGATA array.

ing, a candidate for the last interaction point is chosen exploiting the fact that a photoelectric absorption deposits typically an energy of the order of 100 keV, and the scattering sequence is followed backwards up to the origin of the radiation⁷. In both cases, clusters not satisfying the Compton scattering relation can be discarded, thus improving the P/T ratio of the spectra without the need for Compton suppression shields.

If a large solid angle is covered with segmented Germanium detectors, the combination of pulse shape analysis and γ -ray tracking allows for a very high photopeak efficiency together with a good P/T ratio, as will be shown later. In addition, the precise determination of the initial direction of each photon will allow for a good Doppler correction also at relativistic recoil energies, maintaining the quality of the spectra in conditions which would be prohibitive for the present arrays. This is exemplified by Fig. ??, where the same simulated data set is analyzed performing the Doppler correction at the detector, segment or interaction point level for a recoil velocity $\beta = 50\%$. Only in the latter case the high-energy peaks stand out.

4. Present Status of AGATA

4.1. Geometry

The final detector geometry for AGATA has been chosen and optimized on the basis of detailed Monte Carlo simulations for the full array⁷. The full

AGATA array will be constructed out of 180 crystals, having three irregular hexaconical shapes, grouped into 60 all-equal triple clusters within the same cryostat to minimize the amount of dead material in between. A pictorial view of the final geometry for AGATA is presented in Fig. ??, where each color corresponds to a different detector shape.

According to the simulations, such a configuration will cover 82% of the total solid angle. The efficiency of a tracking array will obviously depend both on the geometrical efficiency and on the tracking algorithm. Using the forward tracking code developed in Padova, one obtains photopeak efficiency values of approximately 43% for a single 1 MeV photons and 28% for a cascade of 30 photons of the same energy. In both cases, the P/T ratio is of the order of 60%. The photopeak efficiency values are impressively much higher than the present generation arrays, which combined with the excellent quality of the spectra already shown in Fig. ??, makes AGATA the ideal instrument to perform high resolution γ spectroscopy in the next future. It should not be forgotten, however, that in most cases additional beam tracking devices will be needed in order to maximize the quality of the spectra, as confirmed by the simulations⁷.

4.2. Prototypes

As mentioned earlier, AGATA will be built out of detectors having three different irregular hexaconical shapes, which will be electrically segmented into 36 parts and hermetically encapsulated under high vacuum. The very first prototype detectors purchased by AGATA have such characteristics, the major difference being that they have a regular hexaconical shape.

At the time of writing, the first three prototypes have been delivered and successfully tested at IKP Köln using the test cryostat shown in Fig. ??. Their performance with conventional electronics is very good, the resolution values for each segment being well within the specifications and the cross-talk between the segments being negligible. The three prototypes are presently being assembled into a triple cluster, which is going to be tested at IKP Köln in an in-beam experiment at the end of Summer 2005.

4.3. Electronics and data acquisition

The approach followed to perform pulse processing in AGATA is quite different than that with conventional detectors. Here, most of the pulse processing will be performed by computer algorithms rather than by dedicated analog electronics, except for the preamplifiers which are being developed

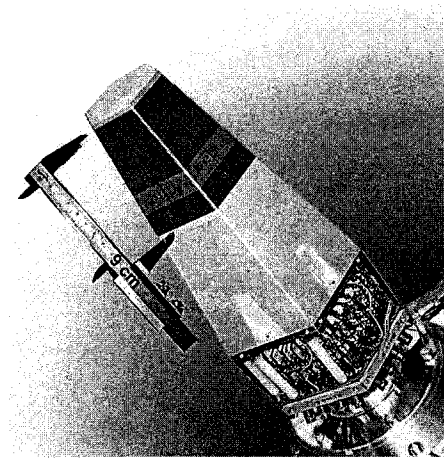


Figure 3. Picture of the first detector prototype for AGATA in its test cryostat.

specifically for the project and will be based on a hybrid design, having a differential output and a fast reset feature to allow for fast recovery in case of signal saturation⁷.

The preamplified signals will be digitized and transferred via optical fibres to powerful computer networks which, after performing pulse shape analysis and γ -ray tracking, will transfer the data to mass storage devices. A global time stamp will be distributed to the digitizers to allow for synchronization of the data coming from the different channels. In principle the system can work triggerless, although the possibility to form and distribute a trigger has been considered for the cases in which the data flux is too high.

The development of the electronics for AGATA is currently frozen until the completion and test of the prototype of the whole data processing chain, which is planned for the first half of 2006.

5. Future Perspectives of AGATA

The present Memorandum of Understanding of the AGATA collaboration covers the period until the end of 2007. The goal of this phase of the project is to prove the feasibility of the operation of a tracking array of Germanium detectors, where pulse shape analysis and γ -ray tracking will be performed on-line. This will be achieved by assembling a small array of AGATA triple clusters, which is normally referred to as the "Demonstrator Array", each

of them associated to the final electronics for AGATA.

According to the present plans, the Demonstrator Array should be composed of 15 crystals (5 triple clusters) with the final shapes for AGATA, which are being delivered starting from autumn 2005. The photopeak efficiency of such a small tracking device will range from 2% to 8% depending on the target to detector distance, meaning that, after the initial set-up phase, the Demonstrator Array could complement or replace existing devices such as CLARA⁷ or RISING⁷, taking advantage of the improved quality of the spectra due to the superior identification of the initial direction of the photons.

Assuming that the Demonstrator Array is successful, a new Memorandum of Understanding will have to be discussed within the collaboration. The full array will be assembled gradually, depending on the rate of funding and of detector production. A possible time schedule, yet unofficial, is to have 15 triple clusters, covering a solid angle of 1π , ready by 2010. Such an array would have a photopeak efficiency larger than 10% and could be used effectively for experiments at the radioactive beam facilities which should be operational at the time such as HISPEC at GSI Darmstadt, SPIRAL-2 at GANIL or SPES at LNL Legnaro. The full AGATA array might be available around 2018.

References

1. C.W. Beausang, J. Simpson, *J. Phys.* **G22**, 527 (1996).
2. Th. Kröll, D. Bazzacco, *Nucl. Inst. and Meth.* **A463**, 227 (2001).
3. Th. Kröll *et al.*, *LNL-INFN(Rep)* **182/2002**, 188 (2002).
4. D. Bazzacco *et al.*, *LNL-INFN(Rep)* **182/2002**, 184 (2002);
Th. Kröll *et al.*, *LNL-INFN(Rep)* **198/2003**, 153 (2003).
5. <http://radware.phy.ornl.gov/greta/news3>
6. R. Venturelli, D. Bazzacco, *LNL-INFN(Rep)* **204/2004**, 220 (2005).
7. http://npg.dl.ac.uk/AGATA/agata_week_talks/
8. G.J. Schmid *et al.*, *Nucl. Inst. and Meth.* **A430**, 69 (1999);
G.J. Schmid *et al.*, *Nucl. Inst. and Meth.* **A434**, 481 (1999).
9. J. Van der Marel, B. Cederwall, *Nucl. Inst. and Meth.* **A437**, 538 (1999);
L. Milechina, B. Cederwall, *Nucl. Inst. and Meth.* **A508**, 394 (2003);
A. Lopez-Martens *et al.*, *Nucl. Inst. and Meth.* **A533**, 454 (2004).
10. E. Farnea, D. Bazzacco, *LNL-INFN(Rep)* **202/2004**, 158 (2004).
11. F. Recchia, E. Farnea, D. Bazzacco, *LNL-INFN(Rep)* **202/2004**, 160 (2004).
12. A. Pullia *et al.*, *IEEE Trans. Nuc. Sci.* **51**, 831 (2004).
13. A. Gadea *et al.*, *Eur. Phys. J.* **A 20**, 193 (2004).
14. H.-J. Wollersheim *et al.*, *Nucl. Inst. and Meth.* **A537**, 637 (2005).

RESEARCH AT ISOLDE AND THE PATH TO EURISOL

P. A. BUTLER*

*ISOLDE, CERN
CH-1211 Geneva 23
Switzerland
<http://isolde.cern.ch>
E-mail: peter.butler@liverpool.ac.uk*

Through the advent of post-accelerated beams with REX-ISOLDE at CERN, probing nuclear properties using transfer reactions and Coulomb excitation of exotic nuclear species is now possible. REX ISOLDE currently provides beams of energy 3 MeV/nucleon into the gamma-ray MINIBALL array, and other instrumentation, at the secondary target position. Examples of research topics currently addressed using REX are presented. Scheduled energy up-grades will increase the physics potential even further. The goal for the next five years will be to accelerate ions up to 5 MeV/nucleon and higher energies. Increase of primary beam intensity will also be achieved in a phased approach, with a significant enhancement provided by the proposed Superconducting Proton Linac as the primary accelerator.

1. Introduction

ISOLDE is a collaboration that contains members from about 80 institutions worldwide. The experimental programme consists of 35–40 active experiments that make use of 5–10 independent spectrometers and other complex instruments in a typical year. The low-energy radioactive beams of exotic nuclei available at ISOLDE, unrivalled for many nuclear species in intensity, purity and beam quality, are crucial vehicles to understand the details of the nuclear many-body system at the extremes as well as increasing our knowledge about nuclear astrophysics and fundamental interactions and being an important tool for research in condensed matter and life sciences.

The experiments carried out at ISOLDE are diverse and state-of-the-art. In addition to a large range of detectors of different types for decay and

* permanent address: Oliver Lodge Laboratory, University of Liverpool, UK

in-beam experiments, there are instruments for laser spectroscopy and nuclear orientation of exotic nuclei, permitting studies of nuclear ground state properties far from stability. The triple-trap ISOLTRAP spectrometer can routinely achieve accuracies of 10^{-8} in mass measurements of unstable nuclei, and is complemented by the MISTRAL spectrometer that is able to measure masses of the most short-lived species such as ^{11}Li . In the last two years the Radioactive beam EXperiment REX-ISOLDE has been operational and is used to test new concepts of post acceleration of radioactive ions as well as use the accelerated beams for experiments in nuclear physics, astrophysics and solid state physics.

For a comprehensive review of activities at ISOLDE see Ref. 1

2. REX-ISOLDE

REX² makes use of the large variety of radionuclides that have been extracted from the on-line mass separator ISOLDE. In order to use these beams significant developments in beam cooling and charge breeding were required, as whereas the output of the ISOLDE primary mass separator is a quasi-DC beam (the intensity varies between the 1.2 s primary proton pulses according to the release characteristics and the nuclide half-life) having charge state 1^+ , the low duty-factor post accelerator requires multiply-charged ($A/q < 4.5$) pulsed beams. A schematic layout of the REX facility is shown in Fig. 1.

The first stage of the preparation of the ISOLDE beam is to continuously inject the beam from the mass separator into REXTRAP³ where it is cooled, accumulated and extracted as bunches. The accumulation and cooling is achieved by collisions with a buffer gas. In the collisions the loss of energy of the ion enables it to be trapped within a potential barrier. The barrier is reduced every 20 ms so that the accumulated ions are ejected as a 20 μs pulse. The transverse emittance of the beam is also reduced by the cooling procedure. This is important because the next stage, REXEBIS⁴(REX Electron Beam Ion Source), has a small acceptance (3 mm mrad). REXEBIS employs a 500 mA 5 keV electron beam that is focussed to a high current density (250 A / cm^2) by a 2 T axial magnetic field. The ion beam is confined longitudinally by applied electric potentials and undergoes stepwise ionization via electron collisions until its mean charge state has the desired value. For $A < 50$ the breeding time in REXTRAP to reach $A/q = 3-4$ is around 20 ms. For ^{133}Cs ions the breeding time was 80 ms.

The yield of the radioactive isotopes from ISOLDE can be several orders of magnitude lower than the amount of residual gas ions from C, N, O and Ar coming out of the EBIS. Therefore, a mass separator is employed with a q/A -resolution of about $1/150$ which is sufficient to select the highly charged rare radioactive ions from rest-gas contaminants.

In the first stage of the REX-ISOLDE linac the ions are accelerated from 5 keV/u to 300 keV/u by a 4-rod RFQ. In order to match the beam from the RFQ into the acceptance of the next stage IH (Interdigital-H-type)-structure (0.8–1.2 MeV/u), a section consisting of two magnetic quadrupole triplet lenses and a rebuncher is required. The high-energy section (0.8–3.0 MeV/u) of the linac consists of three 7-gap resonators and a 9-gap IH structure. Each resonator has a single resonance structure, which consists of a copper half shell and three arms attached to both sides of the shell. The 7-gap linac structures are operated at 101.28 MHz, while the 9-gap IH structure operates at a frequency of 202.56 MHz.

Through the advent of post-accelerated beams with REX-ISOLDE, probing nuclear properties using transfer reactions and Coulomb excitation of exotic nuclear species is now possible. REX ISOLDE currently provides accelerated beams to two secondary target positions, including the HPGe gamma spectrometer⁵ which in its present phase of operation has a full-energy peak efficiency of $\approx 10\%$ for a photon energy of 1 MeV. REX is operational and has already accelerated several species of radioactive ions, *e.g.* 10,000 ions/s of ^{29}Na ; it has the capability to accelerate mass 130 ions and heavier with efficiency of a few percent of the ion source yield. In 2003 REX-ISOLDE was integrated into the standard operation of CERN facilities.

3. Example of the ISOLDE Physics Programme: the Island of Inversion near ^{32}Mg

One of the first experimental evidences for changes in the structure of exotic nuclei from the conventional magic structure came from the observation of extra binding energy in $^{31,32}\text{Na}$ ⁶ at CERN thirty years ago. This was interpreted⁷ by Hartree-Fock calculations as arising from the dominance of intruder components in the ground state over normal components. The filling of the intruder orbits causes an inversion of the standard shell ordering and hence the breakdown of the $N = 20$ shell closure. The question remains, however, as to the exact nature of the mechanism that is mostly responsible for the behaviour of very neutron-rich nuclei, which have extreme

conditions of large N-Z-asymmetry and weak binding.

At ISOLDE recently two experiments have been carried out to elucidate the nature of the island of inversion for nuclei with $Z \approx 12$ and $N \approx 20$: one measuring the ground state properties of ^{31}Mg and one measuring the collective properties of ^{30}Mg .

3.1. Spin and Magnetic Moment of ^{31}Mg

In this experiment, using the online collinear laser spectroscopy setup at ISOLDE and described in Ref. 8 unambiguous values of the spin and magnetic moment of ^{31}Mg were obtained by combining the results of a hyperfine-structure measurement and a β -NMR measurement, both performed with an optically polarized ion beam. These measurements⁸ yielded a precise value for the ground state magnetic moment and a value for the ground state spin of $I = 1/2$. The authors were able to construct a revised level scheme that revealed the coexistence of 1p-1h and 2p-2h intruder states below 500 keV. In fact calculations using the most recent shell model interactions were unable to reproduce the experimentally observed level ordering, although the conclusion was made that the ground state is a nearly pure 2p-2h intruder state, confirming that ^{31}Mg is in the island of inversion.

3.2. Coulomb Excitation of ^{30}Mg

The $B(E2; 0_g \rightarrow 2_1)$ values for neutron-rich Mg isotopes also demonstrate no indication of a shell closure at $N = 20$ for $Z = 12$. There is, however, a rather large uncertainty on the measured values and for $^{30,32}\text{Mg}$ different groups employing the same experimental method (intermediate-energy Coulomb excitation) have obtained different results. This might indicate that systematic uncertainties are present in these measurements, such as the presence of Coulomb-nuclear interference, or the effect of feeding from the many higher-lying states that are excited in the single-step process.

One of the first experiments⁹ employed 2.25 MeV/u ^{30}Mg beams that are Coulomb excited by 1 mg/cm² Ni foils; the γ -radiation was observed using MINIBALL consisting of 8 3-module, 6-fold segmented HPGe detectors. The beam intensity was $\approx 2.10^4$ ions per second for a total irradiation time of 76 hours. In this experiment γ -ray spectra were recorded in coincidence with an annular, segmented silicon detector (CD detector) that detected forward scattered beam particles. The $2^+ \rightarrow 0^+$ transition in ^{30}Mg was clearly identified⁹. Figure 2 shows a comparison of the value of the $B(E2; 0_g \rightarrow 2_1)$ from this measurement with other experimental values for ^{30}Mg

and other Mg isotopes, and compared with theory. The REX-MINIBALL measurement is consistent with some of the measurements carried out using intermediate energy Coulomb excitation, and supports the conjecture that ^{30}Mg lies outside the island of inversion.

4. Future Upgrades of ISOLDE and REX

Scheduled energy and intensity up-grades will increase the physics potential of ISOLDE even further. The goal for the next five years will be to accelerate ions to 5 MeV/nucleon and beyond, with an increase of primary beam intensity to 5 μA or higher. This enhancement of the ISOLDE facility is called "High Intensity and Energy ISOLDE" or HIE-ISOLDE. The energy upgrade can be considered in two phases: (1) to increase the energy to 5.4 MeV/nucleon that enables certain classes of nuclear reactions to be used on a wide range of nuclei and (2) further increases in energy that will enable all reactions to be employed for all nuclei. The ISOLDE hall has already been extended in order to house the additional linac cavity resonators and other instrumentation such as new recoil spectrometers for detection of fusion products. Another new facility, REX*, will provide low energy radioactive ions from a charge breeder ion source either mounted on a high voltage platform or used in conjunction with a variable-energy RFQ. This will provide beams with continuously variable energy from < 100 keV to > 10 MeV for astrophysics and condensed matter studies.

In parallel with the energy upgrade, the proton beam intensity on the primary target will be increased. In the next few years, the available beam intensity from the PS booster, through the provision of H^- injected beam from a new primary injector linac (LINAC 4) and a faster cycling time in the PS Booster, will be increased three-fold, resulting in a significant increase in beam intensity available to ISOLDE. The development of primary target and ion-sources that can withstand these and higher beam intensities will be made in parallel with the intensity upgrade.

5. The SPL Project

CERN is currently considering the scientific case for a high power proton driver, the Superconducting Proton Linac¹⁰. This accelerator will provide > 2 GeV, 11 mA CW proton beams for enhanced injection to the PS and thence to the LHC, and to provide intense proton beams for neutrino production and to a next generation radioactive ion beam (RIB) facility. There are a number of scenarios for neutrino production. In the Neutrino

Factory the proton beam strikes a fixed target producing pions which are captured in a solenoidal channel where they decay into muons. The muons are subsequently cooled and accelerated before injection into a bow-tie or triangle shaped decay ring. A new concept for neutrino beams having strong synergies in accelerator and target technology with a RIB facility is the beta-beam¹¹ in which ${}^6\text{He}$ and ${}^{18}\text{Ne}$ radioactive ions are accelerated to a Lorentz gamma of ≈ 100 before injection into a decay ring, thus producing a flavour-pure beam of anti-neutrinos and neutrinos respectively.

For the next generation RIB facility, the leading European nuclear physics facilities have prepared a preliminary design based on the Isotope Separation On Line approach, called EURISOL¹². EURISOL is currently the subject of a EU VIth framework design study with 20 participating institutions from 14 countries and 21 other contributing laboratories. The high duty cycle of the CERN SPL (at least 150 μs available of the 2.8 ms pulse width, repeated at a frequency of 50 Hz) provides a good match to the specification of the primary driver of EURISOL. This will give a lower peak intensity of the proton beam than the present PS-Booster ISOLDE facility (thereby increasing the target lifetime), while the average current for direct RIB production can be increased to 100 μA or more compared to the present value of $\approx 2\mu\text{A}$. The higher proton energy will give an order of magnitude increase (over that from the existing ISOLDE facility) in the formation cross-sections for the light neutron rich target fragmentation products, while operating the SPL at lower energies than its nominal energy would permit the RIB production cross-section of the spallation products to be optimised. The high power available (4 MW) also allows the use of a spallation neutron target for production of intense beams of fission fragments in a secondary target.

The driver beam will be transported to both the existing ISOLDE facility and a new target area that is located underground. Post-accelerated RIB beams of energies up to and beyond 10 MeV/nucleon will be transported to at least three experimental areas, with possibilities to be explored of injection into the PS Booster to accelerate heavy radioactive ions to 100 MeV/nucleon or to inject into storage rings with electrons, muons, or antiprotons.

6. Outlook

ISOLDE at CERN is currently undergoing a renaissance in terms of its application to studies in nuclear, astro-, and condensed matter physics,

thanks to the advent of the post-accelerator REX. The planned upgrades in terms of beam energy and intensity, first HIE-ISOLDE later this decade and then SPL-ISOLDE, will ensure that ISOLDE remains a leading centre world-wide for research using accelerated radioactive ions.

References

1. D. Forkel-Wirth, G. Bollen (eds), *Hyperfine Interactions*, volume 129, 2000
2. F. Ames et al., CERN report 2005-009 (2005)
3. G. Bollen et al., *Nucl. Instrum. Meth. A*, 368 (1996) 675
4. B.H. Wolf et al., *Nucl. Instrum. Meth. B*, 204 (2003) 428
5. J. Eberth et al., *Prog. Part. Nucl. Phys.* 46 (2001) 389
6. C. Thibault et al., *Phys. Rev. C* 12 (1975) 644
7. X. Campi et al., *Nucl. Phys. A*251 (1975) 193
8. G. Neyens et al., *Phys. Rev. Lett.* 94 (2005) 022501
9. O. Niedermaier et al., *Phys. Rev Lett.* 94 (2005) 172501
10. B. Autin et al.: Conceptual design of the SPL, a high-power superconduction H^- Linac at CERN, CERN-2000-012, 2000
11. P. Zucchelli, *Phys. Lett. B*, 532 (2002) 166
12. J. Vervier et al., <http://www.ganil.fr/eurisol>

This page is intentionally left blank

Part II
Communications

This page is intentionally left blank

VARIOUS TYPES OF MEASUREMENTS FOR ATMOSPHERIC MUONS PERFORMED WITH THE WILLI DETECTOR

A. BERUCI, B. MITRICA, M. PETCU, I. M. BRANCUS, G. TOMA, AND
M. DUMA and J. WENTZ AND H. REBEL and O. SIMA

The electromagnetic calorimeter WILLI (Weakly Ionizing Lepton Lead Interaction), mounted in a rotatory frame measures the charge ratio and the flux of atmospheric muons in the energy range 0.4 - 1 GeV for prechosen azimuthal and zenithal direction. The measuring principle of the muon charge ratio is based on the different decay mechanism of positive and negative muons in matter, while for the flux the calorimetric method is used. The experimental setup permits the observation of the influence of the geomagnetic field on the muon charge ratio observable and fluctuations of the flux of low energetic muons, thus enabling sensitive tests of various simulations codes (e.g. CORSIKA). Recently the procedures of acquisition and analysis were automatized and the detector is ready for continuous data taking.

1. Introduction

Atmospheric muons are the penetrating component of the secondary cosmic radiation arising from the interaction of high - energy particles from the cosmos with the atomic nuclei of the Earth's atmosphere. This radiation is a feature of our environment and has a considerable impact on natural and man-made systems of our globe. More specifically, muons are mainly produced by the free decay of kaons and pions generated in hadronic interactions of primary Cosmic Rays (CR) or hadronic fragments with atmospheric nuclei. Having 2.2 μ s life time they transport valuable information about the CR spectrum and Extensive Air Shower (EAS) development to see level.

The detector WILLI used for the measurements of atmospheric muons is located near sea level at 44°26'N and 26°04'E. It is a prototype electromagnetic calorimeter registering the energy deposit of traversing muons and the decay time of stopped muons. The whole setup is mounted in a rotatory frame enabling directional measurements in a wide range of azimuthal and zenithal directions.

The studies reported here are directed towards two aspects. First the

muon charge ratio, $R_\mu = N(\mu^+)/N(\mu^-)$, is used to investigate simulations of EAS by CORSIKA¹. Secondly a method for measuring the muon flux is proposed for studying short time variation correlated with the solar activity.

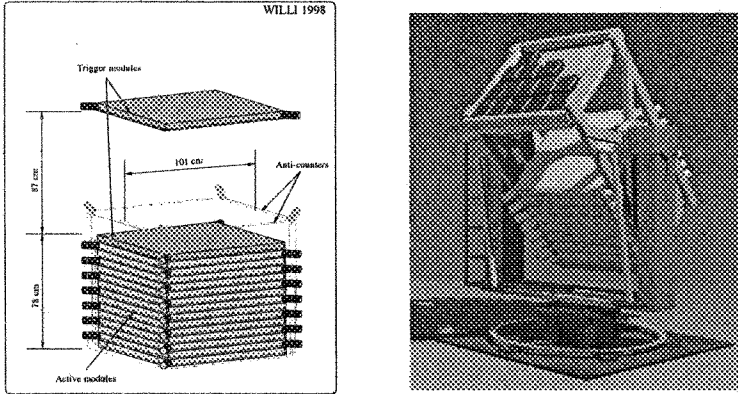


Figure 1. The WILLI detector. Schematic view (left) and artistic view (right)

2. WILLI Detector

The detector (see Fig. 1) is an electromagnetic calorimeter made of 20 scintillator plates. Each plate, a 1 m^2 NE-114 plastic scintillator mounted in a Aluminum box, is read out by two PMTs mounted on opposite corners. The body of the detector consists of 15 plates grouped compactly. The plates are arranged in such a way that the PMT axes of each one is perpendicular to the same axes of the neighboring one. Another plate is situated on top, at a distance of 87 cm from the body, for triggering reasons and 4 plates are situated on sides to provide anti-counter signals.

The information delivered by the detector for each trigger is the analog anode/dynode signal of each PMT and the time interval between the prompt and the delayed signal produced by decay products of stopped muons. The time window is opened for $51\ \mu\text{s}$ and read with a resolution of $20\ \text{ns}$. The detector is calibrated against simulations and the total (muon plus decay products) energy deposited per plate can be estimated for each event.

3. Muon Charge Ratio

The primary CR consist almost entirely of positively charged particles. The muon charge ratio $R_\mu = N_{\mu^+}/N_{\mu^-}$ is modified by the interactions in the atmosphere but it conserves the positive charge excess. At low energies ($E_\mu \leq 5 \text{ GeV}$) the muon charge ratio depends on the geomagnetic latitude and azimuthal direction.

In this studies, a less frequent method, the so called *delayed coincidence* method, is used for determination of R_μ ². It is based on the different decay time of μ^+ and μ^- when they are brought to rest in matter.

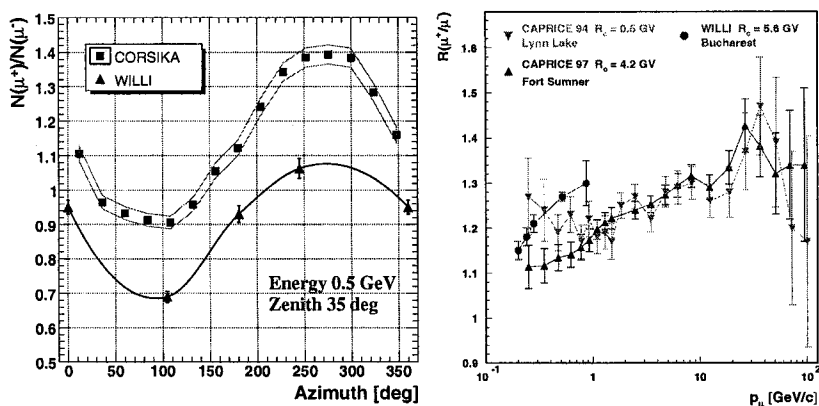


Figure 2. The dependance of the muon charge ratio on the azimuth angle compared with CORSIKA simulations (left). The dependence of muon charge ratio on momentum for vertical measurements of WILLI and CAPRICE (right).

To check our method and systematics, a comparison with CAPRICE data has been realized for vertical muons (see Fig. 2 right panel). In spite of different rigidities of the three measurements, the data are in the same range.

The dependence on the geomagnetic field of the muon charge ratio seen in the azimuthal dependence can be exploited to tune simulations codes of EAS like CORSIKA for consistency of geomagnetic field details. It has been shown that these features are very important when using CORSIKA for application like neutrino flux estimations³ or civil applications⁴. In the left panel of Fig. 2 the measurements done with WILLI are compared with CORSIKA simulations for four approximate directions: North (0°), East (105°), South (181°) and West (245°). A systematic shift of ≈ 0.2 in R_μ

was observed and its explanation is currently under investigation.

4. Muon Flux

The vertical energy spectrum of muons at sea level for low energies ($E_\mu \leq 5 \text{ GeV}$) depends on the geomagnetic latitude and solar activity. We will investigate the last feature by registering short time variations of the flux of stopped muons ($\approx 0.5 \text{ GeV}$). The method for muon flux estimation depends on the following ingredients:

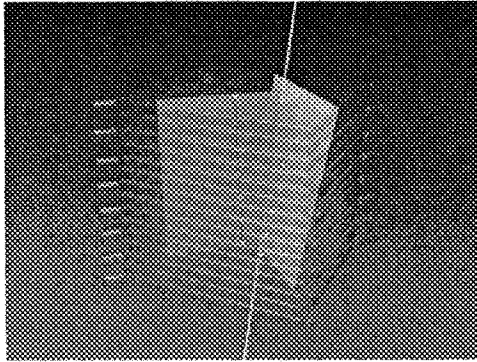


Figure 3. Evaluation of individual muon direction by registering the asymmetries of PMT's amplitude signals.

The energy of individual muons stopped in the calorimeter is determined by the sum of energy deposits in the scintillator plates corrected with CORSIKA simulations. The direction can be determined using the particular PMT's setup. In Fig. 3 the body of the detector is shown and the PMTs are marked by cylinders. It can be seen that half of the plates are oriented, as regard to the PMT axes, on one direction and half on the perpendicular. For each subset a plane can be determined by fitting the most probable impact points on each plate with a straight line. The muon direction is obtained at the intersection of the two planes. After a first evaluation an uncertainty of 10% can be reached for energy and 5% for direction. Data have been collected and will be analysed.

5. Conclusions

The detector WILLI is a small and easy to operate setup, enabling various kinds of studies with atmospheric muons. The muon charge ratio data can

be used for tuning EAS simulations codes like CORSIKA. Our analysis reveals that there are systematic differences between our measurements and estimations from simulations. Further investigations must be done for clarification. Muon flux can be estimated on same data sets as for charge ratio and its time variation can be correlated with the solar activity.

References

1. D. Heck *et al.*, *FZKA-Report 6019*, Forschungszentrum Karlsruhe (1998).
2. B. Vulpesu *et al.*, *Nucl. Instr. Meth. A*, **414** (1998) 205.
3. J. Wentz *et al.*, *Phys. Rev. D*, **67** (2003) 07320.
4. H. H. K. Tang, *IBM J. Res. Devel.*, **40**, no. 1 (1996) 91; J. O. H. Stone *et al.*, *Geochim. Cosmochim. Acta*, **62** (1988) 433.

FEW VALENCE PARTICLE (HOLE) EXCITATIONS AROUND DOUBLY-MAGIC NUCLEUS ^{132}Sn

E. DRAGULESCU AND D. TRANCOTA

Institute of Physics and Nuclear Engineering, P.O. Box MG-6, Bucharest-Magurele, Romania

Development of neutron-rich radioactive beams at the Holifield Radioactive Ion Beam Facility has stimulated experimental and theoretical studies in heavy Sn and Te isotopes. We report here the properties of the even $N=80$ and $N=84$ Sn and Te isotopes calculated in the framework of CVM2, assuming two neutron holes(particles) coupled to the quadrupole vibrator. The obtained energy levels, wave functions and electromagnetic transitions are compared with experimental data and previous calculations.

1. Introduction

It is well known that the doubly-magic ^{132}Sn nucleus shows the strongest shell closure and the nuclei with few valence nucleons around it have simple structure, as in the ^{208}Pb region. The few-valence-particle (hole) nuclei around doubly closed shell offer useful information on single-particle energies, nucleon-nucleon interaction and effective charges in this region of nuclei, being of great interest to study them both theoretically [1–5,10–15] and experimentally [5–9]. The ^{132}Sn region provides an excellent case for the application of spherical shell model in truncated spaces [1–5]. As one goes on increasing the number of valence particles (holes) at two, many collective features can appear. Some even-even nuclei around Pb or Sn show a “vibration like” structure — the violation of the simple harmonic vibrator selection and transition probability rules, the existence of quadrupole moments in excited states and the presence of new levels in the region of two phonon states, which do not show vibrational characteristics. The properties of nuclei from different regions of mass, but having these features, were explained in the framework of the cluster-vibration model for two particles (holes) coupled to a vibrator (CVM2) [10–16].

The region of neutron-rich Sn and Te nuclei with the number of protons and neutrons above and below $Z=50$ and $N=82$ closed shells was recently studied by means of Coulomb excitation of accelerated ion beams at HRIBF Oak Ridge using methods of nuclear γ -ray spectroscopy [5–9]. The results are

unexpected for ^{136}Te ($N=84$), where the $B(E2)\downarrow$ value for the first 2^+ state is low in comparison with the values for the $N=80$ ^{130}Sn and ^{132}Te nuclei.

2. Cluster-Vibration Model for two particles (holes) (CVM2) applied to Sn and Te nuclei around ^{132}Sn

A detailed description of the model is given in [10–14]. The $N=84$ isotones (^{134}Sn and ^{136}Te) are described as two neutron particles and the $N=80$ isotones (^{130}Sn and ^{132}Te) as two neutron holes coupled to ^{132}Sn vibrator. The present calculations were performed with the sets of parameters shown in Table 1. The parameters are chosen so as to obtain the best overall agreement with the observed properties (see Table 2, Figs. 1 and 2). Vibrational states up to three phonons are taken, and the neutron configurations for $N<82$ and $N>82$ used are those from G. A. Leander *et al* [15].

Table 1. Parameters used in present CVM2 calculations for $^{130,134}\text{Sn}$ and $^{132,136}\text{Te}$ nuclei

nucleus	E_2^+ [MeV]	$\hbar\omega_2$ [MeV]	A [MeV]	G [MeV]	e_{sp} [e]	e_{vib} [e]
^{130}Sn	1.221	1.280	0.20	0.20	0.5	0.66
^{132}Te	0.974	1.000	0.20	0.20	0.5	1.96
^{134}Sn	0.725	1.000	0.27	0.16	0.5	0.68
^{136}Te	0.607	0.800	0.35	0.15	0.5	1.23

Table 2. Electromagnetic properties calculated within CVM2 and their comparison with experimental data for $^{132,136}\text{Te}$ nuclei.

transition	^{132}Te		^{136}Te		
	$B(E2)\downarrow$ [e^2b^2]		$B(E2)\downarrow$ [e^2b^2]		
	CVM2	EXP	CVM2	SM [5]	EXP
$2_1^+ \rightarrow 0_1^+$	0.0344	$0.0344 \pm 0.0034^\dagger$ $0.038 \pm 0.006^\S$	0.02057	0.05	0.0206 ± 0.0003
$4_1^+ \rightarrow 2_1^+$	0.0525		0.01687		
$6_1^+ \rightarrow 4_1^+$	0.0033		0.01181		

state	^{132}Te					
	$Q_2(\text{eb})$		$\mu(\text{nm})$			
	CVM2	EXP	[4]	[3]	CVM2	EXP*
2_1^+	-0.008		0.960	0.982	0.756	0.70
4_1^+	-0.06		3.08		0.850	
6_1^+	-0.041		4.97		-1.24	

† Ref. 5, § Ref. 6 *Ref. 9

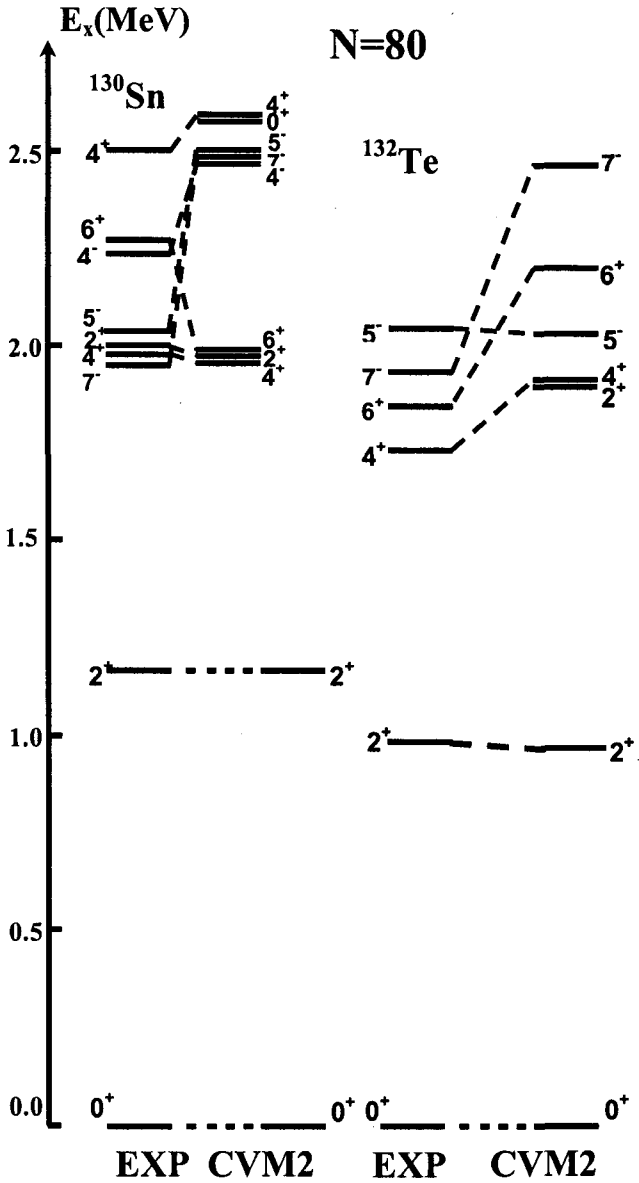


Figure 1. Comparison of the experimental and theoretical energy spectra for ¹³⁰Sn and ¹³²Te N=80 isotones.

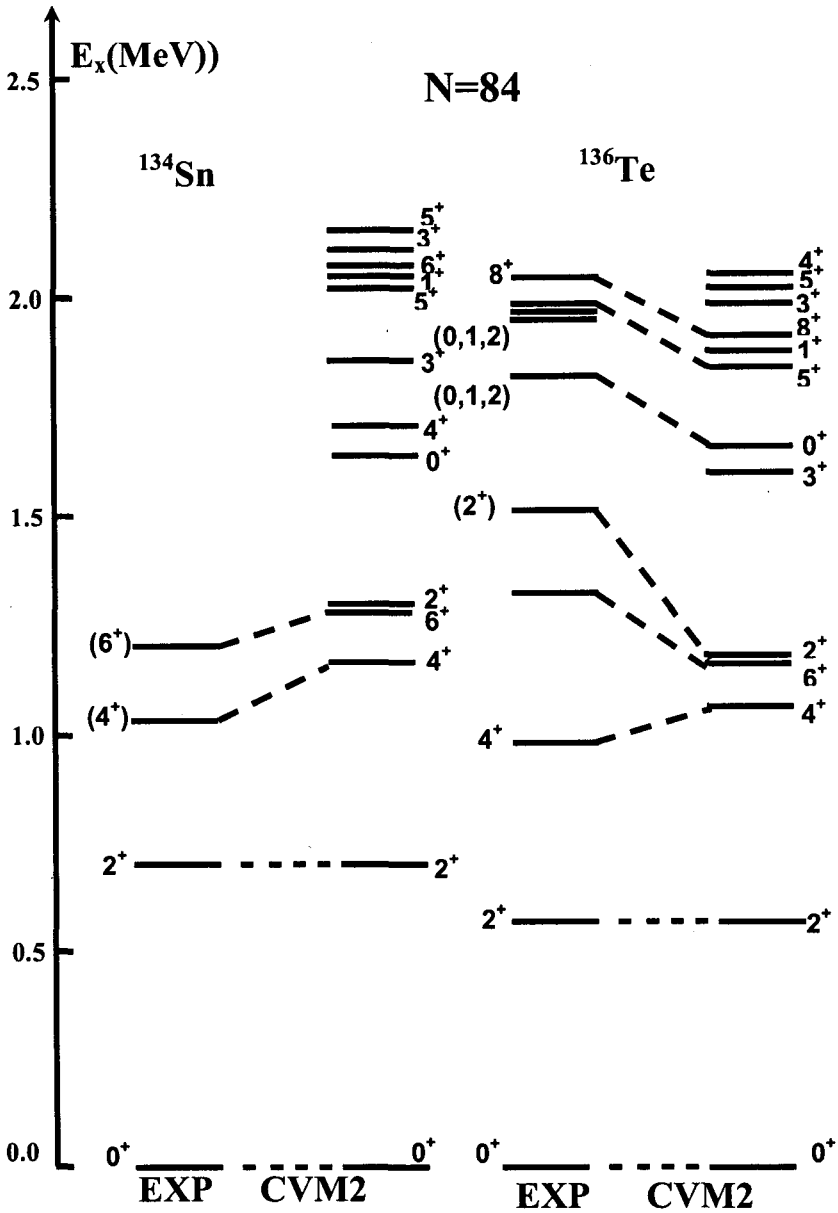


Figure 2. Comparison of the experimental and theoretical energy spectra for ^{134}Sn and ^{136}Te N=84 isotones.

3. Conclusions

The comparison of CVM2 results for energy spectra and for the electromagnetic properties show very good agreement with the existing experimental data for the $N=80$, 84 Sn and Te isotones. The agreement with experiment is comparable with that obtained in recent shell model calculations [2,4] and QRPA calculations [3] as far as spectra are concerned, and is better for the electromagnetic properties. The values of the neutron pairing strength are systematically lower as one crosses the $N=82$ gap. An increased collectivity for ^{132}Te ($N=80$) is due to the fact that two protons are added to ^{130}Sn and the distribution over different orbit is changed. The e_{VIB} is decreased for ^{136}Te ($N=84$) due to the changes produced in the phonon cloud (protons and neutrons) and its interaction with the cluster (two neutrons). We hope that new experimental data on electromagnetic properties, as magnetic and quadrupole moments, would validate our understanding of the structure of nuclei around ^{132}Sn .

References

1. H. Wildenthal and D. Larson, *Phys. Lett.* **B 37**, 266 (1971).
2. S. Sarkar and M.S. Sarkar, *Phys. Rev.* **C64**, 014312 (2001).
3. J. Terasaki *et al.*, *Phys. Rev.* **C66**, 054313 (2002).
4. B. A. Brown *et al.*, *Phys. Rev.* **C71**, 044317 (2005).
5. D.C. Radford *et al.*, *Phys. Rev. Lett.* **88**, 2225 (2002).
6. C. J. Barton *et al.*, *Phys. Lett.* **B 551**, 269 (2003).
7. D.C. Radford *et al.*, *Eur. Phys. J.* **A 15**, 171 (2002).
8. R. O. Hughes *et al.*, *Phys. Rev.* **C69**, 051303(R) (2004).
9. N. J. Stone *et al.*, *Phys. Rev. Lett.* **94**, 192501 (2005).
10. G. Alaga and G. Ialongo, *Phys. Lett.* **B 22**, 619 (1967).
11. G. Alaga, F. Krmpotic and V. Lopac, *Phys. Lett.* **B 24**, 537 (1967).
12. V. Lopac, *Nucl. Phys.* **A155**, 513 (1970).
13. V. Paar, *Nucl. Phys.* **A185**, 544 (1972).
14. V. Lopac and V. Paar, *Nucl. Phys.* **A297**, 471 (1978).
15. G. A. Leander *et al.*, *Phys. Rev.* **C30**, 416 (1984).
16. E. Dragulescu *et al.*, (to be published).

POSSIBLE E(5/4) SYMMETRY IN ^{135}Ba

M. S. FETEA^{1,2}, R. B. CAKIRLI^{2,3}, R. F. CASTEN³ AND D. D. WARNER^{2,4}

¹*Department of Physics, University of Richmond, Richmond, VA 23173, USA*

²*WNSL, Yale University, New Haven, CT 06520, USA*

³*Department of Physics, University of Istanbul, Istanbul, Turkey*

⁴*SERC Daresbury Laboratory, Warrington WA44AD, UK*

The nucleus ^{135}Ba was investigated as a possible candidate for E(5/4), a non-trivial example of critical point symmetry in odd mass nuclei, for the case of a γ -soft liquid drop with quadrupole deformation coupled to a particle with $j = 3/2$. Comparison of the E(5/4), Interacting Boson-Fermion Approximation, Particle-Vibrator Coupling Model and Shell Model calculations with the data are presented.

Dynamic symmetries are related to exactly solvable problems through analytic solutions. In the framework of the interacting boson approximation (IBA)[?], the symmetries behind harmonic vibrators, γ -unstable nuclei, and deformed symmetric rotors have been codified in terms of the U(5), O(6), and SU(3) limits[?]. While symmetries represent stable limits of structure, most nuclei are placed in regions of structural changes. A new class of symmetries^{?,?} describes systems undergoing phase transitions between dynamical symmetries mentioned above.

For even-even nuclei, two analytic solutions for the Bohr Hamiltonian – X(5)[?] and E(5)[?] – expressed in terms of the zeros of the special Bessel functions, offer predictions for energies and electromagnetic transition probabilities. The E(5) symmetry, at the phase transition between the γ -soft U(5) and the O(6) limits, is less explored and only two examples, ^{134}Ba [?] and ^{102}Pd [?] have been proposed. A non-trivial example of a special solution called E(5/4) has been recently worked out[?] for the case of a liquid drop with quadrupole deformation coupled to a particle with $j = 3/2$. It is the purpose of this work to provide the first test of the E(5/4) critical point symmetry for an odd- A nucleus, ^{135}Ba . To provide a perspective for the E(5/4) description, we also performed shell model (SM), interacting boson-fermion approximation (IBFA) and particle-vibrator coupling model calculations (PVCM).

Since ^{134}Ba is an E(5) example, ^{135}Ba is a possible E(5/4) candidate. Because the $d_{3/2}$ neutron is in a "hole" state, the proper core for the ^{135}Ba should be ^{136}Ba , which is not a E(5) core. Also, although ^{133}Ba would have a ^{134}Ba , therefore an E(5) core, its ground state is $1/2^+$, indicating that this nucleus is not suitable for an E(5/4) search. The energy and $B(E2)$ values of the existing data⁷ and the E(5/4) predictions⁷ are shown in the upper left and lower right panels of fig. ??, respectively. For E(5/4), only the $B(E2)$ values of transitions that had a known corresponding value in the data have been plotted. Although related to E(5), except for an overall energy scale factor and an effective charge for the $E2$ rates, the E(5/4) predictions are parameter free⁷. In fig. ??, we fitted the $5/2_1^+$ level in E(5/4) to the corresponding level in ^{135}Ba to get energy levels closer to the experimental ones than when the 2_1^+ energy of E(5) is fitted to the 2_1^+ energy of ^{134}Ba data⁷. A few key $B(E2)$ values and absolute transition rates need to be known before one can make a definite comparison of the E(5/4) with the existing data. An experiment that will allow us to determine absolute transition rates or upper limits for the spin allowed $1/2_2^+ \rightarrow 1/2_1^+$, $1/2_2^+ \rightarrow 3/2_2^+$, $3/2_3^+ \rightarrow 1/2_1^+$, and $3/2_3^+ \rightarrow 3/2_2^+$ transitions, and to re-measure the questionable data on $3/2_3^+ \rightarrow 5/2_1^+$ and $3/2_2^+ \rightarrow 5/2_1^+$ transitions was proposed and has been performed at Yale.

Using the IBFA Hamiltonian $H = H_{sd} + H_F + V_{BF}$, where H_{sd} represents the pure boson part, and H_F is the single nucleon degree of freedom part, and using a simple choice of boson-fermion interaction V_{BF} ⁷, we performed IBFA calculations for a $d_{3/2}$ neutron hole with a single particle energy (SPE) of 0.0 keV, and a $s_{1/2}$ neutron hole with a SPE of 211 keV. Calculations with coupling to either a ^{134}Ba or ^{136}Ba core were carried out. The results are similar except for overall scale and we show the former here. In the notation of IBFA⁷ code ODDA⁷, other parameters used in the calculation are: $pair=0.148$ MeV, $oct=0.002$ MeV, $ell=0.02$ MeV, $eps=0.92$ MeV, $qq=-0.016$ MeV, $chq=0.0$ MeV, $nphmax=5$, $chi=0.0$ MeV, $bfm=-0.32$ MeV, $bfq=0.1$ MeV, and $bfe=0.0$ MeV.

The IBFA wavefunctions indicate that about 99% of the $3/2_1$ state is built on the 0^+ of the core coupled to the $d_{3/2}$ neutron hole and 0.8% of the state is built on the 0^+ of the core coupled to the $s_{1/2}$ neutron hole. Thus, this state, and the others dominated by a $d_{3/2}$ amplitude, should be amenable to the E(5/4) description. In contrast, 18% of the $1/2_1$ state is built on the 0^+ core state coupled to the $d_{3/2}$ neutron hole and 82% of the state is built on the 0^+ core state coupled to the $s_{1/2}$ neutron hole. The $1/2_1$ of E(5/4) therefore corresponds to the $1/2_2$ in the IBFA calculation,

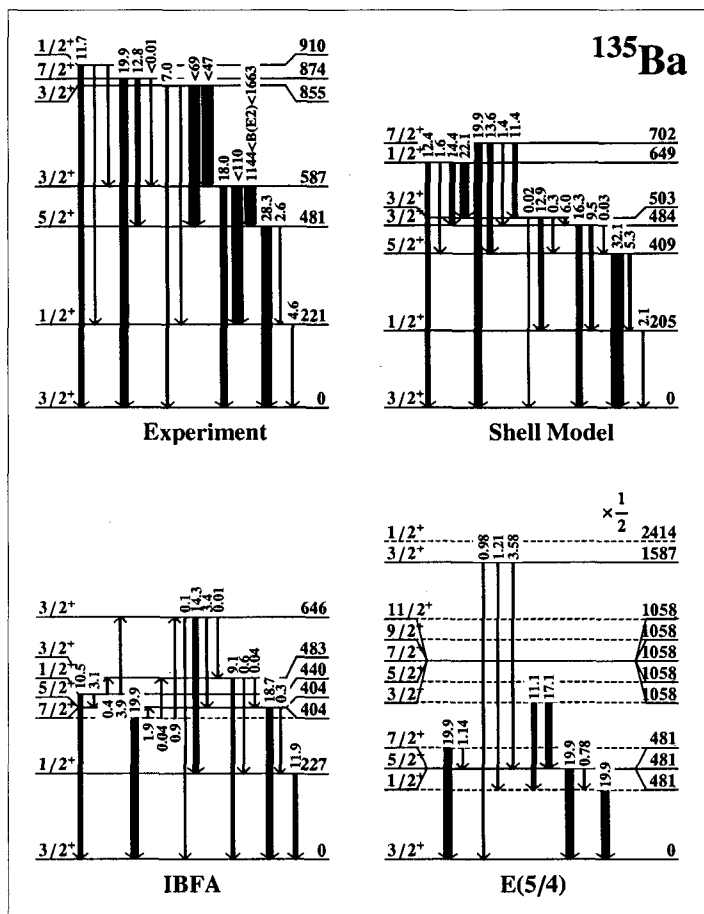


Figure 1. *Upper left*: The low spin levels in ^{135}Ba . The upper limits in $B(E2)$ values have been calculated assuming $E2$ transitions; *Upper right*: SM calculations; *Lower left*: IBFA calculations; and *Lower right*: The low spin levels of $E(5/4)$ symmetry. The $5/2_1^+$ energy of $E(5/4)$ has been fitted to the $5/2_1^+$ energy of ^{135}Ba data. All panels have the same energy scale (keV) except for the lower right panel, in which a 0.5 scaling factor was used. The numbers next to the transition arrows are $B(E2)$ values normalized to the $7/2_1^+ \rightarrow 3/2_1^+$ transition in the ^{135}Ba data, and the arrow widths are proportional to the $B(E2)$ value. Upward going arrows have been used in the IBFA results where the order of the predicted levels is inverted relative to experiment.

and the IBFA-calculated $1/2_1$ corresponds to a single particle state, in agreement with the spectroscopic factor data⁷ for $1/2_1^+$, that is outside the scope of $E(5/4)$. The IBFA calculations are in better agreement with the

data than $E(5/4)$, but significant discrepancies remain. The $7/2_1^+$, $5/2_1^+$, and $1/2_2^+$ are monotonic, which is not the case in the data. Other significant discrepancies cover other level order inversions, and the overpopulation of the $B(E2; 1/2_1^+ \rightarrow 3/2_1^+)$ value.

Energy levels very similar with those in the IBFA are obtained in the PVCMM⁷ calculations. A $d_{3/2}$ and a $s_{1/2}$ neutron hole with SPE of 0.0 keV and 211 keV respectively, have been coupled to a ^{134}Ba core. Pairing parameters 0.940 and 0.608, an $E(2^+)=607$ keV core-energy, anharmonicities 1.49, 0.18, and 0.38 in the 2-phonon state, and seven different particle-core coupling strengths k , have been used. The calculated energies of the six lowest-spin excited states in the IBFA and in PVCMM is given in Table ???. The two models are similar and the conclusions from the comparison of IBFA calculations with the data apply for the PVCMM model too.

Table 1. Energies (in keV) of the lowest-spin excited states in ^{135}Ba , from IBFA and PVCMM ($k = 1$ and $k = 2$) calculations.

	IBFA	PVCMM	PVCMM
		$k = 1$	$k = 2$
$1/2_1$	227	218	237
$5/2_1$	404.3	611	621
$3/2_2$	483	629	690
$3/2_3$	646	830	863
$7/2_1$	404.2	610	620
$1/2_2$	440	616	641

We also performed SM calculations in a model space that gives rough absolute $BE2$ values and spacing in $^{100-132}\text{Sn}$ and reasonable SPE in ^{101}Sn , with the NL3 interaction Hamiltonian⁷, using the code Oxbash^{7,7}. The calculations were performed for a ^{100}Sn core, and we allowed 0 to 6 protons in $1g_{7/2}$, 0 to 2 protons in $2d_{5/2}$, and filled $1g_{7/2}$ and $2d_{5/2}$ with neutrons, and allowed 0 to 4 neutrons in $2d_{3/2}$, 0 to 2 in $3s_{1/2}$ and 0 to 12 in $1h_{11/2}$. The results are shown in upper right panel of fig. ???. The agreement is overall rather good, and certainly the best of the models in Figure ?? for the relative energies and $B(E2)$ values. As in the IBFA calculations, the $1/2_1$ corresponds to a $3s_{1/2}$ single particle state. The observed non-monotonic arrangement of the $1/2_1^+$, $5/2_1^+$, and $7/2_1^+$ is correctly reproduced in the SM calculations.

In conclusion, comparison with data shows that more $B(E2)$ values and

absolute transition rates are needed before a definitive comparison of ^{135}Ba with the E(5/4) is possible. Although E(5/4) reproduces some energy and $B(E2)$ values, the IBFA, PVCMM, and SM calculations give better agreement with the existing data. This is perhaps not surprising since E(5/4) is an extremely simplified, parameter-free prediction. Also, given that nuclear properties change discretely with nucleon number, there is a very small chance that any given nucleus will land precisely at the critical point, just like it is unlikely that any given nucleus will precisely satisfy any of the familiar dynamical symmetries of the IBFA.

Acknowledgments

The authors thank Professors F. Iachello for providing us with the E(5/4) predictions prior to publication, and B.A. Brown for providing the Oxbash code, as well as for many useful discussions. We also acknowledge the financial support from the U.S. NSF Grant PHY 0204811, the Research Corporation grant CC5494, and US DOE Grant No. DE-FG02-91ER-40609.

While David Warner was an integral part of this work, he died before the completion of this study, and did not live to see or comment on the manuscript.

References

1. A. Arima and F. Iachello, *Phys. Rev. Lett.*, **35**, 1069 (1975).
2. R. F. Casten, and D. D. Warner, *Rev. Mod. Phys.*, **60**, 389 (1988).
3. F. Iachello, *Phys. Rev. Lett.*, **85**, 3580 (2000).
4. F. Iachello, *Phys. Rev. Lett.*, **87**, 052502 (2001).
5. R. F. Casten, and N. V. Zamfir, *Phys. Rev. Lett.*, **85**, 3584 (2000).
6. N. V. Zamfir *et al.*, *Phys. Rev.* **C65**, 044325 (2002).
7. F. Iachello, *Phys. Rev. Lett.*, in press (2005).
8. Yu. V. Sergeenkov and B. Singh, *Nucl. Data Sheets*, **84**, 115 (1998).
9. E. A. Henry, *Nucl. Data Sheets*, **15**, 203 (1975).
10. O. Scholten, *Kernfysisch Versneller Instituut, Groningen, Internal Report 63*, (1979).
11. F. Iachello and O. Scholten, *Phys. Rev. Lett.* **43**, 679 (1979).
12. P. Von Ehrenstein *et al.*, *Phys. Rev.* **C1**, 2066 (1970).
13. B. Castel and K. W. C. Stewart, *Nucl. Phys.* **A162**, 273 (1971).
14. G. A. Lalazissis *et al.*, *Phys. Rev.* **C55**, 540 (1997).
15. B. A. Brown *et al.*, *OXBASH for Windows*, MSU-NSCL Report Number **1289**, National Superconducting Cyclotron Laboratory, Michigan State University, East Lansing, Michigan, (2004).
16. B. A. Brown, *Prog. Part. Nucl. Phys.*, **47**, 517 (2001).

COLD FUSION CHANNELS OF $^{290}_{114}$

R. A. GHERGHESCU

*Horia Hulubei National Institute of Physics
and Nuclear Engineering
P. O. Box MG - 6, Bucharest-Magurele, Romania
E-mail: rgherg@ifn.nipne.ro*

Fusion reactions are calculated to synthesize $^{290}_{114}$ elements. Potential energy surfaces are obtained as the result of dynamic minimization with independent deformations of the target and projectile, small semiaxis of the projectile and distance between centers as degrees of freedom. Binary macroscopic-microscopic method is used to obtain the deformation energy and the Werner-Wheeler approximation yield the mass tensor. The highest penetrability values are obtained for cold fusion channels with ^{104}Kr , ^{108}Sr and ^{112}Zr leading to $^{290}_{114}$.

1. Introduction

This work is devoted to the search of the optimal sub-barrier fusion channels towards $^{290}_{114}$. Though it is known that cross section decreases with decreasing E_{CM} , the present calculations take advantage of obtaining the compound nucleus in the lowest excitation energy, close to its ground state. In this way it might be possible for the superheavy nucleus to be more stable against immediate decay. Choosing a neutron-rich isotope, as a projectile, has as a result a substantial change of the cross section¹. A valuable hint about mass-charge combinations in fusion reaction arises from diffusion calculations² and obtaining the intermediate equilibrium N/Z values. The macroscopic-microscopic method is employed, within the subsequent steps: calculation of the deformation energy using independent intermediary spheroidal deformations of the target and projectile ($\chi_T = b_T/a_T$, $\chi_P = b_P/a_P$), where (b_T, a_T) and (b_P, a_P) are spheroid semiaxes, the small semiaxis of the projectile b_P and the distance between center R during the overlapping stage as degrees of freedom. The mass tensor is calculated by means of the Werner-Wheeler irrotational flow method. The action integral is then computed for all isobaric reactions with the lowest static barriers.

2. Total deformation energy

A binary macroscopic-microscopic method is used to calculate the deformation energy. Single particle energy levels are obtained by the deformed two-center shell model. Details of calculation are given in Ref. 5. In the Schrödinger equation:

$$H\Psi - E\Psi = 0 \quad (1)$$

the total Hamiltonian:

$$H = -\frac{\hbar}{2m_0}\Delta + V(\rho, z) + V_{\Omega s} + V_{\Omega^2} \quad (2)$$

is deformation dependent. The deformed two-center oscillator potential for target and projectile regions v_T and v_P reads:

$$V(\rho, z) = \begin{cases} V_T(\rho, z) = \frac{1}{2}m_0\omega_{\rho T}^2\rho^2 + \frac{1}{2}m_0\omega_{z T}^2(z + z_T)^2, & \text{for } v_T \\ V_P(\rho, z) = \frac{1}{2}m_0\omega_{\rho P}^2\rho^2 + \frac{1}{2}m_0\omega_{z P}^2(z - z_P)^2, & \text{for } v_P \end{cases} \quad (3)$$

where z_T and z_P are the centers of the target and projectile, and equality:

$$V_T(\rho, z) = V_P(\rho, z) \quad (4)$$

defines the border between v_T and v_P regions. The Strutinsky method⁶ computes separately the proton and neutron shell corrections. These nuclei survive only due to negative shell corrections, their macroscopic barrier being negligible⁷. The macroscopic part is computed with the Yukawa-plus-exponential model.

$$E_{def} = E_{macro} + E_{shell} \quad (5)$$

where:

$$E_{macro} = (E_C - E_C^{(0)}) + (E_Y - E_Y^{(0)}) \quad (6)$$

3. Mass tensor and penetrability

There are four independent variables describing the configuration of two intersected spheroids: the ratios of the spheroid semiaxes for target χ_T and projectile χ_P , the small semiaxis of the projectile b_P (the target semiaxis b_T results from volume conservation) and the distance between centers R . In order to perform the further action integrals, it is useful to contract the tensor along one of the coordinates. One complies to the variation law of χ_T and χ_P such that at the touching point (start of the process) they take initial (separated nuclei) values χ_{T0} and χ_{P0} . At the end χ_T must be equal

to the compound nucleus value χ_0 , while χ_P ends at an independent χ_{Pf} . This work proposes a simple linear transition:

$$\begin{aligned}\chi_T &= \chi_{T0} + (\chi_0 - \chi_{T0}) \frac{R - R_f}{R_t - R_f} \frac{100}{k_T} \\ \chi_P &= \chi_{P0} + (\chi_{Pf} - \chi_{P0}) \frac{R - R_f}{R_t - R_f} \frac{100}{k_P}\end{aligned}\quad (7)$$

if $R < 0.01(R_t - R_f)k_T$ for χ_T and $R < 0.01(R_t - R_f)k_P$ for χ_P . k_T and k_P are independent number of steps in R direction with $k_T, k_P < 100$, and determines the number of steps (or the distance range in R) along which the semiaxis ratios change. Figure 1 shows different paths of the target (b_T , upper plot) and projectile (b_P) small semiaxes. These considerations lead to the dependence of b_P , χ_T and χ_P on the same parameters. Final contracted total mass inertia becomes $B = B(R)$. The fusion path is obtained as the result of minimization over *all* the possible values (hence all ranges of κ_T , κ_P , i_P) in *any* direction at a fixed R . The penetrability P for a given fusion path is calculated as usual:

$$P = \exp(-K_{ov}) \quad (8)$$

where K_{ov} is the overlapping action integral.

4. Results and discussion

The deformation energy is computed for every possible (A_T , A_P) fusion channel leading to the same compound nucleus. Calculations are performed for $^{290}114$. Mass asymmetries start from $\eta_A=0$ with the symmetric reaction $^{144}\text{Ba}+^{146}\text{Ce}$ up to $\eta_A \simeq 0.84$ corresponding to $^{24}\text{Mg}+^{266}\text{No}$. A very pronounced valley is visible at $\eta_A \simeq 0.31$, around $^{104}\text{Kr}+^{186}\text{Pt}$ with a barrier height at 7.22 MeV. The barrier entrance point is situated deep in the overlapping region compared to more asymmetric reactions. The resulting penetrabilities are presented in Table I, for $^{290}114$. There are small differences between barriers, all being around 7-8 MeV, the average height of the energy valley. On the contrary, penetrabilities display large differences. The most favorable values are obtained for ($^{104}\text{Kr}+^{186}\text{Pt}$), with $\log_{10}P=-7.25$, ($^{108}\text{Sr}+^{182}\text{W}$) with $\log_{10}P=-8.036$ and ($^{112}\text{Zr}+^{178}\text{W}$) with $\log_{10}P=-8.664$. As a final remark, one states that the extreme sub-barrier fusion as an alternative to high energy synthesis reaction has certainly the disadvantage of having a low probability, hence a low cross section. However, the final com-

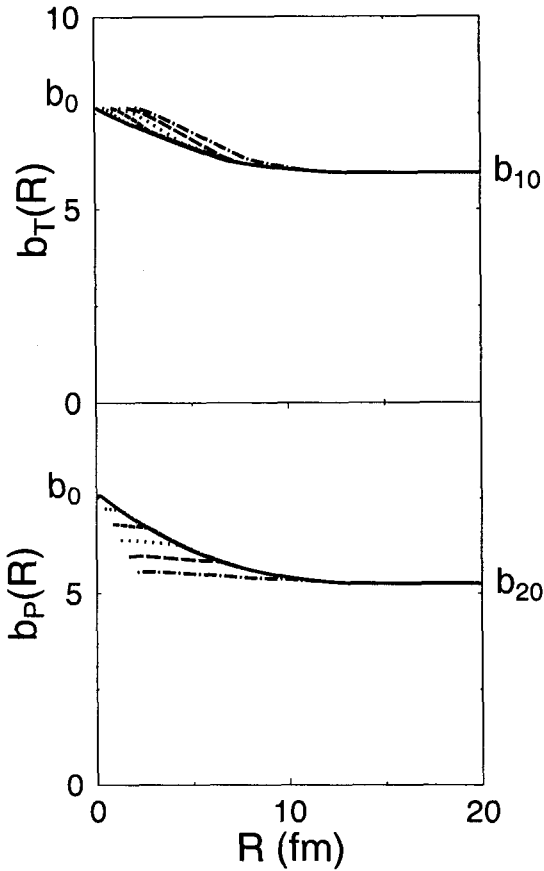


Figure 1. Different paths of variation for the small semiaxis of the target (b_T) and projectile (b_P) as a function of R .

pound nucleus could be synthesized in a more stable state (no excitation), thus it probably lives longer.

5. Conclusions

When nuclei approach each other with a kinetic energy equal to the Q -value of the reaction, chances are to obtain a compound nucleus very close to its ground state. Since no excitation triggers a decay process, the final system could be more stable. The reactions obtained after browsing the

deepest energy valley of (E_{def}, η_A, R) produced narrow barriers and a larger penetrability values. $^{104}\text{Kr}+^{186}\text{Pt}$, $^{108}\text{Sr}+^{182}\text{Os}$ and $^{112}\text{Zr}+^{178}\text{W}$ could be used to obtain $^{290}\text{114}$ in a close to ground state energy, by using a kinetic energy equal to the Q -value.

Table 1. The dynamic barriers E_b and logarithms of penetrabilities $\log_{10}P$ for the energy valley in the synthesis of $^{290}\text{114}$.

$^{104}\text{Kr}+^{186}\text{Pt}$	7.22	-7.250
$^{104}\text{Sr}+^{186}\text{Os}$	7.52	-12.233
$^{104}\text{Zr}+^{186}\text{W}$	7.75	-14.353
$^{104}\text{Mo}+^{186}\text{Hf}$	8.08	-16.106
$^{106}\text{Zr}+^{184}\text{W}$	7.66	-12.976
$^{106}\text{Mo}+^{184}\text{Hf}$	7.93	-12.956
$^{108}\text{Sr}+^{182}\text{Os}$	7.37	-8.036
$^{108}\text{Zr}+^{182}\text{W}$	7.62	-11.245
$^{108}\text{Mo}+^{182}\text{Hf}$	7.91	-12.892
$^{110}\text{Mo}+^{180}\text{Hf}$	7.85	-11.688
$^{110}\text{Ru}+^{180}\text{Yb}$	9.01	-23.688
$^{112}\text{Zr}+^{178}\text{W}$	7.33	-8.664
$^{112}\text{Mo}+^{178}\text{Hf}$	7.77	-10.823

Acknowledgments

The author is grateful to the Deutsche Forschungsgemeinschaft, Bonn, JAERI, Tokai, Japan and Ministry of Education and Research of Bucharest, Romania for financial support.

References

1. S. Hofmann and G. Münzenberg, *Rev. Mod. Phys.* **72**, 733 (2000).
2. G. G. Adamian, N. V. Antonenko and W. Scheid, *Phys. Rev. C* **68**, 034601 (2003).
3. M. Goncalves and S. B. Duarte, *Phys. Rev. C* **48**, 2409 (1993).
4. B. G. Giraud, S. Karataglidis, K. Amos and B. A. Robson, *Phys. Rev. C* **69**, 064613 (2004).
5. R. A. Gherghescu, *Phys. Rev. C* **67**, 014309 (2003).
6. V. Strutinsky, *Nucl. Phys.* **A95**, 420 (1967).
7. A. Sobiczewski, *Phys. Part. Nucl.* **25**, 295 (1994).

PRECISE HALF-LIFE MEASUREMENT OF ^{34}Ar , A SUPERALLOWED β^+ EMITTER*

V.E. IACOB, J.C. HARDY, C.A. GAGLIARDI, V.E. MAYES,
N. NICA, G. TABACARU, L. TRACHE AND R.E. TRIBBLE

*Cyclotron Institute, Texas A&M University
College Station, TX 77843-3366, USA*

We have measured the half-life of the superallowed $0^+ \rightarrow 0^+$ beta emitter ^{34}Ar to 0.08% precision by observing decay positrons from both ^{34}Ar and its daughter ^{34}Cl . This is part of our program of precise measurements aimed at testing the Standard Model *via* the unitarity of the Cabibbo-Kobayashi-Maskawa matrix. A new fitting technique was developed, which allowed us to extract the parent half-life to this precision. Our result is $t_{1/2}(^{34}\text{Ar}) = 843.8(7)$ ms.

1. Introduction

The half life of ^{34}Ar has been determined to unprecedented precision, thus significantly improving the ft -value for its superallowed $0^+ \rightarrow 0^+$ transition. This measurement was performed in the framework of our program to test the Standard Model *via* the unitarity of the Cabibbo-Kobayashi-Maskawa (CKM) matrix. The measured ft -values for the superallowed beta transitions are used to extract a precise value for the up-down quark-mixing element, V_{ud} , of the CKM matrix [1]. For these experiments to be meaningful they must achieve a precision of better than 0.1% and the previously accepted value $t_{1/2}(^{34}\text{Ar}) = 844.5(34)$ ms [2] does not meet this demanding requirement.

2. The experiment

We produced the ^{34}Ar beam using the reaction $p(^{35}\text{Cl}, 2n)^{34}\text{Ar}$. A 30A MeV ^{35}Cl beam from the K500 superconducting cyclotron of TAMU impinged on an LN₂-cooled hydrogen gas target held at 1.5 atm. The fully stripped ^{34}Ar recoils were separated in the Momentum Achromat Recoil Separator (MARS) and then extracted into air, where they passed through a 0.3-mm-thick BC-404 scintillator followed by a stack of aluminum degraders. The degrader thickness was tuned so that >99% of the ^{34}Ar recoils finally stopped in the 76- μm -thick

* This work was supported by the U.S. Department of Energy under Grant DE-FG02-93ER40773 and the Robert A. Welch Foundation under Grants A-1397 and A-1082.

aluminized Mylar tape of our fast tape-transport system. The combined effects of q/m separation in MARS and range selectivity in the degraders resulted in our collecting 99.7% pure samples of ^{34}Ar . Each sample was collected for a short time (either 0.3s, 0.7s or 1.0s), then the beam was turned off and the implanted activity was moved in 175ms to the center of a shielded 4π proportional gas counter located 90 cm away, where the decay positrons were detected and multiscaled for 12s. The collect-move-detect cycle was then automatically repeated until the desired statistics had been accumulated.

The experiment is simple in principle but the desired precision makes it very demanding in practice since every precaution must be taken to eliminate any possible systematic biases. Thus the complete measurement was split into a sequence of separate segments, each containing several million counts from hundreds of cycles, and each accumulated with different settings of important experimental parameters: gas-counter bias, imposed (non-extendable) system dead-time, and detection threshold. Each segment was analyzed independently and compared with the other segments for evidence of systematic differences. No evidence was found for any dependence of the measured half-life on experimental parameters.

3. Data reduction

To extract an accurate half-life for ^{34}Ar we had to face several special challenges:

- ^{34}Ar is a noble gas and might diffuse out of the tape during the detection time, thus simulating a shorter half-life
- The daughter nucleus, ^{34}Cl , is radioactive and has a comparable half-life. Our gas counter records positrons from both ^{34}Ar and ^{34}Cl decays.
- The half-lives of the two species are related by a factor close to 2: viz., $t_{1/2}(^{34}\text{Cl}) = 1.8 t_{1/2}(^{34}\text{Ar})$.

To evaluate possible diffusion, we measured the half life of ^{35}Ar under similar experimental conditions. The collect/move/detect time intervals were 1s/0.133s/35s, and the only impurity present in the collected ^{35}Ar sample was ^{33}Cl at a level of 0.5%. The half-life we obtained for ^{35}Ar was 1.773(3) s, in good agreement with the accepted value of 1.775(4) s [3]. Since our result rules out significant diffusion effects for ^{35}Ar , which has a half-life more than twice that of ^{34}Ar , we can conclude that diffusion must not be a factor for our ^{34}Ar measurement either.

In contrast, the presence of both parent and daughter activities in our time-decay spectra certainly is a factor that must be dealt with. In a separate series of measurements, we produced ^{34}Cl directly *via* the $p(^{35}\text{Cl},pn)^{34}\text{Cl}$ reaction and determined its half-life to be 1.5268(5) s [4]. This was consistent with, but more precise than, previous measurements [1]. We could then use this

result in analyzing the combined ^{34}Cl and ^{34}Ar decay data observed in the present experiment.

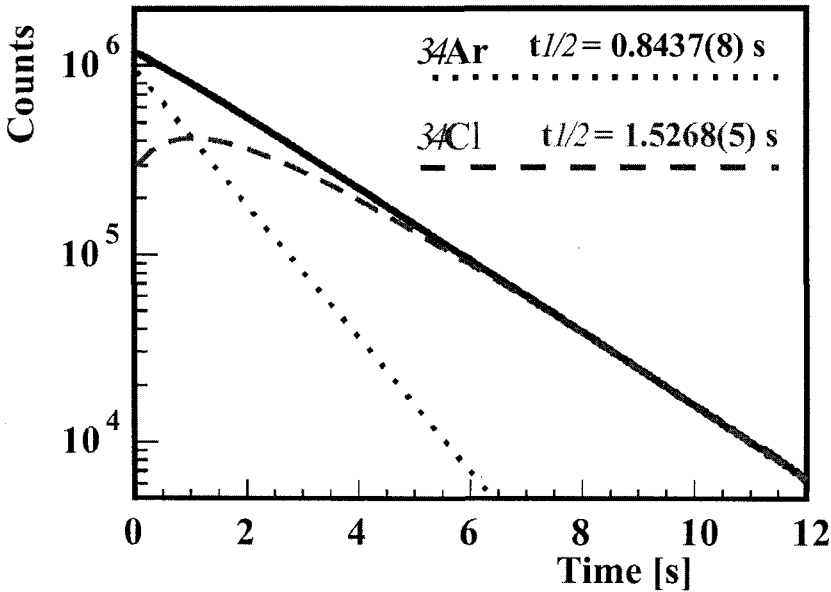


Figure 1. Time-decay spectrum of ^{34}Ar as obtained from our gas counter. The partial contributions from the two activities, ^{34}Ar and ^{34}Cl , are indicated as dotted and dashed lines, respectively

A typical measured decay spectrum is presented in Fig.1. Note that the decay of ^{34}Cl appears to dominate the spectrum, the equal contribution of ^{34}Ar being almost impossible to detect by eye. This is a consequence of the relative magnitudes of the two half-lives. After the collect interval, the combined ^{34}Ar and ^{34}Cl activity is given by

$$\Lambda_{tot} = N_a \lambda_a \frac{2\lambda_b - \lambda_a}{\lambda_b - \lambda_a} e^{-\lambda_a t} + \left(N_b - \frac{N_a \lambda_a}{\lambda_b - \lambda_a} \right) \lambda_b e^{-\lambda_b t} \quad (1)$$

where t is the time after the end of the collect period, $N_{a,b}$ are the numbers of ^{34}Ar and ^{34}Cl nuclei in the source at $t = 0$, and $\lambda_{a,b}$ are the corresponding decay constants. Note that when $\lambda_a = 2\lambda_b$ the first term (the one characterized by the ^{34}Ar decay constant) vanishes. Although not related by exactly a factor of 2, the actual half-lives of ^{34}Ar and ^{34}Cl lead to the coefficient of the $e^{-\lambda_a t}$ term being more than six times smaller than that of the $e^{-\lambda_b t}$ term – and to its being *negative*. This could be a serious limitation in the extraction of a precise half-

life for ^{34}Ar : a simple two-decay-component fit, even with the more than half billion combined ^{34}Ar and ^{34}Cl events we recorded, cannot do better than 0.4% precision, yielding the value 847.0(37) ms for the half-life of ^{34}Ar [5]. This is insufficient for the result to contribute meaningfully to the determination of V_{ud} .

Our first attempt to overcome this problem was to modify our experimental technique. We increased the ratio of ^{34}Ar to ^{34}Cl decay positrons recorded in our counter by making use of the different end-point energies of their associated β^+ spectra (5.04 MeV for ^{34}Ar and 4.47 MeV for ^{34}Cl). We introduced a thin Cu foil between the decaying source and the gas counter, thus attenuating the positrons from both sources, but preferentially from the unwanted ^{34}Cl . We adjusted the foil thickness between 1.25 mm and 1.90 mm and determined the ^{34}Ar to ^{34}Cl ratio and the overall counting rate. For 1.5 mm, the optimum choice, it was found that the ratio of the coefficients in Eqn (1) is improved from 1/6 to about 3, but at the cost of our losing about 95% of the unattenuated counting rate. With a total of 9.5 million combined ^{34}Ar and ^{34}Cl decay events recorded under this condition, we obtained an ^{34}Ar half life of 844.4(47) ms. Even though the decay-spectra obtained were qualitatively better at revealing the ^{34}Ar half-life, this advantage was more than offset by the loss in statistics.

Our second attempt was more successful. We reanalyzed the original data using a different approach. A close look at Eqn (1) reveals that the near cancellation of the coefficient of the $e^{-\lambda_0 t}$ term can actually be turned to our advantage: we can extract the amount by which the ratio of the two half-lives deviates from 2 by analyzing the deviation between the experimental data and a one-component decay characterized by the exponential $e^{-\lambda_0 t}$. We replaced the free fit for the coefficients of the two exponentials in Eqn (1) by one that explicitly connects both coefficients to the experimental implantation time and the half-lives of both nuclides. That is, we require the ratio N_b/N_a to take the value determined by the known collection time for ^{34}Ar and the calculated accumulation of ^{34}Cl as a decay product during the collection time. The associated fitting procedure is more computer-intensive but is effective in increasing the precision of the extracted half-life. To test this new approach, we generated a parallel set of artificial spectra by Monte Carlo techniques: these spectra mimicked our experimental data in statistics, background, dead-time and beam-profile, but with an imposed half-life of 845ms for the parent activity. The results we obtained in fitting this pseudo-data demonstrated our method to be reliable with the uncertainties determined in the fitting procedure.

The method was then applied to the experimental data and was further tested for stability versus various detection settings (dead time, detector bias and discriminator threshold). As seen in Fig. 2, the distribution of the fit results shows no systematic bias in the extracted half life from runs with different combinations of detector biases and discriminator thresholds. A similar test

performed for the possible influence of the dead-time was also devoid of any evidence of systematic dependence. The full fit performed over more than 5×10^8 combined ^{34}Ar and ^{34}Cl decay events yields $t_{1/2}(^{34}\text{Ar}) = 843.8(7)$ ms.

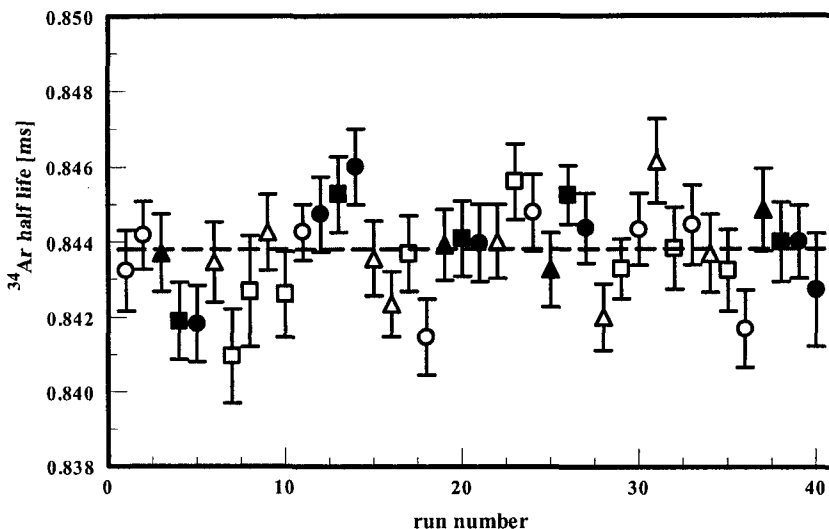


Figure 2. Half-life values for ^{34}Ar obtained in 40 successive runs (less than half our total data) are plotted so as to reveal possible effects from different parameter settings in the detection set-up. Squares, triangles and circles represent the 2400-V, 2550-V and 2700-V detector voltages, respectively. Open or solid symbols represent 150-mV and 200-mV discrimination thresholds, respectively. The normalized chi-square of the distribution is $\chi^2/ndf=1.41$

The reported error contains the statistical error, the uncertainty in the half life of the daughter nucleus ^{34}Cl , the scatter in results extracted from the various independent runs, the uncertainty in the impurity levels and the uncertainty due to the beam profile. Among all these, the contribution of the ^{33}Cl impurity is the most important, its amplitude being twice that of the statistical error, even though the amount of this impurity was a mere 0.25% of the primary activity. This emphasizes the importance of the purity of the radioactive beam in the extraction of a precise half life for such parent-daughter combined decays, as it defines the ultimate precision that can be achieved.

4. Concluding remarks

The half life of ^{34}Ar has been extracted using a constrained-fit procedure. The method makes use of the expected parent-daughter relationship between the contributions of the two activities participating in the decay. Using our new fitting procedure, we obtained the result $t_{1/2}(^{34}\text{Ar}) = 843.8(7)$ ms, in good agreement with the previously accepted value of 844.5(34) ms [2], but with a precision of better than 0.1%, the goal we were seeking.

References

1. J.C. Hardy and I.S. Towner, *Phys. Rev. C* **71**, 055501 (2005).
2. J.C. Hardy et al., *Nucl. Phys.* **A233**, 157 (1974).
3. P.M. Endt, *Nucl. Phys.* **A521**, 1 (1990).
4. V.E. Iacob et al., *Bul. Am. Phys. Soc.* **48**, #2, pg 34 (2003).
5. V.E. Iacob et al., *Bul. Am. Phys. Soc.* **48**, #8, pg 28 (2003).

QUANTUM DEFORMATION OF OPEN SYSTEMS

A. ISAR

*Department of Theoretical Physics,
Institute of Physics and Nuclear Engineering, Bucharest-Magurele, Romania
E-mail: isar@theory.nipne.ro*

W. SCHEID

Institute of Theoretical Physics, University of Giessen, Germany

A master equation for the deformed quantum harmonic oscillator interacting with a dissipative environment, in particular with a thermal bath, is obtained in the microscopic model, using perturbation theory. The coefficients of the master equation depend on the deformation function. The steady state solution of the equation for the density matrix in the number representation is derived and the equilibrium energy of the deformed harmonic oscillator is calculated.

1. Deformed Quantum Oscillators

The generalized deformed quantum oscillators¹ are defined as the algebra generated by the operators $\{1, A, A^\dagger, N\}$ and the structure function $F(N)$, which satisfy the relations: $[A, N] = A$, $[A^\dagger, N] = -A^\dagger$ and $AA^\dagger = F(N+1)$, $A^\dagger A = F(N)$, where $F(N)$ is a positive function with $F(0) = 0$ and N is the Hermitian number operator. For $F(N) = N$ one obtains the relations for the usual harmonic oscillator. For

$$F(N) = \frac{q^N - q^{-N}}{q - q^{-1}} \equiv [N], \quad (1)$$

where q is the deformation parameter, A and A^\dagger are called q -deformed boson annihilation and creation operators^{2,3} and they satisfy the relations $AA^\dagger = [N+1]$, $A^\dagger A = [N]$ and $[A, A^\dagger] = [N+1] - [N]$. If $q > 0$, then $[N] = \sinh(N \ln q) / \sinh(\ln q)$. In the limit $q \rightarrow 1$, q -operators tend to the ordinary operators and we get the usual boson commutation relation $[A, A^\dagger] = 1$. We define the f -deformed oscillator operators⁴ $A = af(N) = f(N+1)a$, $A^\dagger = f(N)a^\dagger = a^\dagger f(N+1)$, where a and a^\dagger are the usual boson operators satisfying $[a, a^\dagger] = 1$, $N = a^\dagger a$ and $[a, N] = a$, $[a^\dagger, N] = -a^\dagger$.

The f -operators satisfy the commutation relation $[A, A^\dagger] = (N + 1)f^2(N + 1) - Nf^2(N)$. The function f is such that when the deformation disappears, then $f \rightarrow 1$ and the usual algebra is recovered. The notion of f -oscillators generalizes the notion of q -oscillators. Indeed, if $f(N) = \sqrt{[N]/N}$, then the operators A, A^\dagger satisfy the q -deformed commutation relations. The Hamiltonian of the f -deformed harmonic oscillator is (ω is the ordinary frequency) $\mathcal{H} = \hbar\omega(AA^\dagger + A^\dagger A)/2 = \hbar\omega[(N + 1)f^2(N + 1) + Nf^2(N)]/2$. It is diagonal on the eigenstates $|n\rangle$ and in the Fock space its eigenvalues are $\mathcal{E}_n = \hbar\omega[(n + 1)f^2(n + 1) + nf^2(n)]/2$. In the limit $f \rightarrow 1$ ($q \rightarrow 1$ for q -oscillators), we recover the ordinary expression $E_n = \hbar\omega(n + 1/2)$.

In Ref. 5, we obtained the following solutions to the Heisenberg equations of motion for the operators a and a^\dagger : $a(t) = \exp[-i\omega\Omega(N)t]a$, $a^\dagger(t) = a^\dagger \exp[i\omega\Omega(N)t]$, where $\Omega(N) = [(N + 2)f^2(N + 2) - Nf^2(N)]/2$. For a q -deformed harmonic oscillator, $\Omega(N) = ([N + 2] - [N])/2$ and for a small deformation parameter τ ($\tau = \ln q$), $\Omega(N) = 1 + \tau^2(N + 1)^2/2$.

2. Quantum Markovian Master Equation

In order to study the dynamics of an open system S, we use a microscopic description of the composite system S+B. As the subsystem S of interest we take the f -deformed harmonic oscillator with the Hamiltonian \mathcal{H} , and B is the environment (bath) with the Hamiltonian H_B . The coupled system with the total Hamiltonian $H_T = \mathcal{H} + H_B + V$ (V is the interaction Hamiltonian) is described by a density operator $\chi(t)$, which evolves in time according to the von Neumann-Liouville equation. When the Hamiltonian evolution of the total system is projected onto the space of the harmonic oscillator, the reduced density operator of the subsystem is given by $\rho(t) = \text{Tr}_B \chi(t)$. For an interaction potential V linear in the coordinate $s_1 = q$ and momentum $s_2 = p$ of the subsystem, the master equation for the density operator of the open system in the Born-Markov approximation has the form^{5,7}:

$$\frac{d\rho(t)}{dt} = -\frac{i}{\hbar}[\mathcal{H}, \rho(t)] + \frac{1}{\hbar^2} \sum_{i,j=1,2} \int_0^t dt' \{C_{ij}^*(t') [s_i, \rho(t) s_j(-t')] + C_{ij}(t') [s_j(-t') \rho(t), s_i]\}, \quad (2)$$

where the coefficients $C_{ij}(t)$ are the correlation functions of the environment operators. Next we use the relations (m is the oscillator mass)

$$q(t) = \sqrt{\frac{\hbar}{2m\omega}}(a^\dagger(t) + a(t)), \quad p(t) = i\sqrt{\frac{\hbar m\omega}{2}}(a^\dagger(t) - a(t)) \quad (3)$$

and insert the equations for $a(t)$ and $a^\dagger(t)$. In the Markov approximation we may replace the upper limit of integration t by ∞ . We define the complex decay rates, which govern the rate of relaxation of the system density operator as follows (we denote $E_+ = \exp[i\omega\Omega(N)t']$, $E_- = \exp[-i\omega\Omega(N)t']$):

$$\int_0^\infty dt' C_{11}(t')E_+ = \int_0^\infty dt' C_{11}^*(t')E_+ = D_{pp}(\Omega), \quad (4)$$

$$\int_0^\infty dt' C_{22}(t')E_+ = \int_0^\infty dt' C_{22}^*(t')E_+ = D_{qq}(\Omega), \quad (5)$$

$$\int_0^\infty dt' C_{12}(t')E_+ = \int_0^\infty dt' C_{21}^*(t')E_+ = -D_{pq}(\Omega) + \frac{i\hbar}{2}\lambda(\Omega), \quad (6)$$

with $D_{pp}(\Omega) > 0$, $D_{qq}(\Omega) > 0$ and $D_{pp}(\Omega)D_{qq}(\Omega) - D_{pq}^2(\Omega) \geq \hbar^2\lambda^2(\Omega)/4$.

In fact, $D_{pp}(\Omega)$, $D_{qq}(\Omega)$, $D_{pq}(\Omega)$ and $\lambda(\Omega)$ play the role of deformed diffusion and, respectively, dissipation coefficients. We assume in the following $\lambda(\Omega) = \lambda = \text{const}$. With these assumptions we obtain the following master equation for the damped deformed harmonic oscillator:

$$\begin{aligned} \frac{d\rho}{dt} = & -\frac{i}{\hbar}[\mathcal{H}, \rho] + \frac{1}{2\hbar^2} \{[(\{D_{pp}(\Omega), q\} \\ & + \frac{i}{m\omega}[D_{pp}(\Omega), p])\rho, q] + [(\{D_{qq}(\Omega), p\} - im\omega[D_{qq}(\Omega), q])\rho, p] \\ & + [(m\omega[iD_{pq}(\Omega) + \frac{\hbar}{2}\lambda, q] - \{D_{pq}(\Omega) - \frac{i\hbar}{2}\lambda, p\})\rho, q] \\ & - [(\frac{1}{m\omega}[iD_{pq}(\Omega) - \frac{\hbar}{2}\lambda, p] + \{D_{pq}(\Omega) + \frac{i\hbar}{2}\lambda, q\})\rho, p] + H.c. \}. \end{aligned} \quad (7)$$

In the limit $f \rightarrow 1$ ($\Omega \rightarrow 1$), the deformation disappears and Eq. (7) becomes the Markovian master equation for the damped harmonic oscillator, obtained in the Lindblad theory for open quantum systems⁸. Expressing the coordinate and momentum back in terms of the creation and annihilation operators and introducing the notations

$$\begin{aligned} D_+(\Omega) & \equiv \frac{1}{2\hbar} [m\omega D_{qq}(\Omega) + \frac{D_{pp}(\Omega)}{m\omega}], \\ D_-(\Omega) & \equiv \frac{1}{2\hbar} [m\omega D_{qq}(\Omega) - \frac{D_{pp}(\Omega)}{m\omega}], \end{aligned} \quad (8)$$

Eq. (7) becomes:

$$\begin{aligned} \frac{d\rho}{dt} = & -\frac{i}{\hbar}[\mathcal{H}, \rho] + \{[[D_+(\Omega)a, \rho], a^\dagger] \\ & - [[a^\dagger(D_-(\Omega) + \frac{i}{\hbar}D_{pq}(\Omega)), \rho], a^\dagger] - \frac{\lambda}{2}[a^\dagger, \{a, \rho\}] + H.c.\}. \end{aligned} \quad (9)$$

In the particular case of a thermal equilibrium of the bath at temperature T (k is Boltzmann constant), we take the diffusion coefficients of the form

$$m\omega D_{qq}(\Omega) = \frac{D_{pp}(\Omega)}{m\omega} = \frac{\hbar}{2}\lambda \coth \frac{\hbar\omega\Omega}{2kT}, \quad D_{pq}(\Omega) = 0. \quad (10)$$

In the limit $\Omega \rightarrow 1$, the deformed diffusion coefficients (10) take the known form obtained for the damped harmonic oscillator in the particular case when the asymptotic state is a Gibbs state⁸.

3. Equation for the Density Matrix

We consider the master equation (9) for the density matrix by means of the number representation. Specifically, we take the matrix elements of each term between different number states denoted by $|n\rangle$ and use $N|n\rangle = n|n\rangle$, $a^\dagger|n\rangle = \sqrt{n+1}|n+1\rangle$ and $a|n\rangle = \sqrt{n}|n-1\rangle$. When $D_-(\Omega(n)) = 0$, $D_{pq}(\Omega(n)) = 0$, the diagonal elements are coupled only amongst themselves and not coupled to the off-diagonal elements. In this case the diagonal elements (populations) satisfy the master equations:

$$\begin{aligned} \frac{dP(n)}{dt} = & -[2(n+1)D_+(\Omega(n)) + 2nD_+(\Omega(n-1)) - \lambda]P(n) \\ & + (n+1)[2D_+(\Omega(n)) + \lambda]P(n+1) + n[2D_+(\Omega(n-1)) - \lambda]P(n-1) \end{aligned} \quad (11)$$

where $P(n) \equiv \langle n|\rho(t)|n\rangle$. The steady state solution of Eq. (11) is

$$P_{ss}(n) = P(0) \prod_{k=1}^n \frac{2D_+(\Omega(k-1)) - \lambda}{2D_+(\Omega(k-1)) + \lambda}. \quad (12)$$

In the particular case of a thermal state, when the diffusion coefficients have the form (10), the stationary solution of Eq. (11) takes the form

$$P_{ss}^{th}(n) = Z_f^{-1} \exp\left\{-\frac{\hbar\omega}{2kT}[(n+1)f^2(n+1) + nf^2(n)]\right\}, \quad (13)$$

where

$$Z_f^{-1} = P(0) \exp \frac{\hbar\omega f^2(1)}{2kT} \quad (14)$$

and Z_f is the partition function:

$$Z_f = \sum_{n=0}^{\infty} \exp\left\{-\frac{\hbar\omega}{2kT}[(n+1)f^2(n+1) + nf^2(n)]\right\}. \quad (15)$$

The distribution (13) can also be written

$$P_{ss}^{th}(n) = Z_f^{-1} \exp\left(-\frac{\mathcal{E}_n}{kT}\right). \quad (16)$$

Expressions (13) and (16) represent the Boltzmann distribution for the deformed harmonic oscillator. In the limit $f \rightarrow 1$ the probability $P_{ss}^{th}(n)$ becomes the Boltzmann distribution for the ordinary harmonic oscillator.

For an q -oscillator weakly coupled to a reservoir kept at the temperature T , the q -deformed partition function can be obtained as a particular case of the partition function Z_f (15):

$$Z_q = \sum_{n=0}^{\infty} \exp\left\{-\frac{\hbar\omega}{2kT} \frac{\sinh(\tau(n+1)) + \sinh(\tau n)}{\sinh \tau}\right\}. \quad (17)$$

We can calculate the equilibrium energy by using the formula

$$\mathcal{E}(\infty) = -\hbar\omega \frac{1}{Z_q} \frac{\partial Z_q}{\partial \beta}, \quad \beta \equiv \frac{\hbar\omega}{kT} \quad (18)$$

and obtain

$$\mathcal{E}(\infty) = \frac{\hbar\omega}{2} \left(\coth \frac{\hbar\omega}{2kT} + \tau^2 c \right), \quad (19)$$

where

$$c = \frac{e^\beta}{(e^\beta - 1)^2} \left[\frac{e^\beta + 1}{e^\beta - 1} - \beta \frac{e^{2\beta} + 4e^\beta + 1}{(e^\beta - 1)^2} \right]. \quad (20)$$

We note that in the approximation of a small deformation parameter τ , the energy of the deformed damped oscillator depends on the oscillator ground state energy $\hbar\omega/2$ and on the temperature T . Evidently, when there is no deformation ($\tau \rightarrow 0$), one recovers the energy of the ordinary harmonic oscillator in a thermal bath^{8,9}. In the limit $T \rightarrow 0$, one has $c \rightarrow 0$, $\mathcal{E}(\infty) = \hbar\omega/2$ and the deformation does not play any role.

References

1. C. Daskaloyannis and K. Ypsilanti, *J. Phys. A: Math. Gen.* **25**, 4157 (1992).
2. L. C. Biedenharn, *J. Phys. A: Math. Gen.* **22**, L873 (1989).
3. A. J. MacFarlane, *J. Phys. A: Math. Gen.* **22**, 4581 (1989).
4. V. I. Man'ko, G. Marmo, E. C. G. Sudarshan and F. Zaccaria, *Phys. Scripta* **55**, 528 (1997).

5. A. Isar and W. Scheid, *Physica* **A310**, 364 (2002).
6. S. Mancini, *Phys. Scripta* **59**, 195 (1999).
7. H. Carmichael, *An Open System Approach to Quantum Optics*, Lecture Notes in Physics m18 (Springer, Berlin, 1993).
8. A. Isar, A. Sandulescu, H. Scutaru, E. Stefanescu and W. Scheid, *Int. J. Mod. Phys.* **E3**, 635 (1994).
9. A. Isar and W. Scheid, *Physica* **A335**, 79 (2004).

SINGLE-PARTICLE EFFECTS IN THE THRESHOLD FISSION CROSS-SECTION

M. MIREA

Institute of Physics and Nuclear Engineering, P.O. Box MG-6, Bucharest-Magurele,
Romania

The dynamic effect due to the radial coupling is quantified in the fission cross-section. A large number of double barriers appears in the fission degree of freedom due to the single particle effects.

1. Introduction

It is well known that the fission barrier in the actinide region exhibits a double humped shape. This double barrier, postulated in the frame of the microscopic-macroscopic model, provided a unified explanation of a great number of experimental results. At excitation energies below or close to the fission barrier top, the properties associated with the double hump shape are more pronounced than in other energy domains. A large number of intermediate resonances appear in the sub-threshold and threshold regions. In the conventional picture, the double barrier is parameterized from experimental data by providing a good model for the nuclear level density. The cross section is proportional with the number of states calculated in the transient point or saddle point configuration. The single particle effects, the dynamics and the dissipation are neglected, despite the fact that it is believed for a long time that these quantities affect drastically all observations. This kind of calculations are good only to obtain evaluations with an accuracy of 30–40%. However, if we expect simulations within better accuracies, the single particle effects, the variations of the effective mass and the dissipation must be taken into account. In the actual model it is clear that a lot of effects responsible for the intermediate structure are not adequately treated and therefore impossible to discern correctly the intermediate resonance. In the following, some improvements are realized to evidence the role of single-particle states. A new formalism [1] is proposed, the main features being described in the following.

2. Single-particle excitations

The neutron single-particle diagram for the fission of ^{235}U with the heavy fragment ^{135}Xe is plotted in Fig. 1. The level scheme is obtained for a minimal

action path. The integral action was minimized using an algorithm similar to that of ref. [2] in a tridimensional configuration space spanned by the most important collective coordinates encountered in fission: elongation, necking and mass-asymmetry. This trajectory begins from a ground state and penetrates the first barrier reaching the region of the second well. In the second well, the necking parameter C starts to change suddenly, the second barrier is penetrated and the configuration of two separated spheres is obtained. The first well is located somewhere at the elongation $R=6.5$ fm. As displayed in the insert of Fig. 1, the sequence of the first experimental levels is reproduced: $7/2^-$ ground state continued by $1/2^+$ and $3/2^+$ levels. Therefore it can be expected that some levels around the Fermi energy are of enough confidence. The following levels in the vicinity of the Fermi energy are selected: 3 levels of projection $\Omega=1/2$ (thick dashed line), three levels of $\Omega=3/2$ (thick dot-dashed line), one level $\Omega=5/2$, two levels $\Omega=7/2$ and one level $\Omega=9/2$ (thick lines).

Between ground state and scission some dynamical effects are produced. The most important one is due to the radial coupling. Single-particle levels with same good quantum numbers cannot intersect but exhibit avoided crossings. A system of equations can qualitatively describe this phenomenon as in Ref. [3]. In Fig. 2, the levels with $\Omega=1/2$ are plotted within their interaction energies. Four avoided crossing regions are selected. A neutron, initially located on ε_1 can follow any path opened by the avoided crossing regions, that is $\varepsilon_1ABD\varepsilon_3$, $\varepsilon_1ABD\varepsilon_2$, $\varepsilon_1ABCD\varepsilon_3$ and so on. A probability of realization can be obtained for each path, and for each path an excitation and a barrier can be associated. Within only the four avoided crossings, 18 energy paths can be obtained and a same number of different barriers. The occupation probability of each barrier was found between 0.1 and 0.25. For $\Omega=3/2$ another 15 barriers are obtained.

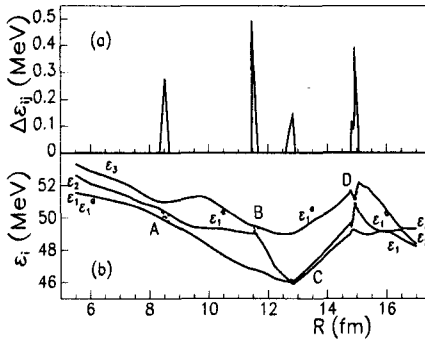


Figure 2. a) Interaction energies in the avoided crossing regions and (b) adiabatic single-particle states with $\Omega=1/2$ and their intersections.

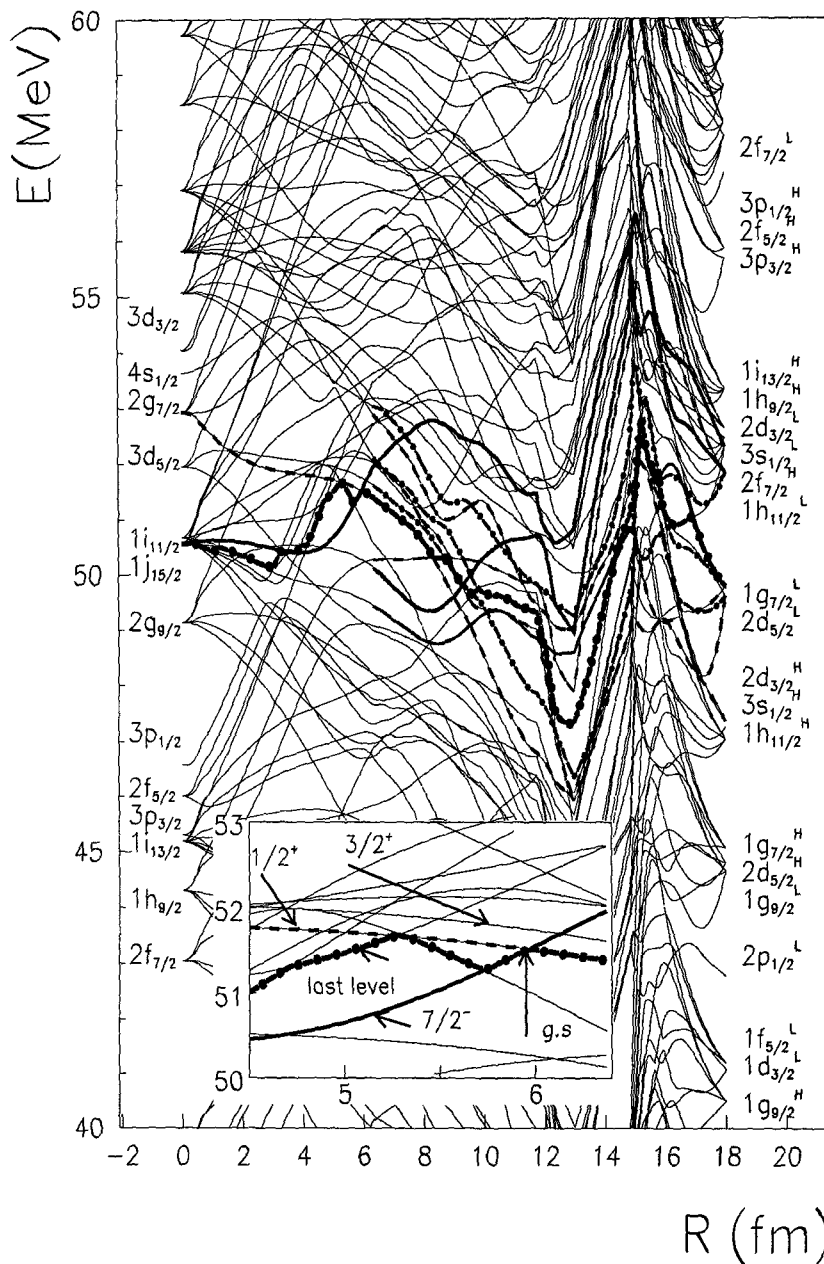


Figure 1. Neutron diagram for the emission of ^{135}Xe from ^{235}U as function of R . The ground-state is marked for $R=6$ fm in the inserted plot.

3. Phenomenological barriers

In cross section evaluations, conventionally the barrier is parameterized as function of a dimensionless parameter within three smoothed joined parabolas.

The height and the stiffness of the parabolas are obtained from experimental data within a good formula for the nuclear level densities and some corrections added in the saddle-point. This simple barrier is suitable for simulations. In the following, the single-particle excitations obtained theoretically are added to such a phenomenological barrier by interpolating between the values obtained at the extremes of the barrier, the ground-state and the exit point. Our phenomenological potential is characterized also by a squared imaginary part located between the turning points of the second well. The main effect of the imaginary part of the potential is to enlarge the widths of the intermediate structure peaks. Usually the magnitude of the imaginary part is obtained by fitting the experimental data. In our calculations, the magnitude of the imaginary part is calculated. It is considered that the transmission through the complex double well P_D divided by the total transmission that reached the second well P_a+P_D is equal to the transmission of the second barrier divided by the sum of all possible channels from the second well. Comparing this ratio with a similar formula based on Bohr-Wheeler transmissions, the magnitude of the imaginary potential can be obtained within an equation.

4. Compound nucleus and fission cross section

In our formalism, we consider that the saddle-point density is an implicit quantity, being determined by the fundamental density through a correspondence allowed by the height of each barrier constructed on fundamental levels with good quantum numbers and a probability of realization of the state associated to these numbers. The same fundamental density can be used for sub-barrier and supra-barrier transmissions. This feature allows us to unfold the initial state versus these quantum numbers, so that the states and the associated transition levels will be assigned by a probability in terms of Clebsch-Gordon coefficients. In order to obtain a mean energy width which takes into account the fact that the spin J of the nucleus is given by the coupling of the collective angular momentum of the core L and the spin of the intrinsic states J_f , the initial states J are unfolded through Clebsch-Gordon coefficients.

For one initial state, several channels become possible depending on L (the orbital momentum of the core), J_f (the spin of the non-rotational nucleus) or Ω (the projection on the nuclear symmetry axis). In the case of the neutron emission, the transmission is written by taking into account an additional channel due to the orbital momentum l carried by the neutron.

5. Results

In the upper panel of Fig. 3, the neutron-induced fission of ^{234}U is displayed in the frame of this model. A steeped rise of the fission cross-section at sub-barrier energies is superimposed on an intermediate resonance structure, as experimentally seen. Moreover, at very low energies, a structure of thin resonances is obtained. The procedure used in this work suggests that the intermediate structure, including the broad resonances, are in fact the result of a superposition of a large number of small resonances due to a huge number of different barriers associated to single-particle effects. Also, it can be suspected that the large number of resonances found in the thermal region can be associated to a large number of fundamental intrinsic states. Some arguments in favor of this hypothesis can be given. In Fig. 3, the weighted transmissions corresponding to all levels with $L=0$ and 1 as function of the excitation energy are displayed in the lower panel. In the vicinity of $E_n=0$ a great number of peaks reside in a small energy interval. These peaks have spin $\frac{1}{2}$ and their transmissions correspond to barriers that differ by energy paths of the unpaired neutron.

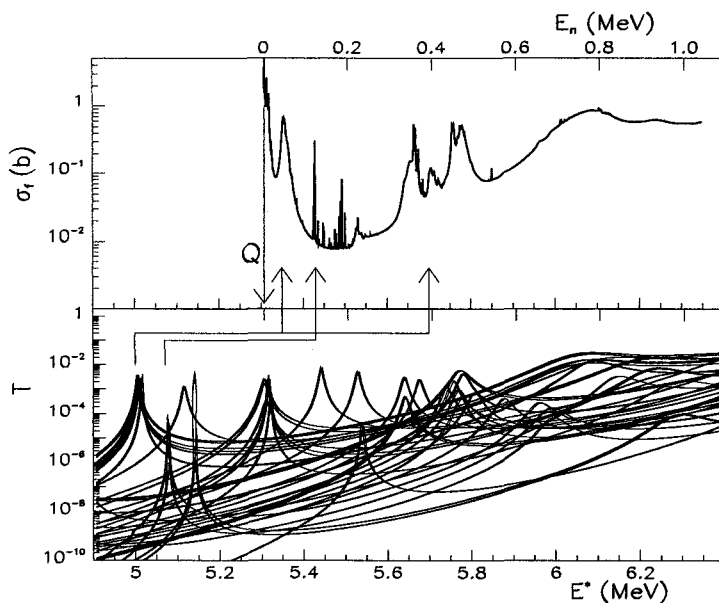


Figure 3. Upper panel: cross section as function of the excitation energy and the corresponding neutron energy. Lower panel: weighted transmissions through the barriers determined in this work for all values of Ω and $L=0,1$. Some patterns determined by combining the beta-excitations with other kind of vibrational excitations (approximated here with a constant value 0.35 MeV as described in text) are marked with arrows.

The double barriers involved in the calculation of these transmissions are characterized by practically the same heights but exhibit differences outside the saddle-points configurations.

6. Conclusions

It is possible that the rich resonant structure of the fission cross-section is due to a rearrangement of orbitals during the process from ground-state up to scission, and the formation of a large number of different barriers. The resonances carry information about the internal structure of the nucleus and the dynamics.

References

1. M. Mirea, L. Tassan-Got, C. Stephan, C.O. Bacri, P.Stoica, and R.C. Bobulescu, *J. Phys. G*, **31**, 1165 (2005).
2. M. Mirea, L. Tassan-Got, C. Stephan and C.O. Bacri, *Nucl. Phys. A***735**, 21 (2004).
3. M. Mirea, *Phys. Rev. C* **57**, 2484 (1998).

EXPERIMENTAL AND THEORETICAL STATUS OF BORROMEAN HALO NUCLEI STRUCTURE INVESTIGATION*

MARIUS PETRASCU

Horia Hulubei National Institute for Physics and Nuclear Engineering POBox MG-6
Bucharest-Magurele, Romania

An introduction to the work performed in pre-emission of neutrons from ^{11}Li halo nuclei will be presented. The standing present problems in the investigation of the structure of Borromean halo nuclei by means of the C_{nn} correlation function are outlined. An investigation of the target screening effect on the pre-emission of halo neutrons will be briefly described. It is shown that due to the diminishing of the screening effect the yield of neutron pair pre-emission is expected to be much larger in the case of ^{12}C than in the case of Si target. It is shown that a new experiment on ^{12}C target will allow to solve the standing problems of C_{nn} and also to test experimentally a recent new theory of C_{nn} [10].

1. Introduction

It was predicted in Ref. [1] that, due to the very large radius of ^{11}Li , and due to the very low binding energy of the halo neutrons, one may expect that in a fusion process on a light target, the halo neutrons may not be absorbed together with the ^9Li core, but may be emitted in the early stage of the reaction. Indeed, the experimental investigation of $\text{Si}(^{11}\text{Li}, \text{fusion})$ has shown that, a fair amount of fusion events [2] are preceded by the pre-emission of one or two halo neutrons. In Ref. [2] was also found that in the position distribution of the halo neutrons, a very narrow forward neutron peak is present. Considering that this peak may be due to neutron pairs, it was decided to investigate the neutron pre-emission in condition of much higher statistics by means of an array detector [3]. Indeed within the narrow forward peak (9 msr) a large number of n-n coincidences was found [4,5]. Trying to build the n-n correlation function, a serious problem appeared connected with the low values of the correlation strength [6,7,8]. A possible explanation could be the residual correlation of the halo neutrons [9]. In Ref. [9] has been proposed an iterative calculation to compensate for the residual correlation. But in Refs. [6,7,8] was shown that the iterative calculation is considerably increasing the error so that is no more possible to draw any conclusion concerning the theoretical predictions. In Ref.

* This work is supported by CERES 3_111 Contract.

[6] an experiment was proposed for getting the intrinsic correlation function by using ^{11}Li and ^{11}Be beams. The halo nucleus ^{11}Be would be ideal for the denominator of the correlation function construction, because it has only one halo neutron and therefore no residual correlation can be possible. In Ref. [6] was also proposed to do the new measurements, by using a C target instead a Si target, because due to the target screening which is lower in the case of C target, the yield of halo neutron pre-emission is expected to be higher. A preliminary estimation quoted in Ref. [6], indicated that for C target, the yield of halo neutron pre-emission is about 2 times higher than for a Si target. It will be shown in the next section, that a more accurate calculation is indicating that the yield of halo neutron pre-emission is expected to be ~ 3.5 times larger in the case of C-target than in the case of Si-target.

Very recently, a new theory for C_{nn} correlation function has been proposed [10]. In this theory, the ^{11}Li halo nucleus is modeled as a three body system consisting of 2 neutrons and a core. It is shown in [10], that an interference minimum is present in C_{nn} , due to the coherence of the 2 halo neutrons. This theory will be briefly considered in sect. 3. Also an analysis of the possibilities to test this new theory, is given. In sect. 4, the conclusions will be presented.

2. Target screening effect investigation

Due to the target screening effect, there is a marked difference between the halo neutron pre-emission probabilities in the fusion of $^{11}\text{Li} + \text{Si}$ and $^{11}\text{Li} + \text{C}$ target. This difference is illustrated in Figs. 1 and 2. In Figs. 1 and 2, the projections of the target nuclei Si and C, on the figure plane are considered. The ^{11}Li halo nuclei are considered as coming from bellow, and producing collisions with the targets in the plane of the figure. One can see in Fig. 1 corresponding to Si target that the halo neutron could escape only in the case if situated between the contour of the Si target (solid line) and the outer dashed line denoting the contour of the ^{11}Li halo. This area will be denoted in the following as S_f meaning "free area" that is, an area not obstructed by the target. Comparing Fig. 1 with Fig. 2, it is visible that $S_f(^{12}\text{C})$ is much larger than $S_f(\text{Si})$. Actually the ratio $S_f(^{12}\text{C})/S_f(\text{Si})$ is almost 3.

A first application of the Sharp Cutoff Model for neutron pre-emission from a halo nucleus was done in Ref. [11]. According to the Sharp Cutoff Model, only the halo neutron being on a "free area" that is an area not obstructed by the Si target, as in the case of Fig. 1a, could escape. The escape probability can be defined as:

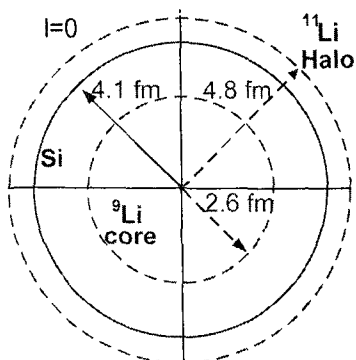


Figure 1: Schematic representation of ^{11}Li halo nucleus collision with Si target, for angular momentum $l=0$ (central collision). Here, the plane projections of the involved nuclei are shown. By the solid line, the contour of Si nucleus is represented. By dashed lines, the core of ^{11}Li and the contour corresponding to the $r^{\text{rms}} = 4.8$ fm of the halo [14] are shown.

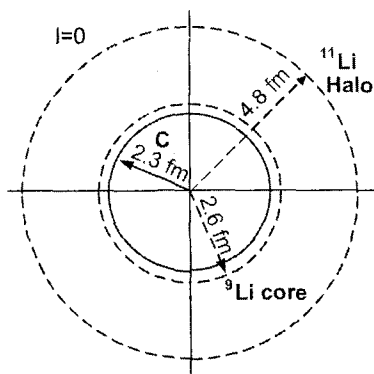


Figure 2: Schematic representation of ^{11}Li halo nucleus collision with ^{12}C target, for angular momentum $l=0$ (central collision). Here, the plane projections of the involved nuclei are shown. By the solid line, the contour of ^{12}C nucleus is represented. By dashed lines, the core of ^{11}Li and the contour corresponding to the $r^{\text{rms}} = 4.8$ fm of the halo [14] are shown.

$$\zeta(l) = \frac{S_f(l)}{S_{\text{tot}}} \quad (1)$$

In Eq. (1), l represents the angular momentum, S_{tot} represents the total area of the halo. One can calculate ζ for the whole range between $l=0$ and $l=l_{\text{cr}}$ by using the sharp cutoff formula for fusion reaction [12]:

$$\zeta = \frac{\sum_{l=0}^{l_{\text{cr}}} (2l+1)\zeta(l)}{\sum_{l=0}^{l_{\text{cr}}} (2l+1)} \quad (2)$$

In our calculations we obtained $l_{\text{cr}}=14$ for Si target and $l_{\text{cr}}=9$ for ^{12}C target. In this calculation [17] we used the simplified formula of Ref. [13]. The probability ζ is related to the probabilities $P^{[1]}$, $P^{[2]}$ and $P_a^{[2]}$ which are correspondingly the probability for pre-emission of 1 halo neutron, two halo neutrons and absorption of two halo neutrons:

$$P^{[1]} = 2\zeta(1-\zeta) \quad (3)$$

$$P^{[2]} = \zeta^2 \quad (4)$$

$$P_a^{[2]} = (1 - \zeta)^2 \quad (5)$$

The results of the performed calculations are provided in Table 1.

Table 1. In this table are provided the values of ζ probabilities (column 4), calculated by the sharp-cutoff formula (2), for 2 targets ^{12}C and Si. (column 1), and for 3 values for the halo radius R_{HALO} . The 4.8 fm value of R_{HALO} is the experimental value taken from Ref. [14]. In column 3, the value of ζ_{exp} is obtained from the number of single detected neutrons and from the number of detected neutron pairs (see Ref. [17]). One can see that ζ_{exp} is in fair agreement with ζ calculated by taking the experimental value of $R_{\text{HALO}}=4.8$ fm. In columns 5, 6, 7 the probabilities $P^{[1]}$, $P^{[2]}$, $P_a^{[2]}$ calculated according Eqs. (3), (4), (5) are given.

Target	R_{HALO} (fm)	ζ_{exp}	ζ	$P^{[1]}$	$P^{[2]}$	$P_a^{[2]}$	$\Sigma P[i]$
^{12}C	4.8		0.701	0.418	0.492	0.089	~1
	4.2		0.610	0.475	0.372	0.151	~1
	3.6		0.469	0.498	0.220	0.281	~1
Si	4.8	0.36±0.06	0.379	0.471	0.144	0.384	~1
	4.2		0.286	0.408	0.081	0.509	~1
	3.6		0.205	0.327	0/042	0.630	~1

As can be seen in Table 1, the increase of $P^{[2]}$ in passing from Si to C target, is mainly due to the decrease of $P_a^{[2]}$ (absorption of 2 neutrons). From Table 1 results that the ratio $P^{[2]}(\text{C})/P^{[2]}(\text{Si})$ is about 3.5. Considering also that the number of C nuclei in the C target is about 2 times larger than in the case of Si target for the same thickness, it follows that one can expect in an experiment performed with C target to acquire a statistics of n-n coincidences of about 7 times larger than one can expect in the case of Si target. With such a statistics of neutron pairs, not available in the past, one is hoping that the standing problem of residual correlations could assuredly be solved [8,9]. In the following section it is emphasized that the very recently published new theory of C_{n-n} could be tested also.

3. Testing the possibility of the recent new 3-body theory of C_{nn}

In Fig. 3 there is presented the C_{n-n} corresponding to the insert of Fig. 2 from Ref. [10].

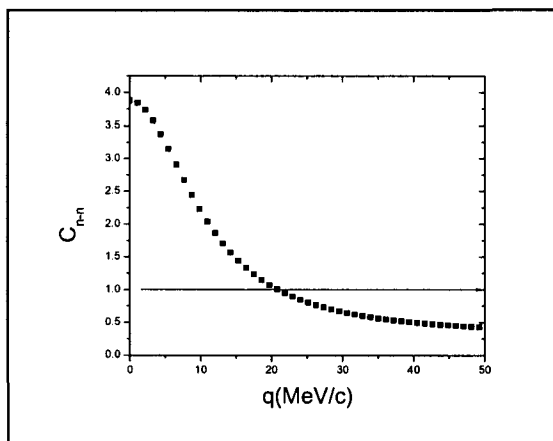


Figure 3: Here is shown the main C_{n-n} correlation function corresponding to the insert of Fig. 2 of Ref. [10]. One can see that this function becomes sub-unitary at q values larger than 20. In Ref.[18] it was obtained that the errors in the q range 20–40 MeV/c approach the value ± 0.2 , when the statistics of neutron pairs becomes ~ 1700 . From this follows that the new theory can be tested by using the most characteristic trait, that is its sub-unitarity.

As it is shown in Fig. 3 the most characteristic trait of the new C_{nn} correlation function is its sub-unitary values at $q > 20$ MeV/c. This trait can be tested [18] within a statistics of ~ 1700 nn coincidences.

4. Conclusions

It is amazing how much can be expected from one pre-emission experiment on a C target !

- The test of the large screening effect of Si target.
- To get answer to the question, could be the target screening, a cause for inflation of C_{nn} [17,18]?
- To make a test of residual correlation by using an ^{11}Be beam.
- To test a new theory of C_{nn} . In fact this theory is the first one worked out in the last 20 years specifically for the Borromean halo nuclei. An important remark is the following: The authors of the new theory have

determined the rms separation between the halo neutrons inside ^{11}Li within their same model [15] and have found 8.5 fm. This is very close to COSMA₁ model rms separation value, 8.3 fm. Consequently the finding of a correlation function of the type shown in the insert of previous Figure will be a confirmation of the ^{11}Li halo structure predicted by COSMA₁ model, [16].

Acknowledgements

This contribution has been worked out together with:

A. Constantinescu, I. Cruceru, M. Giurgiu, A. Isbasescu, H. Petrascu, C. Bordeanu, S. Serban, V. Stoica, HH-NIPNE, Bucharest, Romania, I. Tanihata, ANL USA, W. G. Lynch NSCL, MSU, USA, V. L. Lyuboshits, V. V. Lyuboshits, JINR, Dubna, Russia
M. P is grateful to Dr Lauro Tomio for sending him the C_{nn} numerical values prior to publication.

References

1. M. Petrascu *et al.*, *Balkan Phys. Lett.* **3**(4), 214 (1995).
2. M. Petrascu *et al.*, *Phys. Lett.* **405B**, 224 (1997).
3. M. Petrascu *et al.*, *Rom. J. Phys.* **44** (1-2 Suppl) 115 (1999).
4. M. Petrascu *et al.*, Preprint RIKEN-AF-NP-395 (2001).
5. M. Petrascu, *Yadernaia Fizika*, **66**, no 8, 1572 (2003).
6. M. Petrascu *et al.*, *Phys. Rev. C* **69**, 011602(R) (2004).
7. M. Petrascu *et al.*, *Nucl. Phys.* **A734**, 327 (2004).
8. M. Petrascu *et al.*, *Nucl. Phys.* **A738**, 503 (2004).
9. F. M. Marques *et al.*, *Phys. Lett.* **476B**, 219 (2000).
10. M. T. Yamashita, T. Frederico, Lauro Tomio, *Phys. Rev. C* **72**, 011601(R) (2005).
11. M. Petrascu *et al.*, *J. Phys. G* **25**, 799 (1999).
12. W. Nörenberg and H. A. Weidenmüller, in *Lecture Notes in Phys.* **51**, 1970.
13. J. Wilczynski *et al.*, *Nucl. Phys.* **A373**, 108 (1982).
14. I. Tanihata *et al.*, *Phys. Lett* **287B** 307 (1992).
15. M.T. Yamashita, Lauro Tomio, T. Frederico, *Nucl. Phys.* **A735**, 40 (2004).
16. M. V. Zhukov *et al.*, *Phys. Rep.* **231**, 151 (1993).
17. M. Petrascu *et al.*, *Phys. Rev C* (to be published).
18. M. Petrascu *et al.*, Proc. „*Frontiers in Nuclear Phys. Conf.*” Peterhof, Russia, June-July 2005 (to be published).

Z(4): γ -RIGID SOLUTION OF THE BOHR HAMILTONIAN FOR $\gamma = 30^\circ$ COMPARED TO THE E(5) CRITICAL POINT SYMMETRY

DENNIS BONATSOS, D. LENIS, D. PETRELLIS and P. A. TERZIEV and I. YIGITOGU

*Institute of Nuclear Physics, N.C.S.R. "Demokritos",
GR-15310 Aghia Paraskevi, Attiki, Greece
E-mail: bonat@inp.demokritos.gr*

*Institute for Nuclear Research and Nuclear Energy,
Bulgarian Academy of Sciences,
72 Tzarigrad Road, BG-1784 Sofia, Bulgaria
E-mail: terziev@inrne.bas.bg*

*Hasan Ali Yucel Faculty of Education, Istanbul University,
TR-34470 Beyazit, Istanbul, Turkey
E-mail: yigitoglu@istanbul.edu.tr*

A γ -rigid solution of the Bohr Hamiltonian for $\gamma = 30^\circ$ is derived, its β -part being related to the second order Casimir operator of the Euclidean algebra E(4). The solution is called Z(4), since it corresponds to the Z(5) model with the γ variable "frozen". Parameter-free (up to overall scale factors) predictions for spectra and B(E2) transition rates are in close agreement to the E(5) critical point symmetry, as well as to experimental data in the Xe region around $A = 130$.

1. Introduction

The E(5) critical point symmetry¹ has been obtained as an exact solution of the Bohr Hamiltonian² for γ -independent potentials, while the X(5) model is obtained as an approximate solution for $\gamma \approx 0^\circ$ ³. Another approximate solution, with $\gamma \approx 30^\circ$, called Z(5), has also been obtained⁴. In all these cases, five degrees of freedom (the collective variables β , γ , and the three Euler angles) are taken into account.

In the present work we derive an exact solution of the Bohr Hamiltonian for $\gamma = 30^\circ$, by "freezing" γ (as in Ref. 5) to this value and taking into account only four degrees of freedom (β and the Euler angles). In accordance

to previous terminology, this solution will be called Z(4).

2. The Z(4) model

In the model of Davydov and Chaban⁵ it is assumed that the nucleus is rigid with respect to γ -vibrations. Then the Hamiltonian depends on four variables (β, θ_i) and has the form⁵

$$H = -\frac{\hbar^2}{2B} \left[\frac{1}{\beta^3} \frac{\partial}{\partial \beta} \beta^3 \frac{\partial}{\partial \beta} - \frac{1}{4\beta^2} \sum_{k=1}^3 \frac{Q_k^2}{\sin^2(\gamma - \frac{2\pi}{3}k)} \right] + U(\beta), \quad (1)$$

where β and γ are the usual collective coordinates², while Q_k ($k = 1, 2, 3$) are the components of angular momentum and B is the mass parameter.

Introducing¹ reduced energies $\epsilon = (2B/\hbar^2)E$ and reduced potentials $u = (2B/\hbar^2)U$, and considering a wave function of the form $\Psi(\beta, \theta_i) = \phi(\beta)\psi(\theta_i)$, where θ_i ($i = 1, 2, 3$) are the Euler angles, separation of variables leads to two equations

$$\left[\frac{1}{\beta^3} \frac{\partial}{\partial \beta} \beta^3 \frac{\partial}{\partial \beta} - \frac{\lambda}{\beta^2} + (\epsilon - u(\beta)) \right] \phi(\beta) = 0, \quad \left[\frac{1}{4} \sum_{k=1}^3 \frac{Q_k^2}{\sin^2(\gamma - \frac{2\pi}{3}k)} - \lambda \right] \psi(\theta_i) = 0. \quad (2)$$

In the case of $\gamma = \pi/6$, the last equation has been solved by Meyer-ter-Vehn⁶, with $\lambda = \lambda_{L,\alpha} = L(L+1) - 3\alpha^2/4$, where α are the eigenvalues of the projection of angular momentum on the body-fixed \hat{x}^l -axis. α has to be an even integer⁶. Instead of α it is customary to introduce the wobbling quantum number⁶ $n_w = L - \alpha$, which labels a series of bands with $L = n_w, n_w + 2, n_w + 4, \dots$ (with $n_w > 0$) next to the ground state band (with $n_w = 0$)⁶.

The "radial" Eq. (2) is exactly soluble in the case of an infinite square well potential ($u(\beta) = 0$ for $\beta \leq \beta_W$, $u(\beta) = \infty$ for $\beta > \beta_W$). Using the transformation $\phi(\beta) = \beta^{-1}f(\beta)$, the first equation in Eq. (2) becomes a Bessel equation

$$\left[\frac{\partial^2}{\partial \beta^2} + \frac{1}{\beta} \frac{\partial}{\partial \beta} + \left(\epsilon - \frac{\nu^2}{\beta^2} \right) \right] f(\beta) = 0, \quad \nu = \sqrt{\lambda + 1}. \quad (3)$$

Then the boundary condition $f(\beta_W) = 0$ determines the spectrum, $\epsilon_{\beta;s,\nu} = \epsilon_{\beta;s,n_w,L} = (k_{s,\nu})^2$, $k_{s,\nu} = x_{s,\nu}/\beta_W$, where $x_{s,\nu}$ is the s th zero of the Bessel function $J_\nu(k_{s,\nu}\beta)$. The ground state band corresponds to $s = 1$, $n_w = 0$. This model will be called the Z(4) model.

tations in n dimensions, generated by the angular momenta, symbolically written as $E(n) = T_n \oplus_s SO(n)$ ⁷. One can see that the square of the total momentum, P^2 , is a second order Casimir operator of the algebra, while the eigenfunctions of this operator satisfy the equation

$$\left(-\frac{1}{r^{n-1}} \frac{\partial}{\partial r} r^{n-1} \frac{\partial}{\partial r} + \frac{\omega(\omega + n - 2)}{r^2} \right) F(r) = k^2 F(r), \quad (4)$$

in the left hand side of which the eigenvalues of the Casimir operator of $SO(n)$, $\omega(\omega + n - 2)$ appear. Putting $F(r) = r^{(2-n)/2} f(r)$, and $\nu = \omega + (n - 2)/2$, Eq. (4) is brought into the form

$$\left(\frac{\partial^2}{\partial r^2} + \frac{1}{r} \frac{\partial}{\partial r} + k^2 - \frac{\nu^2}{r^2} \right) f(r) = 0, \quad (5)$$

the eigenfunctions of which are the Bessel functions $f(r) = J_\nu(kr)$. The similarity between Eqs. (5) and (3) is clear.

The ground state band of $Z(4)$ is characterized by $n_w = 0$, which means that $\alpha = L$. Then in $Z(4)$ one obtains $\nu = L/2 + 1$, while in the case of $E(4)$ one has $\nu = \omega + 1$. The two results coincide for $L = 2\omega$, i.e. for even values of L . One can easily see that this coincidence occurs only in four dimensions.

4. Numerical results and comparisons to E(5) and experiment

The level scheme of $Z(4)$ is given in Fig. 1. The similarity between the spectra and $B(E2)$ values of $Z(4)$ and $E(5)$ can be seen by using the extensive numerical results for $E(5)$ given in Ref. 8. The spectra of the ground state band and the β_1 band, as well as their intraband $B(E2)$ s are very similar. One can easily check that the similarity extends to interband transitions between these bands as well, for which the selection rules in the two models are the same.

The main difference between $Z(4)$ and $E(5)$ appears, as expected, in the γ_1 band. The predictions of the two models for the odd levels practically coincide, while the predictions for the even levels differ, exhibiting different staggering.

Predictions of the $Z(4)$ model are compared to existing experimental data⁹ for ^{128}Xe , ^{130}Xe , and ^{132}Xe in Fig. 2. The reasonable agreement observed is in no contradiction with the characterization of these nuclei as $O(6)$ nuclei, since the predictions of γ -unstable models [like $O(6)$] and γ -rigid models [like $Z(4)$] for most observables are similar if γ_{rms} of the former equals γ_{rigid} of the latter¹⁰.

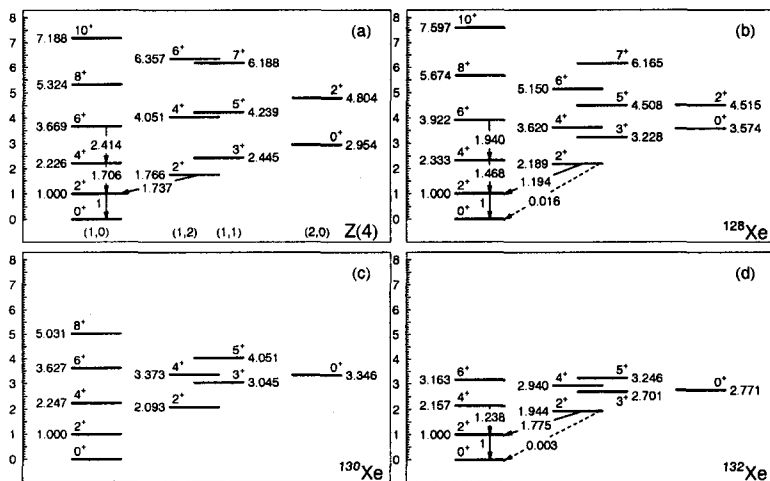


Figure 2. Comparison of the Z(4) predictions for (normalized) energy levels and (normalized) B(E2) transition rates (a) to experimental data⁹ for ^{128}Xe (b), ^{130}Xe (c), and ^{132}Xe (d). Bands in (a) are labelled by (s, n_w) .

5. Discussion

It should be emphasized that neither the similarity of spectra and B(E2) values of Z(4) to these of E(5), nor the coincidence of the ground state band of Z(4) to the spectrum of the Casimir operator of the Euclidean algebra E(4) clarify the algebraic structure of the Z(4) model, the symmetry algebra of which has to be constructed explicitly, starting from the fact⁶ that the Bohr Hamiltonian for $\gamma = 30^\circ$ possesses “accidentally” a symmetry axis.

References

1. F. Iachello, *Phys. Rev. Lett.* **85**, 3580 (2000).
2. A. Bohr, *Mat. Fys. Medd. K. Dan. Vidensk. Selsk.* **26**, no. 14 (1952).
3. F. Iachello, *Phys. Rev. Lett.* **87**, 052502 (2001).
4. D. Bonatsos *et al.*, *Phys. Lett. B* **588**, 172 (2004).
5. A. S. Davydov and A. A. Chaban, *Nucl. Phys.* **20**, 499 (1960).
6. J. Meyer-ter-Vehn, *Nucl. Phys.* **A249**, 111 (1975).
7. A. O. Barut and R. Raczka, *Theory of Group Representations and Applications* (World Scientific, Singapore, 1986).
8. D. Bonatsos *et al.*, *Phys. Rev. C* **69**, 044316 (2004).
9. Nucl. Data Sheets, as of volume **104** (2005).
10. R. F. Casten, *Nuclear Structure from a Simple Perspective* (Oxford University Press, Oxford, 1990).

ISOSPIN DISTILLATION FROM A MICROCANONICAL PERSPECTIVE

AD. R. RADUTA

NIPNE Bucharest, POB MG6, Romania

Fragment average isospin distributions are investigated within a microcanonical multifragmentation model in different regions of the phase diagram. The results indicate that in the liquid phase $\langle N/Z \rangle$ versus Z is monotonically increasing, in the region of phase coexistence it has a rise and fall shape, and in the gas phase it is constant. Characterization of the "free" and "bound" phases vs. fragment charge reconfirms the neutron enrichment of the "free" phase with respect to the "bound" one, irrespective of the localization of the multifragmentation event in the phase diagram.

1. Introduction

In recent years isospin dependent phenomena received much consideration because of their ability to reveal information on the asymmetry term of the nuclear equation of state (EOS). Relying on the fact that in heavy systems in which the neutron density exceeds the proton density the asymmetry term is repulsive for neutrons and attractive for protons, theoretical models of heavy ion reactions predicted different neutron composition of the liquid and vapor phases^{1,2}. More important for studies on EOS, the difference in chemical composition of the gas and liquid phases during a liquid-gas phase transition reflects the magnitude of the asymmetry term and its density dependence.

Trying to identify this process in experimental multifragmentation data, isoscaling techniques based on grandcanonical assumptions have been applied. The results proved the expected increase of neutron concentration in the gas phase with respect to the liquid phase³.

The aim of the present work is to investigate fragment average isospin distributions within a microcanonical multifragmentation model which includes in a realistic way the most important ingredients of the nuclear multifragmentation phenomenon, whose phase diagram was studied previously.

2. Microcanonical Multifragmentation Model predictions

While methods to identify phase transitions in small non-extensive systems accumulate, more importance is given to the fact that in principle the most correct statistical approach to be used for exploding nuclei is the microcanonical one. In the present paper the MMM version⁴ of the microcanonical multifragmentation model^{6,5} is used.

In this model fragments are placed in a spherical container defining the freeze-out volume. All configurations allowed by mass, charge, total energy, total momentum and total angular momentum conservation laws and not forbidden by geometrical constraints are spanned by a Metropolis Monte Carlo trajectory in the configuration space. The key quantity of the model is the weight of each configuration which has a non-analytically tractable form and enters the expression of any physical observable. The break-up fragments relevant for thermodynamics may be excited highly enough to de-excite by sequential particle emission. The present study focuses on the thermodynamically relevant break-up stage of the reaction.

The phase diagram associated with MMM was studied in Ref. 7. For small systems, like (50, 23), irrespectively whether the Coulomb interaction is present or not, the system evolves from the liquid phase present at low excitation energies to the gas phase corresponding to vaporized matter by crossing the coexistence zone. For large systems, like (200, 82), which experience stronger Coulomb fields, the situation becomes more interesting. When one turns the Coulomb interaction off, the system exhibits the same behavior as a small system. When the Coulomb field is activated the critical temperature and pressure decrease such that, for freeze-out volumes up to several tens V_0 , the system may evolve from the liquid phase to gas or supercritical fluid without crossing the phase coexistence zone.

In the following we shall present the MMM predictions on fragment average isospin distributions in different points of the nuclear phase diagram and stress the fact that $\langle N/Z \rangle$ versus Z manifests different behavior in the liquid, phase coexistence and gas regions.

2.1. (200,82) without Coulomb interaction

The phase diagram of the nuclear system (200, 82) without Coulomb and hard-core interactions is represented in Fig. 1 in the temperature-excitation energy and pressure-temperature planes. The solid lines represent iso- βP trajectories for different values of βP . The borders of the phase coexistence region were evaluated using Maxwell construction on the iso- βP caloric

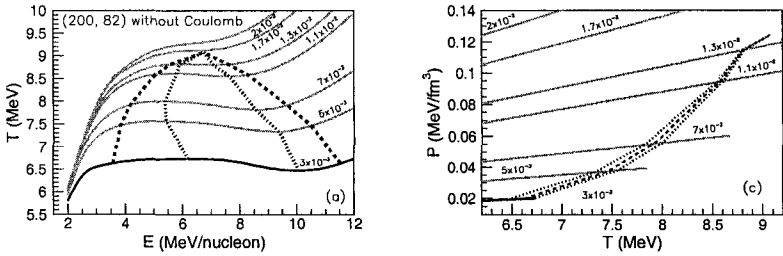


Figure 1. Phase diagram of (200, 82) nuclear system without Coulomb in temperature-excitation energy and pressure-temperature representations. The βP values of the iso- βP curves are labeled in units of fm^{-3} .

curves and are plotted with dashed lines. The borders of the spinodal region are defined as the locus of the inflexion points of $T(E)|_{\beta P}$ curves and are plotted with dotted lines. The critical point is characterized by the following set of values: $T_C = 9.1$ MeV, $P_C = 1.25 \cdot 10^{-1}$ MeV/ fm^3 , $E_C = 6.75$ MeV/nucleon and $(V/V_0)_C = 1.33$.

The shapes of $\langle N/Z \rangle$ versus Z distributions have been investigated along all iso- βP paths represented in Fig. 1. To illustrate the conclusions, we scan the phase space along the trajectory characterized by $\beta P = 3 \cdot 10^{-3}$ fm^{-3} . The states accessed in this way are similar to the ones obtained in nuclear multifragmentation reactions. Thus, as the excitation energy increases from 2 to 12 MeV/nucleon, the temperature ranges around 6 MeV and the average freeze-out volume increases linearly from $2V_0$ to $16V_0$.

Figure 2 represents the fragment average isospin ($\langle N/Z \rangle$) distribution as a function of fragment charge for the above considered excitation energies. Letting apart the average isospin of light charged particles ($Z < 5$) strongly affected by structure effects, one may observe that in the coexistence region $\langle N/Z \rangle$ vs. Z manifests a clear rise and fall behavior and in the gas phase it is constant. Moreover, in the coexistence region the average isospin of a fragment belonging to the liquid is monotonically decreasing with its charge.

The occurrence of the liquid phase at low values of excitation energy and/or freeze-out volume prevents fragment production in the intermediate size domain ($15 < Z < 30$). Moreover, the small values of the total fragment multiplicity make the isospin of clusters whose size is close to the source size sensitive to mass/charge conservation. For these reasons, it was not possible to access conclusive $\langle N/Z \rangle$ vs. Z distributions in the liquid

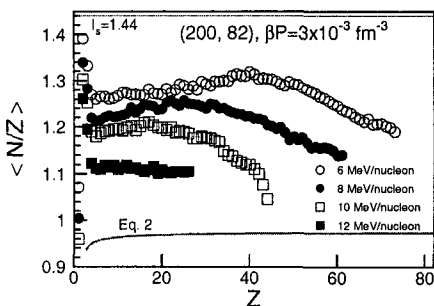


Figure 2. Fragment average isospin distributions as a function of fragment charge for the (200, 82) nuclear system without Coulomb interaction at different excitation energies. The thick line corresponds to the prediction of the liquid-drop binding energy formula, $I(A) = 1 + (a_c A^{5/3} - a_a A) / (2a_i \cdot (a_v A - a_s A^{2/3}))$.

phase.

The effect of excitation energy on $\langle N/Z \rangle$ vs. Z distributions within a given region of the phase diagram is quite trivial. Thus, by increasing the excitation energy the number of emitted neutrons increases such that for conserving the mass and charge of the total system the isospin of the rest of matter is decreasing leading to the observed shift of $\langle N/Z \rangle$ vs. Z distributions toward lower values. The decrease of the turning point where the rising distribution starts to decrease may be understood having in mind the diminish of the liquid part with the excitation energy increase.

2.2. (50, 23) and (200, 82) with Coulomb interaction

To verify whether the obtained results stand valid while modifying the system size and switching the Coulomb interaction on, in the following we shall investigate the (50, 23) and (200, 82) systems with Coulomb interaction.

The corresponding phase diagrams are represented in Fig. 3 in the temperature-excitation energy and pressure-temperature planes. The critical points are characterized by the following set of values: $T_C=4.9$ MeV, $P_C = 7.8 \cdot 10^{-3}$ MeV/fm³, $E_C=4.6$ MeV/nucleon and $(V/V_0)_C=12$ for (50, 23) and, $T_C=3.7$ MeV, $P_C = 1.7 \cdot 10^{-3}$ MeV/fm³, $E_C=7.75$ MeV/nucleon and $(V/V_0)_C=130$ for (200, 82), respectively.

The striking difference between the coordinates of these critical points and the one corresponding to the (200,82) without Coulomb case is the consequence of including the Coulomb interaction. Thus, the Coulomb

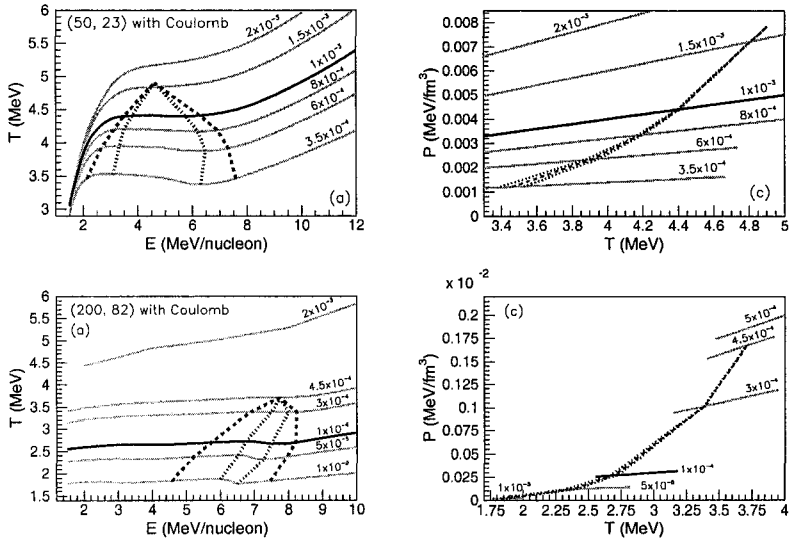


Figure 3. Phase diagrams of $(50, 23)$ (up) and $(200, 82)$ (low) nuclear systems with Coulomb interaction in temperature-excitation energy (a) and pressure-temperature (c) representations. The βP values of the iso- βP curves are labeled in units of fm^{-3} .

field forces the system to occupy a large volume such as to diminish the repulsive effect. If true, a critical volume of several tens V_0 would imply that real nuclear multifragmentation reactions for which the freeze-out volume was estimated to be $3-9 V_0$ take place at super-critical values.

The left panel of Fig. 4 presents $\langle N/Z \rangle$ versus Z distributions corresponding to the liquid, liquid-gas and gas phases of the $(50, 23)$ system along the constant $\beta P = 1 \cdot 10^{-3} \text{ fm}^{-3}$ path. For the coexistence region ($E=5 \text{ MeV/nucleon}$) and for the gas phase ($E=8 \text{ MeV/nucleon}$) the shapes look like the ones obtained for the $(200, 82)$ nucleus: in the phase coexistence $\langle N/Z \rangle$ versus Z has a rise and fall shape and for the gas phase it is almost constant. A striking result is the one corresponding to 2.5 MeV/nucleon which seems to be compatible with the phase coexistence region. The explanation of this apparent paradox lies in the fact that for such a small system and low excitation energies the total fragment multiplicity is around 3, meaning that each emitted light particle will modify drastically the isospin of the residual nucleus. Thus, the observed rise and fall is a consequence of mass/charge conservation.

The right panel of Fig. 4 shows several $\langle N/Z \rangle$ versus Z distributions

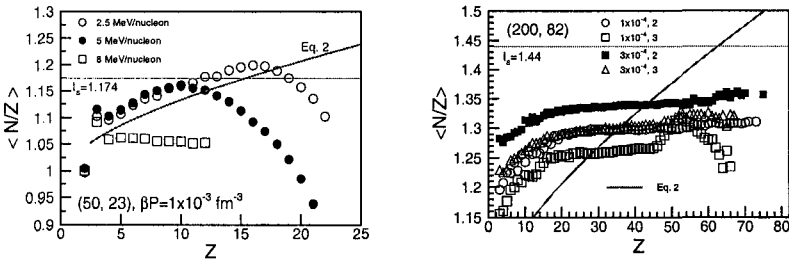


Figure 4. Fragment average isospin distributions as a function of fragment charge for the (50, 23) (left) and (200, 82) (right) nuclear system with Coulomb interaction.

corresponding to the liquid phase of the (200, 82) system that show a clear monotonic increase. The apparent exception corresponding to $\beta P=1 \times 10^{-4} \text{ fm}^{-3}$ and $E=3 \text{ MeV/nucleon}$ is again a manifestation mass/charge conservation due to fission as decay mechanism.

3. Do we have isospin fractionation in statistical multifragmentation models?

Since isospin fractionation was decided by both dynamical models and experimental multifragmentation data analyzing exclusively the isotopic content of light charged emitted clusters, it would be interesting to check to what extent our predictions agree with the reported results. To make this comparison straightforward we adopt one of the methods applied by dynamical models and classify the fragments as part of liquid and gas phases according to their mass. Thus, in the spirit of Ref. 2 we assume that the collection of fragments with $Z \leq 4$ form the "free" phase and the rest of fragments form the "bound" phase. We prefer to call the obtained subsystems by "free" instead of "gas" and "bound" instead of "liquid" because the above mentioned classification may be done irrespective of the localization of the multifragmentation event in the phase diagram.

Fig. 5 depicts the relative neutron enrichment of the "free" phase with respect to the "bound" phase in different points of the phase space. For all considered cases $\langle N/Z \rangle_{free} / \langle N/Z \rangle_{bound}$ is larger than one, meaning that isospin distillation takes place no matter what is the localization of the multifragmentation event in the phase diagram.

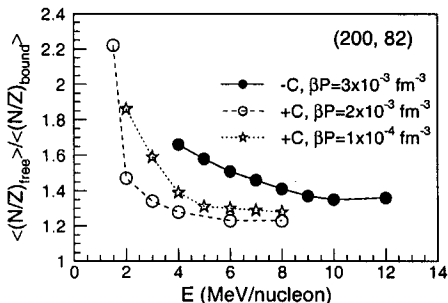


Figure 5. Relative neutron enrichment of the "free" phase with respect to the "bound" phase for the (200,82) nuclear system with and without Coulomb interaction when the associated phase spaces are explored along different βP constant paths.

4. Conclusions

Fragment isospin distributions have been investigated in the framework of a microcanonical multifragmentation model. The obtained distributions manifest different shapes in the liquid, liquid-gas and gas regions of the phase diagram. Deviations from this behavior are caused by mass/charge conservation and manifest at low fragment multiplicities. Phase classification according to the cluster size proves that neutron enrichment of the "free" phase with respect to the "bound" one depends on the source state. Finally, neutron enrichment of the "free" phase is not a signal of phase coexistence since it is observed everywhere in the phase space.

References

1. H. Muller and B. D. Serot, *Phys. Rev. C* **52**, 2072 (1995).
2. A. Ono *et al.*, *Phys. Rev. C* **68**, 051601(R) (2003).
3. H. S. Xu *et al.*, *Phys. Rev. Lett.* **85**, 716 (2000); E. Geraci *et al.*, *Nucl. Phys.* **A732**, 173 (2004); E. Martin *et al.*, *Phys. Rev. C* **62**, 027601 (2000); D. V. Shetty *et al.*, *Phys. Rev. C* **68**, 021602(R) (2003).
4. Al. H. Raduta and Ad. R. Raduta, *Phys. Rev. C* **55**, 1344 (1997); *ibid. Phys. Rev. C* **65**, 054610 (2002).
5. D. H. E. Gross, *Rep. Progr. Phys.* **53**, 605 (1990).
6. J. P. Bondorf *et al.*, *Phys. Rep.* **257**, 133 (1995).
7. Al. H. Raduta and Ad. R. Raduta, *Phys. Rev. Lett.* **87**, 202701 (2001).

ALPHA HALF-TIME ESTIMATES FOR THE SUPERHEAVY ELEMENTS

I. SILIȘTEANU*, A.O. SILIȘTEANU

*Horia Hulubei National Institute of Physics and Nuclear Engineering,
RO-077125, Bucharest-Magurele, Romania,*

** E-mail: silist@theory.nipne.ro*

W. SCHEID

Institut für Theoretische Physik der Justus-Liebig-Universität, Giessen, Germany

B.I. CIOBANU

Gh. Asachi Technical University, Iassy, Romania

The α -decay properties of nuclei are considered and some spectroscopic information on the continuum states populated in the unbound intermediate systems in the decay channel are obtained. The advantages and limitations of current approaches are addressed, with particular regard to quantitative experimental comparisons for superheavy nuclei.

1. Introduction

Our main objective is to make use of measurements and observations on decay reactions in order to derive conclusions concerning nuclear properties. Depending on the experimental approach in production of a radioactive nucleus, our goal is the determination of its existence, its main decay modes and half-life. It is our aim to extend previous developments^{1,2,3} for the case of single channel decay to the case of multi-channel decay. The total decay width for the multi-channel decay state k into a set of $\{n\}$ channels becomes:

$$\Gamma^k = 2\pi_n \Gamma_n^k, \quad (1)$$

where

$$\Gamma_n^k = 2\pi \left| \frac{\int_{r_{\min}}^{r_{\max}} I_n^k(r) u_n^0(r) dr}{\int_{r_{\min}}^{r_{\max}} I_n^k(r) u_n^k(r) dr} \right|^2. \quad (2)$$

In Eq. (2) $I_n^k(r)$ is the particle (cluster) formation amplitude (FA) and $u_n^k(r)$ and $u_n^0(r)$ are the solutions of the systems of differential equations:

$$\left[\frac{\hbar^2}{2m} \left(\frac{d^2}{dr^2} - \frac{l(l+1)}{r^2} \right) - V_{nn}(r) + Q_n \right] u_n^0(r) + \sum_{m \neq n} V_{nm}(r) u_m^0(r) = 0 \quad (3)$$

$$\left[\frac{\hbar^2}{2m} \left(\frac{d^2}{dr^2} - \frac{l(l+1)}{r^2} \right) - V_{nn}(r) + Q_n \right] u_n^\nu(r) + \sum_{m \neq n} V_{nm}(r) u_m^\nu(r) = I_n^\nu(r) \quad (4)$$

where: m is the reduced mass, $Q_n = E - E_D - E_p$ is the emission energy the FA is $I_n^k(r)$, and $V_{nm}(r)$ are the matrix elements of the interaction. The FA is:

$$I_n^k(r) = r \langle \Psi_k | \mathcal{A} | n \rangle = r \langle \Psi_k | \mathcal{A} \{ [\Phi_D(\eta_1) \Phi_p(\eta_2) Y_{lm}(\hat{r})]_n \} \rangle. \quad (5)$$

The matrix $V_{nm}(r)$ are generated by changing the radius of the daughter nucleus R_0 to a dynamical operator :

$$R_0 \longrightarrow R_0 + \hat{O} = R_0 + \beta_2 R_D Y_{20} + \beta_4 R_D Y_{40}, \quad (6)$$

β_2 and β_4 being the quadrupole and hexadecapole deformation parameters.

2. Results

The results of α -decay measurements^{4,5,6} and present estimates are shown in Fig. 1. In the most cases our results are in reasonable good accord to the GSI data for SHE with $Z=110-112$. Our half-time estimates for the SHEs 115 and 116 are shown in Fig.1 and Table 1. Our results are in a good agreement to data^{8,9} and differ significantly from the empirical ones⁷. Figure 3 shows the predicted Q_α -values⁷ for some homologous of groups I, II and VI-VIII versus the total number $N_t = N_p + N_n$ of valence nucleons. We can see that Q_α value decrease with N_t increasing. Clearly that the Q_α -value increases in the main channels of the regions (1,2) when approaching the the magic proton shell, while for the SHE region (3), this decreases. This may suggest the existence of the shell at $Z>114$ contrary to the basic model⁷, but in accord with the mean-field predictions^{10,11}. In Fig.4 we can observe that the Casten factor represents the number of the α -particle over the magic core, and the half-lives for some homologous are almost identical. It was stressed also in¹² that other spectroscopic observables for SHE lie along smooth curves when plotted against this factor.

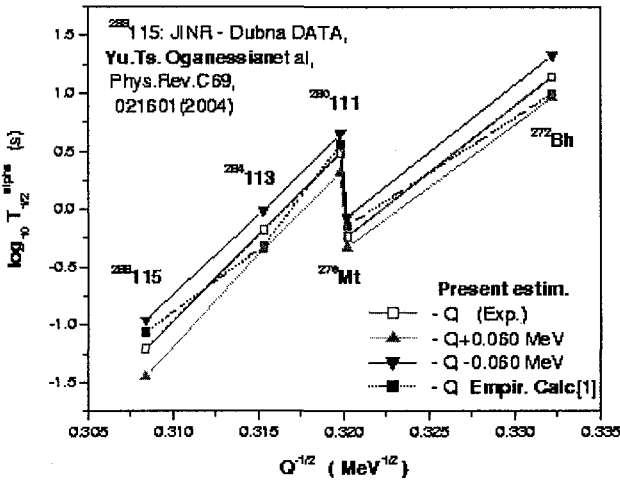


Figure 2. The α -decay data and our present estimates.

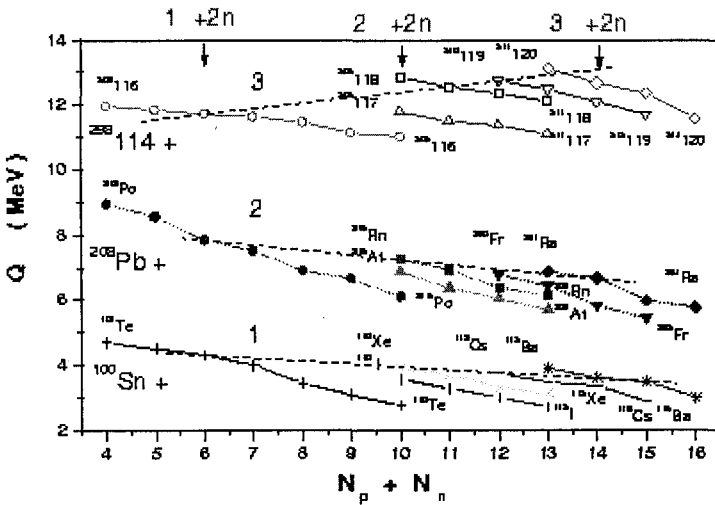


Figure 3. Q_α -values versus the total number of valence nucleons $N_p + N_n$.

3. Conclusions

In most cases, our α -half-time estimates are in excellent agreement to existing data. Such an agreement supports the basic correctness of our unified

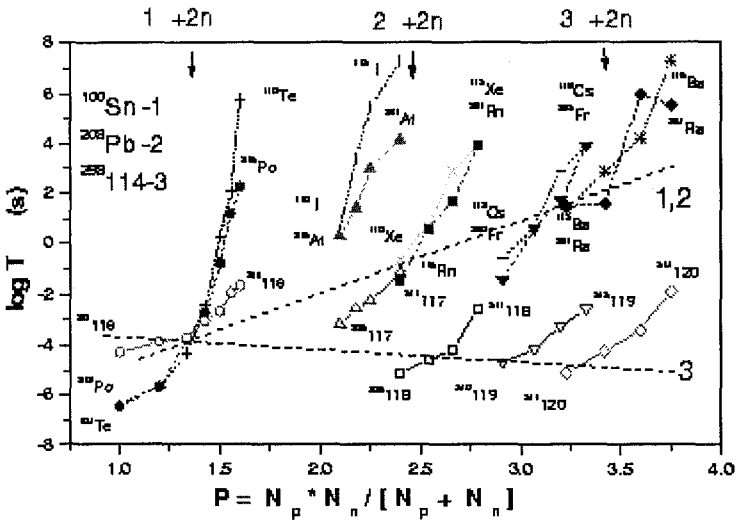


Figure 4. Experimental (full symbols) and estimated (open symbols) α half-lives versus the Casten factor.

picture for heavy-ion and α resonances giving us guarantees for reliable predictions for SHE.

References

1. I. Silişteanu, W. Scheid and A. Sandulescu, *Nucl. Phys.* **A679**, 317 (2001).
2. I. Silişteanu, W. Scheid, *Phys. Rev.* **C51**, 2023 (1995).
3. I. Silişteanu, M. Ivascu, *J. Phys. G./Nucl. Part. Phys.* **15**, 1405 (1990).
4. S. Hofmann *et al.*, *Zeit. Phys.* **A350**, 281 (1995).
5. S. Hofmann *et al.*, *Zeit. Phys.* **A354**, 229 (1996).
6. S. Hofmann and G. Münzenberg, *Rev. Mod. Phys.* **72**, 733 (2000).
7. P. Möller *et al.*, *At. Data and Nucl. Data Tab.* **66**, 131 (1997).
8. Yu. Ts. Oganessian *et al.*, *Phys. Rev.* **C69**, 021601 (2004).
9. Yu. Ts. Oganessian *et al.*, *Phys. Rev.* **C69**, 054607 (2004).
10. K. Rutz *et al.*, *Phys. Rev.* **C56**, 238 (1997).
11. B.A. Brown, *Phys. Rev.* **C58**, 220 (1998).
12. N.V. Zamfir, private communication, 2005.

This page is intentionally left blank

Part III
Conclusions

This page is intentionally left blank

DARK ENERGY - DARK MATTER - AND BLACK HOLES: THE MUSIC OF THE UNIVERSE*

PETER L. BIERMANN

*Max-Planck Institut for Radioastronomy and
Department for Physics and Astronomy
University Bonn, Germany
E-mail: plbiermann@mpifr-bonn.mpg.de*

Here we review the recent evidence for dark energy, dark matter and black holes as components of an expanding universe, for the vantage point of a non-expert; we speculate on a specific DM particle.

1. Introduction

In recent years the evidence for the ubiquity of black holes has become overwhelming, as most galaxies above a certain size appear to have a massive black hole at their center. Observations suggest that such black holes have formed very early in the Universe's evolution.

Similarly, we now have convincing evidence, that galaxies are largely dominated by dark matter, a non-baryonic constituent (Bertone et al. 2005).

And, finally, in very recent years further evidence has accumulated, that a dark energy is trying to rip the universe apart.

Here we review very briefly what we know about these strange constituents of the universe, and speculate on one of them.

2. What holds the Universe together?

Everyday experience shows that gravity holds us down safely, in our chair, in our cars, in our trains and airplanes. The gravitational force of the Earth keeps us down.

*public lecture in celebration of the World Year of Physics 2005 on Mon. June 20th, 2005.

2.1. *Throwing a Ball*

From a child throwing a ball to an artificial satellite flying around the Earth we can describe the orbit with the gravitational pull, the persistent momentum, and the friction in air as well as the upper atmosphere. What is falling down for a ball is curving around the Earth for a satellite or spaceship.

2.2. *An orbit*

Close to the Earth a satellite flies around in about 90 minutes, and from the equality *centrifugal force = gravitational attraction* we can calculate the mass of the Earth. We obtain $5.9723(9) \cdot 10^{24}$ kg (see PDG 2004); in this we use the radius of the Earth 6,378.140 km, already determined in ancient times (although it has to be admitted with a huge error budget not understood at the time). Any child can do an analogous experiment with a pendulum, using a lead-weight and a suspension via a sharp edge on two wires.

2.3. *Sun*

The Earth flies around the Sun, at a distance of $1.495,978,706,60(20) \cdot 10^8$ km, and with a measured velocity of about 30 km/s. Hence we can determine the mass of the Sun to $1.988,44(30) \cdot 10^{30}$ kg. This is about 300,000 times the mass of the Earth. We can also determine the radius of the Sun to $6.961 \cdot 10^5$ km. So light travels from the Sun to us in 8 minutes, longer than the Sun takes to set.

However, with the Sun we can do a test: The Sun sounds like a bell, from its *MUSIC* we determine the structure of the Sun. This is completely analogous to the quality check of a metal bell, which sounds only really nice and harmonious if its structure contains no flaws, and is all homogeneous. Soundwaves run through a bell, and cause waves to propagate though the surrounding air. Similarly soundwaves run through the Sun, also right through the center. So we can determine the structure of the Sun – and can so test our models for the Sun.

Today we have understood and solved the Solar neutrino problem – we understand the Sun – everything fits; one caveat has to be mentioned: we still do not understand the origin of magnetic fields in the universe, and the corresponding challenges of the magnetic plasma near the Sun may provide the avenue to our insight. The neutrino problem then gave deep insight into the properties of neutrinos, their finite mass.

3. Galaxies and Clusters of Galaxies

3.1. *The Milky Way*

The Sun flies around the center of our Milky Way, about once every 250 million years, and at a distance about 20,000 light years.

This motion we can determine within two weeks by measuring foreground stars against background stars using intercontinental radio interferometry. The stars in front rush by the stars in the background, just like trees in the foreground fly by the houses in the background looking out from a railroad car; this is of course especially noticeable if the train goes at 300 km/h.

And so we determine the mass of the Milky Way, and find a mass of about $2 \cdot 10^{11}$ solar masses. This is the mass approximately inside the Solar circle. Please note that such a determination is strictly accurate only for a spherically symmetric distribution of mass; for a rotationally symmetric distribution of mass, for instance, like a flattened disk system, the gravitational force has to be obtained by a suitable integral from zero to infinity. This mass therefore corresponds only approximately to the mass inside 8 kpc.

In fact, from the observation, that the next neighboring galaxy, Andromeda or M31, approaches us already, pulled from the overall expansion of the Universe, we can determine an even higher mass, by about a factor of ten; this mass then corresponds to a radial scale at least about a factor of ten larger than that obtained at the Solar circle.

However, we can also count stars, to try to determine how many stars are there, and if their mass is able to account for the mass that we get from the gravitational pull, exerted on the same stars. In one approximation this was done first by J. Oort, who already noted that there seemed to be a problem: Depending how we count, we miss anything between a factor of 2 and 10 of the mass in stars in the Galaxy.

3.2. *Galaxies and black holes*

We can repeat this exercise using hot gas in early type galaxies, rotation curves of cold gas in late type galaxies, and we always find, that we miss stars.

We can also check for black holes in galaxies, and we always find a central black hole, in galaxies above a certain size or mass. In our Galaxy the mass of the central black hole is about $4 \cdot 10^6$ solar masses. In other galaxies the mass of the central black hole can reach $3 \cdot 10^9$ solar masses.

The mass of this black hole appears to be strictly proportional to the mass of the spheroidal stellar component of the galaxy, with a factor of 1/500. There are several explanations for this proportionality, usually matching star formation in the galaxy with central accretion (see, e.g., the work by Y. Wang).

3.3. Clusters of Galaxies: Mass

Galaxy is just the Greek translation of “Milky Way”, derived from the Greek word for “Milk”; we can consider then the motion of galaxies in clusters of galaxies, and again use both the motions as well as the hot gas to find out how much gravitational pull is necessary to keep the cluster from flying apart.

A typical cluster may have a thousand galaxies moving around several Mega-light-years. From such determinations as well as applying hydrostatic equilibrium models to the X-ray emission of the hot gas we obtain a mass of about 10^{15} solar masses.

3.4. Gravitational Lenses = Glasses

Photons deviate in the gravitational field of the Sun from a straight line path. Light is also bent in its path in and around clusters of galaxies. The bending also gives directly the total mass. We find the same difficulty, only even more pronounced.

3.5. Clusters of Galaxies Problem

We can also count galaxies in clusters, and all the mass in their stars. And again we can use the X-ray emission from the hot gas to get its mass. The hot gas even dominates over the stars in mass, integrated all over the cluster. And the problem is once again: We are missing out on about 90 % of the total mass.

What holds clusters of galaxies together?

4. Matter as You and Me

Matter like you and me we call baryonic matter. The Earth, Sun, Stars, hot and cold gases, all the way to the beginning of the Universe are made up of baryonic matter.

4.1. *Matter Partner Protons*

At the beginning of the Universe – after about 3 minutes – there was a certain fraction of matter in protons and neutrons. Through meeting in binary encounters pairs of nucleons can be formed, and so on to Helium. From today's fraction of Helium in mass we can determine the initial density of nucleons. Therefore we can conclude that about 5 - 10 times as much baryonic matter has to be there, than we can directly observe. Could this be warm gases with about 100,000 K temperature ?

5. Music of the Big Bang

The Universe was very hot at the beginning. Soundwaves just like the waves which carry my words to you ran through the universe. The hot radiation from those early days is still visible. The waves are also visible, a disturbance of 1 part in 100,000. We observe, February 11, 2003 on the internet, the first three tones of the Universe, measured by the satellite WMAP, with incredible precision (astro-ph/0302209, Spergel *et al.* 2003).

This is analogous again of the nice sound from a well built bell, or a violin; a Stradivari sounds wonderful, because of the construction as well as the materials, the special wood, out of which is has been made.

5.1. *Standard Candles*

Stars explode – why, is still contested. For the massive stars this may be due to the magneto-rotational mechanism, proposed long ago (1970) by G. Bisnovatyi-Kogan (many papers 2004/2005), based on an earlier suggestion by N. Kardashev (1964).

Stars like the Sun develop into a white dwarf. White dwarfs in a binary stellar system obtain more mass via tidal forces. When they get too much mass, they collapse, and blow up. This Supernova explosion seems to be always the same – and so we have a standard candle to determine distances in the universe.

For the lamps along a road, that one can observe from some mountain late in the evening, we can determine for every lamp its distance from is apparent brightness, assuming no fog nor haze. And so we find that the universe expands with acceleration, driven by some DARK ENERGY with repelling force. Initially this expansion was slow, for some time it is now accelerating. But why is the factor between DARK MATTER and DARK ENERGY just 3, and just today?

6. Matter?

Normal matter – that you can see directly – you, and me, stars, dust and gases, is an insignificant fraction. Normal matter – that one sees only with great difficulty – probably warm gases, so total normal matter is a fraction of about 0.04. The relative and dimensionless density here is relative to the critical density of the universe, a density which would correspond just to a parabolic orbit without dark energy.

Invisible matter, that we can determine only through its gravitational force, so **DARK MATTER**, of some totally different nature, is about 0.23 in fraction.

Invisible energy, called **DARK ENERGY**, is about 0.73 in fraction.

The sum of these contributions is unity to the best of our understanding (the error budget is about 2 percent).

So the sum of the angles in any large triangle through the universe is 180 degrees – so in the language of mathematics – the universe is flat just like the geometry of a table in a library. Of course one should stay away from black holes for this experiment.

6.1. *Dark Matter Speculation*

As shown in recent work by F. Munyaneza and A. Kusenko with the author (to be published), recently several papers have appeared that seem to converge to a possible solution of the dark matter problem:

- In Kusenko (2004) it has been shown, that a sterile neutrino in the mass range 2–20 keV can explain the kicks pulsars experience at birth, giving them linear velocities along their rotation axis up to 1000 km/s.
- In Munyaneza & Biermann (2005) it has been shown that a Fermion dark matter particle far out of thermodynamic equilibrium in its distribution can explain the early growth of black holes, provided the mass range is 12–450 keV.
- In Abazajian *et al.* (2001), and in Mapelli & Ferrara (2005) it has been shown that the X-ray observations give a constraint for a sterile neutrino mass, with one range allowed to be $\lesssim 14$ keV.

All these lines of reasonings can be summarized as the statement that a sterile neutrino with a small mixing angle in a mass range near 10 keV is a possible dark matter candidate. It appears to fit all observations. Further checks and specific predictions will be presented in a forthcoming paper by

F. Munyanza, A. Kusenko and the present author.

7. Riddle

Let us phrase the riddle in a series of questions:

- What is this repelling force?
- Why is the geometry flat? How is this possible, since the fractions of all components all vary with cosmic time? And yet in the sum always give unity exactly?
- Half the present age of the universe ago dark matter was ten times as important as dark energy, in double today's age of the Universe dark energy will be twice as important as dark matter – will we get the "BIG RIP"? Everything in the Universe will be torn apart, at last even the atoms...?
- Are black holes perhaps important in all this?
- New particles? Do I have to look for new particles in the cosmos instead of at (Geneva) CERN or (Chicago) FERMILAB or (San Jose) SLAC?
- What is the interaction between dark matter and black holes?

7.1. *What We Do not Know*

- Age solar system 4.5 billion years (US billion)
- Age Milky way about 13 billion years
- Age Universe 13.7 billion years
- About 10^{-4} fraction black holes
- About 0.004 visible baryonic matter – Matter like us
- About 0.036 invisible baryonic matter: warm gases?
- About 0.23 non-baryonic matter: What is this?
- About 0.73 dark energy: What is this?
- Future uncertain: What does it mean and what does it bring?

7.2. *The Young Minds*

- **We are looking for an answer**
- What does this all mean?
- Please help!
- Where are our next students?
- Women and men?
- Who wants to help looking?

Acknowledgements

First of all I would like to express my appreciation for the comments on this ms by A. Kusenko and F. Munyaneza, my partners and friends in the DM work. The initial push for the latest stage of this work happened in the inspiring atmosphere at the Aspen Center for Physics, summer 2005; the ACP is funded by the National Science Foundation. Continuing work with F. Munyaneza is funded by the Humboldt Foundation.

P.L. Biermann would like to acknowledge St. Barwick, G. Bisnovatyi-Kogan, D. Cline, T. Enßlin, P. Frampton, T.W. Jones, R. Juszkiewicz, H. Kang, P.P. Kronberg, A. Kusenko, N. Langer, S. Moiseenko, F. Munyaneza, J.P. Ostriker, D. Ryu, Y. Wang, and T. Weiler for intense discussions of these and related questions.

Special support comes from the European Sokrates / Erasmus grants in collaboration with East-European Universities and academy institutes, with partners W. Bednarek, L. Gergely, M. Ostrowski, K. Petrovay, A. Petrusel, M.V. Rusu, and S. Vidrih, and VIHROS through the FZ Karlsruhe. Recent support comes from NATO for a collaboration with S. Moiseenko and G. Bisnovatyi-Kogan (Moscow).

Work with PLB is being supported through the AUGER theory and membership grant 05 CU 5PD1/2 via DESY/BMBF (Germany); further support for the work with PLB has come from the DFG, DAAD, Humboldt Foundation (all Germany).

References

1. Particle dark matter: evidence, candidates and constraints, Bertone, G., Hooper, D., & Silk, J., *Physics Reports*, **405**, 279 - 390 (2005), hep-ph/0404175
2. Pulsar kicks from neutrino oscillations, Kusenko, A., *Int. J. of Mod. Phys. D* **13**, 2065 - 2084 (2004), astro-ph/0409521
3. Fast Growth of supermassive black holes in Galaxies, Munyaneza, F., & Biermann, P.L., *Astron. & Astroph.* **436**, 805 - 815 (2005), astro-ph/0403511
4. Direct detection of warm dark matter in the X-ray, Abazajian, K., Fuller, G.M., & Tucker, W.H., *Astrophys. J.* **562**, 593 - 604 (2001), astro-ph/0106002
5. Background radiation from sterile neutrino decay and reionization, Mapelli, M., Ferrara, A., *Month. Not. Roy. Astr. Soc.* (submitted 2005) astro-ph/0508413
6. First-Year Wilkinson Microwave Anisotropy Probe (WMAP) Observations: Determination of Cosmological Parameters, Spergel, D.N., et al., *Astrophys. J. Suppl.* **148**, 175 - 194 (2003), astro-ph/0302209; and many later papers by the WMAP team

CONCLUDING REMARKS

About the experimental appeal of CSSP05

HEINIGERD REBEL

Institut für Kernphysik, Forschungszentrum Karlsruhe, D 76021 Karlsruhe, Germany

The scientific program of the Carpathian Summer School of Physics 2005 is commented with respect of impacts on the current research of Nuclear Spectroscopy and Astrophysical topics.

1. Introduction

After these nice and beautiful days, a period of very inspiring scientific and personal interactions, updating our views in various subjects of frontier topics in physics, it is a privilege and pleasure for me to conclude the Carpathian Summer School of Physics with some mostly general remarks, from the viewpoint of a, basically, experimental researcher. The remarks are compiled along the talks from my personal point of view and do neither demand to be complete nor do they reflect a balanced evaluation of the new, less new and the brand new messages. Actually I have to apologise at the outset for my fragmentary view, being unable to mention all important issues.

In the very beginning, first I would like to indicate the location of my personal look-out tower. With the bird's view over the Research Centre in Karlsruhe (Fig.1) you may recognize extended arrays of detector stations detecting nuclear particles, distributed over a larger area. It is the detector field of a large scale experiment, comprising the experimentally linked cosmic ray installations of KASCADE (right corner) and KASCADE-Grande (red and green points). The experiments are based on the common efforts of an international collaboration. KASCADE-Grande is an upgrade of KASCADE for a higher energy range for the observations of particles coming from the Cosmos.

In the centre of the original KASCADE array there is a central detector setup, a complicated device, with a heart being a large iron sampling calorimeter for detecting and measuring the interaction of high energy hadrons in the energy range of about 1 to 10 TeV. The experiments observe so-called Extensive Air Showers (EAS), i.e. their soft electron - photon, the penetrating muon and the hadronic components.

THE KASCADE-Grande Experiment

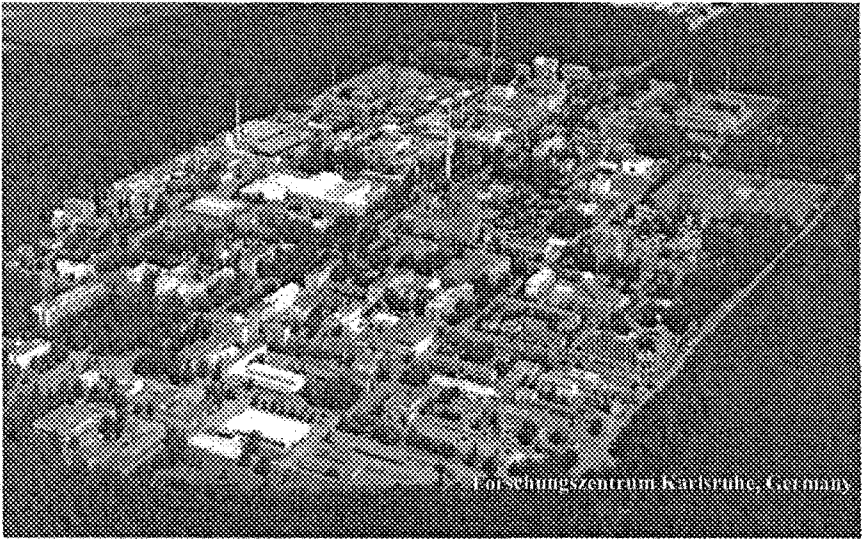


Figure 1. The detector array KASCADE -Grande installed in Forschungszentrum Karlsruhe [1].

*The aim of the investigations is to infer the nature, mass and energy of the primary particles, impinging on our Earth's atmosphere from the Universe, and to explore their interactions with the air target. The energy spectrum of the primary cosmic rays exceeds many orders of magnitude the energies of man-made accelerators. Our experiment concentrates to the energy range between 10^{15} and 10^{17} eV, that is, the region from around the equivalent laboratory energy of the TeV Fermi Lab Collider and the future Large Hadron Collider, therefore, largely in "terra incognita" in what concerns the hadronic interactions. In this energy region the spectrum indicates conspicuous peculiarities, and detailed experimental information on energy and mass composition of cosmic rays in this region are of extreme astrophysical interest to clarify the hitherto largely unknown **origin, propagation and acceleration mechanisms** of cosmic rays.*

Thus, my actual "business card" (or homepage) is coloured with astrophysical interests, with a sight to topics, which have been explored in two interesting laboratories, in the Atomic Nucleus and in the entire Universe by observing various kinds of interactions of various different probes, with perspectives of general and fundamental scientific character.

2. Some general remarks

The close connection between the laws of microphysics, i.e. nuclear and particle physics with the macrophysics, i.e. astrophysics and cosmology is one of the most important insights and discoveries of the last century, being promoted by Albert Einstein and company.

When considering our school program, in fact one laboratory from which we did dominantly report has been indeed the Atomic Nucleus, a collaboration of A nucleons, confined clusters of quarks and gluons, whose interactions carry the Universe. The nucleus as a distinct physical entity has been studied for most of the last century. A casual reviewer of our extended studies may come to the conclusion that the subject is in a mature status and provides now a complete picture of nuclear matter, and that further research is for filling up details and is of less priority. This is also often expressed by colleagues from other specialities, corroborated - we must admit - by occasional immobilities of established sub-branches of our field. Consequently, such a view is also nowadays very often uncritically adopted at public administration offices, surely biased by public opinions in our societies and an irrational understanding of the role of nuclear energy for mankind.

However, the field - this School gives witness - is currently going through an exciting renaissance with the potential of a radical change of our perception of nuclear matter, due to new experimental techniques and new insights and with a rather conclusive demonstration of the relevance and links of nuclear physics with other physical sciences: Astrophysics, Particle Physics and Cosmology. In what concerns Nuclear Physics itself, the renaissance is prompted by the *development of new techniques for probing various degrees of freedom, of production of intensive radioactive beams to investigate nuclear matter at extreme charge-to-mass ratios and new instrumentation to probe nuclei spinning at their limits.*

Even seen from a distant point of view, this renaissance appears to be so remarkable, that nuclear physicists would have no need to justify their jobs only by spin-offs useful for the society, following each public wind to get support. Applications are certainly important and Applied Physics is even challenging and of fascinating interest - what we probably sometimes tend to ignore expressing - but the science of understanding our world, its conserved and broken symmetries, is for itself a service for mankind, for human culture and a basis of common understanding. It should not need artificial spin-offs constructed for the eyes in ministry offices, faking our studies related to the needs of construction firms. This understanding, however, is a matter of culture

of a society, reflected by the political priorities. In Germany we celebrate this year also the Schiller year: Friedrich Schiller died 200 years ago. He says in one of his poems about Science, freely translated: "For one, Science is the adored goddess of truth about us and our world, for the other, just the cow supplying the material for butter production".

3. Ordering the program

The guidelines of this short tour through the landscape of this school are:

- New Developments of Nuclear Spectroscopy and Exotic Nuclei - SuperHeavy Nuclei
- Nuclear Astrophysics: Studies of the Birth of Chemical Elements -Direct and Indirect Laboratory Methods
- Hadronic Matter in various Phases and High Energy Astrophysics
- Large Facilities - currently running and in future
- Messages about the Neutrino

Of course, the issues, even of this selection, are not well separated topics, neither experimentally nor theoretically. It just the charm of this workshop-school to display the lively interplay.

I am going to use in this summary images of full or parts of slides presented at this conference, provided by the authors themselves.

3.1. *Nuclear Spectroscopy*

The first lecture of this workshop by Reiner **Kruecken** (Figs. 2 and 3) did formulate the longstanding current questions, detailed with some studies at the MINIBALL. MINIBALL is a modern gamma ray spectrometer, especially designed for inverse kinematics experiments with radioactive beams. That device is obviously walking through the European laboratories like a travelling circus and economically used for frontier spectroscopic studies.



Long Standing Questions of Nuclear Structure Physics

- What are the limits for existence of nuclei?
 - Where are the proton and neutron drip lines situated?
 - Where does Mendeleev's table end?
- How does the nuclear force depend on varying proton-to-neutron ratios?
 - What is the isospin dependence of the spin-orbit force?
 - How does shell structure change far away from stability?
- How to explain collective phenomena from individual motion?
 - What are the relevant degrees of freedom and symmetries of the many-body system?
- How are complex nuclei built from their basic constituents?
 - What is the effective nucleon-nucleon interaction?
 - How does it connect to QCD?
- What are the nuclei relevant for astrophysical processes and what are their properties?

Figure 2. Longstanding questions of Nuclear Structure Physics.

We have learned with interest that the production and studies of exotic nuclei put again the question of determination of charge, matter and neutron radii of nuclei: The quest is for adequate experimental methods of determination, but also for a clear insight, what is really determined experimentally. Which type of radius is determined by the particular experiment, what is an extrapolation by an adopted form? For this studies we may learn from lessons of the corresponding story of stable nuclei in the past [2].

Wilton **Catford** showed an instructive example of an inverse kinematics experiment: $^{24}\text{Ne}(d,p)^{25}\text{Ne}$ and the question of new magic numbers has been briefly discussed.

The interesting lecture of Juha **Äystö** (Figs. 4-6) presented the newest developments at the Jyväskylä University, Finland, mainly discussing the achievements of nuclear mass measurements with Penning traps. The current development of this field, which I do call, together with high precision measurement of nuclear radii by laser spectroscopy in long isotopic chains [2,3],

"nuclear ground state spectroscopy", is approaching new exciting physics, already now and certainly in the future.

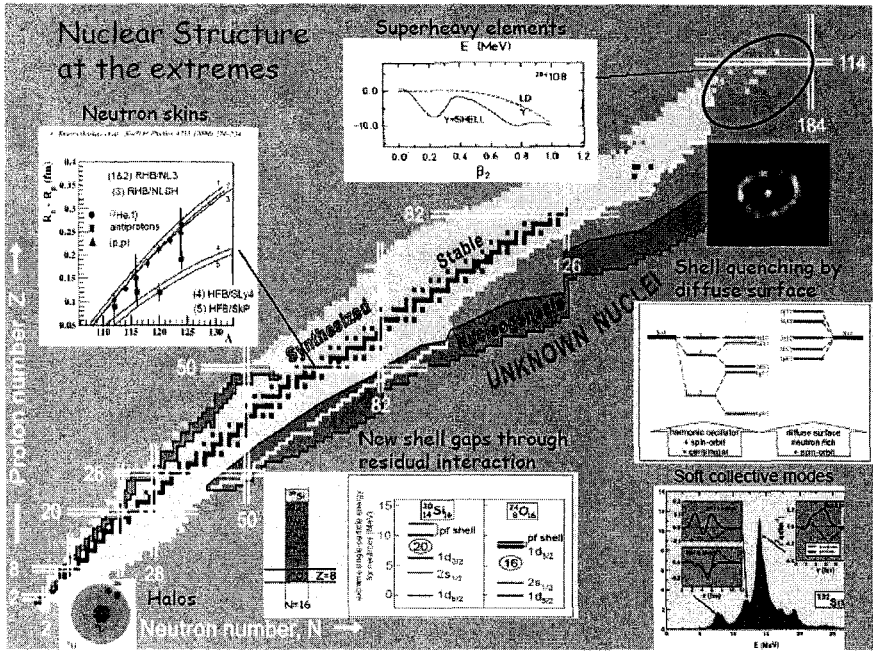


Figure 3. Nuclear structure at the extremes.

Figure 4 indicates the precision needed for attacking different problems of varying fundamental character. It has been said that the efficiency has been enhanced so much that nuclei with a half life of about 100 ms could be efficiently investigated.

A Penning trap is a confining device made of a homogeneous magnetic field superimposed by an electrostatic quadrupole field. The magnetic field B is used for radial confinement. The electric field prevents the ions from escaping along the magnetic field lines and hence leads to axial confinement. The motion in a Penning trap is a combination of three harmonic eigen-motions: an axial oscillation (ω_z) and two circular motions commonly referred to as magnetron (ω_-) and reduced cyclotron motion (ω_+). The sum of the two circular eigen-frequencies equals the cyclotron frequency $\omega_c = \omega_+ + \omega_-$ with $\omega_c = q/m \cdot B$. This frequency is used to determine the mass m of the ion stored in the Penning trap (Fig. 5).

Accuracies requested by physics?

- Fundamental interactions and symmetries
($< 1 \text{ keV}$ or $\delta m/m < 1 \cdot 10^{-8}$)
 - Q-values of nuclear β decay
 - CVC theory and unitarity of CKM matrix
 - Search for scalar and tensor currents
- Charge symmetry in nuclei (1 keV)
 - Isospin multiplets and Coulomb energy differences
- Nuclear structure (10-100 keV)
 - Global correlations (100 keV)
 - Local correlations (10 keV)
 - shell structure, shapes and pairing
 - Drip-line phenomena and halos (10 keV)
- Nuclear astrophysics ($< 10 \text{ keV}$ or $\delta m/m < 1 \cdot 10^{-7}$)

Figure 4. Requested accuracies of measurements of the nuclear mass.

By mass measurements many structure effects, already seen in the measurements of nuclear radii: the deformation effect, the odd-even staggering etc. are revealed by the two neutron separation energies, e.g., in an isotopic sequence.

It was also discussed that precision mass measurement carry information about more fundamental symmetries, about the violation of the conserved vector current and unitarity of the Cabbibo–Kobayashi–Maskawa (CKM) matrix relating weak interaction states and mass eigenstates, which are not exactly the same.

With the Conserved Vector Current theorem superallowed beta decay comes into the play, which has been an issue several times in these days, e.g. here, experimentally by V. **Iacob** et al. and theoretically by Alexandra **Petrovici**.

Principle of a Penning trap

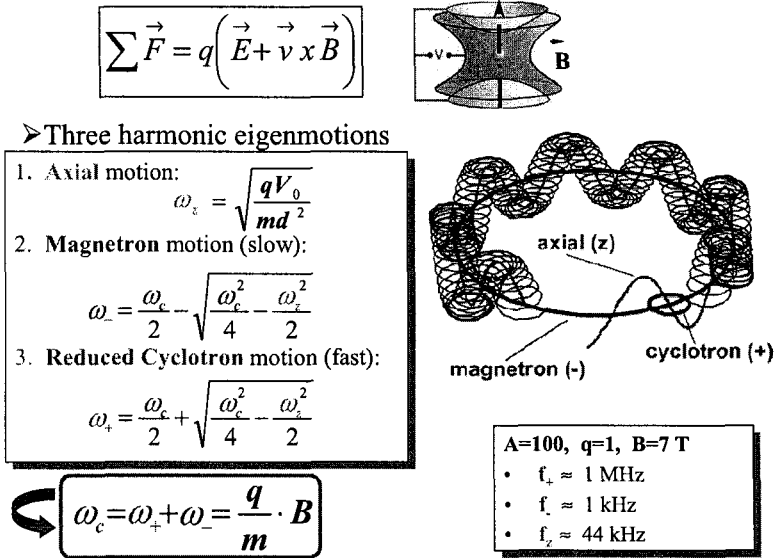


Figure 5. Particle motion in a Penning trap.

Already in the early days, in 1945, Hans Bethe explained the importance of EC for understanding the supernova. Actually till today we are unable to calculate the process with sufficient accuracy and that is for example due to missing knowledge about Gamov Teller strengths.

Conserved vector current (CVC) hypothesis:

Vector part of weak interaction not influenced by strong interaction
 Transition strength, ft value, depends only on the vector coupling constant and the matrix element, and is constant for given T:

$$ft = \frac{K}{G_V^2 \langle M_V \rangle^2}$$

K – product of fundamental constants
 G_V – vector coupling constant
 $\langle M_V \rangle$ – nuclear matrix element
 $f = f(Z, Q_{EC})$ statistical rate function
 $t = f(t_{1/2}, BR)$ partial half life

Plus various corrections (radiative & isospin symmetry breaking)

Measuring the ft value of a superallowed $0^+ \rightarrow 0^+$ β decay allows for a determination of the vector coupling constant G_V .

Figure 6. Superallowed β decay and the Standard model.

Dieter Frekers (Fig. 7) stressed the importance of studies by $(d, {}^2\text{He})$ reactions for astrophysics and also for the double beta decay.

Another example of the interplay of astrophysical questions and solid nuclear physics (communicated by M. Marqués) was the structure of the neutron stars (also highlighted theoretically during this meeting) and the neutron-neutron interaction in the presence of other neutrons. Can we learn something by eventually producing multi neutron clusters in reactions like ${}^7\text{Li} + {}^7\text{Li} \rightarrow {}^{10}\text{C} + 4n$? With this study a lively discussion of 50 years ago [4] about the existence of the tetra-neutron had a revival with new facets.

There have been different presentations about research on superheavy nuclei and the limits of the periodic system: The status of the investigations, the goals, production modes and future were accompanied by theoretical aspects (W.Scheid, D.Poenu). Sigurd Hoffmann presented an example of the GSI activities with velocity separator SHIP. This topic has been further on discussed by Mihail Itkis and Morita-san, about the shape evolution in fusion-fission reactions, the Dubna and Riken activities. Mihail Itkis showed a slide of general interest about the expected limits (Fig. 8).

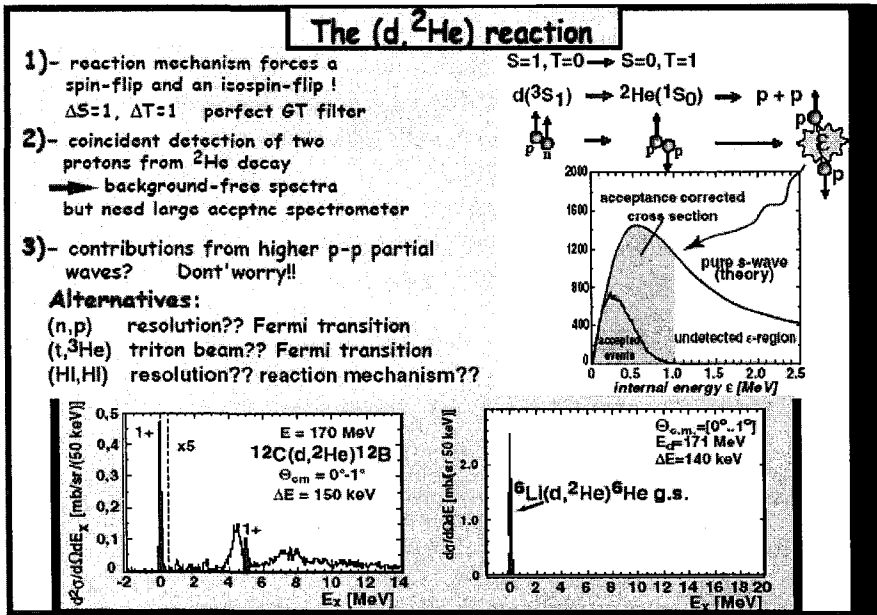


Figure 7. Aspects of studies of the $(d, {}^2\text{He})$ reaction.

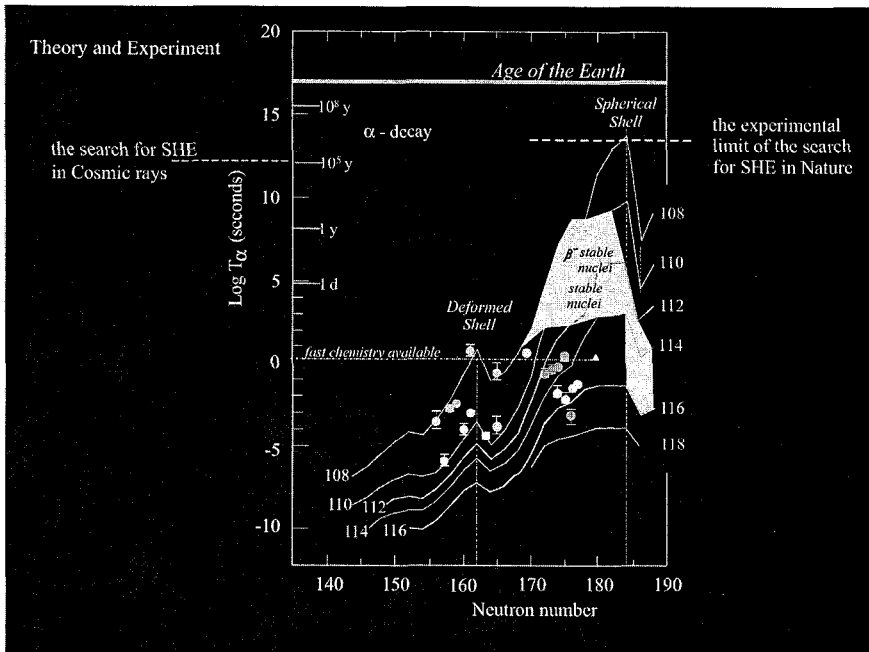


Figure 8. Limitations of Superheavy nuclei production.

3.2. Nuclear Astrophysics

The discussion of this aspect of contemporary nuclear physics has been opened in our school with the quotation of the famous statement of Arthur Eddington (Fig. 9, adopted from J. Görres) which can be considered to be the trigger for Nuclear Astrophysics in the twenties of the last century. The nuclear physics aspect of classical nova explosions has been combined in the excellent talk of Jordi **José**, while Carmen **Angulo** concentrated to the relevance of these explosive astrophysical sites for experimental studies with radioactive nuclei. The experimental methods of studying cross sections for scenarios relevant for nucleosynthesis may be divided in *direct* and *indirect* procedures. We got an impression about the state of the art: about direct methods by Fülöp, Görres, Buchmann, Angulo, and about indirect methods by Motobyashi, Tribble, Spilateri, Liu and Harissopoulos. A scholar lecture has been presented by Joachim **Görres** defining clearly the essential quantities of the problem, in context of specific alpha capture studies. The lecture did also introduce in the basic experimental requirements of modern direct measurements.

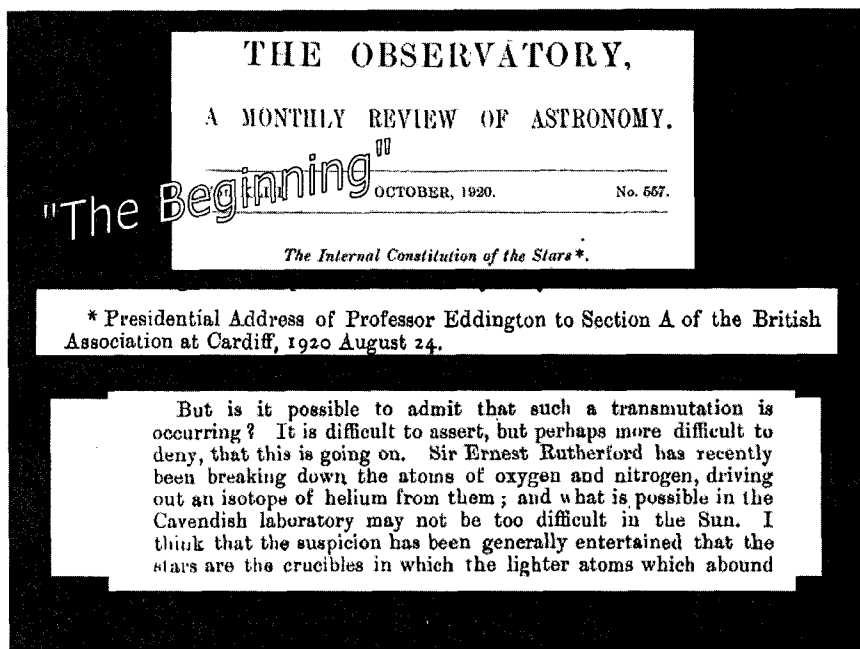


Figure 9. The famous statement of Arthur Eddington.

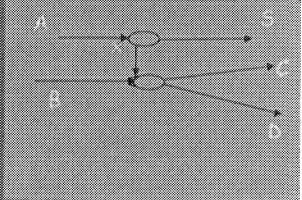
Another example representing the actual experimental status of direct measurements was presented by Zs. Fülöp with an overview about the LUNA project. In his general comments he showed up with a little too much focused view to direct methods, forgetting the merits of alternative indirect procedures. This view has been corrected when Claudio Spitaleri discussed the Trojan Horse Method (Fig. 10) He explained in detail the basis of this procedure. His discussion reminded of various restrictions and uncertainties of direct measurements (screening!) and he warned against too courageous extrapolations of the astrophysical S factor to energies of astrophysical relevance (Fig. 11).

Quasi-Free mechanism \rightarrow Trojan Horse Method

The incoming energy E_A of the incident particle is larger than the Coulomb barrier energy $(E_{AB})_{\text{Coul. Bar}}$

$$E_A > (E_{AB})_{\text{Coulomb Barrier}}$$

The nucleus A can be brought into nuclear field of nucleus B and the cluster x induces the reaction

$$B + x \rightarrow C + D$$


Coulomb effects and electron screening are negligible

G. Baur: Phys. Lett. B178, (1986), 135 18

Figure 10. Principle of the Trojan Horse method.

Bob **Tribble** explained and illustrated the Asymptotic Normalisation Coefficient (ANC) method. This indirect method is based on a skilful factorisation of the cross sections, in a trivial part and the ANCs, which could be inferred from the analysis of transfer cross sections.

Tohru **Motobayashi** presented the Coulomb dissociation method. I have been once involved in the development of this technique (Fig. 12), invented in the eighties exactly for hard-to-measure cross sections, using low intensity beams and avoiding eventual screening problems. Basically one takes advantage of the rich virtual photon field experienced by the passing nucleus in a Coulomb field. Motobayashi reported about the experimental studies of the ${}^7\text{Be}(p,\gamma){}^8\text{B}$ reaction (relevant to the solar neutrino problem) and he presented a compilation what has been done with beams of unstable nuclei (Fig. 13).

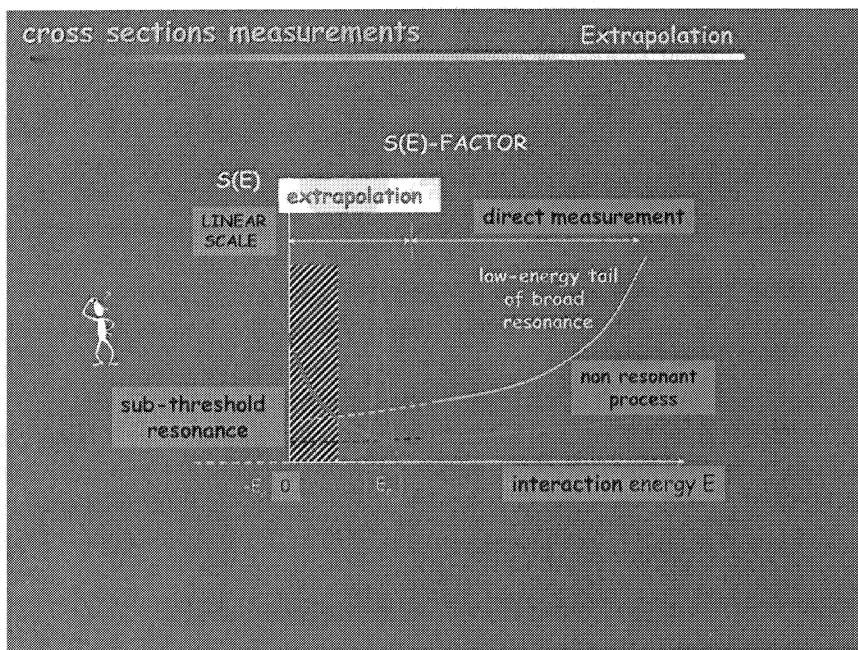
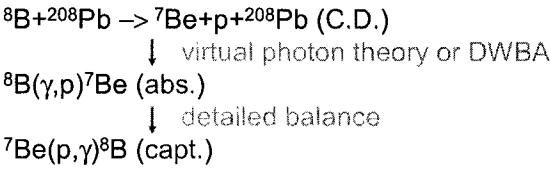
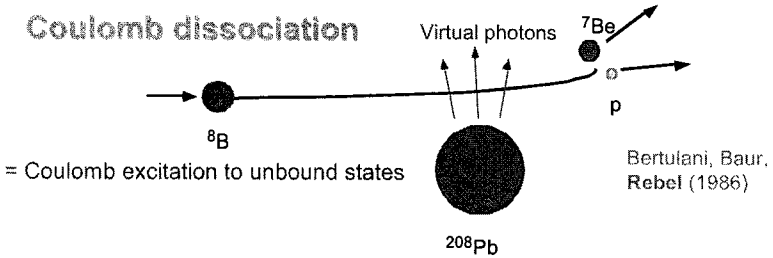


Figure 11. Discussing the uncertainties of extrapolations of direct results.

The ${}^7\text{Be}(p,\gamma){}^8\text{B}$ reaction is one of two most important cross sections - the other is the radiative α -capture on ${}^{12}\text{C}$; Lothar **Buchmann** was loudly thinking about both. The exact value of the S-factor of the proton capture on ${}^7\text{Be}$ plays an important role in the discussion of the observed deficit in the neutrino flux from the Sun. The reaction ${}^{12}\text{C}(\alpha,\gamma){}^{16}\text{O}$ at astrophysical energies carries a key role in the development of biological life. In fact in this sense one should add the triple α - process being equally important. Actually our workshop has to thank Lothar Buchmann, in particular, for many clarifying and valuable comments in the discussions.



large σ
 thick target (intermediate energy) experiments with R.I. beams

Figure 12. Principle of the Coulomb dissociation method.

Stellar reactions studied by Coulomb dissociation using radioactive isotope beams			
Steady burning			
Solar neutrino	${}^7\text{Be}(\text{p}, \gamma){}^8\text{B}$	GSI (254.4MeV) RIKEN, MSU (50-80.4MeV) Notre Dame (3.4MeV)	Direct, ANC
CNO cycle	${}^{14}\text{N}(\text{p}, \gamma){}^{15}\text{O}$ (Coulomb excitation, sub-threshold state)	RIKEN (100.4MeV)	D
Explosive burning			
hot CNO cycle	$\left\{ \begin{array}{l} {}^{12}\text{C}(\text{p}, \gamma){}^{13}\text{N} \\ {}^{13}\text{N}(\text{p}, \gamma){}^{14}\text{O} \end{array} \right.$	RIKEN (78.4MeV)	D
		RIKEN (88.4MeV), GANIL (70.4MeV)	${}_D$
hot pp mode	$\left\{ \begin{array}{l} {}^8\text{B}(\text{p}, \gamma){}^9\text{C} \\ {}^{11}\text{C}(\text{p}, \gamma){}^{12}\text{N} \\ {}^{12}\text{N}(\text{p}, \gamma){}^{13}\text{O} \end{array} \right.$	RIKEN (70.4MeV)	A
		GANIL, RIKEN (70.4MeV)	A
		RIKEN (84.4MeV)	
rp-process	$\left\{ \begin{array}{l} {}^{22}\text{Mg}(\text{p}, \gamma){}^{23}\text{Al} \\ {}^{26}\text{Si}(\text{p}, \gamma){}^{27}\text{P} \end{array} \right.$	RIKEN (50.4MeV)	
		RIKEN (50.4MeV)	
Neutron capture	r-process	${}^8\text{Li}(\text{n}, \gamma){}^9\text{Li}$	MSU (40.4MeV)
	neutron induced CNO cycle	${}^{14}\text{C}(\text{n}, \gamma){}^{15}\text{C}$	GSI (605.4MeV), RIKEN (70.4MeV), MSU (35.4MeV)
	r-process	${}^{18}\text{C}(\text{n}, \gamma){}^{19}\text{C}$	RIKEN (67.4MeV)

Figure 13. Compilation of astrophysically relevant results of the Coulomb dissociation method.

3.3. *Phases of Nuclear Matter and Particle Astrophysics*

When passing to questions of hadronic matter in various phases, to nuclear forces and nuclear structure, we could realize that we met this topic already with the consideration of neutron stars. The present research in laboratories is strongly coupled to the field of heavy ion research, exploring *heated nuclear matter, hot, compressed and excited nuclear matter* on the road to highest densities, to an eventual reproducible short instant of the Early Universe: the *quark-gluon plasma* (QGP).

Before commenting the only experimental research program of this direction, presented here by Zbigniew Majka's talk, let me first mention an interesting approach with *cold* nuclear matter.

Anders Ingemarsson reported about experiments measuring reaction cross sections of various projectiles with nuclei. This is a longstanding experimental problem in classical nuclear projectile-target nuclei interaction studies, and the results could help to constrain the interaction potentials. "Measurements of nuclear reaction cross sections are easy, in principle, but difficult in practice", I noted.

Zbigniew Majka reported about the BRAHMS experiment at RHIC (Relativistic Heavy Ion Collider) at Brookhaven National Laboratory. This experiment is designed to measure charged hadrons over a wide range of rapidity and transverse momentum for studies of the reaction mechanisms of relativistic heavy ions and of the properties of highly excited nuclear matter formed by these reactions. A particular focus was the discussion to which extent the actual results give evidence for the formation of a state of deconfined partonic matter, the QGP. He concluded from the present data the indication that on the way to QGP a new precursor status of nuclear matter, the Colour Glass Condensate (CGC), is formed. Figure 13 simply quotes the original conclusions of Z. Majka.

Figure 14 displays the energy spectrum of primary cosmic rays. From there questions arise, like about the origin of the kink near $3 \cdot 10^{15}$ eV ("knee") and about the appearance of particles, very rare though, above the so called Greisen-Zatsepin-Kuz'min cut-off ($>5 \cdot 10^{19}$ eV) where the spectrum is predicted to end due to the interaction of the particles with the ubiquitous cosmic 2.7 K background radiation. The energy spectrum extends several orders of magnitude the limits of man-made accelerators.

The mystery of the highest energies in Universe, which provides one of the experimental and theoretical challenges of contemporary physics has been brought in our discussion by myself.

Iliana **Brancus** introduced us in the motivation and layout of the KASCADE - Grande experiment (Fig. 1) which is focused to the determination of the energy spectrum and the mass composition of cosmic rays in the energy



Conclusions from the BRAHMS experiments at RHIC:

- **The matter that is created at RHIC differs from anything that has been investigated before.**
- **Results are consistent with strongly interacting deconfined matter.**
- **Indications (model dependent) for a collective gluonic state (CGC) found.**

However

- No direct evidence for chiral symmetry restoration
- No direct evidence for phase transition

Zbigniew Majka, M. Smoluchowski Institute of Physics, Jagiellonian University, Kraków, Poland, ufmajka@cyf-kr.edu.pl

Figure 13. Conclusions of the insights provided by the RHIC experiments.

and the mass composition of cosmic rays in the energy range above the knee, i.e. of cca. 10^{16} - 10^{18} eV, by observing extensive air showers (EAS) induced in the atmosphere. Simulation studies let expect that the correlation of the total number of shower muons with the number of charged particles in regions not too distant from the shower centre is indicative for the mass of the primary particles from the cosmos (Fig. 15).

There is a re-discovery of an EAS detection method by radio pulses emitted in the atmosphere during the air shower development induced by high energy primary cosmic rays [5]. For these tasks to test the technology and to demonstrate the ability of EAS studies the LOPES (LOFAR Prototype Station) [6] radio antenna array has been set up at the area of KASCADE-Grande and is operated in conjunction with the KASCADE-Grande detectors (Fig. 16).

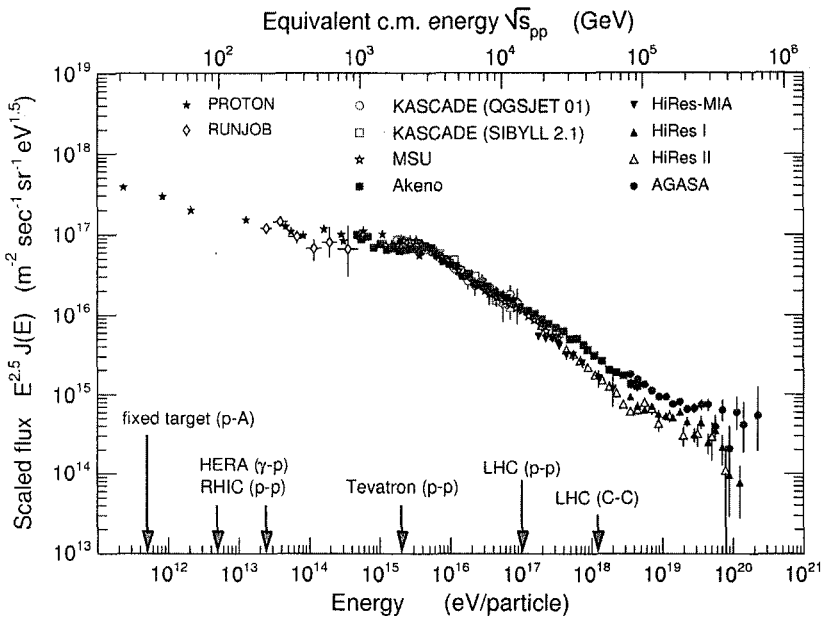


Figure 14. The energy spectrum of cosmic rays.

Ad **van den Berg** discussed in more detail the phenomenon of radio emission from EAS and he outlined the perspectives, in connection with the LOFAR project, of a giant radio telescope. LOFAR started as an innovative effort to force a breakthrough in sensitivity for astronomical observations at radio signals. The basic technology of radio telescopes had not changed since the 1960's: large mechanical dish antennas collect signals before a receiver detects and analyses them. Half the cost of these telescopes lies in the steel and moving structure. A telescope 100 times larger than existing instruments would therefore be unaffordable. New technology was required to make the next step in sensitivity needed to unravel the secrets of the early Universe and the physical processes in the centres of active galactic nuclei.

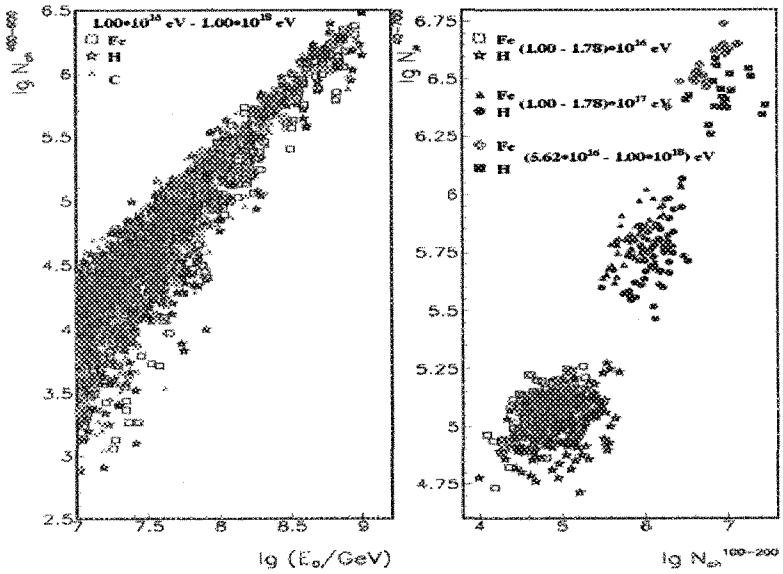


Figure 15. Correlations of air shower observables signaling the mass of the primary cosmic particle.

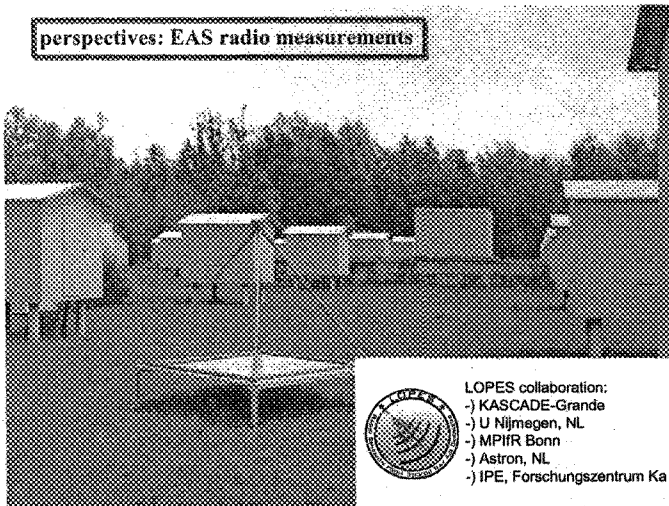


Figure 16. Radio antennas in the area of the KASCADE – Grande detectors: LOPES.

4. Laboratory Reports and Large Facilities

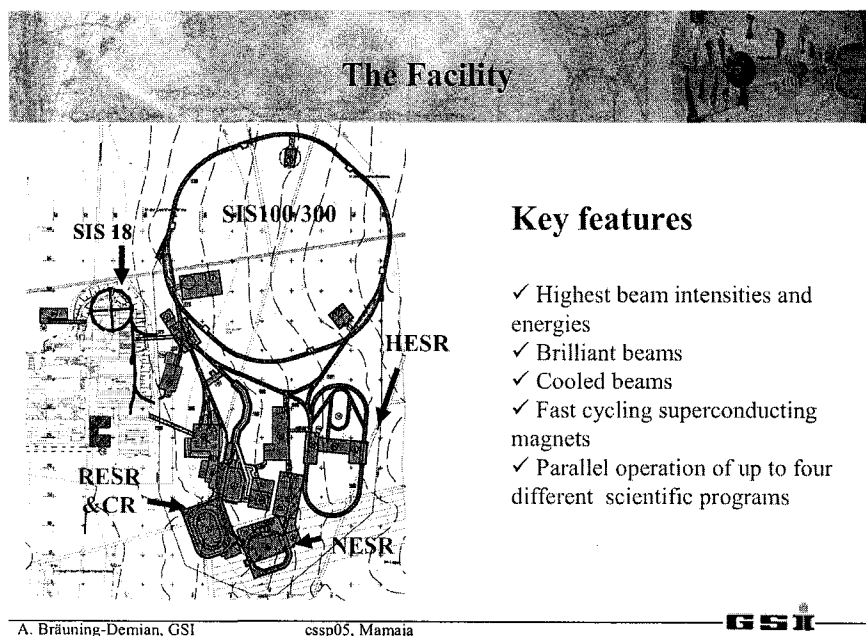


Figure 17. Outline of the FAIR project.

The GSI project **FAIR: Facility for Antiproton and Ion Research** (Fig. 17) was presented by Angela **Bräuning-Demian**, supplemented by Gottfried **Münzenberg's** talk about Nuclear Structure and Astrophysics Research (NUSTAR) at GSI. There have been reports about the developments at RIKEN: the new facility **RIBF (Motobayashi)** and at **ISOLDE (Butler, Fig. 18)**). The modernisation of the facilities at **FLNR Dubna** (around the U 400 M Cyclotron) was instructively presented by M.G. **Itkis**.

L. **Buchmann** reported about the RNB facilities at **TRIUMF**. From experimental/technical point of view I was impressed by the ideas of the **AGATA project (Farnea)** about how the resolution of γ ray spectroscopy should get improved (Fig. 19).

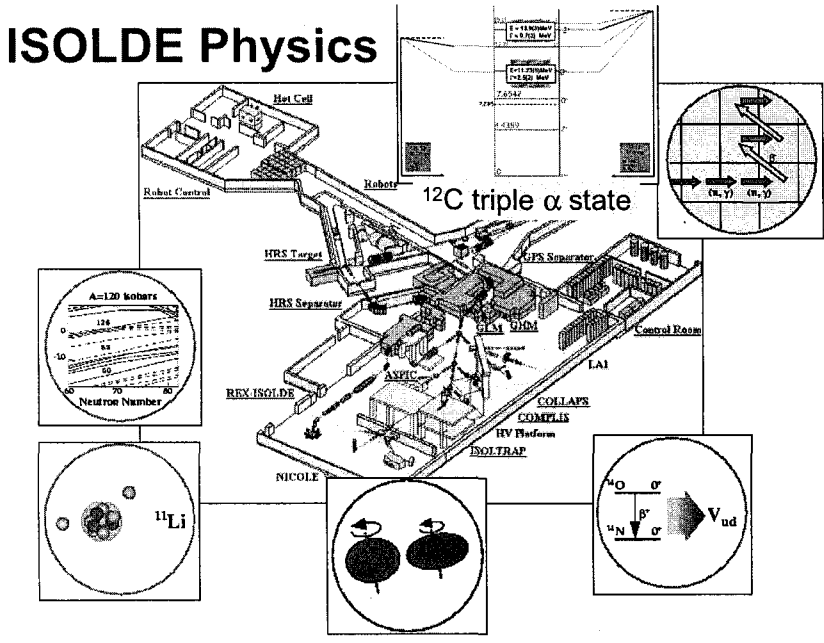


Figure 18. Overview about the physics program at ISOLDE.

Turning to a larger facility of quite different character I do mention **KASCADE-Grande** for Cosmic Ray Research (Fig. 1) with the successful detection of radio flashes induced by air showers with the **LOPES** set up (Fig. 16) presented by Iliana **Brancus**, and my account of the **Pierre Auger Laboratory** [7] to establish the experimental evidence for trans - GZK cosmic particles. With the far reaching perspectives of the radio signal measurements from large air showers, discussed by Ad van den Berg, the **LOFAR** project has been introduced.

In fact there has been a lot of interesting physics communicated in context of the presentations of new experimental devices.

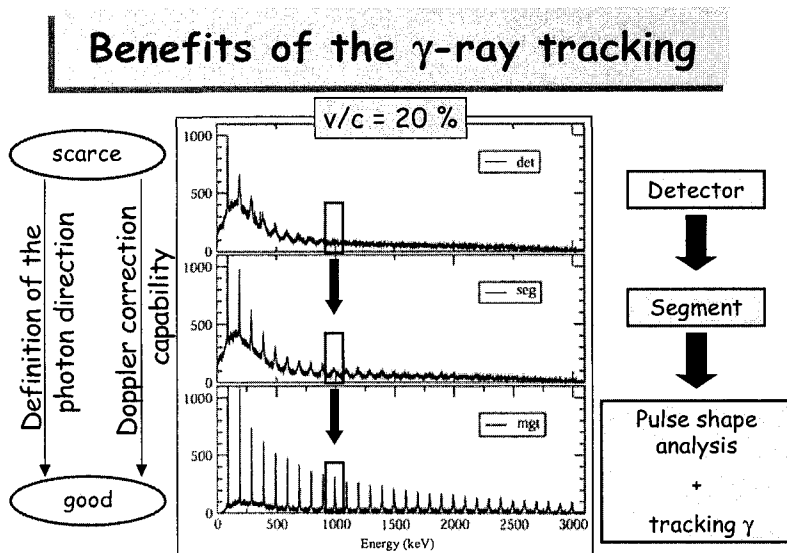


Figure 19. Improving the resolution of γ -ray spectra by tracking (AGATA project).

5. Messages about the neutrino

One of the most interesting examples of a situation of interwoven micro and macro physics is provided by the neutrino. The neutrino plays by its nature (Majorana or Dirac particle?) and its quested mass a key role in modern physics. It is a candidate for nonbaryonic dark matter in the Universe, is important for the energy transport in supernovae, anomalies in the solar neutrino flux and in atmospheric neutrinos and suggests explanations in terms of flavour oscillations. The talk of J. **Suhonen** introduced some views to the field, in particular to double beta decay! The current sharpest direct experimental limits on the electron neutrino mass are resulting from nuclear physics experiments. The WMAP (Wilkinson Microwave Anisotropy Probe) observations invoke theoretical assumptions about the cosmological model. Sabin **Stoica** presented a scholarly lecture about various aspects and compiled the actual status of various approaches each with of own merits. I would disagree with the conclusion that the KATRIN experiment (tritium beta decay) [8] which attempts to lower the upper experimental value of the neutrino mass to $0.2 \text{ eV}/c^2$ in a direct way would be obsolete in view of the results of double beta decay studies. The latter which claim a sensitivity of $1.5 \cdot 10^{-2} \text{ eV}/c^2$ (GENIUS) involve specific

theoretical assumptions and display their own uncertainties. D. **Yakovlev** talked about neutrino emission from neutron stars and Gail **McLaughlin** talked about the role of neutrinos in nucleosynthesis, taking us to the realm of four neutrino flavours. (But all these were theoreticians!)

Certainly the neutrino plays today a role at least as important as in the time when Wolfgang Pauli put forward the neutrino hypothesis. The apparent difference, however is: at that time an eminent physicist missed a meeting in favour of a Christmas ball in Zurich, how Pauli apologised, in his famous letter to the "Dear radioactive ladies and gentlemen", suggesting the existence of the neutrino. Nowadays leading physicists leave earlier or arrive late at our meetings due to important committee commitments! *Quo vadis* intellectual pleasure?

6. Finale

Finally let me remind of some global fundamentals in the background!

Our knowledge of fundamental particles and interactions is such that we can account everything about everyday world, but we explain nothing at all. The current theory of particle interactions, formulated within the standard model, gives a set of explicit rules for computing the forces between the various quarks and leptons, mediated by bosons. Given the masses of quarks and leptons and nine other closely related quantities, that theory can account in principle for all phenomena. On the other hand, we have no explanation, why there are three families, or why they have the masses they have, why the symmetries are broken, why we have no right-handed neutrino?

Flashing briefly the history of the Standard Model, Zbigniew Majka induced me to some thoughts about a peculiar world. Let us imagine for a short moment a world where electrons are as massive as muons, indeed replaced by muons. In this strange world the distance scale would be 200 times smaller, the energy scale would be 200 times greater, but atoms could not be stable due to muon capture, this world would be finally made up of just neutrons and neutrinos. Or imagine, e.g. that the proton would be heavier than the neutron, or in our language the u quark would be heavier than the d quark. Hydrogen would decay, the nucleosynthesis would have happened in quite another way.

Any anthropic principle would have been led ad absurdum. Actually we do not know: Why is it not so? We realize that our present theory is fundamentally incomplete. May be it will remain always an illusion to get rid of arbitrary free parameters. But on the other side the questions may only reflect our current ignorance, and we have to look for the interdependence of seemingly free

parameters. That is the physics beyond the Standard Model that we have to keep in the background of all our speculations about the underlyings of our world.

Acknowledgements

I am aware that it is a reserved privilege of the chairman of the final session to express our common thanks to the organizers, and I do not intend to take this pleasure away from him. But as one of the directors of this CSSP05 is just the chairman of this session, I take the chance to thank personally first him, **Bob Tribble** with **Sabin Stoica**, **Livius Trache** and **Mihai Horoi**, for an extremely interesting outline of the program and for all efforts, and then all the further staff, especially Aurora and Alexandra for the perfect organisation of this school and kind help in personal matters. In particular, I thank various colleagues for some help in preparing my summary. A lot of thanks to **Gabriel Tabacaru** for his patient help, and to **Peter Biermann** and **Gina Isar** for the unsuccessful attempt to organise the adequate transparencies for an ink printer for this talk. Our Romanian colleagues - some of them I have the privilege to call my friends - have again understood to prepare a creative atmosphere mediating the interaction of promising (unfortunately too few) young scientists with established old-timers. That feature is of greatest importance for the future of a lively field. Actually an important role of such meetings is to be a training camp for establishing a healthy style of intellectual exchange and communication, competing in finding out the truth, but not in suppressing the colleagues' achievements. A relaxed and pleasant atmosphere like we experienced here had often prompted important great insights. Isaac Newton found the gravitation when dreaming under an apple tree. My teacher in theoretical physics, Hans Jensen, told that he got the idea of the strong spin-orbit coupling for the shell model during a dancing party, observing the alignments of the rotating pairs. "*Se non è vero, è ben trovato*". May be someone of us has progressed in understanding soliton modes or neutrino oscillations when watching to waves of the Black Sea.

It is a great pity that due to my limitations in understanding and with an obvious restriction of time, I have been unable to comment all communications to the extent they had deserved. I apologise to those which I could not mention in my biased selection of examples. Thus let me end with a quotation of *Publius Ovidius Naso*, the *genius loci* here, indicating why he was banished from Rome:

"Why did I see anything? Why did I make my eyes guilty?

Why did I recklessly learn of a sin?"

(*Ars Amatoria*)

References

1. A. Haungs et al. - KASCADE-Grande collaboration, *Proc. 28th ICRC, Tsukuba, Japan*, Vol. 2 (2003) 945.
2. C.J. Batty, E. Friedman, H.J. Gils, H. Rebel, *Advances Nucl. Phys.* **19**, 1 (1989)
3. E.W. Otten, *Nucl. Phys.* **A354**, 471c (1988).
4. V.I. Goldanskii, *Phys. Lett.* **9**, 184 (1964).
5. H. Falcke et al. – LOPES collaboration, *Nature* **435**, 312 (2005).
6. A. Haungs et al. - LOPES collaboration, *Proc. 22nd Texas Symposium on Relativistic Astrophysics at Stanford University*, Dec.13-17, 2004.
7. *CERN Courier* December 2003, p.11.
8. KATRIN Collaboration: *KATRIN Design Report, Report FZKA 7090* (2004).

TOWARDS TECHNOLOGY IN SOCIETY AND BUSINESS THROUGH SCIENCE AND EDUCATION*

PETER L. BIERMANN ^{1,2}

¹*Max-Planck Institute for Radioastronomy, Bonn, Germany*

²*Department of Physics and Astronomy, University of Bonn*

E-mail: plbiermann@mpifr-bonn.mpg.de

website: www.mpifr-bonn.mpg.de/div/theory

1. Introduction

We will go through three steps in the reasoning, first some examples on how to go from basic research into a business application, then how technology in business arises from long term investment such as education and basic research, and short term investment in hardware, and how these play out in the global competition. We start with three examples.

- **Mathematics:** Number theory: Encryption techniques for sending confidential information over the internet. Scrambling and de-scrambling of optical fiber signals for very high throughput internet (Terabit/second and more).
- **Astronomy:** Big Bang fluctuations: Scan of persons for disease and sickness (e.g. SARS). Infrared observations: Shadows on person in body radiation, airport security. Data analysis: Seismic data analysis for finding oil.
- **Physics:** Plasma physics, cosmic rays: Solar storm predictions, safety of electricity power grids, safety of communication satellites; airplane radiation safety. Scanning of freight containers to control content via cosmic ray secondary particle scattering.

*Notes for the address at the Round Table with scientists, businessmen and politicians organized at the Subcommittee for Science of the Romanian Parliament in Bucharest, Wed. June 22-nd, 2005

1.1. *Investment*

Long term: Education, young people, use of experience of older people.

- Short term: Business hardware and specific expertise.
- Creativity in both long and short term: From diversity, open minds, building bridges.

1.2. *Competition*

Romania in Europe, and Europe versus China, India, United States: World-wide competition for the young minds.

- In my group we have former and present students and young researchers from all continents of this inhabited world; for example now professors in China, India, and Australia (from Romania)!
- In United States, at best universities best graduate students are from Asia and Eastern Europe (in proportion of population).
- We have three years to turn Europe around!
- In Europe East-South is the only hope!

2. Appendix

Here I list a few practical points of experience. These examples are mostly from Germany, some are based on experience with several other countries, and apply only partly to Romania - they do apply to Romanian students and young researchers abroad, however:

- Every first step in any administrative procedure to help should be welcomed; it is a learning experience to become more competitive. Example 1: Some procedure to recognize each others' exams cannot be done, because it would be the "first time ever".
- The conditions to learn and educate should not be confused with rules to protect workers in the workplace. Example 1: Young students are required to prove to the German immigration authorities that they have 575 Euro a month available, while on the other hand the employer is limited to give them 360 Euro a month, with 10 percent tax on top; the 360 Euro have not been changed in 20 years, while the number of 575 keeps rising all the time in step with reality. Example 2: A PhD student cannot be promised a conditional six year contract, because any contract of 5 or more years violates labor protection rules. Example 3: PhD students

can often not be paid a tax free fellowship, but have to pay taxes, so that the cost for the employer is double what the student gets at the end; and yet, all this is part of her/his education.

- Researchers, who work in a country other than their country of national origin, who then marry a partner, perhaps also in research, from yet a third country, are routinely subjected to enormous time consuming bureaucratic difficulties by the immigration and tax authorities in almost all countries. Even the existing international laws and treaties, which are by no means beneficial to international careers, are routinely ignored. Example 1: A wife from a foreign country is told by a government agency that there will be no widow's benefits at all. Example 2: Tax treaties are supposed to prevent double taxation, but if the two tax authorities are of opposite opinion, the tax payer has no recourse. Example 3: A baby can be refused proper registration, if the parents are from different countries - an intervention by diplomats may be required.
- Lifetime career choices are looked upon as personal options, and international competition is incomprehensible to many bureaucrats, especially in a family with several individuals in academia. Pension and health insurance systems for families are usually impossible to maintain due to questions of prior condition, turning an international career into an impossible choice of risks.

We hope that Romania manages to avoid all such pitfalls.

This page is intentionally left blank

LIST OF PARTICIPANTS

Tariq Al-Abdullah
Cyclotron Institute
Texas A&M University
College Station, TX 77843-3366
USA
abdullatq@comp.tamu.edu

Carmen Angulo
Cyclotron Research Center
Université Catholique de
Louvain
B-1348 Louvain-la-Neuve
Belgium
angulo@cyc.ucl.ac.be

Sezgin Aydin
Department of Physics
Cukurova Univ. Art and Science
Balkali/Adana
Turkey
sezgin@nigde.edu.tr

Juha Äystö
Department of Physics
University of Jyväskylä, PO Box 35
FIN-40351 Jyväskylä
Finland
Juha.Aysto@phys.jyu.fi

Laurent Benoit
Laboratoire de Physique
Corpusculaire, IN2P3-CNRS
& Université de Caen
F-14050 Caen cedex
France
laurent@lpccaen.in2p3.fr

Alexandru Bercuci
National Institute of Physics and
Nuclear Engineering - Horia
Hulubei
Bucharest-Magurele, POB MG-6
Romania
alex@muon1.nipne.ro

Ad M. van den Berg
Kernfysisch Versneller Instituut
Rijksuniversiteit Groningen
NL 9747 AA Groningen
The Netherlands
A.M.van.den.Berg@kvi.nl

Peter Biermann
Max Planck Institute for
Radioastronomy, Postfach 2024
D-53010 Bonn
Germany
plbiermann@mpifr-bonn.mp.de

Dennis Bonatsos
Institute of Nuclear Physics
NCSR "Demokritos"
GR-15310 Aghia Paraskevi
Athens, Greece
bonat@inp.demokritos.gr

Ruxandra Borcea
National Institute of Physics and
Nuclear Engineering - Horia
Hulubei
Bucharest-Magurele, POB MG-6
Romania
rborcea@ifin.nipne.ro

Angela Bräuning-Demian
 Gesellschaft für
 Schwerionenforschung
 D-64291 Darmstadt
 Germany
 A.Braeuning-Demian@gsi.de

Iliana Magda Brancu
 National Institute of Physics and
 Nuclear Engineering - Horia
 Hulubei
 Bucharest-Magurele, POB MG-6
 Romania
 iliana@muon1.nipne.ro

Lothar Buchmann
 TRIUMF
 Vancouver BC, V6T 2A4
 Canada
 lothar@triumf.ca

Aurel Bulgac
 Department of Physics
 University of Washington
 Seattle, WA 98195-1560
 USA
 bulgac@phys.washington.edu

Peter A. Butler
 PH-ISOLDE, CERN
 CH 1211, Geneva 23
 Switzerland
 Peter.Butler@cern.ch

Florin Buzatu
 National Institute of Physics and
 Nuclear Engineering - Horia
 Hulubei
 Bucharest-Magurele, POB MG-6
 Romania
 buzatu@ifin.nipne.ro

Florin Carstoiu
 National Institute of Physics and
 Nuclear Engineering - Horia
 Hulubei
 Bucharest-Magurele, POB MG-6
 Romania
 fcarstoiu@ifin.nipne.ro

Wilton N. Catford
 Department of Physics
 University of Surrey
 Guildford, Surrey, GU2 7XH
 United Kingdom
 w.catford@surrey.ac.uk

Iulia Brandusa Ciobanu
 Physics Department
 "Gh.Asachi" Technical University
 Iasi, Romania
 bciobanu@physics.phys.tuiasi.ro

Cristian Ciocarlan
 National Institute of Physics and
 Nuclear Engineering - Horia
 Hulubei
 Bucharest-Magurele, POB MG-6
 Romania
 ccristian@tandem.nipne.ro

Valeriu Ciorba
 Institute of Applied Physics
 Academy of Science
 Chisinau
 Republic of Moldova
 vciorba@phys.asm.md

Doru Delion
 National Institute of Physics and
 Nuclear Engineering - Horia
 Hulubei
 Bucharest-Magurele, POB MG-6
 Romania
 ddelion@ifin.nipne.ro

Pierre Descouvemont
 Physique Nucléaire Théorique et
 Physique Mathématique, CP229
 Université Libre de Bruxelles
 B1050 Brussels
 Belgium
 pdesc@ulb.ac.be

Emilian Dragulescu
 National Institute of Physics and
 Nuclear Engineering - Horia
 Hulubei
 Bucharest-Magurele, POB MG-6
 Romania
 edrag@ifin.nipne.ro

Dana Dumitriu
 National Institute of Physics and
 Nuclear Engineering - Horia
 Hulubei
 Bucharest-Magurele, POB MG-6
 Romania
 dde@ifin.nipne.ro

Enrico Farnea
 INFN, Sezione di Padova
 35131 Padova, Italy
 farnea@pd.infn.it

Mirela Fetea
 Department of Physics
 University of Richmond
 Richmond, VA 23173
 USA
 mfetea@richmond.edu

Daniela Fluerasu
 National Institute of Physics and
 Nuclear Engineering - Horia
 Hulubei
 Bucharest-Magurele, POB MG-6
 Romania
 danny@ifin.nipne.ro

Dieter Frekers
 Institut für Kernphysik
 Westfälische Wilhelms-
 Universität
 D-48149 Münster
 Germany
 Frekers@Uni-Muenster.de

Zsolt Fulop
 ATOMKI
 H-4001 Debrecen
 Hungary
 fulop@atomki.hu

Rodica Maria Georgescu
 Faculty of Physics
 University of Bucharest
 Bucharest-Magurele
 Romania
 rodicab2000@yahoo.com

Radu Gherghescu
 National Institute of Physics and
 Nuclear Engineering - Horia
 Hulubei
 Bucharest-Magurele, POB MG-6
 Romania
 rgherg@ifin.nipne.ro

Dan Ghita
 National Institute of Physics and
 Nuclear Engineering - Horia
 Hulubei
 Bucharest-Magurele, POB MG-6
 Romania
 dghita@tandem.nipne.ro

Joachim Goerres
 Department of Physics
 University of Notre Dame
 Notre Dame, IN 4655
 USA
 jgoerres@nd.edu

Walter Greiner
Frankfurt Institute for Advanced
Studies, J. W. Goethe University
D-60438 Frankfurt/Main
Germany
greiner@th.physik.uni-frankfurt.de

M. Gugiu
National Institute of Physics and
Nuclear Engineering - Horia
Hulubei
Bucharest-Magurele, POB MG-6
Romania
mgugiu@tandem.nipne.ro

Sotiris Harissopulos
Institute of Nuclear Physics
NCSR "Demokritos"
GR-15310 Aghia Paraskevi
Athens, Greece
sharisop@inp.demokritos.gr

Sigurd Hofmann
Gesellschaft für
Schwerionenforschung
D-64220 Darmstadt
s.hofmann@gsi.de

Mihai Horoi
Department of Physics
Central Michigan University
Mt. Pleasant, MI 48859
USA
horoi@phys.cmich.edu

Jorge E. Horvath
IAGCA
Universidade de Sao Paolo
Cidade Universitaria
05508-900 Sao Paolo
Brazil
foton@astro.iag.usp.br

Nathan Hoteling
University of Maryland
College Park, MD 20742
USA
hoteling@wam.umd.edu

Adrian Mircea Iacob
Faculty of Physics
University of Bucharest
Bucharest-Magurele
Romania
adrian.iacob@connex.ro

Sabin Iacob
National Institute of Physics and
Nuclear Engineering - Horia
Hulubei
Bucharest-Magurele, POB MG-6
Romania
iacobs@exotic.nipne.ro

Victor Iacob
Cyclotron Institute
Texas A&M University
College Station, TX 77843-3366
USA
iacob@comp.tamu.edu

Dmytro Iacubovskiy
Bogolyubov Institute for
Theoretical Physics
Kyiv, Ukraine
dima806@ukr.net

Anders Ingemarsson
Department of Radiation Sciences
Uppsala University
75121 Uppsala
Sweden
Anders.Ingemarsson@tsl.uu.se

Aurel Isar
National Institute of Physics and
Nuclear Engineering - Horia
Hulubei
Bucharest-Magurele, POB MG-6
Romania
isar@ifin.nipne.ro

Paula Gina Isar
Max Planck Institute for
Radioastronomy, Postfach 2024
D-53010 Bonn
Germany
pgisar@mpifr-bonn.mpg.de

Alina Istrate
Faculty of Physics
University of Bucharest
Bucharest-Magurele
Romania
alina@iastate.edu

Mikhail Itkis
Flerov Lab. of Nuclear Reactions
Joint Institute for Nuclear Research
141980 Dubna
Russia
itkis@flnr.jinr.ru

Jan Jolie
Institut für Kernphysik der
Universität zu Köln
D-50937, Köln
Germany
jolie@ikp.uni.koeln.de

Jordi José
Dept. de Física I Enginaria Nuclear
& Institut d'Estudis Espacilas de
Catalunya
E-08034, Barcelona
Spain
jordi.jose@upc.edu

Reiner Krücken
Physik-Department E12
Technische Universität München
D-85748 Garching
Germany
Reiner.Kruecken@ph.tum.de

Marco La Cognata
Universita di Catania
& INFN Lab. Nazionali del Sud,
Catania, Italy
Lacognata@lns.infn.it

Livio Lamia
Universita di Catania
& INFN Lab. Nazionali del Sud,
Catania, Italy
Llamia@lns.infn.it

Yulia Lashko
Bogolyubov Institute for
Theoretical Physics
Kyiv, Ukraine
Lashko@univ.kiev.ua

Wei-Ping Liu
China Institute of Atomic Energy,
POBox 275(1)
Beijing 102413
China
wpliu@iris.ciae.ac.cn

Nicola Lo Iudice
Dipartimento di Scienze Fisiche
Universita di Napoli
Napoli, Italy
loiodice@na.infn.it

Zbignew Majka
M. Smoluchowski Institute of Physics
Jagiellonian University
30-059 Krakow
Poland
ufmajka@cvr-kr.edu.pl

Ioana Manea
 National Institute of Physics and
 Nuclear Engineering - Horia
 Hulubei
 Bucharest-Magurele, POB MG-6
 Romania
 manea@ifin.nipne.ro

C. Marinescu
 Faculty of Physics
 University of Bucharest
 Bucharest-Magurele
 Romania
 cmarinescu@yahoo.com

F. Miguel Marqués
 Laboratoire de Physique
 Corpusculaire, IN2P3-CNRS
 & Université de Caen
 F-14050 Caen cedex
 France
 marques@lpccaen.in2.p3.fr

Gail C. McLaughlin
 Department of Physics
 North Carolina State University
 Raleigh, NC 27608
 USA
 gail_mclaughlin@ncsu.edu

Constantin Mihai
 National Institute of Physics and
 Nuclear Engineering - Horia
 Hulubei
 Bucharest-Magurele, POB MG-6
 Romania
 cmihai@ifin.nipne.ro

Mihai Mirea
 National Institute of Physics and
 Nuclear Engineering - Horia
 Hulubei
 Bucharest-Magurele, POB MG-6
 Romania
 mirea@ifin.nipne.ro

Stoyan Mishev
 Bogoliubov Laboratory of
 Theoretical Physics
 Joint Institute for Nuclear Research
 141980 Dubna, Russia
 Mishev@theor.jinr.ru

Bogdan Mitrica
 National Institute of Physics and
 Nuclear Engineering - Horia
 Hulubei
 Bucharest-Magurele, POB MG-6
 Romania
 bmitrica2002@yahoo.com

Howard Moore
 UNESCO ROSTE
 I-30122 Venice
 Italy
 roste@unesco.org

Kosuke Morita
 RIKEN (The Inst. of Physical and
 Chemical Research)
 Hirosawa 2-1, Wako-shi
 Saitama 351-0198
 Japan
 morita@rarfaxp.riken.jp

Tohru Motobayashi
 RIKEN (The Inst. of Physical and
 Chemical Research)
 Hirosawa 2-1, Wako-shi
 Saitama 351-0198
 Japan
 motobaya@rarfaxp.riken.jp

Gottfried Münzenberg
 Gesellschaft für
 Schwerionenforschung
 D-64220 Darmstadt
 Germany
 g.muenzenberg@gsi.de

Tatsuya Nakada
 CERN
 1211-CH, Geneva 23
 Switzerland
 Tatsuya.Nakada@cern.ch

Alina Negoita
 National Institute of Physics and
 Nuclear Engineering - Horia
 Hulubei
 Bucharest-Magurele, POB MG-6
 Romania
 alina@iastate.edu

Florin Negoita
 National Institute of Physics and
 Nuclear Engineering - Horia
 Hulubei
 Bucharest-Magurele, POB MG-6
 Romania
 fnegoita@ifin.nipne.ro

Argyris Nicolaidis
 Department of Physics
 Aristotle University of Thessaloniki
 Thessaloniki, Greece
 nicolaid@auth.gr

Marius Orlandea
 National Institute of Physics and
 Nuclear Engineering - Horia
 Hulubei
 Bucharest-Magurele, POB MG-6
 Romania
 orlandea@cern.ch

Sanziana Paduroiu
 University of Bucharest
 Faculty of Physics
 Bucharest-Magurele
 Romania
 sathya_thar@yahoo.com

Horia Petrascu
 National Institute of Physics and
 Nuclear Engineering - Horia
 Hulubei
 Bucharest-Magurele, POB MG-6
 Romania
 hpetr@ifin.nipne.ro

Marius Petrascu
 National Institute of Physics and
 Nuclear Engineering - Horia
 Hulubei
 Bucharest-Magurele, POB MG-6
 Romania
 mpetr@ifin.nipne.ro

Dimitrios Petrellis
 Institute of Nuclear Physics
 NCSR "Demokritos"
 GR-15310 Aghia Paraskevi
 Athens, Greece
 petrellis@inp.demokritos.gr

Alexandrina Petrovici
National Institute of Physics and
Nuclear Engineering - Horia
Hulubei
Bucharest-Magurele, POB MG-6
Romania
spetro@ifin.nipne.ro

Gianluca Rosario Pizzone
Universita di Catania
& INFN Lab. Nazionali del Sud,
Catania, Italy
rgpizzone@lns.infn.it

Dorin Poenaru
National Institute of Physics and
Nuclear Engineering - Horia
Hulubei
Bucharest-Magurele, POB MG-6
Romania
poenaru@ifin.nipne.ro

Amalia Pop
National Institute of Physics and
Nuclear Engineering - Horia
Hulubei
Bucharest-Magurele, POB MG-6
Romania
a_pop@ifin.nipne.ro

Adrian Sabin Popescu
Faculty of Physics
University of Bucharest
Bucharest-Magurele
Romania
adrianp@astro.aira.ro

Traian Popescu
Faculty of Physics
University of Bucharest
Bucharest-Magurele
Romania
popescutraian@yahoo.com

Oana Georgeta Radu
National Institute of Physics and
Nuclear Engineering - Horia
Hulubei
Bucharest-Magurele, POB MG-6
Romania
oanaradu@ifin.nipne.ro

Adriana Rodica Raduta
National Institute of Physics and
Nuclear Engineering - Horia
Hulubei
Bucharest-Magurele, POB MG-6
Romania
araduta@ifin.nipne.ro

Heinigerd Rebel
Institut für Kernphysik
Forschungszentrum Karlsruhe
Germany
Heinrich.Rebel@ik3.fzk.de

Stefano Romano
Universita di Catania
& INFN Lab. Nazionali del Sud,
Catania, Italy
romano@lns.infn.it

Mircea Rusu
Faculty of Physics
University of Bucharest
Bucharest-Magurele
Romania
mrusu@dnt.ro

Antti Saastamoinen
Department of Physics
University of Jyväskylä, PO Box 35
FIN-40351 Jyväskylä
Finland
ajsaasta@phys.jyu.fi

Chhanda Samanta
 Saha Institute of Physics
 Kalkota, India
 & Virginia Commonwealth Univ.
 Physics Department
 Richmond, VA 23284
 USA
 csamanta@vcu.edu

Nicu Sandulescu
 National Institute of Physics and
 Nuclear Engineering - Horia
 Hulubei
 Bucharest-Magurele, POB MG-6
 Romania
 nsand@ifin.nipne.ro

Tiberiu Sava
 National Institute of Physics and
 Nuclear Engineering - Horia
 Hulubei
 Bucharest-Magurele, POB MG-6
 Romania
 tiberiu@tandem.nipne.ro

Werner Scheid
 Institut für Theoretische Physik der
 Justus-Liebig Universität Giessen
 D-35392, Giessen
 Germany
 Werner.Scheid@theo.physik.uni-
 giessen.de

Ion Silisteanu
 National Institute of Physics and
 Nuclear Engineering - Horia
 Hulubei
 Bucharest-Magurele, POB MG-6
 Romania
 silist@theory.nipne.ro

Claudio Spitaleri
 Universita di Catania
 & INFN Lab. Nazionali del Sud,
 Catania, Italy
 spitaleri@lns.infn.it

Mihai Stanoiu
 INP Orsay
 F-91406, Orsay cedex
 France
 stanoiu@ipno.in2p3.fr

Sabin Stoica
 National Institute of Physics and
 Nuclear Engineering - Horia
 Hulubei
 Bucharest-Magurele, POB MG-6
 Romania
 stoica@ifin.nipne.ro

Gheorghe Stratan
 National Institute of Physics and
 Nuclear Engineering - Horia
 Hulubei
 Bucharest-Magurele, POB MG-6
 Romania
 stratan@theory.nipne.ro

Jouni Suhonen
 Department of Physics
 University of Jyväskylä, PO Box 35
 FIN-40351 Jyväskylä
 Finland
 suhonen@phys.jyu.fi

Gabriel Suliman
 National Institute of Physics and
 Nuclear Engineering - Horia
 Hulubei
 Bucharest-Magurele, POB MG-6
 Romania
 suligab@tandem.nipne.ro

Gabriel Tabacaru
 Cyclotron Institute
 Texas A&M University
 College Station, TX 77843-3366
 USA
 tabacaru@comp.tamu.edu

Dimitar Tarpanov
 INRNE
 Bulgarian Academy of Science
 BG-1784 Sofia
 Bulgaria
 tarpanov@inrne.bas.bg

Cosmin N. Timis
 Department of Physics
 University of Surrey
 Guildford, Surrey, GU2 7XH
 United Kingdom
 C.Timis@surrey.ac.uk

Gabriel Toma
 National Institute of Physics and
 Nuclear Engineering - Horia
 Hulubei
 Bucharest-Magurele, POB MG-6
 Romania
 gtoma@mon1.nipne.ro

Livius Trache
 Cyclotron Institute
 Texas A&M University
 College Station, TX 77843-3366
 USA
 livius_trache@tamu.edu

Robert E. Tribble
 Cyclotron Institute
 Texas A&M University
 College Station, TX 77843-3366
 USA
 tribble@comp.tamu.edu

Ioan I. Ursu
 National Institute of Physics and
 Nuclear Engineering - Horia
 Hulubei
 Bucharest-Magurele, POB MG-6
 Romania
 iursu@opensys.ro

Nguyen G. Van Giai
 IPN Orsay
 F-91406, Orsay cedex
 France
 nguyen@ipno.in2p3.fr

Alexei Voinov
 Bogoliubov Laboratory of
 Theoretical Physics
 Joint Institute for Nuclear Research
 141980 Dubna, Russia
 voinov200@mail.ru

Victor Voronov
 Bogoliubov Laboratory of
 Theoretical Physics
 Joint Institute for Nuclear Research
 141980 Dubna
 Russia
 voronov@theor.jinr.ru

Volker Werner
 Yale University
 Wright Nuclear Structure
 Laboratory
 New Haven, CT 06520-8124
 USA
 vw@mirage.physics.yale.edu

Dmitry G. Yakovlev
 Ioffe Physical Technical Institute
 194021 Saint-Petersburg
 Russia
 yak@astro.ioffe.ru

Nicolae V. Zamfir
National Institute of Physics and
Nuclear Engineering - Horia
Hulubei
Bucharest-Magurele, POB MG-6
Romania
zamfir@tandem.nipne.ro

Vladimir Zelevinsky
NSCL & Dept of Physics and Astr.
Michigan State University
East Lansing, MI 48824-1321
USA
zelevinsky@nscl.msu.edu

This page is intentionally left blank



Carpathian Summer School of Physics 2005
Exotic Nuclei and Nuclear/Particle Astrophysics
 June 13-24, 2005, Mamaia-Constanta, Romania

PROGRAM

Sunday, June 12th, 20:30 - Welcome reception at hotel Savoy

Monday, June 13th, 2005	
Session: Opening session	
Chair: S. Stoica	
9:00	<i>R. Kruecken</i> : Coulomb excitation and transfer experiments with MINIBALL
9:55	<i>J. Suhonen</i> : What has nuclear structure to do with neutrino and dark-matter physics?
10:50 Coffee break	
11:15	Official opening
12:30 Lunch	
Session: Afternoon session	
Chair: J. Aysto	
15:00	<i>Zs. Fülöp</i> : Feasibility of nuclear astrophysics experiments at the LUNA underground accelerator facility
15:55 Coffee break	
16:10	<i>W. Catford</i> : Neutron transfer studied with a radioactive ^{24}Ne beam
17:10	<i>T. Nakada</i> : CP violation in B physics

Tuesday, June 14th, 2005	
Session: Exotic nuclear structure I	
Chair: R. Kruecken	
8:30	<i>V. Werner</i> : Properties of low-lying states: Shape parameters and proton-neutron symmetry
9:30	<i>N. Lölödice</i> : New methods for the exact solution of the nuclear eigenvalue problem beyond mean field approaches
10:25 Coffee break	
10:40	<i>A. Petrovici</i> : Exotic Phenomena in Medium Mass Nuclei
11:40	<i>V. Voronov</i> : Q-phonon approach for low-lying 1- two-phonon states in spherical nuclei
12:35 Lunch	
Session: Exotic nuclear structure II	
Chair: J. Jolie	
15:00	<i>D. Bonatsos</i> : Analytic Description of the Shape Phase Transition from Octupole Deformation to Octupole Vibrations
15:55 Coffee break	
16:10	<i>A. Ingemarson</i> : Reaction cross sections for protons and light ions
17:10	<i>M. Fetea</i> : Possible E(5/4) Symmetry in ^{135}Ba
17:30	<i>D. Petrellis</i> : Z(4): γ -rigid Solution of the Bohr Hamiltonian

Wednesday, June 15th, 2005	
Session: Exotic nuclei	
Chair: D. Bonatsos	
8:30	<i>J. Aysto</i> : Newest developments in nuclear mass measurements far from stability
9:30	<i>D. Frekers</i> : Facets of nuclear charge-exchange reactions. From nucleon-nucleon physics to double-beta decay
10:25 Coffee break	
10:40	<i>M. Marques</i> : Research on neutron clusters
11:40	<i>J. Jolie</i> : Rare Isotopes INvestigations at GSI (RISING) using relativistic ion beams
12:35 Lunch	
Session: Exotic decays	
Chair: D. Poenaru	
15:00	<i>D. Delion</i> : Systematics of proton emission
15:55 Coffee break	
16:10	
17:10	<i>V.E. Jacob</i> : Precise half life measurement of ^{34}Ar , a superallowed β^+ emitter
17:30	<i>Yu. Lashko</i> : Effective attraction and other peculiar manifestations of the Pauli principle in collisions between atomic nuclei
	<i>E. Dragulescu</i> : Few-valence-particle (hole) excitations around doubly magic ^{132}Sn
18:30	<i>SOC CER I: Romania - Rest of the World (on the beach)</i> .

Thursday, June 16th, 2005	
Session: SuperHeavy Elements I	
Chair: G. Muenzenberg	
8:30	<i>W. Greiner</i> : Clusters of matter and anti-matter; a mechanism for cold compression
9:30	<i>S. Hofmann</i> : Synthesis of SHE at SHIP
10:25 Coffee break	
10:40	<i>W. Scheid</i> : Dynamics of mass asymmetry in dinuclear systems
11:40	<i>D. Poenaru</i> : Fission valleys and heavy ion decay modes
12:35 Lunch	
Session: Neutron stars and other	
Chair: W. Catford	
15:00	<i>N. Van Giai</i> : Collective nuclear excitations in unstable nuclei and in the inner crust of neutron stars
15:55 Coffee break	
16:10	<i>N. Sandulescu</i> : Nuclear Superfluidity in the Crust of Neutron Stars
17:10	<i>Communications</i> <i>Ad. Raduta</i> : Isospin distillation from a microcanonical perspective <i>A. Isar</i> : Quantum deformation of open systems
20:00	Public lecture at Ovidius Univ (I): <i>G. Stratan</i> : Einstein's miraculous year <i>L. Buchmann</i> : The cosmic origin of elements

Friday, June 17th, 2005	
Session: Nuclear Astrophysics I & Large facilities I	
Chair: R. E. Tribble	
8:30	<i>J. Jose</i> : The nuclear physics of classical nova explosions
9:30	<i>T. Motobayshi</i> : Recent experimental studies of nuclear astrophysics
10:25 Coffee break	
10:40	<i>A. Braeuning-Demian</i> : GSI Facility for Antiproton and Ion Research (the FAIR Project).
11:40	<i>T. Motobayshi</i> : RIKEN new facilities
12:10	<i>M. Petrascu</i> : Experimental and theoretical status of Borromean halo nuclei structure investigation
12:35 Lunch	
Session: Large facilities II	
Chair: C. Angulo	
15:00	<i>P. Butler</i> : The ISOLDE research programme and the path to EURISOL
15:55 Coffee break	
16:10	<i>E. Farnea</i> : The AGATA project
17:10	<i>M. Itkis</i> : Facilities at FLNR Dubna
17:40	<i>L. Buchmann</i> : RNB facilities at TRIUMF
	<i>TBD</i> : Summary of first week

Saturday, June 18th, all day: boat trip in Danube's Delta, lunch on boat (please register).

Sunday, June 19th, from 17:00: tour of Black Sea resorts by coach and wine degustation at "Crama Murfatlar" in Neptun. Traditional dinner possible (please register).

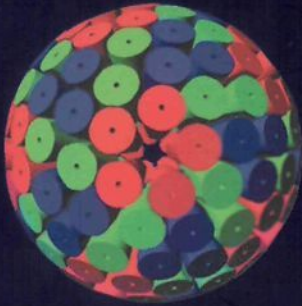
Monday, June 20th, 2005	
Session: SuperHeavy Elements II	
Chair: S. Hofmann	
8:30	<i>M. Itkis</i> : Peculiarities of the fusion-fission process of heavy and superheavy nuclei
9:30	<i>K. Morita</i> : Synthesis of heaviest elements using a gas-filled recoil separator at RIKEN
10:25 Coffee break	
10:40	<i>G. Muenzenberg</i> : NUSTAR at FAIR Nuclear Structure Research at GSI and the Future
11:40	<i>C. Samanta</i> : Mass formulae from normal to hypernuclei
12:35 Lunch	
Session: Nuclear structure	
Chair: M. Itkis	
15:00	<i>V. Zelevinski</i> : From Super-Radiance to Continuum Shell Model
15:55 Coffee break	
16:10	<i>V. Zelevinski</i> : cont'd
17:10	<i>P. Descouvemont</i> : Three-body models in nuclear physics
18:10	Public lecture (II) <i>P. Biermann</i> : Black holes, dark matter and dark energy
19:10-19:30	<i>A. Nikolaidis</i> : Cosmic Rays and new physics

Tuesday, June 21st, 2005	
Session: Nuclear astrophysics II	
Chair: H. Rebel	
8:30	<i>J. Goerres</i> : The role of alpha induced reactions in nuclear astrophysics
9:30	<i>C. Angulo</i> : Experimental methods to nuclear reactions involved in explosive stellar binaries
10:25 Coffee break	
10:40	<i>L. Buchmann</i> : The most important nuclear reactions in astrophysics
11:40	<i>R.E. Tribble</i> : Indirect techniques in measurements of stellar reaction rates
12:35 Lunch	
Session: Nuclear astrophysics III	
Chair: L. Trache	
15:00	<i>C. Spitaleri</i> : Recent applications of the Trojan Horse Method to Nuclear Astrophysics
15:55 Coffee break	
16:10	<i>W.P. Liu</i> : Indirect measurement of astrophysical (n, γ) and (p, γ) reactions
17:10	<i>S. Harissopulos</i> : Global reaction models relevant to the p-process

Wednesday, June 22nd, 2005	
Session: High Energy Cosmic Rays	
Chair: A. Bulgac	
8:30	<i>P. Biermann</i> : Comprehensive picture of cosmic ray origin, critical tests
9:30	<i>H. Rebel</i> : Features of High-Energy Interaction Processes from Extensive Air Shower Observations
10:25 Coffee break	
10:40	<i>I.M. Brancus</i> : Study of Extensive Air Showers in KASCADE-Grande experiment
11:40	<i>Ad van den Berg</i> : Prospects for the detection of high-energy cosmic rays using radio techniques
12:35 Lunch	
Session: Exotic Decays II & Communications	
Chair: Yu. Lashko	
15:00	<i>M. Horoi</i> : Shell Model nuclear level densities
15:55 Coffee break	
16:10	<i>M. Stanoiu</i> :
16:30	<i>R. Gherghescu</i> : Sub-barrier fusion reactions for SHE synthesis
17:00	<i>M. Mirea</i> : Single particle effects in the threshold fission cross section
17:20	<i>I. Silisteanu</i> : Estimates of alpha emission rates with all order coupling for cluster decay reactions
17:40	<i>A. Bercuci</i> : Various types of measurements for atmospheric muons performed with WILLI detector
18:30	<i>SOC CER II (across the street, on the artificial grass field)</i>

Thursday, June 23rd, 2005	
Session: Neutron stars and more	
Chair: G. McLaughlin	
8:30	<i>D.G. Yakovlev</i> : Neutrino Emission from Neutron Stars
9:30	<i>A. Bulgac</i> : A few reasons why the crust of a neutron star is a fun and challenging object to study
10:25 Coffee break	
10:40	<i>Z. Majka</i> : BRAHMS Experiment Quest for Early Universe Phases of Hadronic Matter
11:40	<i>J.E. Horvath</i> : Strange matter in core-collapse supernovae
12:35 Lunch	
FREE afternoon	
19:30	Banquet at restaurant "Nunta Zamferei" in Neptun –Romanian wedding Keynote speaker: <i>J.E. Horvath</i>

Friday, June 24th, 2005	
Session: Neutrino physics Chair: V. Zelevinski	
9:00	<i>G. McLaughlin</i> : Neutrinos and Nucleosynthesis
10:00	<i>S. Stoica</i> : Recent achievements in neutrino properties
11:00 Coffee break	
Closing session Chair: R.E. Tribble	
11:30	Summary experiment: <i>H. Rebel</i>
12:00	Summary theory: <i>A. Bulgac</i>
12:35 Lunch	
Departure from Mamaia to Bucharest	



Proceedings of the Carpathian Summer School of Physics 2005

Exotic Nuclei and Nuclear/Particle Astrophysics

This volume documents an important event in the World Year of Physics 2005 and a continuation of the traditional international summer schools that have taken place in Romania regularly since 1964. On one hand, the study of exotic nuclei seeks answers about the structure and interaction of unique finite quantum mechanical many-body systems. On the other, it provides data that have an impact on the understanding of the origin of the elements in the Universe.

The contributions, written by outstanding professors from prestigious research centers over the world, provide the reader with both comprehensive reviews and the most recent results in the field. Large experimental facilities are discussed together with future research projects. The book offers insights into how experiments in terrestrial nuclear physics laboratories may be combined with observations in outer space to enlarge our basic knowledge.

25 
World Scientific
YEARS OF PUBLISHING
1 9 8 1 - 2 0 0 6



6222 hc
ISBN 981-270-007-2

9 789812 700070
www.worldscientific.com